Structural Integrity 7
Series Editors: José A.F.O. Correia · Abílio M.P. De Jesus

José A.F.O. Correia
Abílio M.P. De Jesus
António Augusto Fernandes
Rui Calçada *Editors*

Mechanical Fatigue of Metals

Experimental and Simulation Perspectives

Springer

Structural Integrity

Volume 7

The *Structural Integrity* book series is a high level academic and professional series publishing research on all areas of Structural Integrity. It promotes and expedites the dissemination of new research results and tutorial views in the structural integrity field.

The Series publishes research monographs, professional books, handbooks, edited volumes and textbooks with worldwide distribution to engineers, researchers, educators, professionals and libraries.

Topics of interested include but are not limited to:

- Structural integrity
- Structural durability
- Degradation and conservation of materials and structures
- Dynamic and seismic structural analysis
- Fatigue and fracture of materials and structures
- Risk analysis and safety of materials and structural mechanics
- Fracture Mechanics
- Damage mechanics
- Analytical and numerical simulation of materials and structures
- Computational mechanics
- Structural design methodology
- Experimental methods applied to structural integrity
- Multiaxial fatigue and complex loading effects of materials and structures
- Fatigue corrosion analysis
- Scale effects in the fatigue analysis of materials and structures
- Fatigue structural integrity
- Structural integrity in railway and highway systems
- Sustainable structural design
- Structural loads characterization
- Structural health monitoring
- Adhesives connections integrity
- Rock and soil structural integrity

Springer and the Series Editors welcome book ideas from authors. Potential authors who wish to submit a book proposal should contact Dr. Mayra Castro, Senior Editor, Springer (Heidelberg), e-mail: mayra.castro@springer.com

More information about this series at http://www.springer.com/series/15775

José A.F.O. Correia · Abílio M.P. De Jesus ·
António Augusto Fernandes ·
Rui Calçada
Editors

Mechanical Fatigue of Metals

Experimental and Simulation Perspectives

Springer

Editors
José A.F.O. Correia
Faculty of Engineering
University of Porto
Porto, Portugal

Abílio M.P. De Jesus
Faculty of Engineering
University of Porto
Porto, Portugal

António Augusto Fernandes
Faculty of Engineering
University of Porto
Porto, Portugal

Rui Calçada
Faculty of Engineering
University of Porto
Porto, Portugal

ISSN 2522-560X ISSN 2522-5618 (electronic)
Structural Integrity
ISBN 978-3-030-13979-7 ISBN 978-3-030-13980-3 (eBook)
https://doi.org/10.1007/978-3-030-13980-3

Library of Congress Control Number: 2019932694

This Springer imprint is published by the registered company Springer Nature Switzerland AG
The registered company address is: Gewerbestrasse 11, 6330 Cham, Switzerland

Preface

Conference Proceedings of the ICMFM XIX. Mechanical Fatigue of Metals—Experimental and Simulation Perspectives

Fatigue represents one of the most important types of damage experienced by materials and structures during normal service, which may lead to fracture. Once today metallic alloys are still the most used materials in the majority of components and structures allowing carrying out highest service loads, the study of the different aspects of metals fatigue attracts permanent attention of scientists, engineers and designers. The International Colloquium on Mechanical Fatigue of Metals (ICMFM) has been organized as a forum for the discussion of the most recent advances in the field. This international colloquium is intended to facilitate and encourage the exchange of knowledge and experiences among the different communities involved in both basic and applied research in this field—the fatigue of metals, looking at the problem of fatigue from a multiscale perspective, and exploring analytical and numerical simulative approaches, without losing the applications perspectives.

The First International Colloquium on Mechanical Fatigue of Metals (ICMFM) was organized in Brno, Czech Republic in 1968. Afterwards, regular Colloquia on Mechanical Fatigue of Metals started in 1972 also in Brno and were originally limited to participants from the countries of the former "Eastern Block". They continued until the 12th Colloquium in 1994 (Miskolc, Hungary) every 2 years. After a break 12 years long, the Colloquia restarted in 2006 (Ternopil, Ukraine), followed by the ones in 2008 (Varna, Bulgaria), 2010 (Opole, Poland), 2012 (Brno, Czech Republic), 2014 (Verbania, Italy), 2016 (Gijón, Spain) and the last one, the 19th colloquium, organized in 5–7 September 2018 at the Faculty of Engineering of the University of Porto, Portugal. The colloquium has reached the status of a truly international science forum with more than 20 nationalities and more than 120 presentations involved in the 19th ICMFM.

This volume of the Springer Structural Integrity book series gathers 52 works presented in the 19th ICMFM which were distributed along 10 parts covering the

following topics: (i) Microstructural Aspects of Fatigue and Thermal and Environmental Fatigue; (ii) Fatigue of Additive Manufacturing Metals; (iii) Fatigue Crack Propagation; (iv) Probabilistic Methods; (v) Fatigue Modelling; (vi) Multiaxial Fatigue; (vii) Very High Cycle Fatigue; (viii) Applications/Case Studies; (ix) Risk Analysis and Safety of Large Structures and Structural Details and (x) Numerical Methods.

The chairmen of the 19th ICMFM want to acknowledge all authors who have contributed to the success of the event and particularly submitted their works to this book series, as well as the symposia organizers, sponsors and members of the organizing, advisory and scientific committees are also fully acknowledged for their support. Also the Springer is fully acknowledged for their support to the Structural Integrity Book Series.

Porto, Portugal
September 2018

Abílio M.P. De Jesus
José A.F.O. Correia
Rui Calçada
António Augusto Fernandes

Contents

Part I Microstructural Aspects of Fatigue and Thermal and Environmental Fatigue

1 Microscopic Strain Localization of Ti-6Al-4V Alloy Under Uniaxial Tensile Loading 3
Guang-Jian Yuan, Peng-Cheng Zhao, Xian-Cheng Zhang, Shan-Tung Tu, Xiao-Gang Wang and Cheng-Cheng Zhang

2 Characterization of the Fatigue and Damage Behavior of Extruded AW6060 Aluminum Chip Profiles 11
Alexander Koch, Philipp Wittke and Frank Walther

3 Micromagnetic-Based Fatigue Life Prediction of Single-Lip Deep Drilled AISI 4140 19
N. Baak, J. Nickel, D. Biermann and F. Walther

4 Relationship Between Microstructural Features and Fatigue Behavior of Al-Based Alloy in Green Chemical Processing 27
Ildiko Peter, Raffaella Sesana and Roberto Maiorano

5 Influence of Heat Treatment Process to the Fatigue Properties of High Strength Steel 35
V. Chmelko, I. Berta and M. Margetin

6 Effect of Heat Treatment on High-Temperature Low-Cycle Fatigue Behavior of Nickel-Based GH4169 Alloy 41
Xu-Min Zhu, Xian-Cheng Zhang, Shan-Tung Tu, Run-Zi Wang and Xu Zeng

7 High Temperature Fatigue Behaviour of Secondary AlSi7Cu3Mg Alloys 49
Alessandro De Mori, Giulio Timelli and Filippo Berto

8 Mean Stress Effect on Fatigue Behavior of Austenitic Stainless Steel in Air and LWR Conditions 57
W. Chen, P. Spätig and H. P. Seifert

9 Characterization of the Fatigue Behavior of Mechanical and Thermal Aged Austenitic Power Plant Steel AISI 347 65
F. Maci, M. Jamrozy, R. Acosta, P. Starke, C. Boller, K. Heckmann, J. Sievers, T. Schopf and F. Walther

Part II Fatigue of Additive Manufacturing Metals

10 As-Built Sharp Notch Geometry and Fatigue Performance of DMLS Ti6Al4V 75
Martin Frkáň, Gianni Nicoletto and Radomila Konečná

11 Impact of Various Surface Treatments on the S-N Curve of Additive Manufactured AlSi12 83
Steffen Greuling, Wolfgang Weise, Dieter Fetzer, Klaus Müller-Lohmeier and Mattias-Manuel Speckle

12 Fatigue Properties of Powder Bed Fused Inconel 718 in As-Built Surface Condition 91
M. Sprengel, A. Baca, J. Gumpinger, T. Connolley, A. Brandao, T. Rohr and T. Ghidini

13 Application of Data Science Approach to Fatigue Property Assessment of Laser Powder Bed Fusion Stainless Steel 316L 99
M. Zhang, C. N. Sun, X. Zhang, P. C. Goh, J. Wei, D. Hardacre and H. Li

14 Influence of Surface Orientation and Segmentation on the Notch Fatigue Behavior of as-Built DMLS Ti6Al4V 107
Gianni Nicoletto and Radomila Konečná

15 Characterization of the Cyclic Material Behavior of AlSi10Mg and Inconel® 718 Produced by SLM 115
M. Scurria, B. Möller, R. Wagener and T. Bein

Part III Fatigue Crack Propagation

16 Review of Current Progress in 3D Linear Elastic Fracture Mechanics 125
Andrei Kotousov, Aditya Khanna, Ricardo Branco, Abílio M.P. De Jesus and José A.F.O. Correia

17 An Improved Prediction of the Effective Range of Stress Intensity Factor in Fatigue Crack Growth 133
Bing Yang, M. N. James, Yongfang Huang, J. M. Vasco-Olmo and F. A. Díaz

18 Short and Long Crack Growth of Aluminium Cast Alloys 139
Martin Leitner, Roman Aigner, Sebastian Pomberger, Michael Stoschka, Christian Garb and Stefan Pusterhofer

19 Evaluation of Strain Controlled Fatigue and Crack Growth Behaviour of Al–3.4Mg Alloy 147
Pankaj Kumar and Akhilendra Singh

20 Numerical Analysis of the Influence of Crack Growth Scheme on Plasticity Induced Crack Closure Results 155
D. Camas, J. Garcia-Manrique, F. V. Antunes and A. Gonzalez-Herrera

21 Towards Quantitative Explanation of Effective Thresholds of Mode III Fatigue Crack Propagation in Metals 161
Tomáš Vojtek, Stanislav Žák and Jaroslav Pokluda

22 Crack Propagation Under Cyclic Bending in Welded Specimens After Heat Treatment 169
Dariusz Rozumek, Janusz Lewandowski, Grzegorz Lesiuk and José A.F.O. Correia

23 Crack Propagation in the Threshold Stress Intensity Region a Short Review 175
Luiz Felipe F. Ricardo, Timothy H. Topper, Luiz Carlos H. Ricardo and Carlos Alexandre J. Miranda

24 A Stress Intensity Factor Study for a Pressure Vessel CT Specimen Using Finite Element Method 181
Patrícia Raposo, Behzad V. Farahani, José A.F.O. Correia, Jorge Belinha, Abílio M.P. De Jesus, Renato N. Jorge and Rui Calçada

25 Micro-notch Size Effect on Small Fatigue Crack Propagation of Nickel-Based Superalloy GH4169 187
J. Wang, R. Wang, Y. Wang, Y. Ye, X. Zhang and S. Tu

Part IV Probabilistic Methods

26 The Interactive Method—Reliable and Reproducible S-N-Curves for Materials 197
Klaus Block

27 Probability Distribution Type for the Accumulated Damage from Miner's Rule in Fatigue Design 205
J. Hoole, P. Sartor, J. D. Booker, J. E. Cooper, X. V. Gogouvitis and R. K. Schmidt

28 Evaluation of Fatigue Properties of S355 J2 and S355 J0 by Using ProFatigue Software 213
Stanislav Seitl, Petr Miarka, Sergio Blasón and Alfonso F. Canteli

29 Updating the Failure Probability of Miter Gates Based on Observation of Water Levels 221
Thuong Van Dang, Quang Anh Mai, Pablo G. Morato and Philippe Rigo

Part V Fatigue Modelling

30 Comparison of Several Optimized Methods for Mean Stress Effect Evaluating the Stress-Life Prediction 231
Jan Papuga, Ivona Vízková, Maxim Lutovinov and Martin Nesládek

31 Application of the Nonlinear Fatigue Damage Cumulative on the Prediction for Rail Head Checks Initiation and Wear Growth 239
Y. Zhou, D. S. Mu, Y. B. Han, X. W. Huang and C. C. Zhang

32 Fatigue Life Prediction for Component with Local Structural Discontinuity Based on Stress Field Intensity 245
Tianyang Lu, Peng Zhao and Fu-Zhen Xuan

33 Low Cycle Fatigue Life Estimation of P91 Steel by Strain Energy Based Approach 253
Bimal Das and Akhilendra Singh

34 Evaluation of Regression Tree-Based Durability Models for Spring Fatigue Life Assessment 261
Y. S. Kong, S. Abdullah, D. Schramm, M. Z. Omar and S. M. Haris

Part VI Multiaxial Fatigue

35 Prediction of Fatigue Crack Initiation Life in Notched Cylindrical Bars Under Multiaxial Cycling Loading 271
R. Branco, J. D. Costa, F. Berto, A. Kotousov and F. V. Antunes

36 Multiaxial Fatigue Analysis of Stainless Steel Used in Marine Structures 279
A. S. Cruces, P. Lopez-Crespo, B. Moreno, S. Bressan and T. Itoh

37 On the Application of SK Critical Plane Method for Multiaxial Fatigue Analysis of Low Carbon Steel 287
A. S. Cruces, P. Lopez-Crespo, S. Sandip and B. Moreno

Part VII Very High Cycle Fatigue

38 Fatigue Testing at 1000 Hz Testing Frequency 297
Markus Berchtold

39 Influence of Microstructural Inhomogeneities on the Fatigue Crack Growth Behavior Under Very Low Amplitudes for Two Different Aluminum Alloys 303
T. Kirsten, M. Kuczyk, M. Wicke, A. Brückner-Foit, F. Bülbül, H.-J. Christ and M. Zimmermann

40 Effect of Ultrasonic Deep Rolling on High-Frequency and Ultrasonic Fatigue Behavior of TC4 311
Yi-Xin Liu, Yun-Fei Jia, Xian-Cheng Zhang, H. Li, Run-Zi Wang and Shan-Tung Tu

Part VIII Applications/Case Studies

41 Microinclusion and Fatigue Performance of Bearing Rolling Elements 321
E. Ossola, S. Pagliassotto, S. Rizzo and R. Sesana

42 Strength Analysis of Tramway Bogie Frame 327
Vaclav Kraus, Miloslav Kepka, Jr., Daniel Doubrava and Jan Chvojan

43 A Study of the Shot Peening Effect on the Fatigue Life Improvement of Al 7475-T7351 3PB Specimens 335
N. Ferreira, J. A. M. Ferreira, J. Jesus, C. Capela and J. D. Costa

44 Investigation of Mechanical Properties and Fatigue of Friction Stir Spot Welded Light Metals 343
Ahmet Atak and Aydin Şik

45 Advanced Development of Hysteresis Measurement Characteristics for Early Detection of Fatigue Damages on Fasting Systems in Concrete 351
Marvin Hoepfner

46 Mechanics and Evaluation of Early Damage 359
Andrei Kotousov, James Vidler, James Hughes, Aditya Khanna, Ching-Tai Ng and Munawwar Mohabuth

Part IX Risk Analysis and Safety of Large Structures and Structural Details

47 Fatigue Damage Factor Calibration for Long-Span Cable-Stayed Bridge Decks 369
A. Nussbaumer, J. Oliveira Pedro, C. A. Pereira Baptista and M. Duval

48 Fatigue Analysis of a Concrete Chimney Under Wind Loads 377
Hermes Carvalho, Victor Roberto Verga Mendes, Sebastião Salvador Real Pereira and José A.F.O. Correia

49 On the Calculation of Offshore Wind Turbine Load Spectra for Fatigue Design 383
Rui Teixeira, Maria Nogal and Alan O'Connor

Part X Numerical Methods

50 The Natural Neighbour Radial Point Interpolation Method to Predict the Compression and Traction Behavior of Thermoplastics 393
D. E. S. Rodrigues, J. Belinha, R. M. Natal Jorge and L. M. J. S. Dinis

51 The Elasto-plastic Analysis of Polymers Subject to Traction and Compression Using Advanced Discretization Techniques 401
D. E. S. Rodrigues, J. Belinha, R. M. Natal Jorge and L. M. J. S. Dinis

52 Fracture Analysis of Semi-circular Bend (SCB) Specimen: A Numerical Study 407
Farid Mehri Sofiani, Behzad V. Farahani and J. Belinha

Part I
Microstructural Aspects of Fatigue and Thermal and Environmental Fatigue

Chapter 1
Microscopic Strain Localization of Ti-6Al-4V Alloy Under Uniaxial Tensile Loading

Guang-Jian Yuan, Peng-Cheng Zhao, Xian-Cheng Zhang, Shan-Tung Tu, Xiao-Gang Wang and Cheng-Cheng Zhang

Abstract In this paper, Plate specimens for tensile tests with two different microstructures (as-received and heat treated) were studied. Micromechanical modelling by using a representative volume element has been adopted to investigate the tensile flow behavior of Ti-6Al-4V alloy. Voronoi tessellation model and actual microstructure model were developed to predict the macroscopic stress versus strain behavior. Kinematic hardening rule was used to simulate the nonlinear hardening. Results showed that Both VT model and actual microstructure model had good ability to predict the stress-strain response. The stress and strain distribution showed that VT model agreed with the microstructure-based model well. Simulation result was consistent with experimental result that measured by digital image correlation test. In addition, the microstructure-level inhomogeneity and incompatible deformation between the hard and soft phases were the main reason for damage.

Keywords Ti-6Al-4V alloy · Micromechanical modeling · Inhomogeneity · DIC

1.1 Introduction

Ti-6Al-4V (TC4) is an $\alpha+\beta$ alloy which exhibits a higher strength compared with α alloys, and a wider processing window as compared to both α and β alloys. It has been widely used in aerospace, automotive and medical sectors due to the low density

G.-J. Yuan · P.-C. Zhao · X.-C. Zhang (✉) · S.-T. Tu
Key Laboratory of Pressure Systems and Safety, Ministry of Education, School of Mechanical and Power Engineering, East China University of Science and Technology, Shanghai 200237, People's Republic of China
e-mail: xczhang@ecust.edu.cn

X.-G. Wang
State Key Laboratory of Advanced Design and Manufacturing for Vehicle Body, Hunan University, Changsha 410082, People's Republic of China

C.-C. Zhang
AECC Commercial Aircraft Engine Co. LTD, Shanghai Engineering Research Center for Commercial Aircraft Engine, Shanghai 201108, People's Republic of China

J.A.F.O. Correia et al. (eds.), *Mechanical Fatigue of Metals*, Structural Integrity 7,
https://doi.org/10.1007/978-3-030-13980-3_1

and high strength at low to moderate temperatures. However, the microstructure and mechanical property of Ti-6Al-4V alloys can vary in a wide range, which are influenced by different heat treatments [1]. Therefore, it is difficult to record the distribution of stress and strain in Ti-6Al-4V alloys quantitatively. Any investigation on the microstructure and material property of Ti-6Al-4V alloys is necessary to predict the mechanical behavior well and hence reduce the experiment costs largely.

Finite-element (FE) models have been widely used to investigate the deformation of materials at the microscale, with the microstructure modelled by using a representative volume element (RVE). To simulate the deformation of the material, the microstructural morphoplogy can be determined by experimental measurement (scanning electron microscope (SEM) or electron backscatter diffraction (EBSD) method) or may be generated artificially (Voronoi tessellation (VT) approach) [2]. Based on our previous work [3], the aim of present work is to investigate the stress and strain distribution of Ti-6Al-4V alloys at the microscale by using VT model and actual microstructure model. The influence of phase induced plasticity and comparison between simulation results and experimental results has been discussed.

1.2 Experimental Procedures

1.2.1 Material

Ti-6Al-4V alloys with two different microstructures were used for tensile tests. The microstructure of as-received alloys, consisted of α and β phases, as shown in Fig. 1.1a. The microstructure of as-received alloy was changed through heat treated (HT) method by two steps: solution annealing and aging treatment. Solution annealing was performed at 955 °C for 1 h, followed by cooling down to room temperature a rate of 50 °C per hour. The second step aging was performed at 700 °C for 2 h to relieve the internal stress and then air cooling. The resulting microstructure consisted of α and β phases with different volume fraction, as shown in Fig. 1.1b.

1.2.2 In-situ Tensile Testing with DIC Method

Plate specimens with gauge length of 8 mm, width of 2.5 mm and thickness of 0.5 mm were used, as shown in Fig. 1.2. Specimens were hand polished on an OPS cloth with colloidal silica for 3 h after initial polishing to #2000 Sic paper. The etching pattern was applied to the surface of the specimen by using Kroll's reagent for approximately 10 s at room temperature. The Kroll's reagent was in a solution of HF, HNO_3 and H_2O with a volume ratio of 5:10:85. In such a case, necessary features of the microstructure can be obtained for successful DIC. In-situ tensile tests were conducted using a SHIMADZU pulser system under scanning electron microscope with a fixed stage. The

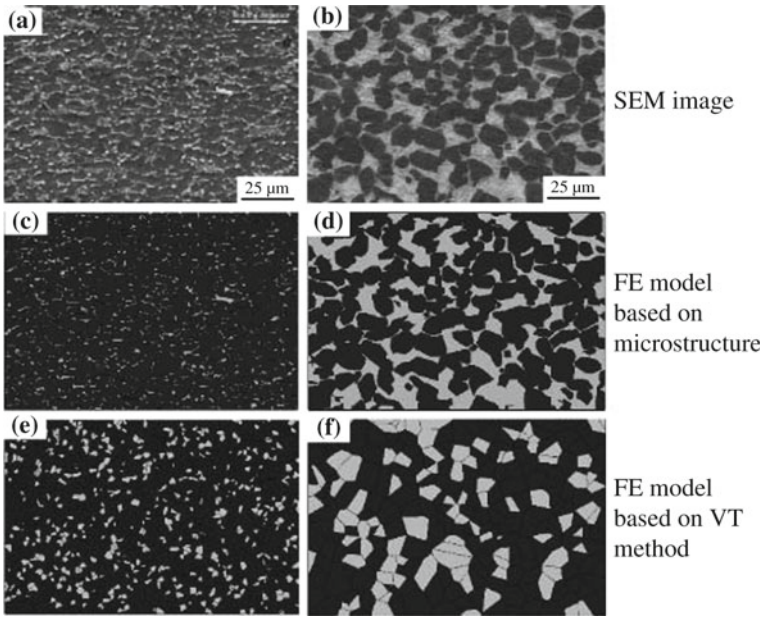

Fig. 1.1 **a** As-received TC4 SEM image, **b** heat treated TC4 SEM image, **c** as-received TC4 FE model based on microstructure, **d** heat treated TC4 FE model based on microstructure, **e** as-received TC4 FE model based on VT method, **f** heat treated TC4 FE model based on VT method

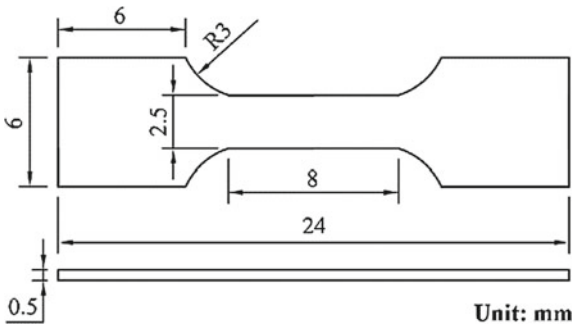

Fig. 1.2 A schematic of the specimen used in the experiment, with gauge length of 8 mm, width of 2.5 mm and thickness of 0.5 mm

force-displacement data were collected and recorded automatically by the computer-based control and data acquisition system during the tensile process. The specimens were loaded in displacement control with a low strain rate of 0.01/min so that the load applied to the specimens could be considered as quasi-static. In addition, the specimens held at each displacement increment for 30 s then images were captured for DIC.

1.3 Micromechanical Modelling of Ti-6Al-4V Alloy

1.3.1 Microstructure-Based RVE Generation

2D representative volume elements were established for the microstructure of both As-received and HT Ti-6Al-4V alloys. Actual microstructure model and VT model were used to generate the polycrystalline aggregate RVEs according to the volume fraction of microstructure, as shown in Fig. 1.1c–f. Plane stress elements (CPS3) were employed for numerical tensile modelling. In order to realize the uniaxial tensile loading of the RVE for actual microstructure model and VT model, boundary constraints are referred to the previous work [4].

1.3.2 Kinematic Hardening Parameters Identification

In the current study, the kinematic hardening model developed by Chaboche [5] is used for Ti-6Al-4V alloy, which can be expressed as:

$$\dot{X} = \sum_{i=1}^{3} \dot{X}_i \tag{1.1}$$

$$\dot{X} = \frac{2}{3} C_i \dot{\varepsilon}_P - \gamma_i X_i \dot{p} \tag{1.2}$$

where the first term in Eq. (1.2) is the hardening moduli and the second term denotes the recall term that represents nonlinear deformation effect. Parameters C_i and γ_i are material parameters that influences the hardening rate during plastic deformation. Here, $\dot{\varepsilon}_p$ denotes the plastic strain rate and $\dot{p}$ is the equivalent plastic strain rate. The index i denotes the individual back stress tensor, which is ranging from 1 to 3. Therefore, the back stress is a summation of three back stress components as:

$$X = X_1 + X_2 + X_3 \tag{1.3}$$

where the first back stress X_1 denotes that the high modulus saturates rapidly at the yielding point. The second back stress X_2 presents the nonlinear deformation of the hysteresis curve. The last back stress X_3 denotes the linear hardening at higher strain range. Therefore, the total flow curve can be described as:

$$X = \sigma_0 + X_1 + X_2 + X_3 \tag{1.4}$$

where σ_0 is the yield stress according to tensile tests. Chaboche determined the material parameters according to the hysteresis loop. However, some researchers [5, 6] estimated the material parameters from monotonic stress-strain curve. The final material parameters has been calibrated as shown in Table 1.1.

Table 1.1 Material parameters for Ti-6Al-4V alloy

Material	C_1 (MPa)	C_2 (MPa)	C_3 (MPa)	γ_1	γ_2	γ_3
As-recieved	10,000	8000	8000	1500	100	1.3
Heat-treated	14,000	1000	2400	2100	300	2.6

1.4 Results and Discussion

The stress-strain curves predicted by using Voronoi tessellation model and actual microstructure model are compared with experimental results, as shown in Fig. 1.3. It can be seen that the predicted results agree well with the experimental data. However, the simulation curve predicted by VT model in HT material exists small discrepancy compared with experimental data, which may be due to the Inhomogeneity of microstructure generated by VT method, as shown in Fig. 1.1f. In addition, the effect of grain size and grain morphology has not been considered.

At the microcale, the stress and plastic strain distribution have been captured for both actual microstructure model and VT model at 8% macro-strain, as shown in Figs. 1.4 and 1.5. Due to the relatively lower mechanical strength, α phase will produce larger plastic strain compared with β phase. Hence, the inhomogeneity of plastic strain will be formed at the boundaries between α and β phases. The existence of intense plastic strain (shear bands) can be clearly seen in Fig. 1.5. Strain localization in these shear bands will promote failure likelihood at the microscale. Hence, the intense plastic strain at the α and β interface will finally lead to the formation of crack, which is similar to the experimental results in previous work [7].

In addition, the shear bands are inclined at angles of 45° to the loading direction, which may finally lead to the ductile fracture. Similar results have been found during

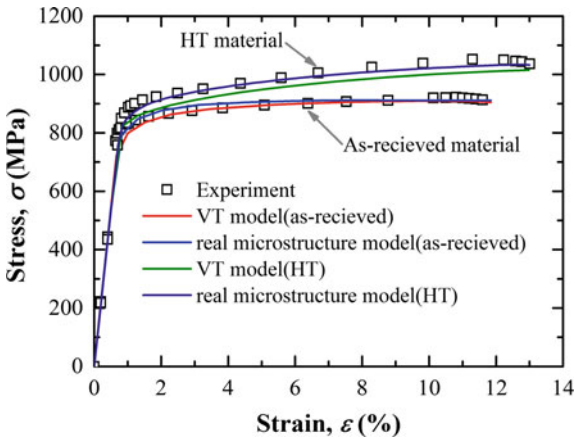

Fig. 1.3 Comparison of stress-strain curve between experiment and simulation results

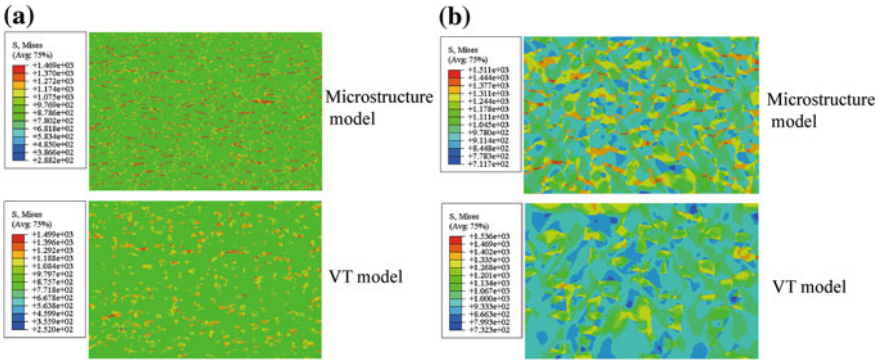

Fig. 1.4 Stress distribution of microstructure model and VT model for (**a**) As-received material and (**b**) HT material at 8% macro-strain

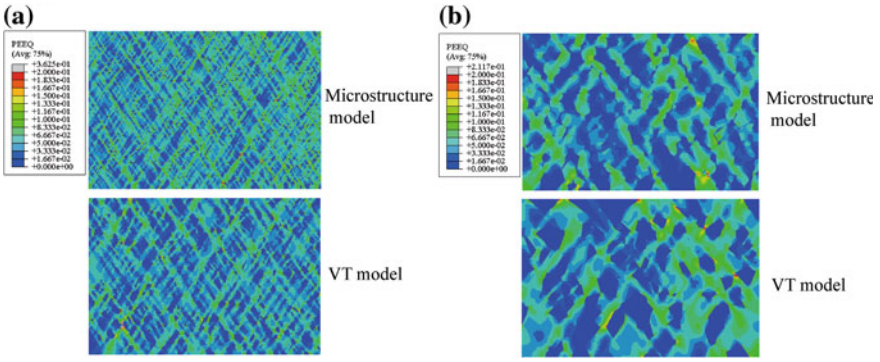

Fig. 1.5 Plastic strain distribution of microstructure model and VT model for (**a**) as-received material and (**b**) HT material at 8% macro-strain

the in-situ DIC test. Figure 1.6 shows the total strain in the whole DIC measurement field at the middle of sample. It can be clearly seen that the total strain measured by DIC method also exhibits shear bands at angles about 45°, which shows that the predicted results agree well with the experimental observation.

1.5 Conclusions

In-situ tensile tests were used to determine the microscopic strain localization of Ti-6Al-4V. FE models generated by actual microstructure and VT method are analyzed to verify the accuracy of these two models. The following results can be obtained:

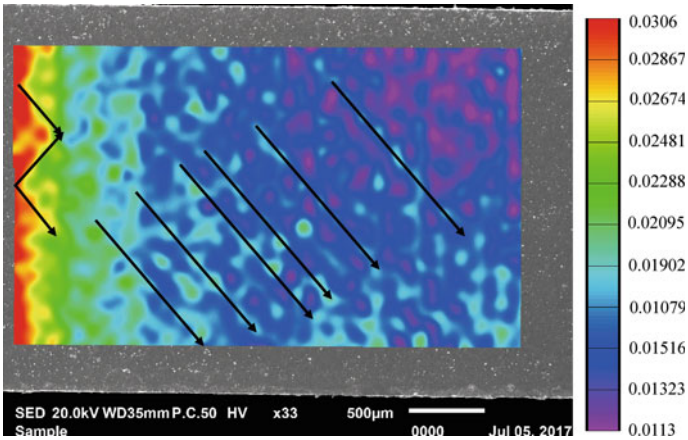

Fig. 1.6 The von Mises strain field at the middle of Ti-6Al-4V HT sample

(1) Both actual microstructure model and VT model can predict the stress-strain curves with sound accuracy. The VT model of HT material has small discrepancy due to the Inhomogeneity of microstructure.
(2) At the microscale, Inhomogeneity of plastic strain can be found in all models, which will leads to the final failure at the α and β interface.
(3) Shear bands exist at the angle of 45° to the loading direction, which is similar to the experimental DIC observation. It will finally cause ductile fracture at the macroscale.

Acknowledgements The authors would like to acknowledge gratefully for the financial support through NSFC of China (51725503,51575183) and 111 Project. Zhang XC is also grateful for the support by Shanghai Pujiang Program, Young Scholar of the Yangtze River Scholars Program, and Shanghai Technology Innovation Program of SHEITC (CXY-2015-001).

References

1. Wu GQ, Shi CL, Sha W, Sha AX, Jiang HR (2013) Effect of microstructure on the fatigue properties of Ti–6Al–4 V titanium alloys. Mater Des 46(2):668–674
2. Barbe F, Decker L, Jeulin D, Cailletaud G (2001) Intergranular and intragranular behavior of polycrystalline aggregates. Part 1: F.E. model. Int J Plast 17(4):513–536
3. Zhang XC et al (2016) Failure mechanism and mode of Ti-6Al-4V alloy under uniaxial tensile loading: experiments and micromechanical modeling. Mater Sci Eng A 676:536–545
4. Sun X, Choi KS, Liu WN, Khaleel MA (2009) Predicting failure modes and ductility of dual phase steels using plastic strain localization. Int J Plast 25(10):1888–1909
5. Chaboche JL (1991) On some modifications of kinematic hardening to improve the description of ratchetting effects. Int J Plast 7(7):661–678
6. Zhang J, Jiang Y (2008) Constitutive modeling of cyclic plasticity deformation of a pure polycrystalline copper. Int J Plast 24(10):1890–1915
7. Mahajan Y, Margolin H (1978) Surface cracking in α-β titanium alloys under unidirectional loading. Metall Trans A 9(3):427–431

Chapter 2
Characterization of the Fatigue and Damage Behavior of Extruded AW6060 Aluminum Chip Profiles

Alexander Koch, Philipp Wittke and Frank Walther

Abstract Due to a great potential for conserving resources, the direct recycling of aluminum chips by hot extrusion is a promising alternative to energy-intensive remelting process. The mechanical properties of cast-based and chip-based specimens of AW6060 aluminum alloy were characterized by means of mechanical quasi-static and cyclic experiments. The response of the material was followed by means of hysteresis, thermometric and resistometric measurements, whereby the fatigue strength could be estimated by alternating current potential drop-technique. The effects deriving from defects in the microstructure, in the form of cavities and seam welds between the chips, could be correlated with the fatigue properties by means of optical and scanning electron micrographs.

Keywords Hot extrusion · Fatigue development · Aluminum chips · Computed tomography · Alternating current potential drop

2.1 Introduction

Due to the increasing scarcity of resources, demands with regard to lightweight construction have significantly increased in recent years [1]. In this context, aluminum is particularly suitable for lightweight-relevant industries because of the excellent strength-to-weight ratio [2]. A disadvantage is the energy-intensive production of primary aluminum as well as recycling by remelting compared to other construction metals [3, 4]. A promising alternative with significantly lower energy consumption is recycling by hot extrusion, in which aluminum scrap produced in machining can be pressed into profiles [5]. The use of such scrap like chips has the distinct advantages of a reduced price compared to raw aluminum and a less material loss due to the high demand of oxides on the surfaces of the chips. The mechanical properties of chip-based specimens depend on the quality of the seam welds occurring between

A. Koch (✉) · P. Wittke · F. Walther
Department of Materials Test Engineering (WPT), TU Dortmund University, 44227 Dortmund, Germany
e-mail: alexander3.koch@tu-dortmund.de

J.A.F.O. Correia et al. (eds.), *Mechanical Fatigue of Metals*, Structural Integrity 7,
https://doi.org/10.1007/978-3-030-13980-3_2

the chips during the extrusion process. Parameters such as shear stress, pressure and local strain in the chips during the extrusion are critical for a satisfactory welding process [6, 7].

Therefore, the aim of this study is to examine to what extent the mechanical properties of chip-based extruded profiles are comparable to conventional cast-based extruded profiles. In this context, quasi-static and cyclic investigations are used to identify possible factors influencing the mechanical properties of chip-based extruded profiles.

Supportive measurands such as the plastic strain amplitude, the change in temperature and the change in alternating current (AC) potential are used in order to draw conclusions about the material behavior during fatigue tests as well as estimate the fatigue strength based on material responses.

2.2 Material and Experimental Methodology

2.2.1 Material and Characterization of Microstructure

To characterize the effect of chips and weld seems on the quasi-static and cyclic deformation and damage behavior, flat-face die profiles with an extrusion ratio of 30.25 were investigated, see [6], using cast-based and chip-based material as the basis for the extrusion process. Cast-based profiles were first homogenized for 6 h at 550 °C following by an extrusion at a temperature of 450 °C using AW6060 aluminum alloy. The chemical composition was analyzed by means of optical emission spectroscopy and is shown in Table 2.1.

To produce the chip-based profiles, the geometrically determined chips with a length of 11 ± 1.7 mm, a width of 7.6 ± 1.2 mm and a thickness of 1.1 ± 0.4 mm, were machined from AW6060 bulk material. Afterwards the chips were cold-compacted to billets with a relative density of 0.78 and a diameter of d_b = 66 mm in order to improve the mechanical properties of the resulting profile. To homogenize the material, the billets were heated up to a temperature of 550 °C for 6 h. Finally, the chip-based billets were extruded to profiles with a diameter of d_p = 12 mm at 450 °C by a hydraulic extrusion press, using a ram speed of 1 mm/s.

The samples for metallographic characterization were taken directly from the profiles as well as from broken specimens and were cold-embedded, ground and polished up to 0.05 μm grit size using colloidal SiO_2 polishing suspension. The grain and chip structures were characterized in micrographs by means of Barker

Table 2.1 Chemical composition of AW6060 in wt%

Si	Fe	Mn	Mg	Zn	Ti	Al
0.4	0.21	0.04	0.42	0.01	0.01	Balance

etching technique under polarized light using a stereoscopic light microscope (Zeiss Axio Imager M1m).

2.2.2 Quasi-static Deformation Testing

In order to analyze the quasi-static deformation behavior and the differences between cast-based and chip-based specimens, tensile tests were carried out according to standard DIN EN ISO 6892-1 using a universal testing machine (Instron 3369) with a maximum load of 50 kN. All tests were performed strain-controlled at a strain rate of $\dot{\varepsilon} = 0.00025\ s^{-1}$ in the elastic region. Above a stress level of 50 MPa (elasto-plastic region) the strain rate was increased to $\dot{\varepsilon} = 0.0067\ s^{-1}$. The strain was measured using a tactile Instron extensometer with a gage length of 25 mm. Figure 2.1b shows the specimen geometry used for the tensile tests, according to standard DIN 50125.

2.2.3 Cyclic Deformation Testing

To characterize the fatigue behavior of the cast-based and chip-based specimens, fatigue tests were conducted on a servohydraulic fatigue testing system (Instron 8872) with a maximum load of 10 kN. All tests were carried out stress-controlled at a stress ratio of $R = -1$ and a frequency of $f = 10$ Hz.

In order to determine the load-dependent deformation and damage behavior incl. cyclic hardening, continuous load increase tests (LIT) and constant amplitude tests (CAT), which are explained in [8], were carried out. The experimental setup (a) as

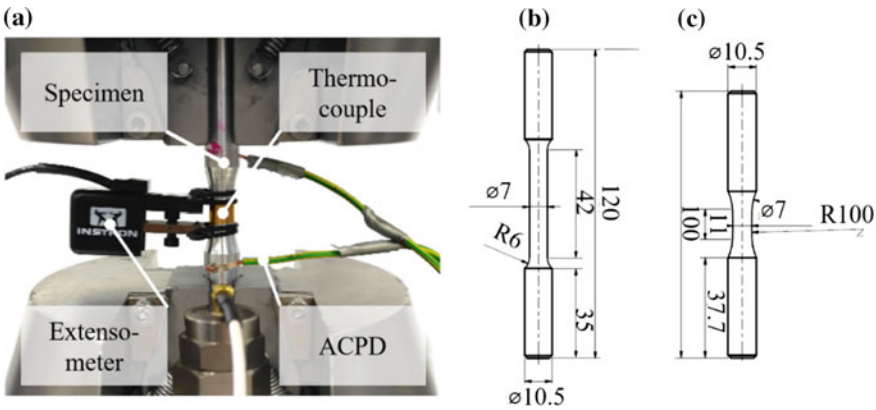

Fig. 2.1 **a** Experimental setup for fatigue tests and specimen geometry for **b** tensile tests and **c** fatigue tests

well as the specimen geometry (c) for the fatigue tests are shown in Fig. 2.1. In order to follow the material response, different measurement techniques were used. The stress-strain hysteresis loops were determined by means of a tactile Instron extensometer, gage length 10 mm. The change in alternating current potential (ACPD) was measured using a Matelect CGM-5 system. Therefore, the contacts were spot-welded to the specimen (see Fig. 2.1a). The current was kept constant at a value of $I = 1.7$ A, with a signal gain of 90 dB and a frequency of $f_{AC} = 0.3$ kHz. For the measurement of the temperature of the specimens, thermocouples were applied at specimen's surface.

2.3 Results and Discussion

The differences in the microstructure between cast-based and chip-based material are illustrated in Fig. 2.2 by representative micrographs. In the cast-based specimen (Fig. 2.2a), the grains have a round shape and there is a gradient of grain size. For the chip-based specimen (Fig. 2.2b) different grain orientations can only be seen in the outer areas. The chips are elongated during the extrusion process. The crack propagates through the grains in case of the cast-based specimens, whereas for the chip-based ones the crack propagates between the chip boundaries. At a specific diameter of the profile, a delamination phenomenon can be detected between the chips, so that a tubular cavity is visible in the cross-section of the chip-based profile (Fig. 2.2c). The pressure during the extrusion process is assumed to be insufficient to secure a proper welding of the chips.

The results of the tensile tests, summarized in Table 2.2, show a higher tensile strength as well as a higher elongation at break for the cast-based specimens, whereas the yield strength is higher for the chip-based specimens. While the seam welds reduce the ultimate tensile strength as well as the elongation at break, the yield strength is increased due to the smaller grains of the chip-based profile.

Figure 2.3 shows the results of the LIT for the cast-based specimen as well as the chip-based specimen. Plastic deformation can be detected above a stress amplitude

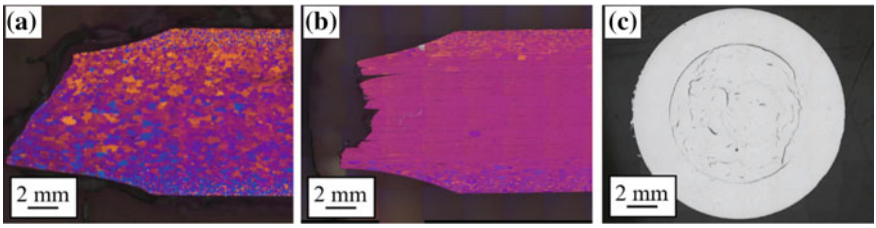

Fig. 2.2 **a** Grain structure of broken cast-based fatigue specimen (longitudinal section, Barker etched), **b** grain and chip structure of broken chip-based fatigue specimen (longitudinal section, Barker etched), **c** defect structure of chip-based profile (cross-section)

Table 2.2 Results of tensile tests

Material	Yield strength (MPa)	Ultimate tensile strength (MPa)	Elongation at break (10^{-2})
Cast-based	45.9 ± 0.5	140.5 ± 1.7	26.6 ± 2.9
Chip-based	54.1 ± 5.4	133.3 ± 5.8	18.2 ± 0.6

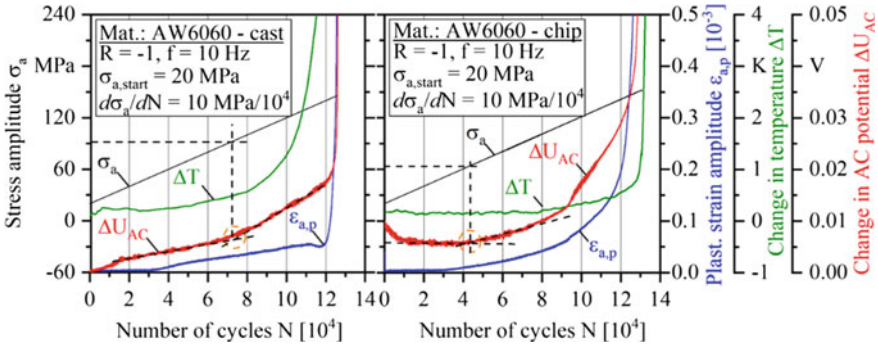

Fig. 2.3 Load increase tests of cast-based and chip-based specimens

of $\sigma_a = 49$ MPa for the cast-based specimen and $\sigma_a = 50$ MPa for the chip-based specimen, which is in good agreement with the results of tensile tests. For the chip-based specimen the plastic strain amplitude increases exponentially with a change in the slope at a stress amplitude of $\sigma_a = 115$ MPa, whereas the increase is linear for the cast-based specimen until it changes into a drastic increase above a stress amplitude of $\sigma_a = 135$ MPa.

The main differences can be seen in the change in AC potential (ΔU_{AC}). For the cast-based specimen, after a short phase of initial rise of AC potential, two regions of linear increase can be distinguished, with a change in the slope at a stress amplitude of $\sigma_a = 93$ MPa. Based on the material response, the fatigue strength can be estimated at about $\sigma_{a,e} = 93$ MPa. It can be assumed that, above this stress amplitude, damage-relevant processes occur in the material, which are responsible for the changes in the measured quantities. The results fit well to the S-N curve (Fig. 2.4a), where a run out occurred in a CAT at a stress amplitude of $\sigma_a = 90$ MPa.

For the chip-based specimen a decrease of AC potential ΔU_{AC} can be observed until a stress amplitude of $\sigma_a = 35$ MPa is reached, presumably due to a compaction of the seam welds. In the stress amplitude region between $\sigma_a = 35$ and 63 MPa, ΔU_{AC} shows a plateau phase, followed by an exponential increase with a change of the slope at a stress amplitude of $\sigma_a = 115$ MPa due to an initiation of a second main crack on the opposite side of the first crack, which could be determined by means of computed tomography investigations. Above a stress amplitude of $\sigma_a = 140$ MPa, ΔU_{AC} shows a drastic increase until failure of the specimen. The change in temperature is constant until $\sigma_a = 105$ MPa is reached, followed by a sharp increase. Analogous to the cast-

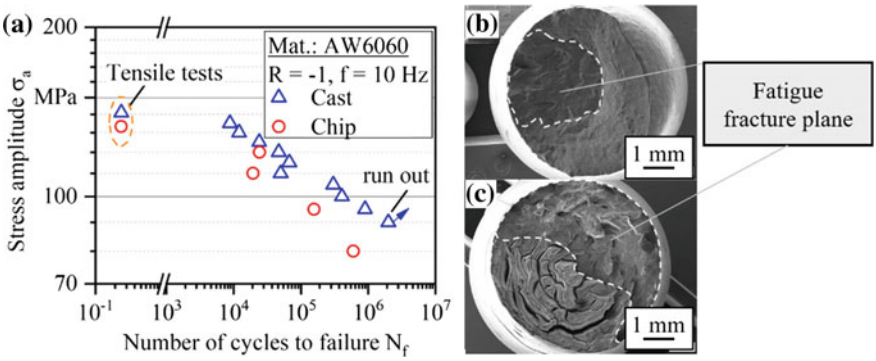

Fig. 2.4 **a** S-N curves of cast-based and chip-based specimens and fractured surfaces as SEM micrographs of **b** cast-based and **c** chip-based fatigue specimens ($\sigma_a = 120$ MPa)

based specimens, the fatigue strength of the chip-based specimens can be estimated at about $\sigma_{a,e} = 63$ MPa, where exponential increase of ΔU_{AC} starts.

Figure 2.4 shows S-N curves (a) as well as fractured surfaces as SEM micrographs of cast-based (b) and chip-based (c) specimens tested at $\sigma_a = 120$ MPa. The chip-based specimens show a significantly reduced lifetime, especially in the HCF-region, compared to cast-based specimens. For both specimens, two areas of fatigue fracture surface and overload fracture surface can be distinguished. In the chip-based specimens (Fig. 2.4c) the cracks propagate between the seam welds, so that individually detached chips can be observed.

2.4 Conclusions and Outlook

Mechanical investigations have shown that both the quasi-static and cyclic properties of chip-based AW6060 profiles are significantly reduced compared to conventionally manufactured cast-based profiles. The reason for this is an insufficient quality of the seam welds occurring in the chip-based profiles, where the chips weld together in the extrusion process. With the help of ACPD-technique, a precise estimation of the fatigue strength in load increase tests as well as a possibility of a tracking of the fatigue progress succeeds. The chip-based specimens show a significant difference in the damage behavior, as the ACPD shows a much earlier beginning of the fatigue progress. As optical as well as scanning electron micrographs have shown, the cracks propagate between the chip boundaries, so that these are the weakest links in the specimens.

In subsequent studies the influences of different extrusion ratios on quasi-static and cyclic properties as well as crack propagation behavior will be investigated.

Acknowledgements The authors thank the German Research Foundation (DFG) for its financial support within the research project "Analysis and extension of the limits of application in metal forming based recycling of aluminum chips" (WA 1672/16-1, TE 508/60-1) and F. Kolpak and A. E. Tekkaya at Institute of Forming Technology and Lightweight Components (IUL), TU Dortmund University, for the provision of profiles in the context of an excellent scientific cooperation within this research project.

References

1. Apelian D, Shivkumar S, Sigworth G (1989) Fundamental aspects of heat treatment of cast Al-Si-Mg alloys. AFS Trans 97:727–742
2. Starke EA, Staley JT (2011) Application of modern aluminium alloys to aircraft. Fundam Alum Metall 24:747–783
3. Schwarz HG (2004) Aluminum production and energy. Encycl Energy 1:81–95
4. Worrell E, Price L, Martin N, Farla J, Schaeffer R (1997) Energy intensity in the iron and steel industry. Energy Policy 25(7–9):727–744
5. Stern M (1951) Direct extrusion applied to light metal scrap. Iron Age 28(6):71–73
6. Güley V, Güzel A, Jäger A, Ben Khalifa N, Tekkaya AE, Misiolek WZ (2013) Effect of die design on the welding quality during solid state recycling of AA6060 chips by hot extrusion. Mater Sci Eng A 574:163–175
7. Donati L, Tomesani L (2004) The prediction of seam welds quality in aluminum extrusion. J Mater Process Technol 153–154:366–373
8. Walther F (2014) Microstructure-oriented fatigue assessment of construction materials and joints using short-time load increase procedure. Mater Test 56:519–527

Chapter 3
Micromagnetic-Based Fatigue Life Prediction of Single-Lip Deep Drilled AISI 4140

N. Baak, J. Nickel, D. Biermann and F. Walther

Abstract Non-destructive testing based on micromagnetic techniques, for example magnetic Barkhausen noise analysis, are quick and reliable possibilities to detect and classify material parameters like hardness and residual stresses. High-strength steels, like AISI 4140 (42CrMo4 + QT), are commonly used for highly dynamically loaded parts. Increasing requirements on weight, performance and efficiency of automotive industry claim increasing demands on material properties. The aim of this study is to evaluate the surface conditions of deep drilled round specimens due to drilling parameters and to predict the resulting fatigue strength by micromagnetic measurements. Furthermore, modified process parameters should enhance fatigue life without the need for expensive processing steps, e.g. autofrettage.

Keywords Micromagnetic technique · Barkhausen noise · Fatigue performance · Surface condition · Single-lip deep hole drilling

3.1 Introduction

Steels are the essential material for highly dynamic loaded components in automotive sector or plant engineering. Quenched and tempered steels, like AISI 4140 (42CrMo4 + QT), for example are used for common rail injectors [1]. Injectors are regularly processed via machining processes like deep hole drilling. Higher sulfur content improves the machining process due to improved chip breaking by formation of manganese sulphides. This requirement is contrary to demands on high fatigue life. In fatigue life high grades of purity are beneficial [2]. To improve the performance without increasing the production costs considerable, surface conditions, for e.g.

N. Baak (✉) · F. Walther
Department of Materials Test Engineering (WPT), TU Dortmund University,
44227 Dortmund, Germany
e-mail: nikolas.baak@tu-dortmund.de

J. Nickel · D. Biermann
Institute of Machining Technology (ISF), TU Dortmund University,
44227 Dortmund, Germany

J.A.F.O. Correia et al. (eds.), *Mechanical Fatigue of Metals*, Structural Integrity 7,
https://doi.org/10.1007/978-3-030-13980-3_3

material structure and residual stresses, should be precisely set during drilling. So far cost-intensive operations like autofrettage are common procedures to improve fatigue life by the introduction of near-surface residual stresses due to plastic deformation [3]. Effort and costs for autofrettage processes increase with smaller diameter and higher depth of the bore [4]. This paper describes the influence of the feed rate during single-lip deep drilling on the surface condition, accordingly the fatigue behavior and the characterization by micromagnetic techniques.

3.2 Testing Strategy

3.2.1 Single-Lip Deep Hole Drilling

Single-lip deep hole drilling is characterized by very good values with regard to the quality of the bore, such as surface roughness, straightness deviation, as well as roundness and diameter of the bore. Due to the asymmetrical design, the single-lip drill is equipped with guide pads which on the one hand allow the tool to guide itself in the bore; on the other hand, the guide pads transmit the cutting and passive forces that occur during process into the bore wall [5]. This smoothes the surface of the bore and at the same time influences the subsurface area by initiating changes in the microstructure and inducing residual stresses. The resulting surface integrity can be influenced according to the process parameters cutting speed and feed rate. The geometry of the drilling tools is another aspect that has an influence on the occurring forces during the machining process and which are transferred to the bore wall [6].

3.2.2 Micromagnetic Techniques

Magnetic Barkhausen noise (MBN) is based on unsteady changes in areal expansion of magnetic domains in ferromagnetic materials. The domains are divided by Bloch walls, which move when an external magnetization occurs. The movement is affected by lattice defects and the magnetostriction. In a constantly changing magnetic field, a characteristic in Bloch wall movement can be observed and traced back to the microstructure and residual stresses. The maximum penetration depth of approximately 100 μm is caused by the skin effect, thus it is important to detect the MBN on the crucially surface [7]. Jiles showed that increasing compressive stresses leads to an increase in coercive field strength and a decrease in maximum of the Barkhausen noise amplitude [8]. The MBN measurement was performed with a custom-build inner-surface sensor with a magnetization from the outer surface. The magnetization frequency was set to 30 Hz and the bandpass filter between 20 and 200 kHz, this assured a uniform magnetic field at the inner surface.

3.2.3 Material

In this study two different melts of AISI 4140 (42CrMo4 + QT, 1.7225) in quenched and tempered condition were evaluated. Both melts meet the standards of DIN EN 10083-3 [9] and significant differences can only be found in sulphur content. The sulpher content according the inspection certificate of melt S110 is 0.011 wt% and of melt S280 is 0.028 wt%.

Table 3.1 displays verification measurements by optical emission spectroscopy. The specimens were machined from round material with a diameter of 50 mm made by continuous casting.

3.2.4 Test Setup

Round specimens with a diameter of 7.5 mm at the measuring length and a single-lip deep drilled bore in longitudinal axis with a diameter of 5 mm were investigated (Fig. 3.1b). The feed rate f was varied between 0.05 and 0.15 mm by otherwise constant parameters. The fatigue tests were performed on a Rumul Testronic 150 kN at a load ratio of R = –1 and a test frequency of $f_{cyc} \approx 75$ Hz. The tests were instrumented with an extensometer, thermocouples and an alternating current potential drop setup (ACPD) system (Fig. 3.2a). For an efficient comparison of the influence

Table 3.1 Chemical compositions of the melts S110 and S280 (wt%)

	C	Si	Mn	P	S	Cr	Mo	Fe
S110	0.41	0.18	0.85	0.011	0.011	1.01	0.18	bal.
S280	0.39	0.17	0.83	0.014	0.028	0.97	0.17	bal.

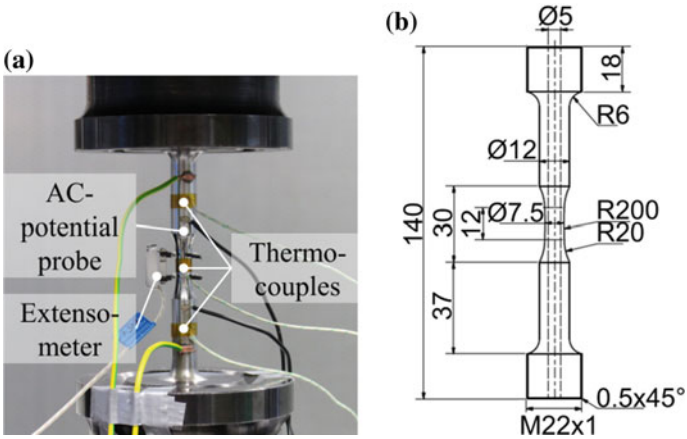

Fig. 3.1 **a** Instrumented fatigue specimen applied in Rumul Testronic 150 kN; **b** Deep drilled fatigue specimen

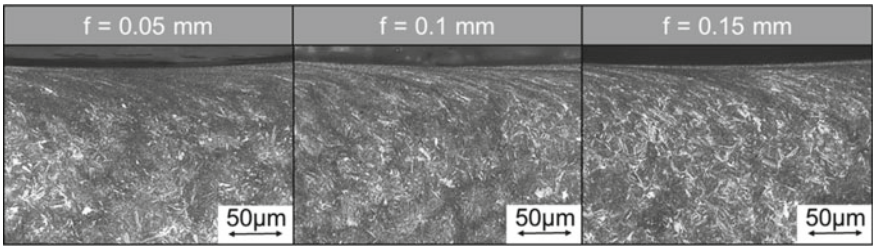

Fig. 3.2 Etched micro-sections of single-lip deep drilled specimen with varying feed rate f

of varying machining parameters, load increase tests (LIT), with a start amplitude $\sigma_{a,start} = 100$ MPa with a load increase of $\Delta\sigma_a = 10$ MPa/10^4 cycles were carried out. Afterwards constant amplitude tests (CAT) for different load amplitudes were performed. These tests were interrupted for micromagnetic testing at $N = 10^4$, 10^5 and 10^6 cycles.

3.3 Results

The varying feed rates lead to differences in the microstructure. Figure 3.2 shows transverse micro-sections of the single-lip deep-drilled specimen. These micrographs reveal an expected deformation of the microstructure in the direction of the cut for all feed rates. Furthermore, the highest feed rate f = 0.15 mm and the related high process forces cause the formation of a white etching layer (WEL).

As seen in Fig. 3.3a the plastic strain amplitude ($\varepsilon_{a,p}$) is a good indicator for first material response in LIT. Figure 3.3b compares the $\varepsilon_{a,p}$ development for the three feed rates in S110. A linear increase in $\varepsilon_{a,p}$ can be seen for all feed rates, for f = 0.05 and 0.15 mm a change from linear to exponential development can be detected at a stress amplitude of 410 MPa. For f = 0.10 mm the gradient in the linear part is significantly lower and the change to exponential increase is shifted to a stress amplitude of 430 MPa. For S280 the change to exponential behavior for specimen of with f = 0.10 mm occurs at the lower amplitude of 380 MPa.

Afterwards CAT tests for S110 with load amplitude of $\sigma_a = 400$ MPa were performed. The results of MBN measurements are displayed in Fig. 3.4. Figure 3.4a displays the coercive field strength Phi_{cm} in a linear scale. The diagram has a significant change during first 10^4 cycles for the feed rates f = 0.05 and 0.10 mm, while Phi_{cm} remains constant for f = 0.15 mm. Figure 3.4b presents Phi_{cm} in a logarithmic scale. This representation allows an evaluation of MBN until 10^7 cycles. All three feed rates show different Phi_{cm} developments. For f = 0.15 mm Phi_{cm} remains constant until 10^7 cycles. The coercive field strength for f = 0.10 mm is constant until 10^5 cycles and decreases afterwards. For f = 0.05 mm Phi_{cm} is nearly constant until 10^6 cycles before it drops. These trends are similar to residual stress relaxation curves known from [10].

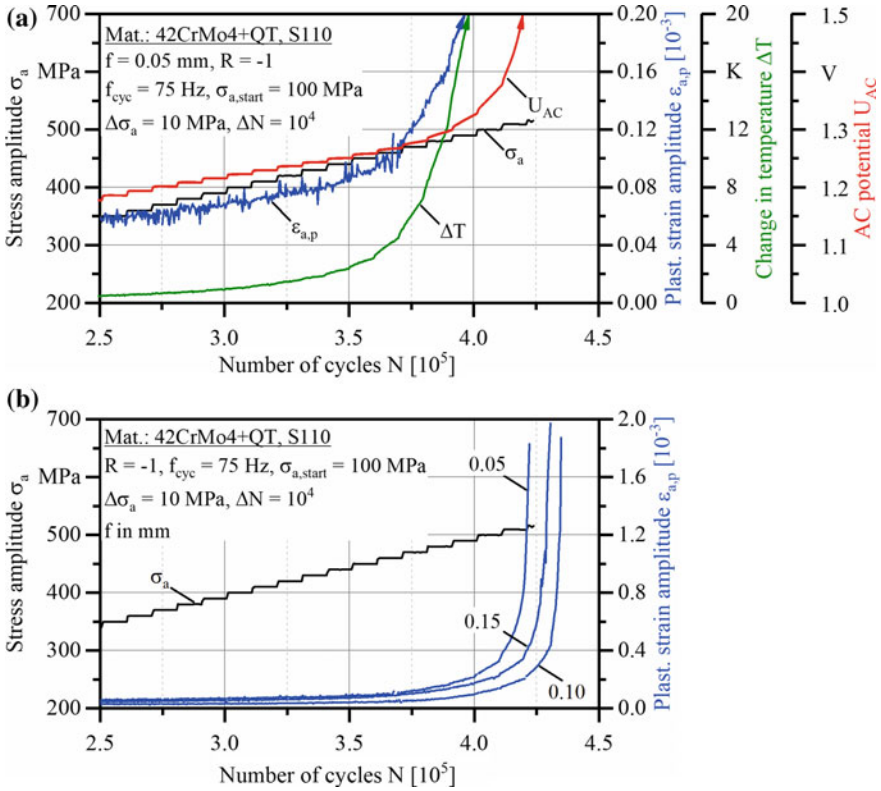

Fig. 3.3 **a** Results of load increase tests on S110 for f = 0.05 mm and **b** results of plastic strain amplitude measurements of load increase tests with varying feed rate

3.4 Summary and Outlook

This study showed that the feed rate of the single-lip deep drilling process has a significant impact on the fatigue behavior of single-lip deep-drilled AISI 4140 specimen. Moreover, the development of micromagnetic parameters changes with the feed rate of the drilling process. The trends of the coercive field strength during fatigue tests for the two lower feed rates resemble known residual stress relaxation curves. For f = 0.05 and 0.10 mm the coercive field decrease significantly in the first 10^4 cycles; a further decreasing can be detected. For f = 0.15 mm no significant change of the coercive field strength can be detected. This leads to the assumption that the drilling process with f = 0.05 and 0.10 mm induce compressive residual stresses, which diminish during first cycles to a level of equivalent surface stress. Maybe the higher process forces for f = 0.15 mm induce residual stresses above the load level or the higher process temperatures may inhibit the formation of residual

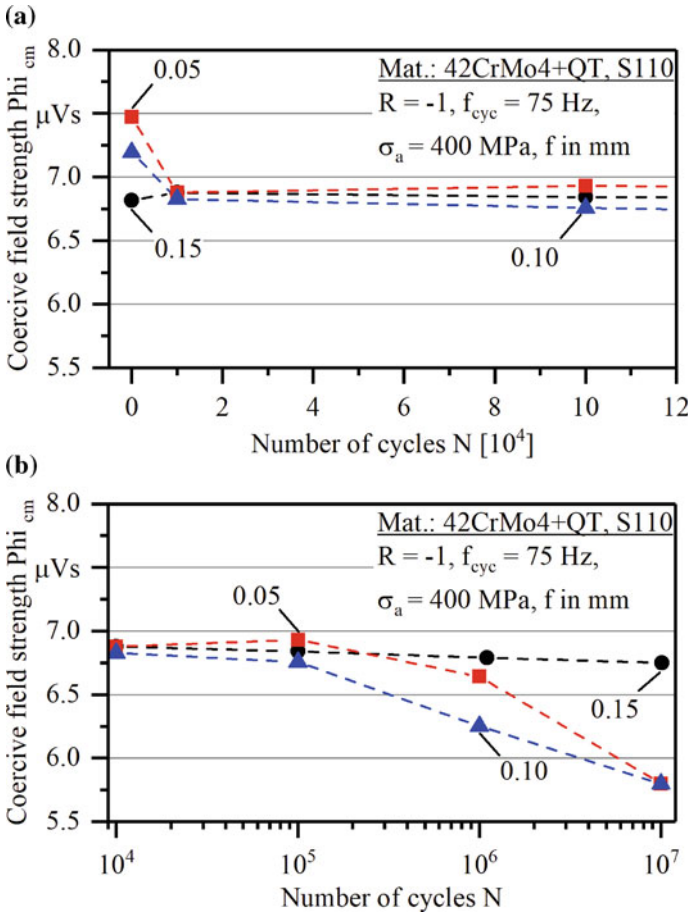

Fig. 3.4 Coercive field strength during fatigue tests with a stress amplitude of 400 MPa for three different feed rates in **a** linear and **b** logarithmic x scale measured on the inner surface

stresses. So neither compressive nor tensile stresses were induced. As expected the higher sulphur content of S280 decreases the fatigue performance by otherwise same parameters.

In subsequent studies the determination of residual stress values and their development should be investigated. Especially the development during the first cycles, from quasistatic investigations up to 10^4 cycles, should be evaluated. With this information a prediction of the trend of residual stress relaxation and relating thereto fatigue life can be possible.

Acknowledgements The authors would like to thank the German Research Foundation (DFG) for financial support within the research project "Investigations on the influence of machining

and sulphur content on the fatigue strength of the quenched and tempered steel 42CrMo4 + QT" (WA 1672/22, BI 493/83).

References

1. Vormwald M, Schlitzer T, Panic D, Beier H (2018) Fatigue strength of autofrettaged diesel injection system components under elevated temperature. Int J Fatigue. Available online 31 Jan (2018). https://doi.org/10.1016/j.ijfatigue.2018.01.031
2. Lei Z, Hong Y, Xie J, Sun C, Zhao A (2012) Effects of inclusion size and location on very-high-cycle fatigue behavior for high strength steels. Mater Sci Eng A 558:234–241
3. Malik M, Kushnood S (2003) A review of swage-autofrettage process. In: Proceeding of ICONE11 International Conference on Nuclear Engineering. Tokyo, Japan, pp. 1–12
4. Leutwein H (2011) Einfluss von Autofrettage auf die Schwingfestigkeit innendruckbelasteter Bauteile aus Kugelgraphitguss, 2nd edn. Ilmedia, Ilmenau
5. VDI guideline 3210. Deep-hole drilling. Beuth (2006)
6. Sakuma K, Taguchi K, Katsuki K, Takeyama H (1981) Self-guiding axtion of deep-hole drilling tools. Ann CIRP 30(1):311–315
7. Cullity BD, Graham CD (2009) Introduction to magnetic materials, 2nd edn. Wiley
8. Jiles DC (1989) The effect of stress on magnetic Barkhausen activity in ferromagnetic steels. IEEE Trans Magn 3455–3457
9. Walther F (2014) Microstructure-oriented fatigue assessment of construction materials and joints using short-time load increase procedure. Mater Test 56(7–8):519–527
10. Holzapfel H, Schulze V, Vöhringer O, Macherauch E (1998) Residual stress relaxation in an AISI 4140 steel due to quasistatic and cyclic loading at higher temperatures. Mater Sci Eng A 248:9–18

Chapter 4
Relationship Between Microstructural Features and Fatigue Behavior of Al-Based Alloy in Green Chemical Processing

Ildiko Peter, Raffaella Sesana and Roberto Maiorano

Abstract In this study, a green chemical milling, Green Etching (Patent pending), is applied to B356.2 Aluminum alloy with the aim to remove a controlled thickness layer from the surface with no buckling and maintaining excellent dimensional tolerances. Comparison of the fatigue life of un-treated and chemically treated samples is performed, with the aim to determine how the above mentioned chemical treatment influences the fatigue resistance of the Al alloy to be used in automotive/aircraft industrial application. The results revealed that the fatigue properties of Al casting alloy are influenced by the presence of casting defects and the fatigue resistance can not be significantly compromised by the milling treatment despite the surface roughness induced by the treatment.

Keywords Al alloy · Green chemical milling · Microstructure · Fatigue resistance · Casting defects

4.1 Introduction

Chemical etching is a chemical process obtained by means of immersion in a tailored solution, used for material removal and lightening of complex shape components. The process allows to operate surfaces which cannot be reached by means of conventional tools and it does not introduce residual stresses. Surface finish can be rough and surface roughness can be higher than the one obtained by means of machining processes, and it is generally related to processed material, chemical solution, temperature and process time [1]. Chemical processing can be operated by means of alkaline [2–5] or acid [1, 6–10] solution. Temperature and time result to be parameter

I. Peter
Department of Applied Science and Technology, Politecnico di Torino, Turin, Italy

R. Sesana (✉)
Department of Mechanical and Aerospace Engineering, Politecnico di Torino, Turin, Italy
e-mail: raffaella.sesana@polito.it

R. Maiorano
RGTech srl, Bruino, Turin, Italy

J.A.F.O. Correia et al. (eds.), *Mechanical Fatigue of Metals*, Structural Integrity 7,
https://doi.org/10.1007/978-3-030-13980-3_4

affecting the performance of the process. In [4] alkaline chemical etching on aluminum is applied to control the surface wettability and to obtain hydrophobic surfaces. An analogous investigation is described in [6] but related to an acid chemical solution. In [7] the property of removing material without interfering with residual stresses of etching allows to indirectly measure the residual stresses in a steel milled specimen. Rectangular pits are obtained after etching both in alkaline [6] and acid [7] chemical etching. In literature few researches are related to how chemical hatching affects aluminum mechanical properties in particular relating HCF. In [5] Al–Mg–Si specimens, processed by means of alkaline chemical hatching, showed a 50% reduction in average LCF lives compared to electropolished Al–Mg–Si specimens. The fatigue-life reduction of the chemically milled specimens is related to early onset of crack nucleation due to pit-induced-stress concentrations. In [10] a similar research is presented with similar results for specimens, processed by means of acid chemical hatching. In [11] also HCF is investigated. It results that HCF behavior is related mainly to surface roughness and to alloying chemical elements.

The aims of this paper are two. Following the suggestions in [1], the first aim is to introduce an innovative chemical alkaline process, Green Etching (GE), for material removal and lightening of aluminum alloys, which allows lower operation temperatures, reusable chemical solution, recycling of processing wastes. The second aim is to present and discuss HCF testing results for an automotive aluminum alloy processed by means of Green Etching which showed an increased HCF resistance. The surface profile and roughness parameters are measured to investigate the possible relation with the HCF behavior.

4.2 Materials and Methods

The investigated alloy, B356.2, (Si: 7.4, Fe: 0.06, Cu: 0.03, Mg: 0.3, Zn: 0.05, Ti: 0.2, Al: balance, wt%) belongs to the Al–Si–Mg system and it is one of the most commonly used gravity cast alloy at industrial level. With respect to the A356 alloy has an equal main alloy content but has decreasing requirement limits related to the impurity content, principally as Fe content regards. Two samples of specimens were prepared. A first sample (Sample A) was obtained by base material specimens, turned, milled and polished. A second set of specimens was obtained by base material specimens, turned, milled and underwent GE (Sample B). GE is a process consisting in a localized chemical attack aiming at removing a thin surface metallic layer in Aluminum components. The surface roughness is increased, but mechanical, chemical and physical properties result to be improved. Microparticles of the same material of which the component is made deposit on the bottom of the tanks and, after being washed, they can be recycled. These operations can be repeated many times and the thickness of the removed layer can be controlled to generate profiles and cavities can be generated. Temperature of the solution is lower than 70 °C, the solution can be reused.

The tensile properties (Yield strength σ_y, ultimate tensile strength *UTS* and elastic modulus *E*) of the un-treated and GE samples have been evaluated by means of Standard tensile tests, according to [12], using an Instron 8801 100 kN universal testing equipment in strain rate control. 3 specimens were tested for base material and surface polished. Fatigue testing was performed by means of a HFP Amsler HFP 422 100 kN vibrophore. Uniaxial tensile fatigue tests have been carried out at room temperature, on both on un-treated and GE samples, according to [13], in load control, stress ratio $R = \sigma_{min}/\sigma_{max} = 0{,}1$ and a load frequency about 158 Hz, run-out condition 10^5 cycles. The fatigue limit has been estimated by Staircase method. In the present paper the term "fatigue limit" for Al alloys is referred to fatigue endurance limit for a 5 milions cycle life. Specimen shape for both monotonic and fatigue tests is dogbone, according to [12, 13]. With respect to [13] a data processing adaptation was performed. As both of them were varied to keep $R = 0.1$ constant, then Staircase data processing was extended to the amplitude data thus obtaining $\sigma_{D0.1}$ fatigue limit. Surface roughness measurements (*Ra, Rm*, *Rt* and *Rz*) were performed by means of an ALPA surface roughness measurement instrument, 0.8 mm cutoff and 5 mm measuring length, 5 measurements on each specimen, one specimen per sample. Profile measurements were performed by means of a PSG200 SM Instruments profilometer. Fracture surface analysis was carried out by Field emission scanning electron microscope (FESEM, ZEISS MERLIN apparatus) equipped with EDS unit.

4.3 Results and Discussion

Tensile testing results are presented in Table 4.1. Fatigue results are reported in Table 4.2. In this table, according to [13], the calculated value of fatigue resistance at 5×10^6cycles, $R = 0{,}1$ and 50% probability of failure, ($\sigma_{D0.1\ 50\ \%}$), 10% ($\sigma_{D0.1\ 10\ \%}$) and 90% ($\sigma_{D0.1\ 90\ \%}$) are reported. If comparing these results with [5, 10] an opposite behavior can be observed. The difference can be due to microstructural properties. In [10] the structure of the Ti alloy results to be exposed to crack nucleation and

Table 4.1 Uniaxial monotonic mechanical characterization results for base material (σ_y Yield stress, *UTS* Ultimate Tensile Resistance, *E* Elastic modulus)

σ_y (MPa)	*UTS* (MPa)	*E* (MPa)
144	250	67,670

Table 4.2 Uniaxial fatigue mechanical characterization results for base material with and without Green Etching

	$\sigma_{D0.1\ 50\ \%}$ (MPa)	$\sigma_{D0.1\ 10\ \%}$ (MPa)	$\sigma_{D0.1\ 90\ \%}$ (MPa)
Base material	42,6	39,2	46,0
Base material with GE	45,7	35,0	56,3

Table 4.3 Surface roughness measurements

		Ra (μm)	*Rq* (μm)	*Rt* (μm)	*Rz* (μm)
Sample A	Average	0,696	0,819	3,866	3,234
	std dev	0,078	0,084	0,543	0,277
Sample B	Average	2,882	3,797	31,368	15,261
	std dev	1,710	2,220	12,915	8,070

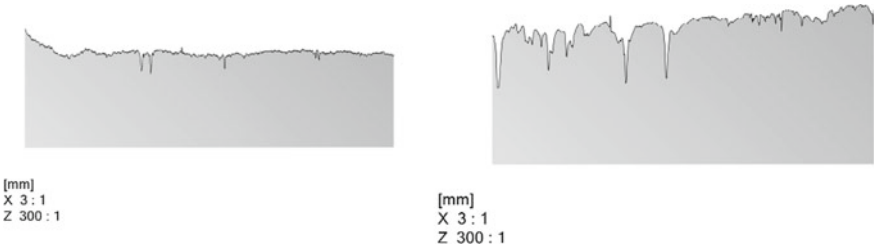

Fig. 4.1 Profile measurements (scale 300:1) for base material (left) and GE base material (right)

propagation in multiple points: the crack nucleation is not directly a consequence of etching but is related to the morphology and composition of the phases present in the structure. A similar observation can be reported for [5]. According to [2], surface appearance, roughness and topology is related to the alloy and solution compositions. Surface measurements are reported in Table 4.3 while profiles are reported in Fig. 4.1. This morphology is coherent with the corresponding reported in [10] for a Ti alloy.

Fracture surface analysis was performed on the specimens submitted to mechanical investigation in order to make a comparison between the microstructural characteristics revealed on the fractured surfaces in the presence or absence of chemical milling, to individuate the presence and the nature of the defects and to analyze the chemical composition and the shape of the particles sited on the fractured surfaces. In particular, two regions of the specimen were observed: in the central part of the specimens, where one has the same conditions, since the chemical milling do not compromise the morphology making possible an evaluation of the production process and of the "healthy" of the specimens produced; on the border of the specimens: following chemical milling it reveals some changes, while with no any treatment looks like as in the former case. The information collected during fracture surface analysis can be directly correlated to the production process and to the mechanical performance of the alloy clarifying the deviation of the tensile and fatigue resistance of the specimens following chemical milling. By analyzing the central part of the specimen it was observed that both of them reveal the presence of the same defect (Fig. 4.2a, b), identified as an interdendritic porosity; such defect is developed in a large area and probably is generated during the manufacturing of the alloy. Generally, such defects are created following an inappropriate feeding of the die with a negative effect on the solidification of the alloy.

Observing the external part of the specimens it is possible to note that the untreated surface, in addition to the presence of porosities, contains a significant amount of oxide, identified as Al_2O_3 (Fig. 4.2c), while the specimen when exposed to GE do not show any presence of $Al_2O_{3:}$ because chemical milling removes such particles (Fig. 4.2d).

Following GE some holes/dips were developed (Fig. 4.3a, b) with different size (130 μm ÷ 190 μm). Additionally, the presence of some different precipitates appears with an elongated shape (Fig. 4.3c) and chemically constituted by Si as detected by EDS analysis. For both specimens a ductile fracture was observed (Fig. 4.4a, c),

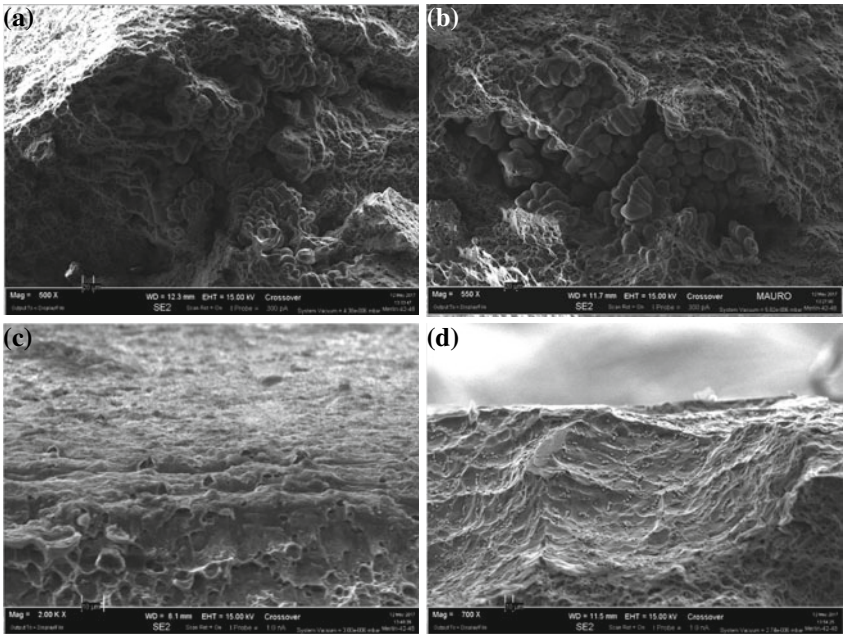

Fig. 4.2 Microstructural details of the fractured surfaces: core of the specimen **a** base material, **b** Green Etched base material and edge of the specimen, **c** base material, **d** Green Etched base material

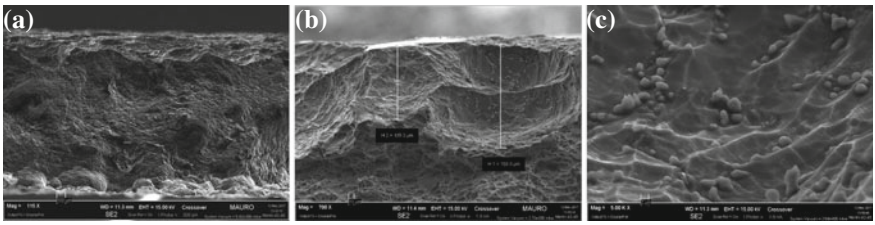

Fig. 4.3 View of the fracture surface of the Green Etched base material showing the modified character near the edge compared to the central part

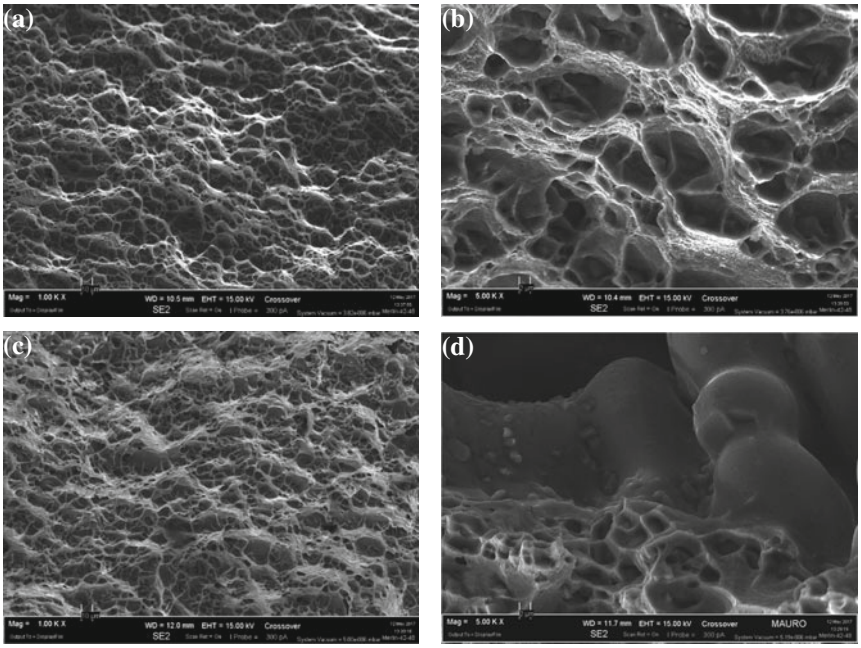

Fig. 4.4 View of the fracture surface of the Green Etched base material showing the modified character near the edge compared to the central part

demonstrating that the GE do not compromises the plasticity of the alloy. As higher magnification the presence of dimples can be observed (Fig. 4.4b, d) and in the case of the GE base material (Fig. 4.4 d) a clear evidence of fresh Al dendrites is observed.

4.4 Conclusions

The comparison of HCF results for the investigated aluminum alloy undergoing GE processing shows an increment in fatigue life resistance. This phenomenon can be attributed to many causes: the rounded shape if surface roughness due to alkaline chemical etching, the chemical action which mechanically removes microinclusions and surface alumina microparticles, the presence of a protective layer generated by chemical actions. Further investigations on other automotive and aerospace aluminum alloys are ongoing.

References

1. Cakır O (2008) Chemical etching of aluminum. J Mater Process Technol 199:337–340
2. Kape JM (1970) Chemical Etching of Aluminium in Caustic Soda Based Solutions. Trans IMF 48(1):43–50
3. Moutarlier V, Viennet R, Rolet J, Gigandet MP, Hihn JY (2015) Power ultrasound irradiation during the alkaline etching process of the 2024 aluminum alloy. Appl Surf Sci 355:26–31
4. Huang Y, Sarkar DK, Grant Chen X (2015) Superhydrophobic aluminum alloy surfaces prepared by chemical etching process and their corrosion resistance properties. Appl Surf Sci 356:1012–1024
5. Spear AD, Ingraffea AR (2013) Effect of chemical milling on low-cycle fatigue behavior of an Al–Mg–Si alloy. Corros Sci 68:144–153
6. Hua B, Suna Y, Guana B, Zhaoa J, Zhanga H, Zhub D, Mab K, Cheng C (2017) Ultrasonic effect on etching tunnel morphology and distribution of aluminum foil. Appl Surf Sci 392:375–383
7. Vilčeka I, Řehořa J, Caroua D, Zemanb P (2017) Residual stresses evaluation in precision milling of hardened steel based on the deflection-electrochemical etching technique. Robot Comput Integr Manuf 47:112–116
8. Jawahir IS, Brinksmeier E, M'Saoubi R, Aspinwall DK, Outeiro JC, Meyer D, Umbrello D, Jayal AD (2011) Surface integrity in material removal processes: Recent advances. CIRP Ann Manuf Technol 60:603–626
9. Kumara A, Gogoib B (2018) Development of durable self-cleaning superhydrophobic coatings for aluminium surfaces via chemical etching method. Tribol Int 122:114–118
10. Sefer B, Gaddam R, Roa JJ, Mateo A, Antti ML, Pederson R (2016) Chemical milling effect on the low cycle fatigue properties of cast Ti–6Al–2Sn–4Zr–2Mo alloy. Int. Jou. of Fatigue 92:193–202
11. Harris WT (1976) Chemical Milling: the technology of cutting materials by etching. Clarendon Press, Oxford
12. UNI EN ISO 6892-1:2016—Metallic materials—Tensile testing—Part 1: Method of test at room temperature (2016)
13. UNI 3964—Room temperature fatigue tests, general principles (in Italian) (1985)

Chapter 5
Influence of Heat Treatment Process to the Fatigue Properties of High Strength Steel

V. Chmelko, I. Berta and M. Margetin

Abstract This paper is devoted to the analysis of static and cyclic properties of two high strength steels (AS 4340). The reason for this analysis was the need to select suitable materials for the power engineering. Analyzed materials had a practically identical chemical composition. The heat treatment process declared by the inspection certificate was very similar too. By the measurements of mechanical properties there were differences in static strength and especially in cyclic properties of compared materials. To explain the significant differences in fatigue properties between materials, it was necessary to analyze their microstructure. The results have shown that a relatively small change in the heat treatment process has a significant effect on the fatigue properties of the steel.

Keywords Fatigue properties · High strength steel · Heat treatment

5.1 Introduction

High strength of the steels and their good mechanical properties are achieved by the heat treatment. It is very difficult to choose such procedure and the type of the heat treatment which leads to the balanced mechanical properties in area of the strength, ductility and fatigue strength. In this study mechanical properties are analyzed for two materials—two steels with the same chemical composition (see Table 5.1) and very similar heat treatment (see Table 5.2).

Analyzed alloy steel AISI 4340 (34CrNiMo-6) is a medium carbon low alloy steel mainly used in power transmission gears and shafts, aircraft landing gear, and other structural parts.

V. Chmelko (✉)
University of West Bohemia, RTI, Univerzitní 22, 30614 Pilsen, Czech Republic
e-mail: vladimir.chmelko@stuba.sk

I. Berta · M. Margetin
Slovak University of Technology, Námestie Slobody 17, 81231 Bratislava, Slovakia

J.A.F.O. Correia et al. (eds.), *Mechanical Fatigue of Metals*, Structural Integrity 7,
https://doi.org/10.1007/978-3-030-13980-3_5

Table 5.1 Comparison of chemical composition of two materials

Chemical elements	C	Mn	Ni	Cr	Al	Si	Mo	Cu	Co	V
Material A	0,42	0,70	1,85	0,82	0,024	0,25	0,26	0,12	0,02	0,01
Material B	0,41	0,72	1,86	0,83	0,010	0,24	0,26	0,14	0,01	0,01

Table 5.2 Comparison of the heat treatment procedure for two materials

Heat treatment	Preheating	Hardening	Tempering
Material A	600/2:30	870/6:00, water	530/8:40, water
Material B	–	890/9:00, polymer	540/11:00, air

Analyzes and measurements include:

- tensile tests and their analysis
- measurement of hardness
- cyclic test in force-controlled mode
- cyclic test in strain-controlled mode
- analysis of microstructure.

5.2 Analysis of Static Strength Properties

One of the required properties of the material was the ductility value minimally of 12%. The lower ductility value reported by certificate of one of the materials led to the need to perform the tensile tests (three samples of each material) and the measurement of their hardness. The tensile curves and the evaluated parameters of both materials are compared in Fig. 5.1.

Differences in ductility values were not documented. The material A exhibited approximately 20% higher tensile strength at practically identical Brinell hardness values.

5.3 Analysis of Fatigue Properties

The cyclic tests of specimen of both analyzed materials were made in loading frame ZUZ-200 of electrohydraulic testing equipment Inova Prague. Force-controlled tensile loading ($R = -1$) was performed at frequency 1–8 Hz together with simultaneous strain sensing by extensometer Sandtner PXA10-1. All load cycles were recorded at sampling frequency, which allow evaluate amplitude of loading cycles with sufficient precision. Basquin's dependency in form [1]

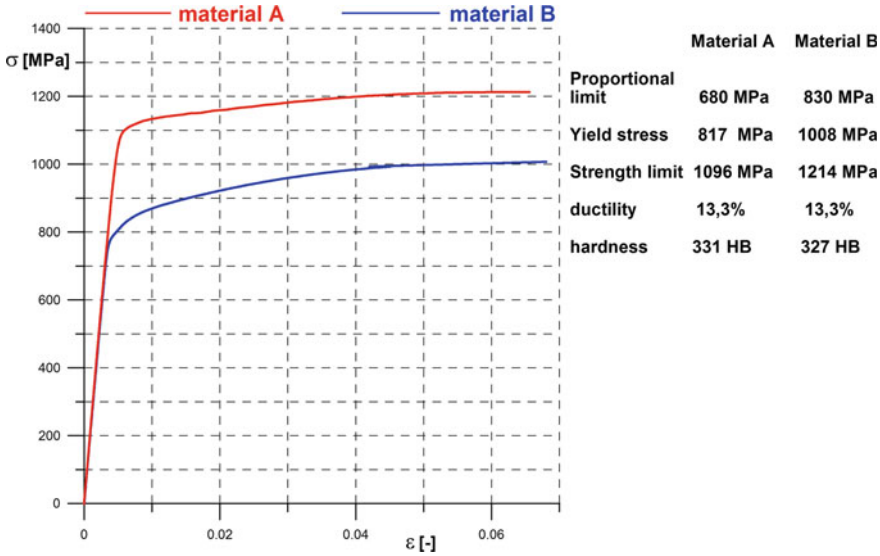

Fig. 5.1 Tensile diagrams of both analyzed materials and obtained mechanical properties

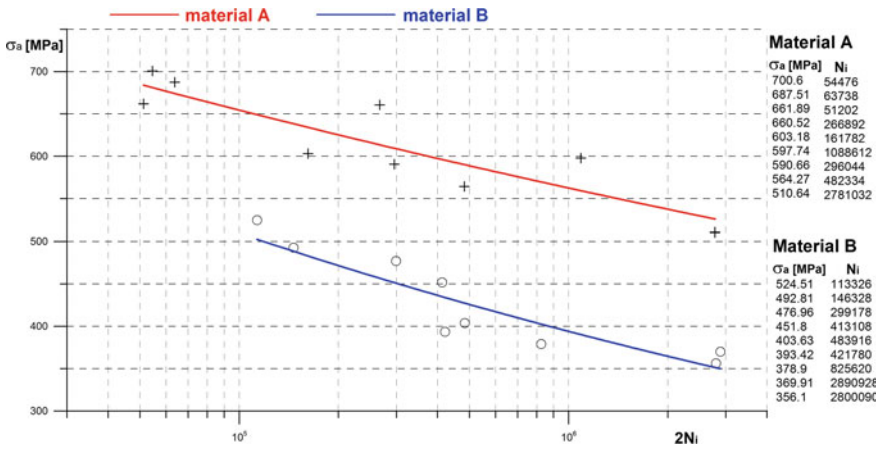

Fig. 5.2 Comparison of the Basquin curves of both analyzed materials

$$\sigma_a = \sigma'_f (2N_i)^b \tag{5.1}$$

were compared in Fig. 5.2. The number of cycles until the crack initiation N_i was evaluated by reverse analysis of the hysteresis loops recorded and the corresponding piston stroke of the hydraulic cylinder.

The results obtained by cyclic tests show a wide difference between the materials under consideration: for lifetime $2 \cdot 10^6$ cycles to initiate crack the corresponding stress amplitude value calculate from regression curves is

$$
\begin{aligned}
{}^{A}\sigma_a^{2\cdot 10^6} &= 520 \text{ MPa for the Material A} \\
{}^{B}\sigma_a^{2\cdot 10^6} &= 330 \text{ MPa for the Material B.}
\end{aligned}
\tag{5.2}
$$

The measured hysteresis loop records enabled to evaluate the cyclic consolidation processes (cyclic hardening or softening)—see Figs. 5.3 and 5.4. Obtained values of strain amplitudes corresponding to the controlled stress amplitudes during cyclic loading indicate a high degree of cyclic stability of both materials [2].

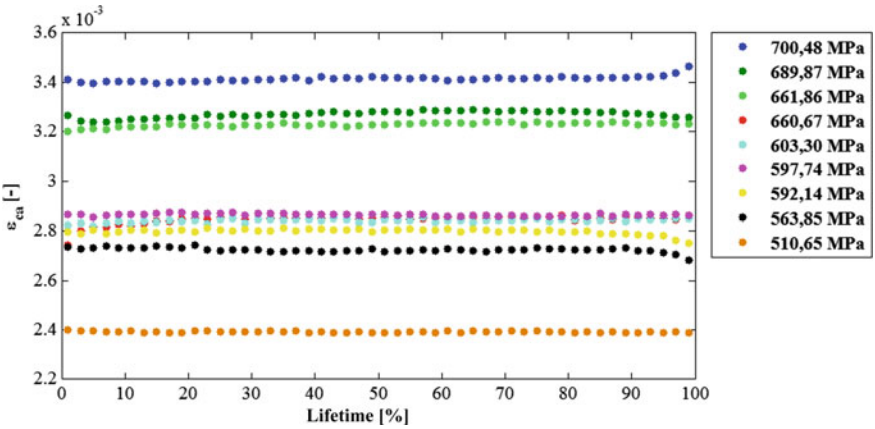

Fig. 5.3 Material A: strain responses for loading amplitudes of stress

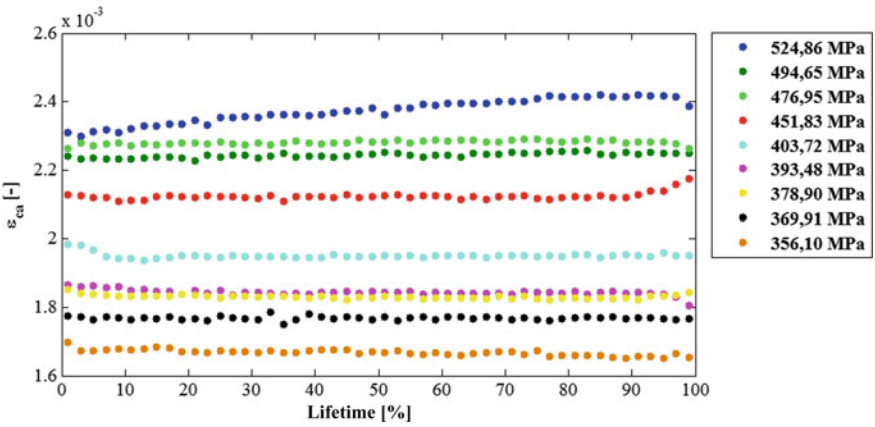

Fig. 5.4 Material B: strain response to loading amplitudes of stress

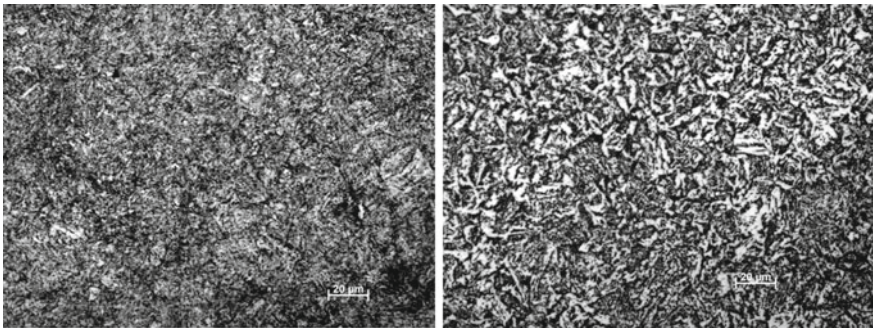

Fig. 5.5 Comparison of microstructure: on the left—the material A: on the right—material B

5.4 Analysis of Microstructure

The explanation of those high differences in cyclic properties for comparing steels is necessary to seek in microstructure of the steels. Specimens of material for metallographic analysis were prepared by conventional techniques—gradual grinding, polishing and etching.

The difference of microstructure is possible to see also from simple optical metallography of both steels (see Fig. 5.5). Microstructure of Material A is the fine grained homogenous sorbitic—typical microstructure after well proper heat treatment process.

Microstructure of Material B reveal the presence of thickened carbides and the boundaries of the original austenitic grains is the result of different temperatures but mainly longer tempering time in the heat treatment process, which can be found by more carefully reading in the Table 5.2 (different time and medium for hardening and tempering processes).

5.5 Conclusions

In this study was present briefly the selected analysis of fatigue properties [3] of steel AISI 4340 (34CrNiMo-6). Properties of steel were analyzed for two ways of their heat treatment. The obtained results remark to the key task of microstructure for the fatigue behavior of steel alloys. Identical chemical composition of metallic materials does not guarantee the identical mechanical properties (mainly cyclic properties). Two ways of heat treatment (with relatively small differences) lead to the non-significant difference in Brinell hardness, 20% difference in tensile strength but between 50 and 60% difference in allowable loading amplitudes throughout the whole lifetime region.

Acknowledgements This work was supported by the Research & Development Operational Programme funded by the ERDF ITMS: 26240220084 Science city Bratislava and by the Slovak Research and Development Agency under the contract No. APVV-17-0666.
The presented contribution has been prepared under project LO1502 "Development of the Regional Technological Institute" under the auspices of the National Sustainability Programme I of the Ministry of Education of the Czech Republic aimed to support research, experimental development and innovation.

References

1. Basquin OH (1910) Proc ASTM 10:625
2. Klesnil M, et al (1993) Cyclic deformation and fatigue of metals. Elsevier
3. Ďurka R, Margetin M, Šulko M (2012) Multiaxial fatigue testing methods. In: Proceedings. of 14th international conference "Applied Mechanics 2012", pp 29–32, Pilsen, The University of West Bohemia

Chapter 6
Effect of Heat Treatment on High-Temperature Low-Cycle Fatigue Behavior of Nickel-Based GH4169 Alloy

Xu-Min Zhu, Xian-Cheng Zhang, Shan-Tung Tu, Run-Zi Wang and Xu Zeng

Abstract The effect of heat treatment on the strain-controlled fatigue behavior of Nickel-based GH4169 alloy at 650 °C was investigated. The volume fraction of δ phase increases as the longer solution annealing time. The maximum phase fraction reaches 13.79% after double-aging heat treatment. At the same time the yield strength and the tensile strength of GH4169 alloy decrease gradually. The heat treatment had almost no effect on fatigue life at strain amplitude higher than 0.6%. However, the fatigue life slightly increased with increasing the solution annealing time at strain amplitude lower than 0.5%. The alloy does not exhibit dual-slope Coffin-Manson relationships at 650 °C. The needle-like δ phase obstruct movement of dislocations. This makes the alloy exhibited the high-temperature fatigue life higher than the room-temperature fatigue life at low strain amplitude.

Keywords High-temperature · Low cycle fatigue · δ phase

6.1 Introduction

The precipitation-strengthened nickel-based superalloy, GH4169, has similar microstructure and mechanical properties to those of Inconel 718. This alloy has been widely used in aviation, aerospace and nuclear industries in China due to its high performance/price ratio, good formability and weldability [1, 2]. The components fabricated by nickel-based superalloy, such as aircraft turbine disks, often undergo fatigue loading. The cyclic loading could cause the low cycle fatigue (LCF) failure. Hence, it is very important to identify the LCF behavior and mechanism of GH4169 superalloy.

Several investigations have been concentrated in reflecting the effects of microstructure, temperature, loading condition on the LCF behavior of Inconel 718 alloy Earlier studies regarding microstructural effect on the deformation behavior

X.-M. Zhu · X.-C. Zhang (✉) · S.-T. Tu · R.-Z. Wang · X. Zeng
Key Laboratory of Pressure Systems and Safety, MOE, East China University of Science and Technology, Shanghai 200237, People's Republic of China
e-mail: xczhang@ecust.edu.cn

J.A.F.O. Correia et al. (eds.), *Mechanical Fatigue of Metals*, Structural Integrity 7,
https://doi.org/10.1007/978-3-030-13980-3_6

and LCF of IN 718 have been reported by Merrick [3], Fournier and Pineau [4], Sanders et al. [5], Worthem et al. [6], Rao et al. [7], Bhattacharyya et al. [8], Xiao et al. [9, 10], and recently Maderbacher et al. [11]. Merrick [3] investigated the grain size effect on LCF life of Inconel 718 alloy. It was found that the fatigue life decreased with increasing the grain size. On the other hand, the GH4169 or Inconel 718 alloy was mainly strengthened by Ni3Nb type γ'' precipitation and partially by Ni3Al type γ' precipitation. A small degree of fatigue hardening quickly followed by fatigue softening was often found during the fatigue process, which might be attributed to the formation of intense slip bands and the shear and possible dissolution of or precipitates [4, 11]. The regularly spaced arrays of deformation bands were often observed at high strain amplitudes [5, 7] and their density generally increased with increase in number of cycles [8]. The experimental results by Worthem et al. [6] and Xiao et al. [9] indicated that the deformation band spacing was obviously influenced by the distribution and movement of dislocation. In addition to the and precipitates, the precipitates at grain boundaries were often formed during heat treatments (HTs) for IN718 alloy [12]. The phase has similar chemical compositions to the primary strengthening phase, implying that the increment of volume fraction of phase could lead to the decrement of volume fraction of phase. It was generally believed that the presence of phase with moderate volume fraction would improve the creep resistance of IN718 since it is beneficial in enhancing ductility and toughness [13].

Fewer reports r regarding the detail of effect of amount and distribution of precipitates on the LCF behavior and C-M relationship of GH4169 or IN718 alloy at high-temperature was available. The aim of this paper was to identify the volume fraction of δ phase on the on high-temperature LCF behavior of GH4169 alloy. The volume fraction of δ phase was changed by changing the parameters used in HTs.

6.2 Experimental Procedures

The material used in this study was Nickel-based GH4169 alloy which was provided by Fushun Special Steel Shares CO, LTD, China. The as-received alloy was supplied in the form of hot rolling bar with the diameter of 60 mm and average grain size of 8–9 μm. The chemical compositions of the alloy were listed in Table 6.1. The alloy has the microstructure consisting of an austenitic face-centered cubic (FCC)-Ni matrix strengthened by the precipitation of γ' [Ll2, Ni3(Ti–Al)] and γ'' [DO22, Ni3(Nb–Ti)] particles and Ni3Nb δ phase. The δ phase usually precipitated at grain boundaries and intragranular twinning interfaces on a certain orientation after HTs.

Table 6.1 Chemical composition (wt%) of GH4169 alloy with a diameter of 60 mm

Ni	Cr	Mo	Al	Ti	Nb + Ta	Mn	Si	C	Fe
52.16	19.05	3.00	0.50	0.93–0.92	5.17	0.03	0.10	0.033–0.031	Other

In order to investigate the effect of volume fraction of δ phase on LCF behavior of GH4169 superalloy, three different heat treatments (HTs) were carried out in an electric resistance-heating furnace equipped with a programmable temperature controller. After the furnace temperature reached a predetermined temperature, the specimens with dimensions of 8 × 6 × 5 mm used for micro structural observation and blank specimens with dimensions of Φ17 × 108 mm used for fatigue tests and tensile tests were put into the furnace. Each HT contained two different steps, the solution annealing and the subsequent aging. The main difference among different HTs was the parameters used in the solution annealing, as listed in Table 6.2, where AC denoted the air cooling. After solution annealing, the specimens were subjected to the conventional ageing treatment at 720 °C for 8 h followed by cooling at 50 °C/h to 620 °C and aging at 620 °C for a further 8 h, and then finishing with an AC to RT.

Cylindrical LCF specimens shown in Fig. 6.1.

LCF tests were performed in air with a symmetrical triangular strain-wave cycle. Tests were carried out at 650 °C with six different total strain amplitudes of ±0.4, ±0.45, ±0.5, ±0.6, ±0.8, ±1.0, ±1.2% at a constant strain rate of 8×10^{-3} s^{-1}. Strain was measured during the LCF test by using an extensometer mounted in the gauge section of specimen.

Table 6.2 The processing parameters used for solution annealing in different HTs

HT1	960 °C for 1 h, AC to 720 °C
HT2	960 °C for 1 h, AC to 900 °C, 900 °C for 4 h, 960 °C for 1 h, AC to 720 °C
HT3	960 °C for 1 h, AC to 900 °C, 900 °C for 20 h, 960 °C for 1 h, AC to 720 °C

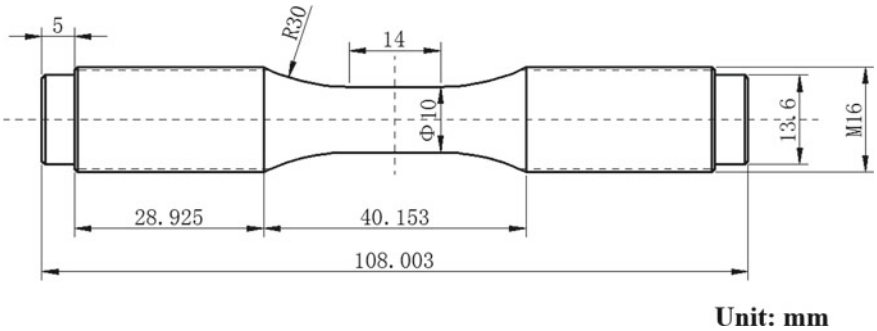

Fig. 6.1 Specimen of low cycle fatigue at 650 °C with a diameter of Φ10 mm

6.3 Result and Discussion

The microstructures of as-received and heat-treated GH4169 alloy are shown in Fig. 6.2. By comparing with the as-received material the grain sizes of the alloy are almost not changed after heat treatments. However, the heat treatment will lead to the precipitation of δ phase at the grain boundaries, as indicated by the arrows in Fig. 6.3a–c. Some discretely short-rod like and granular δ phase precipitates at the grain boundaries within the alloy after HT1. After HT2, the continuous δ phase precipitates along grain boundaries and some needle-like δ phase precipitates along twin boundaries in the grains. After HT3, lots of coarse δ phase precipitates at the grain boundaries. The volume fraction of δ phase in the alloy after three HTs are measured by Image-pro plus software. The volume fractions of δ phase in GH4169 alloy after HT1, HT2 and HT3 are respectively 2.71%, 9.13% and 13.79%. The yield strength as well as the tensile strength of GH4169 alloy decrease gradually with increasing the volume fraction of δ phase in the alloy. As the volume fraction of δ phase increases from 2.71 to 13.79%, the yield strength of GH4169 alloy at room temperature decreases by around 120 MPa. This result indicates that the volume fraction of δ would have an obvious influence on the strength of GH4169 alloy.

After three different heat treatments, the results of high temperature and low cycle fatigue test of alloy GH4169 with different δ-phase content at 650 °C are summarized

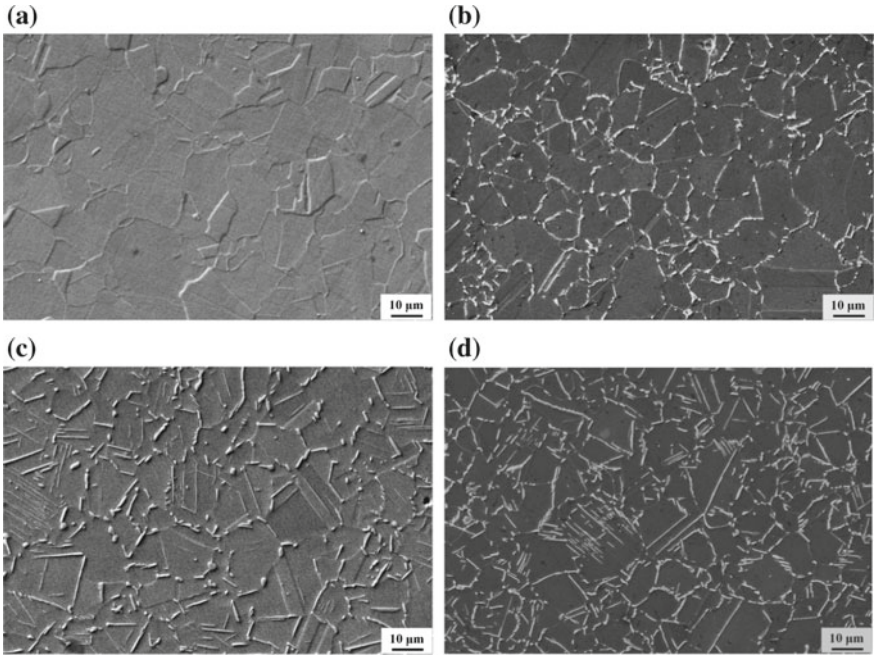

Fig. 6.2 Microstructures of **a** as-received alloy, and alloys after, **b** HT1, **c** HT2, and **d** HT3

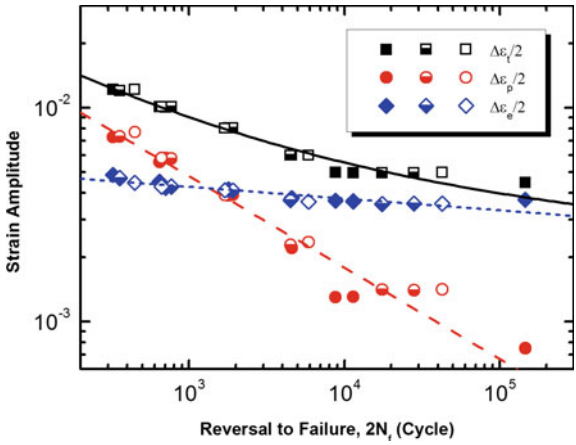

Fig. 6.3 Low cycle fatigue life of GH4169 alloy under 650 °C

in Fig. 6.3. The strain-life curve contains a total of three curves, which are elastic strain-life curve, plastic strain-life curve and total strain-life curve. It can be seen from the figure that the elastic line representing the relationship between the elastic strain amplitude (Δεe/2) and the number of failure reversals (2Nf) of the alloys heat-treated by HT1, HT2 and HT3 is a straight line. The plastic line representing the relationship between the plastic strain amplitude (Δεp/2) and the number of failure reversals (2Nf) is also a straight line.

The results show that the fatigue life of alloys treated with different processes with the increase of strain amplitude decreases. At the same time, the alloys annealed by HT1, HT2 and HT3 showed similar fatigue life at strain rates of 1.2%, 1.0%, 0.8% and 0.6% respectively. At a small strain amplitude of 0.5%, the fatigue life has a certain degree of dispersion, while its life expectancy is significantly affected by the δ phase content. The fatigue life of the HT1 alloy was 5700 cycles and 4382 cycles, respectively. The fatigue life of the HT2 heat-treated alloy is 14,053 cycles and 8759 cycles respectively. The fatigue life of the HT3 heat-treated alloy was 21,345 cycles. It can be seen that from HT1 to HT3 heat treatment, the fatigue life of the alloy at 0.5% of the smaller strain amplitude is gradually increased.

As shown in Fig. 6.4. More secondary cracks appear on the fracture cross-section of the HT1 specimen when the at a strain amplitude of ±0.5%. Non-uniform deformation may cause more secondary cracks at low strain amplitudes. This also make the failure life of HT3 group to be higher than the HT1 and HT2 groups at this strain amplitude although they have higher yield strength.

Temperature is one of the important factors affecting the fatigue properties of materials. Under normal circumstances, at higher temperatures, the material's fatigue resistance decreases with increasing temperature. However, for the GH4169 alloy made from domestic turbine disk, the influence of temperature on its fatigue life is relatively complicated. GH4169 alloy at room temperature and 650 °C low cycle fatigue life comparison shown in Fig. 6.5. On the one hand, the temperature has a great effect on the decrease of fatigue life under high strain amplitude. The fatigue

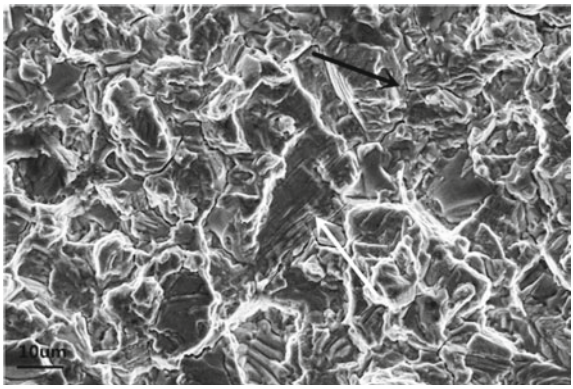

Fig. 6.4 Secondary cracks with HT2 of strain amplitude $\Delta\varepsilon t/2 = 0.5\%$

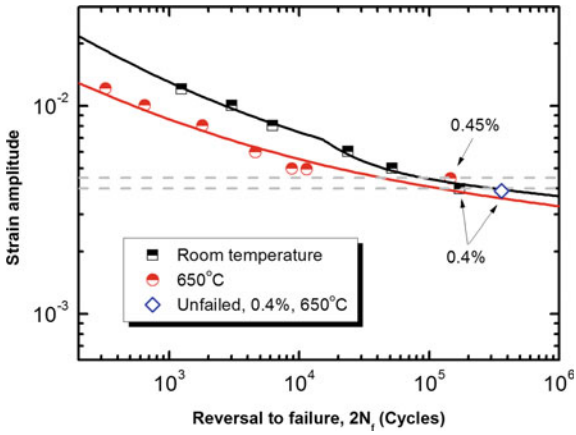

Fig. 6.5 Comparison of low cycle fatigue life of GH4169 alloy between 650 °C and room temperature

life of the alloy at 650 °C is much less than the fatigue life at room temperature. On the other hand, at lower strain rates, the tendency of this fatigue life to decrease rapidly and the effect of temperature on fatigue life reduction at lower strain rates is small. Under the condition of 650 °C and 0.45% strain, the fatigue life of the alloy is 73,054 cycles, which is close to the fatigue life of 0.4% strain at room temperature. However, under the conditions of strain rate of 0.4% at 650 °C, the fatigue life of the alloy exceeds 180,000 cycles without fatigue failure, which is far greater than the fatigue life of the alloy at room temperature. It is possible that the fatigue life of the alloy at 650 °C in the strain amplitude range of 0.4–0.5% is greater than that at room temperature.

6.4 Conclusion

(1) After heat treatment of Φ60 mm GH4169 alloy with HT1, HT2 and HT3, the amount of δ phase precipitated by HT1 was the least, the content increased after HT2 heat treatment, and reached the maximum after HT3 heat treatment.
(2) When the strain amplitude is higher than 0.6%, the effect of volume fraction of δ phase on the fatigue life of GH4169 alloy cannot be distinguished. However, increasing the volume fraction of δ phase had a beneficial effect on the increment of fatigue life at strain amplitude lower 0.5%. In such a case, the fatigue striations cannot be identified and the plastic deformation traces can be discerned on the facets of the fracture surface for the specimen with high volume fraction of δ phase.
(3) The temperature has an important influence on the bilinear behavior of GH4169 alloy. The alloy does not have bilinear behavior at 650 °C. The temperature has a complex effect on the fatigue life of the alloy. The transition from bilinear behavior to single linear behavior leads to complex changes in alloy fatigue life at different temperatures.

References

1. Rao GA, Kumar M, Srinivas M, Sarma DS (2003) Mater Sci Eng A 355:114–125
2. Baccino R, Moret F, Pellerin F (2000) Mater Des 21:345–350
3. Merrick HF (1974) Metall Trans 5:891–897
4. Fournier D, Pineau A (1977) Metall Trans 8:1095–1105
5. Sanders TH, Frishmuth RE, Embley GT (1981) Metall Trans A 12:1003–1010
6. Worthem DW, Robertson IM, Leckie FA (1990) Metall Trans A 21:3215–3220
7. Rao BSK, Kalluri S, Halford GR, McGraw MA (1995) Scr Metall 32:493–498
8. Bhattacharyya A, Sastry GVS, Kutumbarao VV (1999) J Mater Sci 34:587–591
9. Xiao L, Chen DL, Chaturvedi MC (2005) Scr Metall 52:603–607
10. Xiao L, Chaturvedi MC, Chen DL (2005) Metall Trans 36:2671–2684
11. Maderbacher H, Oberwinkler B, Stoschka HP, Mater Sci Eng A586(2013):123–131
12. Azadian S, Wei LY, Warren R (2004) Mater Charact 53:7–16
13. Chen W, Chaturdevi MC (1997) Acta Mater 45:2735–2746

Chapter 7
High Temperature Fatigue Behaviour of Secondary AlSi7Cu3Mg Alloys

Alessandro De Mori, Giulio Timelli and Filippo Berto

Abstract The high temperature fatigue behaviour of secondary AlSi7Cu3Mg alloys has been investigated. The alloy has been solubilized and aged for different times to obtain the age-hardening profile. The peak hardness is reached at 180 °C after 4 h ageing treatment. Further, the hardness stabilizes showing a plateau in the range between 5 and 10 hours of ageing treatment. The heat treatment leads to a complete dissolution of Cu-rich phases, spheroidization of eutectic Si particles and precipitation inside the α-Al matrix. Several fatigue tests have been carried out on selected heat-treated specimens both at room and elevated temperatures (200 and 300 °C). The obtained results show how the fatigue strength decreases with increasing the testing temperature.

Keywords Al–Si alloys · Foundry · High temperature fatigue · Heat treatment

7.1 Introduction

Due to excellent castability, low weight, good corrosion resistance and mechanical properties, the Al–Si foundry alloys are nowadays the most used commercial Al casting alloys for several automotive parts such as engine blocks or cylinder heads [1, 2]. It is well-known how these components are applied at extreme working conditions. Due to high combustion pressure, a temperature up to 300 °C can be reached, far beyond the limit for existing Al–Si casting grades. A temperature of 200 °C is generally considered as the threshold for the rapid degradation of the mechanical properties of Al–Si alloys [1–4]. Therefore, a breakthrough development is needed for engine materials.

A. De Mori (✉) · G. Timelli
Department of Management and Engineering, University of Padova, 36100 Vicenza, Italy
e-mail: alessandro.demori@phd.unipd.it

F. Berto
Department of Engineering Design and Materials, Norwegian University of Science and Technology, 7491 Trondheim, Norway

J.A.F.O. Correia et al. (eds.), *Mechanical Fatigue of Metals*, Structural Integrity 7,
https://doi.org/10.1007/978-3-030-13980-3_7

The post-casting heat treatment plays a key role to improve the high temperature mechanical properties of Al–Si alloys due to precipitation strengthening. One of the most common heat treatment for cylinder heads is the over-aged T7 condition, which is characterised by incoherent precipitation that guarantees higher ductility at the expense of strength [5]. However, the improvement provided by the heat treatment could be limited when using secondary Al alloys, which show lower cost than primary ones, but also small amounts of elements and impurities which can negatively affect the final mechanical properties [6].

Most of research activities paid attention about mechanical properties at room temperature. On the contrary, data regarding high temperature fatigue behaviour of the Al–Si alloys are few, despite their use and diffusion.

The aim of this work is to characterize the high temperature fatigue behaviour of secondary unmodified AlSi7Cu3Mg foundry alloys, generally used for automotive engine production, and to correlate the results with the microstructural properties of the material.

7.2 Experimental Procedure

7.2.1 Casting Parameters

An AlSi7Mg0.3 alloy was used as a baseline material. It was supplied in the form of commercial foundry ingots produced by recycling scrap aluminium. Addition of Ti was made to the melt in the form of commercial Al–10Ti master alloy, which was added to the molten metal as waffle ingots. Commercial purity Cu was also used to achieve the chemical composition of EN AC-46300 alloy (equivalent to the US designation A320).

The material was melted in a 12 kg SiC crucible in an electric resistance furnace set up at 760 ± 5 °C. The melt was stirred and surface skimmed prior to pour. The chemical composition was analysed by optical emission spectrometry on specimens separately poured at the beginning and at the end of the casting trial; the average composition of the alloy is listed in Table 7.1.

The castings were produced by using a steel mould, as proposed in the document CEN/TR 16748:2014 [7]. The cylindrical bars were then sectioned from the castings. A semi-permanent layer of boron nitride coating was sprayed on the steel die walls at temperature of about 200 °C according to standard foundry practice. Before pouring, the temperature of the die was increased to 250 ± 2 °C. The temperature was moni-

Table 7.1 Chemical composition of the investigated AlSi7Cu3Mg alloy (wt%)

Si	Fe	Cu	Mn	Mg	Zn	Cr	Ti	Al
6.713	0.416	3.56	0.287	0.320	0.05	0.013	0.092	bal.

tored by means of thermocouples embedded in the die. The working temperature in the die was in the range of 250–350 °C, which could guarantee an average value of secondary dendritic arm spacing (SDAS) around 20 μm.

7.2.2 Heat Treatment and Hardness Measurements

The produced castings were solution heat-treated inside an air circulating resistance furnace at 485 °C for 24 h and then water quenched at room temperature. The solution temperature was selected according to the results indicated in Ref. [4]. The artificial ageing was performed at 180 °C for different times, in the range between 1 to 10 hours.

In order to obtain the ageing curve for the AlSi7Cu3Mg alloy, Brinell hardness measurements were carried out by using a load of 62.5 kgf, an indenter diameter of 2.5 mm, according to the standard ASTM E10-17. An average over three readings was taken to assess hardness value presented for each condition.

7.2.3 Fatigue Testing

The cyclic tests were performed both at room- and high-temperature on specimens previously aged at 180 °C for 8 h. The fatigue test specimens were machined from produced castings with a total length of 175 mm, a gauge length and diameter of 65 and 10 mm, respectively.

The room-temperature load-controlled fatigue tests were conducted using a 100 kN fatigue testing system at a stress ratio (minimum stress divided by maximum stress) of $R = 0.01$ and frequency of 25 s^{-1}. High temperature fatigue testing was carried out at 200 and 300 °C, respectively, with the aforementioned stress ratio inside an air circulating furnace, integrated in the fatigue testing machine, at a frequency of 50 s^{-1}. Before fatigue testing, each specimen was maintained for 30 min at testing temperature. If the sample survived up to a fatigue cycle of 2×10^6, then the life cycle was considered to have an infinite fatigue life. A sine cyclic waveform was used during testing.

7.2.4 Microstructural Investigations

The microstructures of as-cast and heat-treated specimens were examined with an optical microscopy equipped with a quantitative image analyser. The samples were cut transversally close to final fracture, and mechanically prepared to a 3-μm finish with diamond paste and, finally, polished with a commercial fine silica slurry. The eutectic Si characteristics such as the equivalent diameter and roundness factor, which

is here calculated as $P^2/4\pi A$, where P is perimeter and A is the area of the particle, were measured from different micrographs to obtain a statistical average.

7.3 Results and Discussion

7.3.1 Age-Hardening Response in the AlSi7Cu3Mg Alloy

The hardness of the artificially aged specimens as a function of the ageing time is shown in Fig. 7.1. While the as-cast AlSi7Cu3Mg alloy shows hardness value of 90 ± 3 HB, the as-quenched alloy shows a hardness of 84 ± 3 HB. As reported in literature [5], the age-hardening phenomenon is represented by the hardness increase at the early stage of ageing, followed by the peak-hardness and a decrease due to over-ageing. The ageing treatment generally increases the mechanical response of the alloy; in particular, the maximum value of hardness (138 ± 3 HB) is reached after 4 h at 180 °C. Then, a stable value of about 135 HB is shown when ageing time increases from 5 to 10 hours.

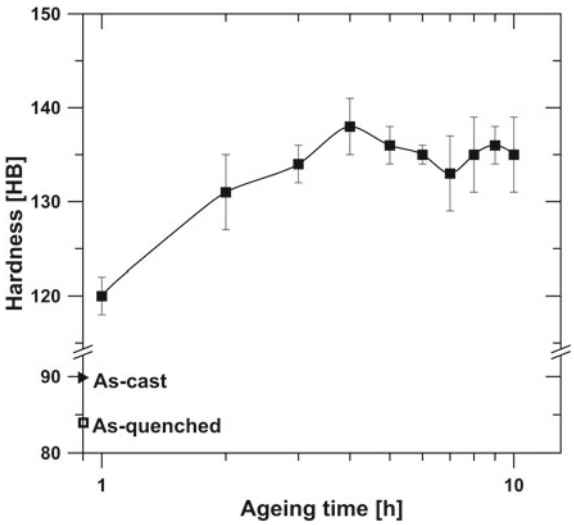

Fig. 7.1 Age-hardening curve of the experimental AlSi7Cu3Mg alloy artificially aged at 180 °C

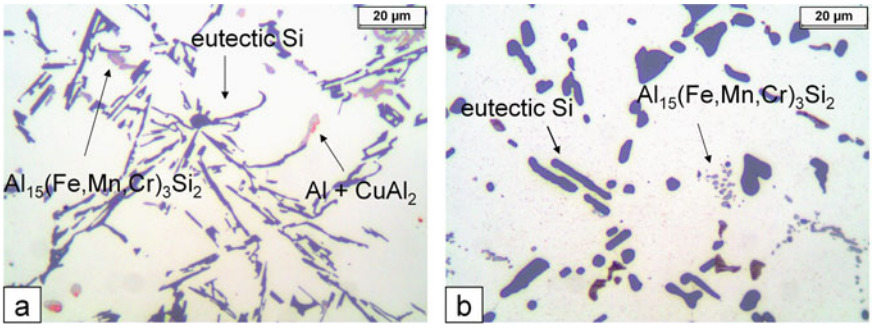

Fig. 7.2 Typical microstructure of the AlSi7Cu3Mg alloy in **a** as-cast and **b** heat-treated conditions

7.3.2 Microstructural Observations

Figure 7.2 shows typical as-cast and heat-treated microstructures observed in the specimens tested at room temperature. Both microstructures consist mainly of primary dendritic α-Al phase and eutectic Si. The morphology of eutectic Si particles changes from unmodified, typical of as-cast temper, to a globular shape after heat treatment. The roundness of eutectic Si particles changes from ~6 in as-cast condition to ~2 in heat-treated alloy, thus indicating that the 24 h solution heat treatment was not sufficient to completely spheroidize the eutectic Si particles. The equivalent diameter of Si particles increases from 3.5 ± 2.3 to 4.8 ± 2.1 μm after heat treatment, indicating coarsening phenomena of the particles [8]. Furthermore, the dissolution of Cu-containing phases due to heat treatment can be also observed, while Fe-rich particles located in the interdendritic regions only partially dissolved, indicating the thermodynamic stability at solution temperatures [1]. The performed heat treatment also led to the precipitation of finely dispersed particles throughout the α-Al matrix [9].

Figure 7.3 shows typical heat-treated microstructures after fatigue testing at 200 and 300 °C, respectively. The permanence at high temperature did not change the characteristics of eutectic Si particle, while the coarsening of the strengthening phases occurred at 300 °C, thus influencing the mechanical response of the material.

7.3.3 Fatigue Characterization

The plot of cyclic stress amplitude and the number of cycles to failure during room- and high-temperature fatigue testing for the investigated AlSi7Cu3Mg alloy is shown in Fig. 7.4.

In general, it is observed how higher stress amplitudes correspond to lower number of cycles before failure. The experimental data show similar trends except the material tested at room temperature where the slope has a steeper gradient. Upon increasing

the testing temperature, the maximum stress amplitude decreases and this is related to a reduction of the material static strength. While the fatigue behaviour at 200 °C is comparable to that at room temperature, the fatigue properties significantly decreases at 300 °C due to the coarsening of strengthening precipitates (see Fig. 7.3).

7.4 Conclusions

The high temperature fatigue behaviour of secondary unmodified AlSi7Cu3Mg foundry alloys has been evaluated together with the microstructural characteristics of the material. The following conclusions can be drawn from this study.

- The alloy reaches the maximum hardness after 4-hours ageing treatment at 180 °C.

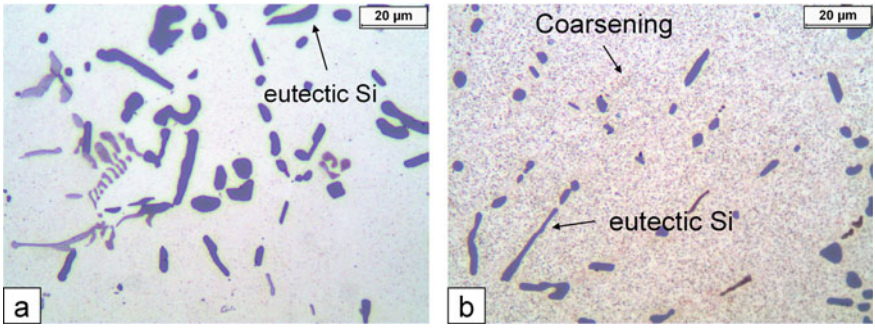

Fig. 7.3 Microstructures of heat-treated AlSi7Cu3Mg alloy after fatigue testing at **a** 200 and **b** 300 °C

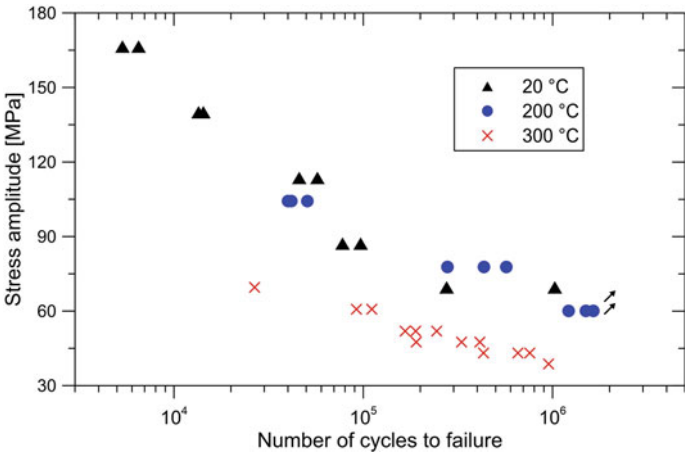

Fig. 7.4 Fatigue life of heat-treated AlSi7Cu3Mg alloy at different testing temperatures

- The solution heat treatment at 485 °C for 24 h does not complete the spheroidization of the eutectic Si particles, but leads to a complete dissolution of Cu-bearing phases. On the contrary, the Fe-rich particles are stable and do not dissolve in the α-Al matrix during heat treatment.
- The fatigue life of the heat-treated alloy decreases with increasing the stress amplitude.
- Increasing the testing temperature from 20 to 200 °C causes the decrease of the fatigue strength. However, while up to 200 °C the behaviour is minimally affected by temperature, the mechanical response at 300 °C significantly decreases due to the coarsening of the strengthening precipitates.

References

1. Shaha SK, Czerwinski F, Kasprzak W, Friedman J, Chen DL (2017) Ageing characteristics and high-temperature tensile properties of Al–Si–Cu–Mg alloys with micro-additions of Mo and Mn. Mater Sci Eng A 684:726–736
2. Yang Y, Zhong S-Y, Chen Z, Wang M, Ma N, Wang H (2015) Effect of Cr content and heat-treatment on the high temperature strength of eutectic Al–Si alloys. J Alloy Compd 647:63–69
3. Gariboldi E, Lemke JN, Rovatti L, Baer O, Timelli G, Bonollo F (2018) High-temperature behavior of high-pressure diecast alloys based on the Al–Si–Cu system: the role played by chemical composition. Metals 8(348):1–20
4. Rakhmonov J, Timelli G, Bonollo F (2017) Characterization of the solidification path and microstructure of secondary Al–7Si–3Cu–0.3Mg alloy with Zr, V and Ni additions. Mater Charact 128:100–108
5. Li RX, Li RD, Zhao YH, He LZ, Li CX, Guan HR, Hu ZQ (2004) Age-hardening behavior of cast Al–Si base alloy. Mater Lett 58:2096–2101
6. Camicia G, Timelli G (2016) Grain refinement of gravity die cast secondary AlSi7Cu3Mg alloys for automotive cylinder heads. Trans Nonferr Metals Soc China 26:1211–1221
7. CEN/TR 16748:2014, Aluminium and aluminium alloys—mechanical potential of Al–Si alloys for high pressure, low pressure and gravity die casting
8. Di Giovanni MT, Cerri E, Saito T, Akhtar S, Åsholt P, Li Y, Di Sabatino M (2016) Effect of copper additions and heat treatment optimization of Al–7% Si Aluminium Alloy. La Metall Ital 108:43–47
9. Yang H, Ji S, Yang W, Wang Y, Fan Z (2015) Effect of Mg level on the microstructure and mechanical properties of die-cast Al–Si–Cu alloys. Mater Sci Eng A 642:340–350

Chapter 8
Mean Stress Effect on Fatigue Behavior of Austenitic Stainless Steel in Air and LWR Conditions

W. Chen, P. Spätig and H. P. Seifert

Abstract In this paper, mean stress influence and cooperative effects associated with light water reactor (LWR) environmental factors were studied through load-controlled fatigue tests with cylindrical hollow specimens. Positive (+10, +50 MPa) and negative (−10, −20 MPa) mean stresses were applied and both showed beneficial influence on fatigue life due to cyclic hardening, which results in smaller strain amplitude under the same stress amplitude. The increase in fatigue life was found to depend on mean stress and testing environments. The increase (1.8–2.2x) in fatigue life with +50 MPa mean stress in boiling water reactor/hydrogen water chemistry (BWR/HWC) is smaller than that in air (3.0–3.4x), while the increase with −20 MPa mean stress in both environments is approximately similar. −20 MPa mean stress enhances the resistance to crack initiation as observed with optical microscopy (OM) observations of fracture surfaces and wall cross-sections of tested specimens.

Keywords Fatigue · Mean stress · Light water reactor (LWR) · Austenitic stainless steel (SS)

8.1 Introduction

Mean stress is normally induced from asymmetric cyclic loading. Dead weight, water pressure and weld residual stress in nuclear power plant (NPP) may create mean stress in the internal components of pressure vessels and reactor coolant piping system [1–4]. These components are mainly fabricated with austenitic stainless steels (SSs) owing to their good corrosion and fatigue resistance. Although a great deal of fatigue studies have been carried out on austenitic SSs in air and LWR environment, mean stress effect and cooperative LWR environmental effects on fatigue life are not fully addressed and understood. JSME and ASME Codes were formed to guide the fatigue design [5–7]. In ANL, JSME and ASME Codes, a margin factor in life design is

W. Chen · P. Spätig (✉) · H. P. Seifert
Laboratory for Nuclear Materials, Nuclear Energy and Safety Research Division,
Paul Scherrer Institute, 5232 Villigen-PSI, Switzerland
e-mail: philippe.spatig@psi.ch

J.A.F.O. Correia et al. (eds.), *Mechanical Fatigue of Metals*, Structural Integrity 7,
https://doi.org/10.1007/978-3-030-13980-3_8

introduced to cover the influence of data scatter, size effect, surface finish and loading history on the basis of mean value of strain-controlled test results in air condition [7]. Mean stress effect is absent or obscurely treated in the standard Codes. Thus it is critical to understand mean stress effect under stress-controlled/strain-controlled conditions from a practical view point. Vincent et al. [1] successfully performed tests at constant mean stress and strain range under strain-controlled condition by adjusting the mean strain during the tests. Their results showed that mean stress shortened fatigue life under the same strain range. However, mean strain might affect fatigue strength and mean strain cannot be so large in actual components due to geometrical constraints [8]. Most of the mean stress studies are based on strain-controlled fatigue tests with laboratory standard specimens in air condition, where mean stress tends to be relaxed [9]. The test condition is far from the actual operation condition of austenitic SS components, where complex thermo-mechanical loading and corrosive environments have to be taken into account.

Positive mean stress generally reduces fatigue life while negative mean stress is beneficial to fatigue life. Goodman [10], Gerber [11], Morrow [12], Soderberg [13] methods are commonly applied to correct mean stress effect on fatigue life. These mean stress correction methods mostly applied to high cycle fatigue in carbon and low alloy steels, whose endurance limit is less than the yield stress. However, these methods are not applicable to SSs without modifications since the endurance limit is generally bigger than the yield stress [10]. Recent findings by Spätig et al. show that +50 MPa mean stress increases fatigue life of 316L SS based on load-controlled fatigue tests in LWR environment and in air [14]. Additionally, Solomon also reported that +100 MPa mean stress extended the fatigue life of 304L SS in air and pressurized water reactor (PWR) environment at 150 °C and 300 °C [15, 16]. The non-standard mean stress effect on fatigue life of austenitic SSs is attributed to cyclic hardening that consequently leads to smaller strain amplitude under the same stress amplitude.

8.2 Material and Experimental Procedure

8.2.1 Material and Specimens Fabrication

A solution annealed (non-sensitized) and quenched low-carbon austenitic SS tube section with 219.1 mm outer diameter and 19.5 mm wall thickness was delivered by Sandvik. The chemical composition is 0.011% C, 0.56% Si, 1.77% Mn, 0.031% P, 0.024% S, 17.20% Cr, 2.02% Mo and 11.14% Ni in wt%. The texture-free material has a high share of twin grain boundaries (31%) and a mean grain size of 53 μm (5.23 in ASTM grain size number). Its 0.2% yield stress is equal to 258 MPa at 20 °C and 146 MPa at 300 °C.

Cylindrical hollow fatigue specimens, with outer diameter of 10 mm, wall thickness of 2.5 or 2 mm and gage length of 18 mm, were cut from the delivered tube with

loading axis parallel to the tube longitudinal direction. The surface roughness was measured 0.41 μm (Ra)/3.57 μm (RzD) at inner surface and 0.15 μm (Ra)/1 μm (RzD) at outer surface.

8.2.2 Fatigue Test Facilities and Experimental Conditions

Two fatigue testing facilities were used for tests in high-temperature water (HTW) and in high-temperature air (HTA) respectively. The facility for tests in HTW is described in detail in [17]. Facility for test in HTA consists of a Schenck RMC 100 type electro-mechanical machine and an ATS series 2961 oven.

The HTW was characterized by 288 °C pressurized high-purity hydrogenated water at 100 bar with 150 ppb dissolved hydrogen (DH). The conductivity of the inlet and outlet water was about 0.055 μS/cm. This HTW is also called BWR/HWC. The specimen was heated by the high-temperature pressurized water flowing through the tube with 30 L/h. An extensometer was attached on specimen surface. A sinusoidal waveform at a frequency of 0.17 Hz was applied for testing cycles $\leq 10^5$. Afterwards, the frequency was adjusted to 1 Hz until life end or running up to 10^6 cycles, considered as fatigue strength (σ_{fs}). Fatigue life was defined when the specimen totally broke into two parts or the measured elongation was larger than 1.0 mm.

8.3 Results and Discussion

8.3.1 Fatigue Tests

Load-controlled fatigue tests were conducted both in HTW (BWR/HWC) and in HTA conditions. Their stress-life (S-N) data is plotted in Fig. 8.1. The stress amplitude is in the range of 170 to 250 MPa, where EAF phenomenon occurs. Positive (+10, +50 MPa), negative (−10, −20 MPa) and 0 MPa mean stress was applied. For the strain-controlled tests, the corresponding average stress amplitudes versus fatigue life data ($\overline{\sigma_a}$ vs. N_f) are depicted with green stars in Fig. 8.1a. Extensive tests in air condition are ongoing to obtain data points in the high cycle fatigue (HCF) regime with $N_f > 10^5$.

Both positive (+50 MPa) and negative (−10, −20 MPa) mean stresses increase fatigue life in the two environments, except for +10 MPa mean stress, where no significant effect was found. This is consistent with the findings of Solomon [14] and Spätig et al. [13]. In HTW, −20 MPa mean stress leads to larger fatigue life increase (5.0–7.5x) than +50 MPa mean stress does (1.8–2.2x) when compared with fatigue life without mean stress tests in LCF regime ($N_f < 10^5$). In HTA, −20 MPa and + 50 MPa mean stresses increase the fatigue life by 5.7–6.5 × and 3.0–3.4x, respectively. Comparing the mean stress effect in the two environments, the mean stress beneficial factors on fatigue life of −20 MPa in HTW is close to those in HTA.

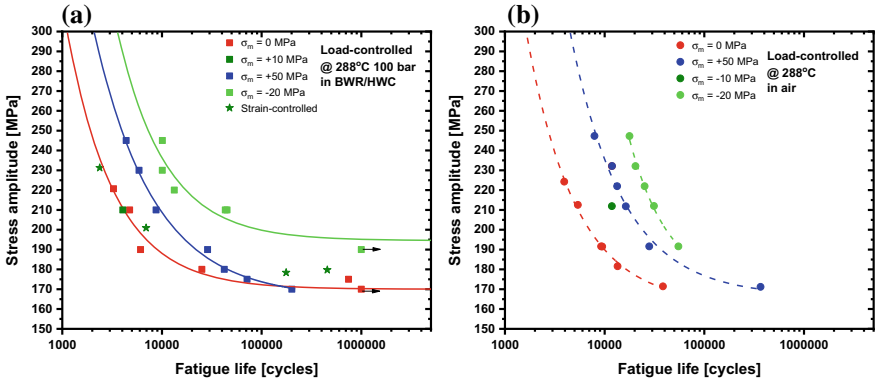

Fig. 8.1 S-N curves of fatigue tests conducted under load-control with different mean stress: **a** in 288 °C BWR/HWC; **b** in 288 °C air condition

However, the beneficial factors of +50 MPa in HTW are smaller than those in HTA. This is due to a larger HTW environment detrimental influence in positive (+50 MPa) mean stress tests than in negative (−20 MPa) mean stress tests. In HTW the fatigue strength (σ_{fs}) increases from 170 MPa at zero mean stress condition to 194 MPa at −20 MPa mean stress. However, +50 MPa mean stress slightly affects fatigue strength in HTW, but more tests with strain amplitude close to the fatigue strength are necessary to assess the mean stress dependence on fatigue strength accurately.

The beneficial effect on fatigue life of both negative and positive mean stresses is tentatively attributed to cyclic hardening reflected as smaller strain amplitude at the same stress amplitude as presented in Fig. 8.2, where the average strain amplitude ($\overline{\varepsilon_a}$) over the whole life was calculated. The slopes of 0 and +50 MPa mean stress data are approximately similar in both environments. In HTW, +10 MPa mean stress slightly

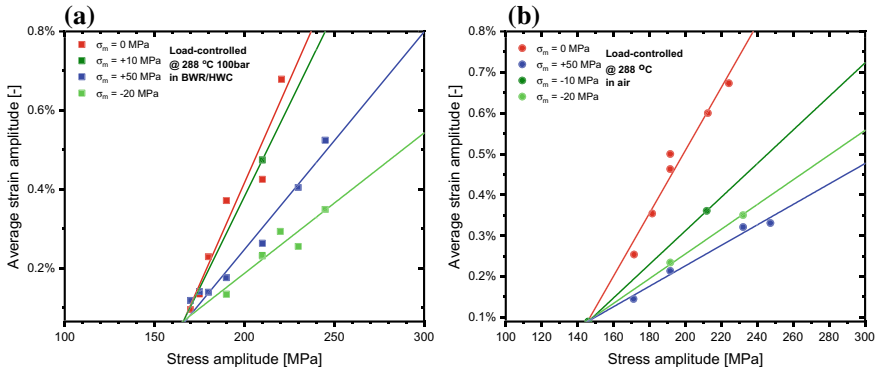

Fig. 8.2 Average strain amplitude versus stress amplitude of fatigue tests (**a**) in 288 °C BWR/HWC (**b**) in 288 °C air under load-controlled condition

hardened the material. −20 MPa mean stress shows stronger hardening effect than +50 MPa mean stress. However, an opposite phenomenon was observed in HTA, where +50 MPa has stronger hardening effect. An approximate −7 MPa mean stress, induced by 100 bar internal water pressure in HTW tests and confirmed via finite element analysis (FEA), may account for the distinct hardening magnitude of −20 and +50 MPa mean stress in the two environments.

8.3.2 Post-test Specimen Characterization

The fracture surfaces of specimens tested in HTW were imaged with optical microscope (OM). Four representative fracture surfaces obtained with $\sigma_a = 210$ MPa and $\sigma_m = 0$, +10, +50, −20 MPa are shown in Fig. 8.3. After long-term exposure to HTW, the oxide layer formed on the fatigue crack surface appears as dark areas that correspond to the fatigue crack shape. All cracks initiated at the inner side and are distributed around the inner wall. However, the fatigue cracking zone of the tests with +10, +50 and −20 MPa mean stresses are smaller than that with zero mean stress, showing a higher resistance to crack initiation. Note that −20 MPa mean stress shows the strongest retardation on crack initiation: except the main crack leading to failure, no small fatigue cracks were observed. This is also confirmed by the OM observations of wall cross-sections along the loading axis in Fig. 8.4, where no crack was observed along the wall cross-section of the specimen with negative mean stress. Larger crack opening and stronger necking in specimens tested with +10 and +50 MPa mean stress is associated with a more intense strain localization and larger ratchetting strain at failure.

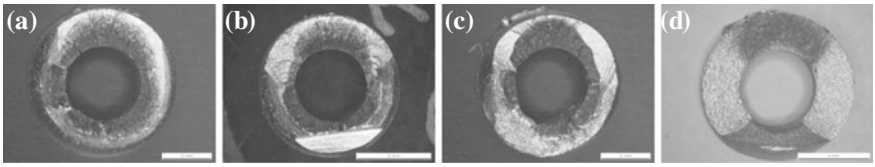

Fig. 8.3 Fracture surfaces of tested specimens with 210 MPa stress amplitude and **a** 0 MPa, **b** +10 MPa, **c** +50 MPa, **d** −20 MPa mean stress under load-control

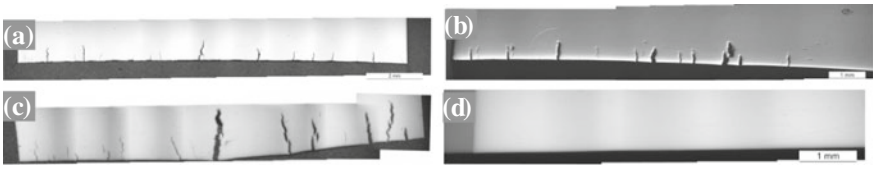

Fig. 8.4 OM images of tested specimens wall cross-sections cut along loading axis. Specimens were tested with $\sigma_a = 210$ MPa, **a** $\sigma_m = 0$ MPa, **b** +10 MPa, **c** +50 MPa, **d** −20 MPa

8.4 Conclusion

In this work, a set of load-controlled fatigue tests with and without mean stress were conducted in BWR/HWC and in air conditions. Both positive (+50 MPa) and negative (−10, −20 MPa) mean stress exhibited a clear increase of fatigue life with dependence on mean stress and testing environment. BWR/HWC shows moderate influence on fatigue life beneficial effect of −20 MPa mean stress. However, the fatigue life increase resulting from the application of +50 MPa mean stress was found smaller in BWR/HWC than in air. The fatigue life beneficial effect of mean stress is attributed to the cyclic hardening, which is reflected as smaller average strain-amplitude at the same stress amplitude. OM observations on fracture surfaces and wall cross-sections show that −20 MPa mean stress strongly retards crack initiation.

Acknowledgements This work was conducted within the frame of the SAFE-II and LEAD research projects and grateful acknowledge goes to the financial support of the Swiss Federal Nuclear Inspectorate (ENSI). The technical assistance and contribution to the mechanical testing of R. Schwenold at Paul Scherrer Institute is appreciated.

References

1. Vincent L, Roux JCL, Taheri S (2012) On the high cycle fatigue behavior of a type 304L stainless steel at room temperature. Int J Fatigue 38:84–91
2. Bae KH, Kim HH, Lee SB (2011) A simple life prediction method for 304L stainless steel structures under fatigue-dominated thermo-mechanical fatigue loadings. Mater Sci Eng A 529:370–377
3. Miksch M, Lenz E, Löhberg R (1985) Loading conditions in horizontal feedwater pipes of LWRs influenced by thermal shock and thermal stratification effects. Nucl Eng Des 48(2):179–187
4. Metzner KJ, Wilke U (2005) European THERFAT project—thermal fatigue evaluation of piping system "Tee"-connections. Nucl Eng Des 235(2–4):473–484 (2005)
5. Miura N (2006) High-cycle fatigue behavior of type 316 stainless steel at 288 °C including mean stress effect. Int J Fatigue 11(28):1618–1625
6. Kamaya M (2017) Influence of strain range on fatigue life reduction of stainless steel in PWR primary water. Fatigue Fract Eng Mater Struct 12(40):2194–2203
7. Magnus D, Bremberg D (2012) Fatigue margins for austinitic stainless steels in ASME boiler and pressure vessel code—a literature study. Swedish Radiation Safety Authority, Sweden
8. Kamaya M, Kawakubo M (2015) Mean stress effect on fatigue strength of stainless steel. Int J Fatigue 74:20–29
9. Facheris G (2014) Cyclic plastic material behavior leading to crack initiation in stainless steel under complex fatigue loading conditions. Doctoral thesis, diss. ETH NO. 21696, ETH Zurich
10. Midmore L (2011) Environmentally assisted fatigue gap analysis and roadmap for future research, 1st edn. Electric Power Research Institute, Palo Alto, California
11. Gerber WZ (1874) Calculation of the allowable stresses in iron structures. Z Bayer Arch Ing-Ver 6:101–110
12. Bae KH (2011) A simple life prediction method for 304L stainless steel structures under fatigue-dominated thermo-mechanical fatigue loadings. Mater Sci Eng A, Struct Mater Prop Microstruct Process (529):370–377
13. Soderberg CR (1930) Factor of safety and working stress. Trans ASME 52(2):13–28 (1930)

14. Spätig P (2015) Mean stress effect on fatigue life of 316L austenitic steel in air and simulated boiling water reactor hydrogen water chemistry environment. In: 17th international conference on environmental degradation of materials in nuclear systems—water reactors. TMS, Ottawa
15. Solomon HD (2005) Influence of mean stress on the fatigue behavior of 304L SS in air and PWR water. In: ASME 2005 pressure vessels and piping conference. ASME, Colorado, pp 87–97
16. Solomon HD (2011) Fatigue limit and hysteresis behavior of type 304L stainless steel in air and PWR water, at 150 °C and 300 °C. In: 15th international conference on environmental degradation. TMS, Colorado, pp 583–603
17. Leber HJ, Ritter S, Seifert HP (2013) Thermo-mechanical and isothermal low-cycle fatigue behavior of type 316L stainless steel in high-temperature water and air. Corros 69(10):1012–1023

Chapter 9
Characterization of the Fatigue Behavior of Mechanical and Thermal Aged Austenitic Power Plant Steel AISI 347

F. Maci, M. Jamrozy, R. Acosta, P. Starke, C. Boller, K. Heckmann, J. Sievers, T. Schopf and F. Walther

Abstract For the comprehensive understanding of the fatigue mechanisms of mechanical and thermally aged materials in power plant reactors, an innovative, resource- and time-optimized approach based on non-destructive testing methods is used. Beside investigations on AISI 347 austenitic stainless steel under cyclic loading, magnetic, resistometric and electrochemical measurement techniques were applied to monitor the proceeding fatigue behavior. Qualitative values indicate surface passivation effects and microstructural changes, which are directly related to fatigue states. In total strain-controlled increase tests, cyclic investigations for the initial and a mechanically and thermal aged condition were carried out under distilled water environment at ambient temperature. In comparison to the initial state, the aging process shows a significant influence on the fatigue behavior with a reduction of the stress amplitude at failure down to 75%.

Keywords AISI 347 · Aging · Strain increase test · Fatigue · Non-destructive testing

F. Maci (✉) · M. Jamrozy · F. Walther
Department of Materials Test Engineering (WPT), TU Dortmund University, 44227 Dortmund, Germany
e-mail: frankel.maci@tu-dortmund.de

R. Acosta · P. Starke · C. Boller
Non-Destructive Testing and Quality Assurance (LZfPQ), Saarland University, 66125 Saarbruecken, Germany

K. Heckmann · J. Sievers
Gesellschaft für Anlagen- und Reaktorsicherheit (GRS) gGmbH, 50667 Cologne, Germany

T. Schopf
Materials Testing Institute (MPA), University of Stuttgart, 70569 Stuttgart, Germany

J.A.F.O. Correia et al. (eds.), *Mechanical Fatigue of Metals*, Structural Integrity 7,
https://doi.org/10.1007/978-3-030-13980-3_9

9.1 Introduction

Materials used in power plants are exposed to aging mechanisms under service conditions that influence the materials' fatigue properties. A cyclic thermal loading, especially through startup and shutdown processes, causes expansions and compressions in a variable high-pressure environment resulting in a reduction of service time due to crack formation and growth. For those applications, generally austenitic stainless steels are well suited, due to their material properties combining high strength, ductility and superior corrosion resistance at elevated temperatures [1]. However, to ensure the integrity of the components throughout the lifetime, innovative, resource- and time-optimized non-destructive testing (NDT) methods are used, with the objective to monitor and estimate the fatigue life during operation. In the study reported here, electrochemical, magnetic and resistometric measurements are combined in order to monitor the proceeding fatigue-related mechanisms, which are relevant for further fatigue life calculation of power plant steels.

9.2 Material and Material Condition

For safety-relevant components in German power plants the niobium-stabilized austenitic stainless steel AISI 347 (X6CrNiNb18-10, 1.4550) is widely used [2]. The chemical composition according to manufacturer's report is given in Table 9.1.

Two material conditions were investigated in form of hourglass specimens (Fig. 9.1). Beside the initial state, an additional aged condition was used. The aging process consisted of cyclic loading under air conditions with the total strain amplitude $\varepsilon_{a,t} = 3 \times 10^{-3}$, constant strain rate $\dot{\varepsilon}_t = 0.4 \times 10^{-3}\ s^{-1}$ and temperature T = 240 °C. After 50% (15,725 cycles) of the specimen's lifetime, the fatigue tests were stopped. This number of cycles was determined statistically in preliminary tests.

Table 9.1 Chemical composition of AISI 347 stainless steel according to manufacturer's report

Alloying elements (wt%)									
C	Cr	Ni	Mn	Si	Nb	P	Co	S	Fe
0.025	18.147	10.064	0.577	0.401	0.402	0.024	0.019	0.0011	Bal.

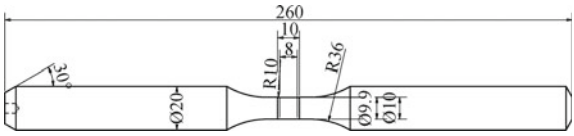

Fig. 9.1 Geometry of fatigue specimen

9.3 Experimental Setup and Procedure

For the characterization of the fatigue behavior, total strain-controlled increase tests (SIT) were carried out under distilled water environment with fully reversed loading, applying the strain ratio $R_\varepsilon = -1$. A servo-hydraulic testing system (Instron 8802, F = ±250 kN) was used. In preliminary calibration tests, the extensometer measured over a gauge length of 89 mm was correlated to a gauge length of 8 mm, positioned within the gauge length of the extensometer and representing the specimen's minimum cross section. For the SIT, the total strain amplitude was increased stepwise starting from $\varepsilon_{a,t,cor,start} = 0.5 \times 10^{-3}$ by $\Delta\varepsilon_{a,t,cor} = 0.5 \times 10^{-3}$ each $\Delta t = 1{,}800$ s under a constant total strain rate of $\dot{\varepsilon}_{t,cor} = 4 \times 10^{-3}\ s^{-1}$ until failure. The temperature during the test was kept constant at 20 °C.

Figure 9.2 shows the experimental setup for fatigue tests performed under distilled water environment using an in situ corrosion cell with measurements taken based on electrochemical, magnetic and resistometric NDT methods.

The working principles of magnetic measurements requires the presence of a magnetic field. Therefore, a constant direct current of $I_{DC} = 10$ A has been applied at the clamping jaws of the testing system. When the current flows through the specimen, the magnetic field can be measured with a Hall sensor. With known voltage and constant direct current, the electrical resistance was determined according to Ohm's law. For the electrochemical measurement a three electrode system is used, which contains the specimen itself acting as a working electrode, a graphite counter electrode and a silver chloride (Ag/AgCl) reference electrode. The data were measured within the separate circuit of the potentiostat (Gamry Interface 1000A).

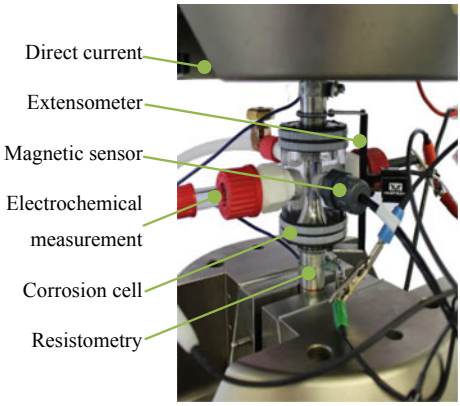

Fig. 9.2 Experimental setup

9.4 Results of Testing and Measurement

From preliminary fatigue tests, lifetime influencing effects can be excluded from the use of distilled water. Therefore, the field of non-destructive testing methods can be extended to characterize the fatigue behavior of AISI 347 stainless steel. Within SIT, a significant influence of the aging process (Fig. 9.4) can be observed when compared to the results shown for the initial state in Fig. 9.3. At the specimens' failure, materials in the initial state achieve a higher strain level of $\varepsilon_{a,t,cor} = 0.95\%$ when compared to the aged condition ($\varepsilon_{a,t,cor} = 0.70\%$). Consequently, the stress amplitude at failure $\sigma_{a,f} = 734$ MPa for the initial state is higher when compared to

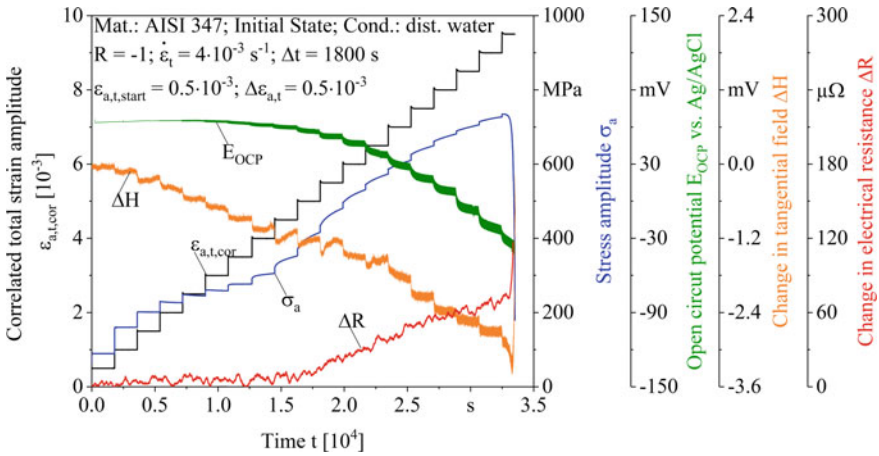

Fig. 9.3 Total strain-controlled increase test for initial state with direct current

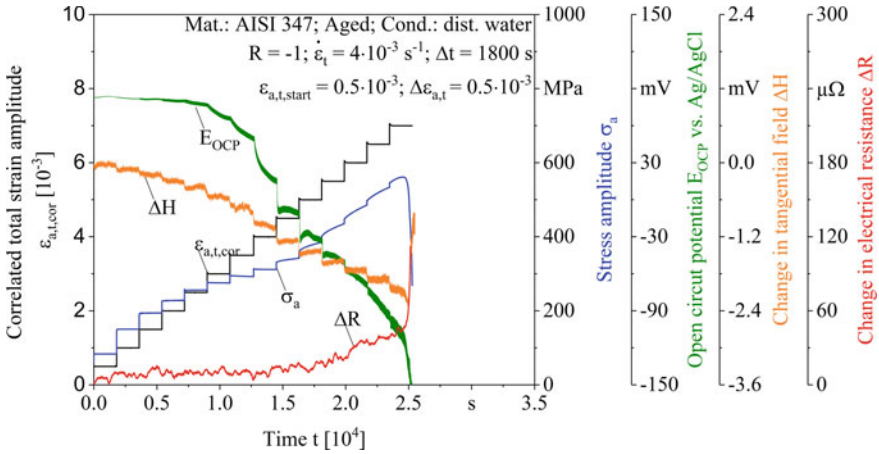

Fig. 9.4 Total strain-controlled increase test for aged condition with direct current

the aged condition ($\sigma_{a,f} = 561$ MPa). Both material states show a qualitatively similar curve in the progression of their stress amplitude. Three sections for the initial state can be determined. At strain levels $0.05\% < \varepsilon_{a,t,cor} < 0.25\%$ an almost analogues relationship between the strain and stress amplitude is observed. The first area represents a linear stress-strain relationship while a transient behavior of the material is observed in the second area respectively. From $0.25\% < \varepsilon_{a,t,cor} < 0.50\%$ a non-analogues relationship of stress-strain is observed. In this second section, the stress amplitude drops and raises again and represents the cyclic softening effect through a decrease in deformation resistance. This is related to dislocation movements on energetically beneficial regions within the microstructure. From $\varepsilon_{a,t,cor} > 0.50\%$ the stress amplitude raises continuously until fracture. This third section represents the cyclic hardening effect that indicates an increase in deformation resistance. This is also related to microstructural changes due to a saturation in dislocation densities and martensitic transformation [1].

For the aged condition, this third section is significantly shorter, resulting in lower stress amplitudes. With the phase transition from paramagnetic austenite to ferromagnetic martensite, the material becomes ferromagnetic, leading to a change in the magnetic field [3]. Generally, with continuous cyclic loading, the resistivity varies with increased defect density. The change in magnetic field and electrical resistance are linked to microstructural changes, which are directly related to the current fatigue state [4, 5]. For both material states the magnetic signal decreases stepwise in accordance with the applied strain, whereas the slope of the electrical resistance is nearly constant up to $\varepsilon_{a,t,cor} = 0.35\%$, which is followed by a continuous increase due to the increase of the defect density. In the SIT for the initial state, the slope of the magnetic signal and the decrease in each step are nearly constant until $\varepsilon_{a,t,cor} = 0.4\%$. From $\varepsilon_{a,t,cor} = 0.4$–$0.7\%$, the slope of each step becomes positive. This behavior is linked to the formation of deformation-induced α'-martensite. At this point, the increase in the defect density can be observed in the increase of the slope of the electrical resistance signal. From $\varepsilon_{a,t,cor} = 0.7\%$, the slope in the magnetic signal changes again, becoming negative. It also gets wider within every step due to the Villari effect and the development of intrusions and extrusions at the specimen surface [3].

In the final step before fracture, a more pronounced decrease in the magnetic signal occurs, indicating the formation of macro cracks which propagated until the specimens' failure. This is also observable in the exponential increase of the electrical resistance [4]. For the aged condition, the magnetic behavior during the test is similar, but through the previous damage from the ageing procedure, the damage evolution process starts earlier and the damage phases described before are shorter. The change in the slope of the signal due to phase transformation starts already at $\varepsilon_{a,t,cor} = 0.25\%$ and shows a positive slope until $\varepsilon_{a,t,cor} = 0.55\%$. For the electrical resistance, it starts already at $\varepsilon_{a,t,cor} = 0.45\%$. From $\varepsilon_{a,t,cor} = 0.55\%$, the magnetic signal changes its slope and gets wider. In the final step, there is also a pronounced decrease in the magnetic signal and increase in the electrical resistance signal before specimen failure.

As an additional reference, the open circuit potential (E_{OCP}) is used to detect surface-related changes i.e. passivation effects and cracks of passive layers, which result in a change in the E_{OCP} signal [5]. The E_{OCP} has been measured and compared

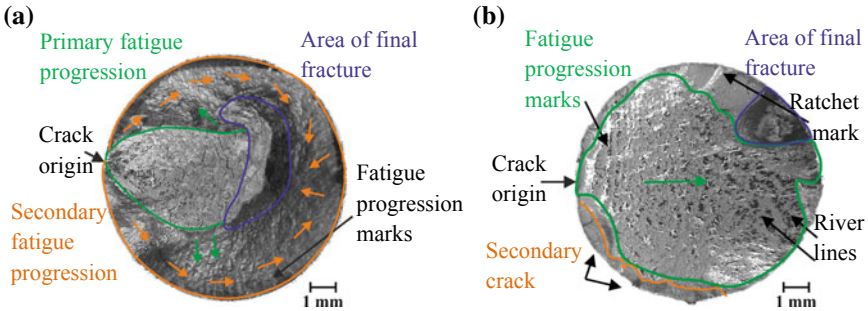

Fig. 9.5 Fractography comparison after SIT for **a** initial state **b** aged condition

for both material states. From $\varepsilon_{a,t,cor} = 0.4\%$, at the beginning of every step, a local decrease can be observed resulting from a fresh and active material surface. In every step, a new open circuit potential is set, being lower than the step before. This pattern repeats until fracture. For the aged condition a clear drop occurs at $\varepsilon_{a,t,cor} = 0.4\%$ followed by an increase in E_{OCP}. This is assumed to be the passivation of a new active surface material as a consequence of crack initiation [6]. For both material conditions the strain related stress amplitudes are similar until fracture, whereas the E_{OCP} signal indicates the crack initiation much earlier. Figure 9.5 shows a significant difference in the area of final fracture and the crack progression path. For the initial state two fatigue progressions paths can be determined, the primary outlined in orange and secondary in green. It is assumed that the ductile fracture occurred stepwise from the crack origin with two different paths. The crack progression for the aged condition occurs on one plain. This implies for the initial state, a slower crack propagation, resulting in higher stress amplitudes due to predomination of cyclic hardening mechanism.

This could be a reason of the decelerated response in the E_{OCP} signal (Fig. 9.3). The aged condition contains multiple crack areas and ratchet marks. It is known, that cyclic hardening effects and especially deformation-induced martensite formation are reduced at elevated temperatures, and crack initiation occurs on lower strain and stress levels [7]. Therefore, due to existing cracks from the aging process the crack propagation starts immediately, which results in a noticeable E_{OCP} signal change for the aged condition (Fig. 9.4).

9.5 Conclusions

The combination of magnetic, resistometric and electrochemical techniques have been successfully applied to monitor and understand fatigue-relevant mechanisms in terms of microstructural changes leading to crack formation, crack growth and rupture under fatigue loading. The high sensitivity of NDT contributes to predict fatigue-related failures of safety-relevant components in nuclear power plants at even very small scales throughout their lifetime.

Acknowledgements The work presented here has been funded by the German Federal Ministry of Economic Affairs and Energy (BMWi, MibaLeb joint project no. 1501528A, 1501528B, 1501528C, and RS1545) on basis of a decision by the German Bundestag. The support is gratefully acknowledged.

References

1. Soppa EA et al (2014) Fatigue mechanisms in an austenitic steel under cyclic loading: experiments and atomistic simulations. Mater Sci Eng A 597:128–138
2. Schuler X et al (2013) Derivation of design fatigue curves for austenitic stainless steel grades 1.4541 and 1.4550 within the German Nuclear Safety Standard KTA 3201.2. In: ASME pressure vessels and piping conference
3. Smaga M et al (2017) Influence of surface morphology on fatigue behavior of metastable austenitic stainless steel AISI 347 at ambient temperature and 300 °C. Procedia Struct Integr 5:989–996
4. Klein M et al (2016) Separation of surface, subsurface and volume fatigue damage effects in AISI 348 steel for power plant applications. Mater Test 58(7–8):601–607
5. Walther F (2014) Microstructure-oriented fatigue assessment of construction materials and joints using short-time load increase procedure. Mater Test 56(7–8):519–527
6. Sun Y et al (2011) Tribocorrosion behaviour of AISI 304 stainless steel in 0.5 M NaCl solution. Mater Chem Phys 129(1):138–147
7. Nebel T et al (2003) Cyclic deformation behavior of austenitic steels at ambient and elevated temperatures. Sadhana 28:1–2, 187–208

Part II
Fatigue of Additive Manufacturing Metals

Chapter 10
As-Built Sharp Notch Geometry and Fatigue Performance of DMLS Ti6Al4V

Martin Frkáň, Gianni Nicoletto and Radomila Konečná

Abstract Metal parts obtained by the layer-wise selective melting of a powder bed are characterized by surfaces that are considerably rougher than conventionally machined parts. Application of lightweight design tools results in complex part geometries with notches, reentrant corners, internal surfaces that are difficult to inspect and whose surface finish may not be improved. To efficiently investigate the fatigue response of as-built DMLS Ti6Al4V in the presence of as-built notches a miniature specimen approach is adopted. Sets of directional mini specimens were manufactured with the long axis parallel and perpendicular to the build direction and heat treated. The sharp notched bar geometry is subjected to cyclic bending. The interaction of directional notch generation, surface quality and geometrical accuracy on the notch fatigue behavior is quantified and discussed.

Keywords Notch fatigue · Direct metal laser sintering (DMLS) · Ti6Al4V · As-built surface

10.1 Introduction

Metal additive manufacturing (AM) appeal has grown enormously in recent years. Components that would not have even been possible just a few years ago can now be made to high standards using a wide range of metals using a powder bed fusion (PBF) technology. No longer only for prototyping applications, PBF is now on the verge of being used for the series production of metal parts.

In the PBF process thin layers of metal powdered are sequentially spread across a build plate before being melted by a laser. Each layer is selectively melted and solidified on top of the preceding layer. The concentrated energy beam of the PBF

M. Frkáň (✉) · R. Konečná
Department of Materials Engineering, University of Žilina, Žilina, Slovakia
e-mail: Martin.Frkan@fstroj.uniza.sk

G. Nicoletto
Department of Engineering and Architecture, University of Parma, Parma, Italy
e-mail: gianni.nicoletto@unipr.it

J.A.F.O. Correia et al. (eds.), *Mechanical Fatigue of Metals*, Structural Integrity 7,
https://doi.org/10.1007/978-3-030-13980-3_10

system is operated according to the CAD part file and therefore it can reproduce the desired geometry of any complexity.

No matter the remarkable progress, metal PBF still involves unique processing, material and part qualification issues still open, namely: (i) complex microstructure due to the layer-wise production and (ii) surface quality that is considerably rougher than conventionally machining and (iii) complex part geometries that are difficult to inspect and whose surface finish may not be post processed and improved.

A major challenge for part qualification is the poor fatigue behavior of as-built parts [1]. In general, the fatigue strength can be reduced for several reasons, a rough surface, an internal defect or a geometrical notch, [2]. Internal defects, being typically small, play a negative role mainly when the surface is machined otherwise fatigue crack initiation starts at as-built surface. Surface roughness depends on several mechanisms of the PBF processing (balling effect, un-melted particles, stair-stepping effect, surface orientation etc.), [3], and reduces significantly the fatigue strength compared to conventional processes as documented in the literature. Still limited is the knowledge of the notch fatigue behavior of PBF metals. The influence of an as-built mild notch (i.e. Stress concentration factor $K_t = 1.63$) on the fatigue behavior of Direct Metal Laser Sintered (DMLS) Ti6Al4V was studied in [4] finding that notch fatigue factors are affected by fabrication direction.

The present study reports an investigation of the fatigue behavior of DMLS Ti6Al4V using as-built specimens containing a sharp notch (i.e. $K_t = 5$). Sets of specimens were fabricated in the horizontal and vertical orientations (i.e. perpendicular and parallel to build direction) and fatigue tested in the as-built state. Directional notch fatigue factors for sharp notch geometry in DMLS-processed material are presented.

10.2 Material and Experimental Details

Material and process. Specimens were manufactured using titanium alloy Ti6Al4V powder supplied by EOS GmbH. The powder particles were spherical, with a diameter range 25–45 μm and with a chemical composition according to standard. The DMLS EOS M 290 system operates a 400 W Yb fiber laser unit with a wavelength of 1075 nm in building chamber filled by argon gas to avoid oxidation of titanium powder. Specimen fabrication used a layer thickness of 60 μm and a chamber temperature of 80 °C. The scan strategy was based on a shell and core concept, where the internal part of the layer is first melted by raster laser motion, followed by geometrical contouring. The hatching directions of subsequent layers were rotated by a 30° angle.

Since the DMLS process generates considerable thermal-related internal stresses [5] in the part, after fabrication the build was stress-relieved. After removal from the build plate, all specimens were heat treated in a vacuum furnace (TAV Italy) to protect the surface from oxidization. The heat treatment consisted of heating to a maximum temperature (740 °C), with soaking period 2 h, followed by a control cooling to a

temperature 520 °C. Last stage consists of fast cooling from a temperature 520 °C to a room temperature by Argon gas. This heat treatment reduces residual stresses of the fabrication process to negligible levels and optimizes the material structure from the mechanical standpoint.

Fatigue specimens. Special miniature fatigue specimens (5 × 5 mm in minimum cross-section and 22 mm in length) were used, [4]. Three sets of specimens were produced according to two orientations with respect to build direction (i.e. horizontal and vertical, see Fig. 10.1) using the same process parameters. The geometrical accuracy and surface roughness of a fine detail, such as the notch, on the fatigue behavior was investigated by applying a cyclic bending loading. Figure 10.2 shows the elastic FE stress distribution in the sharply notched mini specimen due to an applied bending moment. The stress concentration factor for this semielliptical notch (i.e. b/a = 0.25, where a = 2 mm and b = 0.5 mm are the major and minor semi-axes) is $K_t = 5$.

Material characterization. Microstructure of specimens was observed using a light optical microscope Zeiss Axio Observer Z1 M on polished and etched (10% HF for 10 s) specimens that were cut from the fatigue testing samples. Observation of structure was made in order to characterize the degree of material anisotropy, which arises by the peculiar process conditions, (i.e. layer by layer generative principle, short interactions, high temperature gradients and the high localization). Tensile

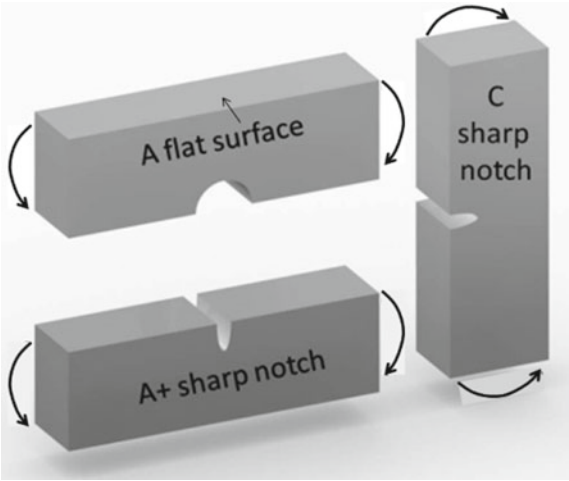

Fig. 10.1 Miniature specimens for fatigue testing of AM metals

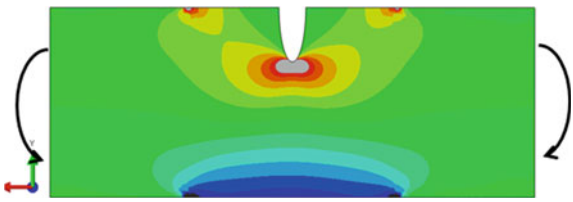

Fig. 10.2 Stress distribution in a mini specimens with a semi-elliptical notch subjected to bending

testing on standard tensile specimens produced in the same job of the fatigue specimens provided the following characteristics: tensile strength $R_m = 1176$ MPa, yield stress $R_{p0.2} = 1104$ MPa and elongation to rupture $A = 12.9\%$.

Vickers hardness testing was performed with a HPO 250/AQ hardness test equipment using 10 kp loading (HV10). The load was applied on the side plane of each specimen on polished surface. All series of hardness tests have uniform results and does not show dependence between orientation and distance throughout the thickness. The mean value from the Vickers hardness measurements are 387 HV10.

Fatigue testing. It was performed at room temperature on modified Schenk-type fatigue testing machine applying a pulsating plane bending (load cycle ratio $R = 0$) to the specimen at a frequency $f = 15$ Hz. The fatigue behavior of notched mini specimens with different build orientation (Fig. 10.1) with rough as-built surface were tested and compared with the fatigue behavior of un-notched mini specimens of type A (A flat surface).

10.3 Results and Discussion

10.3.1 Microstructure

The metallographic analysis after heat treatment showed a two-phase structure formed by the $\alpha + \beta$ phases. Texture of structure is different between parallel and orthogonal plane to the build direction. The microstructure of planes, which are oriented parallel to the build direction is characterized by primary β columnar grains that are filled with fine needles of α phase in β matrix, which are arranged in the Widmanstätten form. This primary β columnar grains, which are several building layers long, are always oriented parallel to the build direction because of the effect of the thermal history during the layer-by-layer fabrication. The microstructure of orthogonal planes shows the primary β columnar grains in cross-section, so they appear as polyhedral grains.

A Widmanstätten microstructure following a β recrystallization annealing provides maximum fracture toughness and fatigue crack growth resistance [6]. This type of microstructure is very similar to our but in our case the microstructure is much finer due to DMLS process. Therefore, the good fatigue crack growth resistance and fracture toughness is expected. On the other hand a bi-modal $\alpha + \beta$ microstructure is preferred to prevent fatigue crack initiation.

10.3.2 Fatigue Behavior

The fatigue test results of in terms of max nominal bending stress vs number of cycles are plotted in Fig. 10.3. The fatigue data appear well-behaved with a reduced

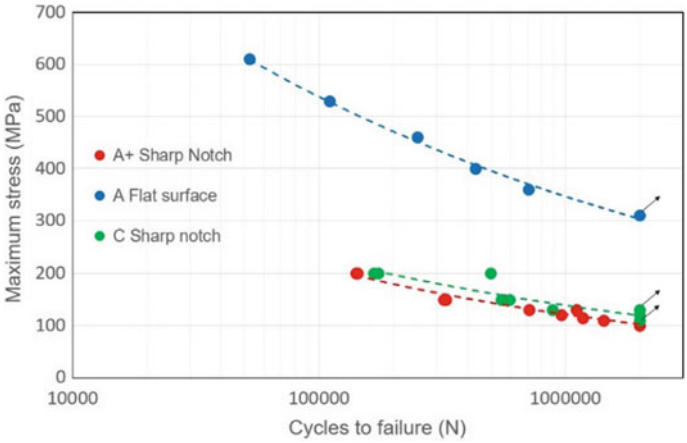

Fig. 10.3 Directional fatigue behavior of SLM Ti6Al4V in the presence of sharp notches

scatter for the Type A notch. The Type C is instead characterized by a larger scatter although the average behavior is not too different from the other direction.

Compared to the reference un-notched fatigue behavior, the notch effect is significant. According an empirical definition of the notch fatigue factor K_f (i.e. ratio between rough as-built un-notched fatigue strength/rough as-built notched fatigue strength), the present mini specimen geometry with a stress concentration factor $K_t = 5$ is associated to $K_{f,A+} = 3$ and $K_{f,C} = 2.4$.

The fatigue behavior is related to the influence of the notch, its geometrical accuracy and its surface quality which depends on the building orientation and DMLS process parameters (i.e. layer thickness) [7]. As shown in the Fig. 10.4a the quality of the notch of Type A+ specimen is high and the shape corresponds to the theoretical geometry from the CAD model (broken line ellipse).

In the case of Type C notch in Fig. 10.4b, the geometrical accuracy of the notch changes along the profile as shown by the comparison with the CAD profile: the notch surface can be split in an accurate up-skin surface (bottom half) and in a highly inaccurate down-skin (top half) surface.

This poor surface quality and accuracy of the down-skin surface is due to a condition involving melting and solidification of loose powder without building supports. Such supports are important in the case of overhangs on top of loose powder and provide a thermal path to dissipate heat, [8].

Although the quality of the A + and C mini specimens is clearly different (Fig. 10.4), the fatigue behavior is similar because the notch root, where the highest stress concentration develops (Fig. 10.2) is very similar for both types of specimens (A+, C). Nonetheless, a larger data scatter is found for C specimens.

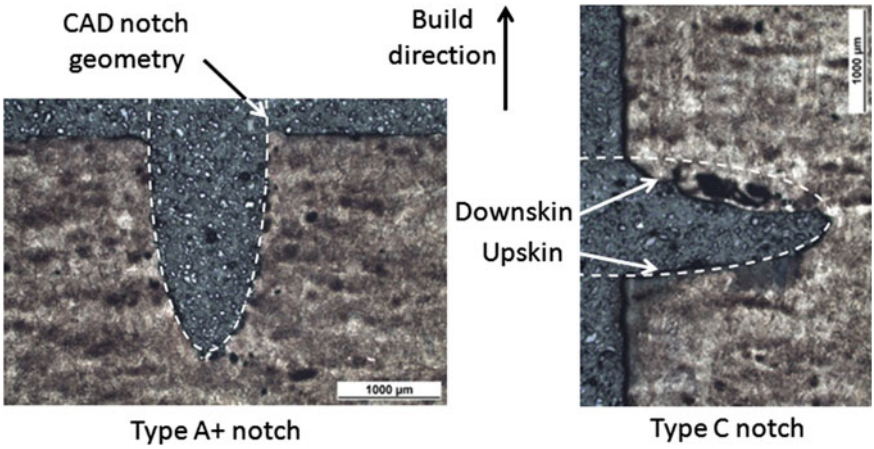

Fig. 10.4 Magnified view of semielliptical notches in mini specimens

10.4 Conclusions

The aim of this study was the determination of the influence of notched mini specimen on the fatigue behavior which is associated by geometrical shape, notch sensitivity of material and aspects related to the manufacturing technology. This study leads to the following conclusions:

- The microstructure of Ti6Al4V specimens prepared by DMLS and then heat treated is characterized by primary β columnar grains that are filled with fine needles of α phase in β matrix arranged in the Widmanstätten form.
- The notch quality of the A + and C mini specimens is directional so is the fatigue behavior.
- Considering the reference un-notched fatigue strength, the directionality of notch fatigue factor was quantified in $K_{f,A+} = 3$ and $K_{f,C} = 2.4$ for $K_t = 5$.

Acknowledgements The research was supported by the project Slovak VEGA grant No. 1/0685/2015. Specimen production by the company BEAM-IT, Fornovo Taro (Italy) (www.beam-it.eu) is gratefully acknowledged.

References

1. Uhlmann E, Fleck C, Gerlitzky G, Faltin F (2017) Dynamical fatigue behavior of additive manufactured products for a fundamental life cycle approach. Procedia CIRP 61:588–593
2. Kahlin M, Ansell H, Moverare JJ (2017) Fatigue behaviour of additive manufactured Ti6Al4V, with as-built surfaces, exposed to variable amplitude loading. Int J Fatigue 103:353–362
3. Król M, Tański T (2016) Surface quality research for selective laser melting of Ti-6Al-4V alloy. Arch Metall Mater 61(3):1291–1296

4. Nicoletto G (2018) Directional and notch effects on the fatigue behaviour of as-built DMLS Ti6Al4V. Int J Fatigue 106:124–131
5. Ali H, Ghadbeigi H, Mumtaz K (2018) Effect of scanning strategies on residual stress and mechanical properties of selective laser melted Ti6Al4V. Mater Sci Eng A 712:175–187
6. Long M, Rack HJ (1998) Titanium alloys in total joint replacement—a materials science perspective. Biomater 19(18):1621–1639
7. Kranz J, Herzog D, Emmelmann C (2015) Design guidelines for laser additive manufacturing of lightweight structures in TiAl6V4. J Laser Appl 27
8. Sames JW, List FA, Pannala S, Dehoff RR, Babu SS (2015) The metallurgy and processing science of metal additive manufacturing. Int Mater Rev 61(5):315–360

Chapter 11
Impact of Various Surface Treatments on the S-N Curve of Additive Manufactured AlSi12

Steffen Greuling, Wolfgang Weise, Dieter Fetzer, Klaus Müller-Lohmeier and Mattias-Manuel Speckle

Abstract Objective of this work is to investigate the behavior of AlSi12 specimens under fatigue loading. It describes the impact of various surface treatments like turning, polishing, shot peening and deep rolling on the S-N curve. Surface treatments, which create compressive residual stresses in near-surface regions show an improved fatigue strength. Deep rolling leads to the best results. Furthermore, the scatter of the S-N curves is discussed. Crack initiation seems to be sensitive to surface treatment. It is concluded, that in the case of rough surfaces the crack starts at surface defects whereas for improved surface conditions, for example polishing, the crack may start at pores in near-surface regions.

Keywords Additive manufacturing · Surface treatment · AlSi12

11.1 Introduction

Additive manufacturing offers unique possibilities to produce complex shaped components, which cannot be realized by conventional processes. Requirements on lightweight design often can be solved by applying aluminum alloys because of low density and their specific weight. The applications of Al-alloys for example in rapid prototyping are well known. However, for serial production in mechanical and automotive engineering a lot of tests still have to be carried out.

Mechanical behavior and metallurgical aspects of AlSi-cast materials are well known and published, e.g. [1]. However, the research on material behavior of AlSi12, which is widely used in mechanical engineering, is still in the beginning. For AlSi10Mg more results are available, because it is used more often in additive

S. Greuling (✉) · W. Weise
Strength of Materials Lab (LWF), Mechanical Engineering Department, Esslingen University of Applied Sciences, Kanalstraße 33, 73728 Esslingen, Germany
e-mail: steffen.greuling@hs-esslingen.de

D. Fetzer · K. Müller-Lohmeier · M.-M. Speckle
Festo AG & Co. KG, 73734 Esslingen, Germany

J.A.F.O. Correia et al. (eds.), *Mechanical Fatigue of Metals*, Structural Integrity 7,
https://doi.org/10.1007/978-3-030-13980-3_11

manufacturing compared to AlSi12. In order to fulfill the requirements in integrity of structures more investigations are required [2–4].

Objective of this work is to determine the fatigue strength of AlSi12 specimens. Especially the impact of various surface treatments on the S-N curve is investigated. Besides measuring the fatigue strength, i.e. determining the S-N curve, the surface conditions are characterized by roughness measurements and applying SEM techniques (scanning electron microscope). The microstructure is investigated and crack initiation is detected by applying SEM.

11.2 Experimental Investigations

The specimens are produced by selective laser melting (SLM) [5, 6] using a SLM 250 HL-machine. Building direction is always 90°, see Fig. 11.1. S-N curves will be determined for additive manufactured AlSi12 specimens applying the following surface treatments:

- Additive Manufactured, AM (no post treatment)
- Turning (rough machined and finished)
- Polishing
- Shot Peening (MHG SMG 25/1, micro glass balls <50 μm, approx. 4 min)
- Shot Peening and und Slide Finishing (Rösler Tub Vibrator)
- Turning and Deep Rolling
- Slide Finishing and Deep Rolling.

For the S-N curve the test results are evaluated according to German standard DIN 50100 [13]. Tests were carried out on a 25 kN resonance testing machine at room temperature. In order to avoid buckling of specimens, tests are carried out with a R-value of 0.1. The testing frequency is in the range of 30–40 Hz. Figure 11.2 shows the specimen's geometry. In these investigations, the S-N curves are determined for finite life regime. Tests for the endurance limit are still running.

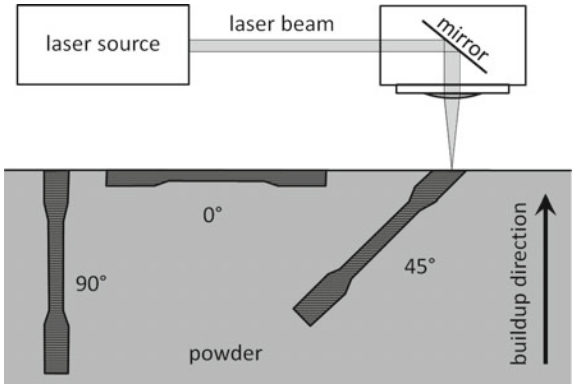

Fig. 11.1 Building directions for SLM process

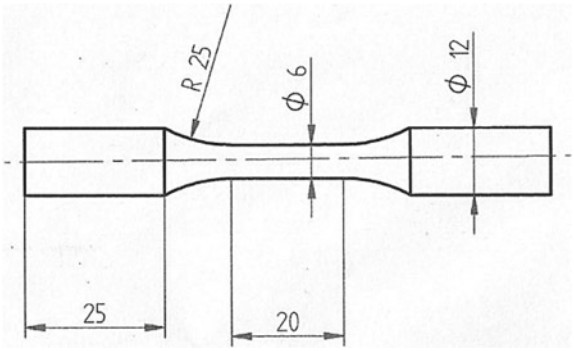

Fig. 11.2 Drawing of specimen

In order to investigate the microstructure, cross sections in longitudinal and transversal directions to the specimen's axial direction were produced. The cross sections were embedded in methyl methacrylate resin, grinded with SiC-foils (120, 320, 600 and 1200) and polished with 3 µm-diamond paste. Etching occurred in 15%-sodium hydroxide solution for 7 s. The microstructure was investigated applying the microscope Olympus UC30. The surface roughness was measured by applying tactile measurement techniques using the testing device MarSurf XR20-GD25. The surfaces after post treatments and fracture surfaces were characterized by applying SEM Phenom G1.

11.3 Results

11.3.1 Chemical Composition

Table 11.1 shows the results of a spectroscopic analysis. Si-concentration of 12.7% is close to the eutectic equilibrium concentration of 12.5% for AlSi-alloys [1].

Table 11.1 Chemical analysis of AlSi12 specimens compared to values of standards, compositions in wt% [7]

	Si	Fe	Cu	Mn	Zn	Ti
Standard	10.5–13.5	0.55	0.05	0.35	0.10	0.15
Specimens	12.7	0.22	0.02	0.01	0.04	0.03

11.3.2 Metallography

Figure 11.3 shows the results of a macroscopic investigation of the cross section. Comparatively many pores are observed. Applying the analysis software of UC30 microscope a pore concentration of 1.5% and maximum pore size of 112 μm is determined. However, measuring the density of AlSi12 related to its theoretical density a pore concentration of 3.4% is detected.

The formation of pores may have many causes and is investigated for AlSi10Mg in [8]. In welding seams of Al-alloys cavities may occur due to shrinkage or pore forms due to hydrogen. Sources for hydrogen can be H-atoms solved in the Al-melt, hydrogen concentrations in shield gas or absorbed water on the powder surface [9]. Absorbed water on powder surfaces may react with molten Al to $Al_2O_3 + H_2$, which was observed in sand casting processes where molding materials contain a certain amount of water [10]. After drying of the powder a density of 99.5% was measured [11]. In addition, impurities in the powder prior to the SLM process might be a reason for pores. Furthermore, process parameters like laser beam energy and scanning velocity have a strong influence on micro porosity [11].

In this investigation pores in additive manufactured AlSi12 probably are caused by hydrogen, when dissolved H-atoms recombine during crystallization of molten Al. This conclusion can be justified, because nearly no pores can be observed in metallographic investigations of the original powder used for this SLM process.

According to Fig. 11.3, a very fine microstructure can be observed. The structure of the additive molten layers can be detected in the micrograph. This very fine microstructure can be explained by a very high cooling rate occurred during the SLM process. At higher magnification (Fig. 11.3, right) it can be seen that we do not observe 100% eutectic phase, which will be expected for AlSi12 material for equilibrium conditions. Primary crystallized AlSi solid solution phases are detected. Due to very high cooling rates, the eutectic composition can be raised up to 13.5% [12]. According to Table 11.1, the AlSi-alloy tested in this work has a composition of 12.7%. For non-equilibrium conditions, which is the case in SLM process, this concentration is below the eutectic composition and therefore the existence of primary crystallized AlSi-phases can be explained.

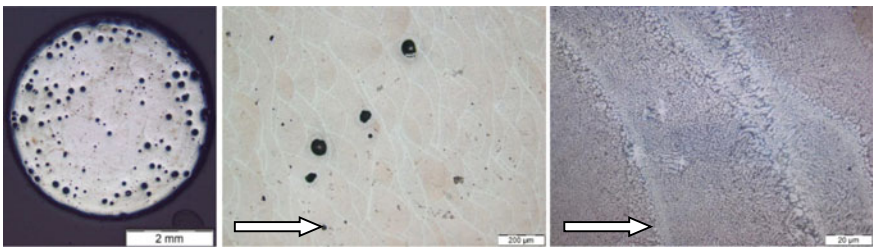

Fig. 11.3 Micrographs of additive manufactured AlSi12-alloys (white arrow: building direction)

11.3.3 Investigation of Specimen Surfaces

The surface roughness is measured using tactile measurement techniques. SEM photographs document the topographies of various surfaces. Figure 11.4 shows the results of surface roughness measurements. Hence, polishing shows low roughness values compared to conditions of additive manufactured specimens and post treatment turning. Even lower roughness values are detected on deep rolled surfaces. Figure 11.5 shows the SEM photographs of various surface treatments. Firstly, the rough surface of the original additive manufactured specimen can be seen, shot peening leads to a typical spherical calotte structure. The polished surface is smooth but pores can be detected. Obviously, pores beneath the surface are opened by polishing. Deep rolling also shows a smooth surface. However, some irregularities can be seen, which might be micro cracks due to strongly cold deformed surface regions.

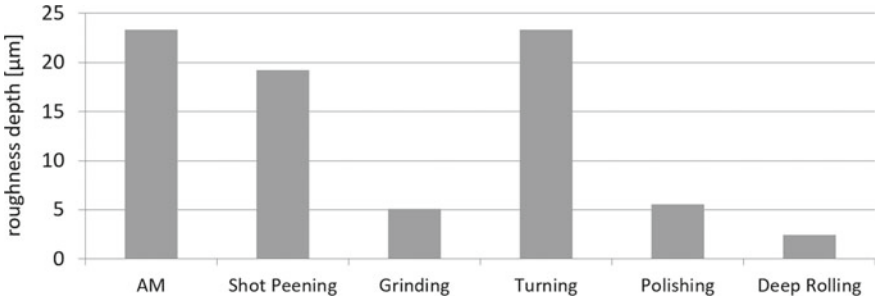

Fig. 11.4 Results of roughness measurements for various surface treatments

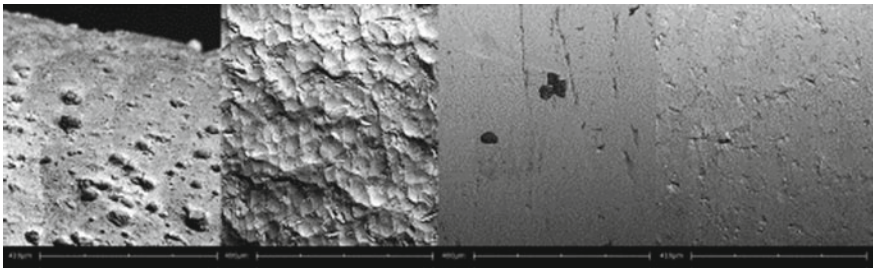

Fig. 11.5 SEM micrographs of specimens for different conditions: additive manufactured, shot peening, polishing and deep rolling (from left to right)

11.4 Results of Fatigue Testing

Figure 11.6 shows the results of all fatigue tests. The S-N curves are evaluated for a failure probability of P = 50% by applying a linear regression method [13]. In general, at least nine tests at room temperature were performed for each S-N curve.

Specimens, which were post treated by shot peening or deep rolling after additive manufacturing, turning and grinding are showing partly much higher fatigue strength then specimens in additive manufactured, polished, rough machined or finished surface conditions. Surprisingly, polishing does not lead to an improvement in fatigue strength. The reason for this behavior is explained with pores in the near-surface regions that will be opened after polishing and act as defects for crack initiation. Shot peening improves fatigue strength probably due to higher compressive residual stresses in near-surface regions. The fatigue strength of shot peened specimens are lying all in the same range neither if they were grinded before shot peening or additive manufactured before shot peening. Even higher residual compressive stresses can be achieved by deep rolling. This leads to higher fatigue strengths.

SEM investigations of the fracture surfaces are carried out in order to detect the location of crack initiation. Two basic mechanisms of crack initiation are observed. Cracks may initiate at the surface in case of very rough surfaces or initiate at a pore in near-surface regions. This is derived from SEM pictures of the fracture surface as shown in Fig. 11.7 (left), where a crack initiated at the surface of an additive manufactured specimen. Figure 11.7 (right) shows the crack initiation at a pore right under the surface in this case for a specimen which were post treated by grinding and shot peening. The evaluation leads to the conclusion that crack initiation occurs at the surface for specimens with high roughness values. This for example was the case for nearly all specimen in the condition AM. For lower roughness values, crack initiation occurs at pores in near-surface regions.

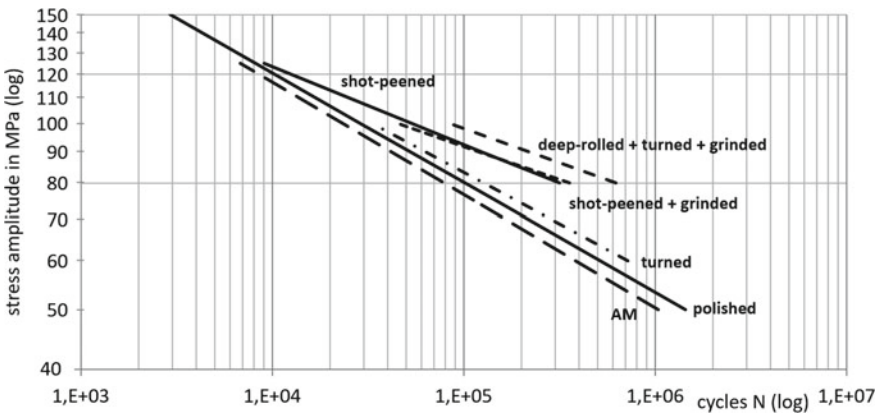

Fig. 11.6 Results of fatigue tests carried out on AlSi12-specimens with various surface post treatments. For each surface condition the S-N curve is depicted for a failure probability of P = 50%

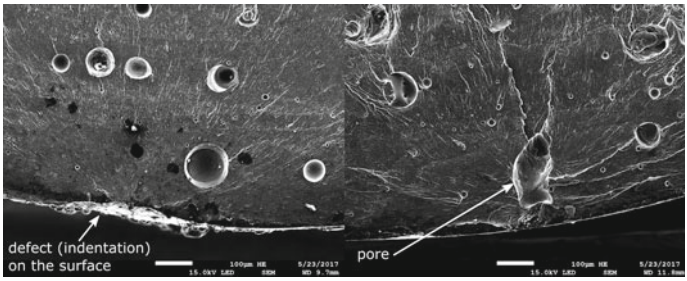

Fig. 11.7 Crack initiation at a surface of an additive manufactured specimen (left) and crack initiation at a pore in near-surface region of a slide finished and deep rolled specimen (right)

A better surface condition, in our case especially produced by deep rolling, leads to higher fatigue strength. However, for specimens and components, which will be exposed to fatigue loading, a micrograph having a low pore concentration and much smaller pores should be achieved. Further research will be focused on materials having a much lower porosity. Furthermore, the influence of various surface treatments on the endurance limit of additive manufactured Al-alloys will be carried out.

References

1. Aluminium Taschenbuch: Band 1 (2011) Grundlagen und Werkstoffe. Verlag Beuth
2. Kaufmann H, Wagener R, Melz T (2016) Anforderung an ein Bemessungskonzept für zyklisch beanspruchte additiv gefertigte Bauteile. DVM-Bericht 401, Berlin
3. Wörner S, Friederich H, Jung U (2016) Additiv gefertigte Bauteile für den Maschinen- und Automobilbau. DVM-Bericht 401, Berlin
4. Spierings AB (2012) SLM Materialeigenschaften: *Aktueller Stand und Trends* "*erweiterte Designmöglichkeiten mit SLM*" 8. SWISS RaPiD Forum
5. Bartkowiaka K, Ullrich S, Frick T, Schmidt M (2011) New developments of laser processing aluminium alloys via additive manufacturing. Phys Procedia 12:393–401
6. Richard H-A, Schramm B, Zipsner T (eds) (2017) Additive Fertigung von Bauteilen und Strukturen, Springer Fachmedien Wiesbaden
7. DIN EN 1706 (2010)
8. Buchbinder D (2013) Selective Laser Melting von Aluminiumgusslegierungen, Shaker
9. Altenpohl D (2005) Aluminium von innen, 5th edn. Alu Media
10. Aluminium Taschenbuch: Band 2 (1999)
11. Buchbinder D, Meiners W (2010) Generative Fertigung von Aluminiumbauteilen für die Serienproduktion. aluGenerativ
12. Hanna MD, Lu SZ, Hellawell A (1984) Modification in the aluminum silicon system. Metall Trans A 15:459–469
13. DIN 50100 (2016)

Chapter 12
Fatigue Properties of Powder Bed Fused Inconel 718 in As-Built Surface Condition

M. Sprengel, A. Baca, J. Gumpinger, T. Connolley, A. Brandao, T. Rohr and T. Ghidini

Abstract The aim of this study was to investigate the fatigue properties of Selective Laser Melted (SLM) processed Inconel 718 (IN718). The joint research activity between the European Space Agency and the company Renishaw, chose IN718 for its suitability in applications for launcher engine components and for Additive Manufacturing (AM) processing. The high-cycle fatigue properties of vertically and horizontally built specimens in as-built condition were investigated and a stress-life (S-N) curve constructed. The fatigue specimens were characterized by X-Ray Computed Tomography (XRCT) and the fracture surfaces analysed by Scanning Electron Microscopy (SEM). The analysis performed shows similar fatigue properties of vertically and horizontally built specimens below 10^6 cycles, despite significant differences in surface roughness.

Keywords Selective laser melting · IN718 · S-N curve · Additive manufacturing

12.1 Introduction

The process of Additive Manufacturing (AM), as defined in ISO/ASTM 52910, is the layer-by-layer manufacturing of a part. Amongst these processes, the Powder Bed Fusion (PBF) process uses thermal energy to selectively fuse areas of a powder bed [1]. Selective Laser Melting (SLM) is a PBF process using a laser to melt the powder. This process enhances significantly the freedom of part shapes and can also

M. Sprengel
The European Centre for Space Applications and Telecommunications (ESA/ECSAT), Fermi Avenue, Harwell-Oxford Campus, Didcot, Oxfordshire OX11 0FD, UK

A. Baca (✉) · J. Gumpinger · A. Brandao · T. Rohr · T. Ghidini
European Space Research and Technology Centre (ESA/ESTEC), Keplerlaan 1, 2200AG Noordwijk, The Netherlands
e-mail: adrian.baca@esa.int

T. Connolley
Diamond Light Source Ltd., Diamond House, Harwell Campus, Didcot OX11 0DE, UK

J.A.F.O. Correia et al. (eds.), *Mechanical Fatigue of Metals*, Structural Integrity 7,
https://doi.org/10.1007/978-3-030-13980-3_12

be used for alloys that are difficult to manufacture such as Inconel 718 (IN718) [2, 3]. As part of the family of Ni-based superalloys, IN718 exhibits high strength at elevated temperatures and resistance to corrosion and is thus used for high temperature applications such as gas turbine components, jet engines and launcher engines [2, 4]. The exceptional mechanical properties are achieved through a two-step precipitation hardening heat treatment aimed at precipitating the $Ni_3(Al,Ti)$ γ' and Ni_3Nb γ'' phases [5]. Amongst the various applications of AM parts, loading scenarios including fatigue loads are most challenging for parts produced by AM [6]. The challenge to overcome has been partly attributed to the surface condition and internal defects of AM parts [1–7]. Surface roughness is seen as one of the most detrimental factors for the fatigue performance of metallic materials [6, 8]. In addition to the influence of surface condition, the presence of sub-surface defects, assumed to be inherent to SLM processed parts, have been reported to decrease the fatigue performance [9]. Although some fatigue data of SLM IN718 is available, the investigations performed rarely focused on as-built specimens that solely received the standard two-step precipitation heat treatment. The novelty of this investigation is the testing of horizontally built specimens in as-built condition, namely without any surface treatment. This situation is faced for launcher liquid propulsion components in some cases and is seen as a potential worst case scenario.

12.2 Materials and Methods

12.2.1 Specimen Manufacture

Cylindrical IN718 fatigue specimens were manufactured in the horizontal and vertical orientation on a Renishaw machine. The specimens were designed according to ASTM E 466. The specimens were built using a laser power of 500 W and a layer thickness of 60 μm. The layers were built using a stripe hatch pattern with a 70 μm hatch distance, two contour lines and a rotation of 67° between each successive layer. The specimens were heat treated according to Renishaw's standard heat treatment based on the AMS 2774 standard. The two-step precipitation heat treatment consists in stress relieving the specimens at 1253 K for 1 h before gas quenching. Then the specimens were heated for a first dwell of 8 h at 993 K and furnace cooling to 873 K for a second dwell of 8 h. The specimens were then gas quenched down to 373 K and then allowed to furnace cool. On the horizontal specimens, the supporting structure was broken off manually with pliers, no other technique was applied. Some relatively small parts were then still connected to the specimens.

12.2.2 Experimental Methods

The specimens were characterized through Non-Destructive (NDI) and Destructive Investigation (DI) methods. The fatigue tests were performed according to ASTM E 466. An Instron 8800 equipped with a 100 kN load cell was used. A stress ratio of R = 0.1 and a frequency of 20 Hz were applied to perform the tests. Based on prior tensile tests, the stress amplitudes 360, 270, 200 and 135 MPa were chosen. With a Zeiss optical microscope, the fracture surface was analysed. X-ray Computed Tomography (XRCT) scans were carried out to analyse the internal defects. The XRCT acquisition was performed using a GE Phoenix V|tome|x M 300 kV at a gun voltage of 230 kV and a current of 150 μA. The voxel size was approximately 25 μm.

12.3 Results and Discussion

12.3.1 XRCT Results

In Fig. 12.1a, the remainders of the support structure is approximately 0.6 mm high and 6.7 mm long. Voids at the interface support structure—specimen can be observed in Fig. 12.1b. The surface of the downward-facing side of the horizontal specimen, where the supporting structure was connected appears very rough compared to the surface of the vertical specimen shown in Fig. 12.1d. The cross sections displayed in Fig. 12.1c, e confirms this finding. Furthermore, sub-surface porosity is visible in (e). An elongated pore and disc shaped void, presumably a lack of fusion defect due to its shape and location, are highlighted by arrows in Fig. 12.1c.

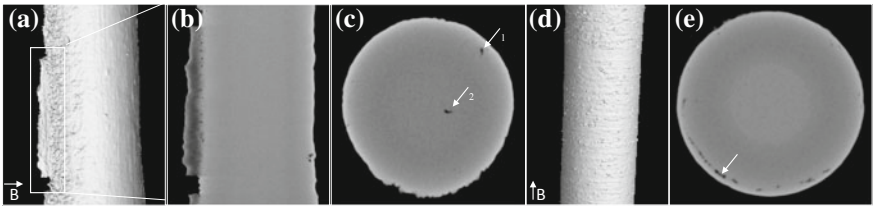

Fig. 12.1 XRCT images—**a** surface of a horizontally built specimen; **b** example of voids located at the interface of the support structure and the specimen; **c** drop shaped void in horizontal specimen (arrow 1) and lack of fusion defect (arrow 2); **d** surface of a vertically built specimen; **e** porosity line in vertical specimen

12.3.2 Fatigue Results

The results of the fatigue testing for vertically and horizontally built SLM IN718 specimens are shown in Fig. 12.2, displayed as an S-N diagram on a plot of stress amplitude versus log number of cycles to failure. The target fatigue life was set to 10^7 cycles. Specimens achieving this number of cycles were categorized as run-outs. The results show near to identical fatigue stress-life behaviour for the two specimen types at stress amplitude levels between 360 MPa and 135 MPa, reaching approximately 10^6 cycles. Furthermore, the endurance limit at 10^6 cycles is less than 135 MPa, with runouts at 10^7 cycles occurring for specimens tested at lower stress amplitudes. Additional testing at these lower amplitudes would be required to confirm the fatigue limit at 10^6 cycles for the tested specimens. Table 12.1 shows superior endurance limits at 10^6 cycles for IN718 reported in literature. However, the specimens used in these investigations were manufactured and tested in different conditions. The main differences being the post processing steps and testing conditions. Although only used as indication, these values emphasize the low fatigue stress-life behaviour of the tested specimens.

Surface roughness and internal defects such as pores and lack of fusion were found to be key aspects that directly affect the fatigue properties [10]. Furthermore, build orientation dependency of SLM IN718 was observed in fatigue tests [11]. The

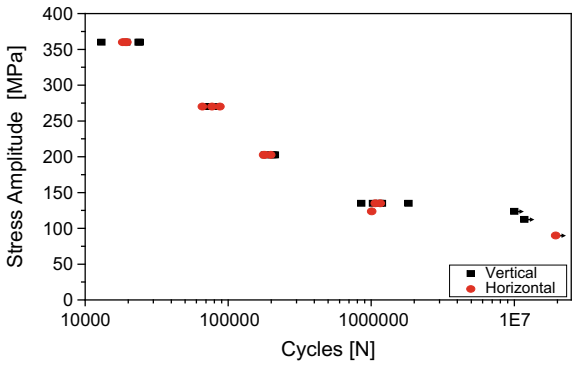

Fig. 12.2 S-N curve of SLM IN718 specimens in as-built and heat treated condition, R = 0.1

Table 12.1 Endurance limits of selected sources, displayed as stress amplitudes of IN718 at 10^6 cycles

Ref.	Process	Endurance limit (MPa)	Stress ratio R
Results	SLM	135	0.1
[6]	SLM	250–300	−1
[11]	SLM	200	0
[9]	DMD	225	0.1
[14]	Wrought	500	−1
[15]	Wrought	380	0.01

above mentioned aspects have been reported to contribute to anisotropic mechanical properties of SLM parts [12, 13]. The herein presented results however show corresponding endurance limits at 10^6 cycles for the two specimen types, independently from the differences in surface roughness and microstructure induced by the build orientation.

12.3.3 Fracture Surfaces

Selected fracture surfaces of horizontal and vertical specimens were analysed with an optical microscope, see Fig. 12.3. The fracture surfaces of the horizontally built specimens appear rougher in comparison with the vertical specimens. This could be resulting from the crack path taken in horizontal specimen, having to go through versus along elongated grains for the vertical specimens, as described in [6, 13]. The crack initiation (1), crack growth (2) and final fracture (3) areas are visible and highlighted in Fig. 12.3a. On all horizontal specimens, the crack initiated close to the interface of the support structures as indicated in Fig. 12.3b. Furthermore, investigating the surfaces with the SEM resulted in the finding of voids and pores in this area, making it difficult to assign the crack initiation precisely to one defect. Elongated defects along the circumference of the horizontal specimen tested at a stress amplitude of 200 and 135 MPa are indicated by an arrow in Fig. 12.3c, d. The occurrence of these drop shaped defects was detected in the XRCT scan displayed in Fig. 12.1d. In Fig. 12.3e, the fracture surface of a vertical specimen tested at 360 MPa is displayed. The surface is scattered with bright areas. Using the SEM, these defects were determined to be lack of fusion. Lack of fusion defects are generally reported to be detrimental for the mechanical properties and contribute to the anisotropy in

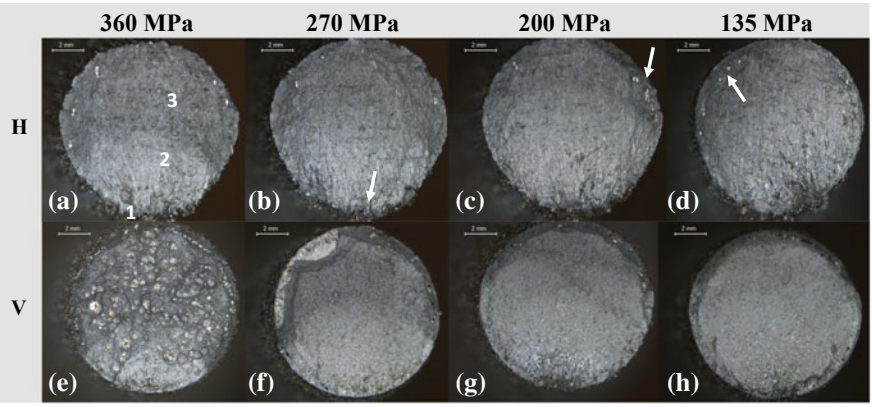

Fig. 12.3 Overview of fracture surfaces of horizontal and vertical SLM IN718 specimens at different stress amplitude levels

SLM specimens [13]. In Fig. 12.3f multiple crack initiation sites are visible and seem to start from sub-surface porosity lines. The presence of these pores between the inner filling and the contour as well as the multiple crack initiation sites were also reported in [6, 7]. The fracture surfaces of vertical specimens tested at 200 and 135 MPa appear to be less crowded with defects and the initiation sites are more distinguishable as shown in Fig. 12.3g, h.

12.4 Conclusions

The fatigue stress-life properties of as-built, heat treated SLM IN718 specimens built horizontally and vertically were assessed. The study aimed at investigating the influence of very rough surfaces on the fatigue properties. The findings reported were:

- The endurance limits at 10^6 of the vertical and horizontal specimens are lower compared to findings of AM and wrought IN718 reported in literature.
- No significant difference in fatigue stress-life behaviour between horizontal and vertical specimens was observed at stress amplitudes above 135 MPa.
- The fracture surfaces of the horizontal specimens appear very rough and are probably linked to the perpendicular crack growth path with respect to the layer orientations. All cracks seem to start in the vicinity of the support structures—specimen interface for horizontally built specimens.

Acknowledgements The authors wish to thank the company Renishaw for providing and the ESTEC workshop for machining the IN718 specimens as well as Diamond Light Source Ltd. for the access to the fatigue machine.

References

1. ISO/ASTM52910-17, Standard guidelines for design for additive manufacturing
2. Anderson M, Patwa R, Shin YC (2006) Laser-assisted machining of Inconel 718 with an economic analysis. Int J Mach Tools Manuf 46(14):1879–1891
3. Caiazzo F, Alfieri V, Corrado G, Argenio P (2017) Laser powder-bed fusion of Inconel 718 to manufacture turbine blades. Int J Adv Manuf Technol 93(9–12):4023–4031
4. Sims CT (1984) A history of superalloy metallurgy for superalloy metallurgists. In: Fifth international symposium on superalloys, pp 399–419
5. Krueger DD (1989) The development of direct age 718 for gas turbine engine disk applications. Miner Met Mater Soc 279–296
6. Yadollahi A, Shamsaei N (2017) Additive manufacturing of fatigue resistant materials: challenges and opportunities. Int J Fatigue 98:14–31
7. Brandão AD, Gumpinger J, Gschweitl M, Seyfert C, Hofbauer P, Ghidini T (2017) Fatigue properties of additively manufactured AlSi10Mg—surface treatment effect. Procedia Struct Integr 7:58–66

8. Romano S, Brückner-Foit A, Brandão A, Gumpinger J, Ghidini T, Beretta S (2018) Fatigue properties of AlSi10Mg obtained by additive manufacturing: defect-based modelling and prediction of fatigue strength. Eng Fract Mech 187:165–189
9. Amsterdam E (2009) Executive summary evaluation of the microstructure and mechanical properties of laser additive manufactured gas turbine alloys Ti-6Al-4V and RTO AVT-163 specialists meeting, October 2009, pp 1–25
10. Uriondo A, Esperon-Miguez M, Perinpanayagam S (2015) The present and future of additive manufacturing in the aerospace sector: a review of important aspects. Proc Inst Mech Eng Part G J Aerosp Eng 229(11):2132–2147
11. Konečná R, Nicoletto G, Kunz L, Bača A (2016) Microstructure and directional fatigue behavior of Inconel 718 produced by selective laser melting. Procedia Struct Integr 2:2381–2388
12. Wang Z, Guan K, Gao M, Li X, Chen X, Zeng X (2012) The microstructure and mechanical properties of deposited-IN718 by selective laser melting. J Alloys Compd 513:518–523
13. Kok Y et al (2018) Anisotropy and heterogeneity of microstructure and mechanical properties in metal additive manufacturing: a critical review. Mater Des 139:565–586
14. Belan J (2015) High frequency fatigue test of in 718 alloy—microstructure and fractography evaluation. Metalurgija 54(1):59–62
15. Ono Y, Yuri T, Sumiyoshi H, Takeuchi E, Matsuoka S, Ogata T (2004) High-cycle fatigue properties at cryogenic temperatures in Inconel 718 nickel-based superalloy. Mater Trans 45(2):342–345

Chapter 13
Application of Data Science Approach to Fatigue Property Assessment of Laser Powder Bed Fusion Stainless Steel 316L

M. Zhang, C. N. Sun, X. Zhang, P. C. Goh, J. Wei, D. Hardacre and H. Li

Abstract The adaptive neuro-fuzzy inference system (ANFIS) was applied for fatigue life prediction of laser powder bed fusion (L-PBF) stainless steel 316L. The model was evaluated using a dataset containing 111 fatigue data derived from 14 independent S-N curves. By using porosity fraction, tensile strength and cyclic stress as the inputs, the fuzzy rules defining the relations between these parameters and fatigue life were obtained for a Sugeno-type ANFIS model. The computationally derived fuzzy sets agree well with understanding of the fatigue failure mechanism, and the model demonstrates good prediction accuracy for both the training and test data. For parts made by the emerging L-PBF process where sufficient knowledge of the material behavior is still lacking, the ANFIS approach offers clear advantage over classical neural network, as the use of fuzzy logics allows more physically meaningful system design and result validation.

Keywords Fatigue · Life prediction · Neuro-fuzzy modelling · Stainless steel 316L · Selective laser melting

13.1 Introduction

Recent progresses in additive manufacturing (AM) have encouraged the use of the technology beyond rapid prototyping to actual part production. Comparing with conventional manufacturing processes, AM systems are associated with added

M. Zhang · H. Li (✉)
Singapore Centre for 3D Printing, Nanyang Technological University, Singapore, Singapore
e-mail: lihua@ntu.edu.sg

C. N. Sun · J. Wei
Singapore Institute of Manufacturing Technology, A*STAR, Singapore, Singapore

X. Zhang
Faculty of Engineering, Environment & Computing, Coventry University, Coventry, UK

P. C. Goh · D. Hardacre
Lloyd's Register Global Technology Centre, Singapore, Singapore

J.A.F.O. Correia et al. (eds.), *Mechanical Fatigue of Metals*, Structural Integrity 7,
https://doi.org/10.1007/978-3-030-13980-3_13

complexities due to the large number of processing parameters. The laser powder bed fusion (L-PBF) method, for example, consists of parameters expanding the laser unit, powder characteristics, scanning pattern, etc., and changes in these parameters could induce different thermal histories and a myriad of physical and mechanical properties in the final parts. In particular, one of the material properties that is strongly affected by L-PBF processing is fatigue as it is very sensitive to manufacturing defects. Many L-PBF materials show inferior fatigue properties to the conventional forms because of premature crack initiation at process-induced lack of fusion defects [1, 2]. This could cause unexpected performance of engineering components and heighten the risk of structural failure.

Computational methods are time- and cost-effective means for solving engineering problems as they are capable of recognizing patterns in complex data [3]. Advanced machine learning algorithms such as the neural network had been used for modelling the input parameter-property relations of processing techniques such as welding [4], hot rolling [5] and casting [6], and could potentially be applied to tackle the intricacies of AM. However, in applying data science methods, it is to be recognized that they adopt attributes of the 'black box'. This is not desirable for modelling novel processes like L-PBF, as the lack of sufficient understanding of the underlying material science can lead to meaningless results. Using fuzzy logics could potentially circumvent this problem. By describing input variables as a set of linguistic terms, the desired physical meaning and system transparency could be realized, and the problem of imprecise and insufficient information could be addressed. For instance, with fuzzy logic, key fatigue assessment indicators, such as porosity and tensile properties, could be related to the fatigue stress-life relations via a set of 'if-then' rules:

Rule 1: If porosity fraction is low and tensile strength is high and stress is low, then fatigue life is long.

Rule 2: If porosity fraction is high and tensile strength is low and stress is high, then fatigue life is short.

The implementation of such rules allows the states between acceptable and non-acceptable porosity and strength conditions to be defined imprecisely by fuzzy boundaries. In this work, the applicability of the adaptive neuro-fuzzy inference system (ANFIS), which incorporates fuzzy logic into the neural network, was examined for fatigue property assessment of L-PBF stainless steel 316L.

13.2 Fatigue Data

A total of 111 fatigue data were adapted from the authors' prior experimental works [7–9]. Stainless steel 316L samples with different tensile stress and porosity conditions were fabricated by varying L-PBF processing conditions, including the laser power, scan speed and layer thickness. 14 independent processing conditions were tested, resulting in 14 sets of S-N curves. Fatigue tests were conducted under load-controlled mode at frequency of 5 Hz and load ratio $R = 0.1$.

13.3 Neuro-fuzzy Modelling of Fatigue Life

13.3.1 Input Variables

Three variables, namely porosity fraction p, static tensile strength σ_b and the maximum cyclic stress σ_{max}, were used as the inputs for the model. Porosity is a key variable defining the crack-initiating defects. For parts with p below a critical level, fatigue fracture of L-PBF stainless steel 316L is characterized by intergranular crack initiation due to dislocations and elemental segregations at dendritic grain boundaries [9], whereas for p above the critical level, the presence of defects triggers defect-driven crack initiation. The resistance to fatigue failure of the specimens is represented by the static tensile strength, where for conventional ferrous metals, the fatigue endurance limit is approximated to be half of the tensile strength [10].

13.3.2 Architecture of the Adaptive Neuro-fuzzy Inference System

Considering the 'if-then' rules described in the Introduction, and prescribing the low level as '1', and the high level as '2', the linguistic rules could be expressed for a Sugeno-type ANFIS model [11] as:

Rule 1: If p is A_1, σ_b is B_2 and σ_{max} is C_1, then

$$f_1 = q_1 p + r_1 \sigma_b + s_1 \sigma_{\max} + t_1 \tag{13.1}$$

Rule 2: If p *is* A_2, σ_b is B_1 and σ_{max} is C_2, then

$$f_2 = q_2 p + r_2 \sigma_b + s_2 \sigma_{\max} + t_2 \tag{13.2}$$

where A_i, B_j, and C_k are the linguistic labels of the variables p, σ_b and σ_{max} respectively, f is the linear consequent function and q, r, s and t are the consequent parameters of the fuzzy rules. Figure 13.1 shows the architecture of the ANFIS model. The first layer specifies the degrees to which the given input parameters belong to each of the linguistic labels via expressions known as membership functions. By multiplying the corresponding membership values, i.e. the outputs of the nodes in Layer1, the firing strength w_i, or the 'degree of fulfilment', of a particular rule is obtained in the second layer. Output of a node in the third layer is equal to the normalized firing strength multiplied by the consequent function f of a rule. The last layer constitutes the summation of all the incoming signals and is equal to the predicted N_f.

The square nodes, i.e. Layer 1 and Layer 3, are adaptive nodes where the parameters are optimized by the adaptive neuro network. A hybrid learning algorithm, consisting the back-propagation and least square methods, were used for tuning the

membership function and the consequent parameters. All computations were performed using the Neuro-Fuzzy Designer app in Matlab.

13.4 Results and Discussion

Of the 111 data points, 78 (70%) were used for training and 33 (30%) for testing the ANFIS model. Training was stopped when the smallest training error, in terms of the root mean squared error (RMSE), was reached. By applying subtractive clustering, four distinct fatigue life clusters were determined, resulting in four fuzzy rules, as illustrated in Fig. 13.1. The input parameters p, σ_b, and σ_{max} were partitioned into 4-3-4 fuzzy sets respectively and the membership functions, in the form of Gaussian distributions, are shown in Fig. 13.2. By correlating with the experimental data, the physical meanings of the membership functions could be interpreted in terms of the fatigue fracture mechanisms. Specifically, a porosity fraction with a high degree of presence in the 'Low' level is associated with the optimum fatigue properties. Mechanistically, this involves crack initiation from microstructural defects. The 'Medium low' level is linked to the transition from microstructure-driven

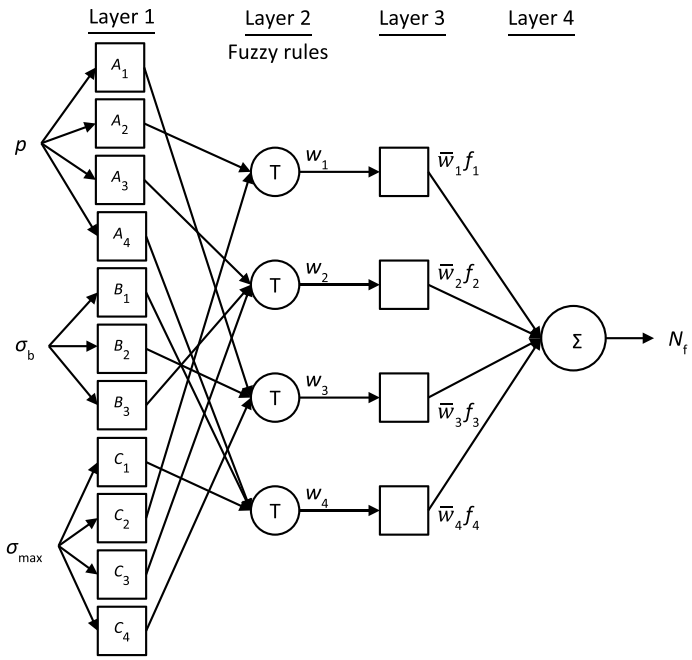

Fig. 13.1 Structure of the adaptive neuro-fuzzy inference system used in this work. The levels of the linguistic labels, from low to high, are indicated by the subscripts of the nodes in Layer 1 in increasing order

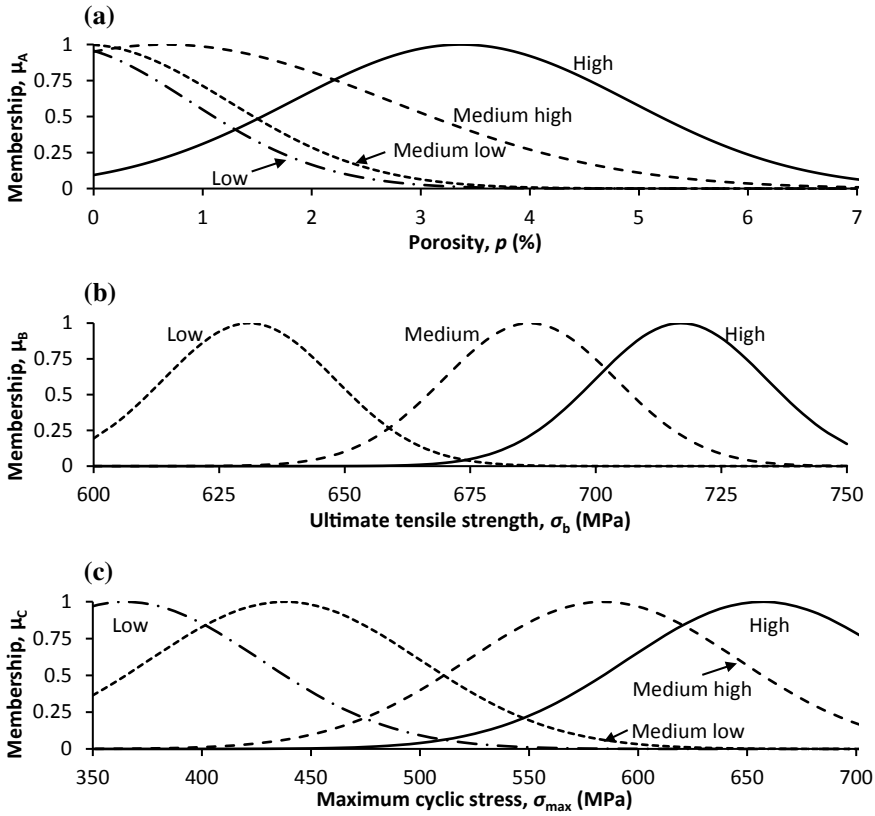

Fig. 13.2 Membership functions for **a** porosity, **b** tensile strength and **c** cyclic stress

to defect-driven failure. The 'Medium high' and 'High' levels correspond to defect-driven failure, where cracks initiate from isolated defects and multiple defects respectively. For the ultimate tensile strength, only three fuzzy categories are applicable. This could imply that fatigue life is less sensitive to tensile strength than to porosity. For the maximum cyclic stress, the fuzzy levels are related to the actual stresses used for fatigue testing.

Relating to the fuzzy rules in Fig. 13.1, the first rule indicates that a medium low porosity and medium low stress will lead to type 1 fatigue life, and the second rule indicates that a medium high porosity, high tensile strength and medium high stress will lead to type 2 fatigue life, and so on. For a given input, all the rules were evaluated in parallel for calculating the fatigue life. As shown in Fig. 13.3, the predicted results compare well with the experimental fatigue lives for both the training and test datasets. The RMSE values for the training and test sets are 13.27% and 13.38% respectively. Such errors on fatigue life could be considered as small relative to the inherent scatter associated with fatigue data (which was evaluated at

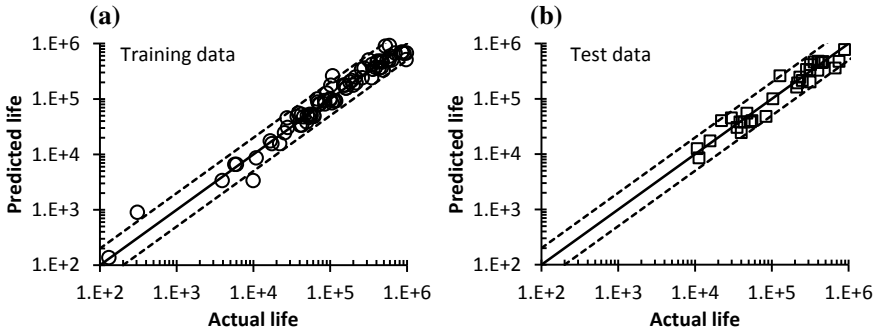

Fig. 13.3 Actual and predicted fatigue life (load cycles) for the **a** training data and **b** test data. Dotted lines represent life factor of two on life

a factor of two on life, as indicated by the dotted lines in Fig. 13.3). This result testifies that the chosen parameters, i.e. the input variables, the number and type of membership functions, rules and the allocation of data for testing and training, are appropriate for the current dataset, and that the ANFIS approach is effective for modelling the fatigue life of L-PBF stainless steel 316L.

13.5 Conclusions

The ANFIS method was applied as a preliminary study for modelling the fatigue life of L-PBF stainless steel 316L using machine learning approaches. Results from this work show that:

1. The neuro-fuzzy system could successfully predict the fatigue life of L-PBF stainless steel 316L with different process-induced porosity and tensile strength properties, and subjected to different cyclic stress levels.
2. The derived membership functions could be interpreted in terms of the fatigue failure mechanisms. Unlike non-fuzzy-based learning approaches, the transparency offered by the linguistic rules enables immediate appreciation of the model, and greatly simplifies the model design and validation process. In addition, the fuzzy boundaries allow better tolerance for imprecise and sparse data, which is relevant to the case of high cycle fatigue tests. This could have contributed to the good prediction accuracy achieved by the present ANFIS model.
3. In future works, the experimental dataset could be expanded to include a larger design space that is more representative of the different types of fatigue failure relevant to L-PBF processing. This will lead to a more complex system such that the use of artificial intelligence methods could be better justified.

References

1. Yadollahi A, Shamsaei N, Thompson SM, Elwany A, Bian L (2017) Effects of building orientation and heat treatment on fatigue behavior of selective laser melted 17-4 PH stainless steel. Int J Fatigue 94:218–235
2. Wycisk E, Solbach A, Siddique S, Herzog D, Walther F, Emmelmann C (2014) Effects of defects in laser additive manufactured Ti-6Al-4V on fatigue properties. Phys Procedia 56:371–378
3. Hkdh B (1999) Neural networks in materials science. ISIJ Int 39(10):966–979
4. Casalino G, Campanelli SL, Memola Capece Minutolo F (2013) Neuro-fuzzy model for the prediction and classification of the fused zone levels of imperfections in Ti6Al4V alloy butt weld. Adv Mater Sci Eng 2013
5. Singh S, Bhadeshia H, MacKay D, Carey H, Martin I (1998) Neural network analysis of steel plate processing. Ironmak Steelmak 25(5):355–365
6. Ozerdem MS, Kolukisa S (2009) Artificial neural network approach to predict the mechanical properties of Cu–Sn–Pb–Zn–Ni cast alloys. Mater Des 30(3):764–769
7. Zhang M, Sun C-N, Zhang X, Goh PC, Wei J, Hardacre D, Li H (2017) Fatigue and fracture behaviour of laser powder bed fusion stainless steel 316L: influence of processing parameters. Mater Sci Eng A 703:251–261
8. Zhang M, Sun C-N, Zhang X, Goh PC, Wei J, Li H, Hardacre D (2018) Elucidating the relations between monotonic and fatigue properties of laser powder bed fusion stainless steel 316L. JOM 70(3):390–395
9. Zhang M, Sun C-N, Zhang X, Wei J, Hardacre D, Li H (2018) Predictive models for fatigue property of laser powder bed fusion stainless steel 316L. Mater Des 145:42–54
10. Tóth L, Yarema SY (2006) Formation of the science of fatigue of metals. Part 1. 1825–1870. Mater Sci 42(5):673–680
11. Takagi T, Sugeno M (1983) Derivation of fuzzy control rules from human operator's control actions. IFAC Proc Vol 16(13):55–60

Chapter 14
Influence of Surface Orientation and Segmentation on the Notch Fatigue Behavior of as-Built DMLS Ti6Al4V

Gianni Nicoletto and Radomila Konečná

Abstract Design and qualification of load-bearing metal parts produced by the additive manufacturing technology is a critical issue. Such metal parts are complex in geometry with notches that are critical locations under fatigue loading. Notch surfaces are typically in the as-built state because post-fabrication surface finishing is not a viable approach in most applications. Here fatigue experiments using notched specimens produced according to different orientations with respect to build direction are presented and used to discuss the notch fatigue behavior of DMLS Ti6Al4V. Notch fatigue factors depend on the process itself and on fabrication details such as up-skin versus down-skin surface orientation, stair-stepping of the notch surface due to the layer-by-layer segmentation and intrinsic as-built surface roughness.

Keywords Direct metal laser sintering · Ti6Al4V · Notch fatigue · Surface quality

14.1 Introduction

The on-going drive for a full exploitation of metal additive manufacturing (AM) technology by industrial sectors such as aerospace, energy, motor racing and medical is pushing for new know-how development supporting the design and qualification of load-bearing metal parts [1].

Powder Bed Fusion (PBF) metal parts for structural applications are expected to have a complex geometry (organic shapes generated by topological optimization, internal cavities, and lattices of different kinds). Their surfaces will be rich of cross sectional changes, variation of orientation with respect to build orientation, rounded notches etc. [2]. Therefore, a critical section of a PBF part will combine a notched geometry and an as-built surface. Fatigue design of notched metal parts obtained by conventional processes and surface finish is well established, widely used in industry

G. Nicoletto
University of Parma, 43126 Parma, Italy

R. Konečná (✉)
University of Zilina, Zilina, Slovakia
e-mail: radomila.konecna@fstroj.uniza.sk; lncs@springer.com

J.A.F.O. Correia et al. (eds.), *Mechanical Fatigue of Metals*, Structural Integrity 7,
https://doi.org/10.1007/978-3-030-13980-3_14

and presented in many textbooks. The topic is however quite unexplored in the case of notched PBF metal parts.

This contribution considers Direct Metal Laser Sintering (DMLS) as the PBF process of choice and addresses the fatigue behavior of DMLS Ti6Al4V in the presence of as-built notches whose surface quality depends on the layer-wise surface generation and directionality with respect to build. Therefore, fatigue experiments using notched specimens produced according to different build orientations are presented and discussed.

14.2 Curved Surface Quality Generated by the PBF Process

Part fabrication by the PBF process surfaces leads to high surface roughness compared to conventional milling or grinding. Roughness measurements, i.e. R_a measured with the standard instrumentation, are typically used to characterize the quality of an as-built PBF surface. Inspection of Fig. 14.1, [3], reveals how the roughness varies in dependence of the surface orientation with respect to the build platform. A vertically oriented surface has the lowest roughness due to adhesion that occurs between loose and melted powder during the localized melting process. Two parameters, δ and υ, are defined in Fig. 14.1 and can be used to character the surface orientation as either up-skin (i.e. $0 < \upsilon < 90$) or as down-skin (angle $0 < \delta < 90$). Down-skin surfaces are considerably rougher than the up-skin counterparts due to the presence of dross. Dross formation is due to the much higher density and weight of the weld pool than the loose powder and sinks into it.

Figure 14.1 shows that up-skin flat surfaces have a roughness that is lower than down-skin flat surfaces but however higher than the vertical orientation. That is the effect of the layer-by-layer PBF fabrication process on an inclined surface. This technological effect influences also the quality of the curved surface of an as-built notch.

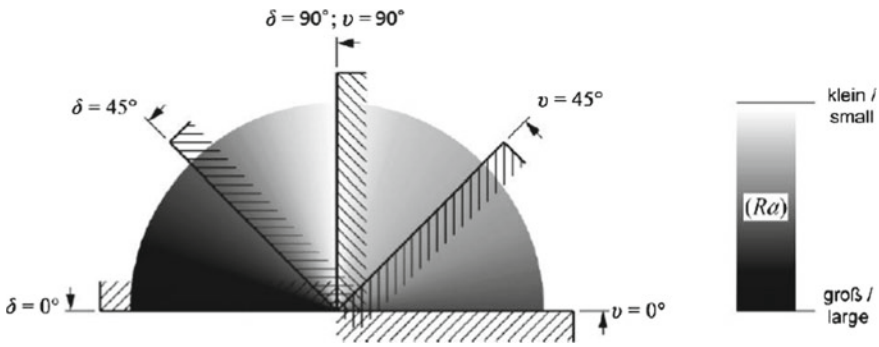

Fig. 14.1 Qualitative dependence of roughness on surface inclination [3]

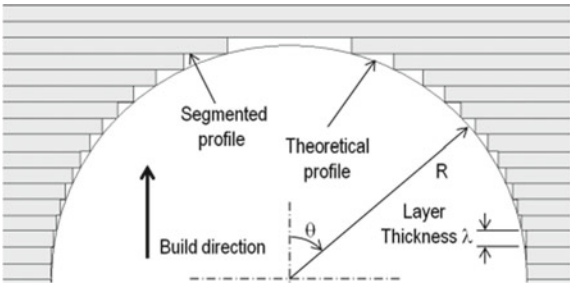

Fig. 14.2 Segmented geometry resulting from the layer-by-layer fabrication of a semicircular detail

While sectioning a notch with a cutting plane perpendicular to the build direction shows an accurate notch geometry, its intersection with a plane containing the z-axis results in stair-stepped notch geometry. Such a stair-stepping derives from the segmentation (or tessellation) of the original Computer-aided Design (CAD) model.

The example of Fig. 14.2 exemplifies how a semicircular geometry (i.e. round notch) of radius R is approximated by segmentation. The stepped profile depends on: (i) the ratio λ/R where λ is the layer thickness and R is the radius, see Fig. 14.2, and (ii) the local orientation θ with respect to the build direction: when θ approaches 0° the local geometry is markedly stair stepped, while for θ approaching 90° the actual geometry merges to the nominal geometry.

According to the previous definition, the notch geometry of Fig. 14.2 is associated to a down-skin surface. Therefore, dross formation is expected after PBF fabrication in addition to the stepped profile. Alternatively, the notch geometry of Fig. 14.2 could be produced according to the up-skin orientation and only the stepped profile would contribute to its surface quality.

14.3 Experimental Details

An experimental approach using a novel specimen geometry is adopted to investigate the interaction of a notch with the as-built surface state and the fatigue behavior. The material considered is Ti6Al4V fabricated with the DMLS process.

The miniature notch specimen geometry proposed in [4] is used here to investigate the as-built notch fatigue behavior in a controlled and repeatable manner. Figure 14.3 shows the miniature specimen ($22 \times 5 \times 7$ mm^3) compared to a standard 80-mm-long rotating bending specimen. The notch is semicircular and has a radius R = 2 mm. The notched specimen geometry loaded in plane bending is characterized by an elastic stress concentration factor $K_t = 1.63$ [5].

The main features of the test method used are: (i) the specimen is small to conveniently generate many specimens with considerable weight and cost savings compared to standard geometries; (ii) the specimen is tested in plane bending so that a

Fig. 14.3 Standard versus miniature as-built fatigue specimens

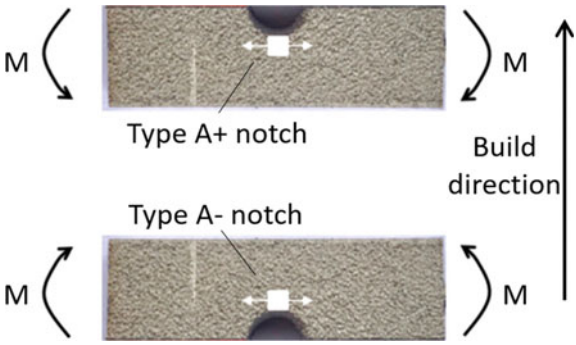

Fig. 14.4 Two types of notched miniature specimen under bending load: Type A+: up-skin notch, Type A−: down-skin notch

selected surface feature (either the notch or the opposite flat surface) is under applied cyclic tensile stress; (iii) the specimen contains a simple notch (semi-circular) so that the unique geometrical parameter R defines it; (iv) the specimen orientation with respect to build direction can be readily selected to generate either up-skin or down-skin notches [5].

Figure 14.4 shows the two types of specimens used in this study with respect to build direction. Type A+ specimen is characterized by the round notch in the up-skin orientation, so that only stair stepping is significant at the location of crack initiation. On the other hand, Type A− specimen has the round notch in the down skin orientation, so that stair stepping and dross formation is expected to influence fatigue crack initiation. Figure 14.4 schematically shows also the cyclic bending moment applied to generate cyclic tensile stress in the respective notch roots.

The two sets of mini specimens were tested in fatigue using an electromechanical plane bending machine under a load ratio $R = 0$ with test run-out fixed at 2×10^6 cycles. The fatigue results obtained by applying tensile cyclic stress to the as-built flat surface opposite to the notch (i.e. reversing the bending moments of Fig. 14.4) in a previous study [4], will be used as the reference un-notched fatigue behavior of as-built DMLS Ti6Al4V.

Mini-specimen fabrication was performed with the DMLS system EOSINT M290 (EOS GmbH, Germany) working with a layer thickness of 60 μm, a max laser power of 400 W and a chamber temperature of 80 °C. The Ti6Al4V ELI alloy powder used here was characterized by spherical powder particles of predominant diameter range

from 25 to 45 μm. After fabrication, a stress relieving heat treatment in a vacuum furnace was applied. The structure was quite isotropic, see [5].

The optical characterization of the as-built notch quality was performed on polished and non-etched specimens with a light microscope Zeiss Neophot 32.

14.4 Results and Discussion

The fatigue test results of in terms of maximum nominal stress σ_{max} versus number of cycles to failure N for the un-notched condition and for the two sets of Type A+ and Type A− notched mini specimens of as-built DMLS Ti6Al4V are plotted in Fig. 14.5. The fatigue data appear well-behaved with a reduced scatter. The up-skin fabrication condition is associated to a slightly better fatigue behavior than the down-skin condition. According the empirical notch fatigue factor K_f definition (i.e. smooth fatigue strength/notched fatigue strength), the notch geometry with a stress concentration factor $K_t = 1.63$ is associated to two notch fatigue factors $K_{f,A+} = 2.0$ and $K_{f,A-} = 2.6$.

It is stressed that differently from conventional metal fatigue here the notch fatigue factor is larger than the stress intensity factor. Furthermore, two notch fatigue factors are due to the different surface quality in dependence of the notch fabrication.

The respective magnified notch profiles of Fig. 14.6 demonstrate that the roughness of these two notch orientations. The down-skin notch surface of Type A− specimen, Fig. 14.6b, is affected by dross formation and is very rough while the up-skin notch surface of Type A+ specimen, Fig. 14.6a, is affected by stair stepping only.

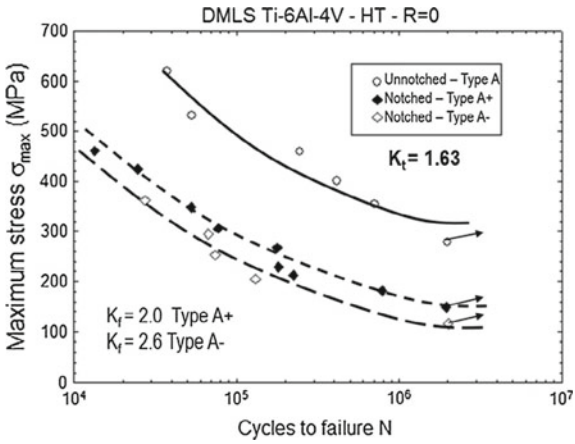

Fig. 14.5 Fatigue behavior of smooth and up-skin versus down-skin circular notches in DMLS Ti6Al4V

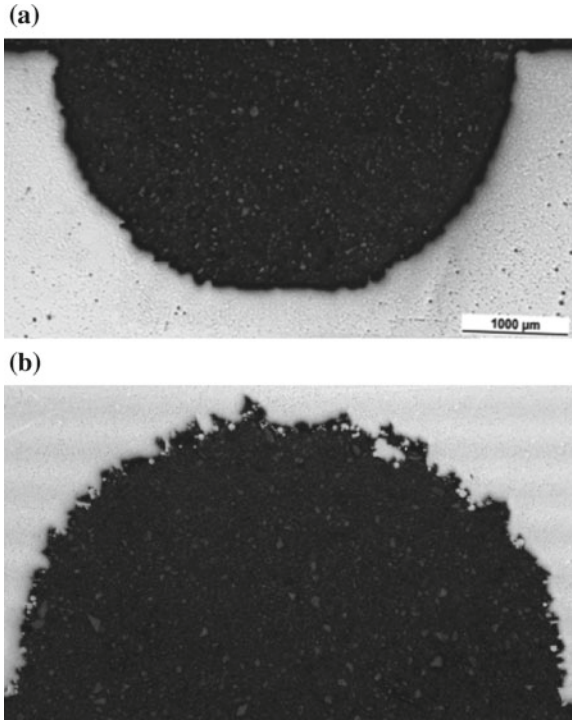

Fig. 14.6 **a** Up-skin round notch; **b** down-skin round notch (R = 2 mm)

14.5 Conclusions

PBF metal parts are typically complex in geometry with notches that are prone to fatigue failure. Their surfaces will be in the as-built condition, as surface finish is not a viable approach. Here the miniature specimen approach proposed elsewhere has been applied to the study of the notch fatigue behavior of DMLS Ti6Al4V. Specimen fabrication was specified so that the notch surface quality is affected by the layer-wise consolidation and by notch directionality with respect to build direction.

The following conclusions are reached:

- The mini specimen concept is suitable for the investigation of the as-built notch fatigue behavior of PBF materials in a controlled way.
- Up-skin and down-skin notches were produced in mini specimens of DMLS Ti6Al4V tested in cyclic bending and their different quality demonstrated by optical microscopy.
- The notch behavior of DMLS Ti6Al4V was quantified by means of two notch fatigue factors, the largest of which is associated to the down-skin notch.
- Both notch fatigue factors are larger than the theoretical stress concentration factor.

Acknowledgements The research was supported by the project Slovak VEGA grant No. 1/0685/2015. Specimen production by the company BEAM-IT, Fornovo Taro (Italy) (www.beam-it.eu) is gratefully acknowledged.

References

1. DebRoy T et al (2018) Additive manufacturing of metallic components—process, structure and properties. Prog Mater Sci 92:112–224
2. Kahlin M, Ansell H, Moverare JJ (2017) Fatigue behaviour of notched additive manufactured Ti6Al4V with as-built surfaces. Int J Fatigue 101:51–60
3. VDI-Guidline 3405 Part 3 Dec 2015, Additive manufacturing processes, rapid manufacturing—design rules for part production using laser sintering and laser beam melting (2015)
4. Nicoletto G (2017) Anisotropic high-cycle fatigue behavior of Ti-6Al-4V obtained by powder bed laser fusion. Int J Fatigue 94:255–262
5. Nicoletto G (2018) Directional and notch effects on the fatigue behavior of as-built DMLS Ti6Al4V. Int J Fatigue 106:124–131

Chapter 15
Characterization of the Cyclic Material Behavior of AlSi10Mg and Inconel® 718 Produced by SLM

M. Scurria, B. Möller, R. Wagener and T. Bein

Abstract The flexibility in design offered by advanced additive manufacturing technologies makes this process more and more attractive for the automotive as well as the aircraft industry, especially for the production of metal components. Nevertheless, while, on the one hand, additive manufacturing paved the way for new design solutions which were not possible before, on the other hand, it represents a new process, which has still not been standardized and, therefore, made exploitable. In this work, the cyclic material behavior of two different metals used for additive manufacturing technologies were evaluated. Small-scale specimens, produced by Selective Laser Melting (SLM) of the Aluminum alloy AlSi10Mg and Inconel® 718 powder, were subjected to Incremental Step Tests (IST) in order to evaluate the cyclic stress-strain behavior of the material. The effects of removed support structures, four building orientations, surface conditions and an additional heat treatment on the cyclic stress-strain behavior of the material were evaluated.

Keywords SLM · AlSi10Mg · Inconel · Cyclic material behavior · IST · Additive manufacturing

15.1 Introduction

Although the term "Additive Manufacturing" is relatively new, the basis of the various technologies that it includes is well known and had already been introduced by the 1980's. The initial idea was to create 3D objects, which represented a scale benchmark of a part (or assembly), by adding material layer by layer. These objects had no structural function and consisted of resin, as in stereo lithography (STL), or

M. Scurria (✉)
Research Group of System Reliability, Adaptive Structures and Machine Acoustic SAM, Technische Universität Darmstadt, Magdalenenstr. 4, 64289 Darmstadt, Germany
e-mail: scurria@sam.tu-darmstadt.de

B. Möller · R. Wagener · T. Bein
Fraunhofer Institute for Structural Durability and System Reliability LBF, Bartningstr. 47, 64289 Darmstadt, Germany

J.A.F.O. Correia et al. (eds.), *Mechanical Fatigue of Metals*, Structural Integrity 7,
https://doi.org/10.1007/978-3-030-13980-3_15

layers of paper, as in the case of Laminated Object Manufacturing (LOM). Many process variations evolved, depending on the material and the principles on which they were based, but the fact that their products were limited to a "visual" rather than "structural" function justified their classification in the Rapid Prototyping category, or more often called 3D Printing. The term Additive Manufacturing (as oppose to Rapid Manufacturing), on the other hand, represented the intention to expand the field of application to parts with a structural function, aiming for series production, i.e. implementing the use of metals. The technology used for this study is Selective Laser Melting (SLM), developed at the Fraunhofer Institute ILT [1].

A layer of metal powder is deposited on a build platform through a rake and then melted by a laser beam. The platform is then lowered by an amount corresponding to the desired layer thickness and another layer of powder is deposited and melted; the process is repeated until the final shape of the object is obtained. The materials investigated here were an Aluminum alloy, AlSi10Mg, and a Nickel superalloy, Inconel® 718. The reasons why the possible use of these metals for additive manufacturing technologies has been widely investigated are different. AlSi10Mg is a hypoeutectic alloy close to the eutectic composition ($\text{weight}_{\%,\text{Si}} = 9–11$) and therefore is already widely used for casting. The properties of additive manufactured AlSi10Mg have already in part been investigated in several studies [2, 3]. Inconel® 718 is a high strength, thermally resistant Nickel-based alloy, widely used in the aircraft industry. Additive manufacturing offers an alternative to the difficulties of machining this alloy, related to its rapid work hardening, and, therefore, several studies have already been conducted [4, 5].

Additively manufactured parts are characterized by defects, which can be internal, such as pores, or surface-related, such as high roughness. The process is still not fully standardized and the variables, which can affect the cyclic material behavior, are several; for example, the process parameters, the presence and removal of support structures, the different microstructures due to different cooling rates, pores, possible heat treatments, surface finish and the anisotropy due to different build directions. This work has focused on the effects of these variables on the cyclic stress-strain behavior of Inconel® 718 and AlSi10Mg.

15.2 Experimental Campaign

15.2.1 Specimens and Reference System

For this investigation, flat small-scale specimens with a thickness of about 2 mm have been used. In order to define the initial conditions, specimens oriented along the powder deposition direction in X (0°, lying), XZ (45°) and Z (90°, standing) directions and specimens lying orthogonal to the powder deposition direction with respect to the building platform (Y specimens) were manufactured using standard process parameters (Fig. 15.1, left).

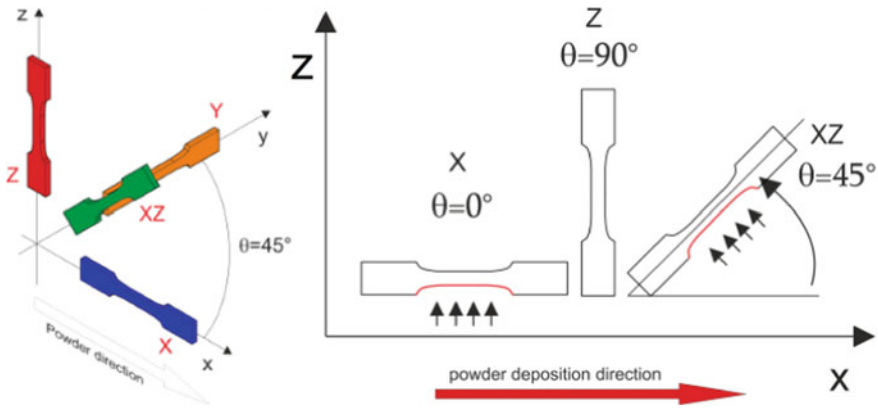

Fig. 15.1 Specimen orientation with respect to the direction of powder (left) and surfaces for which a support structure must be provided (right)

Individually adapted support structures, needed for lying (X and Y directions) and 45° XZ specimens and surfaces with downskin angles up to 45° (Fig. 15.1, right), have been subsequently removed. The specimens were taken from the build platform and the support structures were mechanically removed. The maximum roughness for surfaces as-built ranged from $R_z = 19$ for Z specimens to $R_z = 25$ for X and Y specimens, while, after the removal of support structures, these values could reach peak levels of $R_z = 120$. The subsequent removal of these multiple point joints, in fact, left the surface irregular and with a large amount of defects (Fig. 15.2). A part of the specimens was subjected to a stress relief heat treatment (denoted as 'tempered') while the rest was tested in the as-built state.

15.2.2 Test Equipment

The experimental campaign was carried out using an E-cylinder test rig, developed at the Fraunhofer LBF, which enables strain-controlled fatigue tests using an electric motor. A load cell measures the force, while the strain is measured by an extensometer. An anti-buckling device is used to avoid buckling phenomena when a strain ratio of $R_\varepsilon < 0$ is applied. The test rig and the set up are shown in Fig. 15.3.

Fig. 15.2 Surfaces of an AlSi10Mg specimen built in the X direction: as-built state (left) and after the removal of support structures (right)

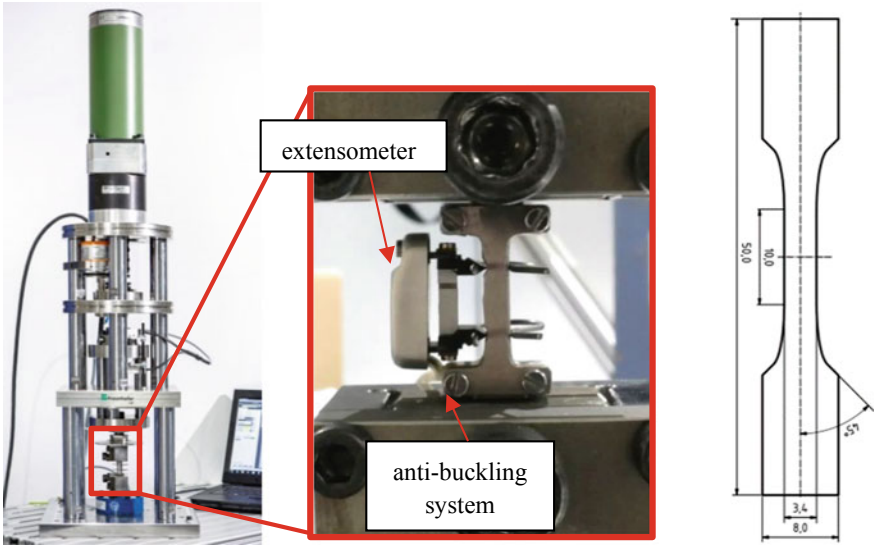

Fig. 15.3 E-Cylinder test rig (left), specimen (right) mounted between the clamping systems including anti-buckling system with applied extensometer (center)

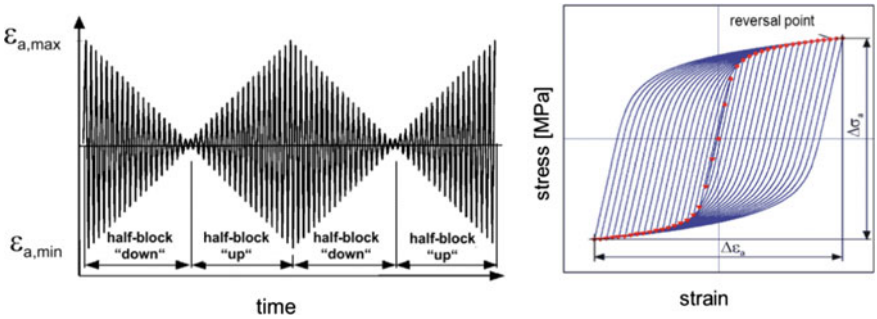

Fig. 15.4 Strain history [9] on the left and reversal points of one block on the right

Incremental Step Tests (IST) [6], a defined load sequence with decreasing and increasing amplitudes, were performed on the specimens, applying a strain ratio $R_\varepsilon = -1$ until failure occurred.

The cycles between two maxima belong to one block (Fig. 15.4, left). The failure corresponds to the *n*-block, in which the maximum force decreased by 10% relates to *n*/2, which is called the *stabilized block* (or *stabilized state*). The reversal points (Fig. 15.4, right) of the stabilized block are used to evaluate the cyclic stress-strain curve by regression of the Ramberg-Osgood equation [7]. The cyclic stress-strain behavior of the material is crucial in simulating the fatigue life of a component and represents the starting point for an assessment using elastic-plastic approaches and, especially, a material-based fatigue approach [8].

15.3 Results

The derived cyclically stabilized stress-strain curves are represented in Fig. 15.5. The different colors correspond to different build orientations (as in Fig. 15.1) and the results are shown for maximum strain amplitudes of $\varepsilon_{a,t} = 0.4$ and 0.8% applied to the two materials after tempering, and on AlSi10Mg also on the as-built state.

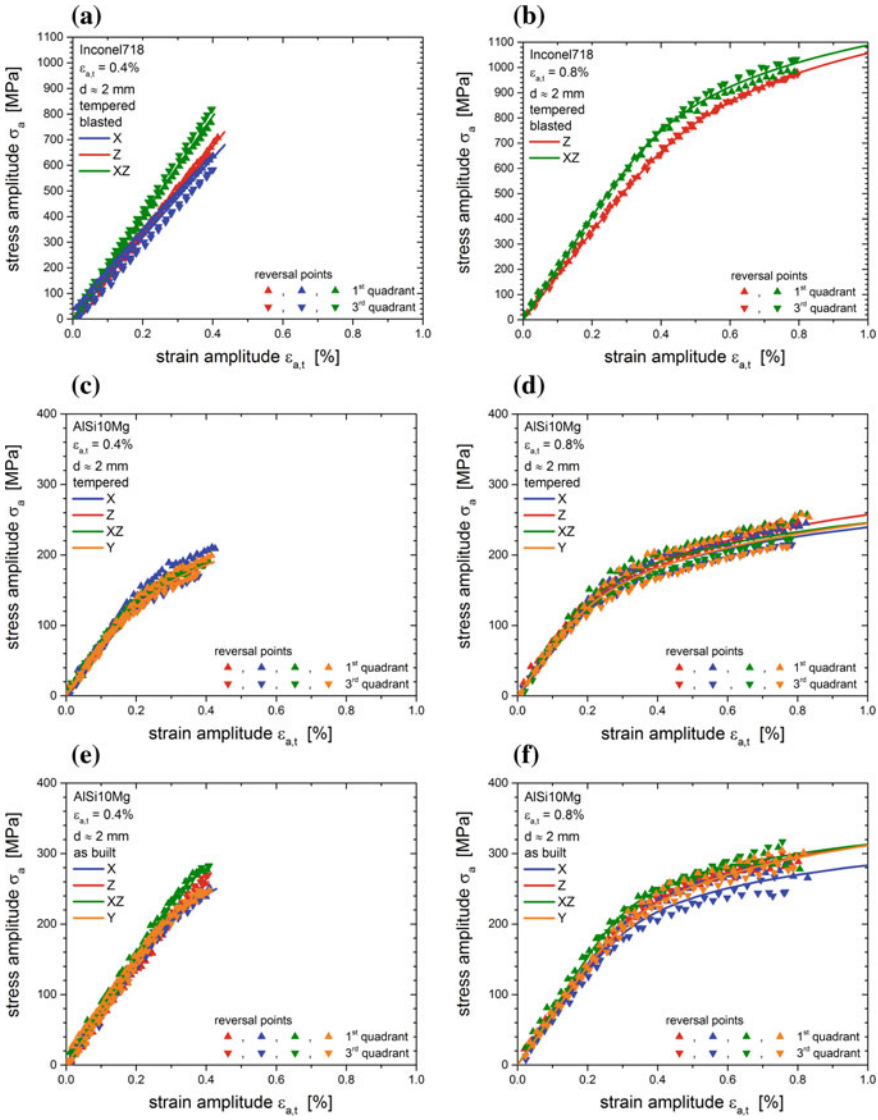

Fig. 15.5 Cyclic stress-strain behavior of blasted and tempered Inconel718 (**a** and **b**), tempered (**c** and **d**) and as-built (**e** and **f**) AlSi10Mg for maximum strain amplitudes of 0.4 and 0.8%

The Young's modulus of Inconel® 718 depends on the build directions; values varying between 180 GPa in the X direction and 230 GPa in the Z direction under cyclic loading conditions have been observed. On the other hand, the Young's modulus of the aluminum alloy specimens is constant which means that the Young's modulus is not influenced by the build direction. Nevertheless, the stress-strain behavior of AlSi10Mg depends on the build direction, especially in the case of the as-built material state. Furthermore, the behavior is different under tensile and compression loading, which is not the case of Inconel® 718.

The tempering of additively manufactured specimens leads to a lower yield strength, compared to the as-built material state, and reduces the different behaviors under tensile and compression loading conditions.

15.4 Conclusions

The cyclic material behavior has been determined by performing Incremental Step Tests on specimens of AlSi10Mg and Inconel® 718. The evaluation of the measured data enables the description of the cyclic stress-strain curves using the equation of Ramberg-Osgood. Summarizing all test results, the stress-strain behavior of additively manufactured specimens and structured depends on the build direction.

In the case of Inconel® 718, the anisotropy is very high and has to be considered for fatigue life assessment in order to enable the light weight potential of additive manufacturing for cyclically loaded structures. Further investigations are necessary, since the influence of the surface quality on the fatigue life seems to be high and an anisotropic behavior was found in some cases. Furthermore, the influence of a heat treatment might have a large influence on the cyclic material behavior and should be investigated in more detail.

Acknowledgements The research and development projects 'VariKa' and 'BadgeB' that form the basis for this publication are funded within the scope of the "PAiCE Digitale Technologien für die Wirtschaft" technology programme run by the Federal Ministry for Economic Affairs and Energy (VariKA) and within the scope of the "Additive Fertigung – Individualisierte Produkte, komplexe Massenprodukte, innovatiove Materialien" (Pro_Mat_3D) by the Federal Ministry of Education and Research (BadgeB). The project VariKA is managed by the DLR project management agency "Gesellschaft, Innovation, Technologie -Informationstechnologien/Elektromobilität" at the German Aerospace Center in Cologne and the project BadgeB by the KIT project management agency "Projektträger Karlsruhe – Produktion und Fertigungstechnologien", respectively. The authors are responsible for the content of this publication.

References

1. Meiners W (1999) Direktes Selektives Laser Sintern einkomponentiger metallischer Werkstoffe, Dissertation, RWTH Aachen

2. Brandl E et al (2012) Additive manufactured AlSi10Mg samples using selective laser melting (SLM): microstructure, high cycle fatigue, and fracture behavior. Mater Des 34:159–169
3. Kempen K et al (2012) Mechanical properties of AlSi10Mg produced by selective laser melting. Phys Procedia 39:439–446
4. Deng D et al (2018) Microstructure and mechanical properties of Inconel 718 produced by selective laser melting: sample orientation dependence and effects of post heat treatments. Mater Sci Eng A 713:294–306
5. Jia Q, Gu D (2014) Selective laser melting additive manufacturing of Inconel 718 superalloy parts: densification, microstructure and properties. J Alloys Compd 585:713–721
6. Landgraf RW, Morrow J, Endo T (1969) Determination of the cyclic stress-strain curve. J Mater JMLSA 4:176–188
7. Ramberg W, Osgood WR (1943) NACA technical note no 902
8. Hell M et al (2015) Fatigue life design of components under variable amplitude loading with respect to cyclic material behaviour. Procedia Eng 101:194–202
9. Masendorf R, Wagener R. Prüf- und Dokumentationsrichtlinie für die experimentelle Ermittlung mechanischer Kennwerte von Feinblechen aus Stahl für die CAE-Berechnung, Anhang Incremental Step Test

Part III
Fatigue Crack Propagation

Chapter 16
Review of Current Progress in 3D Linear Elastic Fracture Mechanics

Andrei Kotousov, Aditya Khanna, Ricardo Branco, Abílio M.P. De Jesus and José A.F.O. Correia

Abstract The aim of this contribution is to provide a brief review of the latest developments in the area of 3D Linear-Elastic Fracture Mechanics. The primary focus of this contribution is on the situations where the classical results, which are normally obtained within the framework of plane theory of elasticity, lead to peculiar results. These situations include analysis of stress and displacement fields near vertex points, generation of the coupled fracture mode under shear loading, application of Williams series expansion to 3D problems as well as fracture scaling.

Keywords LEFM · FE · 3D stress singularities · Plates

16.1 Introduction

Plane problems of elasticity are often treated within the classical two-dimensional (2D) theory of elasticity, which adopts plane stress or plane strain simplifications. However, stress analysis based on this theory occasionally leads to peculiar results due, in part, to the fact that it is an approximate three-dimensional theory even when the plane stress equations are solved exactly [1, 2].

It has been confirmed in many careful numerical studies and is now commonly accepted that the stress and deformation fields in the three-dimensional (3D) plane problems of elasticity can be resolved as a sum of an interior plane stress solution and 3D layer solution as illustrated in Fig. 16.1 [2, 3].

A. Kotousov (✉) · A. Khanna
The University of Adelaide, Adelaide, SA 5005, Australia
e-mail: andrei.kotousov@adelaide.edu.au

R. Branco
University of Coimbra, Coimbra, Portugal

A.M.P. De Jesus · J.A.F.O. Correia
University of Porto, Porto, Portugal

J.A.F.O. Correia et al. (eds.), *Mechanical Fatigue of Metals*, Structural Integrity 7,
https://doi.org/10.1007/978-3-030-13980-3_16

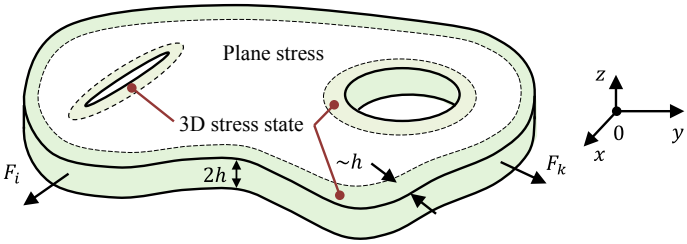

Fig. 16.1 Representation of the exact solution to plane problems of elasticity as a sum of an interior plane stress solution and 3D stress state near boundaries

The region(s) of 3D stress state of characteristic width, h, is normally very small compared to the rest of the structure, and for most situations the in-plane stress components are not very different from their plane stress counterparts. However, this is not true for problems with strong stress concentrators (e.g. elliptical holes with large aspect ratios) and, so called, singular problems such as problems with sharp notches and cracks [4, 5]. The latter problems are the main focus of the present review.

16.2 Stress Singularities

Stress singularities are not of the real world. Nonetheless, they are of a real fact in stress analysis. In general, stress singularities can be associated with a sudden change of boundary conditions or applied loading (e.g. concentrated forces and moments) over vanishingly small areas or volumes, which is often termed as singular loads. This class of stress singularities is well investigated and the nature of their origin and asymptotic behaviour is presently well understood. Another class of singularities is generally not related to singular loads and may occur due to an abrupt change of the geometry; singularities arising in fracture problems belong to this class [1, 2, 4–17].

16.2.1 2D Linear Elastic Fracture Mechanics

The classical plane theory of elasticity provides a powerful tool for analysis of singular problems, and, in particular, problems with cracks. It is based on four basic assumptions: (1) strains and (2) displacements are vanishingly small, (3) the material response is linear (i.e. implying that the strains never exceed the limits of elasticity), and (4) the state of stress near a crack tip follows either the plane stress or plane strain assumptions. Nevertheless, the singular stress state near the crack tip is in violation of all of these assumptions.

The classical Linear-Elastic Fracture Mechanics (LEFM) provides an elegant justification to the implementation of the first three assumptions for failure assessment in the case when the process zone associated with all sorts of nonlinearities is small compared to other characteristic dimensions of the problem. The 3D LEFM deals with the relaxation of the last assumption.

16.2.2 3D Linear Elastic Fracture Mechanics

The 3D stress states near the crack front, see Fig. 16.2, is often represented as a sum of two singular states corresponding to the line (or edge) singularity along the crack front and the 3D corner (or wedge) singularities, which concentrated in the vertex (or angular) points:

$$\sigma_{ik} = \sum_{M=I,II,III} \frac{K_M(\eta)}{\sqrt{r}} f_{ik}^M(\phi) + K^{CS} R^{-\lambda_{CS}} f^S(\vartheta, \varphi) + K^{CA} R^{-\lambda_{CA}} f^A(\vartheta, \varphi), \tag{16.1}$$

where $K_M(\eta)$ are the stress intensity factors in mode I, II and II; K^{CS} and K^{CA} are the intensities of the 3D corner singularity corresponding to symmetric (S) and antisymmetric (A) modes; R is the distance to the vertex point; and r is the distance normal to the crack front. The strength of the 3D corner singularity, λ_C, depends on angle β, Poisson's ratio, ν, as well as the mode of loading, symmetric or antisymmetric. The values of λ_C for different geometries and loading conditions were exhaustively investigated using various semi-analytical as well as numerical approaches [5, 6, 8–10].

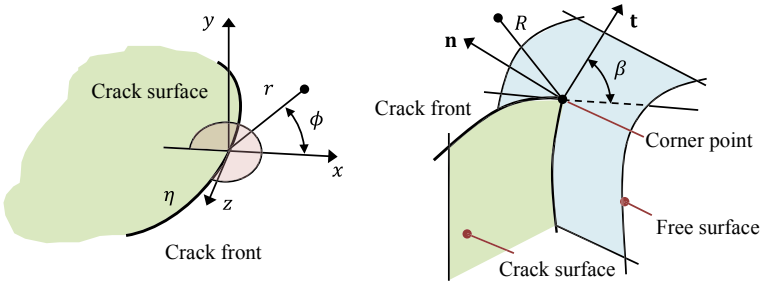

Fig. 16.2 Representation of the stress field near the front of 3D crack

16.3 3D Stress States, Fracture and Fatigue Phenomena

16.3.1 Effect of 3D Corner Singularity of Fatigue Crack Growth

Several researchers suggested in the past that the presence of the 3D corner singularity might lead to a deviation of the fatigue crack front from the orthogonal direction near the free surface. This phenomenon is normally observed in fatigue crack tests for various materials. Energy considerations suggest that during fatigue crack growth the shape of the entire crack front should preserve a $r^{-1/2}$ behavior, including the corner points. This is only possible if the front edge of a fatigue crack intersects the free surface at a certain critical angle, β_c. Particular values and various approximations for β_c as a function of Poisson's ratio are all available in many papers and will not be provided in this paper [9, 11].

The outcomes of experimental verification studies are often controversial. For example, fatigue crack front shapes in specimens of rectangular and trapezoidal beams made of PMMA agree with the energy considerations [9]. Another set of experimental data for surface-breaking cracks performed on steel round bars does not support these considerations [12]. In the latter work the traditional LEFM requirement has been enforced to keep the plastic zone size negligible compared to the ligament. A simple analysis demonstrates, however, that this requirement is not sufficient to separate the plasticity effects from the elastic stress state generated by the 3D corner singularity. Therefore, this particular study cannot be considered as conclusive.

16.3.2 On Evaluation of Edge Singularities Near Vertex Points

An accurate evaluation of singular stress states near the corner point represents a significant computational challenge [8]. As first shown by Benthem [14], the behaviour of the stress intensity factor, K_I, in this can be described as

$$K_I(s) \sim s^{-\lambda_{CI}+\frac{1}{2}}, \tag{16.2}$$

where s is the curvilinear abscissa of the crack front with its origin set at the end point on the free surface. A similar dependence was obtained attracting the matched asymptotic expansion method [8]. Further, based on dimensionless considerations, the variation of the stress intensity factor near the corner points was investigated for through-the-thickness cracks [4, 15, 16]. Moreover, it seems that the similar power function behavior is valid near the vertex point in the case of dissimilar materials [7].

16.3.3 Coupled Fracture Mode (O-mode)

The existence of the coupled out-of-plane mode (O-mode), was exhaustively discussed in the literature. Mode II loading creates tensile and compressive stress states on two sides along the bi-sector line, which leads a scissoring motion due to the Poisson's effect. This generates a new fracture mode, which has similar characteristics to Mode III. However, this is a local mode, which decays very rapidly with the distance from the crack front. As all 3D stress states in plates, it is confined to approximately half of the plate thickness, h, in the radial direction [6, 16], see Fig. 16.3. The influences of the coupled mode as well as the variations of the stress intensity factors across the plate thickness on fracture and fatigue phenomena largely remain unclear [16].

16.3.4 Local Stress Intensity Factor Distribution

The intensities of stress intensity factors vary along the crack front, L. The energy balance equation can provide a link between the remotely applied stress intensity factors, K_I^∞ and K_{II}^∞ from one side and the distribution of the local stress intensity factors, $K_I(\eta)$, $K_{II}(\eta)$ and $K_O(\eta)$ from the other side:

$$\left(K_I^\infty\right)^2 + \left(K_{II}^\infty\right)^2 = \frac{1-\nu^2}{2h}\int_L \left[K_I^2(\eta) + K_{II}^2(\eta)\right]d\eta + \frac{1+\nu}{2h}\int_L K_O^2(\eta)d\eta. \tag{16.3}$$

This relationship is often utilised to verify the quality and accuracy of the numerical simulations [6]. However, it needs to be applied with caution, see Sect. 16.3.6.

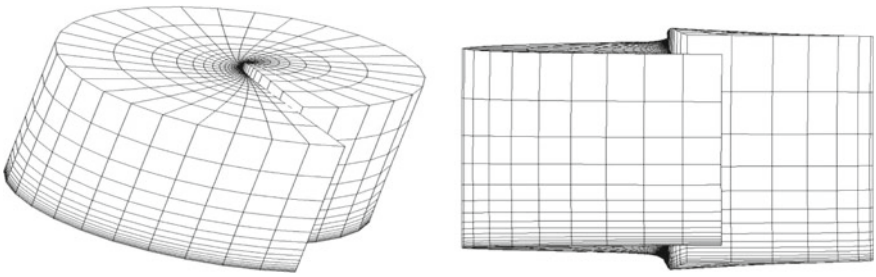

Fig. 16.3 Illustration of the generation of the coupled fracture mode (mode O) due to Poisson's effect for a crack subjected to shear loading

16.3.5 Surface Displacements at Crack Tip

As mentioned in the introduction, plane stress and plane strain theories provide misleading results for the out-of-plane (transverse) displacements, strains and stresses in the near crack tip region. The first theory predicts infinite out-of-plane displacements, u_z, at the crack tip, the second theory (plane strain theory) predicts no the out-of-plane displacements at all. The latest numerical studies supported by experimental investigations indicate that the transverse displacements at the crack tip for mode I are finite (as expected) and the surface displacement can be accurately described by the following equation [10]:

$$u_z \approx -1.34 \cdot \nu K_I^{\infty} \sqrt{h}/E. \tag{16.4}$$

A similar equation was derived for mode II, which was also verified using 3D FE analysis as well as experimental measurements with the DIC method [10, 13].

16.3.6 Williams Asymptotic Series Expansion

This classical result, in general, is not valid in 3D as part of the stress and deformation fields do not follow the plane stress or plane strain simplifications, specifically, in the areas adjacent to the crack faces (Fig. 16.1). This conclusion has many implications for experimental analysis of the stress intensity factor and interpretation of 3D FE calculations [10].

16.3.7 Fracture Scaling Laws in 3D LEFM

The problem of scale effects at brittle fractures was addressed in many studies published in the past. In addition to the classical scaling law in the classical (2D) theory of brittle fracture, dimensionless considerations provide two new scaling laws [4]:

$$K^{CS} \sim K_I^{\infty} h^{1/2-\lambda_{CS}} \text{ and } K^{CA} \sim K_{II}^{\infty} h^{1/2-\lambda_{CA}}. \tag{16.5}$$

The difference $1/2 - \lambda_{\mathrm{CS}} \leq 0$ and $1/2 - \lambda_{\mathrm{CA}} \geq 0$, which implies that the intensity of the corner singularity, K^{CS}, increases boundlessly with a decrease of the plate thickness, and it is expected to affect failure conditions for very thin plates. The intensity of the antisymmetric corner singularity, K^{CA}, has the opposite trend, and it grows boundlessly with an increase of the plate thickness. The presence of two new scaling laws might help to explain the discrepancies between LEFM predictions and test results [17].

16.4 Conclusion

The area of 3D Fracture Mechanics is currently not as well developed as the classical 2D fracture theory. It is largely based on few 3D analytical results, several exact solutions obtained within simplified 3D plate theories and analysis and generalisations of a large number of numerical simulations. This area offers ample opportunities for further research, which can be critical for failure assessment.

References

1. Yang W, Freund LB (1985) Transverse shear effects for through-the-thickness cracks in elastic plate. Int J Solids Struct 21:977–994
2. Kotousov A, Bun S, Khanna A (2017) A new analytical method for the evaluation of transverse displacements and stresses in plane problems of elasticity. Int J Solids Struct 118:89–96
3. Gregory RD, Wan FYM (1988) The interior solution for linear problems of elastic plates. J Appl Mech 55(3):551–559
4. Kotousov A (2010) Effect of plate thickness on stress state at sharp notches and the strength paradox of thick plates. Int J Solids Struct 47(14–15):1916–1923
5. Pook LP (2013) A 50-year retrospective review of three-dimensional effects at cracks and sharp notches. Fatigue Fract Eng Mater Struct 36(8):699–723
6. He Z, Kotousov A, Berto F (2015) Effect of vertex singularities on stress intensities near plate free surfaces. Fatigue Fract Eng Mater Struct 38(7):860–869
7. Luangarpa C, Koguchi H (2016) Analysis of singular stresses at a vertex and along a singular line in three-dimensional bonded joints using a conservative integral. Eur J Mech A/Solids 60:208–216
8. Vu MN, Geniaut S, Massin P, Marigo JJ (2015) Numerical investigation on corner singularities in cracked plates using G-theta method with an adopted θ field. Theor Appl Fract Mech 77:59–68
9. Heyder M, Kuhn G (2005) Numerical and experimental investigations of the influence of corner singularities on 3D fatigue crack propagation. Eng Fract Mech 72:2095–2105
10. He Z, Kotousov A, Berto F, Branco R (2016) A brief review of three-dimensional effects near crack front. Phys Mesomech 19:6–20
11. Hutar P, Ševcík M, Náhlík L, Zouhar M, Seitl S, Knésl Z, Fernández-Canteli A (2010) Fracture mechanics of the three-dimensional crack front: vertex singularity versus out of plain constraint descriptions. Procedia Eng 2(1):2095–2102
12. Lebahn J, Heyer H, Sander M (2013) Numerical stress intensity factor calculation in flawed round bars validated by crack propagation tests. Eng Fract Mech 108:37–49
13. He Z, Kotousov A (2016) On evaluation of stress intensity factor from in-plane and transverse surface displacements. Exp Mech 56(8):1385–1393
14. Benthem JP (1977) State of stress at the vertex of a quarter-infinite crack in a half-space. Int J Solids Struct 13:479–492
15. Garcia-Manrique J, Camas D, Lopez-Crespo P, Gonzalez-Herrera A (2013) Stress intensity factor analysis of through thickness effects. Int J Fatigue 46:58–66
16. Kotousov A, Lazzarin P, Berto F, Pook LP (2013) Three-dimensional stress states at crack tip induced by shear and anti-plane loading. Eng Fract Mech 108:65–74
17. Sinclair GB, Chambers AE (1987) Strength size effects and fracture mechanics: what does the physical evidence say? Eng Fract Mech 26:279–310

Chapter 17
An Improved Prediction of the Effective Range of Stress Intensity Factor in Fatigue Crack Growth

Bing Yang, M. N. James, Yongfang Huang, J. M. Vasco-Olmo and F. A. Díaz

Abstract This paper will summarise the results obtained to date and which demonstrate that the mesoscale CJP model of crack tip fields is capable of providing an improved correlation of fatigue crack growth rates across a range of stress ratios and specimen geometries, compared with the standard stress intensity factor calculations.

Keywords Crack tip field model · Digital image correlation · Shielding

17.1 Introduction

The CJP model is a meso-scale model of crack tip displacement and stress that was proposed a few years ago as an attempt to better characterise the elastic forces induced by the plastic enclave that surrounds a growing fatigue crack and hence enable direct prediction of the effective range of crack driving force. The model was a development of earlier work that had achieved some success in measuring the wake contact pressure arising from the plastic enclave that surrounds a growing fatigue crack [1]. The theoretical model in Mode I loading was extended from a stress-based version that could be fitted to full-field photoelastic images of the crack tip region [2, 3], to one that utilised digital image correlation and could be applied directly to displacement fields on metallic specimens [4]. The next step in the development of

B. Yang
State Key Laboratory of Traction Power, Southwest Jiaotong University, Chengdu, China

M. N. James (✉)
School of Engineering, University of Plymouth, Plymouth, England
e-mail: mjames@plymouth.ac.uk

Department of Mechanical Engineering, Nelson Mandela Metropolitan University, Port Elizabeth, South Africa

Y. Huang
Department of Aeronautics, Xiamen University, Xiamen, China

J. M. Vasco-Olmo · F. A. Díaz
Departamento de Ingeniería Mecánica y Minera, University of Jaén, Jaén, Spain

J.A.F.O. Correia et al. (eds.), *Mechanical Fatigue of Metals*, Structural Integrity 7,
https://doi.org/10.1007/978-3-030-13980-3_17

the model extended it to deal with combined Mode I and Mode II loading which, in principle, would open up its use to include characterising surface roughness-induced shielding as well as plasticity-induced shielding [5].

Experimental verification of the concepts in the CJP model followed a little more slowly than the theoretical developments, reflecting factors such the complexity of phase-stepping photoelastic fatigue experiments, the development of software necessary to automate the CJP model solution from photoelastic and DIC images, and the training of Ph.D. students. Over the last several years, however, researchers from the University of Jaen in Spain, Gifu University in Japan, Southwest Jiaotong University and Xiamen University in China have been making considerable progress in experimental verification of the model [6, 7].

This paper will summarise the results obtained to date and which demonstrate that the CJP model appears capable of providing an improved correlation of fatigue crack growth rates across a range of stress ratios and specimen geometries, compared with the standard stress intensity factor calculations. The model also appears to correctly characterise both plastic zone shape and size and this paper will also briefly discuss the data obtained from overload experiments.

17.2 Background to the Model

The objective of the work described in Ref. [2] was to identify the real influence or effect on the applied elastic field, of stresses arising from plastic deformation associated with crack growth. Reference [4] notes that the CJP model essentially treats the crack as a notional plastic inclusion in an elastic body. This approach leads to the definition of a stress intensity factor perpendicular to the crack plane, called K_F, which drives crack growth in an analogous fashion to K_I and is modified by the incorporation of shielding force components acting perpendicular to the crack. The shielding effect of the plastic enclave is considered via a new retarding stress intensity factor K_R that is defined to account for forces in the plane of the crack that act to retard the crack, and the model also defines an interfacial shear stress intensity factor, K_S, which is included to capture compatibility-induced shear components of shielding that would perhaps be more applicable to Mode II or III loading. This paper will focus on K_F and K_R that have been shown to be applicable to Mode I fatigue crack growth. The model also defines a value for the *T*-stress as this parameter has certain characteristics that affect fatigue crack growth rate; as stated in Ref. [8] these depend on the sign and magnitude of the *T*-stress and can include substantially changing the size and shape of the plane strain crack tip plastic zone, a decrease in fatigue crack growth rate in the Paris law regime with increasing *T*-stress (this reflects the fact that higher positive values of *T*-stress imply higher constraint and smaller plastic zone size), and crack path influences (negative *T*-stress values can stabilise the crack path while, in contrast, positive *T*-stress values induce crack bifurcation). Reference [4] discusses the *T*-stress in the context of using the CJP model to characterise fatigue crack growth in polycarbonate CT specimens. The model can also be used to

investigate the effect of changing values of T-stress on the crack tip field as illustrated in Ref. [2] for the case of photoelastic fringes showing difference in principal stress. Clearly, for a crack tip model to more accurately define plastic zone size and shape, the T-stress is an important parameter.

The intention in developing the CJP model was to elucidate the role and influence of factors such as compatibility-induced interfacial shear stresses and wake contact forces on the effective range of stress intensity factor and any resulting changes observed in the fatigue crack growth rate. There was therefore a dual aim of improved mechanistic understanding of fatigue phenomena such as crack closure, plasticity-induced shielding and overload effects, together with obtaining an improved characterisation of fatigue crack growth in situations where these phenomena are occurring. As an example of improved understanding of the mechanisms that underlie observed phenomena, Ref. [2] indicates that the introduction of interfacial shear stresses causes migration along the crack path of the join between the photoelastic fringe loops on either side of the crack path. This is perhaps more pronounced in the crack wake, but both ahead and behind the crack, the shape of the join between the loops of common fringe order changes from a sharp 'V' to more of a 'U' shape. This phenomenon has been observed before in photoelastic images in the presence of crack closure but the discussion in Ref. [2] is probably the first time that it could be assigned, fairly reasonably, to the effect of interfacial shear stresses. Thus the model offers significant potential in terms of obtaining a better physical understanding of the potential role of the various forces in plasticity-induced shielding.

Further independent evidence of the utility of the model in providing predictions of the effective range of stress intensity factor comes from work recently published by Nowell et al. [9]. In Ref. [9] they discuss the CJP model and present a slightly simplified version of the force diagram given in Ref. [2]. They go on to demonstrate, using DIC data obtained from a growing fatigue crack, that the combined $K_F + K_R$ parameter predicts, a priori, very similar values of ΔK_{eff} throughout a fatigue cycle to those measured experimentally on an existing crack with their technique. Nowell et al. [9] express reservations regarding the split of ΔK into the K_F and K_R terms although they note in their paper that the split into what they call "applied and residual terms" may be helpful, even for measurements taken very close to the crack tip.

In terms of providing an improved characterisation of fatigue crack growth rate, sufficient experimental work has now been performed across a range of stress ratio values, specimen geometries and materials to verify that the model does indeed achieve this, compared with data obtained using the standard Irwin stress intensity value.

This paper will demonstrate this by presenting experimental fatigue crack growth rate data obtained at Plymouth and Jaen over the last two years and it will also summarise current work aimed at predicting fatigue crack growth rates using the CJP model and a calibration curve approach. Other ongoing work has considered the capability of the CJP model to characterise plastic zone size and shape through the application of overload cycles during constant amplitude (CA) fatigue [10], and compared the size and shape results with those given by other commonly used elastic

models of crack tip stresses [11]. The results demonstrate that the CJP model provides a very good characterisation of plastic zone size and shape during CA loading and throughout an overload event, while the accurate prediction of effective stress intensity factor range and the insights offered into the mechanisms operating during shielding allow the influence of other potential causes of crack growth changes during an overload to be identified [10].

17.3 Specimen Geometries and Experimental Techniques

Recent work has focussed on Grade 2 (commercially pure—CP) titanium with a measured yield strength of 390 MPa and a tensile strength of 448 MPa. The elastic Young's modulus E = 105 GPa and Poisson's ratio $\nu = 0.33$. Figure 17.1 shows the three specimen geometries that were used in the tests, i.e. compact tension (CT), double edge-notched tension (DENT) and centre-cracked tension (CCT). Fatigue testing was performed on an ElectroPuls E3000 with the relevant details given in Table 17.1.

The CCD camera used to acquire DIC images was equipped with a 10× magnification macro-zoom lens to provide the necessary spatial resolution in the measurement region surrounding the crack tip. The field of view was 1624 × 1202 pixels (approximately 13.68 × 10.12 mm, with slight specimen-to-specimen variations), giving the spatial resolution for each specimen shown in Table 17.1. Data acquisition involved periodically pausing the fatigue cycling and applying stepwise loading through a fatigue cycle, making DIC measurements at each step and crack tip position was recorded using a travelling microscope on the reverse side of the specimen (resolution ≈ 10 μm). Full experimental and analysis details are given in Ref. [7].

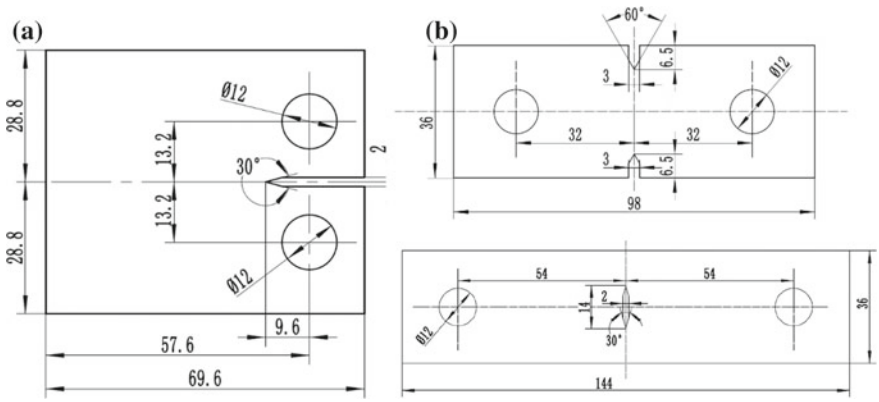

Fig. 17.1 The three specimen geometries used in this work: **a** CT; **b** DENT; **c** CCT

Table 17.1 Fatigue test parameters used in this work

Specimen	P_{max} (N)	R	DIC spatial resolution (μm/pixel)
CT1	700	0.1	8.33
CT2	700	0.3	8.33
CT3	700	0.6	8.22
DENT1	2200	0.05	8.62
DENT2	2200	0.3	8.61
CCT1	2200	0.1	8.88
CCT2	2200	0.3	7.36
CCT3	2200	0.6	7.65

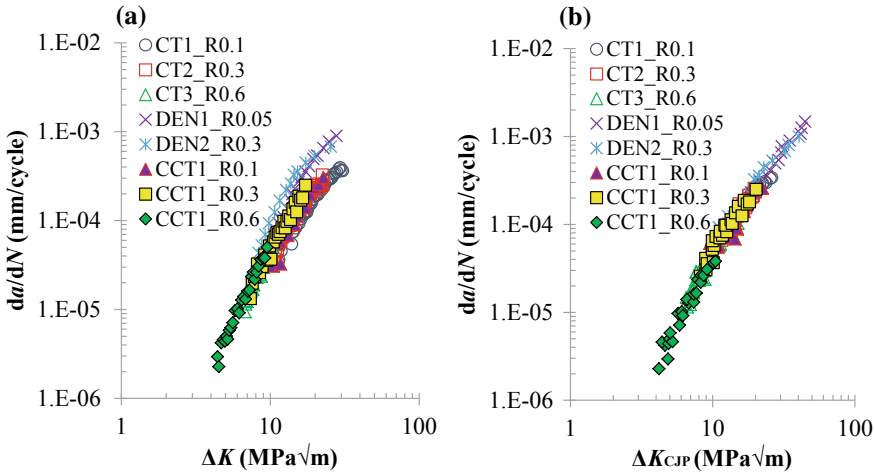

Fig. 17.2 Fatigue crack growth rate data characterised by **a** the standard definition of ΔK; **b** ΔK_{CJP}

Figure 17.2a presents the crack growth rate data characterised in terms of ΔK, while Fig. 17.2b presents the same information characterised using ΔK_{CJP}, which is defined as:

$$\Delta K_{CJP} = \left(K_{F,max} - K_{R,max}\right) - \left(K_{F,min} - K_{R,min}\right)$$

The level of plasticity-induced crack tip shielding in CP titanium is fairly low and hence, on a log-log plot the improvement in the characterisation into a single curve may not appear very high, reflecting the low level of plasticity-induced shielding in CP titanium. However, statistical analysis demonstrates a significant improvement in terms of fitting the data with a single straight line, e.g. from a regression parameter of 0.9504 for the DENT, CT and CCT curves using ΔK to 0.9861 using ΔK_{CJP}. It is also the case that the CJP crack tip field model does not require the incorporation of compliance-based geometry-correction factors in the calculation of stress intensity.

Reference [7] has shown that there are simple relationships between ΔK_{CJP} and ΔK using calibration curves that relate the values of the parameters in the CJP model to the standard ΔK value. These relationships have been determined for CT and DENT specimens of the CP titanium alloy, and they would be affected by influences that change the stress component parameters A, B or D, i.e. changes in the forces that contribute to shielding.

17.4 Concluding Remarks

The work described in Ref. [7] and the additional data on CCT specimens presented here give confidence that the CJP model has significant potential to improve crack growth characterisation where plasticity-induced shielding of the crack tip is occurring. The work reported in Ref. [10] has shown that the CJP model can be used to obtain accurate predictions of both the effective range of stress intensity factor and the changes in plastic zone size and shape that occur during variable amplitude fatigue, and to then assess how well the changes in crack growth rate can be correlated with the effects of plasticity-induced closure.

References

1. Pacey MN, Patterson EA, James MN (2005) A new photoelastic model for studying fatigue crack closure. Exp Mech 45(1):42–52
2. Christopher CJ, James MN, Patterson EA, Tee KF (2007) Towards a new model of crack tip stress fields. Int J Fract 148:361–371
3. Christopher CJ, James MN, Patterson EA, Tee KF (2008) A quantitative evaluation of fatigue crack shielding forces using photoelasticity. Eng Fract Mech 75:4190–4199
4. James MN, Christopher CJ, Yanwei L, Patterson EA (2013) Local crack plasticity and its influences on the global elastic stress field. Int J Fatigue 46:4–15
5. Christopher CJ, Laboviciute G, James MN, Patterson EA (2013) Extension of the CJP model to mixed mode I and mode II. Frattura ed Integrità Strutturale 7(25):161–166
6. James MN, Christopher CJ, Díaz Garrido FA, Vasco-Olmo JM, Toshifumi K, Patterson EA, Interpretation of plasticity effects using the CJP crack tip field model, Solid State Phenom 258:117–124 (2016); In: Proceedings of the 8th international conference on materials structure & micromechanics of fracture, Brno, Czech Republic, 27–29 June 2016
7. Yang B, Vasco-Olmo JM, Díaz FA, James MN (2018) A more effective rationalisation of fatigue crack growth rate data for various specimen geometries and stress ratios using the CJP model. Int J Fatigue
8. Hadj Meliani M, Azari Z, Pluvinage G, Matvienko YG (2010) The effective T-stress estimation and crack paths emanating from U-notches. Eng Fract Mech 77:1682–1692
9. Nowell D, Dragnevski KI, O'Connor SJ (2018) Investigation of fatigue crack models by micro-scale measurement of crack tip deformation. Int J Fatigue
10. Vasco-Olmo JM, Díaz FA, James MN, Bing Y (2018) Crack tip plastic zone evolution during an overload cycle and the contribution of plasticity-induced shielding to crack growth rate changes (in press). Fatigue Fract Eng Mater Struct
11. Vasco-Olmo JM, James MN, Christopher CJ, Patterson EA, Díaz FA (2016) Assessment of crack tip plastic zone size and shape and its influence on crack tip shielding. Fatigue Fract Eng Mater Struct 39(8):969–981

Chapter 18
Short and Long Crack Growth of Aluminium Cast Alloys

Martin Leitner, Roman Aigner, Sebastian Pomberger, Michael Stoschka, Christian Garb and Stefan Pusterhofer

Abstract Fatigue design of AlSi-alloy cast components is a challenging issue due to a great variety of the microstructure depending on the local cooling conditions, which majorly affects the local fatigue behaviour. Therefore, this paper contributes with an experimental evaluation of the short and long crack growth of aluminium cast alloys. At first, single edge notched bending (SENB) crack propagation tests show a distinctive transition of the crack resistance from the small to the long crack regime. At second, in situ fatigue experiments with an optical measurement of the surface crack length augment the crack growth data of the SENB-tests. In addition, the observations reveal that the local material condition, such as micro shrinkage pores or variation in local microstructure, affect the crack propagation as well as the crack path. Summarized, the presented work highlights that the short and long crack behaviour including the influence of microstructural properties needs to be considered thoroughly in order to properly assess the fatigue life of AlSi-alloy cast components.

Keywords Crack growth · Aluminium cast · Crack closure · Resistance curve · Microstructural effects

18.1 Introduction

This paper deals with an experimental characterization of the short and long crack growth behaviour of aluminium AlSi-cast alloys. The work includes four different material types exhibiting a variation of the alloy specification, heat treatment, and eutectic modifiers. In addition, different grades of porosity are established as the samples are extracted from varying components with locally tailored cooling rates,

M. Leitner (✉) · R. Aigner · S. Pomberger · M. Stoschka · S. Pusterhofer
CD Laboratory for Manufacturing Process Based Component Design, Montanuniversität Leoben, Franz-Josef Straße 18, 8700 Leoben, Austria
e-mail: martin.leitner@unileoben.ac.at

C. Garb
Montanuniversität Leoben, Franz-Josef Straße 18, 8700 Leoben, Austria

J.A.F.O. Correia et al. (eds.), *Mechanical Fatigue of Metals*, Structural Integrity 7,
https://doi.org/10.1007/978-3-030-13980-3_18

Table 18.1 Overview of investigated aluminium cast materials

Alloy specification	Heat treatment	Eutectic modifier	Cast component
EN AC-45500	T6	Strontium (Sr)	Cylinder head (ch)
EN AC-45500	T6	Sodium (Na)	Cylinder head (ch)
EN AC-46200	T5	Strontium (Sr)	Cylinder head (ch)
EN AC-46200	T6	Strontium (Sr)	Crank case (cc)

see Table 18.1. Preliminary studies [1, 2] revealed that these cast process parameters can significantly affect the fatigue strength; hence, this paper continuatively focuses on the crack growth characteristics as shown in [3, 4]. The experiments cover both the short and long crack fatigue regime. Within the short crack growth special attention is laid on the effective threshold of the stress intensity factor range $\Delta K_{th,eff}$ [5] as well as the increasing influence of crack closure phenomena [6], such as plasticity- and roughness-induced crack closure effects [7], during crack propagation.

18.2 Crack Resistance Curve

A compression pre-cracking method to generate near-threshold fatigue-crack-growth-rate data [8] is applied to evaluate the resistance (R-) curve [9] of the investigated SENB cast alloy specimens. This R-curve describes the course of the fatigue crack threshold ΔK_{th} starting from the effective value $\Delta K_{th,eff}$ at a crack extension of $\Delta a = 0$ mm up to the long crack growth threshold $\Delta K_{th,lc}$. This short- to long crack growth based change can be described utilizing an exponential approach including the characteristic length l_R [10], see Eq. (18.1).

$$\Delta K_{th} = \Delta K_{th,eff} + (\Delta K_{th,lc} - \Delta K_{th,eff}) \cdot (1 - e^{(-\Delta a/lR)}) \tag{18.1}$$

Further on, if the crack extends and the long crack growth threshold $\Delta K_{th,lc}$ is reached, the common fatigue crack propagation law introduced by Paris and Erdogan [11] is employed. Figure 18.1 (left) depicts the experimental crack growth results for three single-edge-notched-bending samples made of EN AC-45500-T6 Sr (ch) [12]. All fracture mechanical tests are conducted at an alternating load stress ratio of $R = -1$. A subsequent evaluation of the R-curve in Fig. 18.1 (right) shows that the effective threshold values in the short crack regime match well; however, major differences regarding the influence of crack closure effects and the final long crack threshold are recognizable.

Microstructural characteristics significantly affect the fatigue crack growth of aluminium AlSi-cast alloys [13]. Hence, further experiments with optical in situ fatigue crack growth detection according to the procedure given in [14] are conducted.

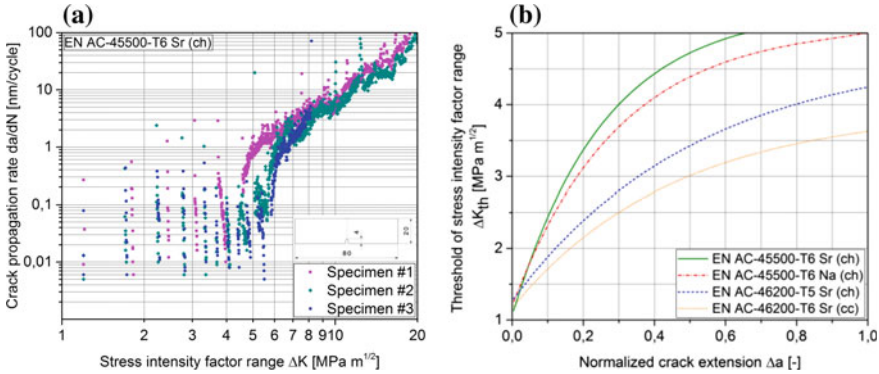

Fig. 18.1 Experimental crack growth results for EN AC-45500-T6 Sr (ch) (left) and evaluation of the fatigue crack resistance curve for the different test series (right)

18.3 In Situ Crack Propagation Tests

In [15], a small-scale rotating bending test-rig was build-up as illustrated in Fig. 18.2. The test rig enables in situ crack propagation analysis utilizing an optical crack measurement based on laser-confocal microscopy. Therefore, round specimens are taken from the very sample position to investigate the surface crack growth.

In order to evaluate the corresponding stress intensity factor range ΔK, the geometry function recommended in [16] is applied, which is valid for round bars under rotating bending load, see Eqs. (18.2) and (18.3).

$$\Delta K = \Delta\sigma \cdot Y(a, r) \cdot \sqrt{\pi s} \; with \; a = 2s/\pi \tag{18.2}$$

$$Y(a, r) = 0.63423 - 0.29743(a/r) + 0.07408(a/r)^2 + 0.48717(a/r)^3 \tag{18.3}$$

Herein, $\Delta\sigma$ is the applied nominal stress range, $Y(a, r)$ is the geometry function, s is the surface crack arc length, a is the crack depth, and r is the radius of the round specimen. Utilizing the measured surface crack arc length from the in situ tests, the stress intensity factor range ΔK at the surface is directly calculable.

Figure 18.3 demonstrates an example of an in situ crack propagation analysis for a round specimen, which is made of a EN AC-45500-T6 Sr (ch) cast alloy. It is observed that the fatigue crack initiated at a micro shrinkage pore at a number of $N_0 \sim 0.1 \cdot N_f$ load-cycles. This observation is in agreement to a study given in [17]. After initiation, the crack propagates within the small-crack growth region (N_1 and N_2) up to a surface crack length of $s \sim 0.2$ mm, which equals a stress intensity factor range ΔK of about 2.3 MPa$\sqrt{\text{m}}$. After reaching the long-crack regime at N_3, the crack growth rate accelerates according to the SENB test data up to final fracture at N_f.

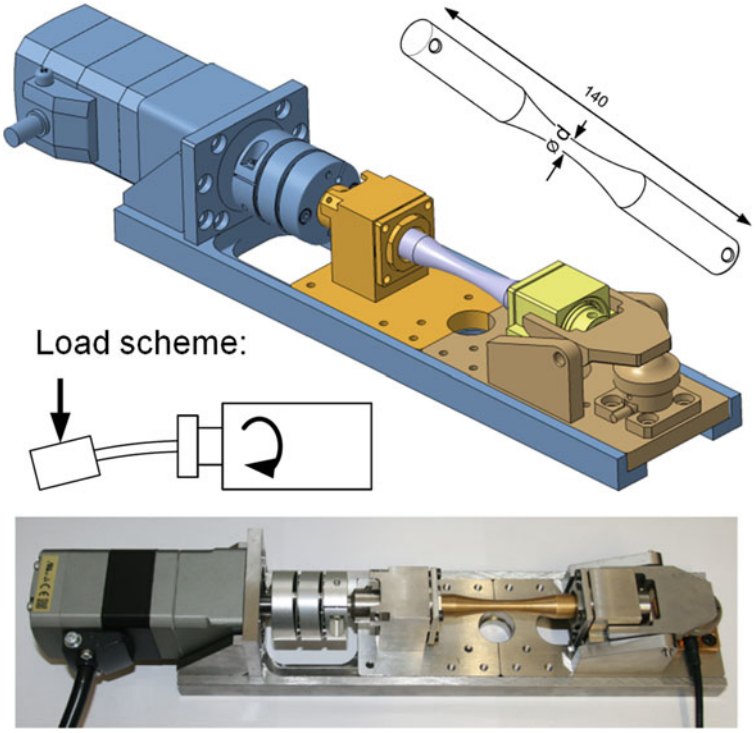

Fig. 18.2 Design of bending test rig for in situ crack propagation tests [15]

To sum up, the investigated in situ fatigue crack growth tests fit well to the evaluated fracture mechanical SENB crack propagation results, which validate the practicability of this data to assess the fatigue life of AlSi-cast materials. However, both the crack propagation rate as well as the crack path may be significantly influenced by microstructural properties, such as shown in [18].

Figure 18.4 (left) highlights the effect of a micro pore on the fatigue crack path. Thereby, the crack strikes the pore on the top-left side within the marked area, and exits on the down-right side, which majorly affected the crack path. Another example is given in Fig. 18.4 (right) showing that not only micro pores, but also the microstructure can have an effect on the crack growth behaviour. Herein, the crack enters on left side within the marked area and grows along a boundary between the α-Al and the eutectic phase up to the right side of the marked area.

Summarized, the results of the in situ optical analysis show that the local material condition, such as micro shrinkage pores or microstructure, influence not only the crack growth rate, but additionally the crack path. Hence, it is essential to cover both the short and long crack fatigue regime to properly assess the lifetime of AlSi-cast alloys, as demonstrated in [12].

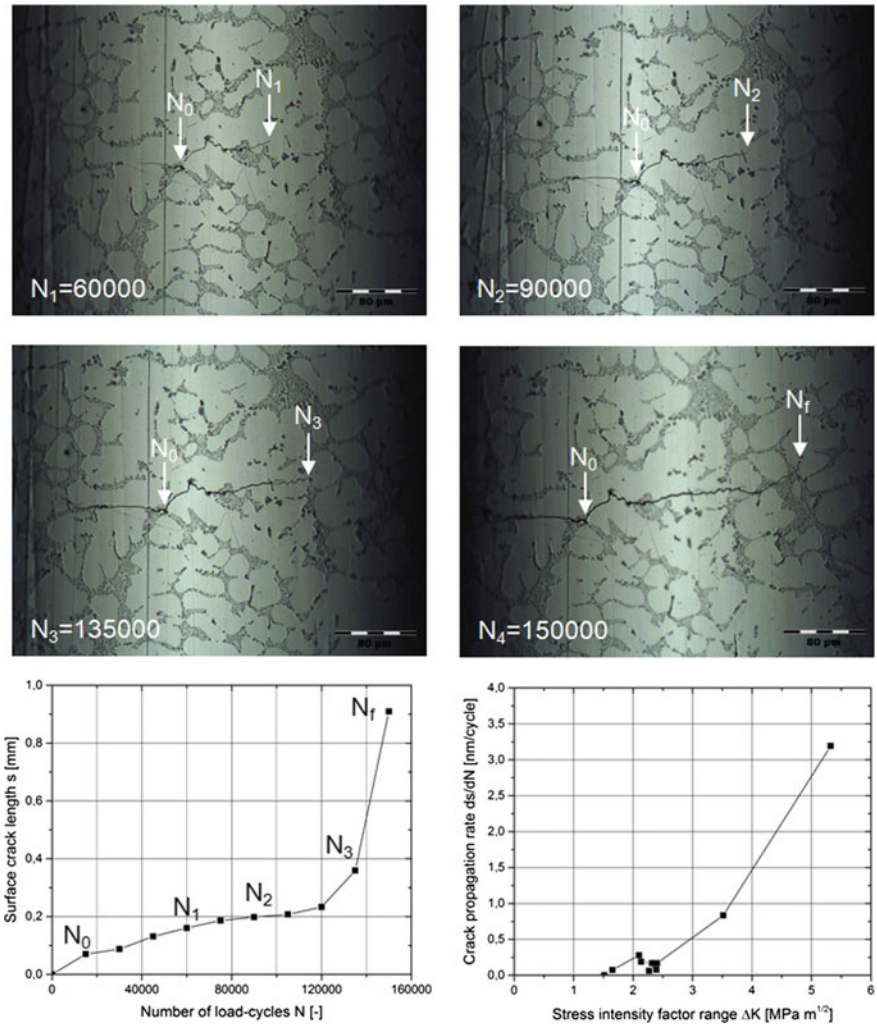

Fig. 18.3 In situ optical detection of crack growth for an EN AC-45500-T6 Sr (ch) cast alloy

18.4 Conclusions

The results of the SENB-crack propagation tests with the investigated AlSi-cast alloys reveal that a distinctive transition from the short to the long crack region occurs. Furthermore, the in situ crack growth experiments validate this finding and highlight that local microstructure can affect the crack propagation as well as the crack path.

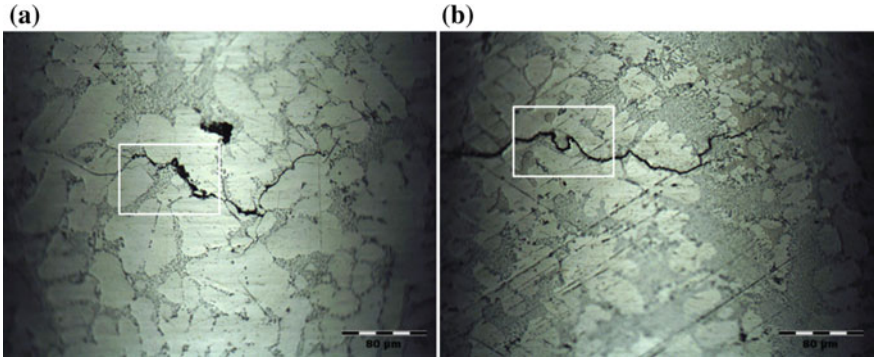

Fig. 18.4 Influence of micro shrinkage pore (left) and microstructure (right) on crack propagation

Acknowledgements The financial support by the Austrian Federal Ministry for Digital and Economic Affairs and the National Foundation for Research, Technology and Development is gratefully acknowledged.

References

1. Garb C, Leitner M, Grün F (2017) Application of $\sqrt{\text{area}}$-concept to assess fatigue strength of AlSi7Cu0.5Mg casted components. Eng Fract Mech 185:61–71
2. Leitner M, Garb C, Remes H, Stoschka M (2017) Microporosity and statistical size effect on the fatigue strength of cast aluminium alloys EN AC-45500 and 46200. Mater Sci Eng A 707:567–575
3. Casellas D, Pérez R, Prado JM (2005) Fatigue variability in Al–Si cast alloys. Mater Sci Eng A 398:171–179
4. Spangenberger AG, Lados DA, Coleman M, Birosca S, Hardy MC (2017) Microstructural mechanisms and advanced characterization of long and small fatigue crack growth in cast A356-T61 aluminum alloys. Int J Fatigue 97:202–213
5. Pippan R (1998) The effective threshold of fatigue crack propagation in aluminium alloys. Philos Mag A 77(4):861–873
6. Pippan R, Hohenwarter A (2017) Fatigue crack closure: a review of the physical phenomena. Fatigue Fract Eng 40:471–495
7. Kim JH, Lee SB (2001) Behavior of plasticity-induced crack closure and roughness-induced crack closure in aluminum alloy. Int J Fatigue 23:247–251
8. Newman JC Jr, Yamada Y (2010) Compression precracking methods to generate near-threshold fatigue-crack-growth-rate data. Int J Fatigue 32:879–885
9. Pippan R, Plöchl L, Stüwe HP (1994) Resistance curves for the threshold of fatigue crack propagation. In: Proceedings of ECF 10—structural integrity, pp 1441–1449
10. Maierhofer J, Gänser H-P, Pippan R (2015) Modified Kitagawa-Takahashi diagram accounting for finite notch depths. Int J Fatigue 70:503–509
11. Paris P, Erdogan F (1963) A critical analysis of crack propagation laws. J Basic Eng 85
12. Garb C, Leitner M, Stauder B, Schnubel D, Grün F (2018) Application of modified Kitagawa-Takahashi diagram for fatigue strength assessment of cast Al-Si-Cu alloys. Int J Fatigue 111:256–268
13. Lados DA, Diran A, Peggy EJ, Major JF (2007) Microstructural mechanisms controlling fatigue crack growth in Al–Si–Mg cast alloys. Mater Sci Eng A 468–470:237–245

14. Huter P, Winter G, Schwab M, Renhart P, Oberfrank S, Grün F, Stauder B (2014) Comparison of microstructural crack paths between hypo-eutectic Al–Si–Cu and Al–Si–Mg cast alloys in high plasticity regimes under rotating bending. Mater Sci Eng A 618:578–585
15. Huter P (2011) Development of a rotating bending testing machine for the in-situ analysis of crack initiation and microstructural crack growth. Master thesis, Montanuniversität Leoben
16. Freitas MM, Francois D (1995) Analysis of fatigue crack growth in rotary bend specimens and railway axles. Fatigue Fract Eng Mater Struct 18:171–178
17. Shiozawya K, Ohda T, Sun S-M (1997) Crack initiation and small fatigue crack growth behaviour of squeeze-cast Al-Si aluminium alloys. Fatigue Fract Eng Mater Struct 20:237–247
18. Zhu B, Leisner P, Seifeddine S, Jarfors A (2016) Influence of Si and cooling rate on microstructure and mechanical properties of Al–Si–Mg cast alloys. Surf Interface Anal 48:861–869

Chapter 19
Evaluation of Strain Controlled Fatigue and Crack Growth Behaviour of Al–3.4Mg Alloy

Pankaj Kumar and Akhilendra Singh

Abstract Present study focuses on fatigue performance of Al–3.4Mg (AA5754) aluminium alloy. Fatigue crack growth (FCG) and strain controlled low cycle fatigue (LCF) tests are performed for as received and precipitation strengthened AA5754 alloy. Precipitation strengthening heat treatment (PSHT) process significantly alters the mechanical and fatigue strength of Al–3.4Mg alloy. Fatigue crack growth (FCG) test is performed at load ratio ($R\text{-}ratio = P_{max}/P_{min}$) of 0.1 and 0.5 using compact tension (CT) specimens. Strain controlled low cycle fatigue (LCF) tests are performed at 1.2 and 1.0% strain ranges. FCG test results depict that PSHT alloys offer higher resistance against crack growth and improvement in fatigue life. LCF test reveals the cyclic hardening behaviour for both as received and PSHT AA5754 alloys. Improvement in fatigue life at both strain ranges is observed for PSHT alloys. Numerical simulations for crack growth analysis are performed by using eXtended Finite Element Method (XFEM). Chaboche kinematic hardening model coupled with finite element method (FEM) is used to simulate the experimental hysteresis loops and fatigue life obtained during strain controlled LCF tests. The present study concludes that lower crack growth rate by FCG test and higher fatigue strength during LCF test is obtained for precipitation strengthened AA5754 alloy as compared with as received alloy. The crack growth simulations by XFEM have good convergence with experimental results. The simulations performed by kinematic hardening model have good agreement with experimental results.

Keywords Fatigue crack growth · Low cycle fatigue · XFEM

19.1 Introduction

Aluminium-Magnesium (Al–Mg) alloys have majority of applications in components of aircraft, ship buildings, automobiles, cryogenic fields etc. due to their better welding characteristics, excellent corrosion resistance and good fatigue properties. Therefore, a relatively new Al–Mg alloy 5754 (AA 5754) is selected to characterize

P. Kumar · A. Singh (✉)
Indian Institute of Technology Patna, Patna 801103, India
e-mail: akhil@iitp.ac.in

J.A.F.O. Correia et al. (eds.), *Mechanical Fatigue of Metals*, Structural Integrity 7,
https://doi.org/10.1007/978-3-030-13980-3_19

their fatigue performance under dynamic loading conditions. The ageing heat treatment allows the reorientation of grain structure due to different phase transformations. Various authors reported that ageing behaviour of Al–Mg alloys significantly affects the mechanical properties of alloy [1, 2]. Starink and Zahra [3] had altered the mechanical properties by performing solution heat treatment at 440 °C for 2 h and post ageing at temperature range of 80–150 °C on Al–Mg alloy. The ease in alteration of mechanical strength via heat treatment of Al–Mg alloys increases its demand in various engineering applications especially in fatigue loading applications. Therefore, design of these components requires knowledge of cyclic loading/unloading responses. In past, researchers contributed their exhaustive work to characterize the fatigue and fracture behaviour of aluminium alloys. Pao et al. [4] observed lower crack growth rate for coarse grained Al–7.5Mg alloy during fatigue crack growth (FCG) test. Recently, higher fatigue life for solution treated AA5754 alloy was reported by Kumar and Singh [5]. Literatures are also available on low cycle fatigue (LCF) characteristics of different aluminium alloys. Nandy et al. [6] studied the influence of heat treatment on LCF behavior on Al–Mg–Si alloy. Several authors have also devoted their substantial work to characterize the fatigue behaviour through numerical methodologies. eXtended finite element method (XFEM) is widely used to model the crack growth behaviour by various authors [5, 7]. Strain controlled LCF performance is modelled by Chaboche kinematic hardening model. This model is widely used by various researchers for predicting the low cycle fatigue behaviour of different alloys [8, 9].

In present study, fatigue performance of Al–3.4Mg (AA5754) aluminium alloy is investigated. FCG and strain controlled LCF tests are performed for as received and precipitation strengthened AA5754 alloy. Numerical simulations for crack growth analysis are performed by using XFEM. Chaboche kinematic hardening model is used to simulate the experimental hysteresis loops obtained during LCF tests.

19.2 Precipitation Strengthening Heat Treatment

Various researchers [2, 3] have provided the following kinetics of phase transformations during precipitation strengthening of Al–Mg alloys

$$\text{SSS}\alpha \longrightarrow \text{GP zones} \longrightarrow \beta'' \longrightarrow \beta'$$

In present study, the Al–Mg alloy 5754 is aged for 3 years at room temperature (30 °C). The aged alloy is then heated at 530 °C for 2 h and then quenched in room temperature water. Quenching results in formation of GP (Guinier-Preston) contains disk shape structure of Mg. Initially, GP zones are modulated structure which is further transformed into ordered GP zones (β''). Thereafter, alloys are further aged at 250 °C for 6 h and cooling in furnace itself and thus, the formation of β' phase occurs. This phase transformation significantly affects the grain structure and mechanical properties of the alloy.

19.3 Experimental Procedure

19.3.1 Fatigue Crack Growth Test

The crack growth behaviour under cyclic loads is experimentally determined by the fatigue crack growth (FCG) test. The schematic of compact tension (CT) specimen is shown in Fig. 19.1. CT specimen is pre-cracked (fatigue crack) by cyclic loading to generate a sharp crack near machined notch tip.

Cyclic loads are applied at two different stress ratios (*R-ratio*) at 5 Hz frequency. A Sigmoidal or Paris curve is plotted by using logarithmic values of crack growth rate (*da/dN*) with respect to change in stress intensity factor (ΔK) range [10]. The slope (m) of stable crack growth regime determines the rate of crack growth.

19.3.2 Strain Controlled Low Cycle Fatigue Test

The specimen preparation and testing procedure is guided by ASTM E606/E606M standard for strain controlled LCF test. The schematic of standard LCF specimen is shown in Fig. 19.1c. A 12.5 mm strain gauge is used for measuring and controlling the strain in the specimen. Fully reversed cyclic loads are applied on the specimen

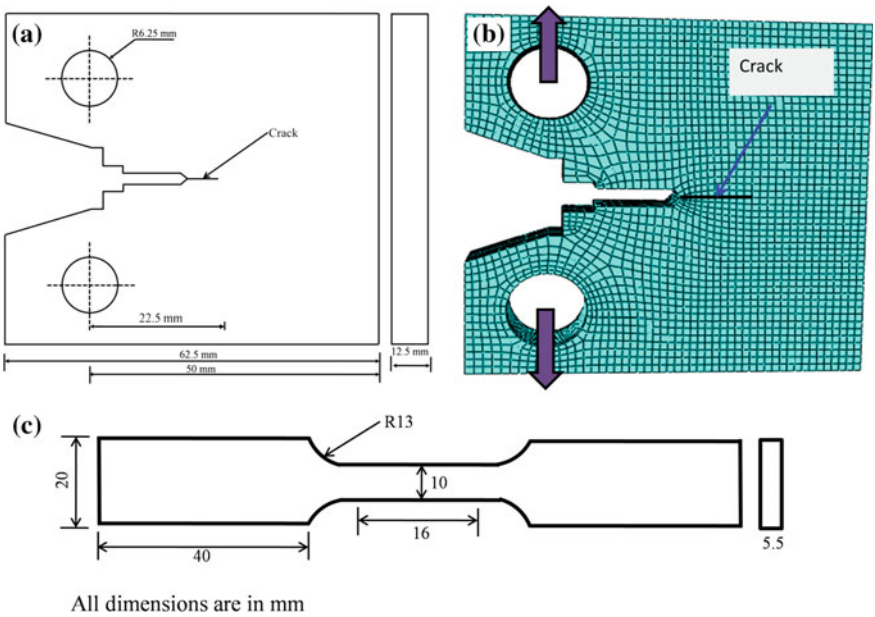

Fig. 19.1 Schematic of **a** experimental **b** meshed compact tension specimen **c** LCF specimen

with the strain ratio of $R_E = \varepsilon_{min}/\varepsilon_{max} = -1$. LCF tests are performed at 0.5% and 0.6% strain amplitudes.

19.4 Numerical Procedure

19.4.1 eXtended Finite Element Method (XFEM)

In XFEM, approximation of primary variable is enriched by additional functions within partition of unity framework [5, 11]. Two types of enrichment functions i.e. Heaviside function for crack surface and asymptotic crack tip functions for crack front are used to model a crack. Mathematically, the enriched displacement approximation at any point can be written as:

$$u^h(\mathbf{x}) = \sum_{j=1}^{\mathbf{n}} N_j(\mathbf{x}) \left[\underbrace{\mathbf{u}_j + (H(\mathbf{x}) - H(\mathbf{x}_j))a_j}_{j \in n_r} + \underbrace{\sum_{\alpha=1}^{4} (\varphi_\alpha(\mathbf{x}) - \varphi_\alpha(\mathbf{x}_j))b_j^\alpha}_{j \in n_A} \right] \quad (19.1)$$

where, $N_j(\mathbf{x})$ is the Lagrange interpolation function; $u^h(\mathbf{x})$ the nodal displacement vector associated with continues part of the finite element solution. $H(\mathbf{x})$, the Heaviside function across the crack surface; a_j is the additional degree of freedom associated with the Heaviside function; $\varphi_\alpha(\mathbf{x})$ is the asymptotic enrichment function taken from the Westergaard-William's solution for displacement field at crack tip and b_j^α is enriched nodal degree of freedom associated with crack tip enrichment function. Heaviside function across the crack surface, $H(\mathbf{x})$, is given as

$$H(\mathbf{x}) = \begin{cases} 1 & if\ (x - x^*)n \geq 0 \\ -1 & otherwise, \end{cases} \quad (19.2)$$

where x is the sample Gauss point; x^* is the point on the crack closest to x and n is the unit outward normal to the crack at x^*.

19.4.2 Kinematic Hardening Chaboche Model

Finite Element Method (FEM) coupled with Chaboche kinematic hardening cyclic plasticity model is used for simulating the hysteresis loop. During cyclic deformation, expansion and contraction of the yield surface is modelled through isotropic hardening model whereas translation of yield surface is reflected through kinematic hardening model [12, 13]. Chaboche kinematic hardening model is superposition of

three Armstrong and Frederick model [13]. Chaboche postulates that the total back stress is summation of three back stresses and written in the form

$$dx = \sum_{i=1}^{3} dx_i \tag{19.3}$$

$$dx_i = \frac{2}{3} c_i d\varepsilon^p - \gamma_i x_i dp \tag{19.4}$$

Here, dx is back stress increment vector, which defines the instantaneous position of the loading surface, γ_i is the kinematic hardening exponent at any point and $d\varepsilon^p$ is plastic strain increment vector. The material parameter c is initial kinematic hardening coefficient.

19.5 Results and Discussion

19.5.1 Experimental Results

Tensile test results depict that tensile and yield strength is increased from 191 MPa to 215 MPa and 257 MPa to 320 MPa for PSHT alloy respectively. FCG test results show the enhanced fatigue life for PSHT alloys at both *R-ratios*. The crack growth rate is higher in as received alloy as compared with PSHT alloys. Decent sigmoidal curves at all test parameters are presented in Fig. 19.2. The Paris constants are evaluated for uniform crack growth regions as illustrated in Table 19.1.

Stabilized hysteresis loops obtained during LCF tests are presented in Fig. 19.3a, b for as received and PSHT alloys. The results presented in Fig. 19.3c, d shows the higher fatigue life for PSHT alloys at both strain ranges. From above results, it can

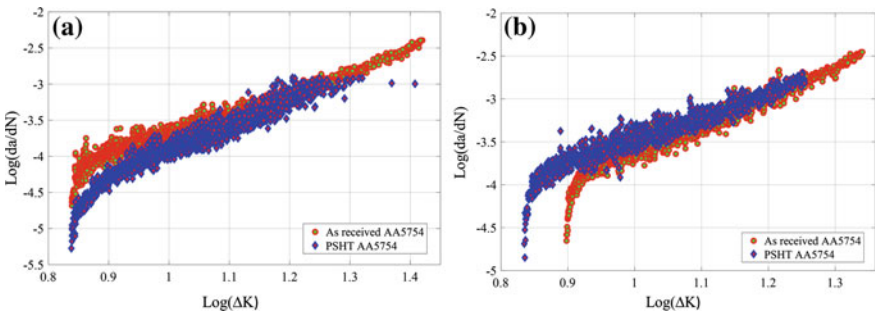

Fig. 19.2 Sigmoidal curve during fatigue crack growth test at stress ratio of **a** 0.1 and **b** 0.5

Table 19.1 Paris parameters evaluated for as received and PSHT alloys

Alloy condition	m		c		Fatigue life (N)	
	0.1	0.5	0.1	0.5	0.1	0.5
As received AA5754	2.39	2.24	4.2×10^{-7}	2.6×10^{-8}	109294	41671
PSHT AA5754	2.19	2.25	3.7×10^{-7}	1.8×10^{-8}	212998	53414

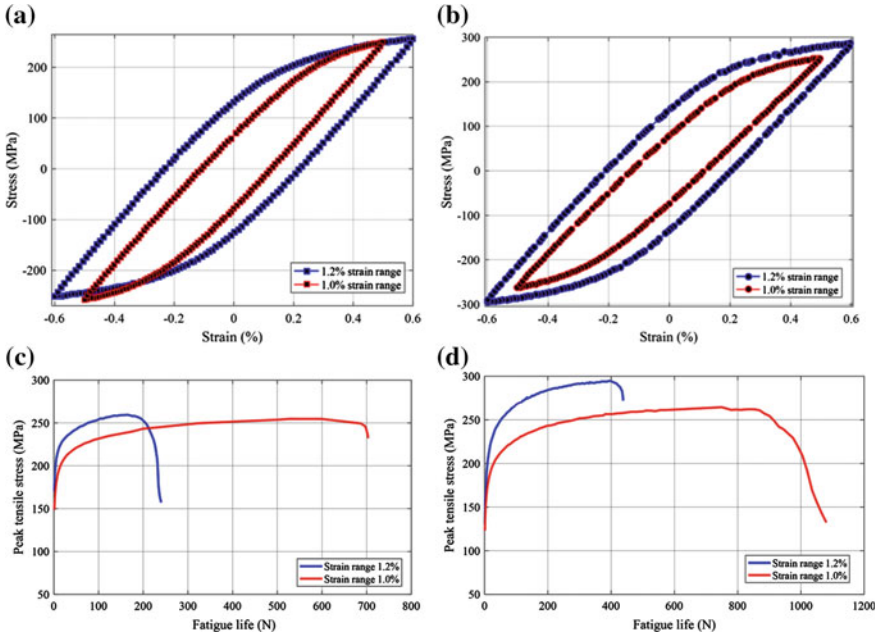

Fig. 19.3 Stabilized hysteresis loops for **a** as received and **b** PSHT alloy and fatigue life for **c** as received and **d** PSHT alloy during LCF tests

be concluded that the improvement in fatigue life during FCG and LCF tests reveals that reorientation of grain structure and phase transformation significantly enhances the fatigue strength of AA5754 alloy.

19.5.2 Numerical Results

Meshed model shown in Fig. 19.1b represents the exact solid model along with boundary conditions during XFEM simulation. The von Mises stress distribution near vicinity of crack tip (Fig. 19.4a, b) is higher for PSHT alloys which shows that PSHT alloys offers higher resistance towards crack growth. The initial cyclic hysteresis loop

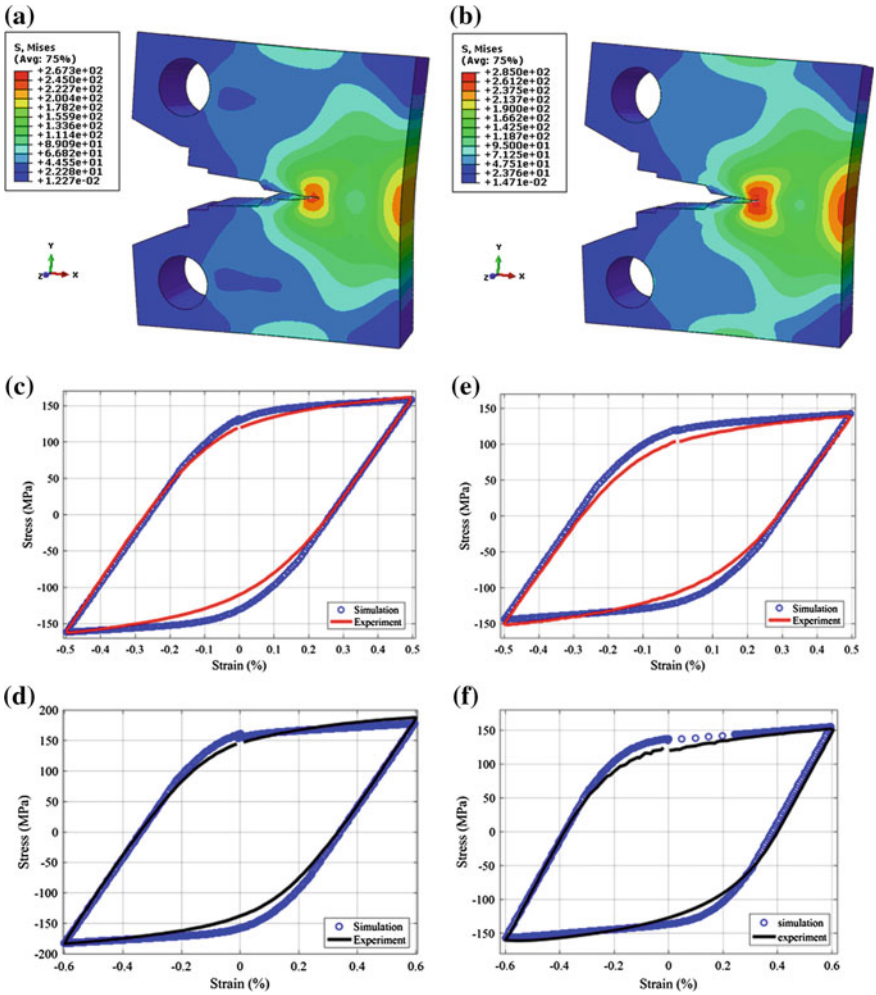

Fig. 19.4 von-Mises stress distribution in **a** as received and **b** PSHT alloys during crack growth simulations by XFEM. Experimental and simulated hysteresis loop at **c** 0.5% and **d** 0.6% strain amplitudes for as received and **e** 0.5% and **f** 0.6% strain amplitudes for PSHT alloy

is simulated by evaluating the material's parameters at highest strain range i.e. 1.2% by using "Chaboche Model". Figure 19.4c–f signifies that the simulated hysteresis loops have good agreement with experimental loops for both strain ranges.

19.6 Conclusions

PSHT is a suitable heat treatment process to enhance the mechanical and fatigue strength of AA 5754 alloy. Almost double fatigue life is obtained at *R-ratio* of 0.1 for PSHT alloys. Lower crack growth rate by FCG test and higher fatigue strength during LCF test is obtained for precipitation strengthened AA5754 alloy. XFEM methodology successfully predicted the crack growth behavior for both conditions of alloy. The numerical hysteresis loops predicted through Chaboche kinematic hardening model have good convergence with experimental loops.

References

1. Nozato R, Ishihara S (1980) Calorimetric study of precipitation process in Al–Mg alloys. Trans Jpn Inst Met 21(9):580–588
2. Sato T, Kamio A (1991) High resolution electron microscopy of phase decomposition microstructures in aluminium-based alloys. Mater Sci Eng A 146(1–2):161–180
3. Starink MJ, Zahra AM (1998) β′ and β precipitation in an Al–Mg alloy studied by DSC and TEM. Acta Mater 46(10):3381–3397
4. Pao P, Jones H, Cheng S, Feng C (2005) Fatigue crack propagation in ultrafine grained Al–Mg alloy. Int J Fatigue 27:1164–1169
5. Kumar P, Singh A (2017) Investigation of mechanical properties and fracture simulation of solution-treated AA 5754. J Mater Eng Perform 26(10):4689–14706
6. Nandy S, Sekhar AP, Das D, Hossain SJ, Ray KK (2016) Influence of dynamic precipitation during low cycle fatigue of under-aged AA6063 alloy. Trans Indian Inst Met 69:319–324
7. Goel S, Kumar N, Fuloria D, Jayaganthan R, Singh IV, Srivastava D (2016) Evaluating fracture toughness of rolled Zircaloy-2 at different temperatures using XFEM. J Mater Eng Perform 25:4046–4058
8. Paul SK, Sivaprasad S, Dhar S, Tarafder M, Tarafder S (2010) Simulation of cyclic plastic deformation response in SA333 C-Mn steel by a kinematic hardening model. Comput Mater Sci 48:662–671
9. Basantia SK, Bakkar MA, Khutia N, Das D (2015) Simulation of LCF characteristic of AA6063 Al alloy under different aging conditions. In: Materials today proceedings. Elsevier, pp 2226–2235
10. Paris PC (1961) A rational analytic theory of fatigue. Trend Eng Univ Wash 13(1):9–14
11. Belytscho T, Black T (1997) Elastic crack growth in finite elements with minimal remeshing. Int J Numer Methods Eng 40:1483–1504
12. Frederick CO, Armstrong PJ (2007) A mathematical representation of the multiaxial Bauschinger effect. Mater High Temp 24:1–26
13. Chaboche JL (1991) On some modifications of kinematic hardening to improve the description of ratchetting effects. Int J Plast 7:661–678

Chapter 20
Numerical Analysis of the Influence of Crack Growth Scheme on Plasticity Induced Crack Closure Results

D. Camas, J. Garcia-Manrique, F. V. Antunes and A. Gonzalez-Herrera

Abstract Plasticity Induced Crack Closure (PICC) has been studied by means of finite element method for a long time. Most of previous work was developed considering bi-dimensional models. During last years, the use of three-dimensional models has been extended. Nevertheless, the methodology employed has been inherited from bi-dimensional analyses. Many previous bi-dimensional analyses studied different numerical parameters and optimized them. Present computational capabilities allow a comprehensive study of the influence of different modelling parameter in a similar way to those bi-dimensional analyses. Moreover, the influence of these parameters on the obtained results along the thickness can be taken into consideration. In particular, one of the key issues is related to the crack growth scheme. A fatigue analysis implies a crack growth. Each change in loading and boundary conditions implies solving a nonlinear problem. It is not feasible to consider all the cycles involved in a real fatigue problem when running a finite element analysis. The computational cost is not acceptable. In the present work, a CT aluminium specimen has been modelled three-dimensionally and several calculations have been made in order to evaluate the influence of the number of load cycles between node releases. The results are analysed in terms of crack closure and opening values.

Keywords Finite element analysis · Fatigue crack closure · Crack growth scheme

20.1 Introduction

Since the early 70s, finite element models have been used to analyse the Plasticity Induced Crack Closure (PICC) phenomenon [1]. This mechanism is usually considered as the fundamental phenomenon that cause crack closure. The yielded material

D. Camas (✉) · J. Garcia-Manrique · A. Gonzalez-Herrera
Department of Civil and Materials Engineering, University of Malaga, Málaga, Spain
e-mail: dcp@uma.es

F. V. Antunes
CEMMPRE, Department of Mechanical Engineering, University of Coimbra, Coimbra, Portugal

J.A.F.O. Correia et al. (eds.), *Mechanical Fatigue of Metals*, Structural Integrity 7,
https://doi.org/10.1007/978-3-030-13980-3_20

produced during crack growth and previous fatigue loading cycles is the main actor that causes the untimely contact of the crack flanks.

First numerical analyses were made considering bi-dimensional models, whether plane strain or plane stress conditions. Some numerical parameters affect the results and it is important to understand and limit their effects. Issues as the mesh size, the plastic wake developed or the number of load cycles between crack increments must be carefully analysed to ensure reliable results. In the literature, a large number of previous bi-dimensional analyses, that optimise these parameters, can be easily found [2–5]. Some three-dimensional studies have been published recently [6, 7] as computational power has grown. However, the methodology usually employed has been inherited from the bi-dimensional optimisations.

Besides, one of the main issues that these numerical models face is the validation with experimental data. Fatigue crack closure measurement have been made employing strain gages located at the back or the mouth of the specimen. In any case, these measurements are taken remotely form the crack tip. Lately, digital image correlation has been used to validate numerical models [8–11]. However, with this technique, only information about what is happening at the surface is available.

The aim of this work is to analyse the influence of the crack growth scheme on the accuracy of the crack closure or opening results when considering a three-dimensional model. The influence of the number of load cycles between node releases on the crack closure results is analysed. This work is a continuation of a previous one in which the influence of the mesh size on PICC results was analysed considering a three-dimensional model [12].

20.2 Numerical Model

In this work, a CT specimen geometry ($W = 50$ mm, $a = 20$ mm and $b = 3$ mm) has been three-dimensionally modelled. The commercial finite element software ANSYS has been used to run the simulations. In Fig. 20.1, a scheme with main dimensions is shown, where a is the crack length and b, the specimen thickness.

The most critical region is the area close to the crack front. In this area there are deep stress and strain gradients. In order to capture properly these variations, the elements close to crack front must be very small. A huge size transition from this area to the most remote ones is mandatory to avoid an unreasonable computational cost. The specimen has been meshed considering two different strategies. Firstly, around the crack front, a homogeneous and structured mesh with hexahedral elements is used, while the volume of the specimen that is working in the elastic region of the material behaviour is meshed considering an unstructured mesh. The size of the first area is determined by the Dugdale's equation (Eq. 20.1).

$$r_{pD} = \frac{\pi}{8}\left(\frac{K_I}{\sigma_y}\right)^2 \tag{20.1}$$

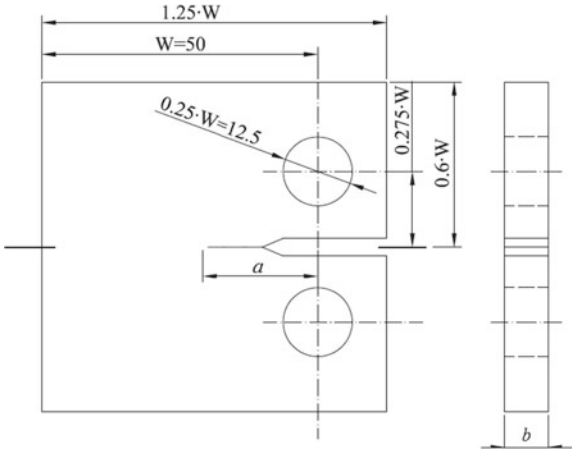

Fig. 20.1 CT specimen scheme

Because of the symmetry of the problem, just a quarter of the model has to be modelled applying appropriates boundary conditions.

Previous fracture mechanic numerical analyses based on the same specimen geometry shown that a fine mesh along the thickness is an important issue to take into account in order to capture properly the transitory behaviour close to the surface [13–15].

The minimum element size along the propagation axis and through the thickness is determined following the recommendations established in a previous study in which the effect of this numerical parameter in PICC results is analysed considering a three-dimensional model [12]. Figure 20.2 shows the mesh considered in this model.

The material considered is an aluminium alloy Al-2024-T351 that shows weak hardening ($E = 73.5$ GPa, $\sigma_y = 425$ MPa, $K' = 685$ MPa, $n' = 0.073$, where K' and n' are the parameter and the exponent of the Ramberg-Osgood yielding model). The cyclic stress-strain curve is considered in the numerical model which has evident savings in computational cost. A three-linear stress-strain curve with an isotropic hardening law has been used to model the material behaviour. There are no differences when the material shows a weak hardening rule as in this case where $H/E = 0.003$.

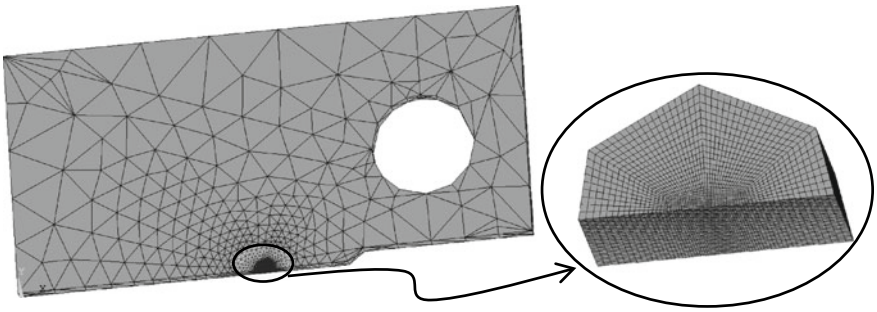

Fig. 20.2 3D finite element mesh

Four different cases have been analysed. For all of them, constant amplitude loading with crack growth is considered. The load applied is which corresponds to a stress intensity factor $K = 25$ MPa m$^{1/2}$ and the stress ratio considered is $R = 0.3$.

Besides, it is necessary to develop a minimum plastic wake to stabilise the results. The plastic wake length considered in this study is 0.4 times de Dugdale's plastic size. The crack advance takes place numerically by releasing nodes. Finally, the minimum element size is 90 times smaller than r_{pD}. In these numerical analyses, it is not possible to consider all the loading cycles involved in a real problem. Four different load cycles between node releases are considered range from 1 to 8 cycles.

20.3 Results

In this section the results are obtained changing the number of load cycles between node releases while the crack is growing, but after realising the last set of nodes, just one last cycle is applied.

The displacements and the y-stresses along the thickness and the effect of the number of load cycles between node releases are going to be analysed. Figure 20.3a shows the u_y displacements of the first node behind the crack front at three different positions along the thickness during the last loading cycle. The values at 1.5 represent the results obtained at the surface, while values at 0.0 refer to the mid-plane. The horizontal line represented in the figure corresponds to the rigid surface which represents the other crack flank. These results are obtained considering just one loading cycle between node releases.

In addition, Fig. 20.3b shows the y-stresses of the nodes at the crack front at the same three positions along the thickness than in previous figure. It can be clearly seen than the closure is prominent at the surface than at the interior of the specimen. The displacements along the thickness evolve, being greater at the interior, in particular at the mid-plane, and lower as the surface is approached. Same behaviour can be seen when y-stresses are analysed. This behaviour along the thickness is influenced by the evolution of the closure values along the crack front. The influence of the number of load cycles between node releases on y-displacements depends on the considered position along the thickness. The influence of the load cycles is greater at the interior of the specimen than at the surface. At the exterior of the specimen the vertical displacements are almost independent of the number of load cycles, while at the mid-plane the displacements slightly decrease when the load cycles between node releases increase. Turning our sight to stress behaviour, there is almost no noticeable influence of the number of load cycles between node releases during the crack growth.

Figure 20.4 shows the influence of the number of load cycles between node releases on node contact closure values. It can be seen that the values are pretty stable, more at the surface than in the interior. However, the relative difference in any case is smaller than 4%. The opening values show even less dependency with the number of load cycles between node releases.

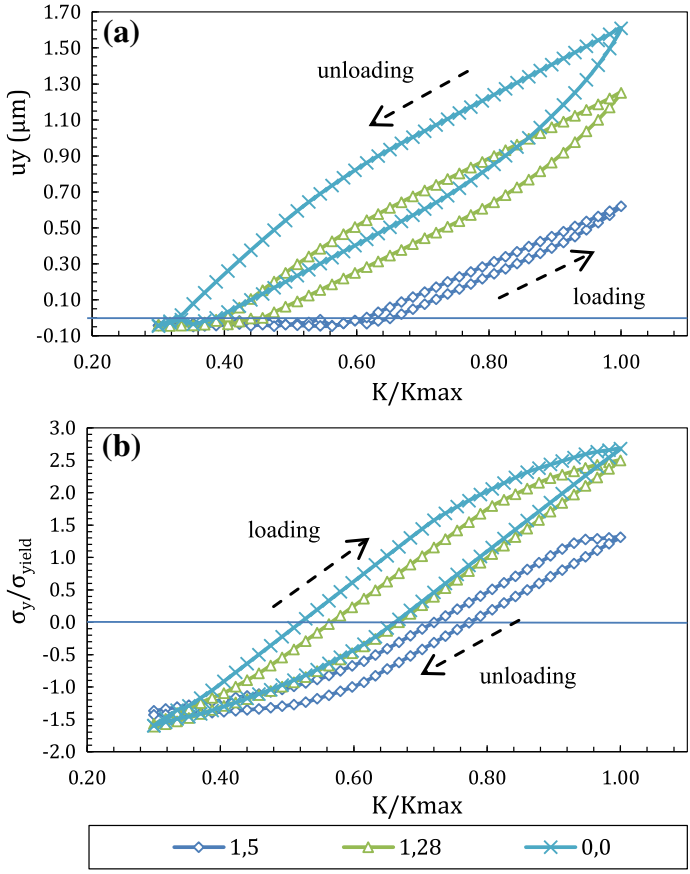

Fig. 20.3 u_y displacements (**a**) and σ_y stresses (**b**) for three nodes at different positions

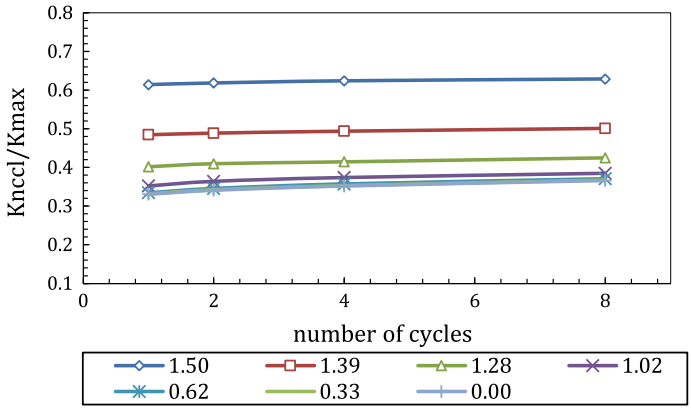

Fig. 20.4 Influence of the number of load cycles between node releases on node contact closure

20.4 Conclusions

This study has pointed out that for the material considered, which shows a weak hardening behavior, the number of loading cycles between node releases during the crack growth has not a significant influence. Neither stresses nor displacements suffer a great dependency on this numerical parameter. Besides, crack opening and closure results based on stresses are more stable than the ones based on displacements, although differences can be neglected compared with the numerical errors introduced by other parameters as the minimum element size.

Acknowledgements This work has been supported by the Ministerio de Economía y Competitividad of the Spanish Government through grant reference MAT2016-76951-C2-2-P.

References

1. Newman JC (1974) A finite-element analysis of fatigue crack closure. NASA Tech Memo X-72005
2. McClung RC, Sehitoglu H (1989) On the finite element analysis of fatigue crack closure-1. Basic modeling issues. Eng Fract Mech 33:237–252
3. Branco R, Antunes FV, Martins RF (2008) Modelling fatigue crack propagation in CT specimens. Fatigue Fract Eng Mater Struct 31:452–465
4. Gonzalez-Herrera A, Zapatero J (2009) Numerical study of the effect of plastic wake on plasticity-induced fatigue crack closure. Fatigue Fract Eng Mater Struct 32:249–260
5. Antunes FV, Camas D, Correia L, Branco R (2015) Finite element meshes for optimal modelling of plasticity induced crack closure. Eng Fract Mech 142:184–200
6. Chermahini RG, Shivakumar KN, Newman JC Jr, Blom AF (1989) Three-Dimensional aspects of plasticity-induced fatigue crack closure. Eng Fract Mech 34:393–401
7. Vor K, Gardin C, Sarrazin-Baudoux C, Petit J (2013) Wake length and loading history effects on crack closure of through-thickness long and short cracks in 304L: Part II—3D numerical simulation. Eng Fract Mech 99:306–323
8. Lopez-Crespo P, Camas-Peña D, Gonzalez-Herrera A, Yates JR, Patterson EA, Zapatero J (2008) Numerical and experimental analysis of crack closure. Key Eng Mater 385–387:369–372
9. Camas D, Lopez-Crespo P, Gonzalez-Herrera A (2011) Numerical study of the influence of the crack front curvature in the evolution of the plastic zone along the CT specimen thickness. Key Eng Mater 465:119–122
10. Camas D, Lopez-Crespo P, Gonzalez-Herrera A, Cruces AS, Moreno B (2016) Study of fatigue cracks with numerical and experimental methods. Procedia Eng 160:13–20
11. Camas D, Lopez-Crespo P, Gonzalez-Herrera A, Moreno B (2017) Numerical and experimental study of the plastic zone in cracked specimens. Eng Fract Mech 185:20–32
12. Camas D, Garcia-Manrique J, Moreno B, Gonzalez-Herrera A (2018) Numerical modelling of three-dimensional fatigue crack closure: mesh refinement. Int J Fatigue 113:193–203
13. Camas D, Garcia-Manrique J, Gonzalez-Herrera A (2011) Numerical study of the thickness transition in bi-dimensional specimen cracks. Int J Fatigue 33:921–928
14. Camas D, Garcia-Manrique J, Gonzalez-Herrera A (2012) Crack front curvature: influence and effects on the crack tip fields in bi-dimensional specimens. Int J Fatigue 44:41–50
15. Garcia-Manrique J, Camas D, Gonzalez-Herrera A (2017) Study of the stress intensity factor analysis through thickness: methodological aspects. Fatigue Fract Eng Mater Struct 40:1295–1308

Chapter 21
Towards Quantitative Explanation of Effective Thresholds of Mode III Fatigue Crack Propagation in Metals

Tomáš Vojtek, Stanislav Žák and Jaroslav Pokluda

Abstract The article presents the state-of-the art of tools for prediction of mode I, II and III effective thresholds for metallic materials. The effective threshold is independent of the stress ratio as well as the yield strength and is, therefore, a universal parameter for a particular metal. It can also be also used to separate the effective and crack closure components of resistance to fatigue crack growth. Results of recent research provided relationships for quantification of mode II and mode III effective thresholds for a wide range of metallic materials which are in a good agreement with experiments. The local crack growth mode has to be taken into account which depends on crystal lattice type and secondary phase type. The mode III cracks propagate by local crack front advances under mode I or mode II which was taken into account in numerical calculation of local stress intensity factors. It allowed explanation of the experimentally obtained values of the mode III effective thresholds.

Keywords Effective threshold · Modes II and III · Local growth mode · Metals

21.1 Introduction

In order to optimise the material microstructure and processing for damage-tolerance design the mechanisms of resistance to fatigue crack propagation need to be known.

T. Vojtek (✉) · S. Žák · J. Pokluda
Central European Institute of Technology (CEITEC), Brno University of Technology, Purkyňova 123, 612 00 Brno, Czech Republic
e-mail: tomas.vojtek@ceitec.vutbr.cz

T. Vojtek
CEITEC IPM, Institute of Physics of Materials, Academy of Sciences of the Czech Republic, Žižkova 22, 616 62 Brno, Czech Republic

J. Pokluda
Faculty of Mechanical Engineering, Brno University of Technology, Technická 2, 616 69 Brno, Czech Republic

Faculty of Special Technology, Alexander Dubcek University of Trencin, Pri parku 19, 911 06 Trenčín, Slovak Republic

J.A.F.O. Correia et al. (eds.), *Mechanical Fatigue of Metals*, Structural Integrity 7,
https://doi.org/10.1007/978-3-030-13980-3_21

These mechanisms can only be understood well when the applied loading is divided into the effective component causing material damage (intrinsic resistance) and the crack tip shielding component (extrinsic resistance) [1]. Kinetic data are usually measured in terms of the applied stress intensity factor (SIF) range and fitted by a Paris-type law. These data, however, represent a superposition of the intrinsic and extrinsic resistance which have physically completely different mechanisms. Therefore, there is a necessity for a separation of these two components. The applied loading characterised by the SIF range $\Delta K = K_{\max} - K_{\min}$ and the stress ratio $R = K_{\min}/K_{\max}$ can be divided into the effective SIF range $\Delta K_{\text{eff}} = K_{\max} - K_{\text{cl}}$, which corresponds to the effective crack driving force, where K_{cl} is the level of crack closure, and the rest of the loading cycle where the crack is closed (between K_{cl} and $K_{\min}$) and no material damage occurs at the crack tip. The closure-free stress ratio corresponds to the case of $K_{\min} > K_{\text{cl}}$ and $\Delta K_{\text{eff}} = \Delta K$. The effective SIF range is *independent of the stress ratio R*.

The crack growth threshold ΔK_{th} is an essential parameter for estimation of the residual fatigue lifetime. The effective threshold $\Delta K_{\text{eff,th}}$ is then a material characteristic important for both the separation and the study of intrinsic and extrinsic components at any given R ratio. The crack closure level can be calculated using a measured effective crack growth rate curve $\mathrm{d}a/\mathrm{d}N - \Delta K_{\text{eff}}$ in addition to a $\mathrm{d}a/\mathrm{d}N - \Delta K$ curve measured for standard stress ratios of 0.1 or -1. The material behaviour can then be derived for any other stress ratios using the relation $K_{\text{cl}} = K_{\max} - \Delta K_{\text{eff}}$, where $K_{\max} = \Delta K/(1 - R)$.

The crack closure component represents a large part of loading at the threshold, sometimes even higher than the effective part. This typically leads to a large scatter of the measured values under various testing conditions. For the mode I loading of metallic materials, the effective threshold is a well predictable parameter. It is independent of both the stress ratio and *the yield stress* [2–4]. The reason for this is that the size of the crack-tip area embracing the cyclic movement of dislocations is smaller than the distance between the characteristic microstructural features. Such independence of the yield stress was first revealed experimentally and later supported by discrete dislocation dynamics simulations [5]. For a particular metal matrix, the strength of the atomic bonds is only slightly affected by the alloying elements. Note that this independence only stands for the effective threshold value and not for the crack propagation rate, which is already dependent on the cyclic yield stress. The dependence of the applied threshold ΔK_{th} on microstructure and yield stress is fully given by the crack closure mechanisms.

The aim of this research is to provide predictive tools for effective thresholds in mode II and mode III. The article focuses on an overview and interpretations of results based on the recent experimental research in this area. A further verification of the theory by an investigation of more materials is the subject of an on-going research.

21.2 Mode II Effective Threshold

For mode I cracks in single-phase metals, the effective threshold can be well predicted using the relationship

$$\Delta K_{\mathrm{Ieff,th}} = 0.75E\sqrt{b}, \tag{21.1}$$

while $\Delta K_{\mathrm{Ieff,th}} = E\sqrt{b}$ holds for alloys. Here, E is the Young modulus and b is the magnitude of the Burgers vector. Under the shear-mode loading, the separation of the effective and the shielding component is even more important, since the friction between the fracture surfaces results in a very high extrinsic component [6]. There are, however, two complications. First, the mode II effective threshold cannot be experimentally measured using the high stress ratio method since the crack still remains closed. Second, a simple theoretical relationship

$$\Delta K_{\mathrm{IIeff,th}}^{\mathrm{ideal}} = G\sqrt{b} \tag{21.2}$$

analogical to Eq. (21.1) is valid only for ideally planar cracks. In the real materials, however, the shear-mode cracks tend to deflect from the original crack plane to possess a certain local mode I component (depending on material). This effect should be taken into account when formulating the relationship for the mode II effective threshold.

Experimental values of the mode II effective thresholds were measured recently using a special and complex experimental methodology where the shear-mode cracks propagated from open precracks generated by cyclic compressive loading. Details of this procedure can be found elsewhere [7]. To take the local SIFs at deflected crack fronts into account, the following equations

$$\Delta K_{\mathrm{IIeff,th}}^{\mathrm{local\ II}} = \frac{G\sqrt{b}}{\frac{1}{2}\cos\frac{\theta}{2}(3\cos\theta - 1)} \quad \text{for}\ \theta < 46^\circ \tag{21.3}$$

$$\Delta K_{\mathrm{IIeff,th}}^{\mathrm{local\ I}} = \frac{0.75E\sqrt{b}}{\frac{3}{2}\cos\frac{\theta}{2}\sin\theta} \quad \text{for}\ \theta > 46^\circ \tag{21.4}$$

were formulated [8], where θ is the mean deflection angle (see also Fig. 21.1 in the next section). It was found that these relationships are in a good agreement with the experimentally obtained effective thresholds when the typical mean deflection angle

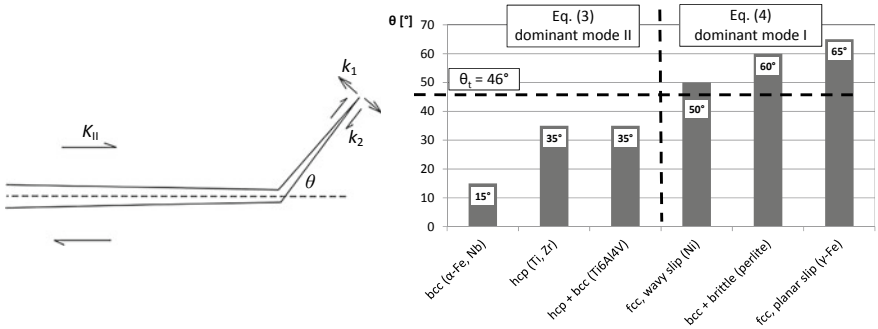

Fig. 21.1 Typical crack deflection angles θ that should be used in Eqs. (21.3) and (21.4) to predict the effective mode II threshold for various metallic materials. The transition angle $\theta_t = 46°$ separates the two dominant local crack growth modes

θ is used as a parameter for a certain type of metallic material depending on crystal structure and phase composition (see the next section). In general, Eq. (21.3) holds for materials with the dominant local shear-mode growth mechanism, characterised by the values of $\theta < 46°$ and Eq. (21.4) stands for materials with the dominant local opening-mode growth mechanism and $\theta > 46°$ [9].

21.2.1 Influence of Crystal Lattice

Under the near-threshold loading, the mode II loaded cracks can propagate coplanarly (along the maximum shear stress plane) if there is a high number of possible slip planes in the crystal lattice and the low angles between these planes then allow a nearly coplanar cyclic single slip through a majority of grains along the crack front. This is the case of bcc metals were the coplanar slip was indeed observed (pure ferritic steel and niobium). On the other hand, the fcc metals have large angles between the slip planes which results in a high crack deflection angle and a multiple slip mechanism of a local mode I crack growth. The stainless steel with a planar slip (low stacking-fault energy) exhibited the highest mean deflection angles corresponding to a nearly pure local mode I growth. Nickel with a wavy slip (high stacking fault energy) had somewhat smaller deflection angles but the crack growth was still under the local mode I dominance. The hcp metals (titanium, zirconium) exhibited medium size angles and a transitional behaviour between the local mode I and the local mode II dominance [10]. The conclusions about the dominant local crack growth mode were supported by fractographical observations where the typical crystallographic patterns indicating a single slip occurred only in materials with the dominant local mode II mechanism [7].

21.2.2 Influence of Secondary Phases

If the primary (matrix) phase allows the local mode II growth the secondary phase can change this behaviour depending on its type. A change towards the local mode I mechanism was observed in the pearlitic steel, where the cementite lamellae represented a brittle phase with a non-coherent phase boundary. Consequently, the effective mode II and mode III thresholds increased in comparison with the purely ferritic steel. On the other hand, the β-Ti lamellae (bcc) in the α-titanium matrix (hcp) of the Ti6Al4 V alloy did not lead to any change of the dominant local mode II mechanism due to a coherent phase boundary which allowed an easy dislocation crossing into the ductile β-Ti phase. The effective mode II and mode III thresholds in this alloy remained approximately equal to those measured for pure α-titanium grade [9]. Figure 21.1 summarizes the typical deflection angles and the local growth mode dominance for various metallic materials.

The knowledge of the dominant growth mode is significant not only for prediction of the effective threshold (Eqs. 21.3 and 21.4) but also for estimation of a further crack propagation behaviour taking the crack tip shielding component into account. In materials with coplanar local mode II crack growth the level of friction between the fracture surfaces is approximately equal in both modes II and III and the measured applied thresholds and crack growth rates are also approximately equal. On the other hand, there is a large difference between the mode II and the mode III crack behaviour in materials with the dominant local mode I growth. The remote mode II cracks grow easily in a mode-I manner after the whole crack front is deflected, while the remote mode III cracks generate a complicated three-dimensional fracture surfaces (factory roofs) with a high level of friction and clamping of asperities resulting in a significant retardation of the crack growth.

Additional experiments are in progress to verify the results for copper alloys (CuZn40Pb2 and CuSn8). Fracture surfaces from the shear-mode loaded specimens made of CuZn40Pb2 should exhibit a local mode I crack growth mechanism, since copper has the fcc crystal lattice and brass has a low stacking-fault energy. The theoretically predicted effective mode II threshold for brass using Eq. (21.4) and the angle $\theta = 65°$ is $\Delta K_{\mathrm{IIeff,th}} = 1.4\ \mathrm{MPam}^{1/2}$.

21.3 Mode III Effective Threshold

The growth mechanism of remote mode III cracks is a complicated procedure and the corresponding effective mode III thresholds are always higher than those of mode II. Behaviour of the mode III cracks is described based on behaviour of the mode II cracks. Since there is no straightforward local mode III crack growth mechanism, these cracks propagate under local mode I or local mode II mechanisms, starting at local asperities of the crack front. The tendency to grow under the local opening or

local shear mode dominance was found to be the same for both mode II and mode III cracks in all tested materials.

The effective mode III threshold can be predicted using the value of $\Delta K_{\mathrm{IIeff,\,th}}$ and the ratio between mode II and mode III effective thresholds $\Delta K_{\mathrm{IIeff,\,th}}/\Delta K_{\mathrm{IIIeff,th}}$. The value of this ratio was found to be approximately 0.65 for all tested materials [11].

For materials with coplanar shear-mode crack growth (bcc metals) this value could be identified with the ratio of local mode II SIFs at the in-plane crack front asperities to the macroscopic mode III SIF for a straight crack front. This ratio depends on the mean angle of these asperities and its measurement on fracture surfaces of the ferritic steel and niobium resulted in average values of 25° and 26°, respectively [11]. The corresponding ratio of the local mode II SIF to the global mode III SIF was 0.7 which is in a good agreement with the experimentally obtained ratio $\Delta K_{\mathrm{IIeff,\,th}}/\Delta K_{\mathrm{IIIeff,\,th}} \approx 0.65$.

For materials with the dominant local mode I growth mechanism the crack propagation is a geometrically much more difficult process, since the factory-roof morphology of the fracture surface is generated by the growth of locally twisted crack front segments. However, for the threshold value it is decisive that the first stages of such a growth must be realized in plane by a creation of local semi-elliptical crack segments. Therefore, the explanation of the value of the ratio $\Delta K_{\mathrm{IIeff,\,th}}/\Delta K_{\mathrm{IIIeff,\,th}}$ formulated for materials with the local mode II growth dominance might also be valid here. For the brass alloy for which the experiments are planned the theoretically predicted effective mode III threshold is $\Delta K_{\mathrm{IIIeff,\,th}} = 2.2\ \mathrm{MPam}^{1/2}$, taking the values of $\Delta K_{\mathrm{IIeff,\,th}}$ predicted in the previous section and the ratio $\Delta K_{\mathrm{IIeff,\,th}}/\Delta K_{\mathrm{IIIeff,\,th}} = 0.65$ into account.

21.4 Summary

Effective threshold is a very useful parameter for studying of mechanisms of fatigue crack propagation and crack closure. Under mode I loading the effective threshold is well predictable for wide range of metallic materials. In this work it was presented the state-of-the art of possibilities of prediction of mode II and mode III effective thresholds for metallic materials. The results are in a good agreement for up-to-date tested materials. Experimental data for more materials are needed to further verify the relationships.

Acknowledgements This work was financially supported by the Czech Science Foundation (GA CR) in the frame of the Project No. 17-15716Y and by the Ministry of Education, Youth and Sports of the Czech Republic under the project CEITEC 2020 (LQ1601).

References

1. Ritchie RO (1988) Mechanisms of fatigue crack propagation in metals, ceramics and composites: Role of crack tip shielding. Mater Sci Eng A 103:15–28
2. Hertzberg RW (1995) On the calculation of closure-free fatigue-crack propagation data in monolithic metal-alloys. Mater Sci Eng A 190:25–32
3. Liaw PK, Lea TR, Logsdon WA (1983) Near-threshold fatigue crack growth behavior in metals. Acta Metall 31:1581–1587
4. Pippan R (1998) The effective threshold of fatigue crack propagation in aluminium alloys. I. The influence of yield stress and chemical composition. Philos Mag A 77:861–873
5. Riemelmoser FO, Gumbsch P, Pippan R (2001) Dislocation modelling of fatigue cracks: an overview. Mater Trans 42:2–13
6. Tschegg EK, Stanzl SE (1988) The significance of sliding mode crack closure on mode III fatigue crack growth. Basic questions in fatigue. ASTM STP 924 1:214–232
7. Vojtek T, Hohenwarter A, Pippan R, Pokluda J (2016) Experimental evidence of a common local mode II growth mechanism of fatigue cracks loaded in modes II, III and II + III in niobium and titanium. Int J Fatigue 92:470–477
8. Vojtek T, Pippan R, Hohenwarter A, Pokluda J (2017) Prediction of effective mode II fatigue crack growth threshold for metallic materials. Eng Fract Mech 174:117–126
9. Vojtek T, Hohenwarter A, Pippan R, Pokluda J (2018) Influence of secondary phase on intrinsic threshold and path of shear-mode fatigue cracks in metals. Acta Phys Polonica A 134:699–702
10. Pokluda J, Pippan R, Vojtek T, Hohenwarter A (2014) Near-threshold behaviour of shear-mode fatigue cracks in metallic materials. Fatigue Fract Engng Mater Struct 37:232–254
11. Vojtek T, Žák S, Pokluda J (2018) Quantitative analysis of intrinsic mode III fatigue thresholds in bcc metals. Int J Fatigue 115:35–41

Chapter 22
Crack Propagation Under Cyclic Bending in Welded Specimens After Heat Treatment

Dariusz Rozumek, Janusz Lewandowski, Grzegorz Lesiuk and José A.F.O. Correia

Abstract The paper presents the tests results on the fatigue crack growth under cyclic bending specimens at constant moment amplitude made of S355 steel with fillet welds. Rectangular specimens with stress concentrators in form of the external two-sided blunt notches and fillet welded joints were tested. The tests were performed under constant value of the stress ratio $R = -1$ without and after heat treatment. This research also presents the test results of the microstructure of welded joints taking into account changes in the material after heat treatment and the impact of these changes on the fatigue life of specimens.

Keywords Crack propagation · Welding · Bending · Heat treatment

22.1 Introduction

Welded joints as a method of joining inseparable technical constructions are commonly used in many areas of human activity. Although the topic has been addressed in publications around the world for many years, due to the ever-increasing requirements for improving the safety of welded structures and to increase fatigue durability, it is still popular [1, 2]. Currently, scientists are focusing on studies on the influence of various factors on the durability of welded joints, i.e. type of load, type of heat treatment, environmental conditions, the influence of weld geometry, etc [3, 4].

This paper presents the results of the fatigue crack propagation obtained for welded specimens made of S355 steel subjected to bending without and after heat treatment.

D. Rozumek (✉) · J. Lewandowski
Opole University of Technology, Mikolajczyka 5, 45-271 Opole, Poland
e-mail: d.rozumek@po.opole.pl

G. Lesiuk
Wrocław University of Science and Technology, Smoluchowskiego 25, 50-370 Wrocław, Poland

J.A.F.O. Correia
University of Porto, Rua Dr. Roberto Frias, 4200-465 Porto, Portugal

J.A.F.O. Correia et al. (eds.), *Mechanical Fatigue of Metals*, Structural Integrity 7,
https://doi.org/10.1007/978-3-030-13980-3_22

22.2 Experimental Procedure

22.2.1 Material and Specimen

The subject of the investigation is the structural S355 steel. Some mechanical properties (σ_y—yield tensile strength; σ_u—ultimate tensile strength; E—Young's modulus; ν—Poisson's ratio; A_5—elongation at fracture) of the tested steel are given in Table 22.1. Shapes and dimensions of the tested specimens with welds are presented in Fig. 22.1. The initial material of test specimens was drawn bar with Ø30 mm diameter, which was used for making two types of components of the specimens, being fixed together by fillet welded joints on both sides (concave and convex welds).

Hand-made welded joints were made by employing the TIG method in an inert shielding gas (argon) using a welding wire marked W-42-2-W2Sil according to EN ISO 636. Visual pre-selection of specimens were carried out before the experimental tests. All the tested specimens were subjected to non-destructive tests by using magnetic particle test method under UV light [5].

The tests allowed to eliminate welded specimens, on the surface of which defects (mainly cracks) that could influence the final result of the experimental research were revealed. Experimental tests were performed on welded specimens without heat treatment (raw—after welding) and on the specimens after heat treatment. The heat treatment was carried out by subjecting the specimens to relief annealing at 630 °C during 2 h.

Hardness distribution of the material was obtained using Vickers method. The measurements were performed using a LECO MH 200 microhardness tester under a load of 100 g, according to the EN ISO 9015-1 requirements. Metallographic tests were performed with the use of an optical microscope OLYMPUS IX70 employing polarized light and phase contrast.

Table 22.1 Mechanical properties of the S355 steel

σ_y (MPa)	σ_u (MPa)	E (GPa)	ν (−)	A_5 (%)
357	535	210	0.30	21

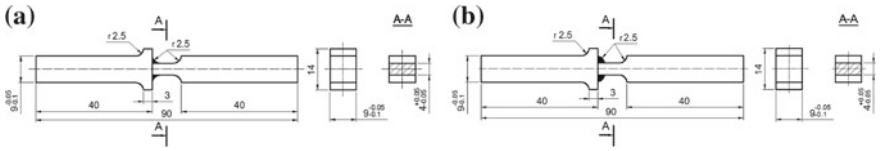

Fig. 22.1 Shapes and dimensions of the welded specimens with: **a** concave welds, **b** convex welds, dimensions in mm

22.2.2 Fatigue Tests

The tests were performed on the fatigue test stand MZGS − 100 [5, 6]. During the tests the force was controlled (in the considered case, the moment amplitude was controlled) works under loading frequency equal to 28.4 Hz. The theoretical stress concentration factor, estimated with use of the model [7], in the solid specimen with concave weld under bending was $K_t = 1.38$ while it was 1.56 for the convex weld configuration. Unilaterally restrained specimens were subjected to cyclic bending with the constant load ratio $R = M_{min}/M_{max} = -1$, and amplitude of moment, M_a, equal to 9.2 N m, which corresponded to the nominal amplitude of normal stress for the net section of $\sigma_a = 383$ MPa (solid specimen). Fatigue crack growth on the specimen surface was observed with the optical method. The fatigue crack increments were measured with the optical method using micrometer mounted on the portable microscope with magnification of 20 times and accuracy up to 0.01 mm. At the same time, a number of loading cycles, N, was recorded and reference image was captured.

22.3 Test Results and Discussion

During laboratory tests, initiation and fatigue cracks growth from one side of the specimen (from top or bottom) were observed, and after a certain period of propagation, the crack growth occurred also on the other side specimen. Figure 22.2 presents the fatigue crack length versus number of cycles for the obtained results of experimental tests on the specimens. In Fig. 22.2 can be observed that the longest fatigue life indicate specimens made of solid material without heat treatment.

In specimens with concave welds (Fig. 22.2a) subjected to relief annealing, the fatigue crack initiation took place at 15100 cycles, and the specimens were damaged

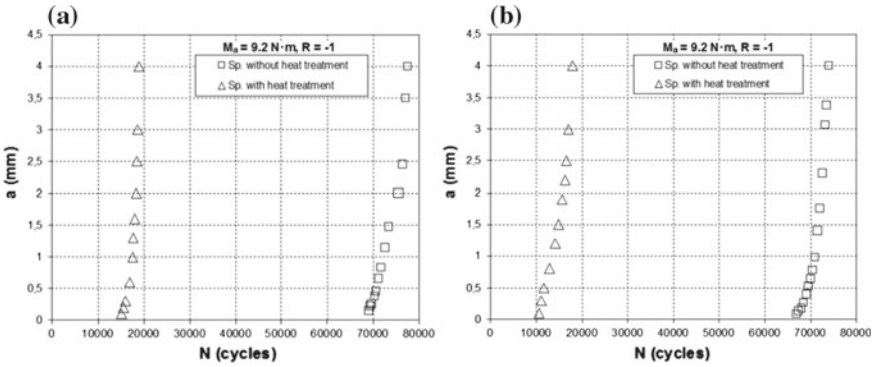

Fig. 22.2 Crack length versus number of cycles under bending for test specimens with: **a** concave welds, **b** convex welds

at 19000 cycles. Specimens without heat treatment showed the highest fatigue life, in which the crack initiation occurred at 69000 cycles, and their damaged at 77500 cycles. Similar behaviour, shown in Fig. 22.2b, is also observed in specimens with convex welds. In specimens subjected to relief annealing, the fatigue crack initiation occurred at 10500 cycles, and the specimens were damaged at 18000 cycles. Specimens without heat treatment also showed the highest fatigue life, in which the crack initiation occurred at 67000 cycles, and their damaged at 74000 cycles.

In specimens with concave joints (Fig. 22.2a) under relief annealing, fatigue crack initiation occurred at cycles number 15100, and specimens were damaged at 19000 cycles. In the case of specimens with convex joints, the initiation of cracks occurred at the cycles number of 10500, and the failed specimens occurred after 18000 cycles and these were the lowest durability (Fig. 22.2b). For each case, two or three specimens were tested. The results of the micro-hardness measurements without and after heat treatment are presented in Fig. 22.3. From Fig. 22.3 it appears that micro-hardness of the welded joints without heat treatment (HT) is not uniform. Micro-hardness of the welds is higher than the base material. The highest values of micro-hardness were measured for heat-affected zone (HAZ) and without HT. It can be seen in Fig. 22.3 that for base material, micro-hardness stayed at the same level 188–189 $HV_{0.1}$, while of HAZ high fluctuations of micro-hardness between 197–274 $HV_{0.1}$ were observed. In the specimens after heat treatment the micro-hardness was lower than the micro-hardness of the specimens without HT and smaller fluctuations were noted. Slight higher micro-hardness is observed for a concave welds than a convex one. The micro-hardness after heat treatment is between 125–154 $HV_{0.1}$ and shows lower fluctuations.

Base material S355 has fine-grained ferritic-pearlite structure with fine equiaxial ferrite grains and very fine pearlite grains of strip pattern. Figure 22.4 presents microstructure of S355 steel in the heat affected zone (HAZ) with observed cracks.

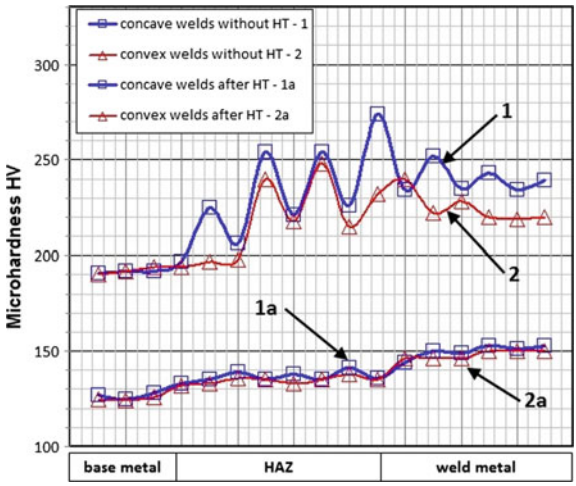

Fig. 22.3 Microhardness distribution with divided into zones without and after heat treatment

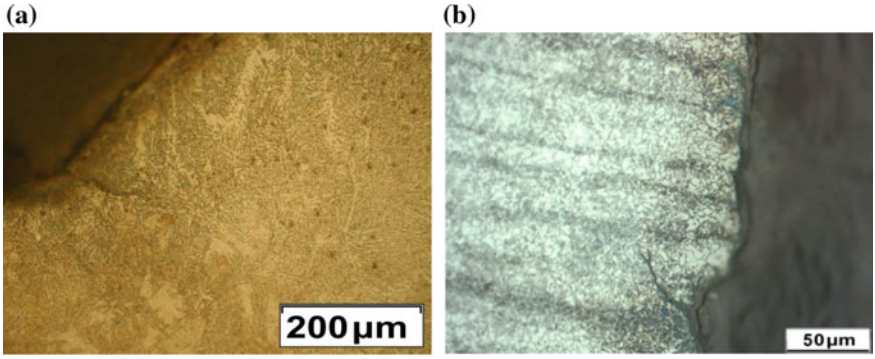

Fig. 22.4 The microstructure of the material in HAZ for **a** without HT, **b** after heat treatment

Main crack initiate in the specimen without heat treatment (Fig. 22.4a—convex weld) was at the bottom of the notch, at weld boundary, i.e. in penetrated zone of Widmanstatten structure and HAZ within bainitic structure and occurred perpendicularly in relation to maximum normal stresses. Main crack had numerous side cracks. Then main crack runs through normalised structure zone, where no side cracks were observed.

Significant decrease in fatigue life of specimens after heat treatment was caused by structural changes occurring in the tested material as a result of heat treatment. In the specimens without heat treatment there was a martensite and bainite microstructure, and after the heat treatment the microstructure of bainite and sorbitol (which occurs in the HAZ—Fig. 22.4b) was observed. The main crack growth was outside the weld and primary HAZ in the area of the specimen with a sorbitol microstructure, enriched with cementite.

22.4 Conclusions

The following conclusions have been made on the basis of the obtained results:

1. The highest material micro-hardness was measured in HAZ on specimens without heat treatment, and the smallest in specimens after heat treatment.
2. The fatigue life of welded specimens without heat treatment was higher than the specimens for which heat treatment was applied.
3. Fatigue cracks growth in all test specimens started on one-side of the specimen, at the place of highest concentration of stresses.

References

1. Carpinteri A, Brighenti R, Huth HJ, Vantadori S (2005) Fatigue growth of a surface crack in a welded T-joint. Int J Fatigue 27:59–69
2. Kawiak M, Balitskii A (2018) Embrittlement of welded joints of tram rails in city environments. Eng Fail Anal 85:97–103
3. Sniezek L, Szachogłuchowicz I, Hutsaylyuk V (2016) Low cycle fatigue properties of AA2519–Ti6Al4 V laminate bonded by explosion welding. Eng Fail Anal 69:77–87
4. Prażmowski M, Rozumek D, Paul H (2017) Static and fatigue tests of bimetal Zr-steel made by explosive welding. Eng Fail Anal 75:71–81
5. Lewandowski J, Rozumek D (2016) Cracks growth in S355 steel under cyclic bending with fillet welded joint. Theoret Appl Fract Mech 86:342–350
6. Rozumek D, Marciniak Z (2008) Control system of the fatigue stand for material tests under combined bending with torsion loading and experimental results. Mech Syst Signal Process 22:1289–1296
7. Thum A, Petersen C, Swenson O (1960) Verformung, Spannung und Kerbwirkung. VDI-Verlag, Düesseldorf

Chapter 23
Crack Propagation in the Threshold Stress Intensity Region a Short Review

Luiz Felipe F. Ricardo, Timothy H. Topper, Luiz Carlos H. Ricardo and Carlos Alexandre J. Miranda

Abstract This work presents a short review of fatigue crack propagation with emphasis on the parameters that influence the threshold stress intensity, ΔKth. This threshold value is dependent on such variables as the material itself, the test conditions, the R-ratio, the environment and crack closure. The crack geometry effects are discussed as well as some crack closure models. A discussion of other parameters that influence the threshold stress intensity regime including short crack thresholds and their respective models and their application will be the subject of a near-future review.

Keywords Fatigue · Design · Threshold stress intensity factor · Crack propagation · Crack closure models

L. F. F. Ricardo (✉)
Metallurgical and Materials Department, UFRJ, Federal University of Rio Janeiro, Cid. Universitária-Centro de Tecnologia, Rio de Janeiro, RJ 21941-972, Brazil
e-mail: luiz.ricardo97@poli.ufrj.br; lchr6060@gmail.com

T. H. Topper
Civil Engineering Department, University of Waterloo, 200 University Avenue West, Waterloo, ON N2L 3G, Canada
e-mail: topper@uwaterloo.ca

L. C. H. Ricardo
Materials Science and Technology Center, IPEN, Nuclear and Energy Research Institute, University of São Paulo, Av. Lineu Prestes, 2242 Cidade Universitária, São Paulo, SP 05508-000, Brazil
e-mail: lricardo@ipen.br

C. A. J. Miranda
Nuclear Engineering Center, IPEN, Nuclear and Energy Research Institute, University of São Paulo, Av. Lineu Prestes, 2242 Cidade Universitária, São Paulo, SP 05508-000, Brazil
e-mail: cmiranda@ipen.br

J.A.F.O. Correia et al. (eds.), *Mechanical Fatigue of Metals*, Structural Integrity 7,
https://doi.org/10.1007/978-3-030-13980-3_23

23.1 Introduction

Modern defect—tolerance design approaches to fatigue are based on the premise that engineering structures are inherently flawed; the useful fatigue life then is the time or the number of cycles to propagate a dominant flaw from an assumed or measured initial size to a critical dimension. In most metallic materials, catastrophic failure is preceded by a substantial amount of stable crack propagation under cyclic load conditions.

The rates at which these cracks propagate for different combinations of applied stress, crack length and geometric conditions of the cracked structure, and the mechanisms which influence the crack propagation rates under different combinations of mean stress, test frequency and environment, are practical interest [1]. Crack propagation is usually described by the relationship/curve of log da/dN versus log ΔK where a is the crack length, N is the number of cycles, and ΔK is the range of the stress-intensity factor in a loading cycle. As depicted in Fig. 23.1, one can identify three regions or crack growth regimes that this curve passes through, named Regions A, B and C. The Paris power law relationship can be applied to the region B that shows a linear variation of log da/dN versus log ΔK. The curve is bounded by two limits, the upper limit (in Region C) being the fracture toughness of the material and the lower limit (in the Region A) being the threshold. Below this threshold there is no crack growth. Several parameters/variables can have influence in this curve. The fatigue crack threshold is discussed by McEvily [2] as a function of a number of variables, including the material, the test conditions, the R-ratio, and the environment. ASTM E 647 defines the fatigue crack growth (FCG) threshold, Δ*K*th, as that asymptotic value of ΔK at which da/dN approaches zero. For most materials an operational, although arbitrary, definition of Δ*K*th is given as that ΔK value which corresponds to a fatigue crack growth rate of 10–10 m/cycle.

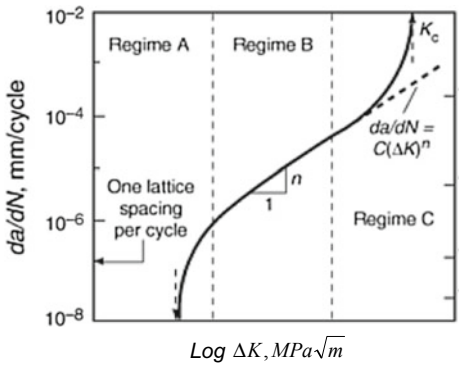

Fig. 23.1 Fatigue crack propagation regimes [2]

23.2 The Threshold Region

The earliest studies of fatigue were concerned with failure of a workpiece after a number of loading cycles. At that time, researchers, most significantly Woehler [3], did not isolate crack growth as a separate phenomenon, before rupture. The approach to evaluate crack growth is simple for long cracks and by passes the unknown details of crack tip atomistic processes (Long cracks are those ones that start growing for a given cyclic loading.). For these it is possible to draw a curve of crack propagation rate (da/dN) versus the range of the alternating stress intensity (ΔK). The curve itself (Fig. 23.1) is a function of R load ratio and it is usually drawn on a log-log scale. Cracked materials are only superficially elastic. There is always plasticity in a region very near the crack tip. Under LEFM this region is so small that it does not affect the overall cracked components stress distribution. Larger scale plasticity is explicitly described by elastic–plastic formulations such as the J-integral or the crack tip opening displacement (CTOD).

The variables K and J are, however, closely related under small scale yielding conditions; the additional work involved in using J has not appeared to yield a commensurate improvement in predictive ability under near-threshold conditions except in special cases. The relative success of LEFM is illustrated by Fig. 23.2 which shows the correlation of da/dN $\times$ ΔK for experimental data for a 2024—T3 aluminum alloy obtained by Paris et al. [4] and Paris and Erdogan [5] from various sources.

Nowadays, with the tools of Fracture Mechanics (specifically LEFM) it is possible to analyze how cracks propagate under cyclic load. Several studies try to simulate how cracks propagate under in a large scale plasticity regime, however this will not be mentioned in this review work. To know more about this regime one can see [6], for instance. Figure 23.1 suggests that the threshold for crack propagation may not be an intrinsic part of the growth (e.g. Paris) relation. For any given material, thresholds are apt to vary more with changing test conditions than do the Paris constants. But,

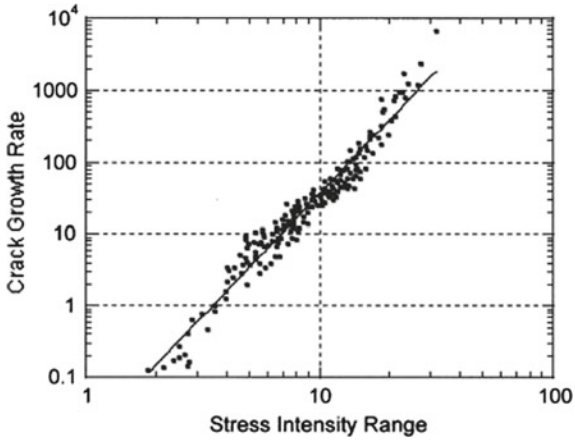

Fig. 23.2 Data for 2024-T3 aluminum from various sources used by Paris et al. [4] and Paris and Erdogan [5]

within the threshold region, extrinsic effects seem to modify the value of an intrinsic threshold. These extrinsic effects have been embraced under the heading of 'crack closure'. As defined by Elber, when closure is present, the effective stress intensity range is not the applied maximum stress intensity minus the applied minimum stress intensity, but rather the applied maximum stress intensity minus a closure stress intensity. The growth of small cracks is even more complicated. It is not unusual in the case of small cracks for crack propagation within the threshold region to be fitted, as with a spline of local small-crack Paris relations defining the mean value of the growth rate for the given conditions [4, 5, 7].

23.3 Effect of Crack Geometry

Considering a small superficial crack the threshold region in metals is generally associated with a reversed-shear mode of growth which at least implies a mode II component. At the same time, plasticity is largely confined to select crystallographic planes, e.g. {111} in Fe–Ni alloys [8].

This gives rise to a faceted fracture surface. Since growth takes place by a shear mechanism on planes inclined to the mode I stress plane, a certain amount of mode II displacement is expected. If this were unreversed, as might happen in a tensile overload, registry of the peaks and troughs between the upper and lower crack faces could be lost and the peaks would contact each other before the crack fully closed.

At stress intensity ranges near the threshold, a large oxide buildup is likely. Several works on this subject are mentioned in [9, 10]. The presence of this oxide, believed to be due to fretting, is thought to increase the crack opening stress [11–15]. At very low fatigue loads, oxide, and at higher loads, misaligned facets act as wedges reducing the effective stress intensity range by preventing the crack from closing. These effects are called, respectively, oxide- and roughness-induced crack closure. In the region close to the fatigue threshold, the stress ratio exerts a strong effect on the crack closure level. Environmental effects similarly reach a maximum at stress intensity ranges near threshold but then diminish [11, 12].

23.4 Crack Closure Models

Since it was proposed by Elber [16] in the early 1970s, the concept of crack closure has been widely used to explain the influence of R load ratio on fatigue crack growth (FCG) [17, 18]. It has been realized for a long time that the degree of crack closure was higher at lower R [19] while it may be negligible at higher R values (i.e., $R > 0.7$) [20–22]. As a result, instead of the conventional ΔK, the FCG rate was correlated with the effective stress intensity factor range ΔK_{eff} [20, 21], i.e., $\Delta K_{eff} = K_{max} - K_{cl}$. Here, K_{max} is maximum stress intensity factor and K_{cl} is the stress intensity when crack is closed. Since then, several crack closure mechanisms have been defined that

include the effect of R, environment, temperature and crack growth mode. Stewart [23] reported that air humidity, corrosive and other gaseous environments provided additive contributions to the effect of R on FCG.

23.5 Conclusions

This paper reviewed and discussed some topics regarding the parameters that influence the threshold stress intensity value in crack propagation under cyclic loading. Among these parameters the effect of crack closure and R-ratio were the main focus of this review. Other topics related to the threshold stress intensity regime including short crack thresholds and the respective models and their applications will be the subject of a future review.

References

1. Suresh S (1991) Fatigue of materials, 1st edn. Cambridge University Press, Cambridge
2. McEvily AJ (1996) Metals handbook. ASM 12:318–334
3. Wöhler A (1860) Versuche zur Ermittlung der auf die Eisenbahnwagenachsen einwirkenden Kräfte und die Widerstandsfähigkeit der Wagen-Achsen, Zeitschrift für Bauwesen, X, 583–616
4. Paris PC, Gomez MP, Anderson WE (1961) A rational analytic theory of fatigue. Trends Eng 13(1):9–14
5. Paris PC, Erdogen F (1963) A critical analysis of crack propagation laws. J Basic Eng 85:528–534
6. Maneschy JE (1998) Integral-J para Carregamentos Cíclicos. PhD dissertation, IPEN/USP (In Portuguese)
7. Chen EY (1996) PhD dissertation, Northwestern University
8. Suresh S, Ritchie R (1984) Propagation of short fatigue cracks. Int Metals Ver 29:445–474
9. Krenn C, Morris JW Jr, Mei Z (1997) The crystallography of fatigue crack initiation in two austenitic Fe–Ni superalloys. In: Soboyejo WO, Srivatsan TS (eds) High-cycle fatigue of structural materials. The Minerals, Metals and Materials Society, Philadelphia (PA, USA), pp 327–337
10. Liaw P (1989) Long fatigue cracks—microstructural effects and closure. MRS Bull 25–35
11. Stewart AT (1980) The influence of environment and stress ratio on fatigue crack growth at near threshold stress intensities in low alloy steels. Eng Fract Mech 13:463–478
12. McEvily AJ, Ritchie RO (1998) Crack closure and the fatigue-crack propagation threshold as a function of load ratio. Fatigue Fract Eng Mater Struct 21:847–855
13. Ford FP, Hoar TP (1973) On the mechanism of corrosion fatigue in aluminum 7 wt% magnesium. In: The microstructure and design of alloys, 3rd international conference on the strength of metals, 1974, vol. 1. The Metals Society, London, UK, pp 467–471
14. Taylor D, Knott JK (1981) Eng Mater Struct 4(2):147–155
15. Dubey S, Soboyejo ABO, Soboyejo WO (1997) An investigation of the effects of stress ratio and crack closure on the micromechanisms of fatigue crack growth in Ti–6Al–4V. Acta Mater 45:2777–2787
16. Elber W (1971) The significance of fatigue crack closure. In: Damage tolerance in aircraft structures, vol 486. ASTM STP, Lutherville-Timonium, MD, pp 230–242
17. Liaw PK, Leax TR, Swaminathan VP, Donald JK (1982) Influence of load ratio on near-threshold fatigue crack propagation behavior. Script Metall 16:871–876

18. Cooke RJ, Beevers CJ (1973) The effect of load ratio on the threshold stresses for fatigue crack growth in medium carbon steels. Eng Fract Mech 5:1061–1071
19. Robinson JL, Beevers CJ (1973) The effects of load ratio, interstitial content, and grain size on low-stress fatigue-crack propagation in a-Titanium. Met Sci 7:153–159
20. Walker K (1970) The effect of stress ratio during crack propagation and fatigue for 2024-T3 and 7075-T6 aluminum. In: Effects of environment and complex load history on fatigue life: a symposium, vol 462. ASTM STP, Lutherville-Timonium, MD, pp 1–14
21. Mishra MP, Packiaraj CC, Ray SK, Mannan SL, Borgstedt HU (1997) Influence of sodium environment and load ratio (R) on fatigue crack growth behaviour of a type 316 LN stainless steel at 813 K. Int J Pres Vessel Pip 70:77–82
22. Ding J, Hall R, Byrne J (2005) Effects of stress ratio and temperature on fatigue crack growth in a Ti–6Al–4V alloy. Int J Fatigue 27:1551–1558
23. Stewart AT (1980) The influence of environment and stress ratio on fatigue crack growth at near threshold stress intensities in low-alloy steels. Eng Fract Mech 13:463–468

Chapter 24
A Stress Intensity Factor Study for a Pressure Vessel CT Specimen Using Finite Element Method

Patrícia Raposo, Behzad V. Farahani, José A.F.O. Correia, Jorge Belinha, Abílio M.P. De Jesus, Renato N. Jorge and Rui Calçada

Abstract This study aims to determine the mode I Stress Intensity Factor, K_I, for a steel alloy specimen extracted from a pressure vessel, so-called P355NL. The geometric and mechanical properties are derived from Compact Tension, CT, specimens available in the relevant literature. The theoretical value of K_I is evaluated through the formulation reported in ASTM E 647-15 ASTM International (Standard test method for measurement of fatigue crack growth rates. West Conshohocken, PA, 2015, [1]) for the geometric properties used in the previous study. Numerically, to solve the CT specimen problem, a Finite Element code software, ABAQUS© is used. Therefore, obtained numerical results are then compared to the theoretical ones, leading to assess the numerical analyses' performance. In this study, distinct crack lengths are considered as; $a = \{8, 9, \ldots, 20 \text{ mm}\}$. Overall, encouraging results were obtained possessing a satisfactory agreement compared to theoretical solution.

Keywords Uniaxial fatigue · FEM · Pressure vessels

24.1 Introduction

The main goal of the Compact Tension (CT) specimen test, which is the use of a notched specimen, is to create a fatigue crack under a uniaxial cyclic load with

P. Raposo · B. V. Farahani (✉) · J.A.F.O. Correia · A.M.P. De Jesus · R. N. Jorge
FEUP- Faculty of Engineering of University of Porto, 4200-465 Porto, Portugal
e-mail: behzad.farahani@fe.up.pt

P. Raposo · B. V. Farahani · J.A.F.O. Correia · J. Belinha · R. N. Jorge
INEGI - Institute of Science and Innovation in Mechanical and Industrial Engineering, Campus FEUP, 400, 4200-465 Porto, Portugal

J. Belinha
ISEP- Instituto Superior de Engenharia do Porto, Rua Dr. António Bernardino de Almeida, 431, 4200-072 Porto, Portugal

R. Calçada
Faculty of Engineering, University of Porto, Porto, Portugal

J.A.F.O. Correia et al. (eds.), *Mechanical Fatigue of Metals*, Structural Integrity 7,
https://doi.org/10.1007/978-3-030-13980-3_24

maximum and minimum values, being $R = \sigma_{min}/\sigma_{max}$. The initiation of the fatigue crack starts in the notch and extends through the specimen. Close to notches and cracks, the fatigue process is governed by highly concentrated strains and stresses in those zones, thus fatigue crack growth can be considered as a process of successive crack increments as a consequence of the damage of the material in this region [2].

The components and structures which are welded or experience processing techniques can introduce inconsistencies in the structure that are well represented by the fatigue crack [1]. The components and structures are commonly flawed or have pronounced notches [3]. Structures can be subjected to dynamic loads which are responsible for local fatigue damage [4].

The CT specimens are used in fracture mechanics and corrosion tests. In order to obtain the material fracture toughness, determined through the stress intensity factor (SIF or K). This property describes the capacity of a material to withstand fracture, being this one of the most important features of structural materials, mechanical components, etc. [1, 5].

Nowadays, structures require the ability to stand a substantial amount of damage, therefore it is important to develop reliable methods to predict the failure of fatigue damaged components/structures [6]. The analysis and estimation of the crack growth and fracture behavior can be done by combining the fracture mechanics theory and Paris law [5–9].

Due to the computers development, the numerical methods have been increasingly used to solve complex engineering problems [3, 10]. In the beginning of study on fracture mechanics with numerical techniques, the Finite Element Method (FEM) was used with remeshing and Boundary Element Methods (BEM) although these approaches presented difficulties handling with cracked structures [11]. After some years, Moës et al. [12] developed an approach to evaluate the crack growth using Haar function where the representation of the whole crack is independent on the mesh [9]. Other approaches such as meshless methods follow a local approximation combined with a flexible domain discretization in comparison with FEM and BEM [9]. In meshless methods, nodes do not build a mesh, since there is no previous relation between them. In the process of solving demanding problems involving high computational efforts, meshless methods possess some advantages, since remeshing is not required and it contributes simplifying the crack propagation [9, 13].

This study tends to evaluate the K_I in addition to the essential variational fields. For this purpose, a steel alloy specimen extracted from a pressure vessel was studied, identified as P355NL, it was previously studied in a Ph.D. Thesis [14], from which were taken the geometric and mechanical properties obtained from CT specimens. The theoretical value of K_I was obtained through the formulation presented in ASTM E 647-15 (Standard Test Method for Measurement of Fatigue Crack Growth Rates) [1] for the geometric properties used in the previous study [14]. To solve the CT model, a FEM code based software, ABAQUS© was used. The numerical results were then compared with the theoretical solution leading to assess the numerical approaches' performance. In this study, several crack lengths were considered: $a = \{8, 9, \ldots, 20 \text{ mm}\}$.

24.2 Analysis and Results

In the fracture mechanics and fatigue fields, the crack propagation is a very significant concept that requires a detailed study. This study needs experimental campaigns in order to obtain the mechanical properties of the materials and extensive numerical studies, calibrated and compared with the experimental/reference values. Hence, a pre-cracked CT specimen made of a mild steel from a pressure vessel S355 was used in this study.

Figure 24.1 presents the CT specimen with the recommended dimensions and in Fig. 34.2, the load application scheme is demonstrated [1]. It was considered that $\Delta P = P_{max} - P_{min} = 1634.1\,\text{N}$ and $R = P_{min}/P_{max} = 0$. Table 24.1 reports the geometric dimensions of the CT specimen considered in this study.

The ΔK reference (theoretical) value was obtained using the equation presented in ASTM E 647-15 standard [1], for different crack lengths of $a = \{8, 9, \ldots, 20\,\text{mm}\}$. Equation (24.1) provides the theoretical K value:

$$\Delta K = \frac{\Delta P}{B\sqrt{W}} \frac{(2+\alpha)}{(1-\alpha)^{3/2}} \left(0.886 + 4.64\alpha - 13.32\alpha^2 + 14.72\alpha^3 - 5.6\alpha^4\right) \quad (24.1)$$

Being ΔP the load amplitude ($P_{max} - P_{min}$), B the specimen thickness, W the dimension as presented in Fig. 24.1 and $\alpha = a/W$. The FEM code software ABAQUS can directly compute the stress intensity factor. The mechanical properties of the studied material were extracted from a previous study carried out by Correia [14], as represented on Table 24.2. Concerning the FEM analysis, it should be noted that

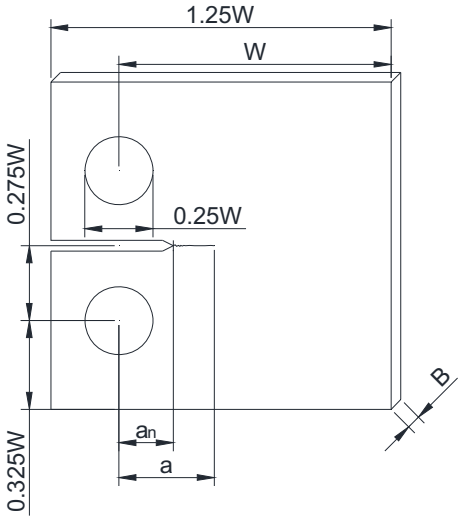

Fig. 24.1 Recommended dimensions for CT specimens according to the test standard

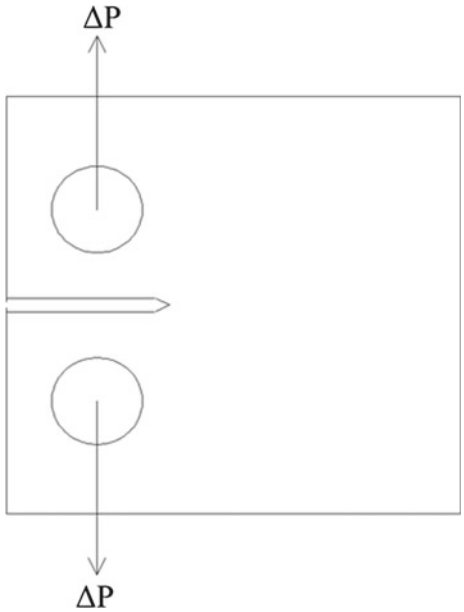

Fig. 24.2 Schematic view of the fatigue test condition

Table 24.1 CT specimen dimensions are in mm, PV P355NL

W	L	$H/2$	0.275 W	B	D	h_e	a_n
40	50	24	11	4.35	10	1.6	8

Table 24.2 Mechanical properties of the steel [11]

Material	E (MPa)	v	f_y (MPa)	f_u (MPa)
PV P355NL	205200	0.275	418.06	568.11

the authors followed the procedure carried out in the former works as extensively described in [6, 9].

The ΔK values were computed relying on the foregoing theoretical equation and also they have been obtained by the FEM formulation analyzed in ABAQUS© as can be seen on Table 24.3. Moreover, Fig. 24.3 demonstrates the von Mises stress and the vertical displacement variation on the fractured CT specimen if $a = 14$ mm.

24.3 Conclusions

This work addresses the calculation of the mode I stress intensity factor, K, through the theoretical expression proposed by ASTM E 647, and by numerical approaches using the Finite Element Methods (FEM). The theoretical expression was used as a

Table 24.3 CT specimen; K_I obtained for each method and the respective error

a (mm)	ΔK_{ASTM} (MPa.m$^{0.5}$)	ΔK_{FEM} (MPa.m$^{0.5}$)	Error (%)
8	255.429	241.456	5.470
9	274.430	289.687	5.560
10	294.117	305.519	3.877
11	314.473	322.558	2.571
12	335.699	340.256	1.357
13	358.031	359.996	0.549
14	381.746	379.195	0.668
15	407.176	402.532	1.140
16	434.711	426.434	1.904
17	464.820	470.597	1.243
18	498.069	502.037	0.797
19	535.141	539.793	0.869
20	576.873	584.069	1.247

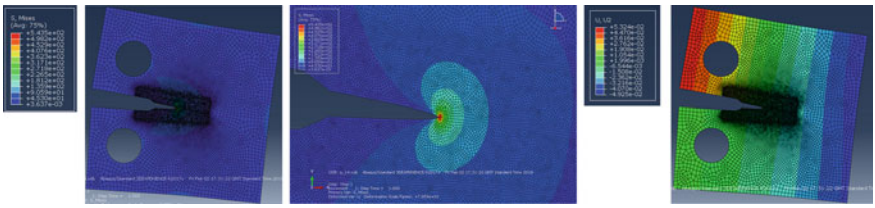

von Mises stress | von Mises stress at the crack tip | vertical displacement, U2

Fig. 24.3 CT specimen with a crack of $a = 14$ mm, FEM ABAQUS

value for comparison and validation of the numerical method. The numerical model was developed with geometry and mechanical properties of CT specimens from a mild Steel from a pressure vessel. For the proposed CT specimen, several crack lengths were simulated The FEM model was solved using the standard FEM based code software ABAQUS© allowing to directly obtain K, assuming the strain energy release rate criterion in the presence of integral contours.

Comparing the calculated theoretical value based on ASTM E647 standard with numerical results, a good agreement between the values was reached.

Overall, the numerical methods are a reliable and robust source of results, leading to accurate predictions of the behavior of materials/components/structures, which with adequate calibration can lead to the reduction of experimental tests, that have very high associated costs.

Acknowledgements The authors acknowledge the Portuguese Science Foundation (FCT) for the financial support through the doctoral grants PD/BD/135257/2017 and PD/BD/114095/2015 and postdoctoral grant SFRH/BPD/107825/2015. The authors gratefully acknowledge the fund-

ing of SciTech: Science and Technology for Competitive and Sustainable Industries, R&D project co-financed by Operational North Regional Program (NORTE2020), through European Fund of Regional Development (FEDER).

References

1. ASTM International (2015) Standard test method for measurement of fatigue crack growth rates. West Conshohocken, PA
2. Mikheevskiy S, Bogdanov S, Glinka G (2015) Analysis of fatigue crack growth under spectrum loading—the UniGrow fatigue crack growth model. Theor Appl Fract Mech 79:25–33
3. Branco R, Antunes FV, Martins RF (2008) Modelling fatigue crack propagation in CT specimens. Fatigue Fract Eng Mater Struct 31:452–465
4. Silva ALL, de Jesus AMP, Xavier J et al (2017) Combined analytical-numerical methodologies for the evaluation of mixed-mode (I + II) fatigue crack growth rates in structural steels. Eng Fract Mech 185:124–138
5. Branco CM, Fernandes AA, de Castro PMST (1999) Fadiga de Estruturas Soldadas, 2nd edn. Fundação Calouste Gulbenkian, Lisboa
6. Farahani BV, Tavares PJ, Moreira PMGP et al (2017) Stress intensity factor calculation through thermoelastic stress analysis, finite element and RPIM meshless method. Eng Fract Mech 183:66–78
7. Tada H, Paris PC (1983) The stress intensity factor for a crack perpendicular to the welding bead. Int J Fract 21:279–284
8. Eslami S, Farahani BV, Tavares PJ et al (2018) Fatigue behaviour evaluation of dissimilar polymer joints: friction stir welded, single and double-rivets. Int J Fatigue 113:351–358
9. Farahani BV, Tavares PJ, Belinha J et al (2018) Compact tension fracture specimen: experimental and computational implementations on stress intensity factor. J Strain Anal 2018:1–18
10. Camas D, Lopez-Crespo P, Gonzalez-Herrera A et al (2017) Numerical and experimental study of the plastic zone in cracked specimens. Eng Fract Mech 185:20–32
11. Farahani BV, Tavares PJ, Belinha J et al (2017) A fracture mechanics study of a compact tension specimen: digital image correlation, finite element and meshless methods. Procedia Struct Integr 5:920–927
12. Moes N, Dolbow J, Belytschko T (1999) A finite element method for crack growth without remeshing. Int J Numer Methods Eng 46:131–150
13. Rao BN, Rahman S (2000) An efficient meshless method for fracture analysis of cracks. Comput Mech 26:398–408
14. Correia JAFO (2014) An integral probabilistic approach for fatigue lifetime prediction of mechanical and structural components

Chapter 25
Micro-notch Size Effect on Small Fatigue Crack Propagation of Nickel-Based Superalloy GH4169

J. Wang, R. Wang, Y. Wang, Y. Ye, X. Zhang and S. Tu

Abstract Nickel based superalloys are used extensively in the hot sections of gas turbines in the aerospace and power generation industries. Some of them are submitted to fatigue circumstances, which may restrict their service lives. Moreover, almost all the structural components have defects. In the past years, the disasters caused by fatigue have aroused consensus. And the safety life design methods have been widely used in the service time design for structures under fatigue load. However, most of those design methods considered the structures were integrated with no defects such as cavities and micro-cracks. While the cracks would initiate and propagate from these defects, which might limit the fatigue life largely. Therefore, a profound understanding of the notch effect on fatigue progress is necessary to build models which can assess the failure period of components in these harsh operating conditions. This paper will discuss notch size effect on fatigue progress in nickel-based superalloys.

Keywords Micro-notch · Fatigue · Small crack

25.1 Introduction

Nickel based superalloy GH4169 is a kind of precipitation enhancement material, owning similar properties to Inconel 718 [1]. It is a multi-component superalloy with

J. Wang · R. Wang · X. Zhang (✉) · S. Tu (✉)
Key Laboratory of Pressure Systems and Safety, Ministry of Education, School of Mechanical and Power Engineering, East China University of Science and Technology, Shanghai 200237, People's Republic of China
e-mail: xczhang@ecust.edu.cn

S. Tu
e-mail: sttu@ecust.edu.cn

Y. Wang · Y. Ye
National Quality Supervision and Test Center of Pressure Piping Components National Quality Supervision and Test Center of Pressure Piping Components (NPCTC), Nanjing 211100, People's Republic of China

J.A.F.O. Correia et al. (eds.), *Mechanical Fatigue of Metals*, Structural Integrity 7,
https://doi.org/10.1007/978-3-030-13980-3_25

complicated structure, containing face centered cubic (FCC) γ'-Ni_3(Al, Ti), body-centered tetragonal (BCT) γ''-Ni_3Nb [2], orthorhombic δ-Ni_3Nb and so on. The phases γ' and γ'' dispersed in the matrix dramatically enhance the tensile properties of GH4169. While the phases δ precipitated at grain boundaries can block the sliding of grain boundaries, which improves its creep properties. Moreover, the superalloy also shows excellent corrosion and oxidation resistance at elevated temperature [3]. Thus, GH4169 is widely used in nuclear industries and aviation.

For instance, the turbine blades in aircraft engines are mainly manufactured by this kind of material. During service process, these components are often subjected to repetitive or fluctuating stresses, which may lead to fatigue failure.

Commonly, the fatigue progress can be divided into three parts: crack initiation, crack propagation, and final fracture. While the crack propagation part could also be distinguished as the small crack propagation and the long part. Due to Suresh's definition [4], small cracks could be generally regarded as microstructurally small cracks, mechanically small cracks and physically small cracks.

Since the 20th century, many crack propagation models have been put forwards. Insides, the most famous models are Paris law [5] and the its derivative models. Considering the stress ratio effect, and the crack closure effect, Walker [6], Forman [7] and Newman [8] modified the Pairs law. These laws are appropriate for long cracks. But for short cracks, they apparently possess higher crack propagation rate than long cracks at the same stress intensity factor. And this should be paid more attention.

This study investigated the small crack propagation regulations with notched specimens, following the work of Deng [9], Ye [10] and Qing [11]. And notch size effect is discussed.

25.2 Experiment Procedure

The material used in this study is rolling Ni-based superalloy GH4169. Its chemical compositions are summarized in Table 25.1. Before experiments, 17 mm diameter round bars were first cut for heat treatment. The heat treatment adopted here was commonly used in industry, where the process was as follow:

(1) Solution annealing at 960 °C for 1 h, air cooling to room temperature.
(2) Aging at 720 °C for 8 h, cooling at 50 °C/h–620 °C.
(3) Aging at 620 °C for a further 8 h, air cooling.

Table 25.1 Chemical composition (wt%) of GH4169 alloy

Fe	Cr	Mo	Al	Ti	Nb + Ta	Mn	Si	C	Ni
19.46	19.05	3.00	0.50	0.93–0.92	5.17	0.03	0.10	0.033–0.031	Bal.

The round bars after heat treatment were then machined into specimens with the dimensions. To ensure the accuracy of the test, the dimensional tolerance and surface roughness were strictly guaranteed. The parallel section of the sample is polished to the mirror to reduce the surface quality effect. Then laser machining method was taken to create the micro-notch at different sizes. Afterwards, the surface with micro-notch would be polished again to remove processing burns. At last, specific corrosion liquid was utilized to expose the metallography of the notched surface.

Fatigue crack propagation tests were conducted in air on an MTS landmark 370.10 hydraulic testing system at room temperature. The frequency of the tests was maintained 5 Hz. The maximum stress here was 800 MPa, while the stress ratio was 0.1.

Replica method was applied to record the original metallography and the crack length of each specific cycles among tests. The detailed procedure of replicating process can be found in Ref. [11].

After the tests, the crack morphologies, which were recorded by the dried replicas, could be observed by using optical microscopy (OM) with a resolution of 0.1 μm when the crack lengths were smaller than 0.3 mm. And the crack propagation rate could be calculated through the crack lengths by observing the replicas at different time intervals. At last, the fractographies of each specimen were observed by using scanning electron microscopy (SEM).

Incremental polynomial method [11] was used to calculate the crack propagation rate. And the stress intensity factor was calculated using the equation proposed by Newman and Raju [8].

25.3 Results and Discussion

25.3.1 Material Properties After Heat Treatment

The microstructures of superalloy GH4169 after heat treatment were displayed in Fig. 25.1. With the SEM and the software Image-Pro Plus, the grain size and the phase distribution were detected. The average grain size was 12 μm. The δ-phase was observed through the software. As was showed in Fig. 25.1b, there was about 12% in area ratio after heat treatment.

Before fatigue tests, tensile test has been carried out. And the result of tensile test was listed as follows: The yielding strength and ultimate strength are respectively 1203.82 MPa and 1437.08 MPa. And the elongation is 25.60%.

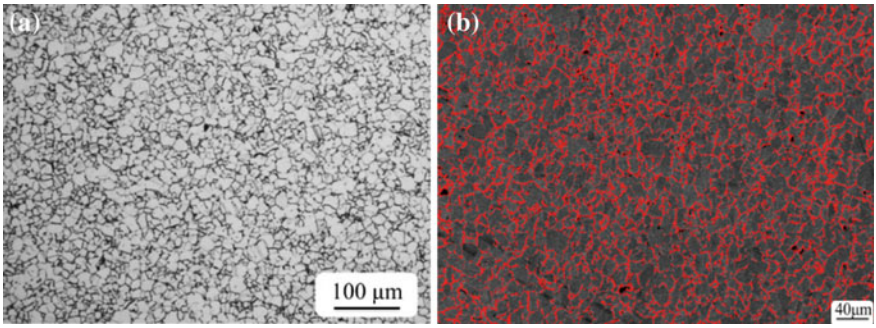

Fig. 25.1 Microstructures of superalloy GH4169 after heat treatment. **a** OM result; **b** SEM result with δ-phase highlight

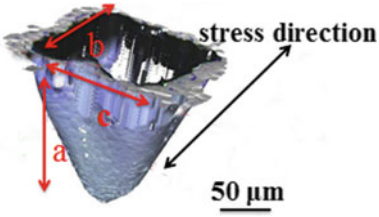

Fig. 25.2 The result of observation of micro-notch by three-dimensional surface profilometer

25.3.2 Effect of Micro-notch Size on Fatigue Life

Excluding the parallel specimens, 21 specimens with different micro-notch size were tested. Figure 25.2 showed the 3D profile of the micro-notch, where a represented for depth direction. b was the width of the notch which was parallel to stress direction. c was the length of the notch, perpendicular to the load and the crack would initiate and propagation in this direction.

For all fatigue specimens, the cracks initiated from the notch. And the previous experimental results indicated that the effect of replica process on the fatigue crack growth rate and fatigue life can be ignored [9–11]. A summary of fatigue lives is displayed in Fig. 25.3. As is shown in this figure, the fatigue life is largely influenced by the length of the defects. With the initial length of the notch increasing, the fatigue life reduces. Moreover, when the length of the notch is small, it shows great impact. However, this impact would decrease, when the length is larger than 200 μm. Comparing the fatigue life with the depth of the notch, it could be realized that the life shortens with the increasing of depth. While the width shows little influence on fatigue life.

FEM method was conducted to calculate the stress concentration factor. Figure 25.4 showed the distribution of fatigue life with increasing stress concentration factor. In this figure, fatigue life and stress concentration factor are correlated.

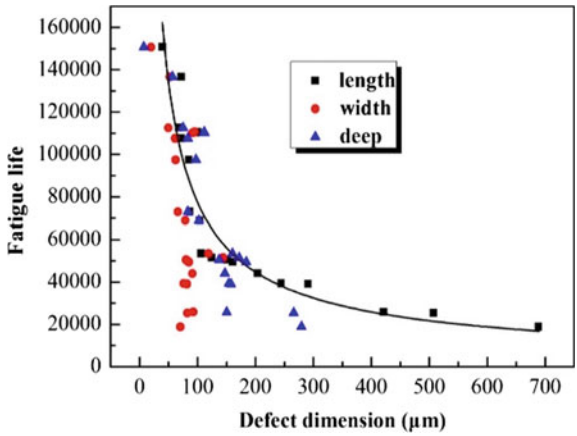

Fig. 25.3 The relationship between dimensions of defects and fatigue lives

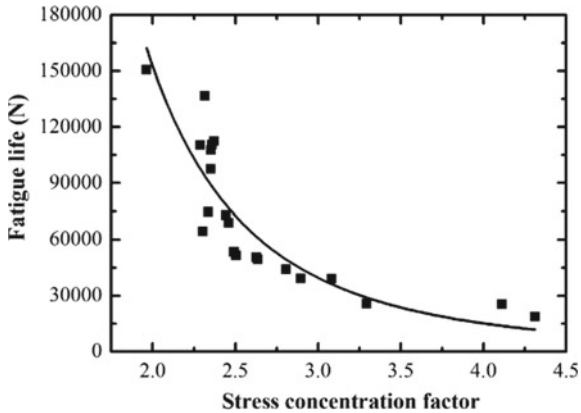

Fig. 25.4 The relationship of stress concentration factor and fatigue life of Specimens

25.3.3 Effect of Micro-notch Size on Fatigue Crack Initiation and Propagation

Figure 25.5 were three photos from replica observed by OM. As is shown in this figure, cracks initiated from the micro-notches, and propagated mostly in a trans-granular way. Influenced by micro-structure, at micro-structure short crack stage, cracks propagated in a zigzag way.

Crack propagation rates and stress intensity factor were calculated according to Newman's method. And the result was exhibited in Fig. 25.6. At micro-structure short crack stage, the propagation rate expressed great volatility. When the crack length came to physical small crack and long crack stage, the crack propagation rate conformed to the Paris law.

As is referred in Ref. [11], the crack propagation progress has two transition point. In this study, it could be observed that both crack initiation life and the two points

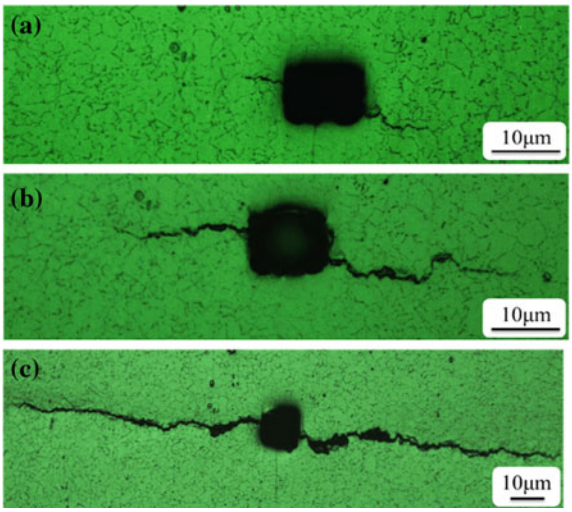

Fig. 25.5 Typical process of crack propagation, **a** 43000 cycles, **b** 7600 cycles **c** 97000 cycles

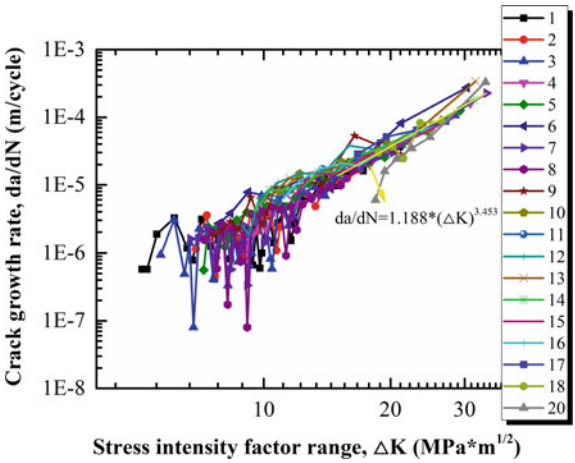

Fig. 25.6 The crack propagation rate with different micro-notch size along with stress intensity factor range

occurred earlier with the increase of length of the notch. And when the initial notch length is long enough, the transition from micro-structure short crack to physical short crack will disappear.

25.4 Conclusions

The multi-scale fatigue crack propagation behavior of GH4169 Nickel-based alloy with different micro-notch sizes was investigated. The following conclusion can be obtained.

1. With the increase of the notch length and depth, the fatigue life drops dramatically. But when each size approaches to some extent, the notch size effect weakens. And the stress concentration factor shows great impact on fatigue life.
2. The crack propagated most in a trans-granular way. Notch size affects crack initiation life and the transition points of different crack stages.

References

1. Lindley TC, Nix KJ (1986) Metallurgical aspects of fatigue crack growth. In: Smith RA (ed) Proceedings of the fatigue crack growth, Pergamon, vol 53
2. Andrews S, Sehitoglu H (2000) A computer model for fatigue crack growth from rough surfaces. Int J Fatigue 22:619
3. Vallellano C, Navarro A, Domínguez J (2000) Fatigue crack notches: i theory. Fatigue Fract Eng Mater Struct 23:113
4. Suresh S (1998) Fatigue of materials, fatigue & fracture of engineering materials & structures, vol 28(12) pp 1153–1160(8)
5. Paris P, Erdogan F (1963) A critical analysis of crack propagation laws. J Basic Eng 85(4):528–534
6. Walker K (1970) The effect aluminium, effects of environment and complex load history on fatigue life: STP 462. ASTM Special Technical Publication, pp 1–14 (1970)
7. Forman RG (1972) Study of fatigue crack initiation from flaws using fracture mechanics theory. Eng Fract Mech 4(2):333–345
8. Newman JC (1981) An empirical surface crack. Eng Fract Mech 15(1–2):185–192
9. Deng GJ, Tu ST, Wang QQ et al (2014) Small fatigue crack growth mechanisms of 304 stainless steel under different stress levels. Int J Fatigue 64(7):14–21
10. Ye S, Zhang XC, Gong JG et al (2017) Multi-scale fatigue modelling. Fatigue Fract Eng Mater Struct 40(11):1928–1941
11. Qin CH, Zhang XC et al (2015) Grain size effect on multi-scale fatigue crack growth behaviour of Inconel alloy GH4169. Eng Fract Mech 142:140–153

Part IV
Probabilistic Methods

Chapter 26
The Interactive Method—Reliable and Reproducible S-N-Curves for Materials

Klaus Block

Abstract Based on a new developed research method—the Interactive Procedure—the characteristic fatigue strength curve (e.g. 5%-quantile obtained at a level of confidence of 90%) was determined directly by test results. As an example new experimental investigations on reinforcing steel were conducted on pure single bars as well as on bars embedded in concrete. The lower stress level was kept constant according to the usual design situation. Another example with a shear loaded fastener system—steel element in concrete—shows that the load bearing capacity increases, if the concrete strength increases. A third example shows the differences between prestressing steel tested without embedment and casted in concrete. For the development of a complete whole S-N-curve for steel 3–5 static and 20–25 cyclic tests are necessary.

Keywords S-N-Curve · Statistical evaluation · Fatigue loaded systems · Quality control

26.1 The Interactive Procedure

The Interactive Procedure is used for determination of the fatigue resistance up to the fatigue limit resistance of materials and systems. A relatively small number of tests can define the fatigue limit resistance as a 5%-quantile each with a necessary confidence level. After only a few tests with different load levels, a prognosis for the final result can be determined. The following new mathematical function was chosen to describe the complete S-N-Curve.

K. Block (✉)
fobatec GmbH, Dortmund, Germany
e-mail: klaus.block@fobatec.de
URL: https://www.fobatec.de

J.A.F.O. Correia et al. (eds.), *Mechanical Fatigue of Metals*, Structural Integrity 7,
https://doi.org/10.1007/978-3-030-13980-3_26

$$\Delta S = \Delta S_D + (\Delta S_1 - \Delta S_D) \cdot a^{(\lg N)^b} \tag{1}$$

with

$\Delta S = f(N)$	amplitude of the fatigue load bearing capacity.
a, b	positive non dimensional values, with $a < 1, 0$.
N	number of cycles.
ΔS_D	amplitude of the fatigue limit bearing capacity.
S_1	statically load bearing capacity.

The method of the least squares is used for determination of the function of the mean values by varying the values a, b and ΔS_D. The only condition to be fulfilled is, that the S-N-Curve is an S-shaped. The fatigue limit bearing capacity ΔS_D can become any value which is realistic for the related system, even zero.

After only 4 tests with different load levels a first approximation of the S-N-Curve as a mean value and an estimation of a x-quantile value is possible. During the following process, tests and calculations are alternating (interaction between calculation and tests). For achieving the final result at least 20 tests are necessary to get reliable and reproducible values for the statistically evaluated meanvalue of the S-N-Curve (Fig. 26.1).

Afterwards the quantile-function can be determined by calculation of single quantiles based on 3 test results each. All these single values can be described by an own function with own values for a, b and ΔS_D. No parallel translation or estimation for certain limits are necessary.

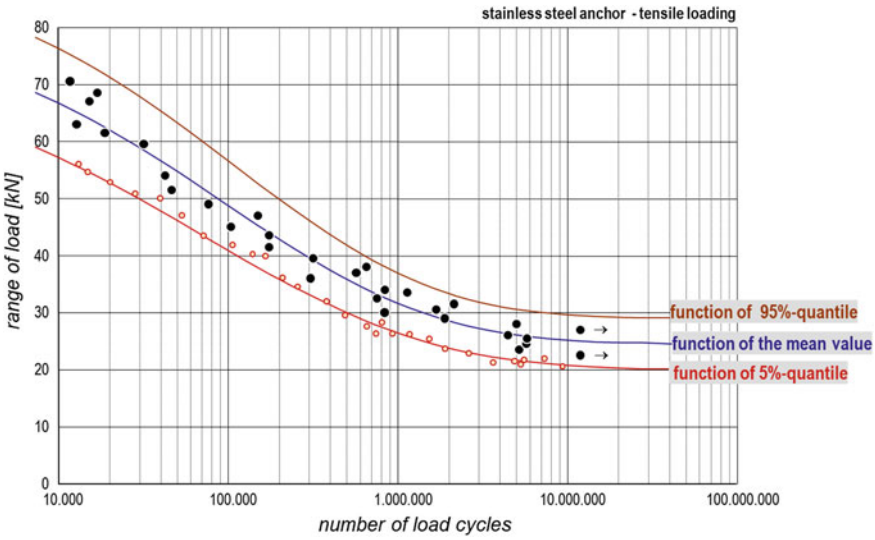

Fig. 26.1 Example of the final results of the S-N-Curve

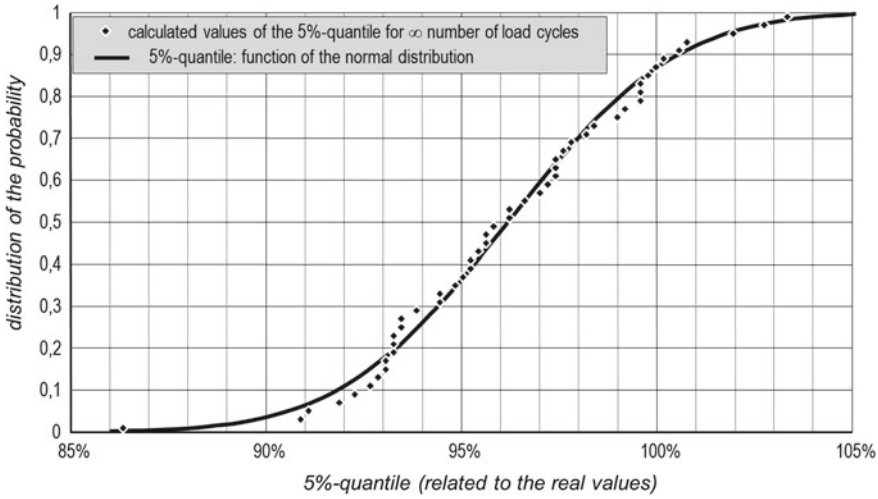

Fig. 26.2 Results of Monte-Carlo-Simulation

This method had been proofed by a Monte-Carlo-Simulation. The result of this check is shown in Fig. 26.2. In detail the Interactive Procedure is described in [1–4].

26.2 Fatigue Resistances of Systems

26.2.1 General

Very often, the material fatigue resistance is transferred to the fatigue resistance of fatigue-loaded systems. In most cases of real applications, systems consisting of different material or different elements are fatigue loaded. A system might fail at different positions, e.g. depending on the kind of manufacturing. Alternatively, another constructive member influences the failing member. In the following chapters, three examples from the field of constructive civil engineering are shown.

26.2.2 Reinforcement Steel for Concrete Structures with Fatigue Tension Actions

Usually steel reinforcement bars are tested uncasted and not embedded in concrete. The positive effect of the force transmission for embedded reinforcement had been taken into account for a comparison with uncasted members. Some test results are

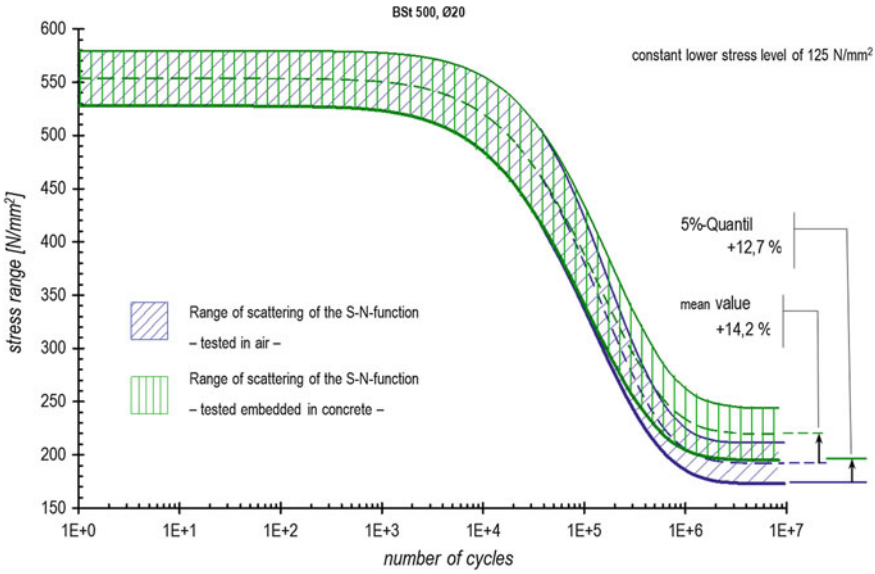

Fig. 26.3 Fatigue-test results of reinforcement steel Ø20 tested uncasted and embedded in concrete

shown in the following Fig. 26.3. Due to the support of the concrete, the fatigue resistance of the steel member increases more than 10%.

The results of this research are described in detail in [5, 6].

26.2.3 Fatigue Shear-Loaded Fastener

Tests and calculations on chemically bonded fasteners were conducted to determine the effect of concrete properties on the fatigue bearing capacity under shear loading (Fig. 26.4). The influence of the concrete compression strength and a crack width of 0.3 mm compared with non-cracked concrete were researched. For each of the four test-series an S-N-Curve was produced.

Some results of this research are shown in Fig. 26.5. The influence of the concrete compression strength is shown depending on cracked and non-cracked concrete. More results are described in [7].

26.2.4 Prestressing Steel Loaded by Fatigue Tension

Prestressing steel is used for concrete structures with a relatively large span, e.g. bridges. In many applications, the prestressing steel is curved like shown in Fig. 26.6.

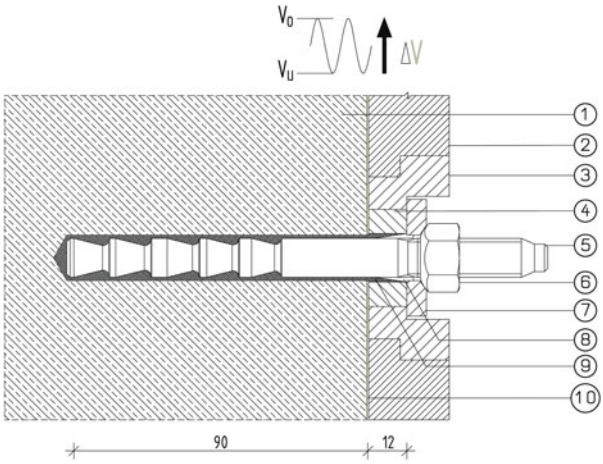

(1) Concrete (2) Attachment (3) Outer bush (4) Inner bush
(5) Fastener rod (6) Nut (7) Washer (8) centering piece
(9) Injection mortar (10) sliding film (plastic layer)

Fig. 26.4 Test structure and fastener properties

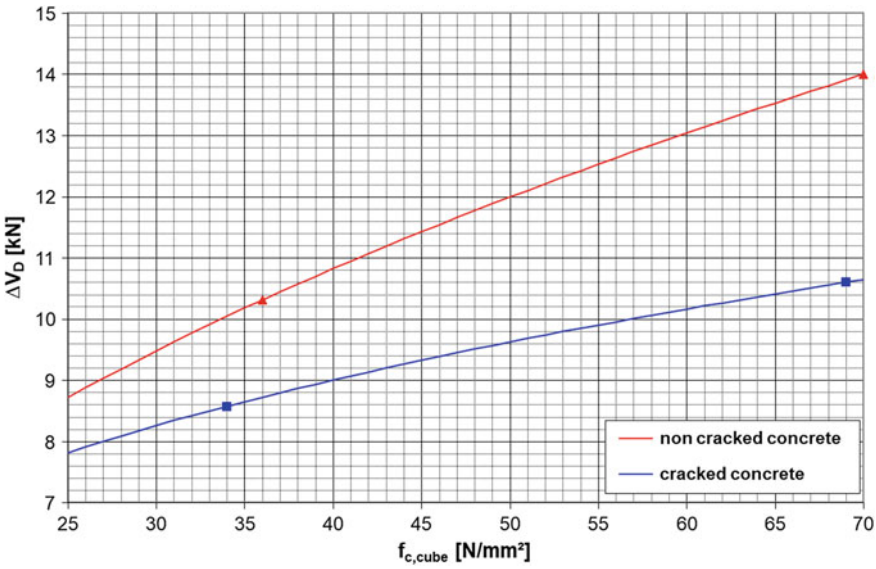

Fig. 26.5 Range of long-term fatigue bearing capacity of a fastener M12 depending on the concrete strength and a concrete crack with of 0.3 mm

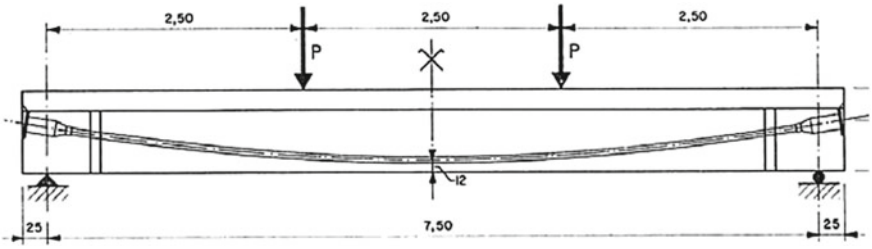

Fig. 26.6 Typically curved prestressing steel (here in a test setup) [8]

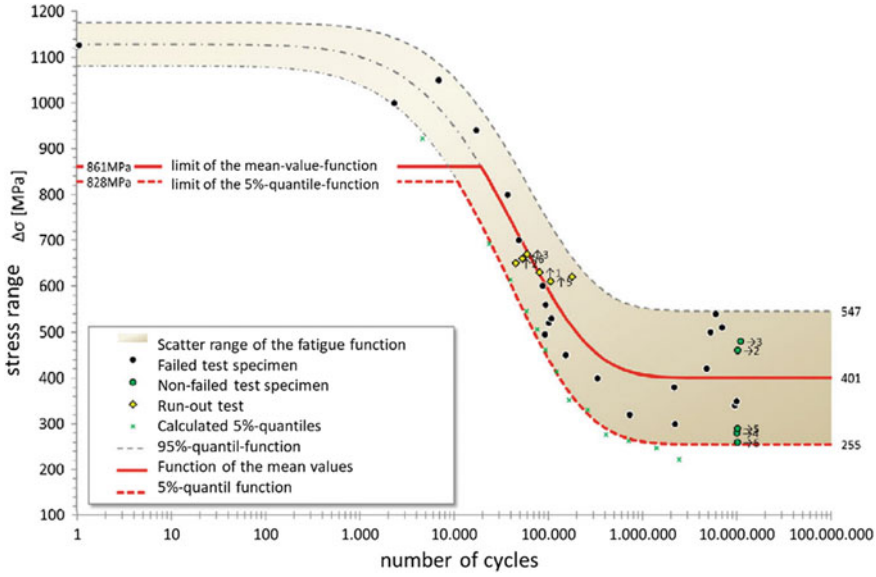

Fig. 26.7 Fatigue test results for single prestressing steel elements including the scatter range (5%-quantile und 95%-quantile) [8]

Heeke [8] investigated the fatigue behaviour of single prestressing steel elements and of prestressing steel in a concrete structure. Figure 26.7 shows fatigue test results for single elements. It can be recognized that for more than 10.000.000 cycles no failure occurred. The non-failed specimen were tested again at a higher stress range and the results lie within the scatter range of test results without a preloading of some million cycles.

Fatigue tests with the same curved prestressing steel in concrete bars show, that failures occur up to 70.000.000 cycles and no horizontal shape of the S-N-Curve can be recognized (Fig. 26.8). The main reason for these differences can be found in the friction between the single steel elements and between steel and mortar.

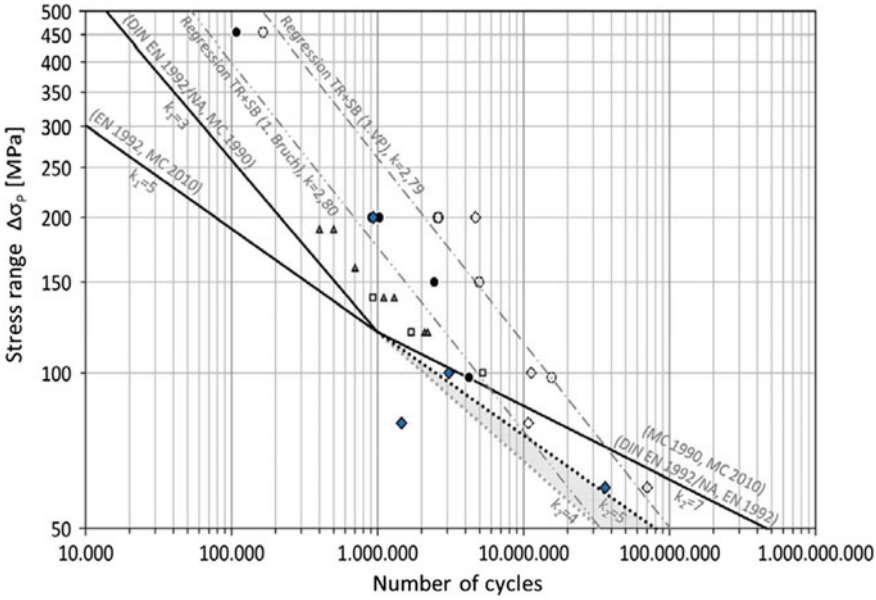

Fig. 26.8 Fatigue tests Results for casted in curved prestressing steel [8]

26.3 Summary

S-N-Curves for materials as well as systems can be determined reliable and reproducible by using the Interactive Procedure. Fatigue properties of materials cannot be transferred readily to system fatigue behaviour.

References

1. Block K, Dreier F (1998) Die Ermüdungsfestigkeit zuverlässig und kostengünstig ermitteln—-Das Interaktive Verfahren. Materialprüfung 40(3):73–77
2. Block K, Dreier F (2003) Das Ermüdungsverhalten von Dübelbefestigungen. Deutscher Ausschuss für Stahlbeton, vol 541. Beuth Verlag, Berlin
3. EOTA EAD 330250-00-0601 (2018) Post-installed fasteners in concrete under fatigue cyclic loading, Draft Jan 2018
4. EOTA EAD 330008-03-0601 (2018) Anchor Channels, Mar 2018
5. Maurer R, Block K, Dreier F (2010) Ermüdungsfestigkeit von Betonstahl—Bestimmung mit dem Interaktiven Verfahren, Bauingenieur, vol 85, pp 17–27
6. Maurer R, Block Klaus Dreier F, Machoczek D, Heeke G (2011) Interactive determination of the fatigue behavior of reinforcing steel. In: Proceedings of the fib symposium Prague 2011. ISBN 978-80-87158-29-6

7. Block K, Dreier F, Bigalke D (2007) Fatigue bearing capacity of anchors exposed to shear loading, Beton- und Stahlbetonbau 2007 Sonderheft engl. Nr 10102
8. Heeke G (2016) Untersuchungen zur Ermüdungsfestigkeit von Betonstahl und Spannstahl im Zeit- und Dauerfestigkeitsbereich mit sehr hohen Lastwechselzahlen. Technische Universität Dortmund, Schriftenreihe Beton, Heft 9

Chapter 27
Probability Distribution Type for the Accumulated Damage from Miner's Rule in Fatigue Design

J. Hoole, P. Sartor, J. D. Booker, J. E. Cooper, X. V. Gogouvitis and R. K. Schmidt

Abstract Variability is present within the stress-life (S-N) fatigue analysis process. This variability propagates through the analysis process into the accumulated damage computed using Miner's Rule. This paper aims to characterise the probability distribution type of the accumulated damage from Miner's rule when accounting for variability in fatigue design parameters using a case study. Whilst the distribution type could not be conclusively selected, considerations regarding the future application of probabilistic methods for fatigue design are presented.

Keywords Probabilistic fatigue · Miner's rule · Skewed distribution

27.1 Introduction

Within the sector of fatigue design, many metallic components are designed to mitigate fatigue failure using 'classical' analysis approaches based upon stress-life (S-N) curves and Miner's Rule. This approach is known as the safe-life fatigue analysis process and is currently used for aircraft landing gear [1], along with components from many other industries. The component 'safe-life' represents the number of applied cycles after which the component must be removed from service. However, the safe-life fatigue analysis process contains many sources of variability within fatigue design parameters, such as materials data, loading and component dimensions [2]. This variability propagates through the process, resulting in significant variation in the accumulated fatigue damage from Miner's Rule and hence the component safe-

J. Hoole (✉) · P. Sartor · J. D. Booker · J. E. Cooper
Faculty of Engineering, University of Bristol, Bristol BS8 1TR, UK
e-mail: jh12317@bristol.ac.uk

X. V. Gogouvitis
Safran Landing Systems, Gloucester GL2 9QH, UK

R. K. Schmidt
Safran Landing Systems, Ajax, ON L1S 2G8, Canada

J.A.F.O. Correia et al. (eds.), *Mechanical Fatigue of Metals*, Structural Integrity 7,
https://doi.org/10.1007/978-3-030-13980-3_27

life. Current research work by the authors aims to develop a probabilistic approach that will compute the probability of failure (P_f) associated with a component safe-life, to better represent the statistical nature of fatigue. A probabilistic approach would model design parameters as probability distributions (e.g. *Normal*, *Weibull*, etc.) and would use probabilistic methods to propagate the variability through to the accumulated damage, enabling the computation of P_f [3]. As the accuracy of the damage probability distribution is vital for producing an accurate value of P_f, this paper aims to characterise the probability distribution type of the accumulated damage from Miner's Rule using a case study.

27.1.1 Stress-Life Fatigue Analysis Process

Stress-Life (S-N) fatigue analysis is a classical approach to fatigue analysis [2]. The loads applied to the component are "blocked" into 'i' blocks defined by the maximum and minimum load-levels (P_{max_i}, P_{min_i}) and the number of times a pair of load levels is applied (n_i). The loads are converted into stress-levels and subsequently into cyclic stress amplitudes (σ_{a_i}) and their associated mean stresses (σ_{m_i}). To convert the stress cycles into equivalent fully-reversed (i.e. $\sigma_{m_i} = 0$) stress amplitudes (σ_{s_i}) a model, such as the Goodman correction, is applied [2]. S-N curves represent how the number of cycles to failure (N_f) varies with the applied cyclic stress of a material. S-N curves are typically based on fully-reversed testing of material coupons. Miner's Rule can then be used to compute the fatigue damage accumulated (d_i) for a cyclic load 'i' as shown in Eq. 27.1 [2]. The total accumulated fatigue damage (D_T) is computed by the summation of the individual damages [2] and failure is assumed to occur when $D_T = 1$ [2].

$$\begin{aligned} D_T &= \sum d_i = \sum \frac{n_i}{N_{f_i}} \\ &= \sum \frac{Number\ of\ times\ cyclic\ stress\ 'i'\ applied}{Number\ of\ cycles\ to\ failure\ for\ cyclic\ stress\ 'i'\ from\ S{-}N\ curve} \end{aligned} \tag{27.1}$$

27.1.2 Probabilistic Methods: Monte Carlo Simulation

A Monte Carlo Simulation (MCS) is a probabilistic method that performs often thousands of evaluations of a process or model, each time randomly sampling different values for the input variables, which are modelled using probability distributions [3]. This results in many values being generated for each individual output of the process. The values for each output can also be statistically characterised using a probability distribution. In the context of this paper, the input variables are the fatigue design

parameters (see Sect. 27.2.1), the process/model is the S-N analysis process, and the output value is the total accumulated damage from Miner's Rule 'D_T'.

27.1.3 Previous Literature on the Probability Distribution Type for the Accumulated Fatigue Damage from Miner's Rule

Previous studies within the literature have proposed the *Normal* [4], *Log-Normal* [5], *3 Parameter Weibull* [6] and *Fréchet* [5] distribution types for the accumulated fatigue damage from Miner's Rule. However, these studies have relied on an assumed distribution type of 'N_f' from S-N data sets [4–6], along with an assumed S-N curve shape [5]. However, the choice of distribution type for N_f is often debated [2] and cannot be assumed a priori for new S-N data sets. Previous studies have also not accounted for variability in fatigue design parameters other than N_f, such as loading and dimensional variability. To extend the work presented in previous studies, this paper aims to present a general method for generating and identifying the probability distribution type of the accumulated damage from Miner's rule, when accounting for material (S-N data), loading and dimensional variability. This objective will be achieved through the use of an MCS applied to an S-N case study. The use of an MCS means that assumptions regarding the N_f distribution type and S-N curve shape do not need to be made a priori.

27.2 Case Study Definition

The case study geometry shown in Fig. 27.1 is the SAE Keyhole specimen [7], manufactured from 4340 steel [8], a typical aircraft landing gear material [1]. The hypothetical load case shown in Fig. 27.1 was constructed to achieve a spread of stress amplitudes across the S-N curve and to ensure that stresses due to loading variability

(a)

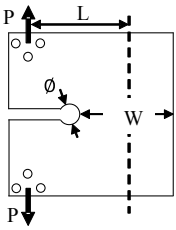

(b)

i	P_{Max_i} (kN)	P_{Min_i} (kN)	n_i	i	P_{Max_i} (kN)	P_{Min_i} (kN)	n_i
1	24.75	-11.00	50	6	22.00	-5.50	500
2	18.70	-11.00	100	7	13.75	-22.00	100000
3	22.00	-16.50	100	8	23.1	-11.00	150
4	24.75	-19.80	25	9	24.75	-16.50	50
5	13.75	-22.00	100000	10	24.75	-22.00	10

Fig. 27.1 **a** SAE Keyhole Geometry. **b** Applied loading

would not exceed the material Ultimate Tensile Strength (σ_{UTS}). Stress analysis equations were sourced from "*eFatigue*" [7], along with a notch stress concentration factor from Ref. [9].

27.2.1 Statistical Characterisation of Fatigue Design Parameters

In order to provide inputs to the MCS, typical fatigue design parameters were statistically characterised, as shown in Table 27.1. Unless stated, all distributions were assumed to be *Normal*, based on the mean (μ) value and a Coefficient of Variation (CoV) defined in Eq. 27.2, where 's' is the sample standard deviation (s values for tolerances were computed assuming the tolerance represented $\pm 3\ s$ as described by Haugen [3]).

$$CoV = \frac{s}{\mu} \tag{27.2}$$

To capture variability in N_f at a given stress-level on the S-N curve, *2 Parameter (2P) Log-Normal* distributions were fitted to the coupon results at each tested stress-level in the ESDU 4340 S-N data (see Fig. 27.2) [8]. For stress-levels that presented 'run-outs' (i.e. tests where the coupon did not fail before a predetermined N_f) [2], a constant $CoV = 0.0323$ was assumed as run-out data requires additional statistical methods [12] beyond the scope of this paper. The fatigue limit (σ_{FL}) was modelled as a *Normal* distribution based upon the 'Probit' method [2], giving a $\mu = 457$ MPa and $s = 13$. For each MCS iteration, a Probability S-N (P-S-N) curve [2] was generated based upon sampling N_f and σ_{FL} values as demonstrated in Fig. 27.2. P-S-N curves assume a constant Probability of Survival (PoS) at all stress amplitudes and at the σ_{FL} [2].

Table 27.1 Statistical characterisation of case study fatigue design parameters

Design parameter	Statistical characterisation
Load levels (P_{Max_i}, P_{Min_i})	Mean load level from Fig. 27.1 with $CoV = 0.08$ (typical variability of aircraft landing gear loads during touchdown [10])
Number of cycles (n_i)	A *discrete uniform* distribution from 0.8 n_i to 1.2 n_i
Nominal width (w)	$\mu_w = 68.6$ mm with ± 0.508 mm tolerance for sawing [3]
Thickness (t)	$\mu_t = 9.5$ mm with ± 0.254 mm tolerance for rolled steel [3]
Hole diameter (Ø)	$\mu_{\emptyset} = 9.5$ mm with ± 0.254 mm tolerance for drilling [3]
Load offset (L)	$\mu_L = 62.1$ mm with ± 0.381 mm tolerance for hole location [3]
UTS (σ_{UTS})	$\mu_{UTS} = 875$ MPa [8] with $CoV = 0.0112$ [11]

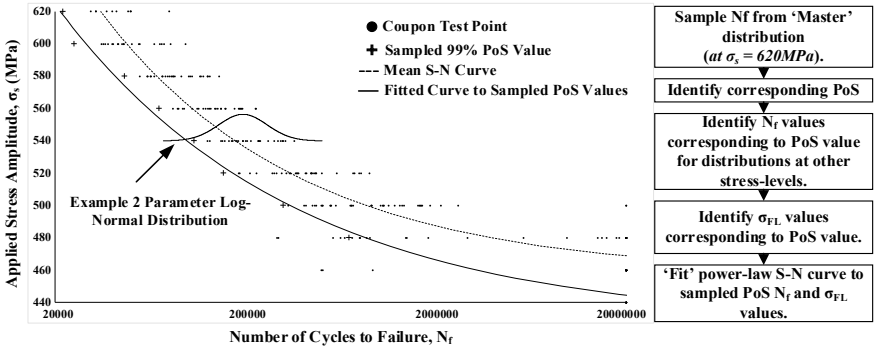

Fig. 27.2 Demonstration of P-S-N representation of S-N curves [2], based upon the ESDU 4340 S-N data [8]. The sampling process used to generate S-N curves for the MCS is also shown

27.3 Results: Statistical Characterisation of Accumulated Damage

The MCS of the case study was repeated for 25,000 evaluations to ensure convergence of the input and output distributions. The resulting histogram of the accumulated fatigue damage from Miner's rule (D_T) is shown in Fig. 27.3a. It can also be of value to identify the distribution of the natural logarithms ($Ln(D_T)$) of the values, as shown in Fig. 27.3b.

As can be seen from Fig. 27.3a, the shape of the D_T distribution is positively skewed (i.e. right-tailed). Candidate distributions capable of demonstrating positively skewed and only zero or positive values (negative damage values are not phys-

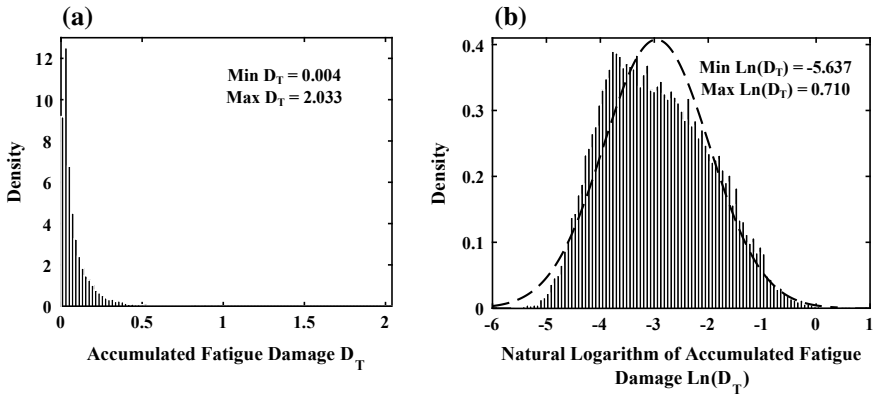

Fig. 27.3 Histograms of the output from the MCS. **a** shows the distribution shape of the accumulated damage from Miner's Rule (D_T) and **b** shows the distribution shape of $Ln(D_T)$ along with a Normal distribution to highlight the positive skew in $Ln(D_T)$

ically possible) were identified [12, 13]: *2P* and *3P Weibull*, *Log-Logistic*, *Gamma*, *Fréchet*, *Birnbaum-Saunders*, *Burr Type XII*, *Inverse Gaussian* and *Pearson Type III*. *Log-Normal* distributions were rejected due to the skew in $Ln(D_T)$ shown in Fig. 27.3b. Maximum Likelihood Estimates (MLE) were used to 'fit' the distribution parameters (e.g. μ and s) [12]. The Cumulative Distribution Functions (CDFs) of each candidate distribution were plotted against the Empirical CDF (ECDF), which is based on the observed frequencies from the MCS [14], to visually assess the 'fit' of the candidate distributions. Only the *3P Weibull*, *Birnbaum-Saunders* and *Inverse Gaussian* provided acceptable visual fits. All other distributions showed a poor visual fit at the upper tail.

The distribution selection and MLE fitting process was repeated for the $Ln(D_T)$ values in Fig. 27.3b. Due to the requirement for positive skew and negative values, the following candidate distributions were identified [12, 13]: *3P Log-Normal*, *3P Weibull*, *Gumbel Maximum*, *Pearson Type III* and *Skew-Normal* [15]. The *Gumbel Maximum* distribution failed to provide an acceptable visual fit to the $Ln(D_T)$ ECDF.

The distribution types found to provide acceptable visual fits were then assessed for 'Goodness-of-Fit' (GoF) using the Chi-Squared (χ^2) test, which compares the frequency of observed values from the MCS results with those expected from the fitted distribution type [14]. This measure is known as the χ^2 statistic (χ^2S). This value is then compared to the critical value (χ^2C) at the 5% significance level and the candidate distribution was rejected if the computed χ^2S exceeded the χ^2C [14]. Table 27.2 shows the χ^2S and χ^2C for each candidate distribution. It can be seen from Table 27.2 that the χ^2 test rejects each of the proposed distribution types. Therefore, despite a number of the candidate distributions presenting acceptable visual fits, the distribution type for the accumulated damage from Miner's Rule could not be selected conclusively using the χ^2 test.

27.3.1 Impact of Results on the Development of a Probabilistic Approach

As Table 27.2 has shown, the wide range of candidate distributions failed to provide an acceptable fit to the accumulated damage from Miner's Rule when using the χ^2

Table 27.2 $\chi 2$ test statistics and critical values for each of the candidate distributions

Result	D_T			$Ln(D_T)$			
Distribution	3P Weibull	Birnbaum-Saunders	Inverse Gaussian	3P Weibull	3P Log-Normal	Pearson Type III	Skew Normal
χ^2S	3478.24	841.11	405.05	981.52	852.16	919.61	849.90
χ^2C	137.70	138.81	138.81	137.70	137.70	137.70	137.70
Decision	Reject	Reject	Reject	Reject	Reject	Reject	Reject

test. Therefore, additional distribution shapes should be considered such as *Beta* and other *Pearson* and *Burr* type distributions [13]. Regardless, the probability of failure (P_f) could still be computed from the MCS results, by identifying the number of evaluations resulting in failure. As there were 12 'failure' evaluations out of 25,000, $P_f = 4.8 \times 10^{-4}$. The case study has also demonstrated that there is a pressing need for the development of a systematic process to 'down-select' the most appropriate distribution type from the wide range of candidate distributions. This is the focus of the authors' future work and could be applied to MCS results and the fatigue design parameters in Sect. 27.2.1.

To identify the cause of the skew in the $Ln(D_T)$ values, the variability in each parameter was isolated one at a time. However, the skew in the distribution persisted. This suggests that the skew is caused by a non-probabilistic element of process. This is expected to be the S-N curve, as it is the single point where all design parameters interact.

27.4 Conclusion

This paper has presented a Monte Carlo Simulation applied to a stress-life analysis case study with the aim of selecting the probability distribution type that best characterises the accumulated damage from Miner's rule. Whilst the distribution type could not be conclusively selected, this work has demonstrated the need to consider a wider range of distribution types than those commonly used in fatigue design, along with the need for a systematic 'down-selection process' to assist engineers in selecting distributions.

Acknowledgements This paper presents work performed as part of the Aerospace Technology Institute (ATI) funded "Large Landing Gear of the Future" project in collaboration with Safran Landing Systems. The authors would like to thank IHS ESDU for their permission to reproduce the 4340 S-N data.

References

1. Braga DFO et al (2014) Advanced design for lightweight structures: review and prospects. Prog Aerosp Sci 69:29–39
2. Shijve J (2009) Fatigue of structures and materials, 2nd edn. Springer
3. Haugen EB (1980) Probabilistic mechanical design. Wiley
4. Rathod V et al (2011) Probabilistic modeling of fatigue damage accumulation for reliability prediction. Int J Qual Stat Reliab 1–10
5. Paolino DS, Cavatorta MP (2014) On the application of the stochastic approach in predicted fatigue reliability using Miner's damage rule. Fatigue Fract Eng Mater Struct 37:107–117
6. Fernádez-Canteli A et al (2014) A probabilistic interpretation of the Miner number for fatigue life prediction. Fraturra ed Integrità Strutturale 30:327–339
7. Socie D (2018) eFatigue, www.efatigue.com. Accessed 25 Apr 2018

8. IHS ESDU (Engineering Sciences Data Unit) (2006) Endurance of high strength steels, data item 04109a
9. Pilkey WD (2008) Peterson's stress concentration factors, 3rd edn. Wiley (2008)
10. Rustenburg JW et al (2001) A comparison of landing parameters from manual and automatic landings of airbus A-320 Aircraft
11. Booker JD et al (2001) Designing capable and reliable products. Butterworth-Heinemann
12. Bury K (1999) Statistical distributions in engineering. Cambridge University Press
13. Johnson NL et al (1994) Continuous univariate distributions, vol 1, 2nd edn. Wiley
14. D'Agostino RB, Stephens MA (1986) Goodness-of-Fit Techniques. Marcel Dekker Inc
15. Figueiredo F, Ivette Gomes M (2013) The skew-normal distribution in SPC. REVSTAT—Stat J 11(1), 83–104

Chapter 28
Evaluation of Fatigue Properties of S355 J2 and S355 J0 by Using ProFatigue Software

Stanislav Seitl, Petr Miarka, Sergio Blasón and Alfonso F. Canteli

Abstract The use of S355 high strength steel in civil engineering to design structures of bridges, cranes or simple engineering parts allows material and economical savings to be achieved meeting the strict construction requirements. The knowledge of the fatigue resistance of material plays the key role during design and maintenance of the bridge structures. In the paper the fatigue behavior of S355 J2 and S355 J0 steels are analyzed using statistical models. The data consist of results from low cycle and high cycle fatigue for a variety of specimens. In particular, the software ProFatigue is used for derivation of the probabilistic S–N field from experimental fatigue data. The program, based on a former regression Weibull model, allows the estimation of the parameters involved in the *S–N* field, providing an advantageous application of the stress based approaches in the fatigue design of mechanical components. The results obtained are compared with the usual used Wöhler-curve, usually used, represented as a straight line in a double-logarithmic scale.

Keywords S355 steel · Fatigue · S–N field · Castillo–Canteli model · ProFatigue software

28.1 Introduction

A number of elements of civil engineering structures are often subjected of fatigue loading. A typical material used for such constructions is S355 steel, which according to the EN 10025-2:2004 [1] standard is manufactured in two grades S355 J0 and S355 J2. Some specific information about its fatigue properties can be found in the literature, see Seitl et al. [2]. The fatigue properties of the S355 steel under

S. Seitl (✉) · P. Miarka
High Cycle Fatigue Group, Institute of Physics of Materials, Academy of Sciences of the Czech Republic, Zizkova 22, 616 62 Brno, Czech Republic
e-mail: seitl@ipm.cz

S. Blasón · A. F. Canteli
Department of Department of Construction and Manufacturing Engineering, Universidad de Oviedo, 33203 Gijón, Spain

J.A.F.O. Correia et al. (eds.), *Mechanical Fatigue of Metals*, Structural Integrity 7,
https://doi.org/10.1007/978-3-030-13980-3_28

bending fatigue loading is analysed in [3]. The S355 steel specimens were subjected to block bending loads, with varying mean load value. Some material hardening was observed, which resulted in changes of material response to the mechanical loading, see Pawlicek et al. [4], even if from a mechanical point of view no structural changes were observed. The contribution by Rozumek et al. [5] showed crack growth characteristics for S355 steel specimens under tension and bending with torsion loading and mixed modes I + II and I + III while a comparison on the basic properties of S355 and S690 steels was done in De Jesus et al. [6] in which contribution was found that the knowledge of the fatigue resistance of the material plays the key role during design and maintenance of the bridge structures.

In the paper, the fatigue behavior of S355 J2 and S355 J0 steels are analyzed using a statistical model. The data consist of results from low cycle and high cycle fatigue for a variety of different specimens. The probabilistic *S–N* field is derived from the experimental fatigue data using the software ProFatigue [7]. The latter, based on a former regression Weibull model, see [8, 9], allows the estimation of the parameters involved in the *S–N* field model to be determined, providing an advantageous application of the stress based approaches to the fatigue design of mechanical components. The obtained *S–N* field is compared with the customary Wöhler curve, represented as a straight line in a double-logarithmic scale (Basquin's model [10]).

28.2 Studied Materials and Specimens

The chemical composition of both steel grades is specified in EN 10025-2:2004 standard and shown in Table 28.1. The fatigue properties of material can be analyzed in terms of the estimated fatigue endurance limit or in terms of the fracture mechanics based approach. The microstructure of the experimental material was created with polyhedral grains of ferrite and pearlite, while the pearlitic colonies are elongated in the rolling direction see in Fig. 28.1.

The fatigue endurance limit is determined from the *S–N* curve whereby the stress range, corresponding to a lifetime of 10^7 cycles is usually considered to be a safe

Table 28.1 Parameters of the Wöhler curves using the Basquin equation and Weibull distribution for S355 steel

		Basquin				Weibull			
Steel grade	Rolling direction	*A*	*B*	R^2	λ	δ	β	B	C
S355J0	A	−70.83	1239.1	0.883	0.02	0.04	1.05	8.93	6.23
	B	−5.01	615.12	0.2183	0.04	0.06	1.02	8.46	6.28
S355J2	A	−7.231	657.12	0.7244	0.18	0.05	1.04	6.31	6.30
	B	−2.264	610.7	0.0849	0.00	0.04	1.02	8.60	6.35

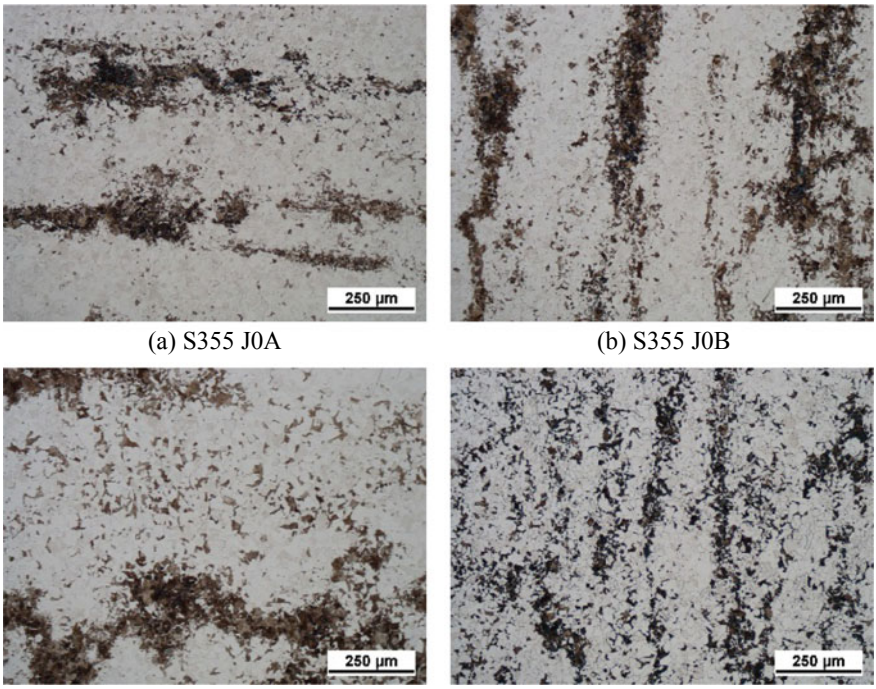

(a) S355 J0A (b) S355 J0B

(c) S355 J2A (d) S355 J2B

Fig. 28.1 Structure of the S355 J0 and S355 J2 steel grades: the crack was propagating in the horizontal direction; Light optical micrography, etched with 2% Nital

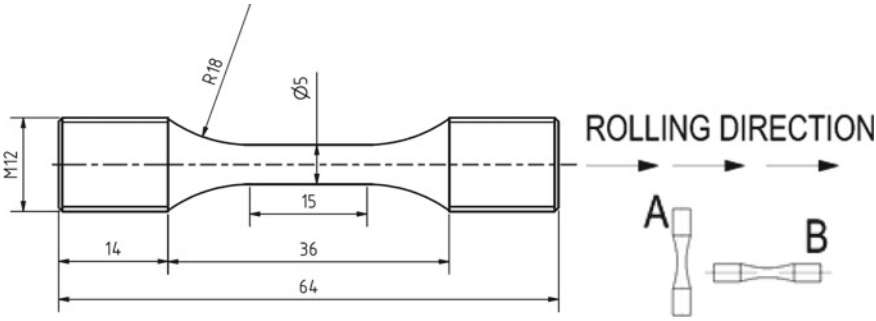

Fig. 28.2 Specimen geometry and rolling direction

reference that not being surpassed ensures non-failure during the whole service lifetime of the component. The testing procedure consists in applying cyclic loading with predefined stress range to determine the number of cycles to failure as described, e.g. in Eurocode 3 standard [11], part 1–9 for the stress ratio $R = 0.1$. The specimen geometry used for the S355 steel tests is shown in Fig. 28.2.

28.3 Applied Models for *S–N* Field Assessment

28.3.1 Wöhler Curve as Fitted Using Basquin's Equation

Often, the Wöhler-curve is represented as a straight line in a double logarithmic plot as the solution provided by Basquin's equation [10]. Accordingly, the relation between stress range and lifetime is given by following equation

$$\Delta\sigma = AN^B, \tag{28.1}$$

where the parameters A and B represent, respectively, the independent term and slope of the resulting straight line in double logarithmic scale.

It is to note that a certain scatter is observed among the results obtained for the same defects induced during the extrusion process, randomness in the specimen manufacturing, etc.

The limited number of S355 steel specimens tested, shown in Fig. 28.3, is typical for this kind of fatigue programs.

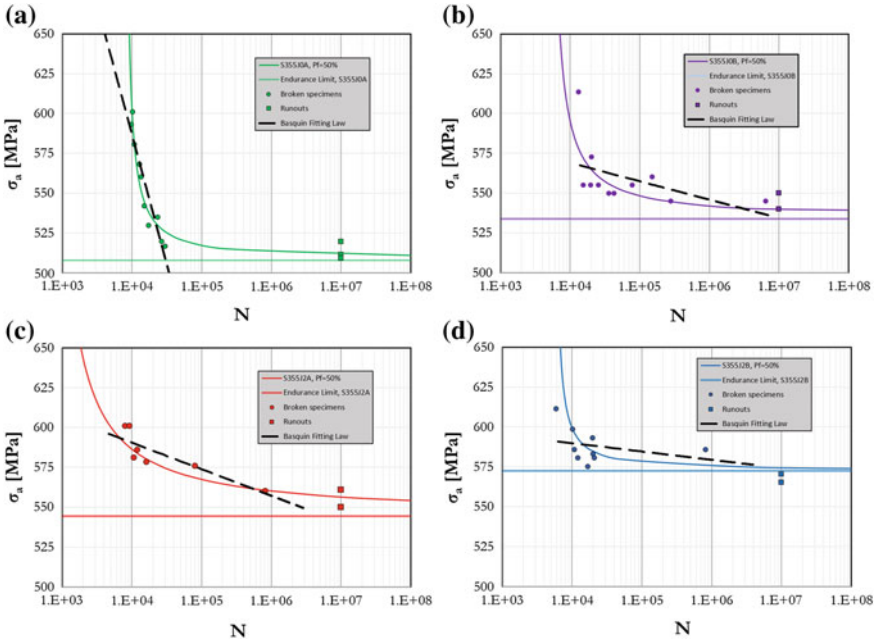

Fig. 28.3 *S–N* field evaluated using Basquin equation and Weibull distribution for S355 steel: **a** J0-A; **b** J0-B; **c** J2-A; **d** J2-B

28.3.2 Probabilistic Model

In this work, the fatigue regression model proposed by Castillo and Canteli [6] is used to perform the lifetime prediction. Using the normalized variable $V = (logN - B)(log\Delta\sigma - C)$ the entire S–N field may be represented by a three parameter Weibull distribution for minima:

$$F(N;\Delta\sigma) = 1 - exp\left[-exp\left(\frac{(logN - B)(log\Delta\sigma - C) - \lambda}{\delta}\right)\right] \tag{28.2}$$

with the following condition:

$$V = (logN - B)(log\Delta\sigma - C) \geq \lambda, \tag{28.3}$$

where B is a threshold lifetime value, C is the endurance, or fatigue limit for $N \rightarrow \infty$, and λ, δ and β are the location, scale and shape Weibull parameters, respectively. The percentiles curves are hyperbolas sharing the asymptotes $\log N = B$ and $\log \Delta\sigma = C$, whereas the zero percentile curve represents the minimum possible number of cycles required to reach failure for the different values of $\log \Delta\sigma$. More information about the model can be found in [8, 9].

In order to facilitate the practical assessment of the *S–N* field from the fatigue data obtained in the experimental program, the free software ProFatigue [7] is applied. The program can be downloaded from the link http://www.iemesgroup.com/download.

28.4 Results Discussion

Figure 28.3a–d. shows the results of the experimental program performed for the S355 steel and the comparison between the fatigue results for $P_f = 50\%$ probability of failure using both Basquin and Weibull models: (a) J2-A; (b) J2-B; (c) J0-A; (d) J0-B. The values for $P_f = 50\%$ give an overview of the basic behavior of the S355 steel. The results from ProFatigue are compared with those from Basquin model Table 28.2 gives the parameters for the different approaches by applying the maximum likelihood method.

Table 28.2 Comparison of the stress fatigue limits for different cases of S355 steel

		Basquin	Weibull	
Steel grade	Rolling direction	Limit 1e7	Limit 1e7	Endurance limit
S355J0	A	97.5	511.2	507.8
	B	543.4	539.5	533.8
S355J2	A	540.6	556.6	554.6
	B	610.7	574.6	572.49

In all cases, a similar description of the experimental results is observed for both models, bilinear Basquin and ProFatigue, in the investigated fatigue region but not so in the high cycle fatigue region where the discrepancies are notorious, on the one side for the S355J0A steel (Fig. 28.3a) due to the lack of failures in the lifetime range between 10^5 and 10^7 $N > 10^7$ in the very high cycle region, and for the $N > 10^7$ in the remaining cases (Fig. 28.3b–d).

According to the results obtained, the Weibull model, as proposed in [8, 9], provides more reliable results than the simple linear *S–N* approach but additionally, probabilistic definition of the *S–N* field information and so that the former one, is recommended for practical applications in civil engineering structural analysis under fatigue, see [12–19].

28.5 Conclusions

The following conclusions are drawn from this paper:

Two different models representing two alternative methodologies for evaluating the *S–N* field are applied to the assessment of fatigue data from two S355 steel grades and the results, compared.

The ProFatigue program, based on the regression Weibull model proposed by Castillo–Canteli, provides a probabilistic analytical way of assessing fatigue results in fatigue. The extrapolation outside the lifetime ranges considered in the tests is possible. In principle, a fatigue limit is implied in this model, although accordingly to the results this limit may prove to be zero or not. The experimental results, represented as *S–N* fields, are relevant when used as input parameters for the sensitivity analysis in the calculation of civil engineering steel structures under fatigue loads.

Acknowledgements The Czech Science Foundation under the contract No. 17-01589S supported this research. The research was conducted in the frame of IPMinfra supported through project No. LM2015069 of MEYS.

References

1. EN 10025-2:2004 Hot rolled products of structural steels—Part 2: technical delivery conditions for non-alloy structural steels
2. Seitl S, Miarka P, Klusák J, Fintová S, Kunz L (2018) Comparison of the fatigue propagation rates in S355 J0 and S355 J2 steel grades. Key Eng Mater (in Press)
3. Lewandowski J, Rozumek D (2016) Cracks growth in S355 steel under cyclic bending with fillet welded joint. Theor Appl Fract Mech 86:350–352
4. Pawliczek R, Prazmowski M (2015) Study on material property changes of mild steel S355 caused by block loads with varying mean stress. Int J Fatigue 80:171–177
5. Rozumek D, Marciniak Z, Lesiuk G, Correia JAFO (2017) Mixed mode I/II/III fatigue crack growth in S355 steel. Procedia Struct Integr 5:896–903

6. de Jesus AM, Matos R, Fontoura BFC, Rebelo C, Simoes da Silva L, Veljkovic MA (2012) Comparison of the fatigue behavior between S355 and S690 steel grades. J Constr Steel Res 79:140–150
7. Fernández Canteli A, Przybilla C, Nogal M, López Aenlle M, Castillo E (2014) ProFatigue: a software program for probabilistic assessment of experimental fatigue data sets. Procedia Eng 74:236–241
8. Castillo E, Fernández-Canteli A (2009) A unified statistical methodology for modeling fatigue damage. Springer
9. Castillo E, Canteli A, Siegele D (2014) Obtaining S-N curves from crack growth curves: an alternative to self-similarity. Int J Fract 187:159–172
10. Basquin OH (1910) The exponential law of endurance tests. In: Proceedings of the ASTM, vol 10, II, pp 625–630
11. European Committee for Standardization (CEN) (2005) EN1993-1-9: Eurocode 3: design of steel structures, part 1-9: fatigue. European Standard, Brussels
12. Kala Z (2017) Identification of stochastic interactions in nonlinear models of structural mechanics. In: AIP conference proceedings, vol 1863, p 480004
13. Kala Z, Omishore A (2016) Fuzzy stochastic approaches for analysing the serviceability limit state of load bearing systems. Int J Math Comput Simul 10:294–301
14. Krejsa M, Kala Z, Seitl S (2016) Inspection based probabilistic modeling of fatigue crack progression. Procedia Eng 145–152
15. Krejsa M, Koubová L, Flodr J, Protivinsky J, Nguyen QT (2017) Probabilistic prediction of fatigue damage based on linear fracture mechanics. Frattura ed Integrita Strutturale 11(39):143–159
16. Krejsa M, Janas P, Krejsa V, Kala Z, Seitl S (2016) DOProC-based reliability assessment of steel structures exposed to fatigue. Perspect Sci 7:228–235
17. Krejsa M, Brozovsky J, Lehner P, Seitl S, Kala Z (2018) Stochastic analysis for short edge cracks under selected loads. In: AIP conference proceedings, vol 1978, p 150006
18. Kala Z, Omishore A, Seitl S, Krejsa M, Kala J (2017) The effect of skewness and kurtosis on the probability evaluation of fatigue limit states. Int J Mech 11:152–166
19. Janas P, Krejsa M, Sejnoha J, Krejsa V (2017) DOProC-based reliability analysis of structures. Struct Eng Mech 64(4): 413–426

Chapter 29
Updating the Failure Probability of Miter Gates Based on Observation of Water Levels

Thuong Van Dang, Quang Anh Mai, Pablo G. Morato and Philippe Rigo

Abstract Hydraulic steel structures, especially lock gates play a significant role in keeping navigation traffic uninterrupted. After a few decades of operation, many of the welded joints may suffer various degrees of deterioration, primarily due to fatigue. To economically combining crack inspection with a scheduled maintenance of the movable parts of the gate, it is valuable to predict inspection time of the welded joints using the historical operations of the gate, i.e. the variation of water levels. Updating failure probability of welded joint is mature in the offshore industry, but it is rarely applied for inland navigation lock gates where the contribution to fatigue failure comes from the variation of water pressures during operation of the lock gates. The scope of this paper is to predict the inspection time of a welded joint using the observed water levels from the operational history. The updating of the failure probability is done for three inspection techniques, considering annual probability and repair decisions. The results show the effects of critical annual probability and the probability of detections (PODs) on the update failure probability for a welded joint.

Keywords Fatigue · Miter gate · Probability of failure · Inspection

29.1 Introduction

There are presently a lot of locks in operation along the inland waterways of Europe as well as all over the world. Many of them were built a couple of decades ago. The most common lock gate type generally used is miter gates consisting of two rotating leaves with vertical hinge axes located in the lock chamber walls. Due to their structural features, miter gates have plenty of welded joints. Damages found with varying degrees of degradation at aging navigation lock gates include cracks in welds, local buckling of flanges and corrosion. Structural inspection and evaluation are required to assure that adequate strength and serviceability are maintained at all sections as long

T. Van Dang (✉) · Q. A. Mai · P. G. Morato · P. Rigo
Department of ArGEnCo/ANAST, University of Liege, Liège, Belgium
e-mail: thuongdv@tlu.edu.vn

J.A.F.O. Correia et al. (eds.), *Mechanical Fatigue of Metals*, Structural Integrity 7,
https://doi.org/10.1007/978-3-030-13980-3_29

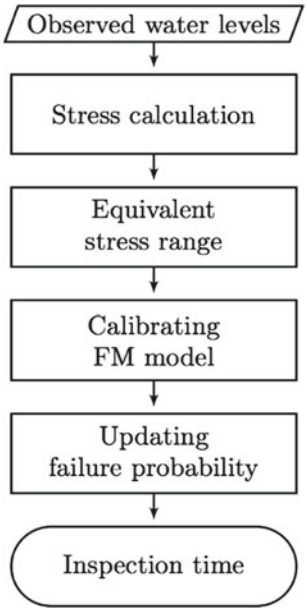

Fig. 29.1 Updating procedure

as the structure is in service. Basically, miter gates are inspected at approximately 5–10 years intervals. This is normally assigned by designers to maintain and replace the movable parts. Cracks inspection can be done and the results of the inspection or the observed degradation provide data to update the failure probability. This paper introduces another technique that inspections and updates the failure probability based on critical annual probability, considering the PODs and repair decisions. The procedure of the present methodology can be found in Fig. 29.1.

29.2 Equivalent Stress Range

For practical fatigue design with the use of nominal stress S-N curves, welded joints are divided into several classes, each with a corresponding design S-N curve. In this study, stresses are calculated from each observed water level by using analytical formulas. Each lockage corresponds to a stress cycle. The relationship between stresses range and the number of cycles over 50 years is built in Fig. 29.2 [1].

The stress in the girder at the connection is parallel and perpendicular to the welds. For a welded joint on a miter gate, the cracks often occur at sharp corners and round-off radii of the vertical and horizontal girders. The properties of welded joint can be found in the detail category $\Delta\sigma_R = 40$ N/mm^2 at 5.10^6 cycles with a slope of m = 3 in Eurocode NEN-EN 1993-1-9 C2, Table 8.3 [2]. Since water levels in front

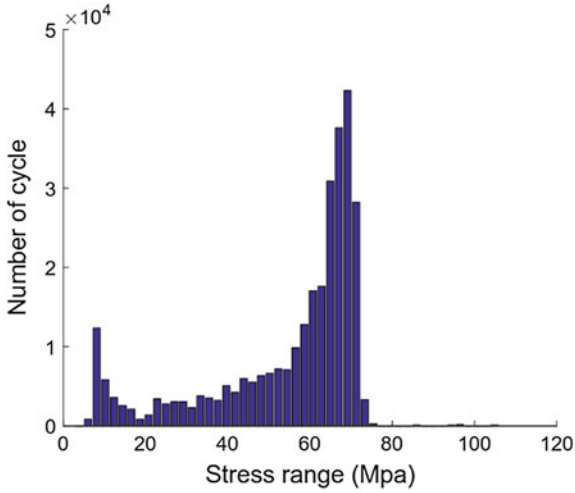

Fig. 29.2 Stress range histogram [1]

and behind the gate are not always the same for every lockage due to seasonal flows of the river, the different stress-ranges occurs during the year are represented by an equivalent stress-range value $\Delta\sigma$, as follows:

$$\Delta\sigma = \sqrt[m]{\frac{D_{tot}C}{nT}} \tag{29.1}$$

where D_{tot} is total accumulated damage, C is a material parameter, n = 7048 is the number of levellings per year and T = 50 years is the time of observations.

29.3 Calibrating Fracture Mechanics Model

Failure probability of the welded joint is first calculated using a limit state function based on Miner's rule [3] (S-N model), Eq. (29.2)

$$g = \Delta - n\frac{B_S^m \Delta\sigma^m}{C} \tag{29.2}$$

where Δ and Bs are the damage criteria and uncertainty load factor, respectively. First order reliability method (FORM) and second order reliability method (SORM) are used to calculate reliability index and the cumulative probability of failure for S-N curve model. The uncertainties involved in the reliability of S-N curve model are presented in Table 29.1.

To incorporate the crack inspection results in assessing failure probability, a fracture mechanics (FM) model is used for crack propagation. The most widely used

Table 29.1 Input data for S-N model

Parameters	Description	Distribution	Mean	Cov
n	No. of cycle/year	Deterministic	7048	
Δ	Uncertainty fatigue damage	Lognormal	1.0	0.3
m	Material parameter	Deterministic	5	
Δσ (MPa)	Stress range	Deterministic	57	
T (Years)	Time service	Deterministic	100	
B_S	Uncertainty load	Lognormal	1	0.25
C	Material parameter	Lognormal	3.5239e11	0.486

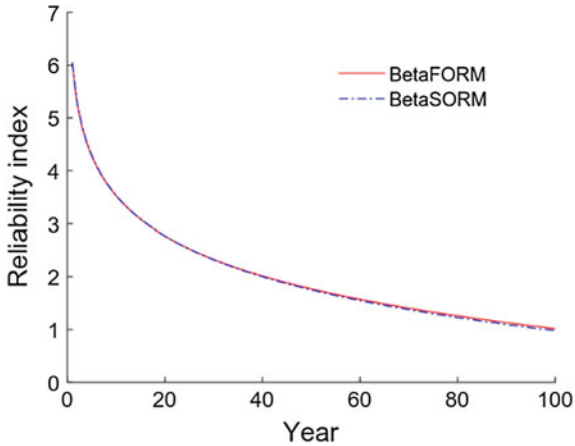

Fig. 29.3 Reliability index

model is the Paris-Erdogan law [4], Eq. (29.3). The results of the calculation reliability index for S-N model are shown in Fig. 29.3.

$$\frac{da}{dN} = C(Y\Delta\sigma\sqrt{\pi a})^m \tag{29.3}$$

where N is the number of cycles, da/dN is the rate of crack growth, C and m are material parameters, Y is geometry function.

Monte Carlo Simulation (MCS) is known as a simple random sampling method or statistical trial method that makes realizations based on randomly generated sampling sets for uncertain variables. The probability of failure is given by Eq. (29.4):

$$P = \frac{1}{N}\sum_{i=1}^{N} I[G(x_i) \leq 0] \tag{29.4}$$

where N is the number of samples, $I[G(x_i) \leq 0]$ is the indicator function.

Table 29.2 Input data for FM model

Parameters	Description	Distribution	Mean	Cov
n	No. of cycle/year	Deterministic	7048	
m	Material parameter	Deterministic	3	
Y	Geometry function	Deterministic	1.12	
B_y	Uncertainty geometry	Normal	1.0	0.649
$\Delta\sigma$ (MPa)	Stress range	Deterministic	57	
T (Years)	Service life	Deterministic	100	
a_0 (mm)	Initial crack size	Exponential	0.16	
a_c (mm)	Thickness	Deterministic	25	
B_S	Uncertainty load	Lognormal	1	0.25
C	Material parameter	Lognormal	2.483e-12	0.664

This method is conducted to determine the probability of failure for FM model. Input data are shown in Table 29.2. Figure 29.4 shows the samples of crack propagation are simulated for the chosen joint by FM model.

The calibration algorithm is carried out by a least-squares fitting in cumulative failure probability space (P_f), as shown in Eq. (29.5).

$$min \sum_{t=1}^{T} (P_{f_{SN}}(t) - P_{f_{FM}}(t; x_1 \ldots x_N))^2 \tag{29.5}$$

where $P_{f_{SN}}(t)$ is the cumulative failure probability at time t, evaluated using the S-N model; $P_{f_{FM}}(t; x_1 \ldots x_N)$ is the cumulative failure probability at time t, evaluated

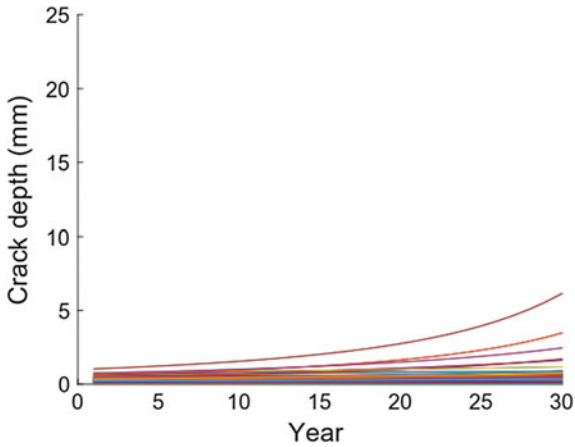

Fig. 29.4 Crack depth propagation

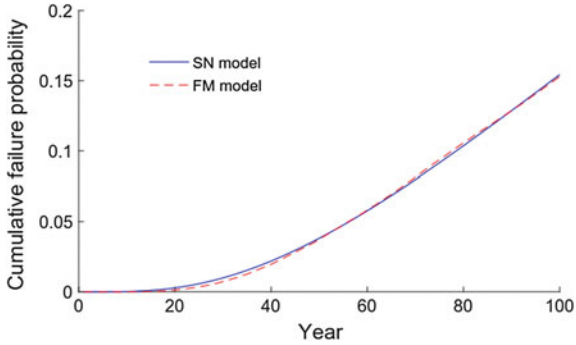

Fig. 29.5 Calibrated result

using FM model with a set of parameters ($x_1 \ldots x_N$) representing initial crack size, C, the uncertainty of geometry function. T is the service life of the considered structures.

The FM model is calibrated to give failure probabilities as obtained from the S-N model analysis. The calibrated result is shown in Fig. 29.5.

29.4 Probability of Detection

The probability of detection is used for quantifying the performance of non-destructive testing. POD curves describe the probability that a certain crack size is detected during inspection. In the present paper the POD curves are assumed to be represented by the Log-Odds-Log scale model [5]:

$$\mathrm{POD(a)} = \frac{\alpha a^{\gamma}}{1 + \alpha a^{\gamma}} \tag{29.6}$$

where a (mm) is the detectable crack and α, γ are regression parameters. To see the effects of PODs on the predicted inspection time, three cases of inspection labelled A ($\alpha = 0.3\ \mathrm{mm}^{-1}$, $\gamma = 3.0$), B ($\alpha = 0.085\ \mathrm{mm}^{-1}$, $\gamma = 3.0$) and C ($\alpha = 0.035\ \mathrm{mm}^{-1}$, $\gamma = 3.0$) are used [6].

29.5 Updating Failure Probability

Normally, the lock gates are often inspected by divers or by de-watering. However, the high costs and downtown associated with these inspection techniques lead to infrequent inspections, typically once every 5–10 years [7]. As a result, the update failure probability may be implemented based on these inspection intervals. This paper provides another technique that updating failure probability based on critical annual probability and inspection techniques. The simulation method is used to

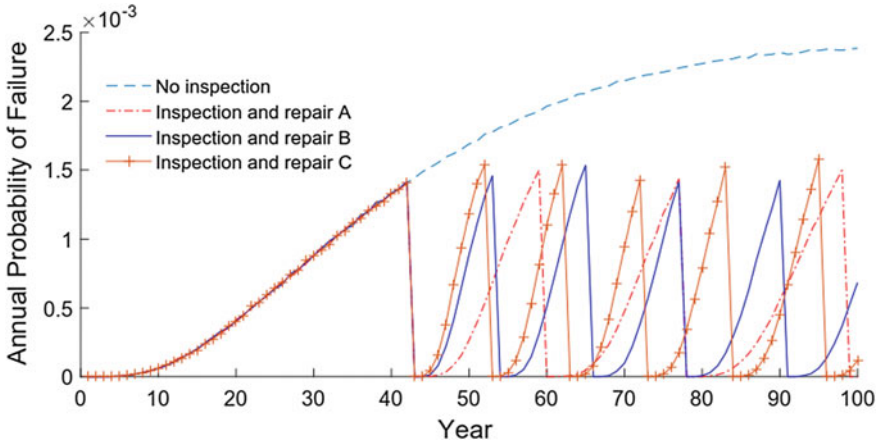

Fig. 29.6 The updating annual failure probability with 90% PODs

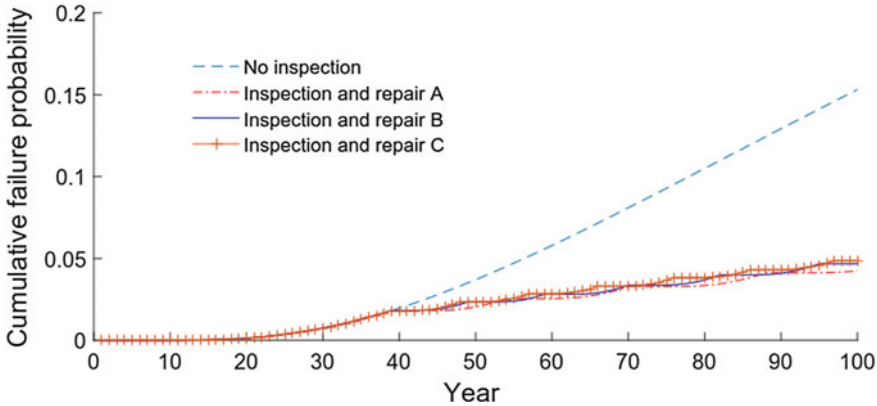

Fig. 29.7 The updating cumulative failure probability with 90% PODs

update the failure probability (P_f), considering POD and repair policies. It is assumed that all detected cracks are repaired. For the case where crack detected and not repaired, as suggested in [8], it should not be considered in the simulation method as an unrealistically large number of samples is required for updating and another method should be employed. The maximum allowable annual probability of failure $P_f = 1.4 \times 10^{-3}$ (equivalent to a target reliability index after 50 years is 1.5 in EN1990) and 90% probability of detection in three inspection techniques are used (Fig. 29.6).

By controlling the annual probability of failure we can choose appropriate inspection time for each POD technique while cumulative failure probability still keeps stable. In this case, after 40 years, the miter gate should be checked and repaired (Fig. 29.7).

29.6 Conclusion

The aging locks on the waterway system have various degrees of deterioration. Therefore, inspection and maintenance to maintain the design life are crucial. However, inspection and repair may costly, so setting up a reasonable inspection plan can play an important role in addressing the issue. This study presented efforts to update the probability of failure for a miter gate based on critical annual probability and inspection techniques. Water level observations data is used to compute stress range and an equivalent stress range. The results have shown that the approach presented in this paper provides an effective method for updating failure probability in miter gates. By considering the cost of welded joint repair and the cost of periodic inspections of the gate, the updated failure probability will be useful for optimizing maintenance plan of lock gates.

Acknowledgements The authors acknowledge the financial support by the Wallonie-Bruxelles International (WBI) for this research.

References

1. Schonfeld D (2013) Fatigue of steel Lock Gates
2. The European Union (2005) European standard EN 1993.1.9, vol 7, no 2006
3. Miner MA (1945) Cumulative damage in fatigue. Am Soc Mech Eng—J Appl Mech 12:159–164
4. Paris P, Erdogan F (1963) A critical analysis of crack propagation laws. J Basic Eng 85(4):528
5. Berens AP, Hovey P (1981) Evaluation of NDE reliability characterization. Dayt. Air force wright-aeronautical lab. Wright-patterson air force base, vol I
6. Kulkarni SS, Achenbach JD (2007) Optimization of inspection schedule for a surface-breaking crack subject to fatigue loading. Probab Eng Mech 22(4):301–312
7. Eick BA et al (2018) Automated damage detection in miter gates of navigation locks. Struct Control Heal Monit 25(1):1–18
8. Mai QA, Sørensen JD, Rigo P (2016) Updating failure probability of a welded joint in offshore wind turbine substructures. In: OMAE2016-54232, pp 1–10

Part V
Fatigue Modelling

Chapter 30
Comparison of Several Optimized Methods for Mean Stress Effect Evaluating the Stress-Life Prediction

Jan Papuga, Ivona Vízková, Maxim Lutovinov and Martin Nesládek

Abstract Four methods for computing the equivalent stress amplitude as the response to the mean stress effect are compared. They all include one additional parameter, which was optimized for 19 different data sets. Trends of the optimized parameters were analyzed, and their estimates were recommended. These recommended values were then checked on the same test set. The final results favor use of the Bergmann and the Walker methods, while the Linear method built as a generalization of the Goodman formula results in a weak output.

Keywords Mean stress effect · Walker method · Goodman method

30.1 Introduction

There are two basic concepts for mean stress effect evaluating in the stress-life prediction. The concept of the reduced fatigue limit amplitude is a traditional solution, which shifts the S–N curve of the fully reversed load case to a new position based on the value for the reduced fatigue limit amplitude $\sigma_{FL,\,red}$. This value is set from the Haigh diagram relevant to the number of cycles at the fatigue limit N_{FL}. Determining the complete reduced S–N curve from the reduced fatigue limit can differ in various applications.

The second approach is in fact much simpler in use. Instead of focusing the Haigh diagram at some given lifetime, it uses the same core formula but with switched meaning of its parameters to compute the equivalent stress amplitude at fully reversed loading. This equivalent stress amplitude should cause the same damage as the cycle described by the stress amplitude and mean stress. The curve in the Haigh diagram goes directly through the loading point, because it is related to the final computed lifetime N_x. The equivalent stress amplitude can be thus immediately used with the S–N curve in fully reversed loading.

J. Papuga (✉) · I. Vízková · M. Lutovinov · M. Nesládek
Faculty of Mechanical Engineering, Czech Technical University in Prague,
Technická 4, 166 07 Prague 6, Czech Republic
e-mail: jan.papuga@fs.cvut.cz; papuga@pragtic.com

J.A.F.O. Correia et al. (eds.), *Mechanical Fatigue of Metals*, Structural Integrity 7,
https://doi.org/10.1007/978-3-030-13980-3_30

Both approaches use the Haigh diagram as the basic part of the solution. Its description by the Goodman formula:

$$\sigma_{a,eq} = \frac{\sigma_a}{1 - \frac{\sigma_m}{S_u}} \tag{30.1}$$

is widely used in the industry for evaluating the mean stress effect (MSE). If conclusions of the relatively recent papers (see e.g. [1–6]) are checked, it becomes apparent that the Goodman method leads to unreliable and in most cases to very conservative results. Often, a new MSE model is suggested and proved to be better than the Goodman method, but the test set used for validating remains small, limited to less than 10 materials [2–5]). If a sufficient number of experimental validation data is used, the data sets contain various issues as discussed e.g. in [7, 8].

The recent work by Dowling et al. [1] is very extensive in comparison with other papers. Its authors compared results for four methods for the MSE inclusion (Goodman, Morrow, SWT and Walker) via the equivalent stress amplitude concept. Goodman, Morrow and SWT methods are strictly defined using the existing material parameters, but the Walker method contains additional fitting exponent:

$$\sigma_{a,eq} = \sigma_{max}\left(\frac{1-R}{2}\right)^{\gamma} \tag{30.2}$$

By using the Basquin formulation of the S–N curve

$$\sigma_{a,eq} = AN^{b} \tag{30.3}$$

Dowling et al. transformed the mix of Eqs. (30.2) and (30.3) to the multiple linear formulation

$$\log N = \frac{1}{b}\left[\log \sigma_{\max} + \gamma \cdot \log\left(\frac{1-R}{2}\right) - \log A\right] \tag{30.4}$$

After completing the regression on collected experimental data in this way, the authors compared computed equivalent stress amplitudes with the stress amplitudes for a fully reversed cycle at the same number of cycles for all experimental points. Use of the linear regression leads to the best fit of the Walker parameter to all data of the given data set. Thanks to it, this method achieved best results in [1].

Papuga et al. [8] recently objected that the comparison of the optimized Walker method with other non-optimized methods could not lead to another conclusion. They decided to give a chance also to the generalized Goodman formula marked as the Linear method (see Table 30.1). M parameter was optimized in the same way, though the formulation enforced a non-linear regression analysis. Results showed that both optimized methods clearly exceeded the prediction quality of any other tested method (9 non-optimized methods were scrutinized) and the results for the Walker method exhibited a lower scatter compared with the Linear method. When

Table 30.1 Formulas for evaluated generalized methods, and names of methods, to which they can degenerate with adequately set material parameters

Method	Can switch to methods	Formula
Bergmann	SWT ($k = 1$)	$\sigma_{a,eq} = \sqrt{(\sigma_a + k \cdot \sigma_m) \cdot \sigma_a}$ (30.5)
Kwofie		$\sigma_{a,eq} = \sigma_a \cdot e^{\alpha \frac{\sigma_m}{R_m}}$ (30.6)
Linear	Goodman, Half-slope, Morrow, Soderberg	$\sigma_{a,eq} = \frac{\sigma_a}{1 - \frac{\sigma_m}{M}}$ (30.7)
Walker	SWT ($\gamma = 0.5$)	$\sigma_{a,eq} = (\sigma_a + \sigma_m)^{1-\gamma} \cdot \sigma_a^{\gamma}$ (30.8)

the proposed estimate for γ was applied to the data, the prediction quality worsened, but it got similar with the Linear method.

This paper goes farther with the evaluation, while placing the question: Could some other trend result in a better approximation of the data than the Walker method does?

30.2 Evaluation and Its Results

30.2.1 MSE Methods

Table 30.1 lists the methods evaluated within this study. The Walker and the Bergmann methods are similar—they are generalized versions of the SWT parameter. It should be noted that while the Bergmann method can also be transformed to the reduced fatigue limit amplitude concept, the Walker method cannot. Two more methods working with an additional regression parameter are present in Table 30.1—the Linear method that have been already analyzed in [8] and the Kwofie method [4].

It can be anticipated that the additional parameter included in the formulation should bring better overall results compared with any non-optimized methods. This statement was confirmed in [8]. On the other hand, the optimized methods are useful only if their parameters can be easily set. If this is not true, they are of limited practical applicability.

30.2.2 Used Experimental Data

The data set used here for the analysis conforms to the testing set described in [8]. It comprises 19 different data sets, which refer to 48 different S–N curves, see their

Table 30.2 Numbers of data sets establishing the test set used here. See more details in [8]

Load case	Plane bending		Push-pull		
Material	Al alloy	Steel	Al alloy	Cast iron	Steel
Number of data sets	3	1	4	2	9

Table 30.3 Mean coefficients of determination R^2 for each group of loadings and materials

Loading	Materials	Kwofie	Linear	Bergmann	Walker
Plane bending	Al alloys	0.829	0.821	0.835	0.832
	Steels	0.833	0.833	0.835	0.832
	Total	0.830	0.824	0.835	0.832
Push-pull	Al alloys	0.844	0.815	0.875	0.876
	Cast irons	0.714	0.673	0.738	0.741
	Steels	0.857	0.861	0.844	0.842
	Total	0.834	0.823	0.838	0.837
Total		0.833	0.824	0.836	0.837

conditions in Table 30.2. The only difference is removing the only experimental case from Ra1 data set with negative mean stresses. It does not have any sense to do any conclusions on validity of any method in the compression region on one set only.

30.2.3 Analysis and the Results

All experimental items in each data set are first used to optimize the sought material parameters. The minimized parameter is the sum of squares of the logarithms of cycles. To compare the ability of each method to conform to the inputted experimental data, this stage is finished by the comparison presented in Table 30.3.

Numbers of S–N curves and data points in each set differ. Table 30.3 thus does not describe the prediction capability, it refers only to the ability to follow some trend.

Dowling et al. [1] checked the prediction quality of different methods by comparing the computed equivalent stress amplitude for each experimental point with the stress computed for the same fatigue life from the optimized Basquin curve (Eq. 30.3). Papuga et al. [8] used a similar solution, and final verdicts stated there correspond to it.

There is an issue anyhow. The optimization leading to final material parameters was controlled by the minimum deviation in fatigue life, but not in fatigue strength. If the relevant parameter had been based on differences in fatigue strength, material parameters obtained would differ. The results obtained in [1] and [8] are thus worth a

Table 30.4 Standard deviations of ΔFL if evaluated for individual data groups

Loading	Materials	Data points	Kwofie (%)	Linear (%)	Bergmann (%)	Walker (%)
Plane bending	Al-alloys	119	4.9	4.9	4.6	4.6
	Steels	71	3.9	3.9	3.8	3.9
	Total	190	4.5	4.6	4.3	4.4
Push-pull	Al-alloys	222	5.8	6.3	4.7	4.6
	Cast irons	130	7.8	8.3	8.5	8.2
	Steels	221	6.7	6.6	9.9	9.8
	Total	573	6.7	7.0	7.9	7.8
Total		763	6.3	6.3	7.2	7.2

further analysis. The parameter used for the comparison here is the fatigue life error ΔFL:

$$\Delta FL = \frac{\log(N_{\text{exp}}) - \log(N_{\text{opt}})}{\log(N_{\text{exp}})} \tag{30.9}$$

N_{exp} corresponds to the fatigue life measured for the given combination $\sigma_a - \sigma_m$. The same stress combination using the formula of the MSE criterion (Table 30.1) provides the $\sigma_{a,\,eq}$. Lifetime N_{opt} is obtained from the Basquin formula with optimized material parameters while using $\sigma_{a,\,eq}$. ΔFL is defined in Eq. (30.9) in this way to keep the rule that positive values mean conservative results (shorter lifetime), negative values are non-conservative. All experimental data points in the set (763 items in total) are evaluated.

Table 30.4 presents the output for the comparison in the form of standard deviations of ΔFL parameter. Because the analysis is done with perfect optimized material parameters, it does not have any sense to compare the mean values for ΔFL over the groups, because they are similarly good.

30.3 Discussion

Results in Table 30.4 support the idea that the previous conclusions in [8] were misleading at least partly. The Walker method (and the Bergmann method) are getting close to the ideal trend compared with the Linear method only for aluminum alloys. For steels, this is on contrary. The Kwofie method works well in both situations.

Such conclusions are anyhow applicable only then, if the derived material parameters are either constant, or if they exhibit some clear dependency on widely available parameters. This paper must keep a limited scope, so only tabular values for ranges of optimized parameters could be shown in Table 30.5 (in parentheses), in addition to the derived values for each material group. Any trends are not very well visible,

Table 30.5 Proposals for estimating material parameters for individual methods. Ranges of optimized values relevant to individual sets are in parentheses. For steels, the last value in parentheses concerns the only test set loaded in plane bending, values for which differ substantially

Param.	Al alloys (7 it.)	Cast irons (2 it.)	Steels (10 items)
γ [–]	0.47 (0.38 ÷ 0.62)	0.42 (0.41; 0.43)	$-0.0004\ S_u + 1.008$ (0.50 ÷ 0.87; PB:0.90)
α [–]	1.12 (0.62 ÷ 1.63)	1.21 (1.00; 1.43)	$0.0009\ S_u - 0.116$ (0.21 ÷ 1.04; PB:0.11)
k [–]	1.10 (0.63 ÷ 1.46)	1.31 (1.21; 1.42)	$0.001\ S_u - 0.202$ (0.16 ÷ 1.00; PB:0.14)
M [MPa]	695 (389 ÷ 1013)	695 (603; 787)	$-0.702\ S_u + 2304.8$ (1054 ÷ 3092; PB:8316)

Table 30.6 Statistics of ΔFL in the case when the material parameters were estimated

Load	Materials	Kwofie		Linear		Bergmann		Walker	
		Mean	Std. dev.	Mean	Std. dev.	Mean	Std. dev.	Mean	Std. dev.
PB	Al	6.1	14.3	3.1	13.5	2.8	6.5	2.6	6.5
	St	13.9	11.1	35.2	27.1	8.5	6.9	7.5	6.3
	Total	9.0	13.7	15.1	25.1	4.9	7.2	4.4	6.9
Ten	Al	0.7	6.9	−2.2	7.7	0.1	5.3	0.0	5.3
	CI	−4.5	9.9	−9.0	11.9	−1.1	8.9	−1.2	8.7
	St	−2.1	11.7	27.4	34.2	−0.8	11.1	−2.2	12.0
	Total	−1.6	9.8	7.7	27.5	−0.5	8.8	−1.1	9.2
Total		1.1	11.8	9.5	27.1	0.8	8.7	0.3	9.0

and thus the average values are proposed in most cases. There are more data items among steels, so simple linear trends are proposed (note anyhow that $R^2 < 0.5$ in all cases).

If these estimates are used in the analysis together with the Basquin curves relevant to S–N curves in fully reversed loading, the results start to differ substantially, see Table 30.6. The results of the Linear method worsened—the method is too conservative and exhibits large scatter. A check was done whether it is not due to the single case of plane bending in steels, but the results did not change much, if this case was removed.

Kwofie's method is better regarding the statistics, though it is still weaker than the other two methods. Kwofie [4] expected α parameter to be close 1. Table 30.5 shows that this assumption is quite close for aluminum alloys and cast irons, but not for most steels.

The Bergmann method and the Walker method exhibit very similar behaviour. Similarly to [1] or [8], their performance is to be rated high above all in the case of aluminum alloys.

30.4 Conclusion

The paper focuses on evaluating the mean stress effect in the high-cycle fatigue life prediction. Four criteria were selected for evaluation through optimizing their material parameters on available experimental data of 19 data sets: the Walker and the Bergmann methods, the Linear method and the Kwofie method. Each of them contains one additional fitting parameter, which was retrieved from the optimization procedure.

To enable practical applicability of the results, the optimized parameters were analyzed and proposals for their estimates stated. Their analyses lead to these conclusions:

1. The Linear method achieves the worst results—too scattered and too conservative.
2. The Kwofie method is closer to the best performing methods, but it remains worse.
3. The methods by Bergmann and by Walker result in a comparable output, and they can be recommended for a general use.
4. More data sets would help in better understanding, whether the observed trends are really universal.

Acknowledgements Authors acknowledge support from the ESIF, EU Operational Programme Research, Development and Education, and from the Center of Advanced Aerospace Technology (CZ.02.1.01/0.0/0.0/16_019/0000826), Faculty of Mechanical Engineering, Czech Technical University in Prague.

References

1. Dowling NE, Calhoun CA, Arcari A (2009) Mean stress effects in stress-life fatigue and the Walker equation. Fat Fract Eng Mater Struct 32(3):163–179
2. Chu CC (2000) Comparison of mean stress correction methods for fatigue life prediction. In: SAE 2000 World Congress. Detroit, SAE International, Michigan pp 1–7
3. Wang SJ, Dixon MW, Huey Jr., Cecil O, Chen SC (2000) The Clemson limit stress diagram for ductile parts subjected to positive mean fatigue loading. J Mech Des 122(1), pp 143–146
4. Kwofie S (2001) An exponential stress function for predicting fatigue strength and life due to mean stresses. Int J Fatigue 23(9):829–836
5. Sekercioglu T (2009) A new approach to the positive mean stress diagram in mechanical design. Materialwiss Werkstofftech 40(9):713–717
6. Niesłony A, Böhm M (2013) Mean stress effect correction using constant stress ratio S-N curves. Int J Fatigue 52:49–56
7. Papuga J (2013) Quest for fatigue limit prediction under multiaxial loading. Procedia Eng 66:587–597
8. Papuga J, Vízková I, Lutovinov M, Nesládek M, Mean stress effect in stress-life fatigue prediction re-evaluated. In: Hénaff G (ed) MATEC Web of Conferences, vol 165

Chapter 31
Application of the Nonlinear Fatigue Damage Cumulative on the Prediction for Rail Head Checks Initiation and Wear Growth

Y. Zhou, D. S. Mu, Y. B. Han, X. W. Huang and C. C. Zhang

Abstract The nonlinear fatigue damage cumulative model was presented by combining the damage curve method considering the wheel-rail loading sequence and the fatigue damage method considering the interaction of the loads. Based on above model and the prediction method for coexistence of fatigue crack initiation and wear of rail, the results for rail head checks (HC) prediction by the linear and nonlinear fatigue cumulative models was analyzed. It was found that the cumulative fatigue damage at the rail material point by the modified nonlinear fatigue damage cumulative model was higher than that of the linear one. Therefore, the HC initiation life was the short. Comparing with the field tests, the results by linear fatigue cumulative model and modified nonlinear fatigue damage cumulative model were close to the upper range value and median of the field test result respectively.

Keywords Rail · Nonlinear fatigue damage cumulative · Head check initiation · Wear · Critical plane

31.1 Introduction

Rolling contact fatigue (RCF) crack, such as head checks (HCs) at rail shoulder and corner and squats at rail crown, and wear are the main defects in rails of the railway and metro systems which influence the rail life and train operation safety. It was found by twin-disc test [1] and field tests [2] that these two rail defects coexisted with the cumulative traffic. Moreover, with the application of the alloy or heat-treated rails, the RCF crack initiated early and propagated rapidly because on one hand wheel-rail contact stress always exceeded the yield limit of rail material, on the other hand the rail had good wear resistance, and then was repressed by wear after large cumulative traffic (more than 100 million gross tonnage, MGT) since the hardening layer was worn away at that time. Therefore, it was considered that the RCF crack could be

Y. Zhou (✉) · D. S. Mu · Y. B. Han · X. W. Huang · C. C. Zhang
Key Laboratory of Road and Traffic Engineering of the Ministry of Education, Tongji University, Shanghai, China
e-mail: yzhou2785@tongji.edu.cn

J.A.F.O. Correia et al. (eds.), *Mechanical Fatigue of Metals*, Structural Integrity 7,
https://doi.org/10.1007/978-3-030-13980-3_31

controlled by both natural and artificial wear (rail grinding) [3] if the crack initiation and propagation life together with wear growth could be predicted accurately. At present, the prediction of the coexistence of crack initiation and wear growth was presented [4, 5] in which the cumulative fatigue damage in rail by traffic was obtained according to the Miner linear fatigue rule. Actually, the wheel-rail contact on the rail by passing vehicles was the variable amplitude load with random loading sequence and interacting by adjacent wheels which should be treated as nonlinear fatigue damage process. Many nonlinear fatigue damage cumulative models were applied in the fields of metal fatigue damage in engineering and so on [6–8].

In this paper, the nonlinear fatigue damage cumulative model was modified by combining the damage curve method considering the wheel-rail loading sequence and the fatigue damage method considering the interaction of the adjacent wheels. Then, a prediction method for coexistence of HC initiation and wear growth in rail was presented. The result was compared with that of by the linear fatigue cumulative model.

31.2 Modification of the Nonlinear Fatigue Damage Cumulative Model

Considering the multiple-level loading of different stress amplitudes, the linear fatigue damage in random material occurs when:

$$\sum D_i = \sum \frac{n_i}{N_i} = 1 \tag{31.1}$$

where n_i is the number of loading cycles at the ith stress level; N_i is the fatigue life at the ith stress level; D_i is the fatigue damage at the ith stress level.

If the loading sequence was considered, the double parameter fatigue criterion model [6] which is based on the damage curve can be applied as follows:

$$D_i = \left(\frac{n_i}{N_i}\right)^{q_i}, q_i = \exp\left[\alpha\left(\frac{n_i}{N_i}\right)^{\beta}\right] - 1 \tag{31.2}$$

where q_i is the damage index; α is the material coefficient; β is stress level coefficient.

If the interaction between adjacent loadings was considered, the Corten-Dolan model [7] can be applied as follows:

$$D_i = m_i r_i n_i^a, N_i = N_1\left(\frac{\sigma_1}{\sigma_i}\right)^m \tag{31.3}$$

where m is the number of damaged nucleation, which is related to stress levels and number of stress interactions; r is the damage growth coefficient; a is a constant

related to the stress level; N_1 is the fatigue life under maximum alternating load; σ_1 is the maximum stress amplitude in multi-stage alternating load.

Then, the load amplitude ratio σ_1/σ_i in Eq. (31.3) is introduced into the exponent q_i of the cycle ratio n_i/N_i of the damage curve model in Eq. (31.2).

Moreover, q_i is defined as:

$$0 < q_i = \left(\frac{N_i}{N_{i+1}}\right)^{\alpha\left(\frac{\sigma_{maxi}}{\sigma_{-1}}\right)} < 1 \tag{31.4}$$

In Eq. (31.4), σ_{maxi} is the maximum stress amplitude acting at the ith stress level; σ_{-1} is the fatigue limit stress of the material. Other parameters are the same as above.

Therefore, the modified nonlinear fatigue damage cumulative model considering both loading sequence and the interaction between adjacent loadings is expressed as follows:

$$\sum D = \left\{ \left(\left(\frac{n_1}{N_{f1}}\right)^{\left(\frac{N_{f1}}{N_{f2}}\right)^{\alpha\left(\frac{\sigma_{max1}}{\sigma_{-1}}\right)}} + \frac{n_2}{N_{f2}} \right)^{\left(\frac{N_{f2}}{N_{f3}}\right)^{\alpha\left(\frac{\sigma_{max2}}{\sigma_{-1}}\right)}} + \cdots + \frac{n_{i-1}}{N_{f(i-1)}} \right\}^{\left(\frac{N_{f(i-1)}}{N_{fi}}\right)^{\alpha\left(\frac{\sigma_{maxi-1}}{\sigma_{-1}}\right)}} + \frac{n_i}{N_{fi}} \tag{31.5}$$

From the multistage stress fatigue test of No. 45 steel with the load from low to high (732–836 MPa) [9], the fatigue damage accumulation was measured as 0.425 after 45,000 cycles and the simulation result was 0.389 by above model. It can be seen that when the load was loaded from low to high, the predicted results by modified nonlinear fatigue damage cumulative model agree with the experimental results.

31.3 Prediction Method for the Coexistence of Rail HC Initiation and Wear

The method for prediction rail HC initiation together with wear growth was presented [5] in which the wheel/rail contact, rail wear, fatigue damage were calculated, the worn rail profile was replaced according to a certain of wear, and finally the nonlinear fatigue damage cumulated in rail material. During the simulation, the fatigue damage in the rail during the wear and profile evolution can be obtained by nonlinear accumulation of Eq. (31.5) instead of the linear one. When the fatigue damage at random point in the rail with $D_{CR} = \sum D = 1$, it can be considered that the HC initiated at this point with the initiation life:

$$N = \sum_{i=1}^{J} n_i \tag{31.6}$$

where N is the crack initiation life, n_i is the cumulative wheel cycles at the ith profile evolution phase (treated as multilevel loading because the rail wear changed wheel/rail contact situation). J is the number of the profile evolution phases.

31.4 Comparison Linear and Nonlinear Cumulative Fatigue Damage Models

With the above method, it was possible to predict the HC initiation life and position together with the wear growth and profile evolution for the U75V heat-treated 75 kg/m rail (with surface hardness of 340–400 HBW) as the high rail in China's heavy-haul railway. In the simulation, the rail parameters were referenced from Ref. [2]. The vehicle axle load was 23 t and its operation speed was 50 km/h. The wheel profile was standard freight vehicle profile which kept constant during simulation. The coefficient of the friction (COF) between the wheel and rail was 0.3. The curve radius was 800 m with a rail inclination of 1:40. No track geometry irregularity or rail surface irregularity was considered in the simulation.

The cumulative fatigue damage in the rail by two models until the HC was initiated at the rail was shown in Fig. 31.1.

The fatigue damage with the wear growth and the HC initiation life were shown in Table 31.1.

From Fig. 31.1 and Table 31.1, it can be seen that the cumulative fatigue damage by the modified nonlinear fatigue damage cumulative model was fast and the fatigue crack initiation life was short. Since the modified nonlinear considered both wheel-

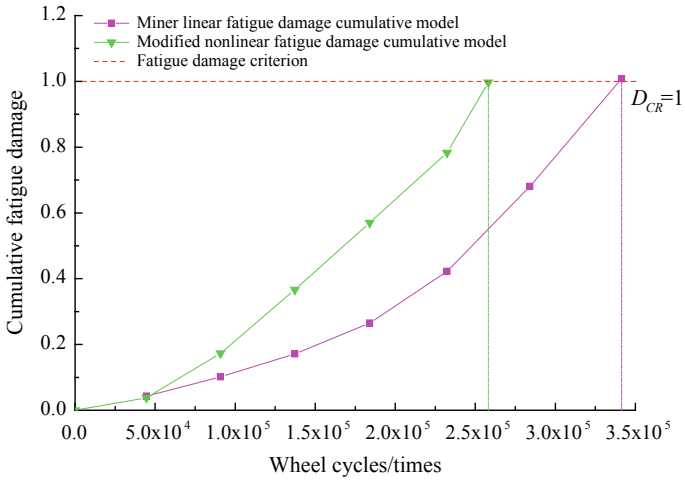

Fig. 31.1 The cumulative fatigue damage of the rail with the accumulation of wheel cycles. D_{CR} is the fatigue damage cumulative criterion which equals 1

Table 31.1 Damage by single wheel cycle and cumulative fatigue damage with the rail profile evolution

Rail profile evolution	Miner linear fatigue damage cumulative model			Modified nonlinear fatigue damage cumulative model		
	Wheel cycles	Damage by single wheel cycle (N_{fi}^{-1})	Cumulative fatigue damage ($\sum D_J$)	Wheel cycles	Damage by single wheel cycle (N_{fi}^{-1})	Cumulative fatigue damage ($\sum D_J$)
R_1	44,547	9.68E−07	0.0431	44,547	8.54E−07	0.0380
R_2	46,276	1.26E−06	0.1014	46,276	2.92E−06	0.1731
R_3	46,427	1.50E−06	0.1711	46,427	4.17E−06	0.3667
R_4	46,794	2.00E−06	0.2647	46,794	4.35E−06	0.5703
R_5	48,312	3.25E−06	0.4217	48,312	4.40E−06	0.7829
R_6	51,716	5.00E−06	0.6803	25,858	8.28E−06	0.9970
R_7	57,339	6.06E−06	1.0277	–	–	–
Sum of wheel cycles	341,411	–	–	258,214	–	–

rail loading sequence and the interaction of the loads, both of them had a great influence on the fatigue damage. In addition, the influence of the previous wheels on the rails did not dissipate and the rear wheels had acted on the same location of rails when the residual deformation of rails existed which lead the rail to be damaged more than the linear model.

31.5 Validation

Prediction of the HC initiation life by the modified nonlinear fatigue damage cumulative model for the U75V heat-treated 75 kg/m rail as the high rail of 800 m curve radius, together with the results of the field tests with the same track condition [10], are shown in Table 31.2.

Table 31.2 HC initiation life of the high rail in heavy-haul railway by prediction and field test

Method	HC initiation life (wheel cycles)
Linear fatigue damage cumulative model	3.41×10^5
Modified nonlinear fatigue damage cumulative model	2.58×10^5
Field tests	1.53×10^5–3.54×10^5

It can be seen from Table 31.2 that the results by linear fatigue cumulative model and modified nonlinear fatigue damage cumulative model were close to the upper range value and median of the field test result respectively.

31.6 Conclusions

The nonlinear fatigue damage cumulative model was modified by combining the damage curve method and the fatigue damage method, which can consider both the wheel-rail loading sequence and the interaction of the loads at the same time. Based on above modified nonlinear fatigue damage cumulative model and the prediction method for predicting the coexistence of HC initiation and wear growth in the rail.

The predicted HC initiation life of the U75V heat-treated rail in high rail was 2.58×10^5 by the modified nonlinear fatigue damage cumulative model. The results of linear fatigue cumulative model were close to the upper range value of the field tests and that of the modified nonlinear fatigue damage cumulative model was close to the median of the field tests.

Acknowledgements We would like to acknowledge the support of the National Natural Science Foundation of China (51678445, 51778484), Key laboratory of Road and Railway Engineering Safety Control (Shijiazhuang Tiedao University) of Ministry of Education of China (STKF201715).

References

1. Donzella G, Mazzù A, Petrogalli C (2009) Competition between wear and rolling contact fatigue at the wheel–rail interface: some experimental evidence on rail steel. J Rail Rapid Transit 31–44
2. Zhou Y, Wang S, Wang T et al (2014) Field and laboratory investigation of the relationship between rail head check and wear in a heavy-haul railway. Wear 315(1):68–77
3. Kalousek J, Magel E (1997) Achieving a balance: the magic wear rate. Railw Track Struct 50–52
4. Zhou Y, Yu M, Jiang J (2016) Effects of rail hardness on rail wear and head check initiation. J Transp Res Board 2545(1):55–65
5. Zhou Y, Han Y, Mu D, et al (2018) Prediction of the coexistence of rail head check initiation and wear growth. Int J Fatigue 289–300
6. Zhu S, Huang H, Xie L (2008) Nonlinear fatigue damage cumulative model and the analysis of strength degradation based on the double parameter fatigue criterion. China Mech Eng 19(22):2753–2761 (in Chinese)
7. Corten HT, Dolan TJ (1956) Cumulative fatigue damage. In: Proceedings of the international conference on fatigue of metals
8. Fan ZC, Chen XD, Chen L, et al (2007) Fatigue-creep behavior of 1.25Cr0.5Mo steel at high temperature and its life prediction. Int J Fatigue 29(6):1174–1183
9. Yan R (2015) Research on reliability modeling and analysis methods based on the performance degradation. University of Electronic Science and Technology of China, Chengdu (in Chinese)
10. Wang J, Xu Y, Lian S, Wang L (2011) Probabilistic prediction model for initiation of RCF cracks in heavy-haul railway. Int J Fatigue 33(2):212–216

Chapter 32
Fatigue Life Prediction for Component with Local Structural Discontinuity Based on Stress Field Intensity

Tianyang Lu, Peng Zhao and Fu-Zhen Xuan

Abstract The impact of notch is one of the major problems that remain to be solved when predicting fatigue life. The zone of notch root has serious stress concentration condition. Stress field intensity (SFI) approach is an advanced volumetric method for fatigue life prediction. This paper makes further research and puts forward a modified approach based on it. A numerical example and an engineering notched specimen are analyzed by finite element approach to prove the validity of new approach. The modified SFI approach shows good fatigue life prediction and is convenient for practical use.

Keywords Notch · Fatigue life · Stress field intensity

32.1 Introduction

Fatigue failure of metal structural component is a common form of structure collapse because it can occur due to cycle stress below the static yield strength. Notch structure has a great reduction effect on fatigue life compared with smooth one. Most engineering designs have to account for the effects of notches on the fatigue life of the component. Notches will cause stress concentration with high local stress and high stress gradients [1]. In a simple fatigue analysis, the maximum stress which can be calculated at notch roots is considered as the critical point to predict fatigue life via stress-life or strain-life curves [2]. This kind of method often gives a poor estimate of the fatigue life [3], which cannot be used in practice. The stress distribution at the notch is very complex which have to be taken into consideration in a realistic fatigue failure criterion.

Stress field intensity (SFI) approach is one of fatigue prediction methods which consider a zone near the fatigue root. It shows great life prediction effect and has

T. Lu · P. Zhao (✉) · F.-Z. Xuan
School of Mechanical and Power Engineering, East China University of Science and Technology, Shanghai 200237, P.R. China
e-mail: pengzhao@ecust.edu.cn

J.A.F.O. Correia et al. (eds.), *Mechanical Fatigue of Metals*, Structural Integrity 7,
https://doi.org/10.1007/978-3-030-13980-3_32

great potential in research [4]. However, the mesh size in notch area is often required to be very small. It makes the calculation time very long. This paper puts forward a modified SFI approach which saves the calculation time and reduces the requirement of high quality mesh.

32.2 Stress Field Intensity Approach

The stress field intensity approach (SFI) was first put forward by Zheng [5] and developed by Yao [4, 6]. This theory assumes that if the stress field intensity at the notch root is the same as that of the smooth one, they have the same fatigue life (see Fig. 32.1).

SFI approach defines the stress field intensity σ_{FI} as:

$$\sigma_{FI} = \frac{1}{V} \int_{\Omega} f\left(\sigma_{ij}\right) \varphi(r) dv \tag{32.1}$$

where Ω is fatigue zone, V is the volume of Ω, $f\left(\sigma_{ij}\right)$ is the failure stress function and $\varphi(r)$ is the weight function.

SFI considers the local high stress zone near the fatigue root as the fatigue zone Ω. From a macro point of view, it can be considered that the zone shape is spherical or ellipsoid. The size can be determined by experimental data and numerical simulation.

Failure stress function $f\left(\sigma_{ij}\right)$ reflects the effect of material and stress distribution on notch root. The value of $f\left(\sigma_{ij}\right)$ depends on the material properties and multiaxial stress field. For ductile materials, such as carbon steel, aluminum alloy and titanium.

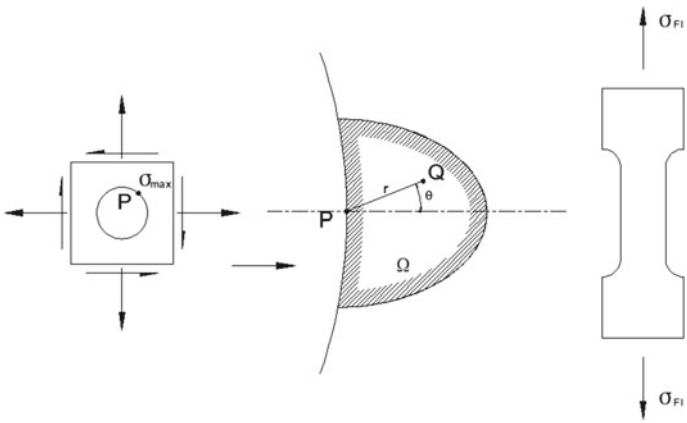

Fig. 32.1 Stress field intensity approach

$f(\sigma_{ij})$ usually uses Von Mises equivalent stress as Eq. (32.2). For brittle materials, such as cast iron and cast steel, $f(\sigma_{ij})$ usually uses maximum major stress.

$$f(\sigma_{ij}) = \frac{1}{\sqrt{2}}\sqrt{(\sigma_1 - \sigma_2)^2 + (\sigma_2 - \sigma_3)^2 + (\sigma_3 - \sigma_1)^2} \tag{32.2}$$

The weight function $\varphi(r)$ represents the contribution of one point in the fatigue zone to the notch root range from 0 to 1. In the notch root, $\varphi(0) = 1$. It means the most influential point in fatigue zone. The form of weight function is varied and has an impact on the zone Ω [7]. The most widely used expression of weight function is Eq. (32.3).

$$\varphi(r) = 1 - \left|\frac{1}{\sigma_{max}}\frac{\partial\sigma(r)}{\partial r}\right| r(1 + sin\theta) \tag{32.3}$$

where θ is the degree between the bisector at the notch root.

32.3 Modified SFI Approach

Consider the arithmetic average method in the same fatigue zone, which ignores the effect of weight function (Eq. 32.4).

$$\bar{\sigma} = \frac{1}{V}\int_{\Omega} f(\sigma_{ij})dv \tag{32.4}$$

Due to the range of weight function, it is evident that:

$$\sigma_{FI} < \bar{\sigma} \tag{32.5}$$

Arithmetic average method doesn't consider that great value has great weight. According to the definition of weight function, the stress intensity should be close to the maximum failure stress which is at the notch root. However, weight function makes every failure stress smaller and the stress intensity is less than that of arithmetic average method. As a result, the volume should be weighted and new equality is:

$$\sigma_{FI} = \frac{\int_{\Omega} f(\sigma_{ij})\varphi(r)dv}{\int_{\Omega}\varphi(r)dv} \tag{32.6}$$

Modified σ_{FI} is greater than $\bar{\sigma}$ and less than σ_{max}. The value is influenced by the weight function. The new weight function used in this study is:

$$\varphi(r) = \left(\frac{\sigma}{\sigma_{max}}\right)^4 \cdot \frac{1}{|sin\theta| + 1} \tag{32.7}$$

The fatigue zone is defined by the value of equivalent stress. The elements whose value exceed the characteristic stress are considered to play the major role to the fatigue failure. The characteristic stress is considered as a property of the material and can be determined by experiments. So the fatigue zone is a set of zone whose failure stress function is greater than characteristic stress:

$$V_{\Omega} = \left\{ \int dv \middle| f\left(\sigma_{ij}\right) \geq \sigma_c \right\} \tag{32.8}$$

In order to predict the fatigue life of the notched parts, it is necessary to define the stress-strain cyclic behavior, S-N curves and the characteristic stress σ_c by basic experiments. Then, the numerical analysis is carried out to find the fatigue zone and calculate the σ_{FI}. Finally, compare the σ_{FI} to the S-N curve to predict the fatigue life.

32.4 Example of Application of Modified SFI Approach

32.4.1 Plate Specimen with a Circle Notch

The plate specimen with a circle notch in the center is made from aluminum alloy LY12-CZ with thickness of 2 mm. Its mechanical properties and fatigue performance are from [8] (see Table 32.1). The left side is fixed and the right side is under a nominal stress. One is tested under 80 MPa and another is under 150 MPa (see Fig. 32.2).

Table 32.1 Mechanical properties of aluminum alloy LY12-CZ

E (GPa)	σ_s (MPa)	σ_b (MPa)	K' (Mpa)	n'
71	332	476	646	0.067

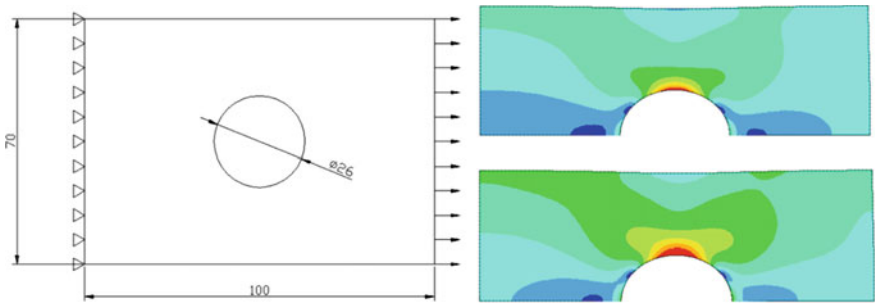

Fig. 32.2 Plate specimen model with a circle notch (left). Von Mises equivalent stress distribution under 80 MPa and 150 MPa loading (right)

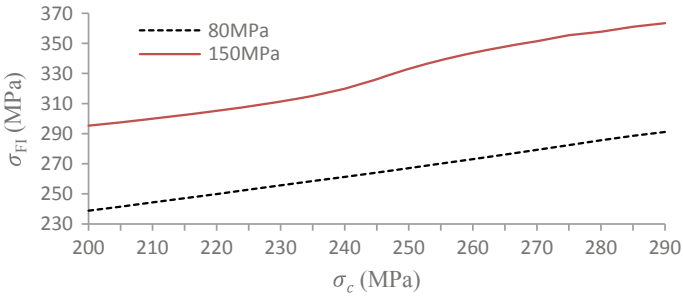

Fig. 32.3 Relationship between σ_{FI} and σ_c

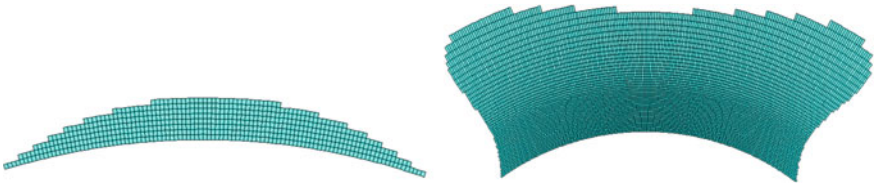

Fig. 32.4 Fatigue zone Ω. 80 MPa (left). 150 MPa (right)

Table 32.2 Analysis result of the example

Loading (MPa)	Conventional σ_{FI} (MPa)	New σ_{FI} (MPa)	Conventional fatigue life (cycles)	New fatigue life (cycles)	Experiment life (cycles)
80	272.4	266.5	96615	111718	135885
150	428.5	330.8	2082	22974	17352

ANSYS is used for elastoplastic analysis to obtain the stress distribution near the circle notch. One-half model is established based on symmetry. Von Mises equivalent stress is taken as the fatigue failure function $f(\sigma_{ij})$ and Fig. 32.2 shows its distribution. The concentration area is on the upper (or lower) side of circle hole.

Calculate σ_{FI} with different characteristic stresses by Eq. (32.6). Figure 32.3 shows the relationship between σ_c and σ_{FI} under two load conditions.

It can be seen that there is a strong linear relationship between σ_c and σ_{FI}. And σ_{FI} is always greater than σ_c. According to the results of experiment, the σ_c of LY12-CZ is 248.3 MPa. The fatigue zone Ω of two loads is plotted in Fig. 32.4.

The S-N curve for LY12-CZ is used in form of $N \cdot e^{\alpha S} = C$. Where $\alpha = 0.0246$, $C = 7.822e+7$. The result is shown in Table 32.2. The example shows that modified SFI approach has good fatigue life prediction accuracy.

32.4.2 Engineering Notched Specimen

Figure 32.5 is an engineering notched specimen in port pressure facilities. The material under investigation is Q345. The experiment uses a 34kN axial load with load ratio, R = 0.1. The section of stress concentration is located on both sides of the middle hole (Fig. 32.6).

According to the results of experiment, the σ_c of Q345 is 312.2 MPa. The fatigue zone Ω is shown in Fig. 32.6. To demonstrate the feasibility and applicability of modified SFI approach, two traditional methods [9] of predicting notched fatigue life, local stress-strain approach and nominal stress approach, are used for comparison in Table 32.3. The engineering example also shows that modified SFI approach has good fatigue life prediction accuracy compared to others.

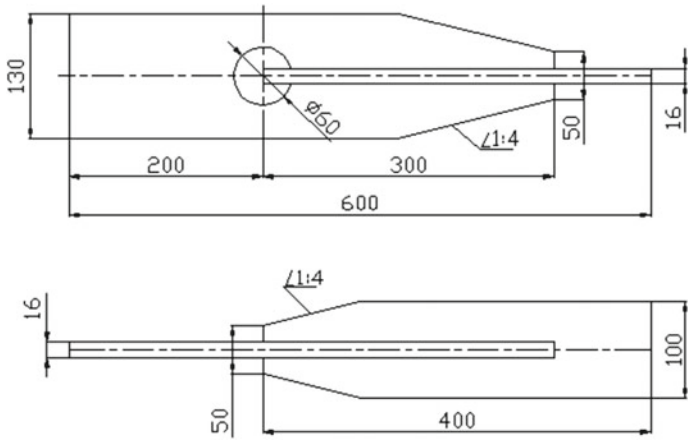

Fig. 32.5 Schematic of the model component with local structural discontinuities

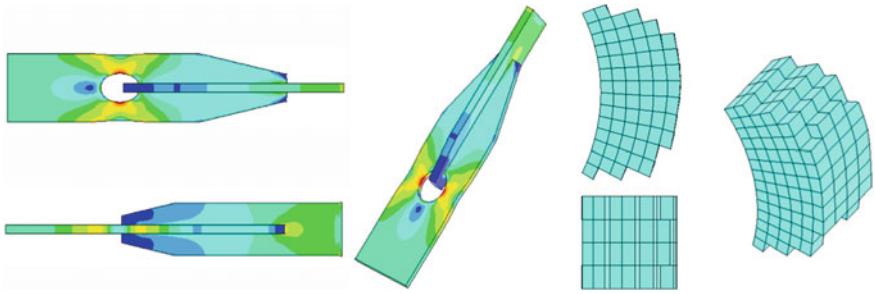

Fig. 32.6 Von Mises equivalent stress distribution (left). Fatigue zone Ω (right)

Table 32.3 Fatigue life comparison between estimation and experiment (unit: cycles)

Methods	Local stress-strain approach	Nominal stress approach	Modified SFI approach	Experimental value
Fatigue life	38741	205213	92534	82043
Deviation	−52.8%	150.1%	12.8%	–

32.5 Conclusion

Modified SFI approach takes into account the stress distribution near the notch root. It shows good fatigue life prediction accuracy. Meanwhile, the new fatigue zone Ω is much bigger than conventional one, which means lower requirement of meshing and can save much time for calculation. The definition of characteristic stress is based on experiments. Application in high cycle fatigue remains to further study.

Acknowledgements The authors are grateful for the supports provided by National Natural Science Foundation of China (51475168).

References

1. Adib-Ramezani H, Jeong J (2007) Advanced volumetric method for fatigue life prediction using gradient effect at notch roots. Comput Mater Sci 39(3):649–663
2. Lim JY, Hong SG, Lee SB (2005) Application of local stress strain approaches in the prediction of fatigue crack initiation life for cyclically non-stabilized and non-masing steel. Int J Fatigue 27:1653–1660
3. Taylor D, Wang G (2000) The validation of some methods of notch fatigue analysis. Fatigue Fract Eng Mater Struct 23(5):387–394
4. Yao WX, Ye B, Zheng LC (2001) A verification of the assumption of anti-fatigue design. Int J Fatigue 23(3):271–277
5. Zheng CH (1984) HCF design method-stress field intensity. Tsinghua Unversity, Beijing
6. Yao WX (1993) Stress field intensity approach for predicting fatigue life. Int J Fatigue 15(3):243–246
7. Guo P, Chen BH, Du CB (2011) Fatigue life assessment of combustor casing rear bush installation seat based on field intensity approach. Aeroengine 6:36–39
8. Yao WX (2003) Fatigue life prediction of structures. National Defend Industry Press, China
9. Neuber H (1961) Theory of stress concentration for shear-strained prismatical bodies with arbitrary non-linear stress–strain law. J Appl Mech Trans ASME 28(4):544–550

Chapter 33
Low Cycle Fatigue Life Estimation of P91 Steel by Strain Energy Based Approach

Bimal Das and Akhilendra Singh

Abstract In the present study strain energy based analytical models are used to predict the fatigue life of P91 steel subjected to strain controlled loading. P91 steel being used in pressure vessel and many other components for ultra-supercritical fossil fired and nuclear power plants are subjected to repeated thermal stresses. In low cycle fatigue regime plastic strain range significantly affects the energy dissipation process during the course of loading. Thus, models based on energy dissipation during first cycle and averages of cycles are developed to assess the fatigue life. Uniaxial strain controlled low cycle fatigue tests at ambient temperature are conducted on P91 steel in the normalized and tempered condition. The material depicted near masing type behaviour as evaluated in terms of variation in bauschinger strain with plastic strain range. The analytically predicted results for fatigue life showed good agreement with experimental fatigue life. The cumulative plastic strain energy or fatigue toughness to failure is seen to increase with increasing number of cycles to failure.

Keywords Low cycle fatigue · Masing · Bauschinger strain · Fatigue toughness

33.1 Introduction

P91 ferritic-martensitic steel is considered as a candidate material for generation IV nuclear reactors and fusion reactors. It is being currently used for steam generators of the Indian prototype fast breeder reactor (PFBR) [1]. Steam generator components being operated at temperature around 623–823 K are subjected to repeated thermal stresses [2]. Cyclic loadings arising due to thermal stresses produces severe strain in the material thereby causing low cycle fatigue (LCF) failure of the engineering components. Since the fatigue failure in the low cycle fatigue regime is mainly caused by the cyclic plastic strain (ε_p), thus plastic strain energy can be considered as a crucial parameter to describe the damage mechanism [3, 4]. Although conventional

B. Das · A. Singh (✉)
Department of Mechanical Engineering, Indian Institute of Technology Patna, Bihta 801106, India
e-mail: akhilendra.singh@gmail.com

J.A.F.O. Correia et al. (eds.), *Mechanical Fatigue of Metals*, Structural Integrity 7,
https://doi.org/10.1007/978-3-030-13980-3_33

strain based approach are widely used to characterize the low cycle fatigue behavior of materials subjected to large magnitude of strain. In recent years researchers have shown great interest in utilizing strain energy as a parameter to characterize the fatigue damage. Energy based approach analyses the low cycle fatigue damage well by considering both stress and plastic strain. Plastic strain (ε_p) being the cause of the energy dissipation may characterize the LCF behaviour well than conventional strain based approach. Golos et al. [3] proposed a single damage criterion based on strain energy density to characterize both low and high cycle fatigue regimes of pressure vessel steel. Callaghan et al. [5] analyzed low cycle fatigue behavior of 2.25Cr–1Mo steel using energy based approach and predicted fatigue toughness to crack propagation. Ontiveros et al. [6] assessed structural integrity of aluminium alloy 7075-T651 by plastic strain energy and thermodynamic entropy generation models. Li et al. [7] showed that it is difficult to determine stable state of cyclic deformation for some materials according to half-life criterion when expressed in terms of strain and stress based parameters. The point of saturation of plastic strain energy was made as a criterion to find the cyclic properties of high strength spring steel. Abdalla et al. [8] carried out low cycle fatigue tests at low and high strain amplitude on BS 460B and BS B500B steel reinforcing bars at various strain ratios. They proposed energy based models to predict the total energy dissipation up to failure using the predicted fatigue life. Thus, in the present study strain controlled low cycle fatigue tests at various strain amplitudes has been conducted and strain energy based models have been employed to predict the fatigue life of P91 steel.

33.2 Material and Experimental Procedures

The material used in this study was received from M/s. Nextgen Steel & Alloys, India in the form of plate having thickness of 6.7 mm. Blocks of (135 mm × 125 mm × 6.7 mm) size were cut from the as received plate and austenized at 1050 °C for 90 min, air-cooled followed by tempering at 760 °C for 60 min. Tensile tests were conducted at a constant displacement rate of 1.5 mm/min in a 100 KN servo-hydraulic test machine (INSTRON 8802). A 25 mm gauge length extensometer was used for strain measurements. The yield and ultimate tensile strength are found to be 546 MPa and 711 MPa respectively. All fatigue tests were carried at constant strain rate of 0.001 s^{-1} until complete separation of the specimens or when the peak stresses got reduced by 30%. Triangular waveform loading was applied with a strain ratio of −1, i.e., fully reversed symmetric cycling. A 12.5 mm gauge length extensometer was used to control strain during the low cycle fatigue tests.

33.3 Low Cycle Fatigue Behavior

The stress-strain response of P91 steel subjected to strain controlled loading at strain amplitudes of 0.3–0.5% are shown in Fig. 33.1. The compressive tip of the stabilised

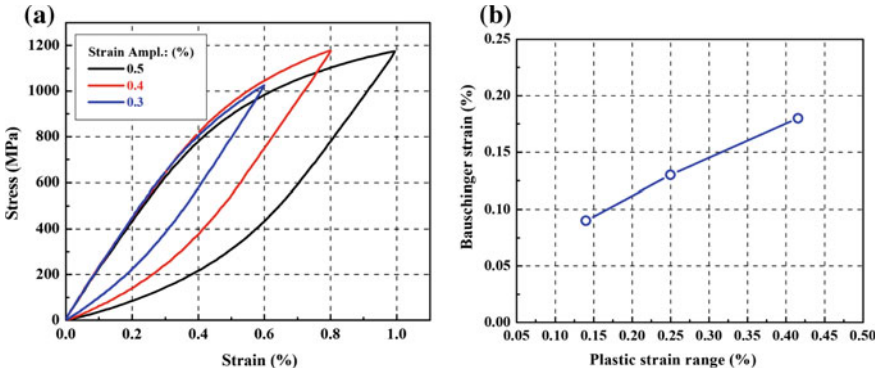

Fig. 33.1 **a** Illustration of masing behaviour of P91 steel, **b** variation of bauschinger strain with plastic strain range

hysteresis loops obtained is translated to a common origin to analyse the masing behavior of the material. Figure 33.1a shows that P91 material shows small deviation from ideal masing type behavior and can be referred as near masing behavior. The masing behavior can be further examined by the variation in bauschinger strain with plastic strain range. Bauschinger strain is defined as the magnitude of plastic strain corresponding to the 75% of the peak tensile stress of the negative part of the stabilised hysteresis loop [9]. The progressive increase in basuchinger strain infers that the P91 steel follows near masing behavior.

33.4 Energy Based Fatigue Models: Background

For over numerous years various methodologies has been adopted to characterize low cycle fatigue behavior based on either stress or strain approach [10]. In these methods parameters such as stress amplitude or plastic strain are usually used to assess the fatigue life. The coherency between stress and strain is not taken into account in the above approaches. Since, elastic strain has negligible effect on fatigue life in the low cycle fatigue regime. Thus, plastic work (area under σ-ε loop) is considered to be a damage parameter to evaluate low cycle fatigue behavior [3–5]. For constant amplitude loading total strain energy per cycle can be divided into elastic and plastic parts of the strain energy per cycle as follows:

$$\Delta W^t = \Delta W^e + \Delta W^p \tag{33.1}$$

where, ΔW is the total strain energy ΔW^e is the elastic strain energy and ΔW^p is plastic strain energy.

33.4.1 Average Plastic Strain Energy

Plastic strain energy has been used to characterize the damage evolution incurred in strain controlled tests for P91 steel [3, 11]. The average plastic strain energy for particular strain amplitude was calculated as the area of the hysteresis loop at half-life ($N_f/2$). The relationship between average plastic strain energy and number of cycles to failure has been presented as follows [4, 7]:

$$W_{av}^{p} = K_p \left(N_f\right)^{\alpha} \tag{33.2}$$

where, K_p and α are measure of plastic strain energy coefficient and plastic strain energy exponent respectively. The values of K_p and α are found to be 707.97 MJm^{-3} and -0.77 respectively.

33.4.2 Prediction of Fatigue Life from Energy

Golos et al. [3] proposed a power law function relating hysteresis plastic energy and number of reversals to failure as follows:

$$\Delta W^{p} = A\left(2N_f\right)^{b} \tag{33.3}$$

where, A is plastic strain energy coefficient and b is plastic strain energy exponent. Plastic strain energy was calculated at various cycles to evaluate the fatigue damage. It will be conservative to predict the fatigue life based on maximum stress when a material shows cyclic softening behavior. Thus, analytical energy models based on energy dissipated in first cycle (W_1^p) and average of the energy dissipated from first to fifth cycle W_{avg}^p. The relationship between energy and number of cycles to failure can be expressed as presented in Eq. 33.3.

$$W_1^{p} = A_1\left(2N_f\right)^{b_1} \tag{33.4}$$

$$W_{avg}^{p} = A_2\left(2N_f\right)^{b_2} \tag{33.5}$$

The energy dissipated in the first cycle and average of cycles are plotted against the number of reversals to failure are shown in Fig. 33.2. The values of A_1 and A_2 are found to be 691.83 MJm^{-3} and 1023.9 respectively.

Figure 33.3a, b shows the accuracy of the predicted number of reversals to failure based on energy dissipated in first cycle and average of cycles. The figure depicts that the above models successfully correlates experimental and predicted fatigue lives within small deviation. The prediction of fatigue life based on the average of cycles is more accurate than energy dissipated in first cycle.

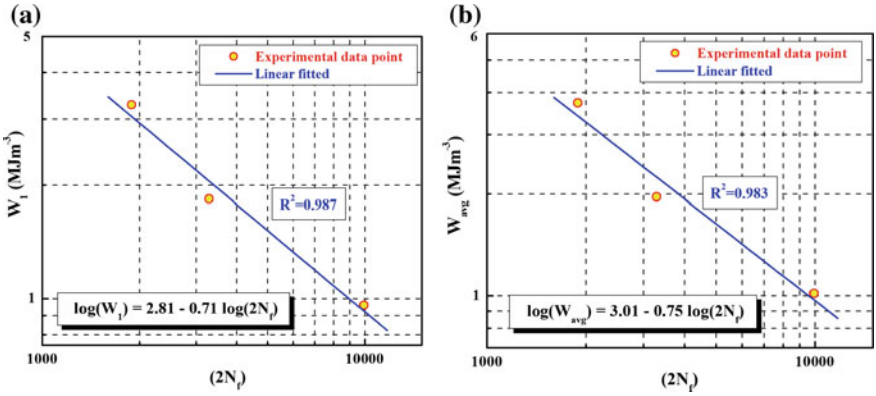

Fig. 33.2 Variation of energy dissipated with number of reversals to failure. Based on **a** first cycle and **b** average of first to fifth cycles

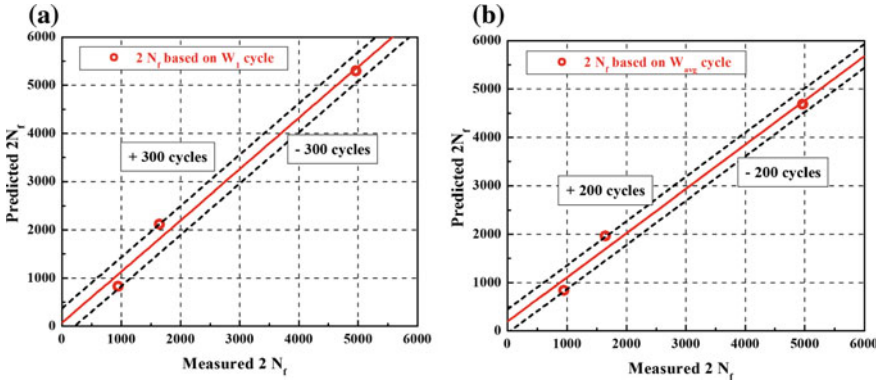

Fig. 33.3 Predicted number of reversals to failure. Based on **a** first cycle and **b** average of first to fifth cycles

33.4.3 Prediction of Fatigue Toughness

The cumulative energy dissipated in the successive cycles till failure can be used to measure the damage incurred due to low cycle fatigue of a material. The total plastic strain energy can be obtained by summing up the area of the hysteresis loop area till failure. This cumulative strain energy till failure can be termed as fatigue toughness, which quantifies the materials ability to resist fatigue failure. The fatigue toughness can be estimated based on the average plastic strain energy obtained at the point of stabilization i.e. half-life as follows:

$$\mathrm{W_f} = \Delta W_{av}^{p} N_f \tag{33.6}$$

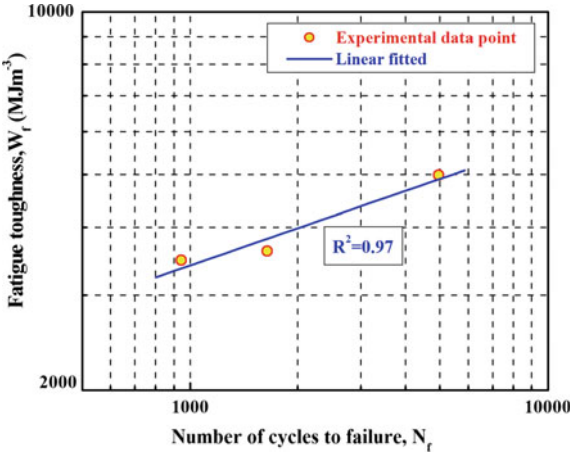

Fig. 33.4 Linear variation of fatigue toughness with number of cycles to failure

where, ΔW_{av}^{p} is the average plastic strain energy and N_f is number of cycles to failure. A power relation can be defined between fatigue toughness and number of cycles to failure as [5]:

$$W_f = W_f^{'}\left(2N_f\right)^t \tag{33.7}$$

where, W is the fatigue toughness exponent. The values of the coefficients obtained through least square technique are: $W_f^{'}$ as 691.83 MJm^{-3} and t as 0.22. The plot of fatigue toughness versus number of cycles to failure is shown in Fig. 33.4. It can be depicted from the figure that fatigue toughness increased with cycles to failure. This can be attributed to the fact that greater amount of energy is required to initiate the fatigue damage.

33.5 Conclusion

In this investigation fully reversed strain controlled low cycle fatigue behaviour of P91 steel has been examined based on energy approach. Analytical models based on energy dissipated in first cycle and averages of cycles (first to fifth) are employed to predict the fatigue lives at various strain amplitudes. Based on the results presented, following conclusions are drawn:

- P91 steel exhibited very small deviation from ideal masing behaviour and can be said to follow near masing characteristics.
- Prediction of fatigue lives based on the energy criterion showed good agreement with the measured fatigue lives.
- The cumulative plastic strain energy or fatigue toughness was found to increase with increasing number of cycles to failure.

- The energy based parameters derived can provide a reliable alternative to strain based approach in quantifying the low cycle fatigue damage of P91 steel.

References

1. Babu MN, Sasikala G, Dutt BS, Venugopal S, Albert SK, Bhaduri AK (2012) Investigation on influence of dynamic strain ageing on fatigue crack growth behaviour of modified 9Cr–1Mo steel. Int J Fatigue 43:242–245
2. Shankar V, Bauer V, Sandhya R, Mathew MD, Christ H (2012) Low cycle fatigue and thermo-mechanical fatigue behavior of modified 9Cr–1Mo ferritic steel at elevated temperatures. J Nucl Mater 420(1–3):23–30
3. Golos K, Ellyin F (1988) A total strain energy density theory for cumulative fatigue damage. J Press Vessel Technol 110(1):36–41
4. Ellyin F, Kujawski D (1984) Plastic strain energy in fatigue failure. J Press Vessel Technol 106(4):342–347
5. Callaghan MD, Humphries SR, Law M, Ho M, Bendeich P, Li H (2010) Energy-based approach for the evaluation of low cycle fatigue behaviour of 2.25Cr–1Mo steel at elevated temperature. Mater Sci Eng A 527:5619–5623
6. Ontiveros VL, Modarres M, Amiri M (2015) Estimation of reliability of structures subject to fatigue loading using plastic strain energy and thermodynamic entropy generation. Proc Inst Mech Eng Part O J Risk Reliab 229(3):220–236
7. Li DM, Nam WJ, Lee CS (1998) A strain energy based approach to the low-cycle fatigue damage mechanism in a high-strength spring steel. Metall Mater Trans A 29:1431–1439
8. Abdalla JA, Hawileh RA, Oudah F, Abdelrahman K (2009) Energy-based prediction of low-cycle fatigue life of BS 460B and BS B500B steel bars. Mater Des 30(10):4405–4413
9. Nandy S, Sekhar AP, Das D, Hossain SJ, Ray KK (2016) Influence of dynamic precipitation during low cycle fatigue of under-aged AA6063 alloy. Trans Indian Inst Met 69(2):319–324
10. Das B, Bakkar A, Khutia N, Das D (2017) Low cycle fatigue performance evaluation of TMT rebar. Mater Today Proc 4(2):2554–2563
11. Plumtree A, Abdel-Raouf HA (2001) Cyclic stress—strain response and substructure. Int J Fatigue 23(9):799–805

Chapter 34
Evaluation of Regression Tree-Based Durability Models for Spring Fatigue Life Assessment

Y. S. Kong, S. Abdullah, D. Schramm, M. Z. Omar and S. M. Haris

Abstract This paper presents an evaluation of pruned regression decision tree for spring fatigue life predictions. The inputs for this regression decision tree models are vehicle ISO 2631 vertical vibrations and suspension frequencies. The design process of a coil spring involved many steps which consume many time and efforts. Hence, there is a need to generate a prediction model to assist spring design. Loading time histories were obtained from a quarter car model simulation for spring fatigue life assessment and ISO 2631 vertical vibrations calculations. The obtained force time histories were used to predict fatigue life of spring using strain-life approaches while acceleration time histories were used to obtain ISO 2631 vertical vibration. Together with spring stiffness sensitivities, the spring fatigue life was modelled using regression decision tree and mean squared error of the generated regression decision tree residuals were analysed. Five sets of independent experimental measurement strain time histories were used to validate the fatigue life predictions using a conservative approach. Most of the validation data points have lied beyond the acceptable region. Therefore, these proposed regression tree models are providing a good prediction on spring fatigue life which could shorten the spring design process.

Keywords Regression tree · Automobile spring · Fatigue life · Vertical vibration

34.1 Introduction

Automobile suspension components tend to fail after experiencing repeated cyclic loadings. This type of failure is known as fatigue failure. Fatigue life of the components are significantly reduced when compared to the desired design life which could

Y. S. Kong · S. Abdullah (✉) · M. Z. Omar · S. M. Haris
Faculty of Engineering and Built Environment, Centre for Integrated Design for Advanced Mechanical System (PRISMA), Universiti Kebangsaan Malaysia (UKM), 43600 Bangi, Selangor, Malaysia
e-mail: shahrum@ukm.edu.my

Y. S. Kong · D. Schramm
Department Chair of Mechatronics, University of Duisburg-Essen, 47057 Duisburg, Germany

J.A.F.O. Correia et al. (eds.), *Mechanical Fatigue of Metals*, Structural Integrity 7,
https://doi.org/10.1007/978-3-030-13980-3_34

cause losses due to warranty claims. Hence, automotive engineers put lots of efforts to evaluate fatigue design of their products. To ensure a realistic fatigue design of an automobile suspension system, Chindamo et al. [1] attempted to bring real road profile to indoor testing. However, the process to collect real data required tedious instrumentation setup and needed to be repeated on different road conditions to reflect customer usage. After tremendous efforts on suspension system analysis have been invested, the data were wasted when a new vehicle variant was released [2].

Towards the fourth industrial revolution, design of automotive suspension component designs was widely assisted by machine learning methods. For example, full factorial design and regression analysis were performed to optimise an automobile suspension system for vehicle ride enhancement [3]. Neural network was utilised to design a controller for automobile suspension system where the performance was compared with proportional-integral-derivative (PID) with genetic algorithm approach [4]. Neural network controller has shown significant improvement of suspension performance. In terms of fatigue optimisation, genetic algorithm was also used to improve fatigue life of an automobile jounce bumper. Overall, most of the machine learning approaches are highly nonlinear and complex to apply [5].

For modelling, decision tree based predictive modelling was preferred due to its simple logical rules. Regression tree is one of the machine learning methods which presented in a tree-like graph used to make decisions. For engineering applications, regression tree was used to predict the required carbon content using temperature, energy and steel composition as input in steel refining [6]. In terms of fatigue application, fatigue strength of steel was predicted using chemical compositions and manufacturing conditions using pruned regression tree [7]. Nowadays, current automotive suspension design considers both vehicle ride and durability of components during design stage. However, the process was lengthy and tedious where the need to have a solution to assist the design process is demanded.

This study aims to generate regression-tree based durability model for automotive coil spring fatigue life predictions with suspension frequency and ISO 2631 vertical vibration as independent variables. If there is a linear relationship between spring stiffness and vehicle ISO 2631 vertical vibration to fatigue life, then the regression-tree based durability models will have high correlation value. Based on the authors' literature study, there is no such regression-tree based durability model has been proposed. The generated model should provide spring fatigue life prediction close to experimental fatigue life to show accuracy of predictions.

34.2 Methodology

The process flow to perform the regression tree-based spring fatigue life prediction is shown in Fig. 34.1. Firstly, the road profile acceleration time histories were collected from different road conditions using a data acquisition system. A sampling rate of 1000 Hz was determined for the data collection process because this frequency range was suitable for steel vibration fatigue analysis [8]. To enhance the analysis, artificial

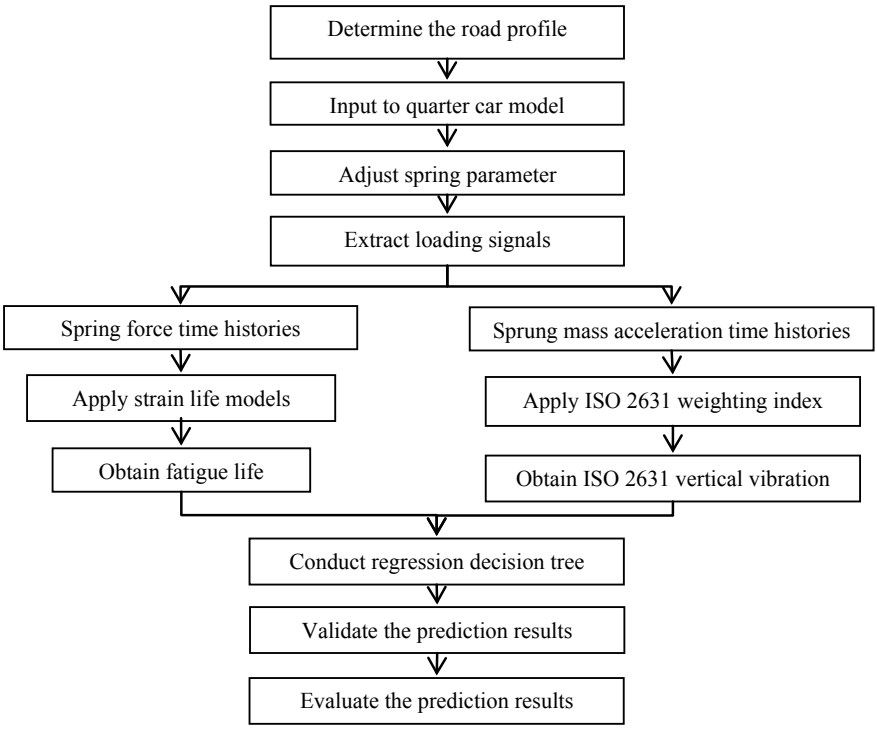

Fig. 34.1 Process flow for spring durability model generation

road profiles class A to D were generated according to ISO 8608 (2016) [9]. Both the measured and artificial generated road profile were used as input to a quarter car simulation model. Through adjusting the spring stiffness, various force signals exerted on the springs and relative sprung mass acceleration were obtained.

The spring force time histories were used as the input to Smith-Watson-Topper (SWT) strain life model for fatigue life predictions. The SWT strain life model could be defined as follows [10]:

$$\sigma_{max}\varepsilon = \frac{\left(\sigma_f{}'\right)^2}{E}\left(2N_f\right)^{2b} + \sigma_f{}'\varepsilon_f{}'\left(2N_f\right)^{b+c} \tag{1}$$

where ε is the plastic strain, $\varepsilon_f{}'$ is the fatigue ductility coefficient, $\sigma_f{}'$ is the fatigue strength coefficient, b is the fatigue strength exponent, c is the fatigue ductility exponent, σ_{mean} is the mean stress, and σ_{max} is the maximum stress. On the other hand, the sprung mass accelerations were weighted according ISO 2631 vibration standard to obtain indicator for vehicle ride assessment.

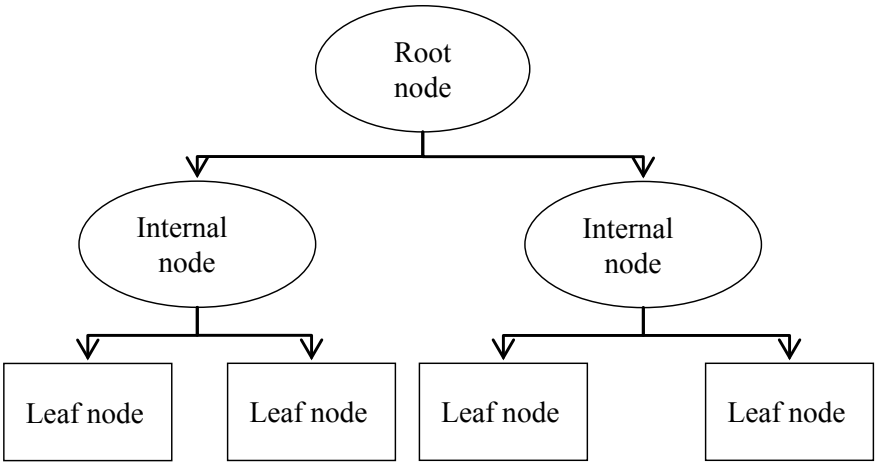

Fig. 34.2 Schematic diagram of a regression tree

After the spring fatigue life and ISO 2631 vertical vibrations were obtained, a regression decision tree method was conducted to analyse the data. The regression tree method performed data analysis through splitting criteria and had a form of tree as shown in Fig. 34.2. The splitting criteria for regression tree is mean square error (MSE) which was defined as follows [11]:

$$\mathrm{MSE} = \frac{\sum_{i=1}^{n}\left(\hat{Y}_i - Y_i\right)^2}{n} \tag{2}$$

where $\hat{Y}_i$ is a vector of n predictions and Y_i is the vector of observed values of the variable being predicted. The splitting algorithm choose an initial value and then divided the data into two subsets. The algorithm determined the lowest MSE value to split the tree and $\hat{Y}_i$ for each subset is the mean value. After the regression tree was generated, a set of five independent measurement data from actual vehicle was used to validate the regression tree predictions.

34.3 Results and Discussions

In this analysis, a total of 90 datasets were used to train the regression tree with suspension frequency and vehicle ISO 2631 vibration as independent variables. During the regression tree analysis, the datasets were discretised into smaller sections where variable interactions are clearer. As for the outcome, the trained regression tree model consisted of 15 nodes and 7 splits which is shown in Fig. 34.3. In Fig. 34.3, the root node has split the critical independent variable which was ISO 2631 vertical

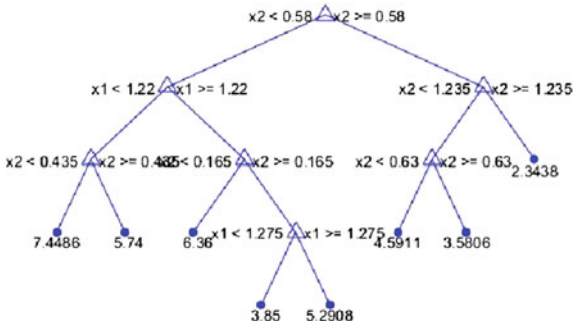

Fig. 34.3 Generated regression-tree based durability model

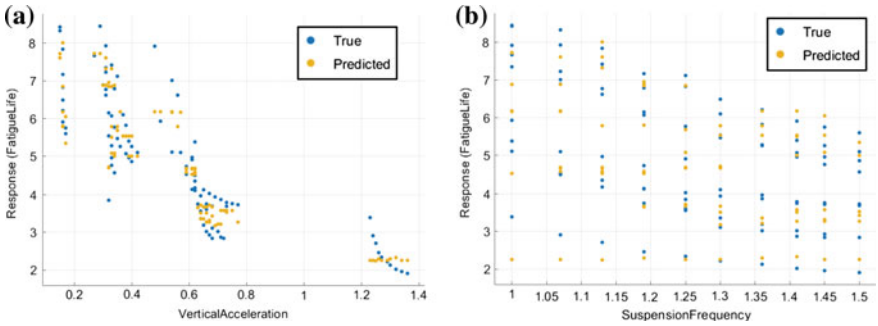

Fig. 34.4 Response plot for independent variables: **a** vertical vibration, **b** suspension frequency

vibration into two groups. Subsequently, the nodes were further split into two groups until a leaf node (fatigue life) was obtained. The process between the root node and leaf node was known as internal node.

The regression tree tended to divide the datasets into subset and then analysed according to MSE. Each of the independent variables was analysed during the regression tree training process. For response plot, the spring fatigue life versus the ISO 2631 vertical vibration is shown in Fig. 34.4a while the fatigue life against the suspension frequency is shown in Fig. 34.4b. The independent variable datasets were scattered around the space and regression tree model attempted to capture the trend and pattern of the distributions. After the regression tree model was obtained, the goodness of fitting was examined to ensure the best fit of the data.

For a good fitted regression model, the model predictions were required to be as close as possible to the true response value. Hence, a regression-tree predicted versus actual response were plotted into Fig. 34.5. As observed, the model consisted of coefficient of determination value (R^2) of 0.85 which shown a strong correlation between model predictions and actual response. As proposed in [13], a R^2 value above 0.80 was considered as a good correlation. Hence, this established regression-tree was considered as having a good relationship. The obtained mean square error (MSE)

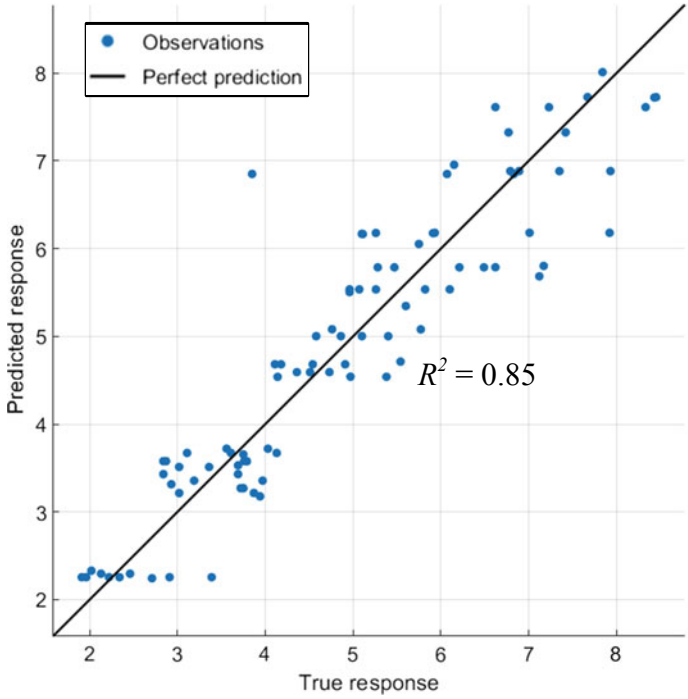

Fig. 34.5 Predicted versus actual response plot

for the response was 0.4347 and the root mean squared error (RMSE) was 0.6593. The datum of dependent variable was ranging from 0 to 8 which was relatively small for this RMSE value. Hence, this regression tree yielded a good fatigue life prediction with low error range.

For any regression analysis, there were no absolute correct prediction outcome. In this case, the difference between the predicted and target value was always existing and known as the residuals. The most useful way to analyse the residuals was using a residual plot where the predicted response is shown in Fig. 34.6. The residual plots were also used to determine the homoscedasticity of datasets [14]. When the residuals were homoscedasticity, the fatigue life predictions were consistent in all the prediction range. To ensure the homoscedasticity of the datasets, linear regression of the residual plots was performed where the regression was linear at zero. This indicating that the residuals were consistent within the range of −3 to 3 throughout the whole predictions. It was suggested that the fatigue life predictions using this regression-tree based model was always within this proposed range.

For the accuracy aspect, the predicted fatigue life using regression tree was analysed using 1:2 or 2:1 scatter plot as shown in Fig. 34.7. This method was widely used in determining the correlation between predicted and experimental fatigue lives because the acceptable tolerance of fatigue life is large [14]. As observed in Fig. 34.7,

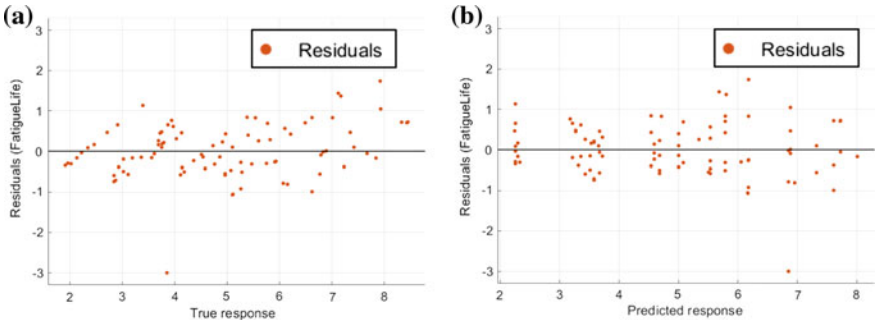

Fig. 34.6 Residual plots for target values: **a** true value, **b** predicted value

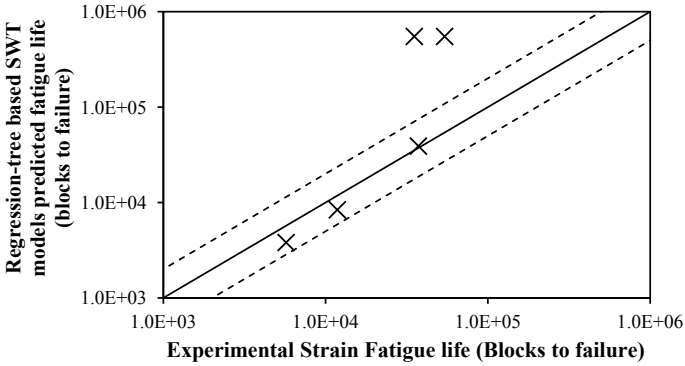

Fig. 34.7 Scatter band for predicted fatigue life

there were five sets of independent datasets were used to validate the established regression tree. There were three datasets were fitted nicely within the 1:2 or 2:1 boundary while two datasets were beyond the datasets. This was because the experimental datasets were collected from a road harsh road condition where the acceleration and strain signals were non-stationary. This shown that the regression tree durability model was less efficient in predicting the stochastic fatigue behaviour. Nevertheless, this method was able to estimate spring fatigue life under stationary signals.

34.4 Conclusion

A regression-tree based durability model has been successfully established for automobile spring fatigue life predictions with a R^2 value as high as 0.85. The residuals of the regression-tree based durability was analysed using a residual plot which proposed that the predictions of fatigue life were consistent. For validation, the predicted

fatigue life was validated using a set of independent experimental measurements and three out of five datasets were fall within acceptable range. This suggested that the proposed regression-tree based durability model could be applied for spring fatigue life prediction using ISO 2631 vertical acceleration and suspension frequencies.

References

1. Chindamo D, Gadola M, Marchesin FP (2017) Reproduction of real-world road profiles on a four poster rig for indoor vehicle chassis and suspension durability testing. Adv Mech Eng 9(8):1–10
2. Ogunoiki A, Olatunbosun O (2015) Characterisation of the effects of vehicle parameter variations on vehicle road load data. SAE Technical Paper 2015-01-0634
3. Mitra AC, Kiranchand GR, Soni T, Banerjee N (2016) Design of experiments for optimization of automotive suspension system using quarter car test rig. Procedia Eng 144:1102–1109
4. Kalaivani R, Sudhagar K, Lakshmi P (2016) Neural network based vibration control for vehicle active suspension system. Indian J Sci Technol 9(1):1–8
5. Al-Jarrah OY, Yoo PD, Muhaidat S, Karagiannidis GK, Taha K (2015) Efficient machine learning for big data: a review. Big Data Res 2(3):87–93
6. Kordos M, Kania P, Budzyna P, Blachnik M, Wieczorek T, Golak S Combining the advantages of neural networks and decision trees for regression problems in a steel temperature prediction system. Hybrid Artif Intell Syst: 36–45
7. Deshpande PD, Gautham BP, Cecen A, Kalidindi S, Agrawal A, Choudhary A (2013) Application of statistical and machine learning techniques for correlating properties to composition and manufacturing processes of steels. In: 2nd world congress on integrated computational materials engineering
8. Putra TE, Abdullah S, Schramm D, Nuawi MZ, Bruckmann T (2015) Generating strain signals under consideration of road surface profiles. Mech Syst Signal Process 60:485–497
9. ISO (2016) Mechanical vibrations—road surface profiles—reporting of measured data. International Organization for Standardization
10. Ince A, Glinka G (2011) A modification of Morrow and Smith-Watson-Topper mean stress correction models. Fatigue Fract Eng Mater Struct 34(11):854–867
11. Gnana Sheela K, Deepa SN (2013) Review on methods to fix number of hidden neurons in neural networks. Math Probl Eng 425740:1–11
12. Sivák P, Ostertagová E (2012) Evaluation of fatigue tests by mathematical statistics. Procedia Eng 48:636–642
13. Srinivasan R, Lohith CP (2017) Main study—detailed statistical analysis by multiple regression. In: Strategic marketing and innovation for Indian MSMEs, pp 69–92
14. Karolczuk A (2016) Analysis of revised fatigue life calculation algorithm under proportional and non-proportional loading with constant amplitude. Int J Fatigue 88:111–120

Part VI
Multiaxial Fatigue

Chapter 35
Prediction of Fatigue Crack Initiation Life in Notched Cylindrical Bars Under Multiaxial Cycling Loading

R. Branco, J. D. Costa, F. Berto, A. Kotousov and F. V. Antunes

Abstract This paper addresses the determination of fatigue crack initiation lifetime in notched round bars under multiaxial loading on the basis of a total strain energy density approach. The *modus operandi* consists of developing a fatigue master curve relating the total strain energy density and the number of cycles to failure from the outcomes of a set of standard strain-controlled fatigue tests. In a second stage, the total strain energy density of the notched sample is computed from representative hysteresis loops obtained via linear-elastic finite-element models. The proposed methodology is tested in cylindrical bars with lateral U-shaped notches and cylindrical bars with blind transverse holes subjected to different constant-amplitude proportional bending-torsion loading. After fatigue testing, specimen surfaces are examined by scanning electron microscopy to identify the main failure micro-mechanisms.

Keywords Crack initiation · Multiaxial fatigue life · Bending-torsion

35.1 Introduction

High-strength steels are ideal for critical components, such as shafts, axles, torsion bars, bolts, crankshafts, connecting rods, etc., due to their excellent strength-to-weight ratio and superior corrosion resistance. The engineering design of such components inevitably contains severe geometric discontinuities, responsible for high

R. Branco (✉) · J. D. Costa · F. V. Antunes
Department of Mechanical Engineering, CEMMPRE, University of Coimbra,
Rua Luís Reis Santos, 3030-788 Coimbra, Portugal
e-mail: ricardo.branco@dem.uc.pt

F. Berto
Department of Mechanical and Industrial Engineering, Norwegian University of Science and Technology, 7491 Trondheim, Norway

A. Kotousov
School of Mechanical Engineering, The University of Adelaide, Adelaide,
SA 5005, Australia

J.A.F.O. Correia et al. (eds.), *Mechanical Fatigue of Metals*, Structural Integrity 7,
https://doi.org/10.1007/978-3-030-13980-3_35

stress concentration phenomena [1]. Therefore, special attention must be given to the fatigue design; otherwise, crack initiation can occur, which is likely to culminate in fatigue failure.

In general, such components undergo complex loading, namely different normal stress to shear stress ratios, and contain various notch configurations, ranging from lateral notches to transverse holes, which cause complex local stress fields, strongly dependent on the geometric discontinuity, and characterised by different stress gradients, and different zones of influence.

Fatigue life prediction models based on local approaches require a detailed evaluation of the stress-strain fields at the critical areas [1–3]. These critical areas vary with the nature of the load, namely with its magnitude, direction, or type. The knowledge a priori of the crack initiation sites is also fundamental to simplify preventive maintenance tasks, reducing the areas to be inspected, and leading to cost savings.

This paper aims at predicting the fatigue crack initiation, based on a total strain energy density approach, in notched cylindrical bars subjected to multiaxial loading. The methodology consists of determining, in a first stage, a fatigue master curve, which relates the total strain energy density and the number of cycles to failure, on the basis of a set of standard strain-controlled fatigue tests. In a second stage, the total strain energy density of the notched samples is computed from representative hysteresis loops obtained via linear-elastic finite-element models. The proposed methodology is tested in notched round bars with lateral notches and blind transverse holes undergoing different proportional bending-torsion loading scenarios. After fatigue testing, specimen surfaces are examined by scanning electron microscopy to identify the main failure micro-mechanisms.

35.2 Experimental and Numerical Procedures

The material employed in this study was the DIN 34CrNiMo6 high-strength steel supplied in the form of 20 mm-diameter bars. Its main mechanical properties are [2]: Yield strength, $\sigma_{YS} = 967$ MPa; Tensile strength, $\sigma_{UTS} = 1035$ MPa; Young's modulus, $E = 209.8$ GPa; Poisson's ratio, $\nu = 0.296$; Cyclic hardening coefficient, $K' = 1361.6$ MPa; Cyclic hardening exponent, $n' = 0.1041$; Fatigue limit stress range, $\Delta\sigma_0 = 353$ MPa; and Stress intensity factor range threshold, $\Delta K_{th0} = 7.12$ MPa $m^{0.5}$.

Low-cycle fatigue tests were performed in a servo-hydraulic machine under: (i) fully-reversed strain-controlled conditions ($R_\varepsilon = -1$), for total strain amplitudes ($\Delta\varepsilon/2$) of 0.4, 0.5, 0.6, 0.8, 1.0, 1.25, 1.5 and 2.0%, at room temperature, using a constant strain rate ($d\varepsilon/dt = 8 \times 10^{-3}\ s^{-1}$); and (ii) fully-reversed stress-controlled tests ($R_\sigma = -1$), with stress amplitudes ($\Delta\sigma/2$) of 540, 560, 580, 600 and 635 MPa. Specimens were fabricated in accordance with the specifications outlined in ASTM E606, with a gage section measuring 15 mm in length and 8 mm in diameter. Stress-strain response was acquired from a 12.5 mm strain-gage extensometer mounted on the gage section. Tests were conducted using the single step method and were interrupted after complete failure of the specimen.

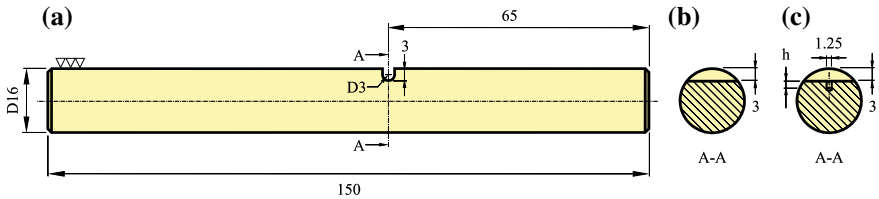

Fig. 35.1 Specimen geometries: **a** round bar with U-shaped notch; **b** cross-section of the round bar with U-shaped notch; **c** cross-section of the round bar with blind transverse hole (dimensions in millimetres)

Multiaxial bending-torsion tests were conducted in a servo-hydraulic testing machine connected to an own-made gripping system, under constant-amplitude pulsating loading ($R_\sigma = 0$), using 16-mm and 14-mm diameter notched specimens with: (i) lateral U-shaped notches of 3-mm diameter and 3-mm depth (see Fig. 35.1a, b); and (ii) 1.25 mm diameter transverse blind holes with depths (h) in the interval 0.3–1.3 mm (see Fig. 35.1c). Two bending moment to torsion moment ratios (B/T) were studied, namely B/T = 2 and B/T = 1, which correspond, respectively, to normal stress to shear stress ratios (σ/τ) of $\sigma/\tau = 4$ and $\sigma/\tau = 2$. For each loading case (i.e. four different geometries and two B/T ratios), three stress levels were tested. The nominal normal stress amplitudes (σ_a) were in the range 90–298 MPa. Notch surfaces were observed in situ throughout the tests using a high-resolution digital camera.

Multiaxial fatigue tests were modelled using a linear-elastic finite-element model (see Fig. 35.2). The mesh was developed in a parametric framework, ultra-refined near the notch and coarser at remote positions, to reduce the computational overhead. The assembled models of the U-shaped notch and the blind transverse hole configurations had, respectively, 99,823 nodes and 76,608 elements, and 97,704 nodes and 89,584 elements. The material was assumed to be homogeneous, linear-elastic and isotropic. Bending moments were applied by two forces (F_B) parallel to the axis of the specimen with the same magnitude and opposite directions. Torsion moments were created by a couple of forces (F_T) with the same magnitude and opposite directions acting on a plane normal to the longitudinal axis of the specimen. Forces were applied at one end of the specimen, while the other was fixed. The B/T ratios were defined by changing the value of λ (see Fig. 35.2), which was equal to 1/2 and 1 for the cases B = 2T and B = T, respectively.

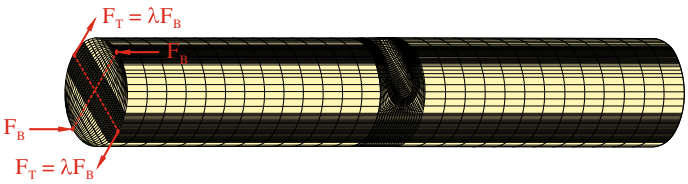

Fig. 35.2 Finite-element model of the 16-mm diameter round bars with U-shaped notches used to replicate the bending-torsion tests

35.3 Results

35.3.1 Crack Initiation Sites and Crack Paths

Figure 35.3 presents examples of the crack paths observed in the experiments for both notch types and the two B/T loading cases. The increase of the B/T ratio, i.e. the increase of the normal stress level, results in straighter crack paths, irrespective of the notch configuration. The dashed lines represent the crack paths predicted numerically on the basis of the first principal stress field [2]. Both the experimental and the numerical crack paths are in good agreement. Crack initiation in the U-notches occurred in the centre of the notch for B/T = 2 (i.e. lower shear stress levels) and close to the border of the notch for B/T = 1 (i.e. higher shear stress levels). In the case of the transverse holes, two cracks tend to initiate, at the hole border, in symmetric locations (see Fig. 35.3c, d); the increase of the B/T ratio (i.e. the increase of the normal stress level) reduces the angle of a virtual line defined by both initiation sites with respect to the horizontal. Experimental crack initiation sites are represented by the small circles and the numerical predictions, i.e. nodes of maximum first principal stress [3], are represented by the squares. The comparison of results shows a very good correlation between both the numerical predictions and the experimental observations.

Figure 35.4a shows the crack initiation site in a geometry with transverse hole. It is possible to distinguish the typical fatigue markings caused by cyclic loading with radial convergence to the vertex (see the arrow). In a subsequent stage, not visible in Fig. 35.4a, this crack joined with another one initiated in a symmetrical position of the hole (see Fig. 35.3c, d). The fatigue crack initiation process, in the case of the

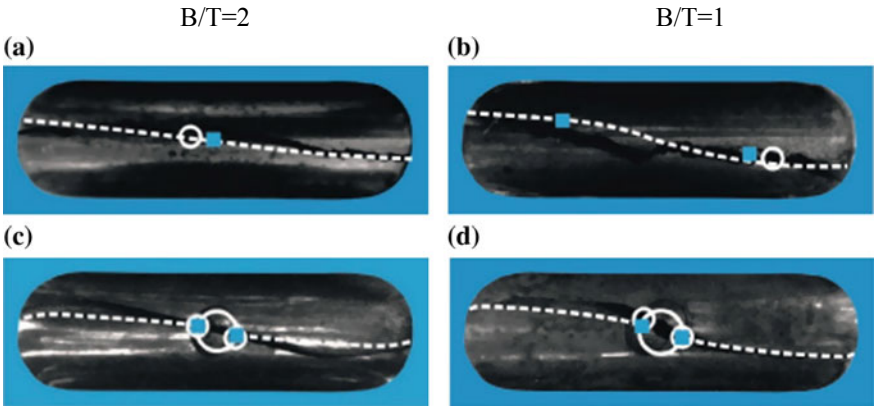

Fig. 35.3 Experimental crack paths: **a** U-shape and B/T = 2; **b** U-shape and B/T = 1; **c** transverse hole and B/T = 2; **d** transverse hole and B/T = 1. Dashed lines and squares represent the numerical predictions of crack paths and initiation sites. Small circles represent the experimental initiation sites; the other circles represent the hole

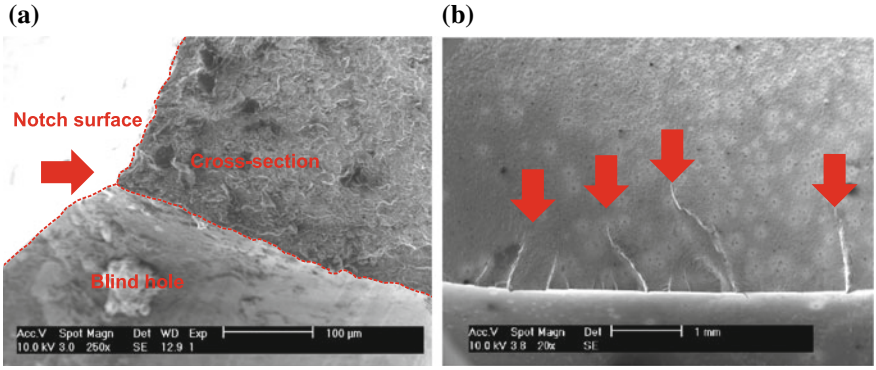

Fig. 35.4 SEM micrographs obtained in the bending-torsion tests: **a** specimen with blind transverse hole; **b** specimen with U-shaped notch

U-shaped notches, is relatively different. As documented in Fig. 35.4b, which shows a macrograph of the fracture surface, it is possible to observe several fracture steps caused by multi-crack initiation (see the arrows) and not only by two cracks.

In order to define the number of cycles to crack initiation, curves relating the crack length versus number of cycles were derived from the high-resolution images collected during the tests. The crack initiation length (a_0) was defined via the El Haddad parameter [4]. For this material, and pulsating loading ($R = 0$), $a_0 = 129$ µm [2]. Fatigue life predictions were performed through the model described in [2]. The modus operandi consists of two main stages: (1) it is developed a fatigue master curve that relates the total strain energy density—accounted for in terms of plastic and elastic positive strain components—with the number of cycles to failure, which is obtained from the outcomes of a set of uniaxial strain-controlled fatigue tests performed using smooth specimens; (2) the total strain energy density of the notched sample is estimated assuming a multiaxial loading scenario. The latter stage can be divided into three steps: (i) reduction of the multiaxial stress state into an equivalent uniaxial stress state by computing the von Mises stress at the theoretical initiation site from the FE models described in the previous section; (ii) definition of an effective stress range based on the Line Method of the TCD; and (iii) generation of a representative hysteresis loop via the ESED concept [5]. After that, the total strain energy of the notched specimen is inserted into the fatigue master curve to estimate the fatigue crack initiation life.

Figure 35.5a shows the fatigue master curve determined from the half-life hysteresis loops obtained in the strain-controlled tests performed using smooth specimens. The fitted function (dashed line) is very well correlated with the experimental observations. Fatigue life predictions obtained via the selected model for the different notch geometries, B/T ratios, and loading levels are exhibited in Fig. 35.5b. Numerical predictions and experimental observations are in good agreement, with all points within a factor of 2 (dashed lines). This fact indicates that the proposed methodology can efficiently predict the fatigue lifetime for different notch configurations and bending-torsion ratios.

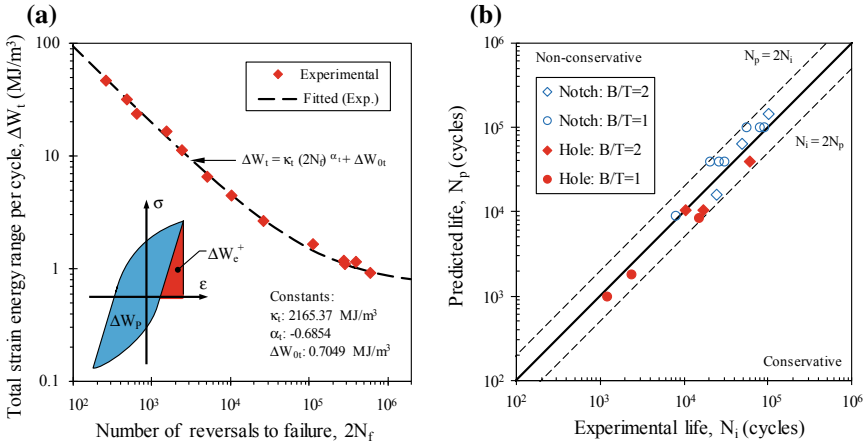

Fig. 35.5 Fatigue master curve defined in terms of total strain energy density and number of reversals to failure; **b** fatigue life predictions using the proposed methodology

35.4 Conclusions

In this paper, fatigue crack initiation in notched samples, with U-notched and transverse holes, subjected to proportional bending-torsion (B/T) loading is studied. The main conclusions can be drawn: (i) fatigue crack paths are strongly affected by the B/T ratio and can be successfully predicted on the basis of the first principal stress field; (ii) crack initiation sites are controlled by the B/T ratio and the notch geometry; (iii) in the U-shaped configuration, a multi-crack initiation phenomenon tends to occur throughout the notch surface while, in the other, there is the nucleation of two cracks, in symmetric positions of the hole, which join each other; (iv) the fatigue initiation life can be successfully predicted using the model based on the total strain energy density evaluated at the notch root.

Acknowledgements The authors would like to acknowledge the sponsoring under the project number 016713 (PTDC/EMS-PRO/1356/2014) financed by Project 3599: Promover a Produção Científica e Desenvolvimento Tecnológico e a Constituição de Redes Temáticas (3599-PPCDT) and FEDER funds.

References

1. Wu SC, Zhang SQ, Xu ZW, Kang GZ, Cai LX (2016) Cyclic plastic strain-based damage tolerance for railway axles in China. Int J Fatigue 93:64–70
2. Branco R, Prates PA, Costa JD, Berto F, Kotousov A (2018) New methodology of fatigue life evaluation for multiaxially loaded notched components based on two uniaxial strain-controlled tests. Int J Fatigue 111:308–320

3. Branco R, Antunes FV, Ferreira JA, Silva JM (2012) Determination of Paris law constants with a reverse engineering technique. Eng Fail Anal 16:631–638
4. El Haddad MH, Topper TH, Smith KN (1979) Prediction of non-propagating cracks. Eng Fract Mech 11:573-84
5. Glinka G (1985) Calculation of inelastic notch-tip strain–stress histories under cyclic loading. Eng Fract Mech 22:839–854

Chapter 36
Multiaxial Fatigue Analysis of Stainless Steel Used in Marine Structures

A. S. Cruces, P. Lopez-Crespo, B. Moreno, S. Bressan and T. Itoh

Abstract This work investigates the fatigue behaviour under multiaxial loading conditions of 316 stainless steel commonly used in offshore and marine structures. Cylindrical hollow specimens were tested under uniaxial tensile stress, hoop stress and different combinations of tensile and hoop stresses. Both proportional and non-proportional loading were studied in the experiments. Prediction of the fatigue life was performed with Wang-Brown, Fatemi-Socie and Liu critical plane models. A detailed analysis and discussion of the performance of the different models is presented with an emphasis on the versatility for different situations.

Keywords Multiaxial fatigue · Stainless steel for marine structures · Critical plane models

A. S. Cruces · P. Lopez-Crespo (✉) · B. Moreno
Department of Civil and Material Engineering, University of Malaga,
C/Dr Ortiz Ramos, s/n, 29071 Málaga, Spain
e-mail: plopezcrespo@uma.es

A. S. Cruces
e-mail: ascruces@uma.es

B. Moreno
e-mail: bmoreno@uma.es

S. Bressan
Graduate School of Science & Engineering, Ritsumeikan University, 1-1-1,
Nojihigashi, Kusatsu-shi, Shiga 525-8577, Japan
e-mail: r0300kf@ed.ritsumei.ac.jp

T. Itoh
Department of Mechanical Engineering, College of Science & Engineering, Ritsumeikan University, 1-1-1, Nojihigashi, Kusatsu-shi, Shiga 525-8577, Japan
e-mail: itohtaka@fc.ritsumei.ac.jp

J.A.F.O. Correia et al. (eds.), *Mechanical Fatigue of Metals*, Structural Integrity 7,
https://doi.org/10.1007/978-3-030-13980-3_36

36.1 Introduction

Even though the loading conditions of real structures often involves loads in different directions and complex spectra [1], most research works focus on the uniaxial fatigue case. Improving the quality of failure predictions in marine and offshore structures subjected to multiaxial cyclic loading can be achieved based on high quality experiments that reproduce as accurately as possible the real service conditions. This requires applying both proportional [2] and non-proportional loads [3] to the cracked structures. These loading scenarios often produce interaction effects that are difficult to account for by classic theories [2, 4]. Critical plane methods are able to incorporate the stress state and other interaction effects that appear during the loading cycle [5, 6]. Critical plane methods can be used to predict the fatigue life and also the cracking orientation and can be classified into stress based, strain based and energy based methods. The efficacy of the predictions depends on the material under study, the experimental information fed into the model and the type of loading conditions [6]. Unlike damage tolerance approach [7, 8] critical plane methods are based on global data and not locally measured variables [9]. A number of different damage parameters (DP) based on critical plane model have been previously presented [10, 11] and are able to include various loading effects. Using reliable experimental information regarding the multiaxial behaviour of the materials is essential for improving the predictions of the models.

This work shows a thorough analysis of the multiaxial fatigue behaviour of a 316 stainless steel often used in marine, piping and offshore structures due to its good corrosion resistance [12]. By applying different load paths on the specimens, the capabilities of the different critical plane models are evaluated, with an emphasis on hardening and mean stress effects.

36.2 Material and method

The experiments were conducted on 316 stainless steel. This material is commonly employed in marine, piping and offshore industries due to its good resistance against corrosion. Hollow cylindrical specimens with the dimensions described in Fig. 36.1 were used. The longitudinal gauge length was polished with 1 μm alumina particles. The inner surface of the specimen was polished with sand papers up to #2000. The experimental work was conducted with a three actuator fatigue loading rig. Such rig allows (i) the introduction of a fluid inside a hollow specimen, (ii) traction and compression forces to be applied and (iii) torsional force to be applied. In the centre of the testing machine, a pressure gauge and a load cell are equipped to measure the inner pressure, axial load and torque. Further details about the experimental have been described previously [13].

Table 36.1 and Fig. 36.2 show the five different load paths applied. These have a combination of axial longitudinal loads and inner pressure. A frequency of 0.2 Hz was

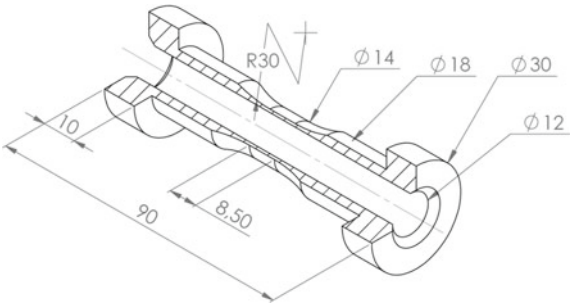

Fig. 36.1 The geometry of the cylindrical specimen. All dimensions are in mm

Table 36.1 Schematic of the six loading paths studied

Path	Id	σ_{Za} (MPa)	$\sigma_{\theta a}$ (MPa)	σ_{Ra} (MPa)	N_f (cycles)
Pull	1	256.35	3.25	−0.5	122,000
Inner-pressure	2A	0	236.35	−36.15	29,300
	2B	0	236.35	−36.15	26,700
Square-shape	4	200.2	236.35	−36.15	3596
Lt-shape	5	173.1	204.35	31.25	14,486
Lc-shape	6A	−200.2	236.35	−36.15	25,770
	6B	−221.55	261.55	−40	13,542
Push-pull	7A	512.7	3.25	−0.5	104
	7B	443.2	3.25	−0.5	393

used in the square shape loads and a frequency of 0.4 Hz was used in the other tests. The inner pressures produce a radial stress σ_r and a hoop stress σ_θ which maximum values are reached inside the tube, the axial load produce an evenly axial tension σ_z in all the area.

The Ramberg-Osgood equation was used in this work to obtain the strain from the stresses applied. The hardening effect is taken into account modifying the cyclic strength coefficient K′ with Eq. 36.1. Non-proportional hardening coefficient α is set to 1 for 316 stainless steel and a non-proportional factor F is set to 1 [14] for the case of π/2 load offset.

$$k'_{np} = k'(1 + \alpha F) \tag{36.1}$$

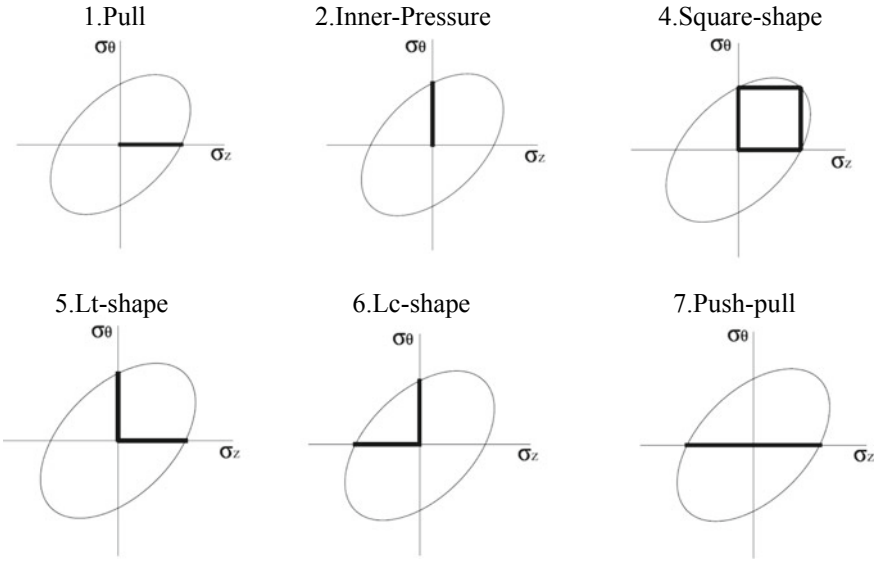

Fig. 36.2 Schematic of the six different loading paths studied

36.3 Introducing Critical Plane Models

36.3.1 Wang-Brown Model (WB)

Wang-Brown model (Eq. 36.2), is a strain type model [15]. The DP is defined on the plane φ^* with the maximum shear strain range $\Delta\gamma$. Both shear strain and normal strain in φ^* are considered to build the DP. According to the authors, the physical explanation of such criterion is that cyclic shear strain promotes crack nucleation. At the same time, crack growth is a consequence of normal strain. S parameter defines the material sensibility to the normal strain in the crack growth.

$$\frac{\Delta\gamma_{max}}{2} + S\Delta\varepsilon_n = [(1+\nu_e) + S(1-\nu_e)]\frac{\sigma_f^{'}}{E}\left(2N_f\right)^b + \\ + \left[\left(1+\nu_p\right) + S\left(1-\nu_p\right)\right]\varepsilon_f^{'}(2N_f)^c \tag{36.2}$$

36.3.2 Fatemi-Socie Model

Fatemi-Socie model (Eq. 36.3) is a strain type model [16], based upon the model proposed by Brown and Miller [5]. They suggested substituting the normal strain component for a normal stress component. The DP is defined on the plane φ^* with the

larger shear strain range $\Delta\gamma$. The normal tension on φ^* is modified by the coefficient $K/\sigma y$ which defined the material sensibility respect from the normal tension on the slip plane.

$$\frac{\Delta\gamma\max}{2}\left(1+k\frac{\sigma_{n,\max}}{\sigma_y}\right)=\frac{\tau_f^{'}}{G}(2N_f)^{b_\gamma}+\gamma_f^{'}(2N_f)^{c_\gamma} \tag{36.3}$$

36.3.3 Liu I and Liu II Model

Liu I (Eq. 36.4) and Liu II (Eq. 36.5) are energy type models [17]. Depending on the failure mode, Liu presents two parameters, one for a normal tension failure ΔW_I and another one for shear tension failure ΔW_{II}. This way distinguishes between brittle and ductile materials. For normal tension failure, plane φ^* will be the one which maximize axial work $\Delta\sigma\Delta\varepsilon$, and for shear tension failure the one which maximize shear work $\Delta\tau\Delta\gamma$. Once φ^* is determined, the DP is obtained as the sum of both works, the axial and shear work.

$$(\Delta\sigma_n\Delta\varepsilon_n)_{\max}+(\Delta\tau\Delta\gamma)=4\sigma_f^{'}\varepsilon_f^{'}\left(2N_f\right)^{b+c}+\frac{4\sigma_f^{'2}}{E}\left(2N_f\right)^{2b} \tag{36.4}$$

$$(\Delta\sigma_n\Delta\varepsilon_n)+(\Delta\tau\Delta\gamma)_{\max}=4\tau_f^{'}\gamma_f^{'}\left(2N_f\right)^{b\gamma+c\gamma}+\frac{4\tau_f^{'2}}{G}\left(2N_f\right)^{2b\gamma} \tag{36.5}$$

36.4 Fatigue Life Results

Figure 36.3 shows the life estimation for each model for different load paths. The solid line presents those points with a coincidence between the experimental life N_{exp} and the calculated N_{calc}. Dashed lines limit the zone with a twice (100%) and half (−50%) deviation of the calculated life respect to the experimental. FS results are represented with blue squares, WB with green triangles, Liu I with black circles and Liu II with purple crosses.

Conservative predictions are observed at low fatigue life, this is for #6 push-pull path tests. This is in agreement with previous analyses conducted on structural low carbon steel [3]. As the test strain value is reduced a better correlation between prediction and experimental life is obtained. In general, FS presents the best results among the models with the exception of the non-proportional load path #3. There is not a clear difference between Liu I and Liu II estimations, although as it was describe previously, they are developed for different failures modes.

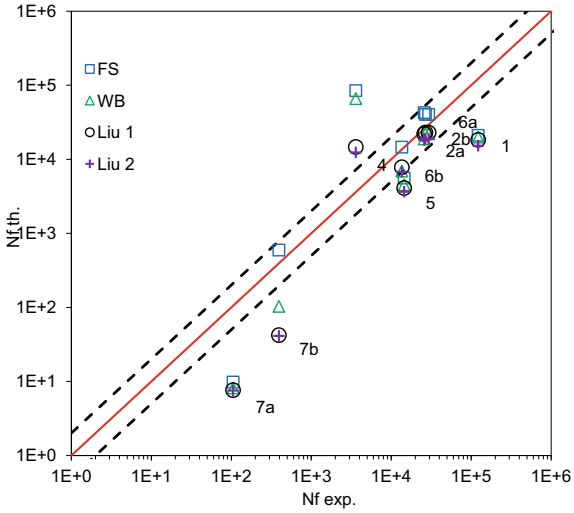

Fig. 36.3 Critical plane model 316 stainless steel fatigue life predictions for different load paths

36.5 Conclusions

Four different critical plane models have been assessed on 316 stainless steel used in marine structures. Different types of proportional loads and non-proportional loads were studied by combining uniaxial loads and inner pressure loads on cylindrical hollow specimens. It was shown that the critical plane models under study produce conservative predictions in the low cycle fatigue regime. While FS model overall generates the best predictions for all cases, Liu models appear to generate improved predictions for non-proportional cases.

Acknowledgements Authors would like to acknowledge the financial support from Ministerio de Economia y Competitividad through grant reference MAT2016-76951-C2-2-P and from Kakenhi Grant-in-Aid for Scientific Research (C) through grant number JP18K03854.

References

1. Moreno B, Martin A, Lopez-Crespo P, Zapatero J, Dominguez J (2016) Estimations of fatigue life and variability under random loading in aluminum Al-2024T351 using strip yield models from NASGRO. Int J Fatigue 91:414–422
2. Lopez-Crespo P, Pommier S (2008) Numerical analysis of crack tip plasticity and history effects under mixed mode conditions. J Solid Mech Mater Eng 2:1567–1576. http://dx.doi.org/10.1299/jmmp.2.1567
3. Lopez-Crespo P, Moreno B, Lopez-Moreno A, Zapatero J (2015) Study of crack orientation and fatigue life prediction in biaxial fatigue with critical plane models. Eng Fract Mech 136:115–130
4. Chen X, Gao Q, Sun XF (1994) Damage analysis of low-cycle fatigue under non-proportional loading. Int J Fatigue 16:221–225

5. Brown MW, Miller KJ (1973) A theory for fatigue failure under multiaxial stress-strain conditions. Proc Inst Mech Eng 187:745–755
6. Socie DF, Marquis GB (2000) Multiaxial fatigue. Society of Automotive Engineers Inc, Warrendale, PA (USA)
7. Ewalds HL, Wanhill RJH (1984) Fracture mechanics. Arnold, London
8. Shterenlikht A, Díaz-Garrido FA, Lopez-Crespo P et al (2004) Mixed mode (KI + KII) stress intensity factor measurement by electronic speckle pattern interferometry and image correlation. Appl Mech Mater 1–2:107–112
9. Mokhtarishirazabad M, Lopez-Crespo P, Moreno B et al (2016) Evaluation of crack-tip fields from DIC data: a parametric study. Int J Fatigue 89:11–19
10. Spagnoli A (2001) A new high-cycle fatigue criterion applied to out-of-phase biaxial stress state. Int J Mech Sci 43:2581–2591
11. Cruces AS, Lopez-Crespo P, Moreno B, Antunes FV (2018) Multiaxial fatigue life prediction on S355 structural and offshore steel using SKS critical plane model. Metals 8(12):1060. https://doi.org/10.3390/met8121060
12. Turski M, Bouchard PJ, Steuwer A, Withers PJ (2008) Residual stress driven creep cracking in AISI Type 316 stainless steel. Acta Mater 56:3598–3612. https://doi.org/10.1016/j.actamat.2008.03.045
13. Yakada Y, Morishita T, Itoh T (2017) Effect of interchange in principal stress and strain directions on multiaxial fatigue strength of type 316 stainless steel. In: Proceedings of fatigue 2017 conference
14. Cailletaud G, Doquet V, Pineau A Cyclic multiaxial behaviour of an austenitic stainless steel: microstructural observation and micromechanical modelling. European Structural Integrity Society
15. Wang H, Brown MW (1993) Under proportional and non-proportional. 16:1285–1298
16. Fatemi A, Socie DF (1988) A critical plane approach to multiaxial fatigue damage including out-of-phase loading. Fatigue Fract Eng Mater Struct 11:149–165
17. Liu KC (1993) A method based on virtual strain energy parameters for multiaxial fatigue life prediction. ASTM STP 1191:67–84

Chapter 37
On the Application of SK Critical Plane Method for Multiaxial Fatigue Analysis of Low Carbon Steel

A. S. Cruces, P. Lopez-Crespo, S. Sandip and B. Moreno

Abstract In this work Suman-Kallmeyer critical plane model is assessed and compared to few other critical plane models. The analysis is based on both in-phase proportional loading and out-of-phase non-proportional loading applied to a low carbon steel. A wide range of loading scenarios were studied by combining axial and torsional loads, producing fatigue lives in the range of 10^3 to 10^6 cycles. The study allowed low and high cycle fatigue regimes to be assessed. In addition, the hardening effect was also investigated. Finally, a comparison with well established critical plane models is also performed.

Keywords Critical plane approach · Multiaxial fatigue · Biaxial fatigue · St52-3N

37.1 Introduction

Fatigue failures are critical in industries where dynamic or cyclic loads are present. Multiaxial loading conditions are often encountered in real structures [1]. As a consequence, general design codes should incroporate either directly or indirectly multiaxial aspects. Taking into account multiple loads into design models requires not only the stress state to be accounted for, but also the material behaviour, the load interaction effects [2] and their impact on the nucleation and the propagation of fatigue

A. S. Cruces · P. Lopez-Crespo (✉) · B. Moreno
Department of Civil and Material Engineering, University of Malaga, C/Dr Ortiz Ramos, s/n, 29071 Malaga, Spain
e-mail: plopezcrespo@uma.es

A. S. Cruces
e-mail: ascruces@uma.es

B. Moreno
e-mail: bmoreno@uma.es

S. Sandip
Propulsion - Mission Systems COLLINS AEROSPACE, 3530 Branscombe Rd, Fairfield, CA 94533, USA
e-mail: sandip.suman@utas.utc.com

J.A.F.O. Correia et al. (eds.), *Mechanical Fatigue of Metals*, Structural Integrity 7,
https://doi.org/10.1007/978-3-030-13980-3_37

cracks [3–5]. A number of multiaxial fatigue theories attempt to integrate this information in so called damage parameters, while other are based on experimental characterisation of some property measured at the crack tip [6]. The damage parameter approach is employed to estimate the damage caused by the load cycles. Developing a single theory to cover all materials, loads configurations and external factors is extremely complicated [7]. Different theories have been proposed for specific loading scenarios. Critical plane methods present the damage in each cycle with a parameter, normally as combination of several stress-strain values, in a plane where is estimated the crack nucleate and growth [8]. They are very useful in predicting the fatigue life and the failure plane [9]. Critical plane methods have shown positive results for different materials and application in the industry [10, 11] and are already implemented in most of the recognized CAE tools. As in uniaxial fatigue, methods with damage parameter based on tension are more suitable to high cycle fatigue and those methods based on strain present better results for low high cycle fatigue as they account for plastic strain and other low cycle life effects [12]. The critical plane model developed by Suman and Kallmeyer [13] is analysed here and then compared to other models such as Fatemi and Socie [14], Wang and Brown [15], and Liu 1 and Liu 2 [16] under different loading conditions. Finally the predictive capabilities of the different methods are tested in terms of fatigue life.

37.2 Description of the Experiments

The experimental work is based on tubular hollow specimens resembling a dog bone shape. Multiaxial fatigue tests were conducted under strain control. This was possible thanks to the use of a biaxial extensometer. The material studied was a low carbon steel type St52-3N. This material has applications in offshore, piping, marine and structural domains. The experimental setup with the fatigue machine, the biaxial extensometer and the cylindrical specimen is shown in Fig. 37.1. Figure 37.1 also shows the sign for the different types of loads applied during the experiments. Twenty one multiaxial tests were conducted with sinusoidal normal-shear strain with

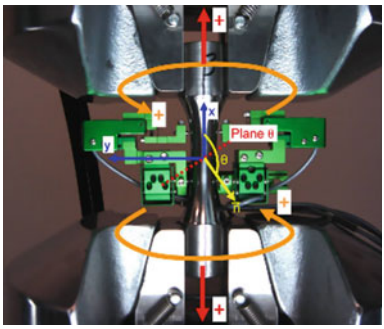

Fig. 37.1 Photo of the key elements employed in the experiments. The system of coordinates is also shown

total inversion in-phase and with 90° out-of-phase. Strain amplitudes ε_a and γ_a were chosen (based on previous results) to obtain a number of cycles to failure between 10^4 and 10^6, hence models will be evaluated for low and high cycle fatigue. Tests were also carried out with the purpose of fitting the parameters of the new critical plane model (SK, see following section).

37.3 Multiaxial Fatigue Analysis with Critical Plane Methods

37.3.1 Suman-Kallmeyer (SK) Critical Plane Method

The recently developed by Suman and Kallmeyer critical plane method is used in this work [17] (see Eq. 37.1). The method is based on the damage parameter where the shear strain range is multiplied by maximum shear stress value at critical plane φ* in their model. The third term in this model is the maximum value of the product of normal stress and shear stress on φ*.

$$(G\Delta\gamma)^{w}\tau_{max}^{(1-w)}\left(1+k\frac{(\sigma\cdot\tau)_{max}}{\sigma_0^2}\right)=AN^b+CN^d \tag{37.1}$$

When a material is loaded close to its yield strength, small changes in stress cause a significant amount of strain under low cycle fatigue. Conversely, for high cycle fatigue, for stress levels well below the yield strength, considerable changes in stress cause small changes in strain. SK model can capture both phenomena by considering the shear strain range and the maximum shear stress term. Hence, SK model appears to be very versatile and can predict the fatigue life of specimen loaded by both high cycle fatigue and low cycle fatigue. It is based on observations that crack initiation phenomenon is dominated by shear stress and strain among microscopic metal grains; however, propagation of micro-crack does not happen only due to cyclic tensile stress, and is the combined effect of both normal and shear stress at the critical plane. Hence, SK model describes this interaction by introducing the product of normal and shear stress at the critical plane in his damage parameter Eq. 37.1. The constants (w and k) are material parameters, and can be influenced by material specification and processing. An optimization process based on a less square error minimization is employed to fit the parameters. Optimization was carried out to minimise the relative error between experimental (left side of Eq. 37.1) and computed fatigue damage (right side of Eq. 37.1). An iterative process was followed with the initial values for k and w parameters ranging between the damage parameter value and the shear tension applied on φ*. When the number of data use to fit the parameters are excessively low, delimiting the values to obtain a correct solution is more relevant.

37.3.2 Wang-Brown (WB) Critical Plane Method

Wang-Brown method Eq. 37.2 is a strain type model [15]. The DP is defined on the plane φ* with the maximum shear strain range Δγ. Both shear strain and normal strain in φ* are considered to build the DP. According to the authors, the physical explanation of such criterion is that cyclic shear strain promotes crack nucleation. At the same time, crack growth is a consequence of normal strain. S parameter defines the material sensibility to the normal strain in the crack growth.

$$\frac{\Delta\gamma_{max}}{2} + S\Delta\varepsilon_n = [(1+\nu_e) + S(1-\nu_e)]\frac{\sigma_f^{'}}{E}\left(2N_f\right)^b + \\ + \left[\left(1+\nu_p\right) + S\left(1-\nu_p\right)\right]\varepsilon_f^{'}(2N_f)^c \tag{37.2}$$

37.3.3 Fatemi-Socie (FS) Critical Plane Method

Fatemi-Socie model (Eq. 37.3) is a strain type model [14], based upon the model proposed by Brown and Miller [4]. They suggested substituting the normal strain component for a normal stress component. The DP is defined on the plane φ* with the larger shear strain range Δγ. The normal tension on φ* is modified by the coefficient K/σy which defined the material sensibility respect from the normal tension on the slip plane.

$$\frac{\Delta\gamma_{\max}}{2}\left(1 + k\frac{\sigma_{n,\max}}{\sigma_y}\right) = \frac{\tau_f^{'}}{G}(2N_f)^{b_\gamma} + \gamma_f^{'}(2N_f)^{c_\gamma} \tag{37.3}$$

37.3.4 Liu 1 and Liu 2 Critical Plane Method

Liu 1 Eq. 37.4 and Liu 2 Eq. 37.5 are energy type models. Depending on the failure mode, Liu presents two parameters, one for a normal tension failure ΔWI and another one for shear tension failure ΔWII. This way distinguishes between brittle and ductile materials. For normal tension failure, plane φ* will be the one which maximize axial work Δσ Δε, and for shear tension failure the one which maximize shear work Δτ Δγ. Once φ* is determined, the DP is obtained as the sum of both works, the axial and shear work.

$$(\Delta\sigma_n\Delta\varepsilon_n)_{max} + (\Delta\tau\Delta\gamma) = 4\sigma_f^{'}\varepsilon_f^{'}\left(2N_f\right)^{b+c} + \frac{4\sigma_f^{'2}}{E}\left(2N_f\right)^{2b} \tag{37.4}$$

$$(\Delta\sigma_n\Delta\varepsilon_n) + (\Delta\tau\Delta\gamma)_{max} = 4\tau_f^{'}\gamma_f^{'}\left(2N_f\right)^{b\gamma+c\gamma} + \frac{4\tau_f^{'2}}{G}\left(2N_f\right)^{2b\gamma} \tag{37.5}$$

37.4 Fatigue Life Results and Discussion

Figure 37.2 shows life estimation for each model in-phase and Fig. 37.3 for out-of-phase. The solid line presents those points with a coincidence between the experimental life N_{exp} and the calculated N_{th}. Dashed lines limit the zone with a twice (100%) and half (−50%) deviation of the calculated life respect to the experimental. SK estimation are represented with red diamonds, FS with blue squares, WB with green triangles, Liu 1 with black circles and Liu 2 with purple crosses.

For in-phase loading, SK gives good estimation, with values near the conservative side, as it can be seen for almost all models with the exception of Liu 2. At low cycle fatigue the response is not as good as for high cycle fatigue, as consequence of

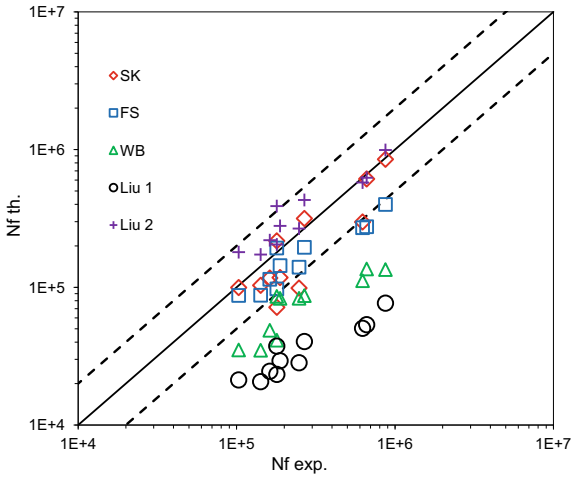

Fig. 37.2 St52-3N fatigue life predicted for in-phase loading

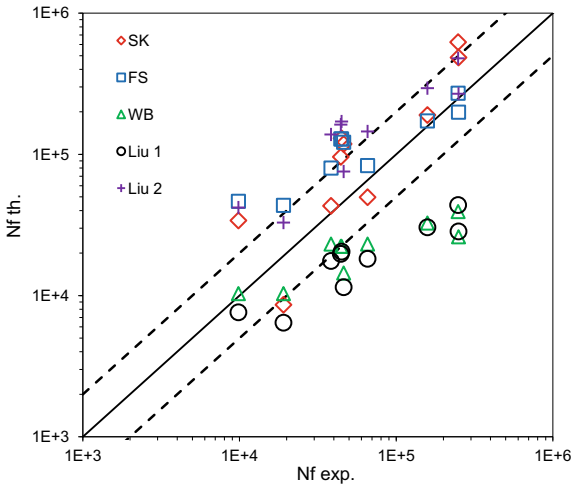

Fig. 37.3 St52-3N fatigue life predicted for out-of-phase loading

a low weight of the shear strains in the DP for the fit obtained. FS returns better predictions at low cycle fatigue than SK, with a conservative tendency as it moves to high cycle fatigue. As we can see, between Liu 1 and Liu 2, the second one gives a better result, showing this way the ductile character of the material. WB based on the same model as FS, shows similar results but more conservative, as previously noted maybe considering the normal stress on φ^* instead of the normal strain reflect better the hardening effect. For out-of-phase, models predictions move up to the non-conservative side respect to the values returns in-phase. Although SK model estimations are not bad, it presents a considerable dispersion, consequence of the sensitive response of the DP with τ_{max} instead of the low weight of $\Delta\gamma$ at low cycles. It is observed that the WB and the Liu 1 models provide very similar results and overestimate the fatigue life in general.

37.5 Conclusions

This work tests the SK critical plane model and compares it agains other well established critical plane methods. Good predictions were observed for SK method both under in-phase and out-of-phase loading conditions. A large sensitivity to the fitting parameters described in the model was observed.

Acknowledgements Financial support from Ministerio de Economia y Competitividad through grant reference MAT2016-76951-C2-2-P is greatly acknowledged.

References

1. Cruces AS, Lopez-Crespo P, Bressan S, Itoh T (2019) Investigation of the multiaxial fatigue behaviour of 316 stainless steel based on critical plane method. Fatigue Fract Eng Mater Struct, accepted for publication. https://doi.org/10.1111/ffe.12991
2. Moreno B, Martin A, Lopez-Crespo P, Zapatero J, Dominguez J (2016) Estimations of fatigue life and variability under random loading in aluminum Al-2024T351 using strip yield models from NASGRO. Int J Fatigue 91:414–422
3. Filippini M, Foletti S, Papadopoulos IV, Sonsino CM (2003) A multiaxial fatigue life criterion for nonsymmetrical and non-proportional elasto-plastic deformation. In: Carpinteri A, Spagnoli A, de-F M (eds) Biaxial/Multiaxial Fatigue and Fracture. Elsevier Science and ESIS, pp 383–400
4. Brown MW, Miller KJ (1973) A theory for fatigue failure under multiaxial stress-strain conditions. Proc Inst Mech Eng 187:745–755
5. Lopez-Crespo P, Pommier S (2008) Numerical analysis of crack tip plasticity and history effects under mixed mode conditions. J Solid Mech Mater Eng 2:1567–1576
6. Lopez-Crespo P, Garcia-Gonzalez A, Moreno B et al (2015) Some observations on short fatigue cracks under biaxial fatigue. Theor Appl Fract Mech 80:96–103
7. Tanaka K, Takahash H, Akiniwa Y (2006) Fatigue crack propagation from a hole in tubular specimens under axial and torsional loading. Int J Fatigue 28:324–334. https://doi.org/10.1016/j.ijfatigue.2005.08.001

8. Lopez-Crespo P, Moreno B, Lopez-Moreno A, Zapatero J (2015) Study of crack orientation and fatigue life prediction in biaxial fatigue with critical plane models. Eng Fract Mech 136:115–130
9. Mokhtarishirazabad M, Lopez-Crespo P, Moreno B et al (2017) Optical and analytical investigation of overloads in biaxial fatigue cracks. Int J Fatigue 100 part 2:583–590
10. Chen X, Gao Q, Sun XF (1994) Damage analysis of low-cycle fatigue under non-proportional loading. Int J Fatigue 16:221–225
11. Chu C (1995) Fatigue damage calculation using critical plane aproach. J Eng Mater Technol 117:41–49
12. Socie DF, Marquis GB (2000) Multiaxial fatigue. Society of Automotive Engineers Inc, Warrendale, PA (USA)
13. Suman S, Kallmeyer A, Smith J (2016) Development of a multiaxial fatigue damage parameter and life prediction methodology for non-proportional loading. Frat Ed Integrità Strutt 38:224–230
14. Fatemi A, Socie DF (1988) A critical plane approach to multiaxial fatigue damage including out-of-phase loading. Fatigue Fract Eng Mater Struct 11:149–165
15. Wang CH, Brown MW (1993) A path-independent parameter for fatigue under proportional and non-proportional loading. Fatigue Fract Eng Mater Struct 16:1285–1298
16. Liu KC (1993) A method based on virtual strain energy parameters for multiaxial fatigue life prediction. In: Advances in Multiaxial Fatigue, ASTM STP 1191. pp 67–84
17. Cruces AS, Lopez-Crespo P, Moreno B, Antunes FV (2018) Multiaxial fatigue life prediction on S355 structural and offshore steel using SKS critical plane model. Metals 8(12):1060. https://doi.org/10.3390/met8121060

Part VII
Very High Cycle Fatigue

Chapter 38
Fatigue Testing at 1000 Hz Testing Frequency

Markus Berchtold

Abstract In 2014 RUMUL could present a new resonant fatigue testing machine, with a testing frequency of 1000 Hz. The dynamic load of maximum 50 kN peak-peak is produced with an electromagnetic system. Similar to established resonant systems which run on testing frequencies from about 40 up to 250 H. The static portion of the load is provided by a mechanical spindle, the maximum load of the system is ±50 kN. Any load ratio can be selected. Flat and round specimen types that are normally used in fatigue testing can be used. The new testing machine offers new possibilities for investigations of material properties in the very high cycle fatigue (VHCF) regime. Compared to other systems used in the field of VHCF testing the RUMUL GIGAFORTE provides several advantages. The size of the machine is smaller and energy consumption less compared to a servo hydraulic system. The actually tested material volume is larger than the material volume that is tested on ultrasonic systems. The testing frequency of 1000 Hz allows normally continuous testing, without stopping for cooling down the specimen. In the past three years the new testing machine was intensively used for example at the laboratory of the Fraunhofer institute IWS Dresden in Germany. Effects of the 1000 Hz testing frequency on the fatigue behaviour of the material were observed. This talk shows some example of heating up of the specimen related to the 1000 Hz testing frequency and highlights some of the found frequency related effects on fatigue strength.

Keywords New resonant fatigue testing machine · Giga cycle (VHCF) · Frequency effects

38.1 Introduction

"There is no infinite fatigue life in metallic materials" [1]. Studies on damage mechanism on higher number of load cycles, in the range of up to 1010 cycles and more could well proof the finding published by Claude Bathias and others. Thanks to the

M. Berchtold (✉)
RUMUL Russenberger Prüfmaschinen AG, Neuhausen am Rheinfall, Switzerland
e-mail: mberchtold@rumul.ch

J.A.F.O. Correia et al. (eds.), *Mechanical Fatigue of Metals*, Structural Integrity 7,
https://doi.org/10.1007/978-3-030-13980-3_38

development of faster testing technics and the shortening of testing time a large number of basic research activities took place in the recent decades. Ultrasonic fatigue testing systems work on the resonant frequency at about 20 kHz, and require relatively small specimens with a specific geometry. Ultrasonic fatigue studies showed that a fatigue limit in the traditional sense does not exist in the Gigacycle regime. Cracks may occur subsurface or on the surface, and may start for example from inclusions in the material [1].

Subsequent with higher testing frequency, an old question of fatigue testing is highlighted and cannot be neglected: "What is the effect of the testing frequency on fatigue life?" Testing on very high testing frequency may lead to different damage mechanism than under real loading condition for example of an engine component.

Since inclusions and imperfection play an important role in VHCF the manufacturing process has a significant effect on fatigue life in the Gigacycle regime. Particularly for relatively inhomogeneous materials the testing of material volumes that represents the scatter of the manufacturing process is a concern.

In 2014 RUMUL could present a new resonant fatigue testing machine, with a testing frequency of 1000 Hz. The dynamic load of maximum 50 kN peak-peak is produced with an electromagnetic system, similar to established resonant fatigue testing systems which typically run on testing frequencies from about 40 up to 250 Hz. The static portion of the load is provided by two mechanical spindles, the maximum load of the system is ±50 kN. Any load ratio can be selected. Flat and round specimen types that are normally used in fatigue testing can be used. The new testing machine offers new possibilities for investigations of material properties in the very high cycle fatigue (VHCF) regime. Compared to other systems used in the field of VHCF testing the RUMUL GIGAFORTE provides several advantages. The size of the machine is smaller and energy consumption less compared to a servo hydraulic system. The actually tested material volume is larger than the material volume that is tested on ultrasonic systems. The testing frequency of 1000 Hz allows normally continuous testing, without intermittently stopping the test for let the specimen cool down (Fig. 38.1).

In the past four years the new testing machine was intensively used for example at the laboratory of the Fraunhofer-Institut für Werkstoff- und Strahltechnik IWS in Dresden in Germany. It is used for testing material samples and small components as well. Some effects of the 1000 Hz testing frequency on the fatigue behaviour of the material were observed [2]. Recently the IWS laboratory developed a small salt spray chamber and mounted it on the GIGAFORTE to preform fatigue testing under corrosive atmosphere.

38.2 Effects of the Loading Frequency on Fatigue Life

What is the effect of the frequency of an alternating load on fatigue life and fatigue testing? This question is probably present since beginning of fatigue testing. And it is clear there are frequency effects. For lower frequencies the effects can be neglected

Technical data:	**RUMUL GIGAFORTE 50**
Max. peak value:	50 kN tension/compression
Max. dynamic load range:	50 kN (+/- 25 kN amplitude)
Max. static load:	+/- 50 kN
Max. dynamic stroke range:	0,2 mm (+/- 0,1 mm)
Test frequency:	approx. 1000 Hz *(+/- 3 %)*
Horizontal daylight:	400 mm
Max. vertical test space:	330 mm *
Control modes:	Load, Stroke, Acceleration
Sample types:	round up to M27x2 with and without tread flat, bending
Total weight:	approx. 1200 kg
Sound insulation cabin:	is required! (up to 120 dB) with cabin 80dB measured

Fig. 38.1 1000 Hz fatigue testing machine RUMUL GIGAFORTE with small sound enclosure

very often, however the sometimes unknown magnitude of some effects led to a quite conservative approach of limiting the testing frequency in some areas of fatigue testing. The frequency effects can be divided in three areas: Temperature and environment as extrinsic factors and strain rate as intrinsic factor [2, 3]. The effects may superimpose, and affecting fatigue life in the same or opposite direction.

38.2.1 Temperature

A higher material temperature lowers usually the fatigue life as the ultimate strength of a material is related to the temperature. Some materials show a temperature depending crystallographic transformation that affects the material properties and fatigue life.

Maintaining the specified temperature range is therefore a basic requirement for fatigue testing.

A material specific basic damping is always present when deforming a solid material. Microscopic plastic deformation during cyclic loading leads to additional damping and it is almost completely transferred to heat. The damping energy and corresponding heat that is produced per load cycle and volume is constant for an even axially loaded specimen. The produced heat per time is proportional to the frequency. The resulting material temperature depends as well on the present heat loss, for example the heat flow to the fixture and to the ambient atmosphere. Convectional cooling can be used to control the temperature during testing.

Some material do not show the above described linear relation between temperature and testing frequency, with higher frequency the temperature does not increase

as expected [4]. This finding may point to hardening (resp. softening) mechanism that belongs to the category "strain rate" in this context.

38.2.2 Environment

There are time related mechanisms such as oxidation, corrosion or creep that may a play role for the formation of a new surface during crack initiation and propagation. Depending on the relevance of such mechanisms a significant frequency effect can be expected. For example, it is reported that some investigations show a significant frequency dependency of aluminium alloys on fatigue life. The Aluminium alloy AW-5083 shows almost now frequency effect at 20 kHz on fatigue life in inert atmosphere but in air [3].

38.2.3 Strain Rate

The strain rate is proportional to the testing frequency. During loading in resonant condition the strain rate is not constant. It follows a sinus function. It is thought that the strain rate of irreversible deformation could affect fatigue life significantly.

An influence of the testing frequency at 20 kHz on fatigue life could be found on quenched and tempered steel 50CrMo4 depending on the strength of the material. It was concluded that the found correlation of fatigue life and testing frequency is related to the strain rate and is typical for cubic body centred metals. The frequency effect is mainly seen on the left side, of finite life of the S–N curve [3].

For metastable austenitic steel (1.4301, AISI 304) a frequency effect related to the transformation of crystallographic structures was found during testing at 1000 Hz with the GIGAFORTE. The analyses showed that higher amounts of strain-induced Martensite and lower plastic strain amplitudes are observed when the cyclic experiments are carried out at lower frequency, promoting higher fatigue strengths [2, 5].

38.3 Temperature Records

RUMUL could look into heating up behaviour of material samples in the last year. The specimens have been provided by interested laboratories. For Temperature recording a type K thermocouple was attached on the specimen. Compressed air was used to mitigate heating up if required. Load ratio was selected −1 for all tests.

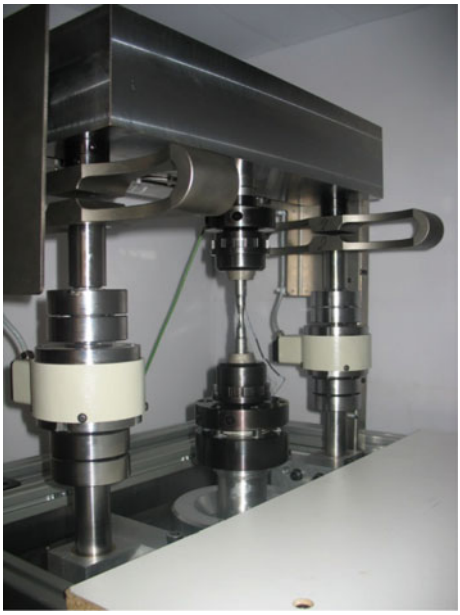

Fig. 38.2 RUMUL GIGAFORTE, round specimen without thread, thermocouple attached with tape

Material	Specimen	Gauge diam. (mm)	Testing condition	Freq. (Hz)	Load amplitude	Temp. (°C)
Nodular Iron	Round, cyl. and hour glass, w. thread	7	Load increasing 0.2 * 10^6 cycles/step compr. air cooling	1011	8.5 kN (220 MPa)	38
9% Cr-steel	Round, hour glass, w. thread	8	Load increasing, 2 * 10^6 cycles/step compr. air cooling	1024	18.6 kN (373 MPa)	26
						54[a]
Ti alloy	Round, hour glass, w. thread	5	Const. load 10^6 cycles/step no cooling	996	5.52 kN (280 MPa)	35
Ferritic steel HV_{30} ~ 220	Round, cyl. w/o thread	8	Load increasing, 10^6 cycles/step no cooling, (Fig. 38.2)	1023	17 kN (337 MPa)	62[b]

[a]Cooling temporarily off
[b]Temperature is not stabilizing, probably softening effect

38.4 Summary and Outlook

The RUMUL GIGAFORTE is an efficient tool for testing very high number of load cycles in a reasonable time. Common specimen types and sizes can be used. Depending on material and load the specimen may heat up. The heating is usually low

or moderate and can be mitigated with compressed air cooling, continuous testing is possible.

The possibility to test on 1000 Hz testing frequency may help to further evaluate frequency effects and further enhance the confidence on fatigue data in the high and very high cycle regime.

References

1. International Journal of Fatigue 93 (2016) 215. In Memoriam Claude Bathias 1938–2015, Haël Mughrabi, Professor Emeritus of Materials Science and Engineering, University of Erlangen-Nürnberg, 91058 Erlangen, Germany
2. Einfluss der Prüffrequenz auf die Rissinitiierung und das Ermüdungsrisswachstum im HCF/VHCF-Bereich am Beispiel des Stahls 1.4301, Tagung Werkstoffprüfung 2016, M. Zimmermann et al. Institut für Werkstoffwissenschaft, Technische Universität Dresden
3. Frequency effect and influence of testing technique on the fatigue behaviour of quenched and tempered steel and aluminium alloy. International Journal of Fatigue 93 (2016) 224–231 N. Schneider et al. State Material Testing Institute and Institute for Materials Technology, Technische Universität Darmstadt, Grafenstr. 2, 64283 Darmstadt, Germany
4. Neue Ansätze für eine Schädigungsenergiehypothese auf der Basis thermischer Messungen, 6. Sitzung des DVM Arbeitskreises Betriebsfestigkeit in Darmstadt, Klaus Stärk
5. Influence of loading frequency and role of surface micro-defects on fatigue behaviour of metastable austenitic stainless steel AISI 304. D.F. Pessoa et. al. Fraunhofer-Institut für Werkstoff -und Strahltechnik IWS, 01277 Dresden, Germany and Institut für Werkstoffwissenschaft, Technische Universität Dresden, 01069 Dresden, Germany

Chapter 39
Influence of Microstructural Inhomogeneities on the Fatigue Crack Growth Behavior Under Very Low Amplitudes for Two Different Aluminum Alloys

T. Kirsten, M. Kuczyk, M. Wicke, A. Brückner-Foit, F. Bülbül, H.-J. Christ and M. Zimmermann

Abstract In the present paper the aluminum alloys EN AW-6082 (peak-aged and overaged) and EN AW-5083 (solution annealed) were investigated regarding the long fatigue crack growth behavior in the range of very low amplitudes and therefore very high number of load cycles. The cracks were initiated at micro notches, prepared by means of focused ion beam technology and examined in situ by a long distance microscope. In first experiments the threshold for each material condition was defined. Subsequently the tests were carried out at constant ΔK values. Further analysis such as electron backscatter diffraction (EBSD) and confocal microscopy were executed to analyze the fatigue crack growth behavior. A microstructural barrier function of the primary precipitates could be detected for each material condition. Grain boundaries seem to influence the crack growth only in case of the work hardening alloy (EN AW-5083), which is the material with smaller average grain size compared to EN AW-6082.

Keywords Ultrasonic fatigue testing · Very high cycle fatigue · Long crack growth behavior

T. Kirsten · M. Zimmermann
Institute for Materials Science, Technical University of Dresden, Dresden, Germany

M. Kuczyk (✉)
Fraunhofer Institute for Materials and Beam Technology, Dresden, Germany
e-mail: martin.kuczyk@iws.fraunhofer.de

M. Wicke · A. Brückner-Foit
Institute for Materials Engineering, University of Kassel, Kassel, Germany

F. Bülbül · H.-J. Christ
Institute for Materials Engineering, University of Siegen, Siegen, Germany

J.A.F.O. Correia et al. (eds.), *Mechanical Fatigue of Metals*, Structural Integrity 7,
https://doi.org/10.1007/978-3-030-13980-3_39

39.1 Introduction

In the course of previous studies on the topic of very high cycle fatigue (VHCF) the behavior of metallic materials at load cycles above 10^7 cycles was thoroughly investigated [1–6]. It has been shown that fatigue cracks can grow even at amplitudes below the classical fatigue limit [7]. A great amount of studies focuses on the crack initiation phase, because of their life determining characteristic. The crack growth phase at low stress amplitudes is therefore not as intensively investigated as of yet.

The aim of the present work is to analyze the fatigue crack growth behavior of two commercially available aluminum alloys (EN AW-6082 and EN AW-5083) at VHCF relevant low stress amplitudes in the near threshold regime at quasi constant stress intensity factors ΔK in order to gain insight into the possible barrier function of microstructural inhomogeneities, such as precipitates and grain boundaries. The test system used in this research is an ultrasonic fatigue testing system, operating at high frequencies, which is therefore predestined for experiments in the VHCF regime. The thresholds for each material were experimentally determined in orientation to ASTM E 647 [8] by means of load shedding method. Here the threshold is determined by continuously decreasing the applied stress amplitude. Applying the load-shedding method to define the long crack threshold can result in threshold values that are slightly overestimated since likely crack closure effects may become effective. However, because of the sample geometry restrictions due to the ultrasonic fatigue testing other methods, such as the method proposed by Tabernig and Pippan [9], were not applicable. Previous studies could show that crack initiation site for aluminum alloys in the VHCF regime may occur in the subsurface region [10]. In order to analyze early crack growth behavior by means of direct optical observation, it is necessary to add an artificial crack starter to the sample surface. Hence a micro notch was inserted by means of focused ion beam technology (FIB).

39.2 Material and Testing

In this study the precipitation hardening alloy EN AW-6082 (Al Si1MgMn) and the work hardening alloy EN AW-5083 (Al Mg4.5Mn0.7) were investigated. Their specific chemical composition can be found in [11].

The microstructure of alloy EN AW-6082 is defined by elongated grains due to the rolling process. The grains are 500–1000 μm long and have a width of about 50–100 μm. The material contains two types of primary precipitates: Mg_2Si and Al(Si,Mn,Fe). In order to investigate the microstructural influence on the crack growth behavior two different aging conditions (peak-aged and overaged) were defined. The heat treatment is given in Table 39.1.

EN AW-5083 was analyzed in the soft-annealed condition with a more globular grain morphology and a size around 25–50 μm. The microstructure is defined by

Table 39.1 Precipitation hardening heat treatment of aluminum alloy EN AW-6082

	Peak-aged	Overaged
Homogenization	540 °C, 1 h	540 °C, 1 h
Quenching	Water	Water
Annealing	200 °C, 4 h	200 °C, 24 h

primary precipitates of type Mg_2Si, $Al_6(Mn,Fe)$. Micrographs of both alloys can be seen in Fig. 39.1.

The fatigue crack growth tests were carried out using an ultrasonic fatigue testing system (BOKU Vienna), which operates at a resonance frequency of about 20 kHz. The electro-chemically polished samples were cyclically loaded in tension-compression mode at a stress ratio of $R = -1$. In order to prevent unintended heating of the samples, the tests were executed in pulse-pause mode without external cooling. In front of the ultrasonic fatigue testing system, a long-distance microscope is installed to monitor the crack growth in situ. The test area is shown in Fig. 39.2a.

The samples have a cylindrical, hourglass shape with a shallow notch in the center area. A micro notch is inserted on the ground of the shallow notch by means of focused ion beam technology to act as a defined crack initiation site (Fig. 39.2b). Due to the

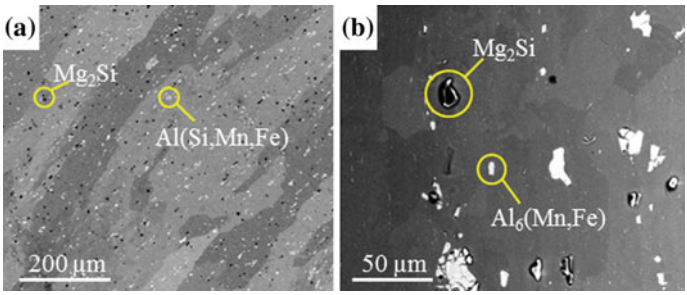

Fig. 39.1 Microstructure with primary precipitates of the investigated material. **a** EN AW-6082, **b** EN AW-5083

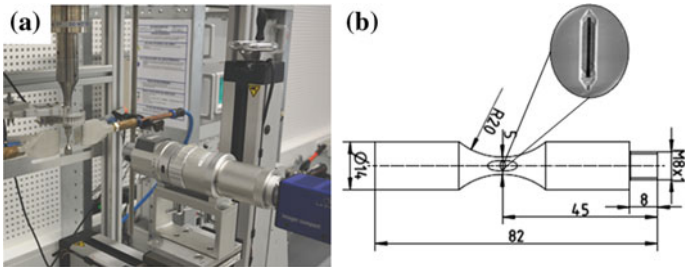

Fig. 39.2 **a** Ultrasonic fatigue testing system with long distance microscope in front. **b** Hourglass shaped sample geometry with micro notch (length: 125 µm)

micro notch the crack propagates in both directions starting from the edges of the FIB notch. For the crack growth curves the overall crack propagation is considered.

In first experiments the threshold for long fatigue crack growth was determined. The threshold was assumed when the crack propagation rate dropped below 10^{-11} m/cycle. Subsequent tests were carried out at quasi-constant stress intensity factors ΔK in the range of the determined thresholds. This was achieved by repeatedly adapting the load amplitude $\Delta\sigma/2$ according to the optical measurements of the crack growth throughout the entire test.

The cracks were afterwards analyzed using scanning electron microscope and electron backscatter diffraction (EBSD) together with an orientation imaging method (OIM) software to gain further insight into the correlation between fatigue crack growth behavior and grain morphology. By determining the slip systems with the highest Schmid factor for grains along the crack path, the crack propagation mode can be defined. Afterwards the samples were cracked under tensile loading to analyze the fracture surface by means of confocal microscopy.

39.3 Experimental Results and Discussion

39.3.1 Fatigue Crack Growth Thresholds

During first experiments the threshold for long fatigue crack growth was determined on the basis of three fatigue crack growth experiments for each material condition. The results are given in Table 39.2.

The results show, that the peak-aged condition has a slightly superior resistance against fatigue crack growth compared to the overaged state regarding the higher threshold value. This is in accordance to the literature [12]. The highest threshold was measured for the work hardening alloy.

Table 39.2 Measured threshold values ΔK_{th} for the materials and heat treatments investigated

	EN AW-6082 peak-aged	EN AW-6082 overaged	EN AW-5083
$\Delta K_{th,1}$ (MPa$\sqrt{m}$)	1.39	1.31	1.45
$\Delta K_{th,2}$ (MPa$\sqrt{m}$)	1.44	1.35	1.56
$\Delta K_{th,3}$ (MPa$\sqrt{m}$)	1.56	1.38	1.69
ØΔK_{th} (MPa$\sqrt{m}$)	1.46	1.35	1.57

39.3.2 Fatigue Crack Growth at Constant Stress Intensity Factors

For analyzing the microstructural influence on the fatigue crack growth behavior the tests were carried out at constant ΔK values. A possible barrier function can be detected by analyzing the crack propagation rate over the crack length as shown in Fig. 39.3. The constant ΔK values for the three materials investigated are all in a similar range compared to each particular threshold. It can be seen that the crack growth rates for alloy EN AW-6082 are showing some slight changes, which can be correlated to microstructural features. Retardations in crack propagation are mainly caused by primary precipitates, especially the Fe-based ones (details can be found in [13]). A pronounced influence of grain boundaries could not be observed for the material. Only in one sample of the overaged condition tested at 1.9 MPa$\sqrt{m}$ the crack growth rate decelerates from $4.7 * 10^{-10}$ to $2.1 * 10^{-10}$ m/cycle near a grain boundary. Since otherwise grain boundaries are not causing any obvious change in crack propagation, it can be assumed, that the effect in the one case is caused not only by the character of the grain boundary itself but more so by its orientation alongside the crack path (details can be found in [13]). Regarding the likely influence of the heat treatment condition, there is no significant difference detectable between the overaged and the peak-aged condition.

In comparison to the aforementioned results, the curve of alloy EN AW-5083 shows a higher variability and in addition demonstrates a smaller average crack growth rate. Reasons for that might be the smaller average grain size of the alloy. Analyzing the crack path by means of EBSD it can be seen that the crack is deflected several times after passing grain boundaries (see Fig. 39.4), which causes a crack growth retardation, especially when the grain size is small and there are many grain boundaries ahead of the crack tip.

It can be seen, that the fatigue crack path depicted in Fig. 39.4 propagates at some points in a shear-controlled manner even though the crack is in long crack growth range (white arrows indicate the direction of highest Schmid factor in Fig. 39.4).

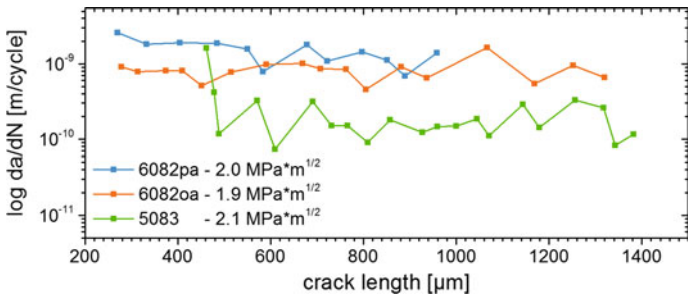

Fig. 39.3 Crack growth rate versus crack length for the three materials investigated at constant ΔK values

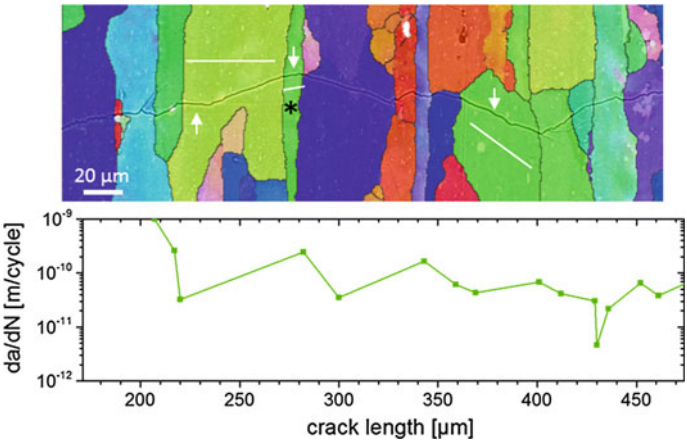

Fig. 39.4 EBSD analysis for EN AW-5083 at $\Delta K = 2.1$ MPa$\sqrt{m}$ (white lines indicate orientation of slip system with highest Schmid factor) and corresponding crack growth curve

For example the crack propagates through the narrow grain in the middle region (*) under an angle of about 15°. The corresponding slip system with the highest Schmid factor (of about 0.42) has the same orientation at this point of the sample surface. Similar phenomena could not be observed for the alloy EN AW-6082, which can most likely be attributed to the larger grain size. As can be seen in Fig. 39.4 the regions of shear-controlled crack growth are however very limited and occur either only in very small grains or in just a part of a larger grain.

For a further understanding of the crack growth behavior—which is overall a 3D process—the fracture surfaces were analyzed also by confocal microscopy, which can depict the altitude differences for a given fracture surface. For EN AW-5083 at 2.1 MPa$\sqrt{m}$ the fracture surface is very smooth with altitude differences of only about ± 50 µm (see Fig. 39.5). Not only because of that, but also because of the pronounced length to depth ratio of 0.9 it can be assumed that the crack was able to propagate quite steadily and easily into the material. However, because of the post mortem character of this analysis, final conclusions as to the correlation between the microstructural topology and the observed fatigue crack growth behavior on the sample surface cannot be made. A computer tomography (CT) analysis during the experiments would be necessary to reproduce the fatigue crack growth into the material to gain further insight into the role of microstructural barriers.

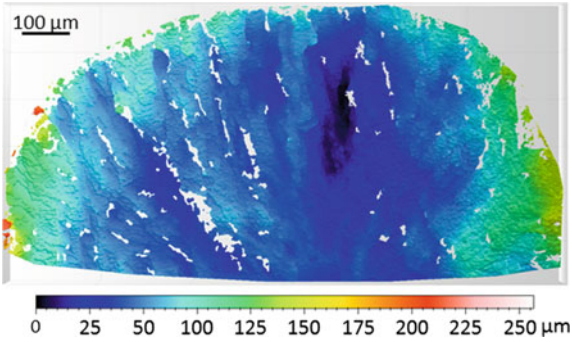

Fig. 39.5 Confocal microscopy analysis of EN AW-5083 at 2.1 MPa$\sqrt{m}$

39.4 Conclusion

The fatigue crack growth behavior for long fatigue cracks in the range of the threshold was investigated. In the present study it could be seen, that there is an influence of the microstructure for all three investigated material conditions. Between the peak-aged and the overaged condition of alloy EN AW-6082 no significant difference was observable. The Fe-based primary precipitates are mainly the cause for a crack growth deceleration. For alloy EN AW-5083 a similar effect of the primary precipitates could be detected, but in addition a minor influence of grain boundaries becomes effective, most likely caused by the smaller grain size and the larger density of grain boundaries. One of the current drawbacks of the results presented is the 2D character of crack path observation. For a further understanding of the fatigue crack growth behavior a CT analysis during the test would give precious new insights into the interaction between primary precipitates and grain morphology.

References

1. Stanzl-Tschegg S, Mayer H (eds) (2001) Proceedings of international conference on fatigue in the very high cycle range, Vienna, Austria
2. Sakai Y, Ochi Y (eds) (2004) Proceedings of 3rd international conference on very high cycle fatigue. Society of Materials Science, Kyoto
3. Allison JE, Jones JW, Larson JM, Ritchie RO (eds) (2007) Proceedings of 4th international conference on very high cycle fatigue. TMS Publications, Ann Arbor
4. Berger C, Christ H-J (eds) (2011) Proceedings of 5th international conference on very high cycle fatigue. DVM-Verlag, Berlin
5. Wang QY, Hong YS (eds) (2014) Proceedings of 6th international conference on very high cycle fatigue. CD-ROM, Chengdu
6. Zimmermann M, Christ H-J (eds) (2017) Proceedings of 7th international conference on very high cycle fatigue. Siegener Werkstoffkundliche Berichte, Siegen
7. Berger C, Pyttel B, Schwerdt D (2008) Beyond HCF—is there a fatigue limit? Materialwiss Werkstofftech 10(39):769–776
8. ASTM E 647-11 (2011) Standard method for measurement of fatigue crack growth rates. American Society for Testing and Materials (ASTM), Philadelphia

9. Tabernig B, Pippan R (2002) Determination of the length dependence of the threshold for fatigue crack propagation. Eng Fract Mech 69:899–907
10. Bach J, Höppel HW, Prell M, Göken M (2014) Crack initiation mechanisms in AA6082 fatigued in the VHCF regime. Int J Fatigue 60:23–27
11. DIN EN 573-3:2013-12, Aluminium und aluminiumlegierungen—chemische zusammensetzung und form von halbzeugen—teil 3: chemische zusammensetzung und erzeugnisformen (EN 573-3:2013)
12. Zaiken E, Ritchie RO (1985) Effects of microstructure on fatigue crack propagation and crack closure behavior in aluminium alloy 7150. Mater Sci Eng 70:151–160
13. Kirsten T, Bülbül F, Wicke M, Christ H-J, Brückner-Foit A, Zimmermann M (2018) Influence of microstructural discontinuities on the behaviour of long fatigue cracks in the VHCF regime for the aluminium alloys EN AW 6082 and EN AW 5083. In: Matec web of conference, vol 165, p 20005

Chapter 40
Effect of Ultrasonic Deep Rolling on High-Frequency and Ultrasonic Fatigue Behavior of TC4

Yi-Xin Liu, Yun-Fei Jia, Xian-Cheng Zhang, H. Li, Run-Zi Wang and Shan-Tung Tu

Abstract A gradient nanostructured (GNS) surface layer was produced on TC4 samples by means of ultrasonic deep rolling (UDR). Grain size refined to nano-scale and increased to macro-scale with the increasing depth. The microstructure of the UDRed sample was observed and the mechanical properties of UDRed samples were measured. The Roughness of samples after rolling is reduced by 60% with the comparison of un-treated sample. The micro-hardness increased with the increasing rolling passes. After the measurement of mechanical properties, the fatigue tests were carried out and the fatigue life of UDRed samples shows were lower than that of un-UDRed samples on high-frequency and ultrasonic fatigue. The fatigue fracture and the initiation of cracks have been investigated to clarify the fatigue mechanism of the UDRed samples. The results showed that the decrement of fatigue life of UDRed samples compared with coarse-grain samples was attributed to the fever in cyclic loading induced by the heterogeneity of the material.

Keywords Ultrasonic deep rolling · Ultrasonic fatigue · High-frequency fatigue

40.1 Introduction

Nano-crystalline materials have higher strength than coarse-grain materials, while the lower tensile plasticity restricted its application. The results of high-cycle fatigue tests and fatigue crack propagation experiments of nano-crystalline Ni [1, 2] showed that the abilities of anti-crack propagation of ultra-fine grained material and nano-crystalline material greatly reduced compared to coarse grain.

As the fatigue cracks usually initiate at material surface and propagate to interior, one may expect to effectively enhance the global fatigue life by introducing compressive residual stress and strain hardening in near the surface layer. Based on

Y.-X. Liu · Y.-F. Jia · X.-C. Zhang (✉) · H. Li · R.-Z. Wang · S.-T. Tu
Key Laboratory of Pressure Systems and Safety, Ministry of Education, School of Mechanical and Power Engineering, East China University of Science and Technology, Shanghai 200237, People's Republic of China
e-mail: xczhang@ecust.edu.cn

J.A.F.O. Correia et al. (eds.), *Mechanical Fatigue of Metals*, Structural Integrity 7,
https://doi.org/10.1007/978-3-030-13980-3_40

this consideration, a novel approach developed to synthesize the gradient surface nanostructure on metallic materials by means of ultrasonic shot peening (USSP) or ultrasonic deep rolling (UDP). Compared to conventional shot peening or deep rolling process, ultrasonic shot peening or ultrasonic deep rolling could produce a surface nanostructure with higher surface hardness, higher residual compressive stress and deeper compressive stress layer. Significantly enhanced fatigue properties have been observed in gradient nanostructure metallic materials in low-cycle fatigue or high-cycle fatigue life [3–5]. Yet, previous work mainly concentrated on low-cycle fatigue or high-cycle fatigue, the fatigue behavior of gradient nanostructure materials in ultrasonic fatigue and high-frequency fatigue need to be further investigated.

Ti alloy is a widely used material in aerospace, military industry, bio-engineering and medical devices, navigation or offshore industry and other fields because of its high corrosion resistance, light weight and high specific strength. The fatigue behavior of the gradient nanostructure Ti alloy in high-cycle and low cycle fatigue have been tested, but there is still a lack of research of the fatigue properties of the gradient nanostructured Ti alloy in high-frequency fatigue and ultrasonic fatigue. In this work, the roughness, hardness, the depth of refinement layer and the residual stress of the gradient nanostructured Ti alloy samples applied to different rolling parameters are investigated. The fatigue properties of GNS Ti alloy and coarse-grained Ti alloy in high-frequency fatigue and ultrasonic fatigue were also compared.

40.2 Experimental Procedure

40.2.1 Sample Preparation and Fatigue Tests

The test specimen in this study was the TC4 alloy with the following chemical compositions (in wt%) of 4.23V, 6.05Al, 0.15O, 0.002N, 0.03Fe and balance Ti. The initial material was heat-treated at 960 °C for 160 min and air cool for $\alpha + \beta$ phase. The ultrasonic deep rolling was used for the surface treatment. A polished cermet ball of 10 mm in diameter was pressed on the surface (with the static force and dynamic ultrasonic force) of a cylindrical sample, which rotated at the velocity of 100 r/mins. Meanwhile, the cermet ball slid along the rod axis from left to right at a constant velocity of 100 mm/min. The cermet ball of the given force to compel a strong plastic deformation on the surface of the material, resulting in a nanostructure formed on the material surface.

The high-frequency fatigue tests were performed on PLG-100C microcomputer control high frequency tensile fatigue testing machine. This kind of universal electro-magnetic excitation resonance fatigue tester that can perform tensile fatigue tests for metallic materials at 80–250 Hz. The Shimadzus USF-2000 ultrasonic fatigue tester was used for the ultrasonic fatigue tests. The 20 kHz vibration waveform generated by piezoelectric element is amplified and then loaded into the samples of ultra-high frequency loading, suitable for long time fatigue test.

40.2.2 Microstructure Observations and Mechanical Measurements

Cross-sectional observations of the treated samples were performed with the Zeiss optical microscope. To clearly observe the microstructure of the TC4, the polished specimens would be etched at room temperature in a solution of 15% nital. The micro-hardness of the nanostructure surface layer of the TC4 samples of different ultrasonic rolling parameters was measured using HVS 1000 micro-hardness tester. The residual stress values along the depth direction from surface to matrix of UDRed samples were determined by X-ray diffraction using the Proto-iXRD MG40P residual stress tester. Electrolytic polishing was used to remove surface materials layer by layer to measure the residual stress at different depths. The electrolytic polishing solution was 5% perchloric acid and 95% acetic acid solution and the voltage was 30 V.

40.3 Results and Discussions

40.3.1 Observations of Microstructure

40.3.1.1 Surface Roughness Analysis

Figure 40.1a shows the original morphology and roughness and Fig. 40.1b shows the morphology of the sample after ultrasonic rolling (static pressure 450 N, amplitude 15 μm, rolling 50 passes). As shown in Fig. 40.1 taken by the 3D profiler, compared with UDRed sample surface with the roughness Ra = 0.282 μm, there are a lot of scratches on the surface of the original sample and the roughness of the samples is Ra = 0.707 μm. The ultrasonic rolling process reduces the surface roughness of the specimen by 60%. The decrement of roughness might because of the plastic flow on the surface of the specimen. The plastic flow significantly fills in micro-defects, flattens the scratches and greatly reduces the surface roughness.

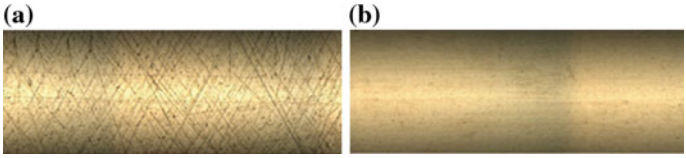

Fig. 40.1 Surface appearance of **a** untreated and **b** ultrasonic deep rolled samples

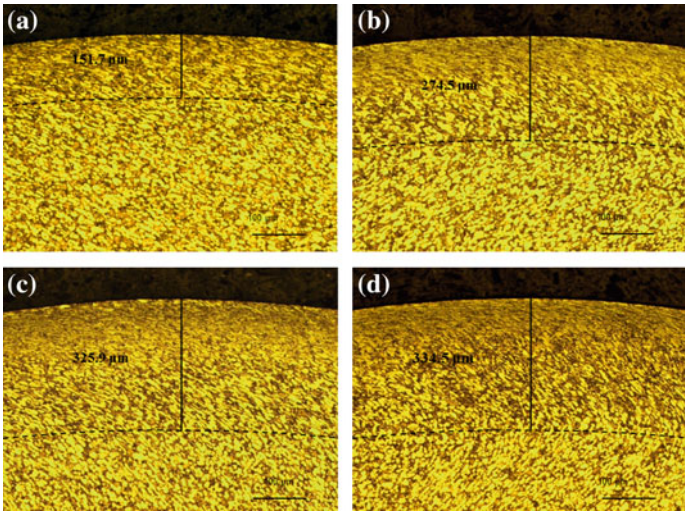

Fig. 40.2 Surface appearance of **a** untreated and **b** ultrasonic deep rolled samples. The cross-sectional microstructure of UDRed TC4 samples with different rolling passs **a** 10, **b** 30, **c** 40, **d** 50 passes

40.3.1.2 Surface Metallographic Observation

As shown in Fig. 40.2, the depth of plastic deformation layers increased with the increasing the number of rolling passes. The surface grains of 30 passes rolled are significantly squeezed and elongated, no longer similar to the matrix grain, as shown in Fig. 40.2b.

As the number of ultrasonic rolling passes is increased to 50 passes, the sheet-like grain structure that has been squeezed and stretched before was further crushed under the repeated impact of the ultrasonic process head, the surface grains were refined to nano-grains by the repeated incision of twin boundaries and dislocations. Meanwhile, the continuous application of the impact on the sample increased the depth of plastic deformation layer, and eventually formed a gradient nanostructure layer from the surface to inside with the gradually reduced plastic deformation (Fig. 40.2d).

40.3.1.3 Micro-Vickers Hardness Distribution

Figure 40.4 shows the hardness distribution along the depth direction of TC4 specimens with different rolling passes. The hardness of TC4 specimen increases with the number of passes. And the subsurface but topmost surface (is about 20 μm from surface) is the site of the maximum hardness value of the UDRed specimen. The maximum hardness values of 40 passes and 50 passes reached 412 HV and 439 HV

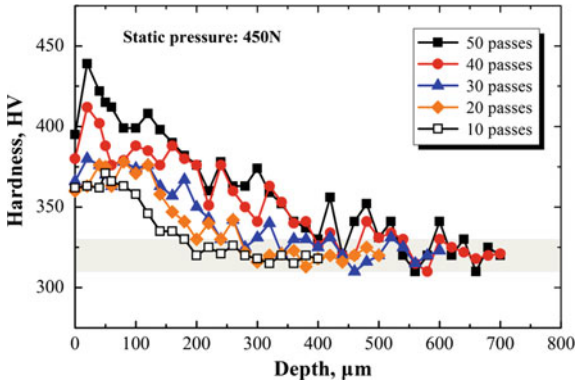

Fig. 40.3 Hardness along depth direction of UDRed TC4 with different rolling passes

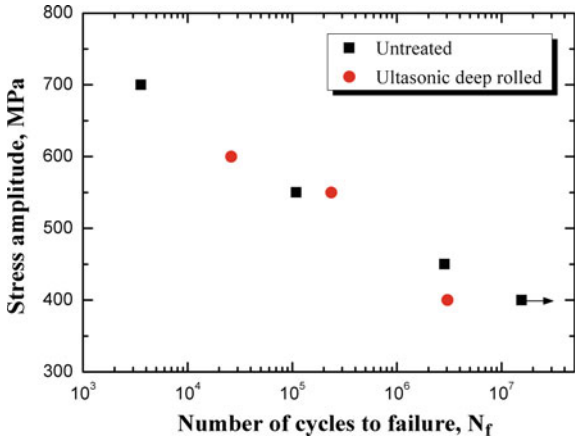

Fig. 40.4 S-N fatigue curves for UDRed and un-treated TC4 under high-frequency fatigue

(Fig. 40.3). Compared to the original sample, the surface hardness increased by 31% and 37%, respectively.

40.3.2 Fatigue Properties of High-Frequency Fatigue

The S-N curves of the UDRed samples are compared with the S-N curves of the untreated samples of high-frequency fatigue (axial tension loading, stress ratio R = −1, loading frequency f = 100 Hz) as shown in Fig. 40.4. Even high-frequency fatigue life has large distribution, the fatigue life of UDRed samples is still generally lower than that of un-treated samples. It is noteworthy that during the fatigue test, even at the sample stress amplitude and frequency, the UDRed sample have severe fever while the un-treated samples did not overheat. That might due to, the surface layer is severe deformed after ultrasonic rolling process, and the severe deformation surface layer needs more energy to further deform.

Therefore, the surface of the sample will elastic re-covery after fatigue tests, and the binding force and density between the surface The fatigue fractures morphologies of the UDRed samples and the un-treated samples were observed as shown in Fig. 40.5. The fatigue crack initiates at the surface and propagates to matrix of the un-treated samples shown in Fig. 40.5a. The clear river patterns of Fig. 40.5b is one of characteristics of cleavage fracture. Different from the fracture morphology of the un-treated sample, the fatigue crack initiates at the sub-surface, and radiate around (see Fig. 40.5c). The cleavage step can be clearly seen in Fig. 40.5d.

40.3.3 Fatigue Properties of Ultrasonic Fatigue

The S-N curves of the UDRed samples with different rolling passes are compared with the S-N curve of the untreated samples of high-frequency fatigue (axial tension loading, stress ratio $R = -1$, loading frequency $f = 20$ kHz) shown in Fig. 40.6. The surface refinement layer and residual stress layer of 50 passes rolled samples are deeper than that of 30 passes rolled samples, but the fatigue life of both is still lower than fatigue life of un-treated samples.

Different from the fatigue fracture in high-frequency fatigue shown in Fig. 40.5, the fatigue crack of URDed samples and un-treated sample in ultrasonic fatigue both

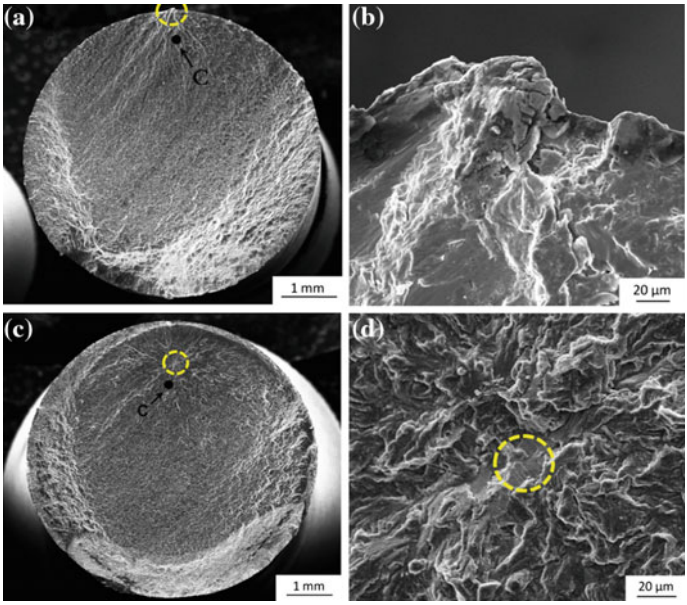

Fig. 40.5 SEM images of the fracture surface of TC4 samples under high-frequency fatigue **a**, **b** un-treated **c**, **d** ultrasonic rolled sample

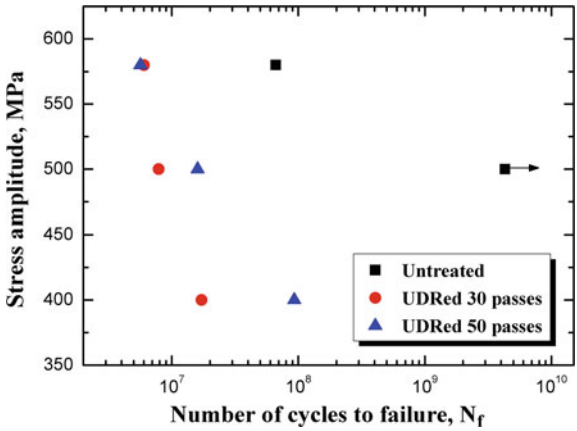

Fig. 40.6 S-N fatigue curves for UDRed and un-treated TC4 under axial loading with 20 kHz

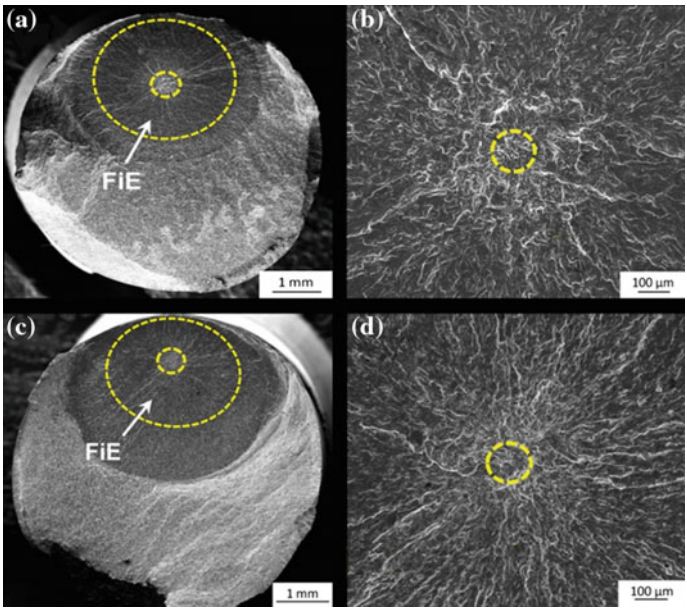

Fig. 40.7 SEM images of the fracture surface of TC4 samples under ultrasonic fatigue **a**, **b** un-treated **c**, **d** ultrasonic rolled sample

initiate at the subsurface as shown in Fig. 40.7. The fish-eye patterns can be clearly seen in the fracture morphology of un-treated sample, and a lot of micro holes formed near the cracks initiation site. And compared to fracture morphology of un-treated samples, many cleavage facets exist near the crack initiation site of UDRed sample.

References

1. Hanlon T, Kwon YN, Suresh S (2003) Grain size effects on the fatigue response of nanocrystalline metals. Scripta Mater 49(7):675–680
2. Hanlon T, Tabachnikova ED, Suresh S (2005) Fatigue behavior of nanocrystalline metals and alloys. Int J Fatigue 27(10–12):1147–1158
3. Tao NR, Wang ZB, Tong WP, Sui ML, Lu J, Lu K (2002) An investigation of surface nanocrystallization. Acta Mater 50:4603
4. Li WL, Tao NR, Lu K (2008) Fabrication of a gradient nano-micro-structured surface layer on bulk copper by means. Mater 59:546
5. Villegas JC, Shaw LL (2009) Nanocrystallization process and mech. Acta Mater 57

Part VIII
Applications/Case Studies

Chapter 41
Microinclusion and Fatigue Performance of Bearing Rolling Elements

E. Ossola, S. Pagliassotto, S. Rizzo and R. Sesana

Abstract Many phenomena are involved in damage of rolling elements of bearings. Rolling contact fatigue is the main cause of failure, along with contact pressure related fatigue and dimensional instabilities effect. Most of those are well known, and are described by wide experimental, analytical and numerical literature. Damage phenomena are related to material properties and manufacturing processes, respectively. Particularly, the damage evolution might be affected by some microinclusions present in the material. This influence is related to mechanical properties, dimension, composition, shape and location of inclusions. This research activity is focused on the 100Cr6 steel alloys. Relation between microinclusions and fatigue life is here investigated. Results of experimental testing run on some test bench are compared to some analytical models for given set of operation conditions. Failures are then analysed to relate life of rolling elements to the microinclusion parameters. The research activity is aimed to investigate whether a microinclusion threshold parameter could be defined, to be related to the life bearing requirements. This analysis is performed by comparing analytical and experimental results of several models and different alloys.

Keywords Fatigue · Bearing · Microinclusion · Structural damage

41.1 Introduction

Bearing fatigue life is influenced by a number of different damage phenomena, including tribological conditions, surface and sub-surface defects and environmental aspects (temperature, corrosion and humidity) [1]. In optimum working conditions, the main cause of damage is Rolling Contact Fatigue (RCF) [2]. Two different phenomena are observed, surface pitting and sub-surface spalling.

E. Ossola · R. Sesana (✉)
DIMEAS, Politecnico di Torino, Turin, Italy
e-mail: raffaella.sesana@polito.it

S. Pagliassotto · S. Rizzo
Central Lab - Product Development, Tsubaki Nakashima, Turin, Italy

J.A.F.O. Correia et al. (eds.), *Mechanical Fatigue of Metals*, Structural Integrity 7,
https://doi.org/10.1007/978-3-030-13980-3_41

In well-lubricated bearing rolling elements, the predominant factor of RCF damage is related to non-metallic inclusions located in the subsurface, where the shear stress due to the Hertzian contact is maximum. Inclusions act as stress risers, causing crack initiation and propagation in the material [3]. Even if steelmaking processes have been improved increasing steel cleanliness [4, 5], oxides and non-metallic inclusions cannot be completely removed.

Several experimental, analytical and numerical studies explored the detrimental role of inclusions on fatigue life, considering the effect of size, shape, location and composition [6] of inclusions. It resulted that RCF is influenced by the size of the largest inclusion present in the material or predicted by statistic methods [4]. In this context, in [7] experimental activities conducted on bearing ball steel subjected to different deoxidation post-processes are described. Chemical composition and size of inclusions using X-ray spectroscopy and destructive testing, and the specimens in RCF conditions are tested. It turns out that specimens with larger defects have a lower fatigue life and the chemical composition of the inclusions affects the damage as well. In particular, steel containing Al_2O_3 or Al_2O_3 CaO inclusions exhibited a worse fatigue behavior if compared to specimen containing SiO_2 Al_2O_3 inclusions.

The different performance could be related to the presence of cavities in the former steels (and not in the latter), which act as stress risers around the inclusions. In order to investigate the effect of inclusion size on fatigue life, other researchers [5] are investigating the possibility to simulate controlled defects by drilling small holes in the material. Recently, experimental and numerical activities were described in [8], investigating the stress state in the material near the inclusion, where microstructural changes are observed, referred as "butterfly wings". FEM and Voronoi tessellation were used to develop a model to predict stress distribution near the defect and simulate crack initiation. Varying size, location and composition of the inclusion, it was found that RCF life is strongly affected by defect stiffness and depth. The maximum Von Mises stress is found when high elastic modulus inclusions are present and located at a depth equal to 0.5 times the contact half width. Different inclusion sizes (ranging from 8 to 16 μm) were studied, but no strong influence on stress concentration was found. The experimental evidence of the harmful effect of larger inclusions on fatigue life is mainly due to the fact that statistically they are more likable to lie at the critical depth. In [9] the effect of size, depth and elastic modulus of aluminum oxide inclusions in a steel matrix are explored on stress distribution and crack propagation. Similarly to [8], it was observed that high elastic modulus inclusions cause higher stress peaks. In addition, a critical value of defect depth (0.75 times the contact half width) exists, where the Von Mises stress is maximum. A larger range of inclusion size (5–20 μm), was investigated observing variation in stress areas, but not in maximum stress values. The interaction between multiple inclusions (pairs, clusters and stringers) have been investigated in [10], basing on the Eshelby method.

The current work investigates the effect of micro-inclusions on fatigue life of a steel alloys (100Cr6) for bearing rolling elements. Fatigue damage and failure mechanisms are studied by experimental testing on test bench and analytical models are considered, to relate life of rolling elements to the micro-inclusion parameters. A dedicated 3d model implementing Eshelby model was developed to estimate the

stress distribution surrounding microinclusion. The simulated load corresponds to experimental load applied to a set of ball bearing undergoing fatigue testing. The calculated stresses will be used as input for a life estimation model to estimate the life of the ball bearing. Then experimental and calculated cycle to failure are compared and failure microscopic analysis, along with residual stresses evolution will be performed. It has to be observed that microinclusion position, shape and dimension are introduced in the numerical model after experimental failure observation. This procedure aims at validating numerical model and life estimation model on bearing balls. The complete project is developing an industrial NDT procedure to detect subsuperficial microinclusions, presence, position and shape. Aim of the research is investigate whether a micro-inclusion threshold parameter could be defined.

41.2 Materials and Method

A 3D numerical Matlab solver was developed, implementing Eshelby model [11–13] to estimate the stress distribution around the microinclusion. The main script handles the input data and calls the Eshelby solver and presents the results. The model inputs material and microinclusion mechanical properties, microinclusion geometry and distance from matrix free surface, loading history. The a microinclusion-matrix model was build corresponding to a case study of an experimental failure, as follows.

For what concerns experimental testing, a set of 8 ACBB axially loaded underwent fatigue testing on a test rig. The ball and bearing races are made of 100Cr6 (Young Modulus 210 GPa, Poisson ratio 0.35, Elastic limit up to 2500 MPa).

Axial loading (30,000 N) blocks were applied to the bearings. At the end of each loading blocks, the bearings were disassembled, the balls were inspected to detect superficial microcracks, dimensional variations, superficial defects. Then inner and outer races were substituted with new ones and the new loading block was applied until failure.

Each bearing included a set of regular balls and one including microinclusions. After failure the microinclusions were analyzed.

The case study presented in this paper is a Alumina Al_2O_3 (Young Modulus 375 GPa, Poisson ratio 0.22) spherical microinclusion, 25 μm diameter, 192 μm subsurface, from which the crack nucleated (Fig. 41.1). The failure occurred after 3 milions of cycles.

For what concerns analytical stress estimation, according to Hertz theory, the stresses were calculated in case that no microinclusion was present in the matrix. The resulting estimated stresses are reported in Fig. 41.2. In case of the presence of a microinclusion, which characteristics match with the investigated case study, the calculated equivalent von Mises and Tresca stresses are reported in Fig. 41.3a, b respectively and in Table 41.1. According to Zaretsky model [14], in these conditions, expected life is 1.88 milions cycles.

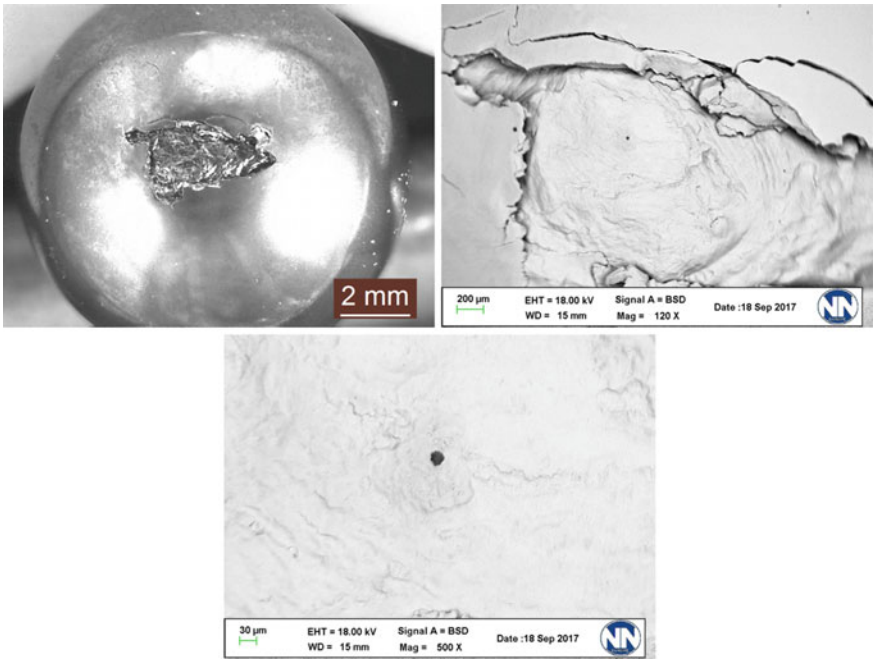

Fig. 41.1 Case study failure surfaces

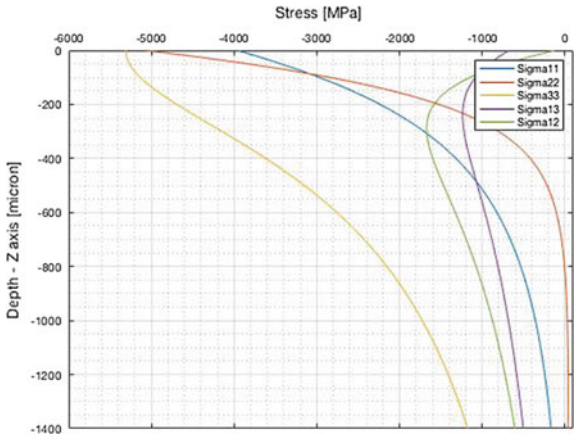

Fig. 41.2 Stress distribution in case of no microinclusions

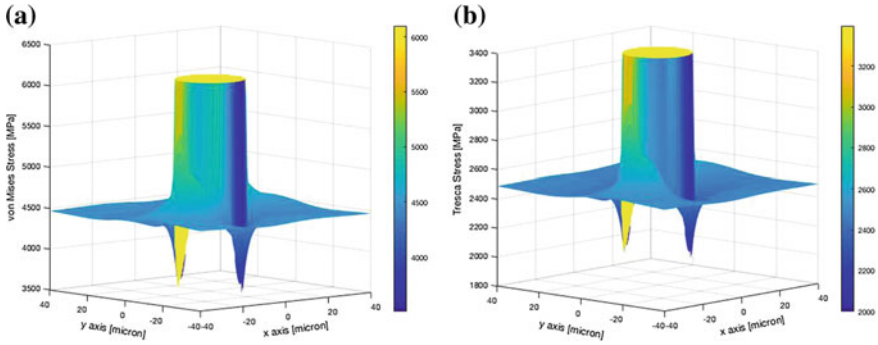

Fig. 41.3 Equivalent calculated stresses in presence of microinclusion: **a** Tresca and **b** Von Mises

Table 41.1 Equivalent stresses

Heading level	No microinclusions (MPa)	With microinclusions (MPa)	% increment
Tresca	2495	3398	36.2
Von Mises	4478	6100	36.2

41.3 Discussion and Conclusions

Numerical stress simulation shows a steep stress gradient in the matrix volume surrounding the microinclusion, and an equivalent stress intensity factor (ratio between equivalent maximum stress and equivalent nominal stress) of 1.36 for both Tresca and Von Mises equivalent stresses. In this condition, the stress reaches the plastic range and, in the matrix, crack can nucleate. Failure surface observation shows that the inclusion appears not affected by failure process. This means that the plastic phenomena could have affected the interface between matrix and inclusion. The consequent stress release can have restored nominal stresses in the matrix and then crack can have propagated in the matrix, slowly, until failure. This experimental observation along with comparison with numerical and analytical results, give important information for a damage and failure model of the ball in presence of microinclusions. In the present research project, more alloys are investigated and further results will be presented in further papers.

References

1. Halme J, Andersson P (2010) Rolling contact fatigue and wear fundamentals for rolling bearing diagnostics-state of the art. Proc Inst Mech Eng Part J J Eng Tribol 224(4):377–393
2. Arakere NK (2016) Gigacycle rolling contact fatigue of bearing steels: a review. Int J Fatigue 93:238–249

3. Tsunekage N, Hashimoto K, Fujimatsu T, Hiraoka KS, Beswick J, Dean W (2010) Initiation behavior of crack originated from non-metallic inclusion in rolling contact fatigue. J ASTM Int 7(2):1–9
4. Unigame Y, Hiraoka K, Takasu I, Kato Y (2007) Evaluation procedures of nonmetallic inclusions in steel for highly reliable bearings. Bearing steel technology-advances and state of the art in bearing steel quality assurance. ASTM Int 7
5. Makino T, Makino T, Neishi Y, Shiozawa D, Kikuchi S, Okada S, Kajiwara K, Nakai Y (2016) Effect of defect shape on rolling contact fatigue crack initiation and propagation in high strength steel. Int J Fatigue 92:507–516
6. Hashimoto K, Fujimatsu T, Tsunekage N, Hiraoka K, Kida K, Costa Santos E (2011) Study of rolling contact fatigue of bearing steels in relation to various oxide inclusions. Mater Des 32(3):1605–1611
7. Ebert FJ (2010) Fundamentals of design and technology of rolling element bearings. Chin J Aeronaut 23(1):123–136
8. Murakami Y, Naoko NY (2002) Influence of hydrogen trapped by inclusions on fatigue strength of bearing steel. Bearing Steel Technology, ASTM International
9. Moghaddam MS, Sadeghi F, Paulson K, Weinzapfel N, Correns M, Bakolas V, Dinkel M (2015) Effect of non-metallic inclusions on butterfly wing initiation, crack formation, and spall geometry in bearing steels. Int J Fatigue 80:203–215
10. Courbon J, Lormand G, Dudragne G, Daguier P, Vincent A (2003) Influence of inclusion pairs, clusters and stringers on the lower bound of the endurance limit of bearing steels. Tribol Int 36(12):921–928
11. Eshelby JD (1957) The determination of the elastic field of an ellipsoidal inclusion, and related problems. Proc R Soc Lond A 241:376–396
12. Meng C, Heltsley W, Pollard DD (2012) Evaluation of the Eshelby solution for the ellipsoidal inclusion and heterogeneity. Comput Geosci 40:40–48
13. Guan J, Wang L, Zhang C, Ma X (2017) Effects of non-metallic inclusions on the crack propagation in bearing steel. Tribol Int 106:123–131
14. Zaretsky E (2010) Rollling bearing life predictions, theory and application. Recent developments in wear prevention, friction and lubrication 37:2

Chapter 42
Strength Analysis of Tramway Bogie Frame

Vaclav Kraus, Miloslav Kepka, Jr., Daniel Doubrava and Jan Chvojan

Abstract The aim of this contribution is to present the development of bogie frames for rail vehicles from the viewpoint of their strength and fatigue life. The manufacturer of the frames described here pays major attention to these aspects during the design, testing and test runs of vehicles. The manufacturer also collaborates with other specialised research facilities. In practice, the development process consists of three stages. The first stage involves stress calculations, the second stage comprises static and fatigue tests and the third one is focused on validating fatigue life data by stress monitoring during test runs on an actual track.

Keywords Tram bogie frame · Strength analysis · Laboratory tests · Stress measurement · Fatigue life prediction

42.1 Introduction

The method of evaluating strength and fatigue life is demonstrated on an example of development of a tramway powered bogie.

42.2 Stress Calculation

The tramway bogie frame of interest is shown in Fig. 42.1. The manufacturer performs computational stress analyses while designing the bogie frame. The company SKODA TRANSPORTATION prefers the ANSYS software.

V. Kraus · M. Kepka, Jr. (✉)
Regional Technological Institute, University of West Bohemia, Pilsen, Czech Republic
e-mail: kepkami1@rti.zcu.cz

D. Doubrava
R&D, SKODA TRANSPORTATION, Pilsen, Czech Republic

J. Chvojan
Research and Testing Institute, Pilsen, Czech Republic

J.A.F.O. Correia et al. (eds.), *Mechanical Fatigue of Metals*, Structural Integrity 7,
https://doi.org/10.1007/978-3-030-13980-3_42

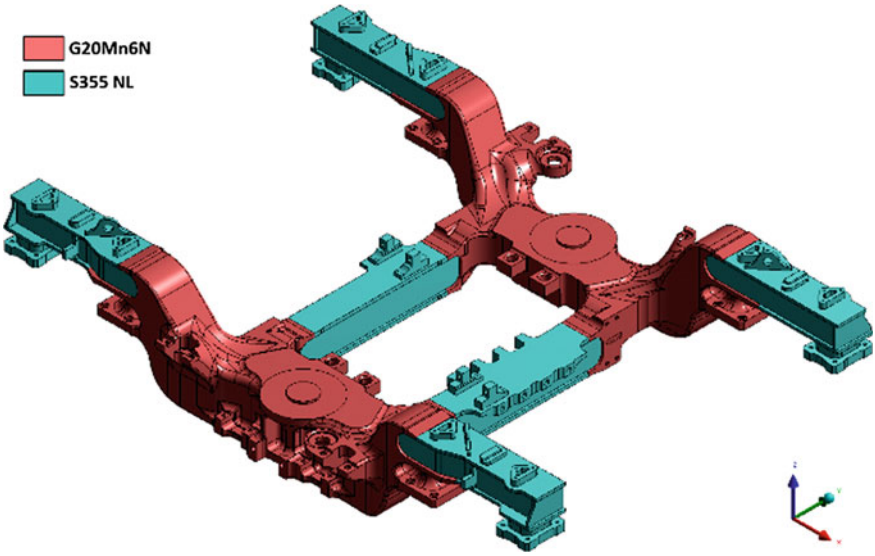

Fig. 42.1 Tramway bogie frame and types of its materials

The bogie frame is modelled using solid elements. The computational model of the frame is presented in Fig. 42.2.

In some locations, typically around weld joints, the mesh is finer to enable stresses in the required distances from the weld joint to be determined; depending on the approach chosen (the nominal approach is the most widely used one). Stress and strain calculations must not be distorted by inadequately defined boundary conditions. An entire sequence of calculations is carried out. Effects of exceptional loads on the

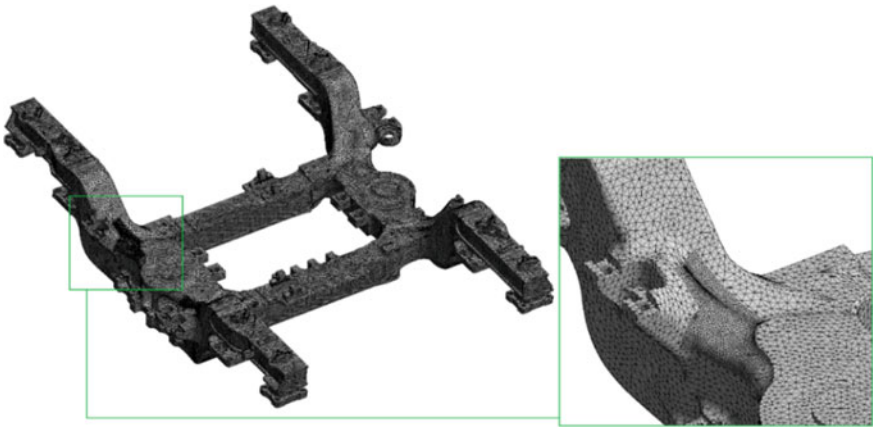

Fig. 42.2 Computational model of bogie frame

bogie frame are analysed and the frame's response to cyclic service loads, which threaten fatigue failure, are examined.

This frame was analysed under 34 separate loading states. Eighteen of those were models of exceptional loads for evaluating static strength. Sixteen loading states were used for evaluating fatigue strength [1]. Forces for these loading states are determined in line with applicable rules. In this case, the standard [2] was used.

Strength and fatigue life are evaluated by combining the results of calculations for individual loading states. The stress state induced by exceptional loads is compared against the allowed values derived from yield stress and ultimate strength of the material of the frame. The resistance of the frame to cyclic loading is evaluated based on its stress response to service loads. Design computations of bogie frames of rail vehicles aim at meeting the endurance limit. In this case, the procedure outlined in [3] was used.

The main limitation to the fatigue life of a bogie is the presence of welds. Before the computation, all weld joints in the bogie frame are classified into notch categories, taking into account the stress and safety categories according to [3].

The upper stress σ_{MAX}, the lower stress σ_{MIN} and the stress ratio R_σ are calculated for all service load combinations. The results are compared with permitted fatigue stress levels. Figure 42.3 is a graphic rendering of this comparison.

Weld joints are assessed using MKJ (Moore-Kommers-Jasper) diagrams, in which the absolute values of the highest principal stress are plotted. These diagrams show the dependence of the limits of the highest principal stress on the stress ratio for individual categories of welds. The curves are plotted for specified levels of probability of survival and safety, as shown in Fig. 42.4.

Calculated results, which are below 75% of the limit value for the relevant MKJ diagram, are considered acceptable.

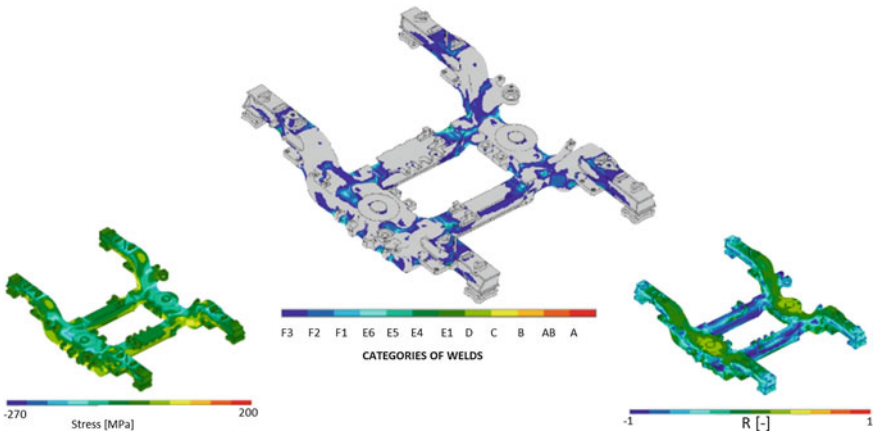

Fig. 42.3 Graphic representation of imported data in the FE model (left: upper normal stress, right: stress ratio and exceedance of endurable upper stress)

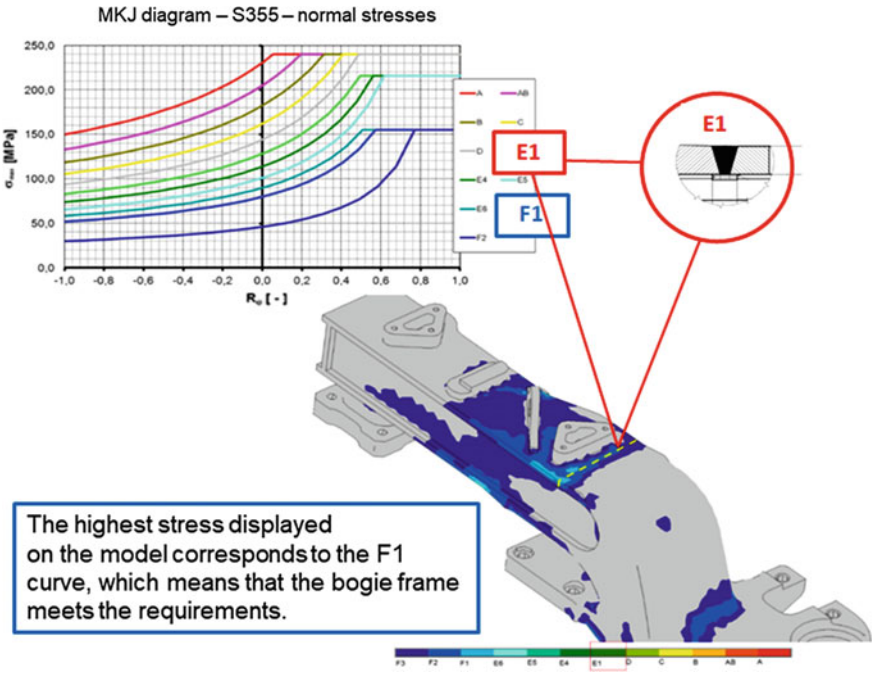

Fig. 42.4 Verification of weld joints according to Haigh diagrams

Where the calculated values exceed this 75% threshold, the stress in the weld joint must be examined more thoroughly, in terms of stresses in individual directions, Fig. 42.5. Using stress calculations, critical regions of the bogie frame are identified. These regions are then fitted with strain gauges for measuring stress levels during laboratory static and fatigue tests and for final measurement during test runs in actual service.

42.3 Static and Fatigue Tests

Before the bogie frame is put into operation, it is tested in a laboratory in static and fatigue tests. The test loads correspond to the loading states employed for computational stress analysis. The laboratory testing methodology was presented in [4]. Static testing involves stress measurement in selected locations of the bogie frame and checking the readings against the values calculated in the previous stage. If these values are in agreement, fatigue testing of the bogie frame proceeds in line with the requirements [2]. The fatigue test setup for this bogie frame is shown in Fig. 42.6.

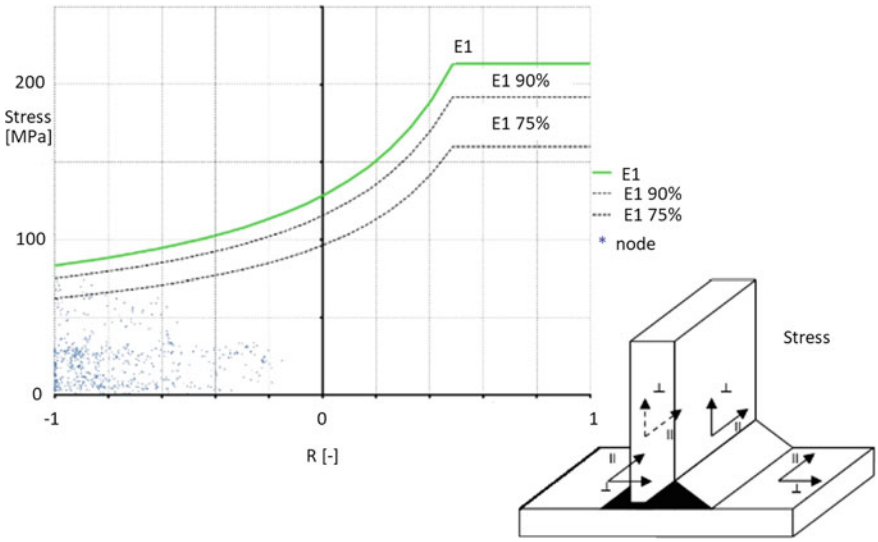

Fig. 42.5 Evaluation for stresses in individual directions

Fig. 42.6 Fatigue test setup

42.4 Fatigue Service Life

Fatigue service life data are validated exclusively on customer's tracks. Before the actual test, a typical load spectrum is determined, which accounts for riding on straight tracks, negotiating curves, short runs in a depot, drive-aways and braking. On-track tests also account for passenger occupation [5]. In these tests, stresses are measured in bogie frame locations identified by the stress analysis and monitored by

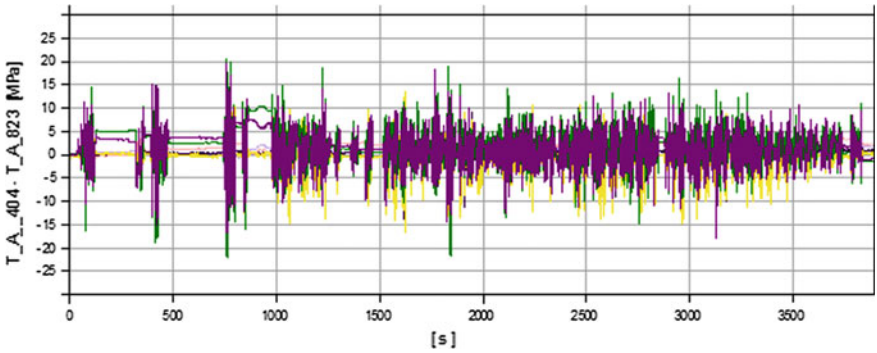

Fig. 42.7 Measured stress-time histories

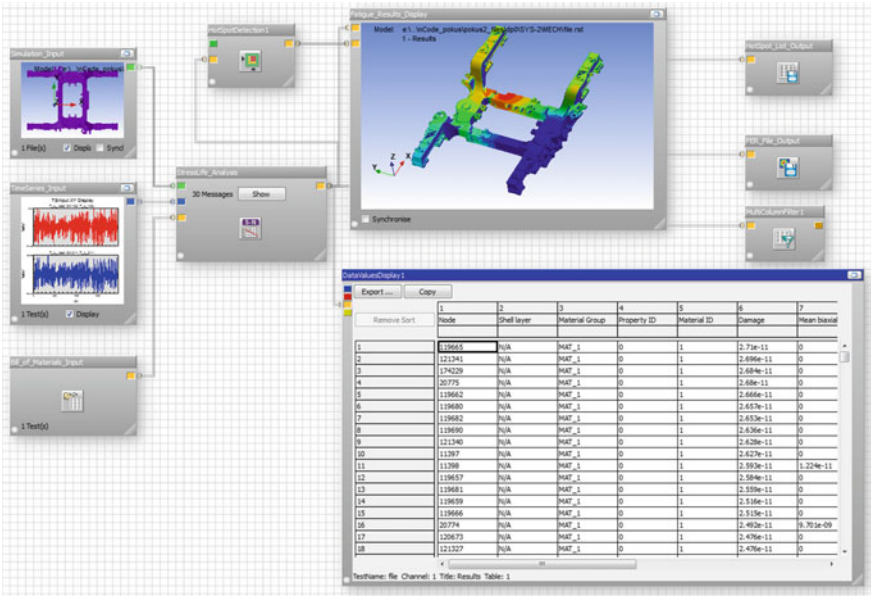

Fig. 42.8 Schematic representation of fatigue life calculation (nCode software)

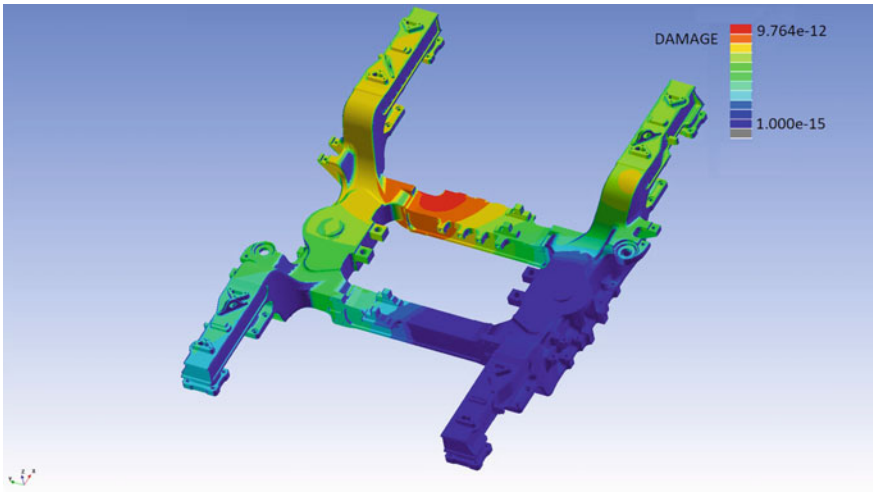

Fig. 42.9 Predicted fatigue life shown on the computational model

strain gauges in fatigue tests. Examples of measured stress-time histories are plotted in Fig. 42.7.

Using the rain-flow method, stress-time histories are converted into stress spectra. The stress spectra and S-N curves for structural details of interest are input into fatigue life calculations based on cumulative fatigue damage according to the Palmgren-Miner rule [6]. A typical fatigue life specification by a customer is between 30 and 40 years (using this value and an estimate of the utilisation in service, the required mileage is derived). The calculation of fatigue life of the bogie frame from measured data is schematically illustrated in Fig. 42.8.

The predicted fatigue life data are reported in the form of tables and, for the sake of clarity, visualized on the model, seen Fig. 42.9.

Acknowledgements The present contribution has been prepared under project LO1502 Development of the Regional Technological Institute under the auspices of the National Sustainability Programme I of the Ministry of Education of the Czech Republic aimed to support research, experimental development and innovation.

References

1. Kraus V, Doubrava D (2014) Strength analysis of the powered bogie frame of 30T tram, SKODA TRANSPORTATION research report (in Czech)
2. CSN EN 13749, Railway applications—wheelsets and bogies—method of specifying the structural requirements of bogie frames, © CNI, July 2005 (in Czech)
3. DVS1612, Gestaltung und Dauerfestigkeitsbewertung von Schweißverbindungen an Stählen im Schienenfahrzeugbau, DVS-Verlag GmbH, August 2014

4. Kepka M, Chvojan J (2015) Remarks to testing of strength and fatigue life of rail vehicle structures. In: Proceeding of the 6th international conference on mechanics and materials in design. LusoImpress, Avintes, S.A., pp 83–84. ISBN 978-989-98832-2-2
5. Kraus V, Cuchy P, Drasky T (2015) On-track strength demonstration test of powered bogie of 30T tram, SKODA TRANSPORTATION research report (in Czech)
6. FKM-Richtlinie (2012) Rechnerischer festigkeitsnachweis für maschinenbauteile aus Stahl, eisenguss—und aluminiumwerkstoffen; 6. Auflage

Chapter 43
A Study of the Shot Peening Effect on the Fatigue Life Improvement of Al 7475-T7351 3PB Specimens

N. Ferreira, J. A. M. Ferreira, J. Jesus, C. Capela and J. D. Costa

Abstract Shot peening is a widely used mechanical surface treatment in the automotive and aerospace industries to improve the fatigue life of metallic components. This work aims to further improvement of the fatigue life on AA7475-T7351 alloy specimens by applying shot peening process using different beads size and bead materials. A systematic study was carried out on the roughness, surface hardening, residual stress profiles and fatigue life. Three point bending (3PB) fatigue tests were conducted. Residual stresses were evaluated by X-Ray diffraction, and the fracture surface was observed and analyzed with a Scanning Electron Microscope. The fatigue test results were plotted in terms of the stress amplitude versus the number of cycles to failure. Since, for this type of loading the initiation of the fatigue process is much localized, the roughness is as or more important than the residual stresses resulting from the shot peening. It was concluded that shot peening does not introduce significant improvement on fatigue life and that the use of glass beads is potentially beneficial.

Keywords Aluminium alloys · Shot peening · Fatigue

43.1 Introduction

Aluminium alloy, AA7475-T7351, is a new aerospace material with improved mechanical properties compared to others, such as 7050 and 7075 alloys [1, 2]. The strengthened aluminium alloys, despite their high tensile strength, have a relatively low fatigue resistance. Shot peening is a widely used mechanical surface treatment to

N. Ferreira · J. A. M. Ferreira (✉) · J. Jesus · C. Capela · J. D. Costa
Department of Mechanical Engineering, CEMMPRE, University of Coimbra, Rua Luís Reis Santos, 3030-788 Coimbra, Portugal
e-mail: martins.ferreira@dem.uc.pt

C. Capela (✉)
Department of Mechanical Engineering, ESTG, Instituto Politécnico de Leiria, Morro do Lena, Alto Vieiro, 2400-901 Leiria, Portugal
e-mail: carlos.capela@ipleiria.pt

J.A.F.O. Correia et al. (eds.), *Mechanical Fatigue of Metals*, Structural Integrity 7,
https://doi.org/10.1007/978-3-030-13980-3_43

improve the fatigue life of metallic components. Each impact produces local plastic deformation whose expansion is constrained by the adjacent material, resulting in a field of surface compressive stresses, with positive effect on fatigue strength [3].

The main shot peening process parameters are the beads material and diameter, process intensity, exposure time, coverage, air pressure, impact angle and nozzle characteristics [4, 5]. Like in steels, fatigue life improvement on shot peening aluminum parts can be, mainly attributed to the compressive residual stresses in the surface region, which very often overcompensates the worsening of surface morphology [6–9]. The shot peening in aluminium alloys causes the work hardening that will be responsible for enhanced resistance to crack initiation, but contrary it causes lower crack growth resistance due to material embrittlement. Then, peening of aluminium alloys, with steel shot can be quite detrimental to fatigue performance. Luo et al. [10], using steel beads, obtained only an increase of 7% in fatigue life for 7075-T6 aluminium specimens, while, on the contrary, Sharp et al. [6], peening with lighter materials, such as glass or ceramic beads, decreased surface roughness and improved the fatigue strength significantly.

The understanding of the improvement in fatigue strength due to surface peening needs still to be better studied in order to enable the development of less conservative designs based on more accurate fatigue life and prediction models. The objective of this paper is to evaluate the shot peening effect, using two different bead diameters and bead materials on the fatigue strength of aluminium 7475-T7351 alloy subjected to pulsating bending.

43.2 Materials and Experimental Procedures

The material used in current work was conducted the 7475 aluminum alloy with a T7351 heat treatment. Table 43.1 indicates the chemical composition of the alloy, according the manufacturer.

Fatigue tests were carried out, using round bone dog specimens 8 mm diameter in center region and tested in three points bending (3PB) as shows Fig. 43.1. All tests were conducted in load control mode, in air and room temperature, at a frequency of 10 Hz and with the stress ratio R = 0.1, using a Instron EletroPuls E10000 machine. Figure 43.1 shows the main dimensions of the specimens and a schematic view of the testing apparatus.

Five batches of samples were prepared: A reference batch of ground and polished specimens and others four with shot peened surfaces. Table 43.2 indicates the bead diameters and bead materials used in different batches. Bead size are according to

Table 43.1 Chemical composition of the 7475-T7351 aluminum alloy (wt%)

Si	Fe	Cu	Mn	Mg	Cr	Zn	Ti	Al
0.1	0.12	1.2–1.9	0.06	1.9–2.6	0.18–0.25	5.2–6.2	0.06	Remaining

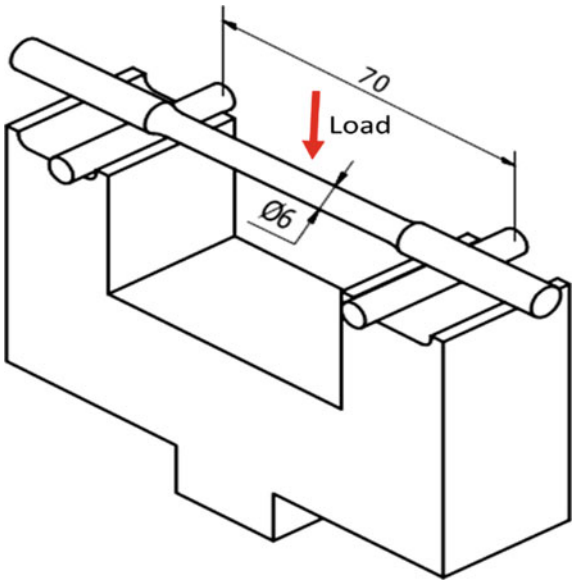

Fig. 43.1 Fatigue testing apparatus

Table 43.2 Parameters for the different shot peening batches

Code	Bead material	Bead size (mm)	Average R_z (μm)
Polished	–	–	4.6
Iron bead—S170	Iron	0.71	24.2
Iron bead—S110	Iron	0.50	20.9
Glass bead—AGB35	Glass	0.50	22.6
Glass bead—AGB8	Glass	0.106	9.3

the specifications and recommendations on ASM 2430 standard for the shot peening of aluminium alloys. Shot peening was done in OGMA, Indústria Aeronáutica de Portugal S.A., using a SURFATEC machine, and with an Almen strip type A. The samples were manually rotated in order to promote the impact angle of the beads on surfaces next to 90° in all zones. The coverage is achieved at 100% when this analysis shows a surface completely attained by the particles. Almen intensity was 0.007 mmA, according ASM 2430 standard.

The microstructure around the surface was observed in microscopy in order to study the effect of the shot peening on. Figure 43.2a–c show exemplary photos.

Figure 43.2a shows the microstructure of the aluminum alloy, presenting the elongated grains, typical of rolled metals. Figure 43.2b, c highlight the surface area where the shot peening occurred in the cases of beads AGB9 and S170, respectively. It was noticed, that S170 beads, with much higher grain size promotes a larger damaged area than the AGB9 beads.

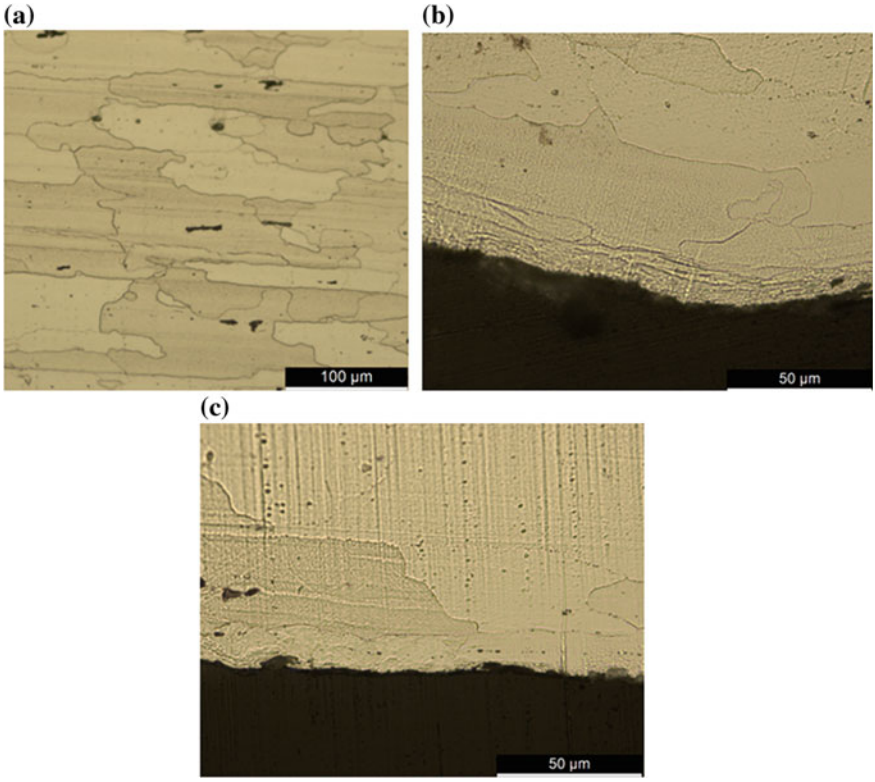

Fig. 43.2 Microstructures: **a** aluminum alloy; **b** peened with S170; **c** peened with AGB9

43.3 Results and Discussion

Figure 43.3 shows the average roughness parameters for the different batches. The results indicated in Fig. 43.3 together with shown in Fig. 43.2 indicate that even the much higher roughness caused by S170 beads the surface profile is smoother, with fewer localized notches than AGB9 beads.

Shot peening promotes usually important changes in hardness and introduce compressive residual stresses. The hardness distribution obtained for the different samples batches, around the surface is presented in Fig. 43.4. The results show some variation from point to point, but they are not influenced by the type of bead used. Unlike normal in most metals is not found hardening caused by the plastic deformation of the grains.

The fatigue test results are plotted in terms of the stress amplitude versus the number of cycles to failure, and are summarized in Fig. 43.5. As usually occurs, and particularly for the type of loading studied in current work, the initiation of the fatigue process is much localized, causing a significant scatter of the results in result of the

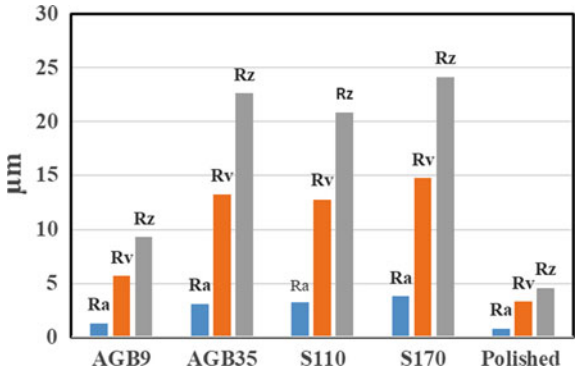

Fig. 43.3 Average roughness parameters for the different batches

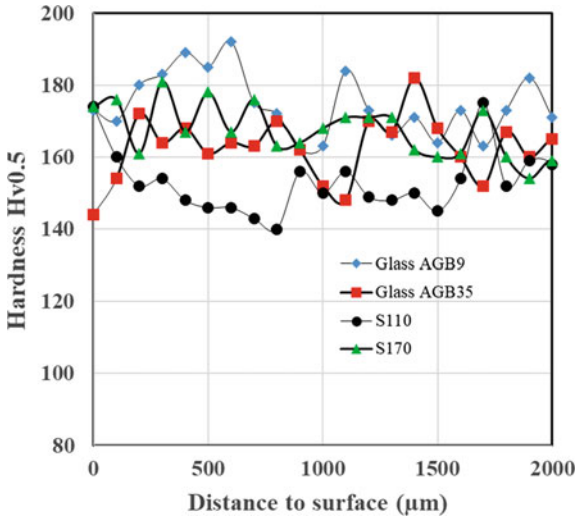

Fig. 43.4 Hardness distribution for the different beads

local residual stresses, hardness and roughness. It was observed that the roughness is as or more important than the residual stresses resulting from the shot peening. It was concluded that shot peening does not introduce significant improvement on fatigue life and that the use of glass beads is potentially beneficial.

43.4 Conclusions

A systematic study was carried out about the roughness, surface hardening, residual stress and fatigue life on three point bending of round specimens of AA7475-T7351 aluminum alloy. The main conclusions were drawn:

- No significant hardening around surface caused by shot peening was observed;

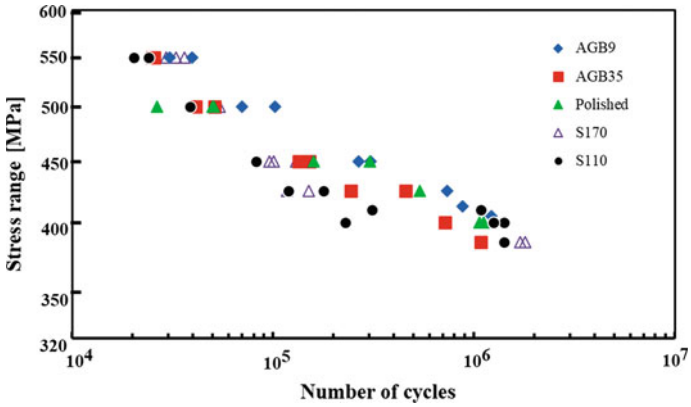

Fig. 43.5 S-N curves for the batches with different shot peening beads and the reference polished samples

- Surface roughness lays an as or more important role than the residual stresses resulting from the shot peening;
- Shot peening does not introduce significant improvement on fatigue life, but the use of glass beads is potentially beneficial.

Acknowledgements The authors would like to acknowledge OGMA-Indústria Aeronáutica de Portugal, Alverca, Portugal, for the collaboration in the supply of samples used in this project. The authors thank also the sponsoring of this research by FEDER funds through the program COMPETE—Programa Operacional Factores de Competitividade—and by national funds through FCT—Fundação para a Ciência e a Tecnologia—under the project UID/EMS/00285/2013.

References

1. Heinz A, Haszler A, Keidel C, Moldenhauer S, Benedictus R, Miller W (2000) Recent development in aluminium alloys for aerospace applications. Mater Sci Eng A 280(1):102–107
2. Kim CY, Choi JM, Song JH (2013) Fatigue crack growth and closure behavior under random loadings in 7475-T7351 aluminum alloy. Int J Fatigue 47:196–204
3. Miková K, Bagherifard S, Bokůvka O, Guagliano M, Trško L (2013) Fatigue behavior of X70 microalloyed steel after severe shot peening. Int J Fatigue 55:33–42
4. Kumar H, Singh S, Kumar P (2013) Modified shot peening processes—a review. Int J Eng Sci Emerg Technol 5(1):12–19
5. Lundberg M, Peng RL, Ahmad M, Vuoristo T, Bäckström D, Johansson S (2013) Influence of shot peening parameters on residual stresses in flake and vermicular cast irons. Mater Sci Forum 768–769:534–541
6. Sharp PK, Clayton JQ, Clark G (1994) The fatigue resistance of peened 7050-T7451 aluminium alloy-repair and retreatment of a component surface. Fatigue Fract Eng Mater Struct 17(3):243–252
7. Wagner L (1999) Mechanical surface treatments on titanium, aluminum and magnesium alloy. Mater Sci Eng A 263:210–216

8. Benedetti M, Bortolamedi T, Fontanari V, Frendo F (2004) Bending fatigue behavior of differently shot peened Al 6082 T5 alloy. Int J Fatigue 26:889–897
9. Turnbull A, de los Rios ER, Tait RB, Laurant C, Boabaid JS (1998) Improving the fatigue resistance of wasp alloy by shot peening. Fatigue Fract Eng Mater Struct 21:1513–1524
10. Luo W, Noble B, Waterhouse RB (1988) The effect of shot peening intensity on the fatigue and fretting behaviour of an aluminium alloy. In: Niku-Lari A (ed) Advances in surface treatments, vol 2. Pregamon Press, Oxford, pp 145–153

Chapter 44
Investigation of Mechanical Properties and Fatigue of Friction Stir Spot Welded Light Metals

Ahmet Atak and Aydin Şik

Abstract The Light metals such as aluminum and magnesium alloys find extensive use in land and air transport vehicles, electronics, computer and sporting goods industries. In order to reduce weight and thus save fuel, many studies are carried out on the development of new engineering materials, which have lightweight and high fatigue strength, especially for the automotive and aviation industry. One of the first metals remembered in this field is magnesium, which has lower density. In contrary to these advantages, joining of light metal alloys with fusion based welding methods have some problems. Since the fusion welding of light metal sheets is difficult, friction stir welding (FSW) method frequently used for joining of these. Studies has shown that shoulder profile of welding tool, which apply pressure on material, affects the welding quality in FSW method. In order to understand these effects various shoulder profile has been studied and understood. FSW method has been investigated and used for joining of materials since about 50 years. In this paper, the pinless shoulder profile designs of stir tool and the mechanical properties and fatigue strength of magnesium and aluminum alloy sheets, which are joined with these stir tools, are aimed to investigate. In order to realize this, shoulder profiles were designed and manufactured accordingly. Subsequently, magnesium and aluminum alloy sheets for automotive and aviation applications were joined with friction stir spot welding (FSSW). Finally, mechanical properties of joined materials such as tensile, tensile shear, bending and fatigue strength were tested. As a result, it has been verified that light metal alloys such as magnesium alloy AZ31B with good ductile and fatigue strength can easily be joined with FSSW. Moreover, joining of light metals with FSSW method has been demonstrated with comparative test and analysis in engineering applications.

A. Atak (✉) · A. Şik
Faculty of Architecture, Department of Industrial Design, Gazi University,
Eti Mahallesi Yükseliş Sokak No: 5, 06570 Maltepe Ankara, Turkey
e-mail: ahmet.atak@gazi.edu.tr

J.A.F.O. Correia et al. (eds.), *Mechanical Fatigue of Metals*, Structural Integrity 7,
https://doi.org/10.1007/978-3-030-13980-3_44

Keywords Friction stir spot welding · Joining of magnesium · Joining of aluminum · Fatigue of light metals · Welding of light metals

44.1 Introduction

Light metals such as aluminum and magnesium alloys generally find extensive use in the field of aerospace industries [1]. Main reason of extensive use of these materials is weight saving and subsequently fuel saving [1–3]. However, significant fatigue strength reduction caused by fusion welded joining (increase of material brittleness and burning) limits the use of these light metals [4, 5]. Other types of joining methods such as rivets, screw connections still have very low fatigue strength caused by notch factor of holes. Use of light metal joining in aerospace, and land vehicles which expose cyclic dynamic loads is quite limited as a consequence of low fatigue strength. In recent years, friction stir welding of light metals are investigated extensively to solve the joining problems of light metals and started to use in many fields [1–5]. FSW joining technique is principally transformation of mechanical energy to heat energy. Main principles of friction spot welding is joining of materials without melting even well below the melting point. This is realized through the heat generated by rotating welding tool on the work piece which softens and plastically deforms the work piece. Since FSW materials are joined at very low temperature, their fatigue strength are generally very high compare to fusion welded materials [6–9].

In this study, FSSW were performed with tool tips having new screw less and different type shoulder profiles, since the tool tip shoulder profile design influences the joining quality. It is aimed to have better fatigue strength with friction stir spot welding (FSSW) compare to fusion spot welding. This study targets to investigate mechanical and fatigue tests of both raw material and joined material. As a result of successful preliminary welding tests, regular and standardized tests were carried out under normal ambient conditions for AZ31B magnesium alloy and the effects were investigated by the following tests:

1. Raw material and FSSW joined material tension test
2. Raw material and FSSW joined material tension test fatigue test.

Magnesium alloy AZ31B which is used in aerospace and automotive to investigate was selected to investigate the mechanical properties of FSSW joining and its effect on fatigue strength. The chemical and mechanical properties of this material are given below according to the standards. The mechanical properties of the material have been verified by the raw material tension tests.

Table 44.1 Chemical properties of magnesium alloy AZ31B [10]

Alloy	Al	Ca	Cu	Fe	Mn	Ni	Si	Zi	Mg
%	2.5–3.5	0.04	0.05	0005	0.2–1.0	0.005	0.1	0.6–1.4	Kalan

Table 44.2 Mechanical properties of magnesium alloy AZ31B [10]

Temper	Tension stress (MPa)	Yield stress (MPa)	Expansion ratio (%)
T4	240	145	≥7

44.2 Material Properties (AZ31B)

Tables 44.1 and 44.2 show the standard chemical composition and mechanical properties of AZ31B sheet material [10].

44.3 Static Tension Tests

Table 44.3 and Fig. 44.1 show the static test results of raw material.

Additionally Table 44.4 shows the static tension/shear test results of FSSW joined sheets.

Table 44.3 Static tension test results of raw material

	Thickness (mm)	Width (mm)	Yield stress (MPa)	Load @ yield stress (MPa)	Tensile stress (MPa)	Load @ tensile stress (N)
Static	1.75	9.92	212	3684.7	290	5032

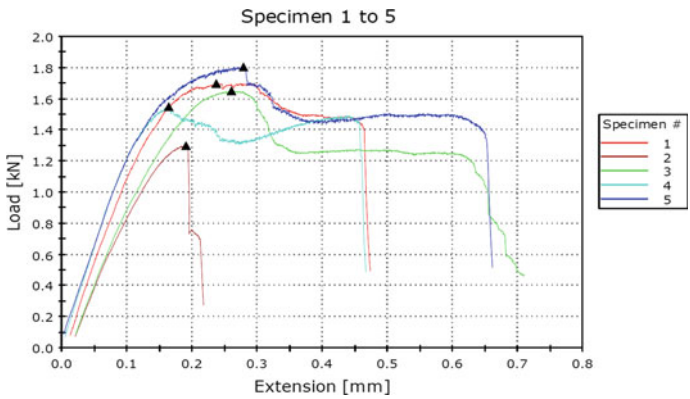

Fig. 44.1 Static tension test results of raw AZ31B magnesium alloyed sheets

Table 44.4 Static tension test results of lab joined FSSW material

	Weld diameter (mm)	Max. load (N)
Static	8	1697.9
		1300.4
		1651.8
		1550.0
		1805.4
	Average	1601.1

Stress distribution calculation in the joining area of fillet welded materials is complicated. Besides, notch factor on this area even makes the calculation more complicated-ted. Therefore only the force dependent fatigue test strength is shown for fillet welded materials. Fatigue strength was measured based on average tension—shear forces of 1601.1 N as shown in Table 44.4.

44.4 Fatigue Tests

Table 44.5 and Fig. 44.2 shows the fatigue test results of raw sample materials.

Table 44.6 and Fig. 44.4 show the fatigue test results of FSSW joined AZ31B samples.

Figure 44.3 shows also the fatigue test results of raw material. Figure 44.4 shows also the fatigue test results of lab joined material.

Table 44.5 The fatigue test results of raw sample materials

	Thickness (mm)	Width (mm)	Max. load (N)	Percent of yield load (%)	Stress (MPa)	Life (Cycles to failure)
Fatigue	1.75	10.2	3280	89.0	184	6.424
	1.75	10.05	2735	74.2	156	30.107
	1.75	10.14	2190	59.4	123	46.927
	1.75	9.99	1917	52.0	110	206.049
	1.75	9.81	1643	44.6	96	1.026.252[a]
	1.75	10.11	1095	29.7	62	1.284.233[a]

[a]Run-out

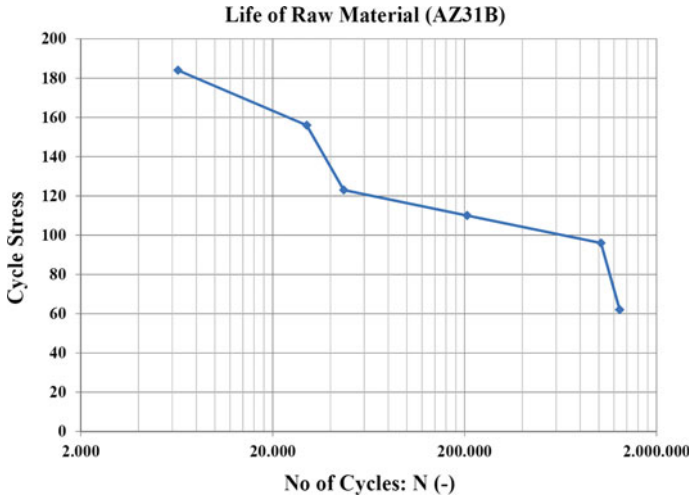

Fig. 44.2 Fatigue test results of raw AZ31B magnesium alloyed sheets

Table 44.6 Fatigue test results of FSSW joined materials

	Weld diameter (mm)	Max. load (N)	Percent of static failure load average (%)	Stress (MPa)	Life (Cycles to failure)
Fatigue	8.0	1209	75.5	*	11.217
		1040	65.0	*	36.814
		871	54.4	*	75.516
		702	43.8	*	121.023
		533	33.3	*	322.831
		364	22.7	*	671.567

*Stress value has to be calculated specific for welding

44.5 Results

- Mechanical properties of AZ31B Magnesium alloy were verified with standard tension test
- Fatigue life of AZ31B magnesium alloy was measured
- Fillet welding of AZ31B magnesium alloy sheets were realized by using FSSW method. Both static strength and fatigue strength of these welded samples were also measured
- Notch effect, which occur with lab joined and spot welding, reduces both the static strength and fatigue life of material. However, this does not mean that the joining is inadequate.

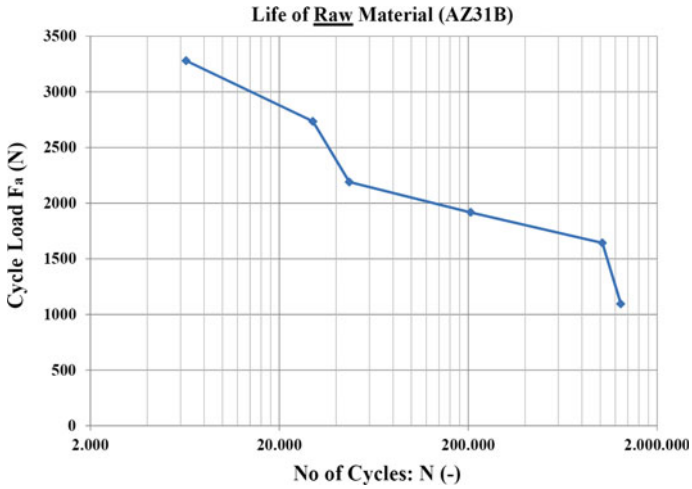

Fig. 44.3 Fatigue test results of raw AZ31B magnesium alloyed sheets

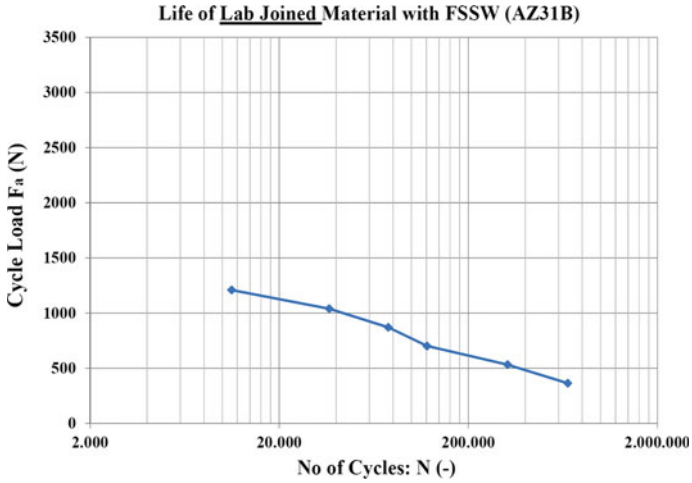

Fig. 44.4 Fatigue test result of FSSW lab joined AZ31B magnesium alloyed sheets

References

1. Atak A, Şik A, Özdemir V (2018) Joining of magnesium alloys with friction stir spot welding (FSSW) method used in automotive sector. In: 9th International automotive technologies congress, OTEKON 2018, Bursa-TURKEY
2. Şik A, Kayabaş Ö (2003) Investigation of fatigue bending endurance of the friction stir welded joint of Aluminum. J Ind Arts Educ Fac 11(12):30–43
3. Şik A (2010) Examination of mechanical properties of magnesium plates joined by friction stir welding. J Sci 14(2), 134–140

4. Su P, Gerlicha A, North TH, Bendzsak GJ (2005) Friction stir spot welding of Aluminum and magnesium alloys. Mater Forum 29, 290–294
5. Külekçi MK, Şik A, Kaluç E (2008) Effects of tool rotation and pin diameter on fatigue properties of friction stir welded lap joints. Int J Adv Manuf Technol 36(9), 877–882
6. Bozkurt Y, Bilici MK (2013) Application of taguchi approach to optimize of FSSW parameters on joint properties of dissimilar AA2024-T3 and AA5754-H22 Aluminum alloys. Mater Des 51, 513–521
7. Tozaki Y, Uematsu Y, Tozaki K (2007) Effect of tool geometry on microstructure and static strength in friction stir spot welded Aluminum alloys. Int J Mach Tools Manuf 47:2230–2236
8. Lathabai S, Painter MJ, Cantin GMD, Tyagi VK (2006) Friction spot joining of an extruded Al-Mg-Si alloy. Scr Mater 55(10), 899–902
9. Bilicim K, Bakir B, Bozkurt Y, Çaliş İ (2016) Taguchi analysis of dissimilar aluminum sheets joined by friction stir spot welding. Pamukkale Univ Müh Bilim Derg 22(1), 17–23
10. ASTM B 107/B 107 M-07, Standard Specification for Magnesium-Alloy Extruded Bars, Rods, Profiles, Tubes, and Wire. Copyright © ASTM International, 100 Barr Harbor Drive, PO Box C700, West Conshohocken, PA 19428-2959, United States

Chapter 45
Advanced Development of Hysteresis Measurement Characteristics for Early Detection of Fatigue Damages on Fasting Systems in Concrete

Marvin Hoepfner

Abstract This paper presents an advanced hysteresis measurement model for the characterization of fatigue failures and corresponding, time-dependent damage processes until final failure of fastening systems in concrete. The developed hysteresis model is based on analytical-physical principals with viscoelastic material properties, four adjustment parameters in combination to secondary additive function components (determined through regression analysis) and uses the measurement data, respective hysteresis loops, in accordance with defined conformation criteria for the first step of approximation. Thus conventional characteristic values of the hysteresis measurement procedure, displacement, cyclic stiffness's and energies could also be defined, even for certain incorrectly and local limited faulty courses, e.g. measurement errors. In a first step, the suitable predictive hysteresis model was applied to experimental fatigue tests of anchor channels in concrete. Further investigations of the four variable parameters led to the potential to identify an indicator for experimental predictions, in relation to specific changes and processes in the shape and area of hysteresis loops at an early stage during the test.

Keywords Fatigue damage · Hysteresis measurement method · Fastening systems

45.1 Introduction

The continuous development of the construction sector with new techniques and structures, as well as its pronounced durability, increases with the requirements by owners and stakeholders, respective societal changes with sustainable use of limited material and financial resources. As a result, the principle of optimal utilization of economical and filigree systems and elements, taking their lifetime into account, is thus observed. To that end, new engineering methods and technologies have been a vehicle for the delivery of advanced systems with optimized performance, particularly against long-term loads, such as repetitive cyclic and dynamic actions.

M. Hoepfner (✉)
Technische Universität Dortmund, August-Schmidt-Str. 8, 44227 Dortmund, Germany
e-mail: marvin.hoepfner@tu-dortmund.de

J.A.F.O. Correia et al. (eds.), *Mechanical Fatigue of Metals*, Structural Integrity 7,
https://doi.org/10.1007/978-3-030-13980-3_45

Structures are dimensioned more efficiently, leading to an increasingly important and critical property of the fatigue resistance, which depends on complex mechanisms. Beyond the fatigue resistance as a single material property, the fatigue failure phenomenon rises in complexity for multi-element systems with combinations of different material, geometries and interactions (as the case is in fastening systems). In order to quantify the characteristics and mechanisms of the damage procedure and to estimate the degradation processes, an advanced hysteresis measurement model is required. In particular, anchor channels, which are under focus in the present study are of great interest since they develop various different failure modes, as well as multiple element failures due to load redistributions.

45.2 Basic Principals

45.2.1 Fatigue and the S/N Curve

Fatigue in general can be described as the physical reaction under varying and periodic mechanical load with properties and phenomenon of structure, composition and materials. The importance and high risk thereby, the load can lead to initial local failure and subsequent global and brittle failure. In structural engineering, mechanical fatigue results from e.g. traffic, wind, periodic machine sequences or other periodic or harmonic load types. The fatigue mechanisms are very specific to the individual material groups. In case of structural steel, the fatigue limit capacity typical is approximately 20% of its short-term strength [1]. Concrete, can exhibit fatigue strength of approx. 40%, thus a significantly longer damage process in relation to steel. Accordingly, when both materials are combined in a constructive system, concrete acts as a confining influence to the system, while the primary influence to the system's fatigue is associated to steel processes [4]. The individual material's fatigue, can solely describe an idealized material property, so it can only be used to a limited extent in characterizing the performance of constructive systems.

In order to describe the fatigue resistance of systems as well as materials, it is commonplace to evaluate the relationship between the number of cycles and the amplitude of load using the S/N curves. In this context, the *Interactive Procedure* by *Block* and *Dreier* was developed in order to evaluate the fatigue resistance after a small number of experimental tests using a statistically robust and accurate regression analysis [1, 7].

45.2.2 Viscoelastic Material Model

In the ideal case of a purely linear, elastic material behaviour, the condition after loading and unloading is fully reversed, and the achieved and stored energy is completely

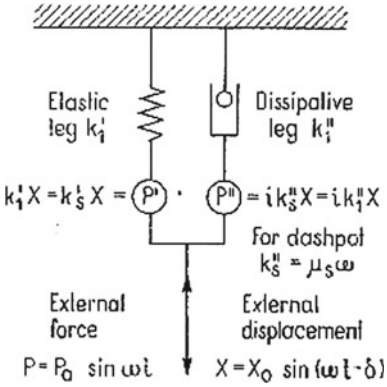

Fig. 45.1 Voigt-type model for viscoelastic materials [6]

returned. In case of multiple cyclic loading even at low loads, inelastic processes in the material occur and the achieved and stored energy will not completely return [2]. If the force-displacement relation is measured for the load cycles, the so-called hysteresis loops result. These illustrate an irreversible energy dissipation through a non-congruent loading and unloading curve in a special loop form. The shape of these hysteresis loops can vary greatly and it depends on the material, respectively the system and a general mechanical description of the mechanisms is highly non-linear and complex. Simplified approaches are based on the typical viscoelastic material model (see Fig. 45.1), which contains properties of viscosity (right side by a damping coefficient k_1'') and elasticity (left side with the spring constant k_1').

Assuming the harmonic sine function is used to describe the external displacement $X(t)$, the force $F(t)$ can be transformed into an elastic component, represented by the spring constant c_f, and the dissipative component, represented by the damping coefficient d according to *Lazan* [6], using the complex exponential form and the assumption of linear material response. The viscoelastic material model representing the special hysteresis ellipse centered in the origin.

As seen in *Lazan's* derivation of the viscoelastic hysteresis loop, the force components of spring stiffness and damping have a certain sine function phase offset by 90° to each other. This effect emerges due to the assumption of a purely linear material response, but complex nonlinearities are inherent to the materials steel and concrete, significantly influencing the shape of the hysteresis loops. However, portions of the stiffness and the dissipative processes, i.e. damping procedures with heat conversion or irreversible deformations, can be allocated [6].

45.3 Hysteresis Model

Fatigue and the associated damage processes can be identified and analyzed through laboratory measured mechanisms of the displacement and force functions, as well as

the hysteresis loops. Herein such an analytical and mechanical model is proposed. This model ensures that conformance criteria are satisfied against test measurement data (appropriate flexibility on loop shapes and correction of measurement errors). Based on the viscoelastic hysteresis model described in the previous chapter, the time function of the elementary imposed displacement $X(t)$ is determined.

In the actual phenomenon, as measurement data show, deviations occur successively at every load step between the extreme values. The realistic simulation of the hysteresis loop requires, that a modification function is used to readjust the sine function with respect to the alternating path amplitude, yet without affecting the extreme values of the sine curve at $x = \sin(\pi/2)$ and $x = \sin(3\pi/2)$. In addition, the equivalence of the function's periods must also be observed. Based on *Lapshin* [5], the modelling of the hysteresis loops can be supplemented by a secondary component in addition to the regular sinusoidal function, i.e. a cosinusoidal function. The unknown adjustment parameters for the sinusoids shape a, b, d and e are determined by least squares regression analysis [3] and are included in the modification functions. Finally, Eqs. 45.1 and 45.2 can provide an optimized approximations of the measured cyclic behavior.

$$s(t) = s_m + s_0 \cdot [\sin(\Omega t + \delta) + a \cdot (\cos(\Omega t + \delta))^{n/2} + b \cdot (-\cos(\Omega t + \delta))^{n/2}] \tag{45.1}$$

$$F(t) = \frac{C_{zyk}}{b_m} \cdot s_m + C_{zyk} \cdot s_0 \cdot [\sin(\Omega t + \delta_1) + (a - d) \cdot (\cos(\Omega t + \delta_1))^{n/2} + (b - e) \cdot (-\cos(\Omega t + \delta_1))^{n/2}] \tag{45.2}$$

where s_m mean displacement; s_0 displacement amplitude; Ω = excitation angular frequency; a, b, d, e = weighting factors; n = power exponent; and $b_m = s_m/\left[\left(F_{max}/C_{cyc}\right) - s_0\right]$ = factor for the mean displacement increase.

45.4 Characteristics of the Adjustment Parameters

The adjustment parameters related to the hysteresis loop curves, exhibit trivial sensitivity on the shape properties and the structural mechanisms on the loading/unloading phase without influence on one another. The influences and characterization of the hysteresis loops through these parameters are presented in Table 45.1.

As mentioned in Sect. 45.2.2 the hysteresis loop can be segregated to an elastic and a viscous component. In the same sense, the advanced hysteresis model discussed herein, and the modification functions can be proportionally elaborated on the basis of energy exchanges. For the parameter combination $a = b = d = e = 0$, and particularly for $a = b$ and $d = e$, the loop consists of a single curve without a circumscribed area, and respectively no damping effect.

In respect to test results, the parameters a and b represent a primarily symmetric development, mirrored over a specific, imaginary axis. A basically opposite behavior

Table 45.1 Parameters and hysteresis loop behaviour

Parameter	Hysteresis loop behavior
$a < 0$, $(a > 0)$	Greater curvature of the loading phase at the lower (upper) half
$b < 0$, $(b > 0)$	Greater curvature of the unloading phase at the lower (upper) half
$d < 0$, $(d > 0)$	Loading curve with a right (left) curvature
$e < 0$, $(e > 0)$	Unloading curve with a right (left) curvature

is shown with a probability of approx. 70% for the entire test group of 15 tests. The geometric properties of the hysteresis loop are affected by the mean value function $W_{sp} = 1/2 \cdot (a + b)$. If a positive value W_{sp} occurs during force-regulated tests, the curvature of the displacement function in the upper half is smaller than in the lower half. If a negative value is obtained, the curvature is opposite.

45.5 Results

Overall, the developed hysteresis model could be applied to the experimental tests of anchor channels and analyzed. With exception of defect measured hysteresis loops an average coefficient of determination of $\bar{R}^2 = 0.9925$ could be realized for a number of 1493 periods. The analysis of the mean value function W_{sp} indicates a significant relationship between the hysteresis shape and the test result. In case of tests, which are loaded on level of fatigue limit bearing capacity without failure, a permanently negative value W_{sp} developed. On the other hand, tests with final failure showed positive values (see Fig. 45.2). This criterion was already confirmed in the entire test group after a low number of cycles and could be used as an early indicator (Table 45.2).

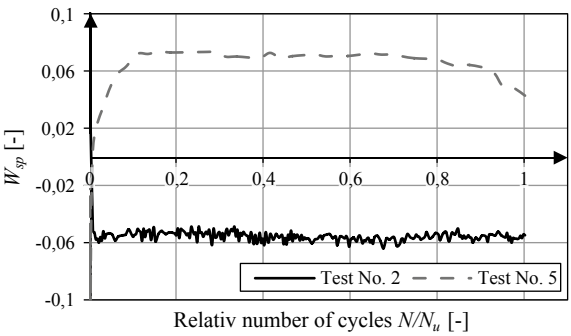

Fig. 45.2 Value W_{sp} for a test on load level of fatigue limit capacity (No. 2) and a test with final fatigue failure (No. 5)

Table 45.2 Hysteresis centroid and value W_{sp} in accordance with the test results

Final result	Number of tests	W_{sp}
No failure, load on level of fatigue limit capacity	4	–
Steel failure	11	+

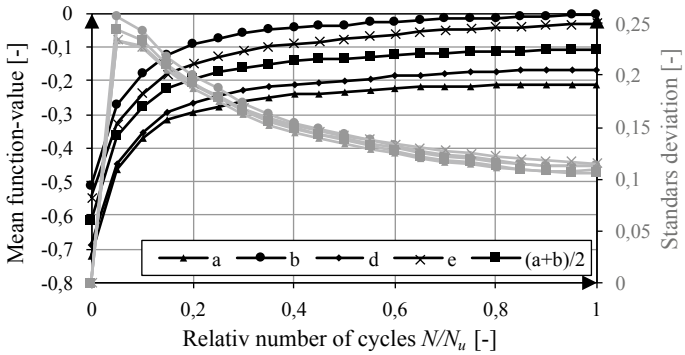

Fig. 45.3 Mean function-value of the adjustment parameters

In the next step, the stabilization of the adjustment parameters is analyzed in order to generate a robust and reliable criterion for the indicator. If the mean function-values of the parameters are determined in relation to the relative number of cycles N/N_u, all tests begin with an initial scatter. In 14 of 15 tests, the values stabilize in the further course and show a horizontal plateau (see Fig. 45.3). The tests with a final failure reach this stage after approx. 50% of N_u, tests on level of fatigue limit capacity (DT) after approx. 30%, respective 2.5×10^6 cycles. In addition, the hysteresis model must be analyzed and further developed with regard to the determination hysteresis function and associated model uncertainties in order to obtain more precise approximations and results, as well as stable and continuous curves of the parameters with a lower scatter.

45.6 Conclusion

A hysteresis model for energetic and detailed investigation of properties and mechanisms of hysteresis loops could be developed and successfully applied with fulfilment of conformance criteria. Additional investigations of the four adjustment parameters can be carried out with regard to the characteristics of the hysteresis centroid and special geometric curvature of the loading and unloading phase and provide indicators for test predictions in relation to the test result, failure or stabilization at an early stage. A basically opposite course of two parameters could be determined in

all tests with a probability of about 70%. The distribution for the early indicator of test results reach a final value for the determined mean function-value at a minimum level of approx. 30%, respective 2.5×10^6 cycles. This generated criterion could be used in the fatigue tests examined. For this purpose, the parameters and associated physical mechanisms are to be verified and stabilized in a next step by using stochastic models.

References

1. Block K, Dreier F (2003) Das Ermüdungsverhalten von Dübelbefestigungen. Beuth Verlag, Berlin
2. Dratschmidt F, Ehrenstein GW (1997) Polymer engineering and science_threaded joints in glass fiber reinforced polyamide. Universität Erlangen-Nürnberg
3. Grossmann W (1969) Grundzüge der Ausgleichsrechnung nach der Methode der kleinsten Quadrate nebst Anwendung in der Geodäsie. Springer Verlag, Berlin, Heidelberg
4. Klausen D, Weigler H (1979) Betonfestigkeit bei konstanterund veränderlicher Dauerschwellbeanspruchung. Beton + Fertigteiltechnik 45, Heft 3
5. Lapshin RV (1995) Analytical model for the approximation of hysteresis loop and its application to the scanning tunneling microscope. Rev Sci Instrum, Am Inst Phys 66(9) (1995)
6. Lazan BJ (1968) Damping of materials and members in structural mechanics. Pergamon Press, New York
7. Maurer R, Block K, Dreier F, Machoczek D, Heeke G (2011) Interactive determination of the fatigue behaviour of reinforcing steel. In: fib Symposium Prag, concrete engineering for excellence and efficiency

Chapter 46
Mechanics and Evaluation of Early Damage

Andrei Kotousov, James Vidler, James Hughes, Aditya Khanna, Ching-Tai Ng and Munawwar Mohabuth

Abstract This chapter describes the microstructural mechanisms leading to damage and the formation of fatigue cracks as well as the methods available to monitor these processes. The evaluation of early damage is especially important for structures with long service life spans, where the crack nucleation stage can dominate the total fatigue life.

Keywords Early damage · Crack nucleation · Fatigue

46.1 Introduction

The decomposition of the total fatigue life, N_T, is commonly represented by two main stages:

$$N_T = N_n + N_p, \tag{46.1}$$

where N_n is the number of cycles required to nucleate a crack and N_p is the number of cycles required to propagate the crack to failure. N_p can be further divided into microstructurally small crack, physically small crack and long crack propagation stages. This chapter is concerned with the crack nucleation stage only. From a microscopic point of view, crack nucleation is a complex process characterised by a transition from an uncracked to a cracked lattice, which can result into crack formations from 1 to 100 μm long in the high cycle fatigue (HCF) regime and from 0.1 to 1 μm in the low cycle fatigue (LCF) range. Crack incubation and crack formation are also often used interchangeably to describe this process [1]. The distinction between crack nucleation and the early stages of crack propagation is difficult to make. N_n can also incorporate the number of cycles required to propagate the crack beyond the first few strong microstructural barriers that can restrict further crack advance.

A. Kotousov (✉) · J. Vidler · J. Hughes · A. Khanna · C.-T. Ng · M. Mohabuth
The University of Adelaide, Adelaide, SA 5005, Australia
e-mail: andrei.kotousov@adelaide.edu.au

J.A.F.O. Correia et al. (eds.), *Mechanical Fatigue of Metals*, Structural Integrity 7,
https://doi.org/10.1007/978-3-030-13980-3_46

The latter might have a significant impact on the fatigue limit and the total fatigue life [2].

The dominant view on fatigue life in the past was that, in all materials, defects are present from the start; so the cracks will propagate right from the first load cycle and therefore, the crack nucleation stage is insignificant in the total fatigue life, or $N_n \ll N_T$. This view is often the case at relatively short life spans, or at high levels of applied cyclic stress [3]. However, if the life span is long, the fatigue crack nucleation stage then occupies an appreciable portion of the total fatigue life. For instance, N_n can range from 5 to 50% of the total fatigue life, in the HCF regime and can fully dominate the fatigue life in the ultra high cycle fatigue (UHCF) regime. It is well known that crack nucleation is also strongly affected by the loading spectra. However, there have been few attempts to assess the effect of variable stress amplitudes on the crack initiation process [4, 5].

The crack nucleation mechanisms can be very different in different materials and these can be advanced or delayed depending on the applied loading. In single crystals as well as in polycrystalline materials, the accumulation of irreversible plastic deformations is considered as one of the most common crack nucleation mechanisms. It involves the localisation of plastic micro-strains within slip bands that normally form intrusions/extrusions at surface grains or impinge on grain boundaries for non-surface grains. The crack nucleation is considered to be the result of progressive microstructural and topological changes due to the accumulation of irreversible plastic micro-strains during repeated load cycles. These progressive microstructural and topological changes in the material during cyclic loading will be termed here as early damage.

The practical significance of the evaluation of early damage, which precedes the crack propagation stage, is obvious, specifically for long life spans or in the HCF and UHCF regimes. This evaluation is critical in situations when subsurface crack nucleation and growth dominates the fatigue life, as many traditional NDT techniques are rendered inappropriate or ineffective for internal defects. In these situations, a damage tolerance approach seems to be difficult or impossible to apply in order to predict the fatigue life and address the structural failure risks with appropriate maintenance and inspection strategies.

46.2 Phenomena Associated with Progression of Early Damage

Cyclic strain localisation and strain accumulation has been proven to be a substantial feature of early damage accumulation. Several phenomena accompanying the latter process can be utilised for the detection and characterisation of its severity as well as the evaluation of structural integrity.

46.2.1 Surface Roughness

In ductile metals, cyclic strain localisation in the form of persistent slip bands (PSB) at the free surface frequently occurs and leads to crack nucleation. The PSB normally consist of a central extrusion and two parallel intrusions, as illustrated in Fig. 46.1, producing a distinct surface morphology. Therefore, the fatigue-induced roughness, in principle, can be distinguished from the initial roughness or machined surfaces [2, 3].

The kinetics of extrusions and intrusions has been studied extensively over the past decade. It was reported in a number of studies that during cyclic loading, the w/h ratio increases with increasing fatigue cycles at a diminishing rate and the ratio normally saturates at about 0.5–1 for fatigue cycles greater than 10^4. Thus, the evolution of surface roughness during fatigue can potentially be utilised as an early damage parameter [5]. Both experimental and numerical studies indicate that an area with high surface roughness may be a precursor of surface crack formation or the transition to the crack propagation stage. However, this approach seems to be inappropriate and ineffective for the evaluation of subsurface crack nucleation, specifically in the UHCF regime which is dominated by interior crack initiation.

46.2.2 Temperature Evolution

As mentioned above, fatigue damage of ductile materials is intimately related to some kind of irreversibility which can be the result of a number of microscopic mechanisms, e.g. cross slip of screw dislocations or mutual annihilation of dislocations. A certain fraction of the work associated with irreversible plastic deformations and other damage mechanisms results in heat generation and this process is often called intrinsic heat dissipation. After the initial shakedown stage of the first load cycles, the

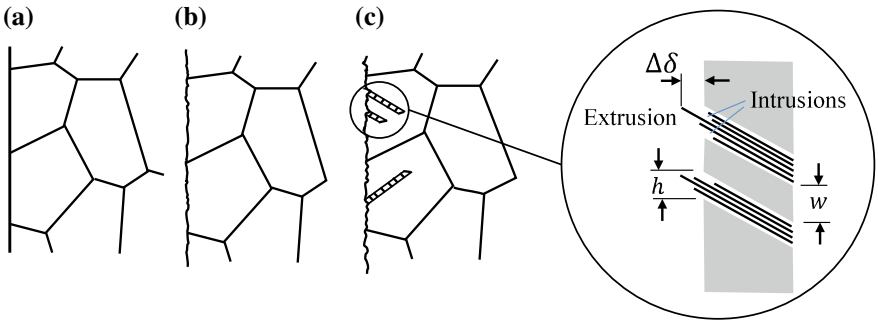

Fig. 46.1 Schematic illustration of surface roughness development [2, 5]: **a**—initial stage; **b**—early stage of surface roughening; **c**—PSB formation. $\Delta\delta$ is the cycle slip displacement, h and w are the slipband width and spacing respectively

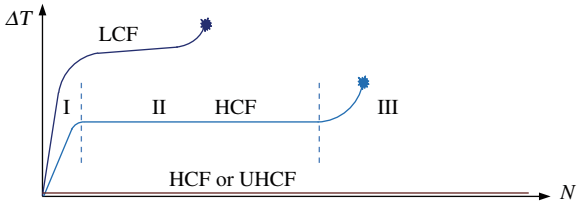

Fig. 46.2 Temperature evolution in different fatigue regimes (constant amplitude of loading)

temperature rise, ΔT, or intrinsic heat dissipation is considered to be representative of the thermal equilibrium state and can therefore be used for damage evaluation.

Extensive studies have demonstrated that there are normally three stages of temperature evolution during fatigue loading if the applied stress range is above the fatigue limit, see Fig. 46.2 [6]. In the initial stage I, the temperature of the specimen's surface increases very quickly until an equilibrium is reached between the heat generation and heat loss. It leads to a stage II which is largely characterised by a stable temperature in the HCF regime or a slight increase of the temperature in the LCF regime. In the final stage III before failure, there is normally a rapid temperature growth associated with the propagation of a macro-crack. The temperature rise depends strongly on the applied stress range and the frequency of loading. In laboratory tests conducted at 1–100 Hz, the temperature rise is typically in the range of 1–50 °C; so these changes can be easily detected by a standard infrared camera.

Experimental observations in the UHCF regime or in the HCF regime at stress ranges below the fatigue limit demonstrate a much smaller magnitude of the temperature rise, largely due to a cessation of cyclic micro-plasticity. Therefore, temperature measurement techniques can be quite effective in the establishment of fatigue limits for different materials working in the HCF regime. But at the same time, it is difficult to apply $\Delta T(N)$ diagrams for the evaluation of progressive damage because in stage II, which dominates the fatigue life, there might be no detectable change in the temperature or heat dissipation. An alternative approach for damage evaluation would be to utilise the initial fatigue stage with rapid temperature changes, i.e. stage I. However, this approach requires a relatively high frequency of the applied loading, which might not be possible in practical situations [6].

46.2.3 Change of Material Constants with Damage Accumulation

It is well known that the total strain tensor, $\bar{\varepsilon}_{ij}$, in a homogeneous solid material of volume, V, containing an arbitrary shear slip system can be written as

$$\bar{\varepsilon}_{ij} = \varepsilon_{ij} + \frac{1}{2V} \sum_r \int_{s_r} (u_i n_j + u_j n_i) ds, \tag{46.2}$$

where ε_{ij} is the microscopic strain tensor, V is the volume of the solid, S_r is the surface of the r-slip band, and u_i and n_j are the displacement and normal vector components at the slip surface, S_r.

Different procedures and methods can be applied to evaluate the effective elastic properties of the solid in the presence of shear slip bands. For uniaxial loading, these averaging procedures normally result in the following equation:

$$E = E_0 \big/ (1 + \kappa\rho), \tag{46.3}$$

where E is the effective elastic modulus of the solid, E_0 is the elastic modulus of the solid without the presence of defects (e.g. slip bands), κ is a constant related to the shape and intensity of the slip bands and ρ is the density of the slip bands. Parameter κ has to be a function of the applied strain, which initiates shear deformations at the slip bands and ρ has to be a function of the accumulated damage, i.e. $\rho = 0$ for undamaged materials. In the case of weak changes in the elastic constants, the effective elastic modulus can be written using the expansion of Eq. (46.3) as

$$E = E_0(1 + \kappa_0\rho) - E_0\kappa_1\varepsilon\rho + O(\varepsilon^2), \tag{46.4}$$

where κ_0 and κ_1 are constants.

The link between the uniaxial stress and strain can now be written as

$$\sigma = E_0(1 + \kappa_0\rho)\varepsilon - \beta\varepsilon^2 + O(\varepsilon^3). \tag{46.5}$$

Experimental observations demonstrate that the change in the elastic moduli (second-order elastic constants) in HCF and UHCF is negligible, i.e. $\kappa_0\rho \ll 1$. The parameter β is the non-linearity constant, which is related to the third-order elastic constants, and is much more sensitive to damage. It can be decomposed as a sum: $\beta = \beta_0 + \beta_d$, where β_0 is the virgin non-linearity (mainly due to the anharmonic response of the lattice) and β_d is the non-linearity due to damage. Therefore, by monitoring the evolution of the non-linearity constant (or, more generally, the third order elastic constants) during fatigue loading, it may be possible to link these changes to damage [7–9].

The non-linearity constant (or, the third-order elastic constants) cannot be determined from ordinary stress-strain diagrams due to the very small changes in the linear response for most structural materials. However, there are two methods based on the generation and sensing of high-frequency ultrasonic waves, which can be utilised for the evaluation of β and subsequently, for monitoring the progression of fatigue damage [9].

The first method exploits the change in the wave speed with the applied strain (i.e. acoustoelastic effect). Bulk, Rayleigh or Lamb waves can be used for accurate evaluation of the non-linearity constant under incrementally applied strains. However, incremental or well-controlled loading is not always possible in real-world applications.

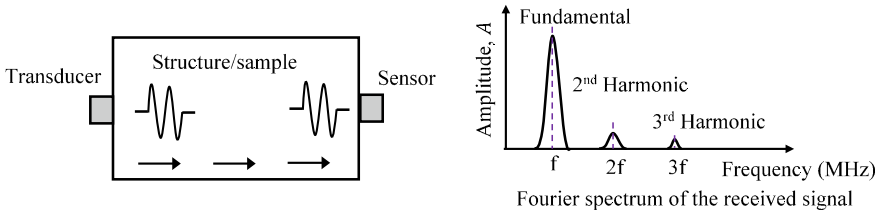

Fig. 46.3 Distortion of the harmonic wavefront in a weakly-non-linear elastic solid

The second method makes use of nonlinear phenomena generated by a strong ultrasonic pulse, e.g. higher harmonic generation. The incident wavefront becomes distorted by the non-linear response, so that higher harmonics are generated as illustrated in Fig. 46.3. The theory predicts that the non-linearity constant $\beta \sim x A_2 / A_1^2$, where x is the distance between the transducer and sensor, and A_1 and A_2 are the amplitudes of the fundamental and the second harmonic respectively. The outcomes of the measurements are normally presented in terms of the ratio of β / β_0 as a function of the fatigue life. There is substantial evidence that this ratio can be used to monitor the microstructural evolution leading to macroscopic damage [7, 8].

The experimental evaluation of β / β_0 is very challenging since the amplitude of the second harmonic is several orders of magnitude smaller than the amplitude of the fundamental frequency. This ratio is also affected by the surface roughness and the diffraction and attenuation of the ultrasonic wave in the propagating medium. Recent studies have reported that the application of non-contact excitation and sensing systems, based on air-coupled ultrasonic transducers and lasers, has considerably improved the signal to noise ratio of the measurements and has reduced the scatter in the experimentally evaluated dependence of β / β_0 upon fatigue damage accumulation. However, it seems that models for predicting the remaining fatigue life or damage based on non-linear ultrasonic measurements are yet to be developed [8].

46.3 Conclusion

This chapter provided a brief overview of the methods available to detect and monitor early damage, i.e. damage which precedes the crack propagation stage. These methods are essential for the safe and efficient operation of machines and structures working in the HCF and UHCF regimes. Various physical phenomena can be utilised to monitor early damage. It can be stated that all these methods are currently in the initial stages of their development. The most promising methods rely on the evaluation of higher-order elastic constants, which are quite sensitive to mechanical damage, as well as measurements of surface roughness, which is directly linked to the accumulation of irreversible plastic deformation at the surface. However, the

latter method might not be efficient in the UHCF regime, where fatigue cracks are formed below the surface.

References

1. McDowell DL, Dunne FPE (2010) Microstructure-sensitive computational modeling of fatigue crack formation. Int J Fatigue 32:1521–1542
2. Mughrabi H (2013) Microstructural fatigue mechanisms: cyclic slip irreversibility, crack initiation. Int J Fatigue 57:2–8
3. Polák J, Mana J (2016) Experimental evidence and physical models of fatigue crack initiation. non-linear elastic damage analysis. Int J Fatigue 91, 294–303
4. Chan KS (2010) Roles of microstructure in fatigue crack initiation. Int J Fatigue 32:1428–1447
5. Meneghetti G, Ricotta M (2012) The use of the specific heat loss to analyse the low- and high-cycle fatigue behaviour of plain and notched specimens made of a stainless steel. Eng Fracture Mech 81:2–16
6. Kim J-Y, Qu J, Jacobs LJ, Littles JW, Savage MF (2006) Acoustic nonlinearity parameter due to microplasticity. J Nondestruct Eval 25(1):29–37
7. Torello D, Thiele S, Matlack KH, Kim J-Y, Quc J, Jacobs LJ (2015) Diffraction, attenuation, and source corrections for nonlinear Rayleigh wave ultrasonic measurements. Ultrasonics 56:417–426
8. Mohabuth M, Kotousov A, Ng CT (2016) Effect of uniaxial stress on the propagation of higher-order Lamb wave modes. Int J Non-Linear Mech 86:104–111
9. Mohabuth M, Kotousov A, Ng CT, Rose LRF, Implication of changing loading conditions on structural health monitoring utilising guided waves. Smart Mater Struct 27(2), 025003

Part IX
Risk Analysis and Safety of Large Structures and Structural Details

Chapter 47
Fatigue Damage Factor Calibration for Long-Span Cable-Stayed Bridge Decks

A. Nussbaumer, J. Oliveira Pedro, C. A. Pereira Baptista and M. Duval

Abstract Part 2 of the Eurocode 3 (EN 1993-2) proposes a straight forward fatigue verification method using a single heavy vehicle model (FLM3) and a damage equivalent factor, λ, to represent the fatigue damaging effects of the real traffic on road bridges. The method is very appealing for bridge design. However, the λ-factor has limitations and is not defined in the EN1993-2 for some load cases or "span lengths" above 80 m, renamed here as "critical lengths". This is the case of cable-stayed bridge decks, where a combination of two internal forces—bending and compression (induced by the stays)—is a characteristic of this bridge system, and stay-cables, with specific shapes of influence lines. To address the above issues a variant solution of the Vasco da Gama Bridge is taken as the case study. In this paper, the results of the λ-factor computed for different critical lengths are compared with previous studies and the original work that led to the current EN formulas for λ. Based on these results, a constant λ value for critical lengths above 80 m is proposed to update the EN for the "mid-span case". For the fatigue design of stays and steel girders, recommendations are given for determining the critical length based on the influence line of the bending moments.

Keywords Fatigue of road bridges · Damage equivalent factor · Long-span · Stays

A. Nussbaumer (✉)
RESSLab, EPFL, Lausanne, Switzerland
e-mail: alain.nussbaumer@epfl.ch

J. Oliveira Pedro
Instituto Superior Técnico, Lisbon, Portugal

C. A. Pereira Baptista
GRID International, Lisbon, Portugal

M. Duval
Losinger Marazzi SA, Lausanne, Switzerland

J.A.F.O. Correia et al. (eds.), *Mechanical Fatigue of Metals*, Structural Integrity 7,
https://doi.org/10.1007/978-3-030-13980-3_47

47.1 Introduction

Fatigue safety verification is an important part in the steel highway and railway bridge design. Part 2 of the Eurocode 3 (EN 1993-2) proposes a simple and fast fatigue verification procedure. It consists in determining the value of the maximum stress range at the location of a specific detail, based on the passage of a unique fatigue load model (FLM3). This stress range is then multiplied by a λ-factor, called damage equivalent factor, to represent the fatigue damaging effects of the real traffic on that bridge detail. This resulting action effect is used in the fatigue verification against the resistance, expressed in terms of stress range of the fatigue detail. It is therefore a straight forward and appealing verification method for bridge design.

One shall mention that a difficulty arises when using the FLM3 Heavy Vehicle (4 axles of 120 kN each) for influence lines of moments over intermediate supports of continuous beams for spans lengths over 40 m, since one passage generates two large consecutive cycles [1]. To keep the number of cycles constant, the additional fatigue damage was expressed instead in terms of stress range, which led to a modified FLM3 in EN 1991-2, by adding a second similar vehicle with a reduced axle load of 36 kN.

In the Eurocode road traffic backgrounds [1, 2], the λ-factors are shown to be related to the bridge static system and influence line shape, represented in the EN 1993-2 by the so-called "span length L" and other characteristics of the relevant influence line (such as internal force type, bridge type, span or support region).

The determination of the "span length L" is function of a number of rules, which are both incomplete and subject to debate. First, to avoid misunderstanding, as the span length is often not to be used as is, the terminology "critical length, L_{cr}" is preferred. Second, the rules are still subject to debate as one main background document is a study for Eurocode 1, railway loads [3]; it contains simulations of railway traffic on bridges, with loading cases and thus effects on influence lines different from road bridges. Third, the rules have no general applicability, their use outside the cases given is thus a matter of interpretation which may lead to errors, and it only considers critical lengths in the range 10–80 m. Fourth and last, no advice is given for the case of cable-stayed bridge decks, with two internal forces combined: bending and compression (induced by the stays). Indeed, it is not clear which one best determines the maximum and minimum stresses to consider.

To address the above problems in the domain of medium to long spans, i.e. excluding the infinite life issue (λ_{max}-factor) typically governing for short influence lines, exploratory studies were carried out using the case study of a variant steel-concrete composite deck solution for the Vasco da Gama Bridge, as well as different typical influence lines of continuous beam type bridges.

47.2 Modeling Traffic Simulations

47.2.1 Modeling of the Cable-Stay Bridge

The Vasco da Gama main bridge has two lateral spans of 204.5 m and a main span of 420 m for an overall length of 829 m between expansion joints, two towers and six piers (three in each side span), which prevent excessive tower's bending and controls the main span deformability, as shown in Fig. 47.1.

For the longitudinal analysis a 2D model is used, with the deck supported by two sets of 32 stays in a semi-harp arrangement. The towers and the piers are in reinforced concrete. For the variant deck, a steel-concrete composite solution is used, with two main steel girders 2.5 m deep for a 30.9 m wide deck (Fig. 47.1) [4, 5]. The stays are directly linked to the main steel girders and are spaced by 13.125 m at the deck level.

The 2D model adopts one half of the deck with a steel concrete composite beam with a concrete deck of 0.25 m thickness and 7.5 m effective width. Since the structure is symmetrical, reference is made only to the left tower and stays, with stays numbered from L1 to L16 for lateral span and from C1 to C16 for central span, starting with the closest one to the tower.

47.2.2 Modeling of the Traffic

To evaluate new λ-factor values for different influence line cases, the method consisted of calculating a stress range with a fatigue load model (FLM3). Then, a realistic continuous design traffic, with vehicles and spacings as shown in Fig. 47.2, was ran-

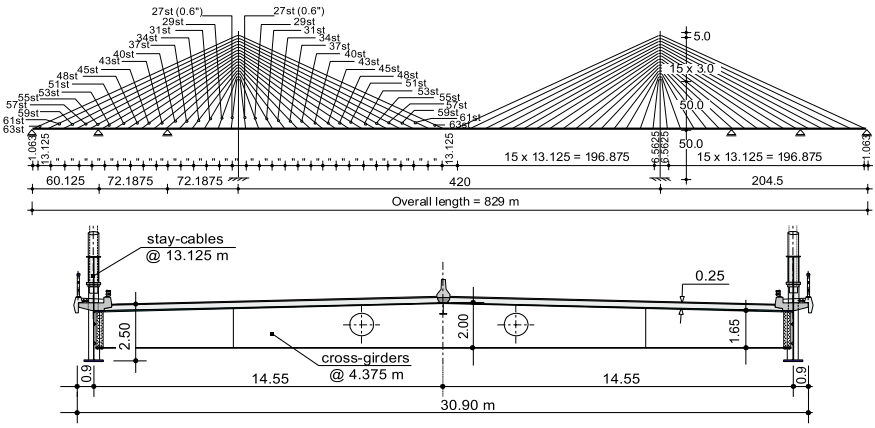

Fig. 47.1 Vasco da Gama Bridge—Variant solution with a steel-concrete composite deck [4, 5]

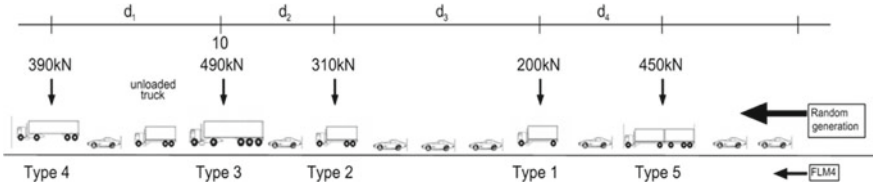

Fig. 47.2 Traffic generation using FLM4

domly generated as a combination of the five Heavy Vehicles (HV) from FLM4 also defined in EN 1991-2, and light vehicles, as described in [6], or using more vehicle types [7].

For the HV's, the traffic composition was defined to represent a worst case scenario, i.e. fatigue design life of 100 years, in accordance to [1]. To do so, the FLM4 long distance HV percentages were used to generate the traffic, with 2/3 of the HV taken as fully loaded and 1/3 as empty, and the HV were assumed to represent 25% of the total traffic in the slow lane. The above assumptions come from a traffic analysis made to develop a probabilistic highway traffic model for fatigue analysis by Baptista [6]. Comparisons with more complex traffic generation showed that a continuous traffic based on FLM4 Heavy Vehicles with the above assumptions was a good approximation of real traffic fatigue effects. In different studies, several simulations of either free-flowing or partially jammed (with stop and go waves) with random distances between vehicles, were used. For long influence lines, i.e. above 40 m, a mix traffic may lead to higher damage, but this was considered not possible in the present studies, were free-flowing traffic was used.

47.2.3 Computation of Damage Equivalent Factor λ

Using an S-N curve with two slopes as in EN 1993-1-9, the damage due to the passage of one typical week of load history was evaluated with the continuous traffic, and then the total damage for 100 years was obtained. One typical week was found to be both sufficiently accurate and efficient, based on the comparison of results with simulations with 1 day, 1 and 10 years. By adapting the S-N curve, a total damage equal to unity can be obtained. When computing stresses, no dynamic amplification factor was considered. The corresponding value of the stress range at 2×10^6 cycles, or say "detail category", is called $\Delta\sigma_{E,2}$. Then the damage equivalent factor λ was evaluated as the ratio between two stress ranges as follows:

$$\lambda = \frac{\Delta\sigma_{E,2}}{\Delta\sigma(Q_{FLM3})} \tag{47.1}$$

where $\Delta\sigma(Q_{FLM3}) = \sigma_{max} - \sigma_{min}$ is the max. stress range resulting from FLM3.

47.3 Results for the Case Study

47.3.1 Critical Length and Stress Range in the Main Deck Girders

Stress influence lines were determined as a combination of both bending and compression influence lines. One can define the stress history in one element, at a specific location, under a 1 kN moving vertical load, and compare their shapes, see Fig. 47.3.

It was found that the axial stress history due to the compression force has little impact on the total stress history and stress range. As it can be seen in Fig. 47.3, the influence line of the total stress in the bottom flange of the deck main girder has a peak very similar to the bending moment influence line. Investigating all positions along the deck, it was found that bending stress accounted for 70–90% of the total stress range. Thus, the bending influence line can be used to define the critical length value; in the presented case, it is similar to a midspan moment of a continuous girder with unequal spans, with the main span equal to $L_{cr} = 27.5$ m. The stress range at each detail can be conservatively obtained by adding the bending stress range with the associated normal stress range (even if the peak stresses are not synchronized).

47.3.2 Critical Length and λ-Factor for the Stay-Cables

The evaluation of the stay's influence lines of Fig. 47.4 show that the lateral stays and the central ones have different shapes, with lateral stays having several humps, whereas central ones have essentially only one hump. The corresponding critical lengths are indicated in the Fig. 47.4 legend. They are similar to an end-span or midspan moment of a continuous girder for the lateral stays, and that of a single span for the central stays. The results of the λ-factor computed for different critical lengths are shown in Fig. 47.5.

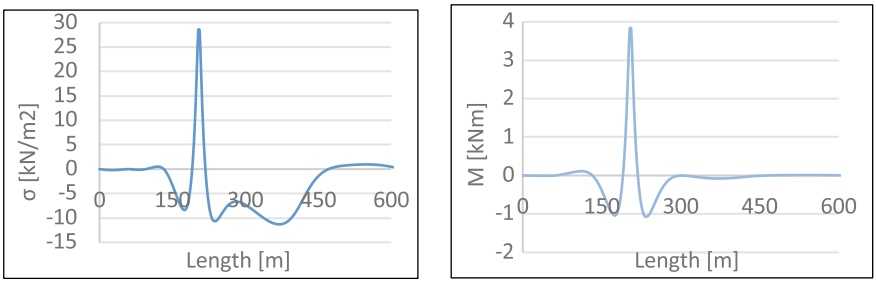

a) Total stress in the bottom flange b) Bending moment in the deck

Fig. 47.3 Example of comparison of main deck girder influence lines (at the tower section)

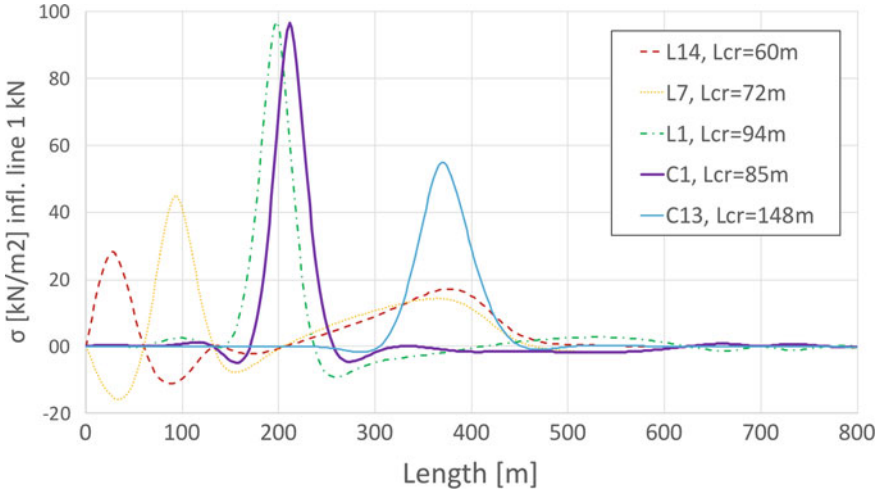

Fig. 47.4 Typical stays influence lines (L = lateral, C = central)

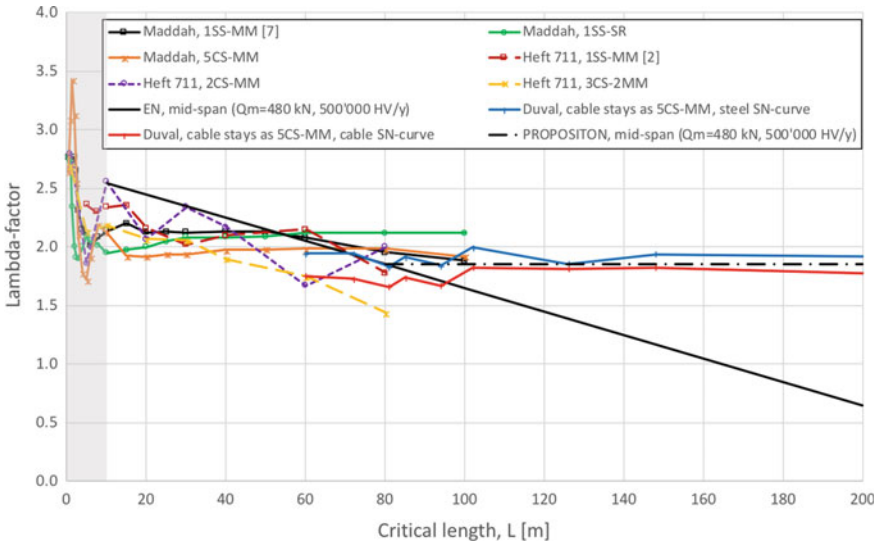

Fig. 47.5 Comparison of λ-factor for the EN 1993-2 "mid-span case", for different stays, previous studies [2, 7] and the new proposition (Legend: 1SS-MM = single span, mid-moment, 2CS = 2 continuous spans, SR = support reaction, 2MM = 2nd span mid-moment, etc.)

All results were adapted to obtain λ-factors for 500'000 HV/year in the slow lane as the standard, and an average HV weight of 480 kN. In order to do so, the EN 1993-2 formula for partial factor λ_2 was used as a first approximation to scale the results from the different studies; thus the absolute values obtained are estimates but the trends shown are deemed correct. Also shown in the figure are the original computations made for establishing the current EN lambda formula, from Heft 711, 1995 [2], as well as simulations made by Maddah [7]. The new proposition for the "mid-span case" is to use a constant value for critical lengths above 80 m. For stay-cables, both steel and cable constructional details are present, thus computations using two different S-N curves where carried out: (1) $m_1 = 3$; $m_2 = 5$; and cut-off limit, and (2) $m_1 = 4$; $m_2 = 6$; no cut-off limit, respectively. They indicate that a new partial factor λ_5 to be multiplied by the existent λ_1–λ_4 could account for a 2nd slope different then 5 [8]:

$$\lambda_5 = 0.02^{\left(\frac{1}{5} - \frac{1}{m_2}\right)} \quad m_2 > 5 \tag{47.2}$$

47.4 Conclusions

- For the stay-cables and steel girders, the influence line of the bending moments can be used for evaluating the critical length (with the sum of the peak stresses from the moment and normal force to determine the stress range);
- The damage equivalence factor shows a constant trend for lengths above 80 m for "mid-span case";
- The different shapes (slopes) of the S-N curves could be accounted for with new a partial factor λ_5, to multiply the existent λ_1–λ_4 factors.

The comments and support of Martin Garcia and Pierre Lorne during this work were appreciated and are acknowledged.

References

1. Sedlacek G et al (2008) Background document to EN 1991—Part 2—traffic loads for road bridges—and consequences for the design. JRC scientific reports, Ispra, Italy
2. Sedlacek G, Merzenich G (1995) Hintergrundbericht zum Eurocode 1—Teil 3.2: 'Verkehrslasten auf Straßenbrücken'. Heft 711. Bundesmin. für Verkehr, Bann-Bad Godesberg
3. Campion, Cocciaglia, Fila, Kirstein, van Maarschalkerwaart, Quoos, Ramondenc, Reber (1992) Eurocode 1 Loads. Railway loads, fatigue assessment. Background document. UIC, Switzerland
4. Oliveira Pedro JJ (2007) Pontes atirantadas mistas—Estudo do comportamento estrutural, PhD thesis, IST Lisbon, Portugal
5. Oliveira Pedro J, Reis A (2010) Nonlinear analysis of composite steel-concrete cable-stayed bridges. Eng Struct 32(2010):2702–2716
6. Pereira Baptista CA (2016) Multiaxial and variable amplitude fatigue in steel bridges, PhD thesis n° 7044, EPFL Lausanne, Switzerland

7. Maddah N (2013) Fatigue life assessment of roadway bridges based on actual traffic loads, PhD thesis n° 5575, EPFL Lausanne, Switzerland
8. Maddah N, Nussbaumer A (2013) Fatigue Life Assessment of Roadway Bridges Based on Actual Traffic Loads. Office fédéral des routes, Berne

Chapter 48
Fatigue Analysis of a Concrete Chimney Under Wind Loads

Hermes Carvalho, Victor Roberto Verga Mendes, Sebastião Salvador Real Pereira and José A.F.O. Correia

Abstract In most cases, tall structures are slender, demonstrating flexible behavior and, consequently, weather-related loads such as wind become a major component. Since these structures are flexible, they may become susceptible to wind induced fatigue. The effect of wind presents itself as dynamic load and can affect structures randomly in an infinite number of cycles, producing significant stress variations. The aim of this work is to present an evaluation of fatigue of a reinforced 180-meter-concrete chimney, at its most critical section, through a non-linear dynamic analysis. The method provides a full dynamic analysis which takes into account the geometric nonlinearities, the aerodynamic and structural damping. The numerical results were evaluated according to the fatigue limit specified by ABNT NBR 6118:2014.

Keywords Concrete chimney · Fatigue · Aerodynamic damping · Nonlinear dynamic analysis

48.1 Introduction

Usually, the analysis of structures under wind loading is performed using an equivalent static analysis, where the influence of floating response is taken into account by the gust factor. This methodology can be used in case of rigid structures for not presenting a considerable dynamic response [1]. More flexible structures, in particular those lightly damped, may show an important resonant response and their dynamic properties must be considered in the analysis [2]. For the analysis of fatigue life it is necessary to know the history of the load as well as the total response of the structure to these loads.

The response of the structures subjected to the wind loads can be divided by a mean and a floating component. The mean component, generally in the wind direction, is

H. Carvalho (✉) · V. R. V. Mendes · S. S. R. Pereira
Structural Engineering Department, University of Minas Gerais, Belo Horizonte, Brazil
e-mail: hermes@dees.ufmg.br

J.A.F.O. Correia
University of Porto, Porto, Portugal

J.A.F.O. Correia et al. (eds.), *Mechanical Fatigue of Metals*, Structural Integrity 7,
https://doi.org/10.1007/978-3-030-13980-3_48

related to the average wind speed and depends mainly on the velocity intensity, and its main effect is the production of a large structural deflection. The floating component of the response is caused by the joint action of wind turbulence and vortex formation. The floating component can be further subdivided into non-resonant floating, caused mainly by large low frequency gusts and resonant fluctuation, caused by elements present in the turbulence, which excite the structure at one of its natural frequencies. The latter is responsible for the occurrence of buffeting forces and may be aggravated by phenomena such as vortex shedding and galloping. Since high-magnitude vibrations can occur at both frequent and moderate velocities, structures are subject to a large number of stress cycles, which can lead overtime to accumulated damage and result in structural failure, even without exceeding any ultimate limit state.

Several studies have correlated fatigue damage to dynamic wind action. Davenport and Freathy [3] introduced a simple relationship between gust response and wind-induced fatigue damage using conventional static design parameters. Patel and Freathy [4] proposed a simplified procedure for estimating structural wind-induced fatigue damage. Repetto and Solari [5] proposed a mathematical model aiming to obtain a stress cycle histogram, accumulated damage and fatigue life of slender vertical structures exposed simultaneously to vibrations due to frontal and cross winds.

The aim of this paper is to present fatigue life evaluation through dynamic analysis of concrete chimney under wind loading, considering the geometric nonlinearity, the vibration caused by the kinetic energy of wind gusts and the aerodynamic damping due to the relative movement between this structure and the wind. The formulation proposed is applied on a 180-meter-high concrete chimney.

A numerical procedure in ANSYS [6] was developed for dynamic analysis with variable wind forces in time and space. Superimposed on the structural damping, aerodynamic damping was considered directly in determining the dynamic wind pressures, through the use of relative velocities between the structure and the wind.

48.2 Dynamic Analysis Procedure

The dynamic analysis involves the next stages [7]:

1. Gravitational forces are gradually implemented. The final configuration of the cable is obtained from a non-linear static analysis (dynamic effects are disabled at this structural loading stage).
2. The aerodynamic forces, which correspond to the average portion of the wind speed, are implemented in the cable as nodal forces. At this stage, the analysis is already dynamic which implies some additional observations. The loads must be slowly introduced, in small increments, in a way that the cable speed, at this stage, is not expressive, and, therefore, does not interfere in the results of the next stage.
3. Wind forces, composed by average and random component, are included, as an arbitrary function of time, for every cable node. The dynamic analysis is processed in a transient regime.

The formulation for aerodynamic damping as proposed in the study is directly considered in the wind pressure calculation, with the use of relative speed between wind and structure, both in the same direction. The basic formulation for wind pressure [8] and relative speed calculus is presented in the next equations.

$$q_{vento} = \frac{1}{2}\rho\, V_R^2 = 0.613\, V_R^2 \tag{48.1}$$

$$V_R = V(t) - V_{estr} \tag{48.2}$$

where: q_{vento} is the dynamic pressure; ρ is the specific mass of the air under normal conditions of pressure (101,320 Pa) and temperature (15 °C); V_R is relative speed between wind and structure, in the node considered; $V(t)$ is wind speed; V_{estr} is structure speed, in wind direction, in the considered node.

For the accomplishment of a nondeterministic dynamic analysis in time domain, the creation of time functions for the floating portion of the longitudinal wind speed is necessary. To create an aleatory sign with a null average, from a given energy spectrum, a Fourier series is used. The function $v(t)$ can be generated from the following equation [9]:

$$v(t) = \sqrt{2}\sum_{i=1}^{N}\sqrt{S^V(f_i)\,\Delta f}\cos(2\pi\, f_i\, t + \theta_i) \tag{48.3}$$

where: $S^V(f_i)$ is spectral density function; N is the number of frequency intervals Δf considered in the specter; f_i is frequency i, in Hertz; t is time, in seconds; Δf is frequency increment, in Hertz; θ_i is aleatory lag angle, between 0 and 2π.

For the determination of the spectral density function $S^V(z, f)$ (*PSDF*—"*Power spectral density functions*"), a formulation proposed by Kaimal is used, shown in the following equation [10]:

$$\frac{f\, S^V(z, f)}{u_*^2} = \frac{200\, x}{(1 + 50x)^{5/3}} \quad ; \quad x(z, f) = \frac{z\, f}{\bar{V}_z} \tag{48.4}$$

where: f is frequency, in Hertz; u_* is friction speed, in m/s; z is height above ground, in meters.

48.3 Description of the Chimney Structure and Numerical Model

An industrial chimney made of reinforced concrete was evaluated in the present work. The structure model is schematized as a cantilever beam, coaxial in the direction z, with height of 180 m and circular hollow cross-section. The external diameter

is 4.8 m throughout the height, while the inferior internal diameter varies linearly from 4.3 m, at the basement, to 4.5 meters, at the top. The reinforcement area is 480 cm^2, distributed in two layers of 49 reinforcement bars with 25 mm of diameter. An elasticity modulus equal to 26.22 GPa and Poisson's Ratio coefficient equal to 0.2 were adopted for the concrete. The specific mass of reinforced concrete is 2.500 kg/m^3, resulting in a total weight of 1.247.464.0 kg. The critical damping ratio adopted was $\zeta = 0.01$. The forces due to wind action were obtained in accordance to the standard ABNT NBR 6123:1988. The chimney was classified as a structure with a dimension larger than 80 m and basic wind speed velocity V_0 was considered equal to 32.0 m/s.

As the application of the proposed procedure to the chimney structure, a finite element model was developed using beam elements (BEAM3). The masses were considered concentrated in numerical model nodes, through MASS21 elements. The boundary conditions were translation and rotation prevented and the wind forces were applied in axis X positive direction.

The average velocity adopted in the analysis, from the weighted average, was equal to 33.45 m/s. The timestep used in the solution was equal to 0.1 s. The critical damping ratio of $\zeta = 0.01$ resulted in multiplicative coefficients of mass and stiffness matrices, α and β, equal to 0.032 and 0.00021, respectively.

48.4 Results

The natural frequencies of the chimney structure were determined through the numerical model. The values obtained are 0.37 Hz, 0.93 Hz and 1.75 Hz, respectively, for the 1st Mode, 2nd Mode, 3rd Mode. Figure 48.1 shows the temporal evolution of the displacements, velocities and accelerations of the top node of the chimney, and the support reactions of the base node of the 180 m-high structure with a wind velocity equal to 32 m/s. Table 48.1 shows the maximum values for each temporal evolution.

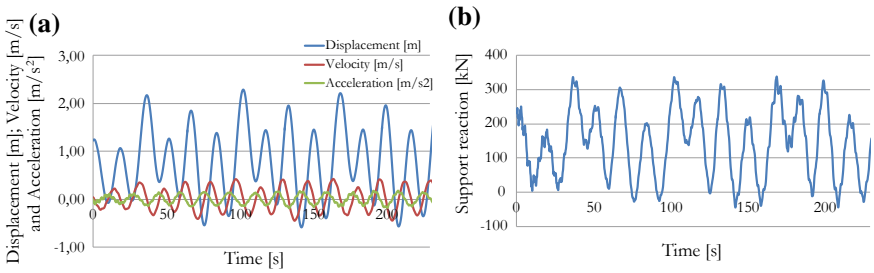

Fig. 48.1 Temporal evolution of displacement, velocity, acceleration (**a**) and support reaction (**b**)

Table 48.1 Maximum values of displacement, velocity, acceleration, support reaction and bending moment

Variable	Max. value
Displacement (m)	2.29
Velocity (m/s)	0.42
Acceleration (m/s^2)	0.17
Horizontal reaction F_x (kN)	347.52
Bending moment M_z (kN m)	57850.58

48.5 Fatigue Analysis on the Basis of ABNT NBR 6118:2014

The standard NBR 6118 [11] specifies that the limit state of interest for security requirements in case of dynamic loads is the one associated with reinforcement fatigue. The standard allows that fatigue verification can be done considering a frequent combination of actions, Eq. 48.5.

$$F_{d,ser} = \sum_{i=1}^{m} F_{gik} + \psi_1 F_{q1k} + \sum_{j=2}^{n} \psi_{2j} F_{qjk} \tag{48.5}$$

where: $F_{d,ser}$ is the combined service load; F_{gik} is ith permanent action, in kN; F_{q1k} is the principal variable action, in kN; ψ_1 is the reduction factor associated with the principal variable action for frequent combination in SLS; F_{q1k} is jth variable action; ψ_2 is the reduction factor for quasi-permanent combination in SLS.

Factor ψ_1 equal to 0.3 was adopted, resulting in a bending moment equal to 17.355 kN m at the basement. It was observed that, for such level of stress, the cross-section partially cracked. The reduced moment of inertia of 3.5 m^4 for the cracked condition of the cross-section was obtained after 10.000 days, according to ABNT NBR 6118. Figure 48.2 shows the cross-section and the neutral axis at the cracked condition. Once the loads and moment of inertia in the cracked condition are defined, the stresses in the reinforcement were determined, as shown in Table 48.2.

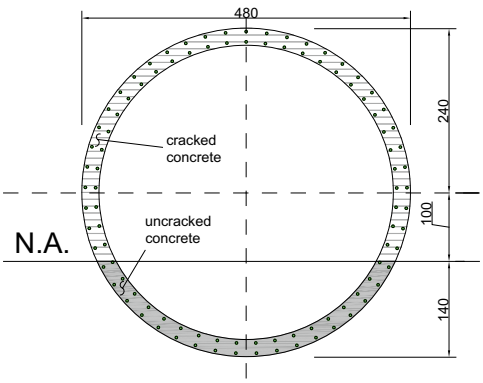

Fig. 48.2 Cross-section in cracked condition

Table 48.2 Normal stress at the basement of the chimney

Limit stress imposed by ABNT NBR 6118:2014 [11] (MPa)	Range stress calculated (MPa)
105	94

48.6 Conclusion

As a consequence of the elevated height of the concrete chimney, the structure presents high flexure stresses due to wind action at the basement, causing cracking in the sag region. The concrete starts to work in stage II, increasing the amplitude of stress in the steel reinforcement. Aiming to study the security of the structure, a fatigue analysis was performed in the most critical cross-section of the chimney. The evaluation consists of a numerical nonlinear dynamic analysis, which resulted in time series showing the behavior of the bending moments and horizontal force the support. Considering that the limit of stress variation $\Delta\sigma$ of 105 MPa for reinforcement bars, specified by ABNT NBR 6118:2014, it was possible to verify the fatigue at the basement through the maximum time history values. In case of tall structures, such as concrete chimneys, the dynamic response due to wind force cannot be neglected for fatigue analysis, evidencing that the reinforcement design is determined by serviceability limit state associated with fatigue.

References

1. Simiu E, Scanlan RH (1986) Wind effects on structures: an introduction to wind engineering, 2nd edn. Wiley, New York
2. Hirsh G, Bachman H (1995) Wind induced vibrations. Vibration Problems in Structures. Institut fur Baustatik und Konstruktion. Birkhauser Verlag Basel, Zurich
3. Davenport K, Freathy P (1988) A simple relationship between the gust response factor and fatigue damage. J Wind Eng Ind Aerodyn 30:45–54
4. Patel K, Freathy P (1984) A simplified method for assessing wind-induced fatigue damage. Eng Struct 6:268–273
5. Repetto MA, Solari G, Directional wind-induced fatigue of slender vertical. Structures (2004) J Struct Eng ASCE, 1032–1040
6. Ansys-12.1 (2009) Release 1.0 documentation for Ansys. Canonsburg, United States
7. Carvalho H (2015) Efeitos do vento em linhas de transmissão. PhD thesis. Department of Structural Engineering, Federal University of Minas Gerais, Belo Horizonte (2015)
8. Associação Brasileira de Normas Técnicas. NBR 6123 (1988) Forces due wind in buildings. Rio de Janeiro
9. Pfeil MS, Battista RC (1995) Aerodynamic stability analysis of cable-stayed bridges. J Struct Eng 121:1784–1788
10. Blessman J (2005) Introdução às ações dinâmicas do vento, 2nd edn. Editora UFRGS, Porto Alegre
11. Associação Brasileira de Normas Técnicas. NBR 6118 (2014) Design of concrete structures—Procedure. Rio de Janeiro

Chapter 49
On the Calculation of Offshore Wind Turbine Load Spectra for Fatigue Design

Rui Teixeira, Maria Nogal and Alan O'Connor

Abstract The present work researches on the definition of the load spectra used for offshore wind turbine low SN slope materials' fatigue design. Uncertainty in the sample sized used to scale fatigue life is analyzed for the tower component. Damage density is investigated for different environmental conditions in order to understand the importance of the different regimes of operation. Damage density is identified to be a heterogeneous function of the loading environmental conditions. In some cases, even for low SN slope materials, most of the damage occurs due to high load ranges. To study on the influence of this heterogeneity, different statistical tail fits are used to compare the influence of accurately defining the tail region on a reference design time (T). Results show that OWT fatigue is highly dependent on the t shorter that T time used to approximate T. This is mainly related to the fact that fatigue design depends not only on scaling stress ranges, but also cycle counts. Effort on the design phase should be applied in the definition of the uncertainty of the load spectra due to the limitation imposed by using low sample sizes to cover the extensive joint distribution of environmental parameters.

Keywords Offshore wind · Fatigue design · Miner's rule · 5 MW baseline OWT

49.1 Introduction

Structural fatigue on OWTs is mainly divided in two major problems. For materials with high SN slopes (here considered as materials with SN slope $m > 10$) the problem of fatigue approaches a problem of extrapolation, where the high loads contribute for almost all the fatigue damage density (% of Miner's fatigue contribution). Whereas for low slope materials (here considered as materials with SN slope $m < 6$), fatigue damage density is spread over different loading ranges.

Wide research on fatigue analysis of OWT has focused on the definition of the extrapolation techniques for composite materials [1–3]. For low SN slope materials,

R. Teixeira (✉) · M. Nogal · A. O'Connor
Trinity College Dublin, College Green, Dublin, Republic of Ireland
e-mail: rteixeir@tcd.ie

J.A.F.O. Correia et al. (eds.), *Mechanical Fatigue of Metals*, Structural Integrity 7,
https://doi.org/10.1007/978-3-030-13980-3_49

such as steels, knowledge on fatigue design techniques were transferred from the one already existing on offshore engineering. In particular, [3] reported that no additional accuracy was attained by spending effort on definition of the load spectra tail for low m materials. To note that the authors use a sample size per environmental loading condition larger than the recommended by the current design standards.

The current paper proposes to research on how the sample size influences fatigue calculations. Additionally, as the tail region is identified to be influent in some operational points, the *trade-off* of spending time on defining it is studied. To fulfill this goal, Sect. 49.2 presents the fatigue design calculation process, Sect. 49.3 presents the results on its uncertainty for 25 points of operation, and Sect. 49.4 presents the main conclusions.

49.2 Fatigue Design Methodology

Design of offshore wind turbine (OWT) towers to structural fatigue is an effort demanding procedure. The current design practices recommend the definition of load distributions, extrapolation of loads and cycles when required, to be used with the widely known linear damage summation rule, Eq. 49.1 [4, 5].

$$D_T = \sum_{i=1}^{S_k} \frac{n_E(S_i)}{n_{SN}(S_i)} \tag{49.1}$$

$n_E(S_i)$ is the number of cycles at a certain stress range S_i, which is compared with the admissible number of cycles $n_{SN}(S_i)$ at that same stress range. $n_{SN}(S_i)$ is calculated based on the a material specified SN curve and k is the total number of stress ranges.

The calculation of $n_E(S_i)$ frequently involves using a cycle counting technique, being the most common the rainflow cycle counting technique. Cycle counting techniques allow for the definition of a stress or load range spectra. Furthermore, as it is not feasible to perform the calculations replicating all the operational states an OWT may experience during its T lifetime, calculations are performed for a limited number of environmental conditions and then scaled up for T.

The definition of the load spectra enables the assessment of D_T using an integration technique, Eq. 49.2.

$$D_T = \int_{\Theta} \int_{S} \frac{f(\Theta) f(S|\Theta)}{n_{SN}(S)} dS \, d\Theta \tag{49.2}$$

being $f(\Theta)$ the distribution function of operational conditions that load the OWT. This distribution is integrated along with the distribution of stress ranges $f(S|\Theta)$. $f(S|\Theta)$ is estimated from the stresses and cycles obtained at Θ, being conditional on

it. As multiple Θ load the OWT, the calculation procedure is expensive even when $f(S|\Theta)$ is defined with small sample sizes.

49.2.1 OWT Model

The analysis presented uses the NREL 5 MW baseline turbine installed on a monopile [6]. As a non-linear coupled code, it replicates the randomness of the OWT tower operational loading. Its non-linear behavior is of relevance to replicate non-linear loading behavior that may be of relevance for structural fatigue design. This is particularly important for high SN slope materials. However, it may be also of relevance for low SN slope materials.

References [4, 5] recommend the usage of at least six distinct seeds in order to define the design loads of OWTs to operational fatigue. Lower frequency loading effects have negligible influence on fatigue life [7]. Damage that occurs within this reference time t of 600 s much shorter than T is identified as D_t.

49.3 Analysis of Fatigue Load Spectra Uncertainty

Short term fatigue follows a lognormal distribution. As many repetitions occur within the T period, cumulated fatigue converges to a single value that is related to the mean of $f(S|\Theta)$. Most of the times defining the mean value of $f(S|\Theta)$ maintaining practicable computational effort results in uncertainty in the estimation.

The approximation of the fatigue design calculations to a problem of mean value was considered before for wind turbines in [2]. Figure 49.1 presents the uncertainty in the calculation of the mean using 8 repetitions ($n_r = 8$) of six different seeds for the cumulative damage calculation. The mean wind speed (U) and the turbulence intensity (I) were selected to compute the results as these are expected to be the most influential variables in terms of fatigue of the tower [8].

It can be seen in Fig. 49.1 that the variability of the mean within the n_r calculations can be relatively high when using 6 seeds. In particular for high values of I this variability is more prominent. To note that offshore I is correlated negatively with U, therefore, the most turbulent operational states are expected to occur at less damaging winds. Nevertheless, even for the Θ where the variability of D_t is relatively smaller (near the cut-out speed of 25 m/s) deviations of $\pm 10\%$ are frequently identified. The calculations at D_t are used to scale up D_T depending on the occurrences of $f(\Theta)$. Thus, eventual errors in the estimation of the D_t will be propagated to D_T. These errors are expected to average over 0, however, if an inefficient description of $f(\Theta)$ occurs, or important fatigue damaging states are underestimated, relevant errors may be propagated to the design value D_T.

As the value of m increases, the uncertainty in the cumulated damage increases for the same initial sample. This is connected to the influence of the higher quantiles

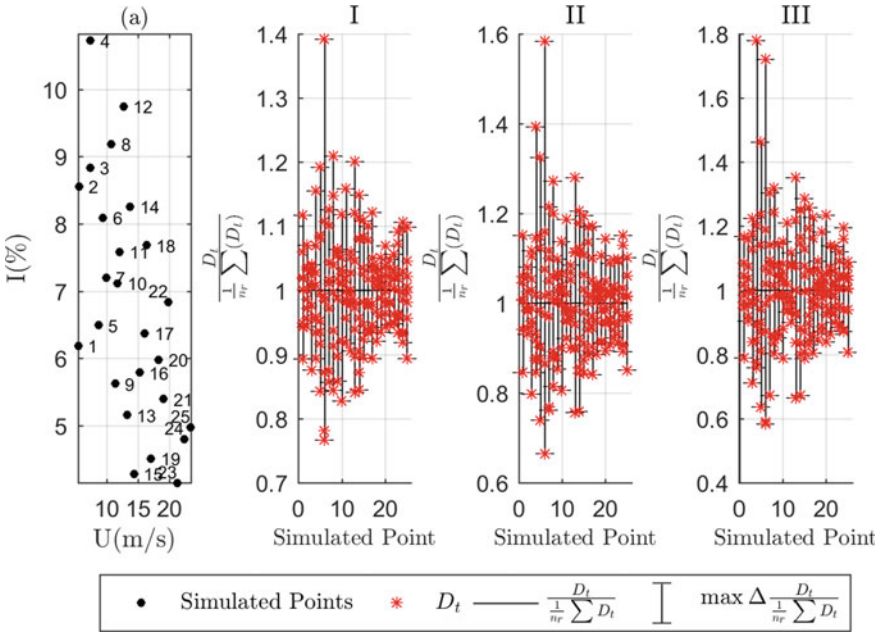

Fig. 49.1 Uncertainty in the cumulated damage (D_t) resulting of 6 seeded simulations of 600 s for $n_r = 8$. **a**—Simulated Points. (I–III)—SN m = 3, 4, 5 respectively

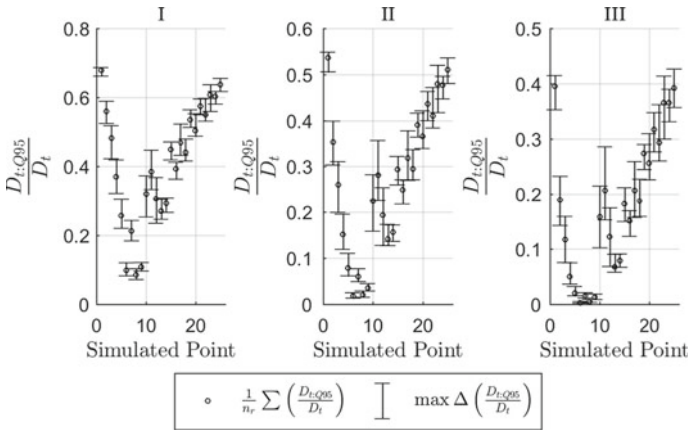

Fig. 49.2 Density of D_t for the lower 95% stress ranges and respective variation within n_r repetitions. (I–III)—SN m = 3, 4, 5 respectively

of stress range. Figure 49.2 presents the damage density of the lower 95% quantile of the stress ranges ($D_{t:Q95}$) compared with the respective cumulative D_t using 6 seeds, and its variability for n_r.

As m increases, influence of larger stress ranges increase. The variation of this percentage within the different simulated points is relatively low, which indicates that it is characteristic of each Θ. Damage density in the tail can be as high as 95%. It is then of interest to infer if design effort on the tail region should be spent for all the operational states, or even some, in order to have more accurate predictions of the D_T.

Characterization of the load spectra tail can be performed through extreme value theory or data truncation, being the second well accepted for wind engineering [3]. The challenge of extrapolation with truncation of data has been widely discussed before [3, 9, 10]. It is commonly assumed that low SN materials do not require the usage of extrapolation techniques to fit the tail distribution. Results from scaling the load spectra, considering and not considering extrapolation, from t with 6 seeded simulations to T equal to 50 simulations are discussed for low SN materials in the following section. The question to answer is if there is a significant advantage in terms of accuracy from adding the extra effort on an accurate load spectra tail estimation.

49.3.1 Scaled Results of D *from* t = *3600 s to* T = *60,000 s*

Comparative results from approximating the 100 points D_T using t of 6 seeded simulations at the same Θ state are presented in Table 49.1. The Peak-Over-Threshold (POT) methodology is applied and loading quantiles of 95 and 99% as threshold (u) value. Extensive considerations about the POT procedure are given in [10]. The choice of these quantiles, previously identified as inappropriate [9], is due the systematic character required for the procedure.

The u value of 95% can significantly overestimate the approximation to the tail, $\Theta = 5, 8$. The challenge of extrapolation for OWT is that of accurately predicting, not only the tail loading, but also the number of cycles. As a result, the confidence in the extrapolation is bounded to the number of initial samples applied. In the case of dealing with the tail region, six was proven to not be adequate by [3]. Up to 30 simulations the mean number of loading occurrences above the 99% quantile is highly variable. In most cases, no significant improvements occur in accuracy of the extra effort of studying the tail spectra region for the tower component. In the cases 9–12, where the simple scale up of the load spectra for $\frac{T}{t}$ is non-conservative, the usage of the POT with 95% quantile u improves the estimation at T. Nonetheless, due to the complexity of analyzing with the POT, and variability in the accuracy, it may be more interesting to direct the design effort to quantify the uncertainty in the initial t used. Further works, also for high m values, should discuss the approximation of the extrapolated stress ranges and cycles simultaneously. It may be of interest to study the definition of u based not only on quantiles of loading but also, or jointly, on a minimum number of expected cycles in order to implement extrapolation.

Table 49.1 Estimation of D for $T = 30{,}000$ s using $t = 3600$ s. D_{GP}, D_W and D_E are relative to the tail fit with the generalised pareto, the weibull and the exponential distributions

	m = 3							m = 5						
	$\times^T/_t$	$u = Q95$			$u = Q99$			$\times^T/_t$	$u = Q95$			$u = Q99$		
Θ	D	$D_{GP}D_{GP}$	D_W	D_E	D_{GP}	D_W	D_E	D	D_{GP}	D_W	D_E	D_{GP}	D_W	D_E
1	0.94	1.04	1.02	1.05	0.95	0.95	0.95	0.92	1.39	1.20	1.45	0.96	0.97	0.97
2	0.86	1.30	1.45	1.12	0.88	0.88	0.89	0.86	3.96	6.46	2.06	0.92	0.94	1.00
3	1.06	1.68	2.33	1.36	1.11	1.13	1.13	1.29	5.90	18.86	2.63	1.55	1.59	1.72
4	0.95	1.63	1.43	1.71	1.02	1.07	1.05	0.93	3.70	2.33	4.35	1.20	1.34	1.48
5	1.12	2.34	2.07	2.09	1.19	1.19	1.28	1.45	8.18	5.88	6.05	1.70	1.67	2.51
6	1.00	1.99	2.87	1.40	1.13	1.18	1.22	1.12	5.19	13.77	2.18	1.48	1.59	2.14
7	0.95	1.59	1.28	1.62	1.00	1.01	1.05	0.76	2.96	1.41	3.16	0.89	0.90	1.15
8	1.20	1.86	1.79	3.08	1.26	1.28	1.26	1.25	3.28	2.51	12.61	1.39	1.43	1.41
9	0.79	0.99	0.97	1.36	0.80	0.81	0.80	0.65	1.03	0.97	2.90	0.68	0.69	0.67
10	0.88	1.00	0.97	1.03	0.89	0.89	0.89	0.84	1.17	1.03	1.34	0.86	0.87	0.86
11	0.83	0.93	0.91	0.97	0.84	0.84	0.84	0.78	1.02	0.93	1.24	0.79	0.79	0.79
12	0.85	1.00	0.98	1.20	0.86	0.86	0.86	0.79	1.13	1.08	2.24	0.80	0.80	0.80

(continued)

Table 49.1 (continued)

	m = 3							m = 5						
	$\times^{T}/_{t}$	$u = Q95$			$u = Q99$			$\times^{T}/_{t}$	$u = Q95$			$u = Q99$		
Θ	D	$D_{GP}D_{GP}$	D_W	D_E	D_{GP}	D_W	D_E	D	D_{GP}	D_W	D_E	D_{GP}	D_W	D_E
13	0.91	1.12	1.10	1.26	0.92	0.92	0.92	0.76	1.32	1.18	2.07	0.78	0.79	0.82
14	0.98	1.25	1.20	1.41	1.00	0.99	1.00	0.97	1.76	1.46	2.80	1.01	1.00	1.05
15	1.06	1.20	1.17	1.25	1.07	1.08	1.07	1.02	1.47	1.33	1.77	1.06	1.08	1.07
16	0.96	1.18	1.13	1.24	0.99	1.00	1.00	0.98	1.79	1.42	2.24	1.05	1.07	1.07
17	0.97	1.17	1.11	1.16	0.99	0.99	0.99	0.89	1.65	1.29	1.60	0.94	0.94	0.93
18	1.06	1.37	1.32	1.56	1.10	1.07	1.13	1.29	2.55	2.15	4.30	1.45	1.33	1.77
19	0.93	1.04	1.04	1.11	0.94	0.94	0.94	0.90	1.30	1.22	1.78	0.92	0.92	0.92
20	0.95	1.06	1.05	1.14	0.96	0.96	0.96	0.95	1.30	1.25	1.84	0.97	0.98	0.99
21	0.91	1.03	0.98	1.01	0.92	0.92	0.92	0.86	1.44	1.09	1.28	0.89	0.89	0.90
22	1.03	1.15	1.13	1.17	1.04	1.05	1.04	1.01	1.49	1.33	1.64	1.06	1.09	1.07
23	1.05	1.12	1.11	1.15	1.05	1.05	1.06	1.08	1.39	1.28	1.55	1.11	1.09	1.11
24	0.98	1.06	1.04	1.07	0.99	0.99	0.99	0.99	1.32	1.16	1.39	1.01	1.01	1.01
25	1.02	1.08	1.07	1.11	1.02	1.03	1.03	1.02	1.24	1.20	1.42	1.04	1.06	1.05

49.4 Conclusions

The current paper investigated uncertainty in the definition of loading spectra for offshore wind turbine tower component fatigue calculations. Variability due to sample statistical significance, with reference to the design standards, was studied. Damage density for different environmental conditions was also analyzed jointly with the improvement in accuracy resulting from the application of different statistical approximations. This was justified due to the heterogeneity of the damage density for different environmental conditions.

Results showed that, if practicality limits the design effort, resources should be focused on assessing uncertainty in the load spectra due to the sample size used to define it. Usage of complex statistical techniques, such as extrapolation, in certain circumstances improves the design accuracy, however, on its own, does not contribute for a robust design procedure and the resulting accuracy is highly case-specific.

Acknowledgements This project has received funding from the European Union Horizon 2020 research and innovation programme under the Marie Sklodowska-Curie grant agreement No. 642453.

References

1. Sutherland HJ (1999) On the fatigue analysis of wind turbines. Technical report. Sandia National Labs, Albuquerque, NM (US); Sandia National Labs., Livermore, CA (US)
2. Lange CH (1999) Probabilistic fatigue methodology and wind turbine reliability. Technical report. Sandia National Labs, Albuquerque, NM, United States
3. Moriarty PJ, Holley W, Butterfield S (2004) Extrapolation of extreme and fatigue loads using probabilistic methods. National Renewable Energy Lab, Golden, CO (US)
4. IEC (2005) Wind turbines part 1: Design requirements. Technical report 61400-1, International Electrotechnical Commission, Geneva, Switzerland
5. IEC (2009) Wind turbines part 3: Design requirements for offshore wind turbines. Technical report 61400-3, International Electrotechnical Commission, Geneva, Switzerland
6. Jonkman J, Butterfield S, Musial W, Scott G (2009) Definition of a 5-mw reference wind turbine for offshore system development. National Renewable Energy Laboratory, Golden, CO, Technical Report No. NREL/TP-500-38060
7. Veldkamp HF (2006) Chances in wind energy: a probabilistic approach to wind turbine fatigue design
8. Teixeira R, O'Connor A, Nogal M, Krishnan N, Nichols J (2017) Analysis of the design of experiments of offshore wind turbine fatigue reliability design with kriging surfaces. Procedia Struct Integr 5:951–958
9. Embrechts P, Resnick S, Samorodnitsky G (1999) Extreme value theory as a risk management tool. N Am Actuar J 3(2):30–41
10. Teixeira R, Nogal M, O'Connor A (2018) On the suitability of the generalized Pareto to model extreme waves. J Hydraul Res 56(6):755–770

Part X
Numerical Methods

Chapter 50
The Natural Neighbour Radial Point Interpolation Method to Predict the Compression and Traction Behavior of Thermoplastics

D. E. S. Rodrigues, J. Belinha, R. M. Natal Jorge and L. M. J. S. Dinis

Abstract Nowadays, the Finite Element Method is the most used discretization technique in structural computational mechanics. However, recently, new discretization techniques—such as meshless methods (Belinha in methods in biomechanics: bone tissue remodelling analysis. Springer International Publishing, Porto, Portugal, 2014 [1])—have been proposed. These numerical techniques are able to efficiently handle some of the FEM's drawbacks, such as the remeshing requirement in crack propagation or large deformations problems. Meshless methods only require an unstructured nodal mesh to discretize the problem domain, and the numerical integration of the discrete system of equations obtained from the Galerkin weak form is performed using a background integration mesh. Additionally, the nodal connectivity is imposed using the influence-domain concept, which allows to construct the interpolation functions. The Natural Neighbor Radial Point Interpolation Method (NNRPIM) is a recently developed truly meshless method, which in this work is used to analyze a thermoplastic

D. E. S. Rodrigues (✉) · J. Belinha · R. M. Natal Jorge · L. M. J. S. Dinis
Institute of Science and Innovation in Mechanical and Industrial Engineering (INEGI), Rua Dr. Roberto Frias, Campus da FEUP, 400, 4200-465 Porto, Portugal
e-mail: drodrigues@inegi.up.pt

J. Belinha
e-mail: job@isep.ipp.pt

R. M. Natal Jorge
e-mail: rnatal@fe.up.pt

L. M. J. S. Dinis
e-mail: ldinis@fe.up.pt

J. Belinha
School of Engineering, Department of Mechanical Engineering, Polytechnic of Porto (ISEP), Rua Dr. António Bernardino de Almeida, 431, 4200-072 Porto, Portugal

D. E. S. Rodrigues · R. M. Natal Jorge · L. M. J. S. Dinis
Faculty of Engineering of the University of Porto (FEUP), Department of Mechanical Engineering, R. Dr. Roberto Frias, s/n, 4200-465 Porto, Portugal

J.A.F.O. Correia et al. (eds.), *Mechanical Fatigue of Metals*, Structural Integrity 7,
https://doi.org/10.1007/978-3-030-13980-3_50

assuming an elasto-plastic behavior. Benchmark numerical examples are solved in both traction and compression, and in the end, the NNRPIM results obtained are compared with FEM solutions.

Keywords Polymers · Elasto-plasticity · Meshless methods

50.1 Introduction

The finite element method (FEM) is the most used numerical tool in computational mechanics. The FEM discretizes the problem domain in smaller parts called elements. In opposition to the FEM, in the meshless methods, the nodes are distributed and the field functions are approximated within an 'influence-domain' rather than an element [1]. 'Influence-domains' are areas or volumes concentric with interesting points and whose overlap ensure the nodal connectivity. Since meshless methods are not mesh reliant, they present some advantages over FEM, particularly when the problem involves transitory geometry (for instance, large deformations or fracture mechanics).

In this work, the Natural Neighbor Radial Point Interpolation Method (NNRPIM) [1] and the FEM are used to perform elasto-plastic analyses on a polypropylene (PP) [2], which is a polymeric material that behaves differently under compression and tension. [2]. The PP is used in many engineering applications in which tensile and compressive loads may be relevant. The strength of the PP under compression can be up to 30% higher than when a tensile load is applied to the material [3]. Thus, this fact highlights the importance of characterizing polymeric materials in different stress states and the use of adequate constrains [2]. Thus, a non-linear algorithm (Newton-Raphson Method) is used within the formulations of the FEM and the NNRPIM, to study the behavior of the PP under tension and compression loads. Assuming a linear elastic-linear plastic material behavior with an isotropic hardening, the von Mises criterion as yield criterion and the Prandtl-Reuss flow rule, the numerical simulation of standard tensile and compression tests are performed. The numerical solutions are compared with experimental data [2]. In the end, is proved the accuracy of the NNRPIM.

50.1.1 The Natural Neighbor Radial Point Interpolation Method (NNRPIM)

In the NNRPIM, the concept of 'influence-domain' used in the Radial Point Interpolation Method (RPIM)—in which the NNRPIM is based—is replaced by the 'influence-cell' concept [1]. In order to obtain the 'influence-cells' the NNRPIM uses geometrical and mathematical constructions, such as the Voronoï diagrams

and the Delaunay tessellation [1]. Thus, because of the way the nodal connectivity is enforced, the displacement and the stress fields obtained using the NNRPIM are generally smoother and more accurate when compared to the solutions obtained with other methods [1]. For shape functions, the NNRPIM makes use of a combination of the multiquadric (MQ) radial basis functions (RBF) with polynomial basis functions. The obtained shape functions possess the delta Kronecker property, which simplifies the enforcement of boundary conditions. To integrate the integro-differential equation from the Galerkin weak form, the NNRPIM uses an integration mesh constructed from the Voronoï diagram. The meshless discrete system of equations, obtained from the Galerkin weak form, has the same standard form as in the FEM, for a static problem: $\boldsymbol{K}_0\,\boldsymbol{u} = \boldsymbol{f}$, being $\boldsymbol{K}_0 = \int_\Omega \mathbf{B}^{\mathrm{T}}\,\boldsymbol{D}\,\mathbf{B}\ \mathrm{d}\Omega$ the initial stiffness matrix (where $\boldsymbol{D}$ is the elastic constitutive matrix and $\mathbf{B}$ is the deformation matrix), $\boldsymbol{u}$ the displacement vector and $\boldsymbol{f}$ the load vector.

50.1.2 Elasto-Plastic Formulation

An elasto-plastic problem is solved within numerical methods considering increments of load. For a load increment that produces an elastic response of the material, the discrete system of equations is solved. Once the material reaches the elastic limit, the stiffness matrix needs to be updated to consider the effects of plastic deformation. In this work, the non-linear elasto-plastic problem is solved using a variation of the incremental-iterative Newton-Raphson method: the initial stiffness in each increment (KT1) algorithm. In the beginning of each load increment after the material pass the elastic limit, this algorithm computes an updated stiffness matrix considering the effects of plastic deformation. The KT1 algorithm is described below:

(i) Verify if any integration point of the domain reached the yield point in the previous increment. If not, it is assumed an elastic behavior of the material and the displacement field is obtained for the load increment i,

$$\boldsymbol{K}_0\,\boldsymbol{u}_i = \boldsymbol{f}_i \Rightarrow \boldsymbol{u}_i = \boldsymbol{K}_0^{-1}\boldsymbol{f}_i \tag{50.1}$$

If there are points of the material that reached the yield stress in the previous increment, the flux vector, $\boldsymbol{a}$, of the previous increment is read $\boldsymbol{a}^T = (\partial F/\partial\boldsymbol{\sigma})^T$:

$$\boldsymbol{a}^T = \left(\frac{\partial F}{\partial \boldsymbol{\sigma}}\right)^T = \left\{\frac{\partial F}{\partial \sigma_{xx}}, \frac{\partial F}{\partial \sigma_{yy}}, \frac{\partial F}{\partial \sigma_{zz}}, \frac{\partial F}{\partial \tau_{xy}}, \frac{\partial F}{\partial \tau_{xz}}, \frac{\partial F}{\partial \tau_{yz}}\right\} \tag{50.2}$$

being F the mathematical expression of the yield surface. In this case, a new stiffness matrix, $\boldsymbol{K}_i^1$, is constructed using: (1) the elasto-plastic constitutive matrix, $\boldsymbol{D}_{ep} = \boldsymbol{D} - (\boldsymbol{d}_D\boldsymbol{d}_D^T)/(A + \boldsymbol{d}_D^T\boldsymbol{a})$—with $A = E_T/(1 - E_T/E)$, where E and E_T represent the elastic and tangent modulus, respectively—for the plasticized integration points, and (2) the elastic constitutive matrix, $\boldsymbol{D}$, for the remaining points:

$$\boldsymbol{K}_i^1 \boldsymbol{u}_i = \boldsymbol{f}_i \Rightarrow \boldsymbol{u}_i = \left[\boldsymbol{K}_i^1\right]^{-1} \boldsymbol{f}_i \tag{50.3}$$

(ii) The stress field is obtained for the points that not reached the yield point using: $\boldsymbol{\sigma}_i = \boldsymbol{D}\boldsymbol{B}\,\boldsymbol{u}_i$; and for the points beyond the plastic limit using: $\boldsymbol{\sigma}_i = \boldsymbol{D}_{ep}\boldsymbol{B}\,\boldsymbol{u}_i$.

(iii) For each integration point, a yield criterion is applied. Thus, if the yield criterion is verified, the material remains in the elastic regime and the stress increment is updated ($\Delta\boldsymbol{\sigma} = \boldsymbol{\sigma}_i$). If not, the material reached the plastic regime and the stress must be returned to the yield surface using the "backward-Euler" procedure [4] ($\Delta\boldsymbol{\sigma} = \boldsymbol{\sigma}_i^{(r)}$, being $\boldsymbol{\sigma}_i^{(r)}$ the new stress field after the stress return algorithm is run).

(iv) The new stress vector, $\Delta\boldsymbol{\sigma}$, is added to the stress of the previous increment (which is null if the present increment is the first one):

$$\boldsymbol{\sigma}_i = \boldsymbol{\sigma}_{i-1} + \Delta\boldsymbol{\sigma} \tag{50.4}$$

(v) Using the new stress field, residual forces are obtained, $\boldsymbol{f}_i^{res}$,

$$\boldsymbol{f}_i^{res} = \boldsymbol{f}_i - \int_{\Omega} \boldsymbol{B}\,\Delta\boldsymbol{\sigma}\,\mathrm{d}\Omega \tag{50.5}$$

if the material rests in the elastic regime, $\boldsymbol{f}_i^{res} = 0$ and the algorithm moves to the next load increment. On the other hand, if at least one of the integration points reached the yield point, $\boldsymbol{f}_i^{res} \neq 0$. A tolerance must be defined to compare the residual forces with the incremental forces within the domain, formed by n nodes:

$$\mathrm{TOL} = \sqrt{\sum\nolimits_{m=1}^{n} \left(\boldsymbol{f}_i^{res}\big|_m\right)^2} \Big/ \sqrt{\sum\nolimits_{m=1}^{n} \left(\boldsymbol{f}_i\big|_m\right)^2} \tag{50.6}$$

If TOL is still higher than a predefined value, the algorithm enters in the iterative phase. If not, the algorithm passes to the next load increment.

(vi) Iterative process:

(1) New field variables are calculated using the residual forces of the increment i, $\boldsymbol{f}_i^{res}$, and the stiffness matrixes $\boldsymbol{K}_i^1$ or $\boldsymbol{K}_0$, depending if there are or there are not points beyond the elastic limit of the material in the previous increment, respectively.

$$\boldsymbol{u}_i = \boldsymbol{K}_0^{-1} \boldsymbol{f}_i^{res} \quad \text{or } \boldsymbol{u}_i = \left[\boldsymbol{K}_i^1\right]^{-1} \boldsymbol{f}_i^{res} \tag{50.7}$$

(2) Repeat step (ii). On the first iteration of each increment, the flux vector, $\boldsymbol{a}$, to be used in the following increment, is calculated. The flux vector is needed to obtain the elasto-plastic constitutive of the next increment.

(3) New residual forces are calculated, $\boldsymbol{f}_i^{res}$, based on the residual force applied in step (1), $\boldsymbol{f}^{res}$, and a new tolerance is determined:

$$\boldsymbol{f}_i^{res} = \boldsymbol{f}^{res} - \int_{\Omega} \boldsymbol{B}\Delta\boldsymbol{\sigma}\, d\Omega \tag{50.8}$$

$$\text{TOL} = \sqrt{\sum_{m=1}^{n} \left(\boldsymbol{f}_i^{res}\big|_m\right)^2} \Big/ \sqrt{\sum_{m=1}^{n} \left(\boldsymbol{f}^{res}\big|_m\right)^2} \tag{50.9}$$

If TOL is still higher than a predefined value, the algorithm begins a new iteration. If not, it passes to the new load increment.

50.2 Numerical Results

As previously mentioned, using the NNRPIM and the FEM, uniaxial tensile and compression tests were simulated (using the FEMAS software [5] and MATLAB® code) and numerical stress-strain curves were obtained. The linear elastic-linear plastic material model was adjusted knowing the experimental stress-strain curves from the literature [2]. Thus, the mechanical properties were estimated for the uniaxial tensile test (E = 1332.645 MPa, σY0 = 19.730 MPa and ET = 194.693 MPa) and for the compression test (E = 886.539 MPa, σY0 = 50.079 MPa and ET = 40.877 MPa). The specimen used in the uniaxial tensile test has a geometry according to the norm ISO 3167—Type B, while the specimen of the compression test has a cylindrical shape with diameter 8 and 12 mm of length, according to Jerabek et al. [6]. The specimen of the uniaxial tensile test is discretized in a nodal mesh (in the NNRPIM analysis) and a finite element mesh, each one having a total number of 2397 nodes. For the compression test, the specimen is discretized using 2145 nodes. In the incremental-iterative process, ten load increments are considered, as well as a tolerance of 0.01. Figure 50.1 contains stress-strain experimental and numerical curves, as well as the elasto-plastic model adopted in both mechanical tests:

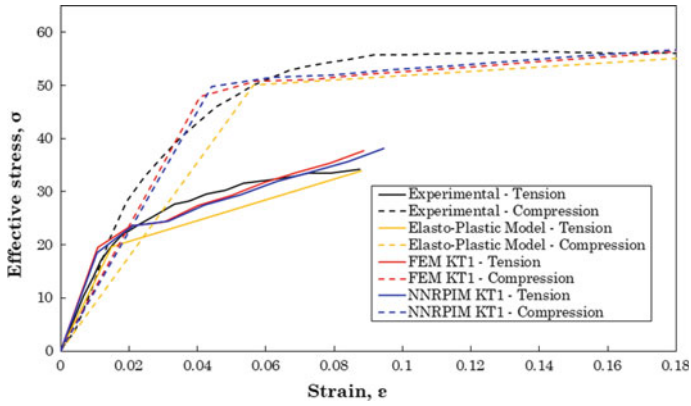

Fig. 50.1 Stress-strain curves of tensile and compression tests performed on specimens, using different numerical methods and non-linear solution algorithms

From Fig. 50.1 it is visible that the NNNRPIM curves are closer to the experimental ones than the FEM curves, especially in the yield point and in the post-yield regime. Thus, using the same discretization level, the NNRPIM can obtain more accurate solutions than the FEM. Regarding the linear elastic-linear plastic model, the results show that it captures satisfactorily the non-linear paths of the experimental stress-strain curves.

50.3 Conclusions

Using elasto-plastic models adjusted to the experimental data found in the literature, several stress-strain curves were obtained using the FEM and the NNRPIM, for the uniaxial tensile and compression tests performed on specimens of polypropylene. The developed elasto-plastic algorithms were successfully validated, since the numerical curves follow the paths of the experimental stress-strain curves. Additionally, from the comparison established between the FEM and NNRPIM curves, it can be concluded that the NNRPIM revealed to be more accurate than the FEM, using the exact same number of nodes. Thus, the meshless method under study proved to be a robust and accurate numerical tool, and can be used as an alternative to the FEM. Additionally, the NNRPIM possesses considerable advantages, especially in problems involving transitory geometry, since NNRPIM does not need re-meshing. Furthermore, as stated in Sect. 50.1.1, the stress fields obtained with NNRPIM are smoother than the ones obtained using the FEM, as can be seen in Fig. 50.2, in which it is represented the distribution of the von Mises stress through the specimen used for the tensile test.

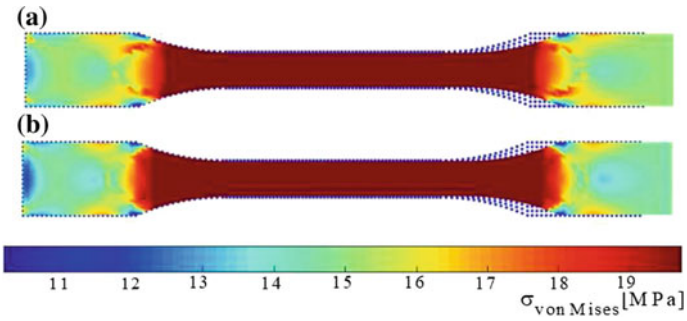

Fig. 50.2 Distribution of the von Mises stress on the specimen, computed with the (**a**) FEM and the (**b**) NNRPIM at the end of the fourth load increment in the incremental-iterative process

Acknowledgements The authors truly acknowledge the funding provided by Ministério da Ciência, Tecnologia e Ensino Superior—Fundação para a Ciência e a Tecnologia (Portugal), under grants: SFRH/BD/121019/2016, and by project funding MIT-EXPL/ISF/0084/2017. Additionally, the authors gratefully acknowledge the funding of Project NORTE-01-0145-FEDER-000022—SciTech—Science and Technology for Competitive and Sustainable Industries, co-financed by Programa Operacional Regional do Norte (NORTE2020), through Fundo Europeu de Desenvolvimento Regional (FEDER).

References

1. Belinha J (2014) Meshless methods in biomechanics: bone tissue remodelling analysis. Springer International Publishing, Porto, Portugal
2. Jerabek M, Tscharnuter D, Major Z, Ravi-Chandar K, Lang R (2010) Multiaxial yield behaviour of polypropylene. EPJ Web Conf. 6:03005
3. Appelsved P (2012) Investigation of mechanical properties of thermoplastics with implementations of LS-DYNA material models. Degree Proj Solid Mech 48
4. De Borst R, Crisfield MA, Remmers JJC, Verhoosel CV (2012) Non-linear finite element analysis of solids and structures. Wiley Ser Comput Mech
5. Jorge Belinha (2018) FEMAS—Finite element and meshless analysis software. http://jbelinha.webs.com/femas. Accessed 18 May 2018
6. Jerabek M, Major Z, Lang RW (2010) Uniaxial compression testing of polymeric materials. Polym. Test. 29(3):302–309

Chapter 51
The Elasto-plastic Analysis of Polymers Subject to Traction and Compression Using Advanced Discretization Techniques

D. E. S. Rodrigues, J. Belinha, R. M. Natal Jorge and L. M. J. S. Dinis

Abstract Materials such as thermoplastics often have different behaviors when subjected to traction and compression. In those cases, yield criterions for nonlinear behavior need to be appropriately selected. In this work, a thermoplastic for a particular additive manufacturing process—the fused filament fabrication (FFF)—is investigated. Traction and compression tests are performed using two numerical tools and two variations of the Newton-Raphson method for the elasto-plastic incremental-iterative process. The stress-strain curves are compared with experimental data provided in the literature. The numerical tools used are the Finite Element Method (FEM) and the Radial Point Interpolation Method (RPIM), which is a meshless method [1]. In order to discretize the problem domain, meshless methods only require an unstructured nodal distribution. The numerical integration of the Galerkin weak form is performed using a background integration mesh and the nodal connectivity is enforced by the overlap of influence-domains defined in each integration point. In the end, a comparison study is performed between the results obtained using the meshless method and the finite element method.

D. E. S. Rodrigues (✉) · J. Belinha · R. M. Natal Jorge · L. M. J. S. Dinis
Institute of Science and Innovation in Mechanical and Industrial Engineering (INEGI), Rua Dr. Roberto Frias, Campus da FEUP, 400, 4200-465 Porto, Portugal
e-mail: drodrigues@inegi.up.pt

J. Belinha
e-mail: job@isep.ipp.pt

R. M. Natal Jorge
e-mail: rnatal@fe.up.pt

L. M. J. S. Dinis
e-mail: ldinis@fe.up.pt

J. Belinha
Department of Mechanical Engineering, School of Engineering, Polytechnic of Porto (ISEP), Rua Dr. António Bernardino de Almeida, 431, 4200-072 Porto, Portugal

D. E. S. Rodrigues · R. M. Natal Jorge · L. M. J. S. Dinis
Department of Mechanical Engineering, Faculty of Engineering of the University of Porto (FEUP), s/n, R. Dr. Roberto Frias, 4200-465 Porto, Portugal

J.A.F.O. Correia et al. (eds.), *Mechanical Fatigue of Metals*, Structural Integrity 7,
https://doi.org/10.1007/978-3-030-13980-3_51

Keywords Thermoplastic · Elasto-plasticity · Radial point interpolation method (RPIM)

51.1 Introduction

Thermoplastics, such as the ones used in additive manufacturing (AM) processes like the fused filament fabrication [2, 3] (for example, the polypropylene), present a highly non-linear behavior. Generally, their mechanical properties are different when compressed or stretched, since the long molecular chains tend to orient in different ways depending on the load conditions. For instance, when the material is compressed, their chains have a tendency to orient in a normal plane to the load direction, causing a higher strength (which can be up to 30% higher than when a tensile load is applied to the material) [4]. In the mentioned AM process, the material is loaded in different ways during the construction of the final product (including tension and compression loads). Thus, it is important to characterize the material and find proper yield criterions and elasto-plastic models to simulate their behavior. The elasto-plastic behavior of a material is characterized by an initial elastic response and, after the yield stress is obtained, a plastic behavior. The plastic behavior can be modelled using different types of models. In this work, a linear elastic-linear plastic model is implemented combined with two numerical tools: the Finite Element method (FEM) and the Radial Point Interpolation Method (RPIM), which is a meshless method. By opposition to the traditional FEM, in meshless methods the concept of mesh or element is inexistent. In these methods, the nodes can be arbitrary distributed and the field functions are approximated within an 'influence-domain' rather than an element [5]. The 'influence-domain' is an area or volume concentric with an integration point. Also in opposition to the FEM, in the meshless methods the nodal connectivity is imposed by the overlap of the 'influence-domains' [5]. Since they are not mesh reliant and because of their higher nodal connectivity, meshless methods represent solid alternatives to the FEM, especially in problems involving large deformations or fracture mechanics—which frequently are associated, in the FEM, with re-meshing procedures. Thus, the potentialities of the RPIM are explored in the isotropic elasto-plastic study performed in this work. The polypropylene, whose experimental stress-strain curves for the uniaxial tension and compression tests can be found in the literature [6], is the material analysed. Using the FEM and the RPIM combined with the Newton-Raphson non-linear algorithm, the objective of this work is to obtain numerical stress-strain curves using different numerical methodologies, establish a comparison between the experimental and numerical data, and ultimately compare the FEM and the RPIM accuracies.

51.1.1 The RPIM Formulation

Most of the meshless methods, such as the RPIM, follow a standard procedure. First, the problem domain is discretized with a nodal mesh. In the particular case of the RPIM, after the nodal discretization, a background integration mesh is constructed using the Gauss-Legendre scheme, in order to integrate the differential equations of the Galerkin weak form. In the RPIM, the nodal connectivity between each node is achieved with the overlap of the 'influence-domains', created following the nodal discretization and the definition of the background integration mesh. In 2D problems, for instance, the 'influence-domains' can be concentric areas with the points of interest. In this work fixed-size 'influence-domains' are used, containing a total of sixteen nodes per interest point. Then, within each 'influence-domain', shape functions are constructed—in its formulation, the RPIM uses a combination of a multiquadric (MQ) radial basis functions (RBF) with polynomial basis functions. From the Galerkin weak form, a meshless discrete system of equations is obtained, which can be written as: $\boldsymbol{K}_0\,\boldsymbol{u} = \boldsymbol{f}$ for a standard static problem, being $\boldsymbol{K}_0$ the initial stiffness matrix, $\boldsymbol{u}$ the displacement vector and $\boldsymbol{f}$ the load vector.

51.1.2 Elasto-plastic Constitutive Model

The elastic behavior of a material can be described using the Hooke's law. To describe the stress-strain relation after plastic deformation, a plastic constitutive tensor needs to be established. Thus, three fundamental topics need to be considered: the yield criterion, a hardening rule and a plastic flow rule. Consider a yield criterion defined in which the yield surface, $F(\boldsymbol{\sigma}, \alpha)$, depends on the magnitude of the load applied and of a hardening parameter α:

$$F(\boldsymbol{\sigma}, \alpha) = f(\boldsymbol{\sigma},\alpha) - \sigma_Y(\alpha) = 0 \tag{51.1}$$

In order to occur plastic flow, the following relation must be valid:

$$dF = \left(\frac{\partial f}{\partial \boldsymbol{\sigma}}\right)^T d\,\boldsymbol{\sigma} - \frac{\partial \sigma_Y}{\partial \alpha} d\alpha \Leftrightarrow \boldsymbol{a}^T d\,\boldsymbol{\sigma} - A d\lambda = 0 \tag{51.2}$$

where $A = \frac{1}{d\lambda}\frac{\partial \sigma_Y}{\partial \alpha} d\alpha$ defines an hardening parameter, $d\lambda$ is the plastic strain multiplier (according to the associated Prandtl-Reuss flow rule) and $\boldsymbol{a}$ is the flux vector, normal to the considered yield surface, defined for a three-dimensional stress state as:

$$\boldsymbol{a}^T = \left(\frac{\partial f}{\partial \boldsymbol{\sigma}}\right)^T = \left\{\frac{\partial F}{\partial \sigma_{xx}}, \frac{\partial F}{\partial \sigma_{yy}}, \frac{\partial F}{\partial \sigma_{zz}}, \frac{\partial F}{\partial \tau_{xy}}, \frac{\partial F}{\partial \tau_{xz}}, \frac{\partial F}{\partial \tau_{yz}}\right\} \tag{51.3}$$

Decomposing the strain increment into the sum of an infinitesimal elastic and plastic strain increments, $d\boldsymbol{\varepsilon}^e$ and $d\boldsymbol{\varepsilon}^p$, respectively: $d\boldsymbol{\varepsilon} = d\boldsymbol{\varepsilon}^e + d\boldsymbol{\varepsilon}^p$, Eq. (51.4) is established:

$$d\boldsymbol{\varepsilon} = \boldsymbol{D}^{-1} : d\boldsymbol{\sigma} + d\lambda \frac{\partial f(\boldsymbol{\sigma})}{\partial \boldsymbol{\sigma}} \Leftrightarrow d\boldsymbol{\sigma} = \boldsymbol{D}_{ep} d\boldsymbol{\varepsilon} \quad , \quad with \quad \boldsymbol{D}_{ep} = \boldsymbol{D} - (\boldsymbol{d}_D \boldsymbol{d}_D^T)/(A + \boldsymbol{d}_D^T \boldsymbol{a}) \tag{51.4}$$

being $\boldsymbol{D}$ the elastic constitutive matrix, which linearly relates the six components of the stress with the six components of strain and $\boldsymbol{D}_{ep}$ is the elasto-plastic constitutive matrix and $d_D^T = a^T \boldsymbol{D}$. This work uses a "linear elastic-linear plastic" hardening model, and the von Mises yield criterion ($F(\boldsymbol{\sigma}, \alpha) = \sqrt{3J_2} - \sigma_Y(\alpha) = 0$, being J_2 the second invariant of that deviator stress tensor). In those conditions, $A = E_T/(1 - E_T/E)$, where E and E_T represent the elastic and tangent modulus, respectively.

In this work, the formulation previously presented is implemented through an incremental-iterative form, using the Newton-Raphson method, in order to solve the non-linear equation system. Two variations of the mentioned non-linear solution method are used: the initial stiffness (KT0) and initial stiffness in each increment (KT1). The first one calculates the stiffness matrix only once: in the first iteration of the first load increment. The second one calculates a new stiffness matrix each time the algorithm enters the next load increment, using the elasto-plastic constitutive matrix—Eq. (51.4). For both Newton-Raphson method variants (KT1 and KT0), stress is forced to return to the yield surface using the "backward-Euler" procedure [5].

51.2 Numerical Results

In this work, the material under study is a development grade polypropylene (PP) homopolymer, manufactured and delivered by Borealis Polyolefine GmbH (Linz, A) [6]. In this section, simulations of a specimen of this material (injection moulded, with geometry according to the norm ISO 3167, Type B) being subjected to a uniaxial tension test are performed. The same material is also analyzed using a uniaxial compression test configuration, which consists in compressing a cylindrical specimen between two plates. The considered diameter of the specimen was 8 mm and the length was 12 mm, according to Jerabek et al. [7]. In the literature [6], experimental stress-strain curves were found. Based on those experimental stress-strain curves, linear elastic-linear plastic models are constructed for the two standard tests—Fig. 51.1. For that to be possible, the Young modulus, the tangent modulus and the initial yield stress have to be estimated for the uniaxial tensile test ($E = 1332.645$ MPa, $\sigma_{Y0} = 19.730$ MPa and $E_T = 194.693$ MPa) and for the compression test ($E = 886.539$ MPa, $\sigma_{Y0} = 50.079$ MPa and $E_T = 40.877$ MPa).

The experimental stress-strain curves of Fig. 51.1 highlight the importance of characterizing polymeric materials in different stress states since the stress-strain

curve of the uniaxial compression test surpasses that of tension and significantly larger stress levels are observed [6].

The specimen of the uniaxial tensile test is modelled as a 2D solid using a plane stress state and discretized in a nodal mesh (for the RPIM analysis) and a finite element mesh, each one having a total number of 2397 nodes. For the compression test, the specimen is modelled as a 3D solid and discretized using 2145 nodes. The estimated mechanical properties of the PP are introduced in the FEMAS software [8], the computational tool used to perform the analysis, which runs in MATLAB® environment. For the incremental-iterative process, ten load increments are considered. Figure 51.2 contains stress-strain curves obtained numerically when the RPIM and the FEM are combined with the KT0 and KT1 algorithms.

As can be observed in the mentioned Fig. 51.2, almost all the numerical curves follow the same paths of the correspondent experimental one. The only exception seems to be the KT0 solutions for the uniaxial tensile test, in which the curves diverge from the experimental one. Despite the similarly of the FEM and RPIM solutions, it can be visualized that the RPIM curves are always slightly closer to the experimental

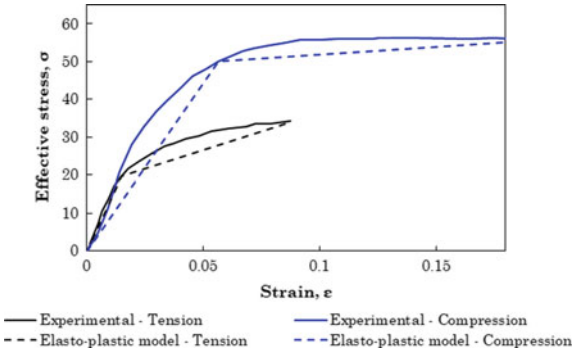

Fig. 51.1 Experimental stress-strain curves for the uniaxial tension and compression tests, and the adjusted elasto-plastic models

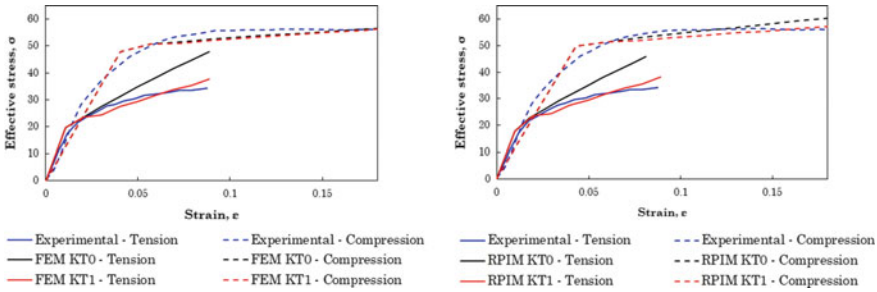

Fig. 51.2 Stress-strain curves of tensile and compression tests performed on specimens, using different numerical methods and non-linear solution algorithms

curves than the FEM curves. This fact proves the accuracy of the RPIM, since it can obtain more accurate solutions than the FEM, using the same total number of nodes discretizing the problem domain in both methodologies.

51.3 Conclusions

The algorithms developed for the elasto-plastic analysis using two numerical methods and two non-linear solution methods were successfully validated, based on the experimental data. Thus, the Radial Point Interpolation Method (RPIM) revealed to be a robust and accurate numerical tool, constituting as a strong alternative to the traditional FEM, since it can obtain solutions slightly more accurate than the FEM, using the same number of nodes discretizing the problem domain, as it was shown in Sect. 51.2. For the uniaxial tension and compression tests, the linear elastic-linear plastic model seems to be sufficient to capture the behavior of the material, since the solutions obtained are closer to the experimental stress-strain curves. Regarding the mechanical behavior of the material in study, it can be concluded that it has a wide range, depending on the material loading conditions, which emphasizes the importance of using adequate constraints on the specimen [6].

Acknowledgements The authors truly acknowledge the funding provided by Ministério da Ciência, Tecnologia e Ensino Superior—Fundação para a Ciência e a Tecnologia (Portugal), under grants: SFRH/BD/121019/2016, and by project funding MIT-EXPL/ISF/0084/2017. Additionally, the authors gratefully acknowledge the funding of Project NORTE-01-0145-FEDER-000022—SciTech—Science and Technology for Competitive and Sustainable Industries, co-financed by Programa Operacional Regional do Norte (NORTE2020), through Fundo Europeu de Desenvolvimento Regional (FEDER).

References

1. Belinha J (2014) Meshless methods in biomechanics: bone tissue remodelling analysis. Springer International Publishing, Porto, Portugal
2. Salinas R (2014) 3D printing with reprap cookbook
3. De Ciurana J, Serenó L, Vallès È (2013) Selecting process parameters in RepRap additive manufacturing system for PLA scaffolds manufacture. Procedia CIRP 5:152–157
4. Appelsved P (2012) Investigation of mechanical properties of thermoplastics with implementations of LS-DYNA material models. Degree Proj Solid Mech 48
5. De Borst R, Crisfield MA, Remmers JJC, Verhoosel CV (2012) Non-linear finite element analysis of solids and structures. Wiley Ser Comput Mech
6. Jerabek M, Tscharnuter D, Major Z, Ravi-Chandar K, Lang R (2010) Multiaxial yield behaviour of polypropylene. EPJ Web Conf 6:03005
7. Jerabek M, Major Z, Lang RW (2010) Uniaxial compression testing of polymeric materials. Polym Test 29(3):302–309
8. Jorge Belinha—FEMAS, finite element and meshless analysis software http://jbelinha.webs.com/femas. Accessed 18 May 2018

Chapter 52
Fracture Analysis of Semi-circular Bend (SCB) Specimen: A Numerical Study

Farid Mehri Sofiani, Behzad V. Farahani and J. Belinha

Abstract A variety of numerical analysis has been carried out by Finite Element Method (FEM), and Extended FEM (XFEM) on Semi-circular Bend (SCB) specimens to evaluate its material behavior, in particular fracture characterization. This work concentrates on calculating stress intensity factor (SIF) assuming an elastic brittle behavior. In order to obtain the required variable fields, FEM formulation was extended to the linear elastic fracture mechanics (LEFM) for the plane stress status. The problem is solved using standard FEM formulation in ABAQUS© to obtain the numerical solution of SIFs, the results are compared to the previous work available in the literature. An acceptable agreement was accomplished leading to verify the proposed computational methodology.

Keywords Fracture characterization · FEM · SIF

52.1 Introduction

The ability to tolerate a substantial amount of damage is a demand for contemporary structures, hence it has become increasingly important to enhance methodologies to anticipate failure in fatigue damaged components. Damage tolerance analyses can be carried out within linear elastic fracture mechanics (LEFM) concepts where the stress intensity factor (SIF) plays a substantial role. The fracture mechanics theorem in conjunction with crack growth laws, i.e. Paris' law, is normally employed to

F. Mehri Sofiani (✉) · B. V. Farahani
FEUP, Faculty of Engineering, University of Porto, Dr. Roberto Frias Street, 4200-465 Porto, Portugal
e-mail: up201600432@fe.up.pt

B. V. Farahani · J. Belinha
INEGI, Institute of Science and Innovation in Mechanical and Industrial Engineering, Dr. Roberto Frias Street, 400, 4200-465 Porto, Portugal

J. Belinha
Mechanical Engineering Department, School of Engineering, ISEP, Polytechnic of Porto, Rua Dr. António Bernardino de Almeida, 431, 4249-015 Porto, Portugal

J.A.F.O. Correia et al. (eds.), *Mechanical Fatigue of Metals*, Structural Integrity 7,
https://doi.org/10.1007/978-3-030-13980-3_52

analyze and predict crack growth and fracture behavior of structural components. To study crack growth and evaluate the remaining life of a certain structural component, rigorous numerical analyses have to be performed to evaluate SIFs [1, 2].

52.1.1 SIF Determination Using Numerical Approach

Crack propagation is a significant concept in fracture, fatigue and damage mechanics. Hence, numerical simulations are required to anticipate the failure phenomenon. The computational approaches are applicable to perform the numerical simulation so, the fracture response and the reliability of cracked constructions are determined [3–6]. In the early age of the fracture mechanics, two numerical techniques have been applied to the solution of cracked problems consisting of FEM with remeshing and Boundary Element Methods (BEM). However, these methods have some substantial disadvantages dealing with the cracked structures. For instance, in FEM, it is cumbersome to automatically remesh finite elements. In the same way, remeshing on a large part associated with the finite elements are restricted in BEM analyses [7].

The FEM formulation is mostly applicable for elastic plate problems with the restriction that it is not suitable to handle stress singularities in its conventional formulation. However, meanwhile, special elements were deployed to tackle the singularities caused by cracks [8]. The SIF calculation for intricate crack configurations in finite plates generally presents significant difficulties. Thus, Byskov [8] proposed an comprehensive numerical FEM to resolve such mentioned problems by focusing on specific cracked elements, in which the stiffness matrix is associated with the crack elements. In 1976, Hillerborg et al. [9] focused on the crack formation analysis in concrete by fracture mechanics theory combined with FEM. Moreover, an new resolving method has been proposed by Belytschko and Black [10] to analyse the 2D cracked problems within FEM, in which a minimal remeshing was required.

Furthermore, Moës and Belytschko [11] simulated arbitrary cohesive crack propagations for three-point-bending concrete beams relying on the extended finite element method (XFEM). They found out that the XFEM associated with the J-integral domain produced more accurate results compared to the classical FEM. Moreover, since the crack might be located arbitrary respecting the mesh in XFEM, no remeshing is required as the crack propagates. Dolbow et al. [12] employed the XFEM equations to numerically model the cracked problem domains for those which are not dependent on the finite element mesh. They proposed an iterative procedure to compute the crack growth stages in the presence of the frictional contact on the interface formed by crack faces.

In the literature, there are several proper work focused on the fracture characterization of the fractured structural components. As an illustration, a coupled numerical method on fracture mechanics was presented by Farahani et al. [1, 2, 13, 14]. They employed the FEM and meshless formulations to study the material behavior in the vicinity of the crack and in areas far away from the crack. Therefore, the SIF was evaluated for the mode I loading states for the 2D cracked models.

52.2 Solid Mechanics, Basis and Formulation

The 2D plane stress deformation theory is assumed here. Considering FEM theory and in accordance with Hooke's law with regard to $\boldsymbol{C}$ as the fourth order material constitutive tensor in plane stress state, it is conceivable to formulate the strain and stress fields as presented in Eqs. (52.1) and (52.2), respectively [15]. The Poisson's ratio and Young's modulus are defined as E and ν, respectively. Therefore, the relation of the stress vector could be written as: $\boldsymbol{\sigma} = \boldsymbol{C}\boldsymbol{\varepsilon}$.

$$\boldsymbol{\varepsilon} = \boldsymbol{L}\boldsymbol{u} = \begin{bmatrix} \frac{\partial}{\partial x} & 0 \\ 0 & \frac{\partial}{\partial y} \\ \frac{\partial}{\partial y} & \frac{\partial}{\partial x} \end{bmatrix} \begin{Bmatrix} u_x(x, y) \\ u_y(x, y) \end{Bmatrix} = \begin{Bmatrix} \frac{\partial u_x}{\partial x} \\ \frac{\partial u_y}{\partial y} \\ \frac{\partial u_x}{\partial y} + \frac{\partial u_y}{\partial x} \end{Bmatrix} = \begin{Bmatrix} \varepsilon_{xx} \\ \varepsilon_{yy} \\ \gamma_{xy} \end{Bmatrix} \tag{52.1}$$

$$\boldsymbol{C} = \frac{E}{(1+\nu)(1-\nu)} \begin{bmatrix} 1 & \nu & 0 \\ \nu & 1 & 0 \\ 0 & 0 & \frac{1-\nu}{2} \end{bmatrix} \tag{52.2}$$

52.3 Analysis and Results

A semi-circular bend (SCB) specimen was considered here as seen in Fig. 52.1. It aimed at SIF evaluation for different crack sizes. The material properties and the geometrical characteristics followed the values reported on Table 52.1. Some

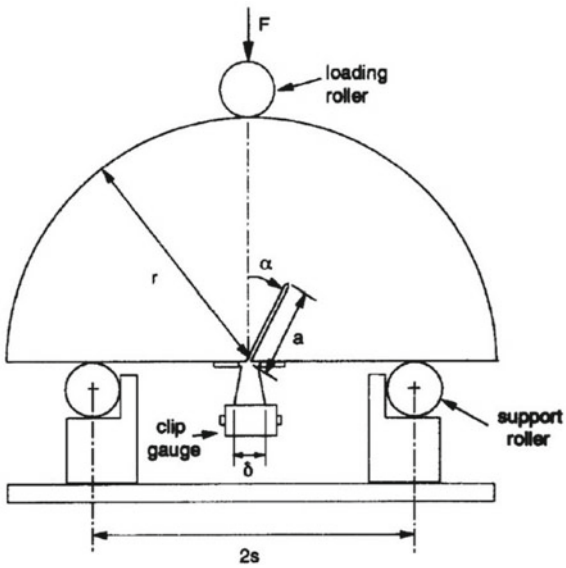

Fig. 52.1 Experimental set-up for a semi-circular specimen under three-point bending

Table 52.1 Geometrical characteristics and material properties

Young's modulus, E	75,500 (MPa)
Poisson's ratio, ν	0.3
Radius of the disk, r	25 (mm)
Thickness of the disk, B	1 (mm)
Crack length, a	7.5, 10, 12.5, 15, 17.5, 20 (mm)
Span, s	0.5, 0.6, 0.7 (mm)
Concentrated load on disk, F	1 (kN)

advantages of the SCB specimens are convenient sample preparation (directly from rock cores), simple geometry and loading configuration, the straight forward testing procedure and application of compressive load, which is more suitable for rocks, rather than tensile load. Furthermore, SCB is a suitable specimen to measure the rock fracture toughness at elevated temperatures, high strain rates, and high confining pressure.

52.3.1 The First FEM Study

As the first numerical analysis, the model was considered with different mesh types where CPS3 triangular elements were considered on the cracked region and the rest of the model was meshed considering CPS4R quad elements. It was intended to evaluate result for s/R = 0.5, 0.6, and 0.7, focused on a/R = 0.3 to a/R = 0.6. Due to the symmetry, half of the disk was analyzed under 3-point bending condition assuming crack lengths of 7.5, 10, 12.5, 15, 17.5 and 20 for 3 s/R sizes (0.5, 0.6, 0.7). The FEM analysis has been simulated in a commercial software ABAQUS©. The obtained results of mode I SIF related to the first analysis are reported in Table 52.2.

52.3.2 The Second FEM Study

As the second study on this topic, the previously defined mesh of the model has been refined to improve the results. The new mesh type was considered as CPS4R quad element for any region including the cracked area. As a matter of fact, a/R = 0.7 and 0.8, are not practical, so in this study, they have been neglected. On the other hand, s/R = 0.7 is not so much used by scientists, so it has been removed from the study. The obtained solutions of SIF are shown in Table 52.2.

It must be noted that all obtained results of SIF have been compared to the previous related studies available in the literature as Table 52.2 demonstrates.

Table 52.2 Mode I SIF calculated from the FEM formulation compared to the literature

a/R	s/R	Presented results (study 1)	Presented results (study 2)	Ayatollahi et al. [16]	Lim et al. [17]
0.3	0.5	2.105	2.579	2.644	2.725
0.3	0.6	3.083	3.298	3.010	3.264
0.3	0.7	3.909	3.991	4.020	4.102
0.4	0.5	3.216	2.925	2.912	2.842
0.4	0.6	3.768	3.735	3.812	3.814
0.4	0.7	4.379	4.415	4.731	4.314
0.5	0.5	4.143	3.612	3.539	3.913
0.5	0.6	4.799	4.566	4.493	4.696
0.5	0.7	5.121	5.166	5.142	5.098
0.6	0.5	5.393	4.835	4.185	4.398
0.6	0.6	5.836	6.031	5.214	5.078
0.6	0.7	6.435	6.654	6.960	7.002
0.7	0.5	6.228	–	5.089	6.102
0.7	0.6	6.762	–	7.128	7.010
0.7	0.7	7.272	–	8.010	8.200
0.8	0.5	12.004	–	12.901	13.464
0.8	0.6	12.579	–	13.201	12.426
0.8	0.7	14.433	–	16.020	17.010

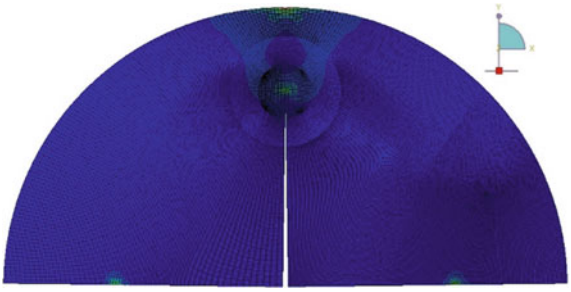

Fig. 52.2 Final Contour for a/R= 0.6, s/R= 0.5, showing the distribution of von Mises stress

Moreover, a closer view to the obtained results, it is possible to visual the profile of von Mises stress variation on the fractured specimen when a/R = 0.6, s/R = 0.5, as Fig. 52.2 depicts. In addition to that, Fig. 52.3 demonstrates the distribution of the first principal stress distribution at the crack tip region if a/R = 0.6, s/R = 0.6. The obtained profile is smooth and stable.

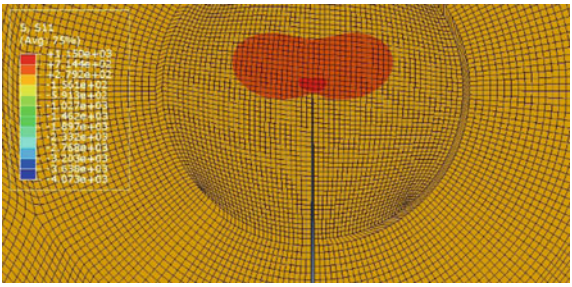

Fig. 52.3 Principal stress distribution in xx axis at the crack tip region, a/R= 0.6, s/R= 0.6

52.4 Conclusion

The present study has focused on calculating stress intensity factor determination for a SCB specimen in mode I condition. A 2D model was analysed relying on a numerical method, FEM, to validate the results in literature. Lim et al. [17] and Ayatollahi et al. [16] presented some results for different crack lengths and spans. The boundary conditions applied to the geometry, were similar to those used by the previously mentioned authors; a concentrated force (1 kN) on top of the disk, and fixed points on bearings of the disk in Y direction, only.

The numerical analyses were implemented for crack length of 7.5, 10, 12.5, 15, 17.5 and 20 mm in a FEM code software, ABAQUS©. The simulation was accomplished for two different meshes properties. Indeed, the maximum energy release rate was the criteria to calculate the stress intensity factor.

As a final remark, in first study, the crack tip region was meshed by 3-node elements and in the 2nd one, the crack tip region was meshed by 4-node elements. By increasing the density of mesh, the results were improved and finally good agreement with the results, presented by others, was obtained.

References

1. Farahani BV, Tavares PJ, Moreira PMGP, Belinha J (2017) Stress intensity factor calculation through thermoelastic stress analysis, finite element and RPIM meshless method. Eng Fract Mech 183:66–78
2. Farahani BV, Tavares PJ, Belinha J, Moreira P (2018) Compact tension fracture specimen: Experimental and computational implementations on stress intensity factor. J Strain Anal (In Press) 1–18
3. Farahani BV, Belinha J, Pires FMA, Ferreira AJM (2018) A radial point interpolation meshless method extended with an elastic rate-independent continuum damage model for concrete materials. Mech Adv Mater Struct 25(10):855–867
4. Farahani BV, Belinha J, Amaral R, Tavares PJ, Moreira P (2018) A digital image correlation analysis on a sheet AA6061-T6 bi-failure specimen to predict static failure. Eng Fail Anal 90:179–196

5. Farahani BV, Belinha J, Amaral R, Tavares PJ, Moreira PMPG (2018) Extending radial point interpolating meshless methods to the elasto-plastic analysis of aluminium alloys. Eng Anal Bound Elem
6. Farahani BV, Belinha J, Andrade Pires FM, Ferreira AJM, Moreira PMGP (2016) Extending a radial point interpolation meshless method to non-local constitutive damage models. Theor Appl Fract Mech 85(Part (A)):84–98
7. Belytschko T, Gu L, Lu YY (1994) Fracture and crack growth by element free Galerkin methods. Model Simul Mater Sci Eng 2(3A):519–534
8. Byskov E (1970) The calculation of stress intensity factors using the finite element method with cracked elements. Int J Fract Mech 6(2):159–167
9. Hillerborg A, Modéer M, Petersson P-E (1976) Analysis of crack formation and crack growth in concrete by means of fracture mechanics and finite elements. Cem Concr Res 6(6):773–781
10. Belytschko T, Black T (1999) Elastic crack growth in finite elements with minimal remeshing. Int J Numer Methods Eng 45(5):601–620
11. Moës N, Belytschko T (2002) Extended finite element method for cohesive crack growth. Eng Fract Mech 69(7):813–833
12. Dolbow J, Moës N, Belytschko T (2001) An extended finite element method for modeling crack growth with frictional contact. Comput Methods Appl Mech Eng 190(51):6825–6846
13. Farahani BV, Tavares PJ, Belinha J, Moreira PMGP (2017) A fracture mechanics study of a compact tension specimen: digital image correlation, finite element and meshless methods. Procedia Struct. Integr 5:920–927
14. Farahani BV, Tavares PJ, Moreira PMGP (2016) SIF determination with thermoelastic stress analysis. Proc Struct Integr 2:2148–2155
15. Belinha J (2014) Meshless methods in biomechanics: bone tissue remodelling analysis, vol 16. Springer, Netherlands
16. Ayatollahi MR, Mahdavi E, Alborzi MJ, Obara Y (2016) Stress intensity factors of semi-circular bend specimens with straight-through and chevron notches. Rock Mech Rock Eng 49(4):1161–1172
17. Lim IL, Johnston IW, Choi SK (1993) Stress intensity factors for semi-circular specimens under three-point bending. Eng Fract Mech 44(3):363–382